METALS, SUPERCONDUCTORS

Internal friction and change in Young's modulus in the alloy Mg–Ni–Y due to a transition from an amorphous to a nanocrystalline state

N. P. Kobelev and I. G. Brodova

Institute of Solid-State Physics, Russian Academy of Sciences 142432 Chernogolovka, Moscow District, Russia

Ya. M. Soĭfer*) and A. N. Manukhin

Institute of Metal Physics, Russian Academy of Sciences 620219 Ekaterinburg, Russia
(Submitted September 21, 1998)
Fiz. Tverd. Tela (St. Petersburg) **41**, 561–566 (April 1999)

The effect on the internal friction and Young's modulus of the evolution of the structure of the amorphous alloy $Mg_{84}Ni_{12.5}Y_{3.5}$ (relaxation of internal stresses, devitrification, nucleation and decay of nanocrystalline phases) was investigated as it was heated. The measurements were performed on ribbon samples by flexural oscillations. Irreversible peaks of the internal friction and anomalies in the behavior of Young's modulus as a function of temperature were observed. The position of the anomalies correlates with the characteristic temperatures of restructurings observed by differential thermal and x-ray diffraction. Possible internal-friction mechanisms associated with various types of structural relaxation and nanocrystallization processes in the alloy are discussed.
[S1063-7834(99)00104-5]

Interest in magnesium alloys by rapid quenching is mainly due to the fact that, while the strength, plasticity, and corrosion resistance of these alloys obtained by conventional metallurgy are quite low, with rapid quenching these properties can be improved substantially.[1–3] In the process, new materials are actually obtained by formation of nonequilibrium structures consisting of amorphous, quasicrystalline, or nanocrystalline phases. The actual expectations are associated with obtaining mixed structures of these nonequilibrium phases and are based on their unique mechanical and corrosion properties. It is well known that internal friction is a very structure-sensitive method and can be used to study structural relaxation, the transition to a glassy state, and the crystallization of amorphous alloys. In the present work, the behavior of the internal friction and Young's modulus of an amorphous Mg–Ni–Y alloy, which are associated with structural relaxation and crystallization of this alloy, is investigated.

1. EXPERIMENTAL PROCEDURE

The alloy $Mg_{84}Ni_{12.5}Y_{3.5}$ in the form of a 0.025 mm thick and 3–5 mm wide ribbon was investigated. The alloy was obtained by rapid quenching with a cooling rate 5×10^6 K/s from temperature 880 K on a copper wheel in vacuum.

All measurements of the elastic and dissipative properties of the samples were performed by the flexural oscillations (vibrating-reed) method[4] at frequencies of the order of 250 Hz in the temperature range 300–650 K in a 10^{-3} torr vacuum. The dimensions of the samples cut from the amorphous ribbon obtained were $10\times1.5\times0.025$ mm. The samples were secured in a measuring head. The required electrode–sample gap was set using a regulating screw. To excite flexural oscillations at the resonance frequency of the sample, a voltage from a low-frequency generator was applied to a capacitor formed by the sample and the electrode. The amplitude of the oscillations was regulated by the amplitude of the applied voltage. Tuning to resonance was automatic. A high-frequency generator, whose feedback circuit contained an LC loop formed by the sample–electrode capacitor and a calibrated high-Q inductance coil, was used to record the excited oscillations. The carrier frequency was modulated by low-frequency oscillations of the sample. The frequency-modulated signal was applied to a meter used for measuring the frequency deviation, after which the parameters of the detected signal were measured — the period and amplitude of the oscillations, the decay of the oscillations with time, or the parameters of the resonance curve (which made it possible to estimate the internal friction $Q^{-1}=\delta/\pi$). Young's modulus of the sample was determined from the expression

$$E=Kl^4\rho f/h^2,$$

where K is a numerical factor, l is the length of the sample, h is the thickness, ρ is the density, and f is the resonance frequency.

The structure of the phases was determined by an x-ray diffraction method using a PW 1050/70 Philips diffracto-

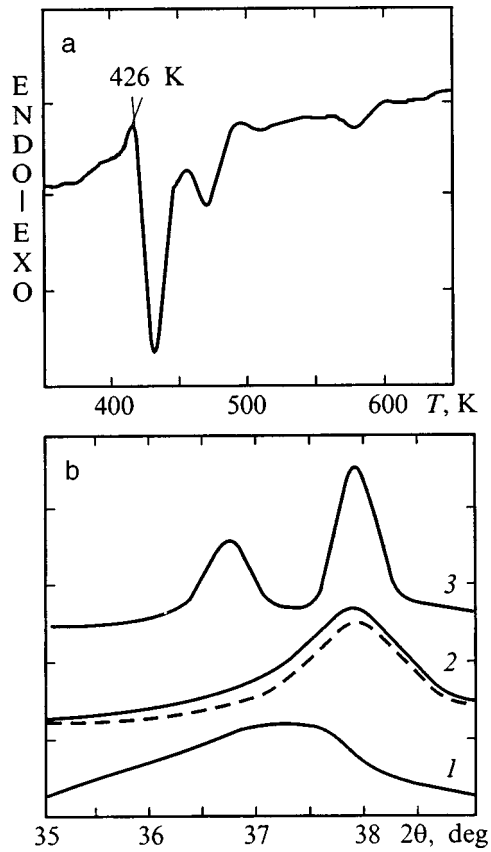

FIG. 1. a — DTA curve of the amorphous alloy $Mg_{84}Ni_{12.5}Y_{3.5}$ on heating at the rate 4 K/min; b — intensity of x-ray scattering near the first maximum in the alloy $Mg_{84}Ni_{12.5}Y_{3.5}$ in the amorphous state (1) and after annealing at 438 K (2) and 478 K (3). The dashed curve corresponds to scattering by the nanocrystalline phase $Mg_xNi_yY_z$. The peak at $2\theta = 36.2°$ corresponds to the (101) line of α Mg and the peak at $2\theta = 37.8°$ corresponds to the $Mg_xNi_yY_z$ phase.

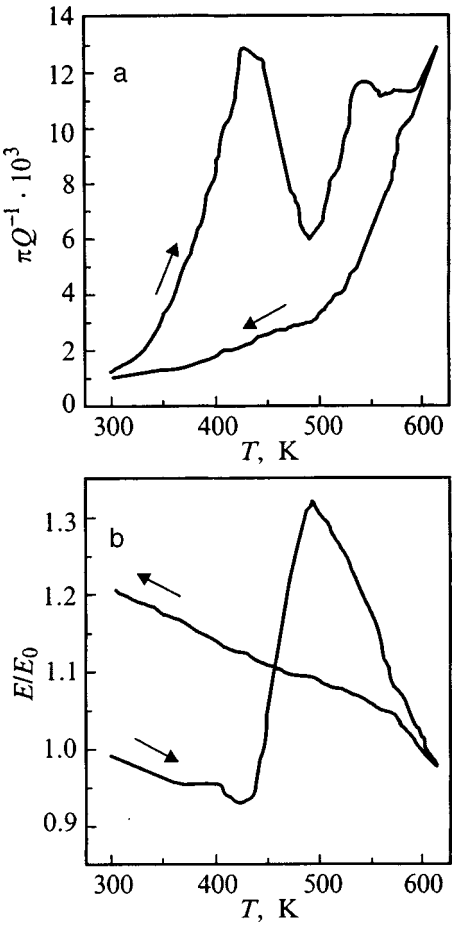

FIG. 2. Temperature dependences of the internal friction Q^{-1} (a) and relative change of the Young's modulus E (b) on heating and cooling at the rate 2 K/min in the temperature 300–615 K of the amorphous alloy $Mg_{84}Ni_{12.5}Y_{3.5}$.

meter with Cu $K\alpha$ radiation at temperature 300 K after 5-min anneals of the samples at prescribed temperatures.

Differential thermal analysis (DTA) for studying the crystallization of the $Mg_{84}Ni_{12.5}Y_{3.5}$ samples was conducted in an argon atmosphere at a rate of 4 K/min.

Differential scanning calorimetry (DSC) was used for the same purposes.

2. RESULTS AND DISCUSSION

The evolution of the structure of the alloy $Mg_{84}Ni_{12.5}Y_{3.5}$ heated from room temperature to 650 K is illustrated in Fig. 1, where data from the investigations of crystallization of the samples from the amorphous state by the DTA method and the results of x-ray diffraction by the same samples at various anneal temperatures are displayed. As one can see from Fig. 1a, which displays the DTA measurements with constant heating at a rate of 4 K/min, at least two large (at 430 and 474 K) and one small (at 580 K) exothermal peaks are observed in the temperature range up to 625 K. According to the analysis of the x-ray diffraction patterns (Fig. 1b), the observed exotherms correspond to different stages of crystallization of the amorphous alloy $Mg_{84}Ni_{12.5}Y_{3.5}$. The first stage (430 K) corresponds to the appearance of a metastable crystalline phase $Mg_xNi_yY_z$ (the exact structure was not determined) with average grain size of approximately 6 nm. It should be noted that the first exotherm (at $T_x \simeq 430$ K) is preceded by an indistinct endotherm, which can be attributed to devitrification characterized by a glass-formation temperature T_g. This conclusion is also confirmed by the DSC measurements, where this endotherm is more clearly manifested, but even in this case the difference between T_g and T_x is negligible and does not exceed 8–10 K. The second stage (475 K) corresponds to precipitation of nanocrystalline Mg; here, a grain of the metastable phase $Mg_xNi_yY_z$ grows approximately to 14 nm. At 580–600 K the metastable phase decomposes into stable phases.

The characteristic form of the temperature dependences of the internal friction Q^{-1} and the relative change in the Young's modulus E/E_0 (E_0 is Young's modulus of the initial sample at room temperature) during a single heating–cooling sample in the temperature range from 300 to 615 K is displayed in Fig. 2. Two wide internal-friction peaks (which we call P_1 and P_2) are observed at temperatures 425 and 530 K during the heating cycle. On cooling, the peaks vanish (i.e. they are of an irreversible character), the temperature dependence of the internal friction becomes monotonic, and the main decrease of damping occurs in the region 600–500 K. The temperature variation of Young's modulus

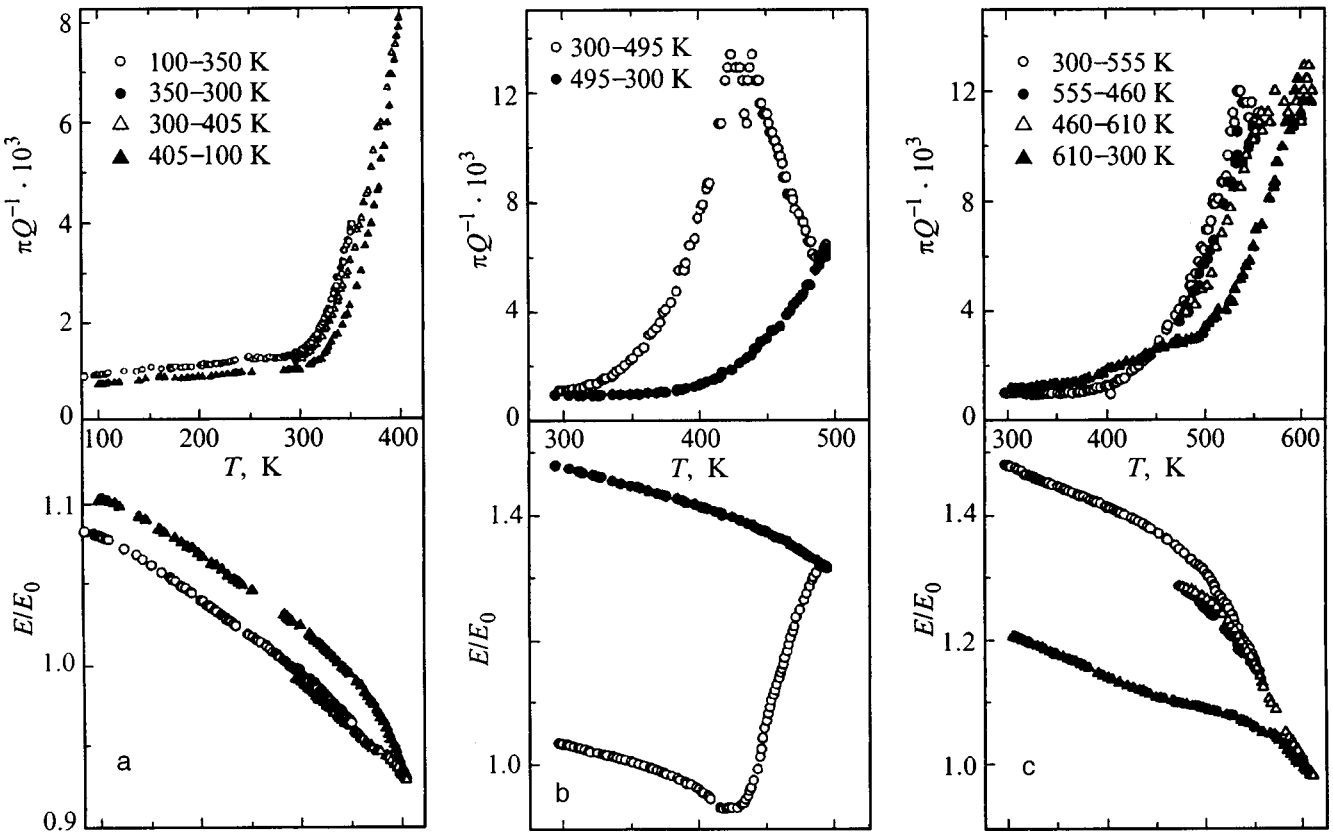

FIG. 3. Temperature dependences of the internal friction Q^{-1} and relative change of the modulus E/E_0 in a sample of the amorphous alloy $Mg_{84}Ni_{12.5}Y_{3.5}$ with thermal cycling at the rate 2 K/min and a systematic increase of the maximum temperature in a cycle. The open symbols correspond to heating cycles and the filled symbols correspond to cooling cycles.

is quite complicated. In the heating cycle up to temperatures of approximately 350–360 K the modulus decreases virtually monotonically with increasing temperature. A small feature (''shelf'' in the temperature dependence) is observed in the region 360–390 K, after which the modulus once again decreases with temperature, but above 415 and up to 490 K the modulus increases very sharply (by almost a factor of 1.5), after which it once again decreases as heating continues up to 616 K. No anomalies are observed in the behavior of Young's modulus on cooling; it increases monotonically with decreasing temperature, but the room-temperature value is approximately 20% greater than the initial value measured in the as-quenched state.

Comparing the data obtained with the results of the investigation of the change in structure of these same samples as a function of temperature shows that the anomalies in the internal friction and Young's modulus are observed approximately at the same temperatures as the exothermal peaks, i.e. at temperatures corresponding to different stages of crystallization from the amorphous state of the alloy $Mg_{84}Ni_{12.5}Y_{3.5}$. Therefore the elastic and inelastic phenomena in the experimental temperature range are determined by the same structural changes that occur in the sample during heating.

To specify the character of the observed changes in Q^{-1} and E/E_0 and to establish the relationship between them and the structure of the alloy, measurements were performed of the temperature dependences of the internal friction and Young's modulus in the course of several heating–cooling cycles on the sample with the maximum temperature in a cycle increasing. The results of such an experiment are presented in Fig. 3. We shall examine in greater detail the data presented in this figure. For convenience, we shall discuss each temperature cycle separately.

1) 100–400 K. In this temperature interval (up to 400 K) the x-ray diffraction data do not show any traces of crystallization. However, the changes in both the internal friction and Young's modulus at these temperatures are already quite noticeable. Up to temperatures of about 130 K the changes in the behavior of the temperature dependences of the internal friction and Young's modulus are reversible, but starting approximately at this temperature and up to 400 K, heating leads to an appreciable (about 3.5%) irreversible increase of Young's modulus and a corresponding irreversible decrease of the internal friction (Fig. 3a). Since the alloy does not crystallize up to 400 K, it can be inferred that the observed changes in Q^{-1} and E/E_0 are due to the structural rearrangement in the amorphous structure of the sample. Structural relaxation of this kind in amorphous materials has been observed in a variety of alloys[5–8] and explained on the basis of ''topological and chemical ordering'' models.[9] Topological ordering in the amorphous material is due primarily to a decrease of the ''free volume'' on annealing, which is conducted at comparatively low temperatures (below the glass-formation temperature T_g and the crystallization temperature T_x) and leads to irreversible changes of various physical

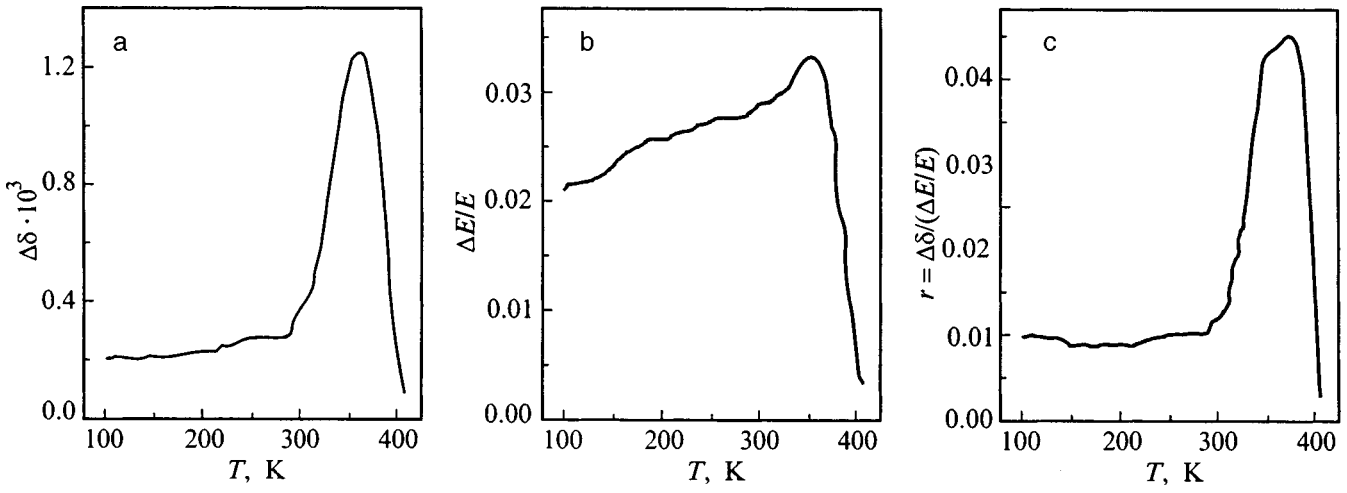

FIG. 4. Temperature dependences of the irreversible part of the damping decrement $\Delta\delta = \pi(Q_h^{-1} - Q_c^{-1})$ (a) and Young's modulus $\Delta E/E = (E_c - E_h)/E_h$ (b) in the amorphous alloy $Mg_{84}Ni_{12.5}Y_{3.5}$ as a result of heating the alloy up to 450 K and the temperature dependence of their ratio $r = \Delta\delta/(\Delta E/E)$ (c). (The indices h and c correspond to the values of the internal friction and Young's modulus in the course of heating and cooling cycles, respectively).

properties, including a decrease of the internal stresses in the material and a quite appreciable increase of the elastic moduli and decrease of the internal friction. Chemical ordering is ordinarily observed in multicomponent structures and is attributed to an irreversible change in the positions of various atoms with respect to one another.

Since the internal friction is due to inelastic phenomena in the sample, a decrease in the internal friction during ordering is caused by either the liquidation of sources of such anelasticity or a decrease in their efficiency. For low-frequency internal friction (which is our concern) the sources can be structural defects whose mobility determines the anelastic behavior of the material. These can be structural defects of different kinds, such as topological dislocations, boundaries of clusters of amorphous material, and so on. A temperature increase results in, on the one hand, an irreversible increase of the mobility of structural defects and correspondingly irreversible changes in the internal friction and elastic moduli and, on the other, to a restructuring-induced decrease in the number of such defects or a transition of the defects to a more stable state in which they become less mobile, which decreases the anelasticity and internal friction determined by E/E_0 and Q^{-1}.

It is evident that a sharp temperature dependence of the internal friction is first observed at room temperature, and the reversible and irreversible components of the internal friction are comparable in magnitude. The temperature-dependent part of the reversible component of the internal friction, which remains after annealing at 400 K, can be described quite well by an expression of the type $\Delta Q^{-1}(T) \sim \exp(E/T)$ with activation energy ~ 0.4 eV. This energy is close in order of magnitude to the migration energy of the atoms, as is confirmed by the assumption that the processes leading to thermal-activation ordering in a system of point defects influences the internal friction.

The irreversible contributions to the internal friction and Young's modulus are presented in Fig. 4. As one can see, the main irreversible changes occur in the temperature range 350–380 K, where a peak of the internal friction and an increase of Young's modulus with temperature are observed. This behavior could be due to the fact that even though crystallization is not observed at these temperatures, structural rearrangement of the amorphous material, consisting of a decrease of the density of the sources of anelasticity, nevertheless takes place. On the basis of the available experimental data it is impossible to draw any unequivocal conclusions concerning the specific physical models of such sources. Nonetheless, it is evident even now that the mechanisms of internal friction which are due to these sources can differ substantially in different temperature ranges. Thus, it is evident from Fig. 4 that below 300 K (in contrast to the region 300–400 K) the irreversible contribution to the damping is virtually temperature-independent, and the value of its ratio to the change in modulus $r = \Delta\delta(T)/(\Delta E/E(T))$ is approximately 0.01 and is virtually independent of temperature in the range 100–300 K. This behavior is usually characteristic for hysteresis mechanisms of internal friction, and it can be attributed to forced activation above small potential barriers.

2) 400–500 K. This temperature range is characterized by devitrification and onset of the first stage of crystallization with appearance of a metastable crystalline phase $Mg_xNi_yY_z$ and precipitation of nanocrystalline magnesium. These processes lead to quite sharp irreversible changes of both the internal friction and Young's modulus (Fig. 3b).

In a heating–cooling cycle a very wide internal-friction peak, whose maximum falls in the temperature range 425–440 K, is obseved on heating. In the temperature dependence of Young's modulus, in the region 400 K a deviation from a linear temperature dependence (more rapid decrease with temperature) is observed first, but a very substantial (up to 45%) increase of the modulus commences at approximately 415 K. This growth continues up to about 490 K. The observed increase in modulus is irreversible, and the difference in the values of Young's modulus of the initial amorphous sample and the sample heated up to 490 K is about 50% at room temperature.

There is no doubt that the observed changes are due to

devitrification and crystallization of the amorphous alloy Mg–Ni–Y. It is known that devitrification results in a sharp change in the viscosity of the material near the glass-formation temperature T_x and, correspondingly, to a sharp change in its elastic-dissipative properties.[10] An irreversible internal-friction peak and a corresponding decrease of Young's modulus should be observed near the temperature T_x on the basis of the viscoplastic friction model.[11] To a first approximation the change in the internal friction can be described on the basis of this model by a Debye-type expression $Q^{-1} \sim \omega\tau/(1+(\omega\tau)^2)$, where ω is the angular frequency, $\tau \sim \eta$, and η is a time- and temperature-dependent viscosity.

In turn, the crystallization of the alloy influences to an even greater extent than vitrification the elastodissipative properties of materials, leading to substantial, primarily irreversible, changes in these properties. There exist several models of internal-friction mechanisms due to structural rearrangement caused by crystallization. These models are based on the assumption that internal friction should be proportional to the rate of phase crystallization during the time of the measurements. It is obvious in this approach that the crystallization should result in irreversible peaks of the internal friction caused by precipitation of a $Mg_xNi_yY_z$ phase and nanocrystalline magnesium.

Unfortunately, the existing experimental data do not make it possible to distinguish the possible contributions to the damping. The crystallization and vitrification processes must be distinguished more accurately. For the system Mg–Ni–Y the temperatures T_x and T_g depend strongly on the chemical composition, and small variations of the latter are the most effective method for distinguishing these processes, which at present is the basic problem.

We call attention to the very high value of Young's modulus in the new structure formed (nanocrystalline phase $Mg_xNi_yY_z$ and the residual amorphous phase). This structure is uncharacteristic of ordinary magnesium alloys.

3) 500–610 K. This temperature range corresponds to new stages of continuing crystallization of the alloy $Mg_{84}Ni_{12.5}Y_{3.5}$. It should be noted that starting at 490 K Young's modulus decreases with increasing temperature (Fig. 3c). This decrease is partially irreversible. The main irreversible decrease in the modulus occurs at a temperature above 550 K, at which the peak of the internal friction is observed, as is indicated by the results of partial temperature cycling in the region 460–555 K. The irreversible decrease of the modulus after heating to 555 K was about 5%. After heating to 610 K Young's modulus at 300 K is approximately 25% lower than for the sample annealed at 490 K. This result is not surprising, considering the fact that according to x-ray diffraction measurements the phase $Mg_xNi_yY_z$ decomposes precisely near 600 K. This confirms once again that the phase $Mg_xNi_yY_z$ possesses very high elastic characteristics. For this reason, the determination of the exact of the composition and crystallographic structure of this phase could be extremely important for producing magnesium alloys with attractive mechanical properties.

In summary, the results obtained attest to a strong effect of the structure of amorphous-nanocrystalline materials on the formation of their elastic-dissipative properties. This makes it possible to use measurements of the elastic characteristics and damping as an extremely informative tool for investigating the kinetics of crystallization processes in amorphous alloys. The same results show that special heat treatment can be used to control the elastic and mechanical properties of Mg–Ni–Y alloys.

We thank the Russian Fund for Fundamental Research for partial support of this work (grants Nos. 98-02-16644 and 95-15-96806).

*)E-Mail: soifer@issp.ac.ru

[1] A. Inoue and T. Masumoto, Mater. Sci. Eng. A **173** (1993) [*sic*].
[2] A. Inoue, K. Ohetera, M. Kohinata *et al.*, J. Non-Cryst. Solids **117/118**, 712 (1990).
[3] T. S. Srivatsan, Li Wei, and C. F. Chang, J. Mater. Sci. **30**, 1832 (1995).
[4] N. P. Kobelev, Ya. M. Soifer, V. G. Shteinberg, and Yu. B. Levin, Phys. Status Solidi A **102**, 773 (1987).
[5] A. S. Aronin, N. P. Kobelev, A. V. Serebryakov, and Ya. M. Soĭfer, Fiz. Tverd. Tela (Leningrad) **30**, 3160 (1988) [Sov. Phys. Solid State **30**, 1819 (1988)].
[6] B. Porscha and H. Neuhauser, Scr. Metall. Mater. **32**, 931 (1995).
[7] L. Kempen, U. Harms, H. Neuhauser *et al.*, J. de Phys. IV C **8**, 643 (1996).
[8] N. P. Kobelev and Ya. M. Soifer, Nanostruct. Mater. **10**, 449 (1998).
[9] A. van den Beukel, Acta Metall. Mater. **39**, 2709 (1991).
[10] He Yizhen and Li Xiao-Guang, Phys. Status Solidi A **99**, 115 (1987).
[11] J. Perez, J. de Phys. C **10**, 427 (1985).

Translated by M. E. Alferieff

Drift of scanning cycles of microwave absorption in high-T_c superconductors

M. I. Shirokov[a] and A. V. Shendrik

Institute of Solid State Physics, University of Latvia LV–1063 Riga, Latvia
(Submitted July 22, 1998)
Fiz. Tverd. Tela (St. Petersburg) **41**, 567–571 (April 1999)

A change in the position and shape of the hysteresis line of magnetically modulated microwave absorption accompanying repeated magnetization reversal of a high-T_c superconductor was observed. The shift of the signal increases with the magnetic field, and its modulation amplitudes and scanning times vanish at T_c, obeying the basic laws of the temperature dependence of the line in single crystals and ceramics. Its appearance is correlated with the attainment of the critical state of modulated screening currents of weak-link loops separated on the surface of the sample and can be interpreted as their interaction on the basis of a generalized surface barrier model. The observed anisotropy indicates a Néel interaction mechanism. © *1999 American Institute of Physics.* [S1063-7834(99)00204-X]

The possibility of practical applications of microwave devices based on high-T_c superconductors (HTSCs) — fast transistor, magnetic memory cells, magnetic suspension of a high-speed rotor[1] — is determined both by their minimum losses and their stability under repeated switching and modulation of the controlling magnetic field. As a very simple example, let us consider the microwave absorption signal accompanying cyclic scanning of a modulated magnetic field (first harmonic of the EPR of the detected signal). The cycle consists of a reversible nonresonant line and a loop of hysteresis losses, often attributed to magnetic hysteresis of the static magnetization $M_{\pm}$.[2–5] It is well known that the latter varies strongly with repeated magnetization reversal of ferromagnets (FMs). The effect of repeated scanning or modulation cycles on the absorption signal and magnetization of HTSCs is clearly seen in individual spectra.[6–9] In one case[6] it was concluded that there is a variance in the parameters of the sample, and in other cases[7–9] it was left, apparently, as an artifact without comment. At the same time it is assumed that the transient processes observed in experiments on magnetization relaxation in HTSCs are not, as a rule, of an instrumental nature, but rather they are of a physical character.[10–12] Logically, the slow relaxation of nonuniformly distributed domains, which is responsible for the drift of a hysteresis loop, in FMs has a direct correspondence in HTSCs — magnetic-flux creep.[13] It has been established that thermally activated creep of magnetic flux with sharp retardation of the field scanning $\Delta H/\Delta\tau < 10^{-2}$ Oe/s gives rise to a logarithmic decrease of the absorption hysteresis in time, while an instantaneous acceleration $\Delta H/\Delta\tau > 10^2$ Oe/s restores the loop in a new position as a result of creep associated with nonuniform demagnetizing factors.[3,14] The contribution of creep to the formation of a signal has not been observed with ordinary scanning rates $\Delta H/\Delta\tau \sim 10$ Oe/s.[15] Moreover, drift of the force–distance hysteresis, analogous to magnetization–field hysteresis and not reducible to creep, has been observed in experiments on levitation of a magnet above a HTSC undergoing magnetization-reversal.[16] In this connection, in the present work a systematic study is made of the evolution of the EPR of the detected signal from a HTSC in the course of successive magnetic-field scanning cycles.

1. EXPERIMENT

The main measurements were performed with an RE-1307 spectrometer with a TE_{102} cylindrical resonator, field scanning range $\Delta H = 0.5 - 10.5$ kOe, modulation amplitude $h_m \leqslant 20$ Oe at 100 kHz, and microwave power $W \leqslant 800$ mW. Varian and Radiopan spectrometers with a flat resonator and a resonator rotated by 90°, respectively, were also used for control. Flat Y-1-2-3 and Tm-1-2-3 crystals ($0.1–0.4 \times 3 - 3$ mm and $T_c \sim 90$ K) and samples of the ceramic Y-1-2-3 ($T_c \sim 89$ K) with the same shape were secured, so as to soften the mechanical effects, in polyethylene tubes with cuts at the end, which gave essentially no resonance signal. The heating of a thermally insulated sample was monitored with a copper-constantan thermocouple. The maintenance of the quality of the filled resonator was followed both automatically and by the resonance signals of the sample and marker. The samples were frozen in a quartz cryostat in liquid nitrogen, as a rule in a zero magnetic field, and oriented with the c axis parallel or perpendicular to the microwave field h. Next, the resonance field H_0 was switched on and repeated scanning in the interval $H_0 \pm \Delta H$ at a rate $\Delta H/\Delta\tau \sim 1 - 60$ Oe/s at temperature 77.3 K was performed.

2. RESULTS

The microwave-absorption hysteresis loop cycles can be reproduced to within the noise accompanying the signal if the modulation amplitude does not exceed the critical value $h_m < h_0$ with a given magnetic field. When $h_0(H)$ is reached, successive cycles of displacement of the loop appear and the slope of the magnetic absorption changes in both the forward and reverse directions of the scanning cycles (Fig. 1). The displacements increase with the magnitude, the modulation amplitude, and the scanning time of the magnetic field and vanish at $T \approx T_c$. This makes it possible to attribute them to

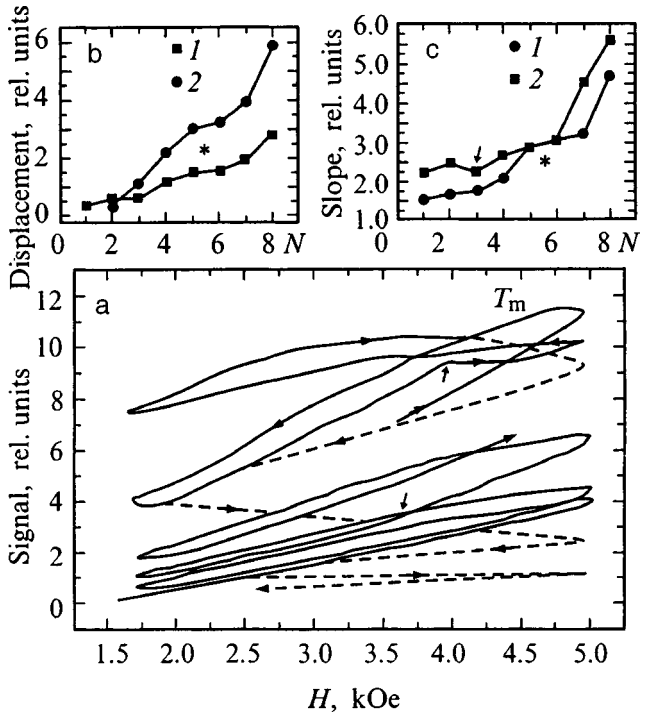

FIG. 1. Pattern of displacements of cycles with subsequent slow heating of the sample from $T=77.3$ K to room temperature. The dashed line shows the cutoff of the line at $T \geqslant T_m \approx 88.5$ K and emergence on the zero line at $T \geqslant 92$ K (a); displacements (b) and slopes (c) of cycles for the left-hand (*1*) and right-hand (*2*) scanning edges, respectively. An asterisk shows the saturation region of the displacements. The arrows mark irregularities. Tm-1-2-3 single crystal, sample No. 1, 1.6 kOe scanning range, $h \parallel c$, $\times 320$, $h_m = 20$ Oe, $\tau = 2$ min.

the superconducting properties of the material. Figure 2 shows the typical behavior of the displacements on the right-hand scanning edge, where, as a rule, they are maximum. For convenience, some cycles (Figs. 1–2) are omitted. The arrows indicate the scanning direction. The continuous increase in the slope of the magnetoabsorption line rules out the possibility that the displacements are due to external factors that degrade the Q of the resonator. The absorption spectrum of the single crystal (Figs. 1b and 1c) shows that saturation of the displacements occurs at the cycle 5–6. Then heating of the sample commences. Here the displacements have a pronounced temperature maximum with an upper limit $T_m \sim 88$ K, and cycle after cycle they relax, approximately linearly in time, to the zero line at $T_m \leqslant T \leqslant T_{cr}$ (dashed line in Fig. 1). The cutoff of the absorption level occurs much more rapidly than the temporal evolution of the cycles: over two cycles as opposed to ten. The slope of the line has irregularities, marked by an arrow (Figs. 1a and 1c). The drift of the line observed during heating of the sample corresponds, on the whole, to the temperature dependence of the absorption signal of a single crystal with a narrow maximum near T_c:[15] $T_m \sim 88.5$ K, $T_c \approx 90$ K, and it is directed predominantly opposite to the displacements. This is especially clearly seen for the ceramic where the signal decreases monotonically as $T \to T_c$.[6] Uncontrollable heating of the sample by the modulation field, by the microwave, or by breakdown of thermostating is unlikely — the motion of the absorption cycle is not accompanied by an increase of the thermal fluctuations, which is inevitable in such a case. The effect of the modulation or vibrational frequency of the sample remained outside the scope of the present measurements. However, it was established that under otherwise equal conditions nonsuperconducting samples of the experimental materials do not exhibit nonstationary behavior of the line.

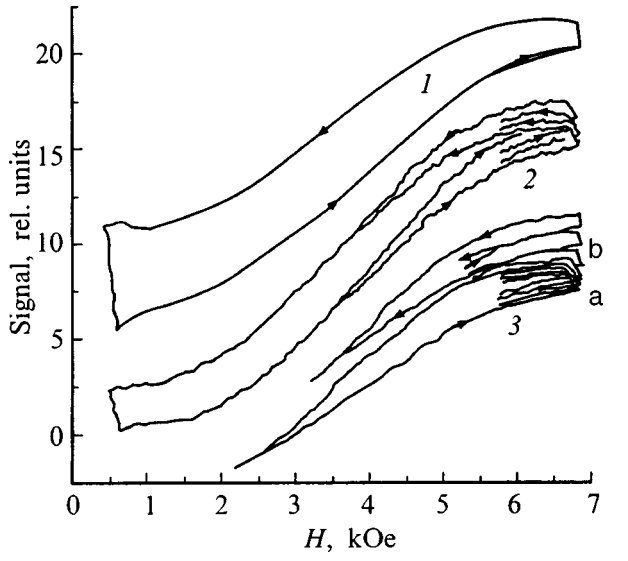

FIG. 2. Line shape and displacement of the microwave absorption signal versus the modulation amplitude h_m, Oe: *1* — for 0.12 with $\times 5.000$, $\tau = 2$ min; *2* — 0.4 with $\times 1.500$, $\tau = 5$ min; *3* — 0.8 with $\times 800$, $\tau = 2$ min (a) and 5 min (b). Y-1-2-3 ceramic in the form of a single crystal.

The shape of the hysteresis loop was recorded simultaneously with the displacements. As is well known, the hysteresis loop changes from a narrowing loop for a signal linear in h_m, which ultimately reflects an upper critical field, to closure or funnelling of the edge (Fig. 2) in the nonlinear regime $h_m > h^*$. The latter is attributed to the screening currents of the weak-link loops on the surface of the superconductor attaining a critical state. Comparing the data (Fig. 2) shows a clear correlation $h_0 \sim h^*$, where $h^* \leqslant 0.1$ Oe, close to the previously observed values ~ 0.05 Oe.[6] The mechanism of the nonlinear h_m dependence of the hysteresis amplitude has been repeatedly discussed.[2,3,6,14] Here it must be attributed to a different circumstance — the simultaneous appearance of displacements of the loop for $h_m > h^*$. Their resolution is all the better, the longer the scanning time $\Delta\tau$ is (Fig. 2). In the process, the jump of the hysteresis substantially decreases, right down to collapse of the line edge (Figs. 2–3). It is interesting to compare the observed evolution of the line with the criterion for detecting the first harmonic of EPR of the detected signal $p = 2h_m \Delta\tau / \Delta H_0 \tau_0$, where τ_0 is the relaxation time of the nonstationary signal.[4] In a developed nonlinear regime $h_m \sim 3-6h^*$, indeed, as $\Delta\tau$ and h_m increase, the amplitude of hysteresis decreases somewhat more slowly than $\sim 1/p$ (Fig. 2). At the same time, a strong transformation $1 \to 3(b)$ of the hysteresis loop and decrease in its amplitude on cycling are also observed. Numerous measurements also show that the loop vanishes and is replaced by a hysteresis of the slope of the line (zig zag) as the scanning range ΔH near H_0 decreases. The residual loop

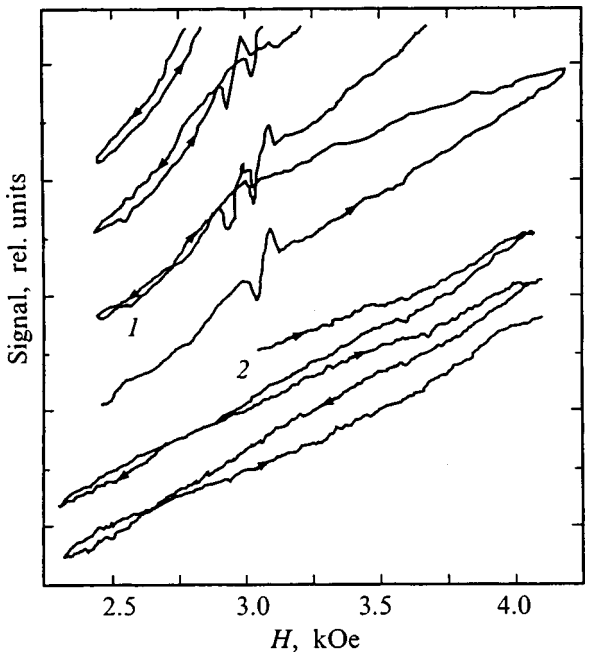

FIG. 3. Displacements of cycles of the microwave absorption signal (zig zag) with a residual loop. Tm-1-2-3 single crystal, $h \parallel c$, scanning range 1.6 kOe, $h_m = 20$ Oe: *1* — sample No. 1, ×500; *2* — sample No. 2, ×320.

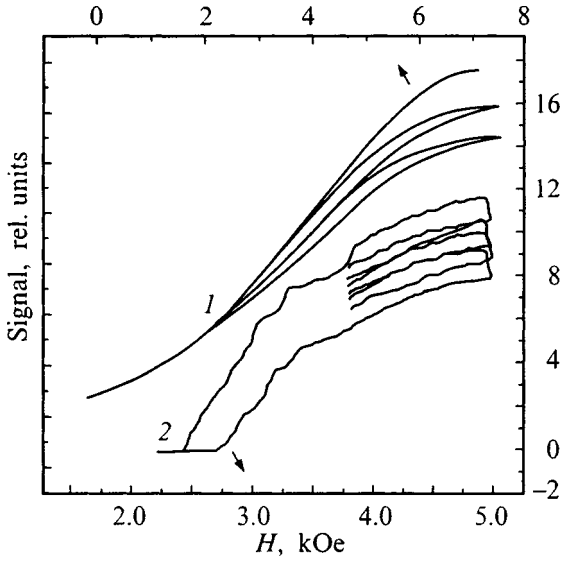

FIG. 4. Microwave absorption cycles for the ceramic Y-1-2-3: *1* — ellipsoid of revolution, 7 kOe scanning range, ×50, $h_m = 20$ Oe, $\tau = 5$ min; *2* — bead, scanning range 3.2 kOe, ×70, $h_m = 20$ Oe, $\tau = 2$ min.

remains at the lower scanning edge with the slope in the forward direction exceeding the slope in the reverse direction and vice versa (Fig. 3). It is easy to verify that the direction around the loop and the zig zag are the same in the first case, while they are opposite to one another in the second case. The same trend occurs when $\Delta\tau$ and h_m are increased further. The data for the parameter τ_0 are extremely inconsistent ranging from $3 \cdot 10^{-3}$ s to 0.5 h.[10–12] The criterion $p \leqslant 0.1-1.0$ gives an estimate $\tau_0 \sim 1.0-0.1$ s for our ceramic samples.

The motion of the cycles can be associated with the slow relaxation of the magnetization of a surface layer, observed in superconductors with nonuniformly distributed demagnetizing factors.[14] To check this supposition, samples were prepared in the form of Y-1-2-3 ceramic beads from the same batch as the wafers whose shape was the same as that of the single crystals. Their diameter $\delta \leqslant 1$ mm corresponded to the surface of the wafers. The main features of the motion of the cycles remained the same: For $\Delta\tau = 2$ min, the displacements are of the order of the amplitude of the loop and, for $\Delta\tau = 5$ min, the typical pattern of sharply narrowed loops (zig zags) following one another arises (Fig. 4). Apparently, this is due to the characteristic mechanisms of relaxation of microwave absorption. Scanning with the lower edge in weak fields also indicates this. For $(H_0 \Delta H) \leqslant 2$ kOe a virtually undisplaced section of a loop is observed, after which the displacement increases approximately linearly in accordance with the criterion $h_m = h_0(H)$ (Fig. 2).

The effect of the anisotropy of the demagnetizing factors was studied on ceramic plates having the same shape as the single crystals. This made it possible to determine the effect of crystallographic anisotropy. The shape and width of the loop turned out to be insensitive to the orientation in a magnetic field. The displacements of the loops, however, have a pronounced maximum for $\vartheta \approx 45°$ above the background for $\vartheta = 0$ and 90° (Fig. 5a). In this connection, similar measurements were performed on a thick single-domain Tm-1-2-3 single crystal. These measurements showed a similar angular dependence of the loop amplitude itself — asymmetry with respect the sign of ϑ (Fig. 5b). Measurement errors were eliminated by reproducing the signal with the sample rotated by 180°. The features near $\vartheta = 0$[17] had virtually no effect on the analysis of the results. An asymmetric pattern of absorption hysteresis can be easily seen in Fig. 5 in Ref. 15, left in this respect without comment. The displacement approximately followed the behavior of the amplitude of the loop and as a rule it stopped at the third cycle.

3. DISCUSSION

At present a theory making it possible to interpret such phenomena does not exist. The phenomenology developed by Néel for FMs showed that the motion of the magnetization reversal cycles $M_{\pm}(H)$ is due to a pair interaction of quite strongly differing domains, and their sequence approximately corresponds to the distribution of such pairs.[18] It has been shown that the nonuniform distribution of weak links with trapping of magnetic flux in the course of the field scanning cycles plays an important role for magnetic hysteresis of the absorption signal.[19] The large role of the variance of the weak-link loops in the microwave absorption hysteresis signal has been shown for the example of h^* in the linear Portis model $\Delta P \sim I$ (Ref. 16) and later developed in the generalized surface barrier model with a quadratic current dependence $\Delta P \sim I^2$.[14] Taking account of the contribution of the interaction of the most strongly differing mutually orthogonal loops oriented parallel and perpendicular to the axis of the single crystal, we arrive at the dependence of the additional contribution to hysteresis on the direction of the current

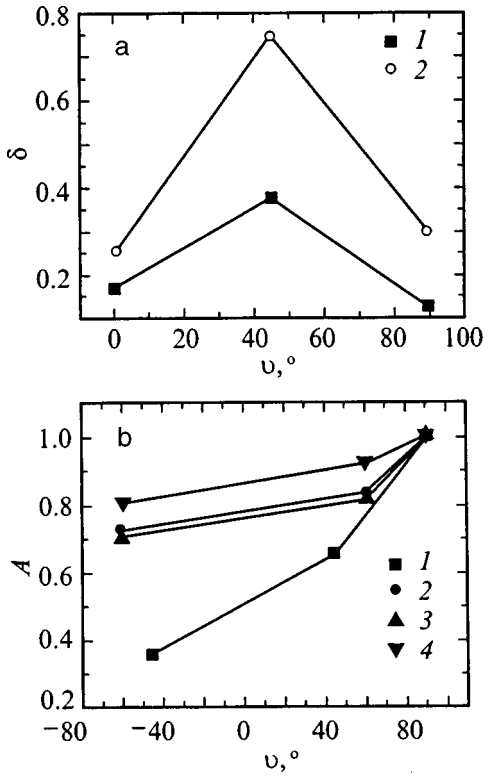

FIG. 5. Anisotropy of microwave absorption signal. a — Displacements of cycles in two different cases of the tuning of the resonator in a flat Y-1-2-3 ceramic sample in the form of a single crystal, scanning range 7 kOe, ×300, $h_m=20$ Oe, $\tau=2$ min (δ — displacement/amplitude hysteresis); b — amplitude of the hysteresis line A: *1* — thick Tm-1-2-3 single crystal, scanning range 7 kOe, ×3.200, $h_m=20$ Oe, $\tau=4$ min; *2* — Y-1-2-3 single crystal from Ref. 15; *3* — same in the surface-barrier model;[14] *4* — in the Portis model.[6]

$$\Delta P_{\text{int}} \sim I_{\parallel} I_{\perp} \sim \alpha \sin 2\vartheta. \tag{1}$$

Comparison with experiment on the angular dependence (Fig. 5b), $\Delta P(\vartheta)=\Delta P_0(\vartheta)+\Delta P_{\text{int}}(\vartheta)$, far from $\vartheta=0(\vartheta=45, 90°)$ shows a quadratic law $\Delta P_0 \sim \sin^2\vartheta$ and $\alpha \sim 0.15$. The data of Ref. 17 ($\vartheta=60, 90°$) have a relative deviation from the Portis model ~ 0.12 with $\alpha \sim 0.1$ and a relative deviation from the quadratic model ~ 0.04 with $\alpha \sim 0.07$. Thus, the phenomenological approach (1) most likely agrees with the generalized surface barrier model[14] in combination with magnetic transparency $I \sim H\sin\vartheta$.[17] The smallness of α corresponds to a low efficiency $\sim d/l$ of the interaction of transverse loops with dimensions $\sim l,l$ and l,d, respectively, where l is the wafer size and d is the wafer thickness. This effect has been observed in a thick single-domain single crystal (d — 0.4 mm, l — 2.5 mm) and in Ref. 7 ($d \sim 0.1$ mm, $l \sim 1.0$ mm).

If these considerations are extended to the experiment with a ceramic plate with the same geometry, then the position $\vartheta=45°$ in isotropic material has, in our view, a single feature — a maximum variance of the interacting loops with respect to geometric type. The average (over the ceramic sample) odd term $\langle \Delta P_{\text{int}} \rangle = 0$, while the cycle drift acquires an additional term, quadratic in the interaction in a separate pair of maximally (by the factor d/l) differing loops, with a higher relaxation rate — creep of nonuniformly distributed magnetic flux. The residual displacement level for orientations $\vartheta=0$, 90° (Fig. 5a) is then due to the characteristic variance of loops of each type. Inclined loops are less effective here. Apparently, their role is likewise limited by the well-known fact that there are no inclined structures of magnetic vortices in HTSCs. In a crystal the contribution of the interaction should be maximized by the basic dependence $I \sim H\sin\vartheta$, which is not small near $\vartheta \sim 45°$. The wide variance of the loops on the surface of a ceramic should, in principle, give a more pronounced pair distribution. In this case, correspondingly, a virtually continuous sequence of cycles (ceramic) and two or three cycles (single crystal) is observed. The first variant, however, was also observed in a variety of single-crystal samples. The distribution of magnetic vortices and the associated weak-link loops is very sensitive to the details of the surface structure[20] and could reflect its defectiveness in these samples. A large variance of the loops is characteristic, specifically, for spherical samples, where a more pronounced pattern of displacement of the signal than in a flat sample is indeed observed (Fig. 3).

We note that if $h_m > h^*$, then the loops always divide into two groups: critical and subcritical, $I_{\text{cr}}/h_m \leqslant K \leqslant I_{\text{cr}}/h^*$ and $K < I_{\text{cr}}/h_m$ respectively, in the notations of Ref. 14. Thus, drift of the line exists irrespective of whether or not, for example, the field scanning is symmetric, in contrast to the case of FMs. Moreover, if the displacement of the cycles of magnetization reversal of FMs can be regarded as equivalent to slow relaxation of the magnetization in time,[19] then in HTSCs the existence of a hysteresis loop is itself due to the turning of the screening currents accompanying a change in the field scanning direction,[7] and a displacement of the loop is therefore due to the interactions in which the currents can participate in this case. It is easy to see that the latter is all the more successful, the slower the scanning and the interaction is all the stronger, the greater the degree and amplitude of the modulation of the field, which agrees qualitatively with our observations. The angular asymmetry of hysteresis (Fig. 5b) corresponds to the relative turning of the screening currents and is most likely caused by surface and not by bulk properties.

On account of the pair interaction of the screening currents distributed on the surface of a superconductor and, in accordance with the tendency for a critical state of the medium $I=I_{cr}$ to be established,[4] the magnetic energy should be redistributed so as to equalize these two systems of loops. The corresponding redistribution of magnetic vortices, including in the skin layer, can give rise to an additional nonstationary microwave absorption on weak links.[7,21] Such a scenario presumes a spontaneous transition of the loops into a critical state, which should decrease the amplitude of the hysteresis loops and produce irregular behavior (Fig. 1). The interaction of the systems of smothed systems of loops can give rise to admixing for $p \geqslant 1$ of the second-harmonic signal, which for $I_m > I_0 \sim I_{\text{cr}}$ is subject to line-slope hysteresis (zig zag). The latter condition can be satisfied either for $h_m \gg h^*$ or with increasing magnetic field as a result of a decrease in $I_{\text{cr}}(H)$. The divergence of the cycles is indeed observed experimentally either with a finite field H^* or for large excesses $h_m \gg h_0$ in any field (curve *1* in Fig. 2). The

observation of displacements of cycles sheds light on the reason why absorption vanishes at a temperature different from T_c:[3] As the sample is heated, first absorption vanishes and then the nonuniformally trapped magnetic flux relaxes cycle after cycle.[22] Thus our preliminary results show that the observed motion of the scanning cycles of microwave absorption in HTSCs is qualitatively consistent with existing ideas about the wide distribution of screening current loops on the surface of a sample and on their pair interaction with the establishment of a universal critical state. The specific character of the temporal evolution on reaching equilibrium is a separate problem. Other contributions to absorption drift are also possible: mechanical vibrations of the sample including vibrations associated with the modulation field,[23] jumps of magnetic vortices,[24] and so on. The direct effect of a controllable surface state of the sample and the shape of the sample, taking account of the real, complicated picture of the penetration of the magnetic field and distribution of magnetic vortices, on the effect considered here is interesting.[20]

*)E-mail: mish@acad.latnet.lv

[1] J. S. Martens, G. K. G. Hohenwarter, J. B. Beyer, J. E. Nordman, and D. S. Ginley, J. Appl. Phys. **65**, 4057 (1989); A. Shaulov, D. Dorman, and R. Bhargava, Appl. Phys. Lett. **57**, 724 (1990); F. C. Moon and D.-Z. Chang, Appl. Phys. Lett. **56**, 397 (1990).
[2] M. Pozek, A. Duląic, and B. Rakvin, Solid State Commun. **70**, 8891 (1989).
[3] A. Duląic, R. H. Crepeau, and J. H. Freed, Phys. Rev. B **39**, 4249 (1988).
[4] I. M. Zaritskiĭ, A. A. Konchits, S. P. Kolesnik, O. A. Mironov, L. Yu. Sipataov, A. I. Fedorenko, and S. V. Chistyakov, Supercond., Phys. Chem. Technol. **4**, 1400 (1991).
[5] T. Yuan, H. Jiang, A. Widom, C. Vittoria, A. Drehman, D. Crisey, and J. Horwitz, Physica C **242**, 197 (1995).
[6] M. Warden, M. Stalder, G. Stefanicki, A. M. Portis, and F. Waldner, J. Appl. Phys. **64**, 5800 (1988); M. Warden, V. A. Ivanshin, and P. Erhart Physica C **221**, 20 (1994).
[7] Yu. N. Shvachko, D. Z. Khusainov, A. A. Romanyukha, and V. V. Ustinov, Solid State Commun. **69**, 611 (1989).
[8] T. Nagashima, K. Watanabe, M. Watahiki, and Y. Fukai, J. Appl. Phys. **28**, L-183 (1989).
[9] V. F. Masterov, I. L. Likholit, A. F. Fedorov, N. M. Shibanova, E. L. Dukhovskaya, and V. V. Potapov, Supercond., Phys. Chem. Technol. **5**, 2235 (1992).
[10] H. L. Ji, Z. X. Shi, X. Jin, X. X. Yao, X. S. Rong, Y. M. Ni, and Z. X. Zhao, J. Appl. Phys. **75**, 1671 (1994).
[11] A. Gurevich, H. Kupfer, B. Runtsch, R. Meier-Hirmer, D. Lee, and K. Salama, Phys. Rev. B **44**, 12090 (1991).
[12] Y. Itoh and U. Mizutani, Jpn. J. Appl. Phys. **35**, 2114 (1996).
[13] P. W. Anderson, Phys. Rev. Lett. **9**, 309 (1962).
[14] V. A. Atsarkin, V. V. Demidov, and N. E. Noginova, Supercond., Phys. Chem. Technol. **5**, 305 (1992).
[15] A. A. Koshta, A. A. Romanyukha, Yu. N. Shvachko, N. A. Viglin, V. V. Ustinov, and S. V. Naumov, Supercond., Phys. Chem. Technol. **3**, 838 (1990).
[16] T. Nikihara and F. C. Moon, Physica C **250**, 121 (1995).
[17] E. Silva, S. Sarti, R. Fastampa, M. Giura, and R. Marcon, Physica C **243**, 303 (1995).
[18] L. Néel, Compt. Rend. Acad. Sci. **246**, 2313 (1958); J. Phys. Radium **20**, 215 (1959).
[19] M. El-Hilo and K. O'Grady, J. Appl. Phys. **73**, 6653 (1993).
[20] V. K. Vlasko-Vlasov, M. V. Indenbom, V. I. Nikitenko, A. A. Polyanskiĭ, R. L. Prozorov, I. V. Grekhov, L. A. Delimova, I. A. Liniĭchuk, A. V. Antonov, and M. Yu. Gusev, Supercond., Phys. Chem. Technol. **5**, 1637 (1992).
[21] M. Cardona, J. Gittleman, and B. Rosenblum, Phys. Lett. **17**, 92 (1965).
[22] V. Sesho Bai, P. V. Patanjali, S. M. Bhagat, and S. Tyagi, J. Supercond. **8**, 299 (1995).
[23] Ch. Pool, Jr., *Electron Spin Resonance* (Interscience Publishers, John Wiley & Sons, N. Y., 1967; Mir, Moscow, 1970), p. 491.
[24] V. D. Kuznetsov, V. V. Metlushko, and I. E. Kuznetsov, Supercond., Phys. Chem. Technol. **2**, 41 (1989).

Translated by M. E. Alferieff

Effect of loading on the chemical potential of oxygen atoms in $YBa_2Cu_3O_{6+x}$ (YBCO) and $PrBa_2Cu_3O_{6+x}$ (PBCO)

Yu. M. Gerbshteĭn and N. E. Timoshchenko

A. F. Ioffe Physicotechnical Institute, Russian Academy of Sciences, 194021 St. Petersburg, Russia
(Submitted August 4, 1998)
Fiz. Tverd. Tela (St. Petersburg) **41**, 572–576 (April 1999)

The effect of loading on the chemical potential of oxygen atoms has been studied in the YBCO and PBCO isostructural compounds, with the former exhibiting HTSC, and the latter, not. Application of a load to both YBCO and PBCO in the orthorhombic phase causes an increase in the chemical potential within the $0.5<x<0.8$ interval, which is interpreted as a phase-separation region. This effect is associated with an increase in the fraction of an ordered phase possessing a smaller specific volume. It is also related to the additional compressibility of the material. In the tetragonal phase this effect is observed only in YBCO. The absence of the effect in PBCO implies the electron-phonon coupling in this material has a different nature. © *1999 American Institute of Physics.* [S1063-7834(99)00304-4]

A characteristic feature of YBCO and PBCO is the inverse proportionality of sample volume to oxygen content x. According to Le Châtelier's principle, application of a load to such a sample should cause absorption rather than release of oxygen, and the chemical potential of oxygen atoms should decrease in this process and not increase. We observed this phenomenon in YBCO and showed that within the $0<x<0.5$ region it is associated with an increase of the electronic chemical potential, and for $0.5<x<1$, with the ortho-tetra phase transition.[1]

This paper reports a study of this phenomenon within a broader x range on the YBCO and PBCO isostructural compounds, the former of which is a high-T_c superconductor, while the latter is not. An analysis is made of the relation of this effect to compressibility and phase separation.

The increment of the chemical potential $\Delta\mu_0$ can be obtained by differentiating the increment of the Gibbs thermodynamic potential with respect to the number of particles. For an isolated isotropic (polycrystalline) sample at room temperature one can write

$$\Delta\mu_0 = v\Delta\sigma, \tag{1}$$

where $\Delta\sigma$ is hydrostatic loading, and v is a constant characterizing the sample material. In the case of uniaxial loading, an effective load equal to one third of the uniaxial one should be inserted in Eq. (1). (This is valid for $\Delta\mu_0 \ll kT$, which in our experimental conditions is certain to be met.) The constant v of a simple substance can be calculated by dividing the sample volume by the number of atoms it contains (in doing this, one should take the volume of an undeformed sample, in which case the work of the load expended in deformation will enter $\Delta\mu_0$). This method of calculation of v is obviously inapplicable to a complex substance. In this case we shall define $\Delta\mu_0$ as the work done by the load in removing a particle. Then v will acquire the meaning of the increment of sample volume associated with removal of one particle, but taken with the opposite sign. Strictly speaking, this requires that the expression for $\Delta\mu_0$ be obtained at a constant load. However for a solid undergoing a small deformation this lack of rigorousness may be disregarded.

1. EXPERIMENT

The increment of the chemical potential of oxygen atoms can be measured with a high-sensitivity ZrO_2 pickup. The experimental method used is essentially as follows. After equilibrium has been attained in the sample–gas–pickup-electrode system, a common chemical potential sets in among the oxygen atoms. Accordingly, the increment of the chemical potential caused by application of a load to the sample should be the same for all components of the system, and it can be measured in the form of the increment of the electrical potential at the pickup electrode.

Loading drives the system out of equilibrium and gives rise to a redistribution of oxygen between the gas and the sample, thus causing a change in oxygen content in the sample from x to $x+\Delta x$, and of the chemical potential, from μ to $\mu+\Delta\mu$. For a given sample mass m, oxygen pressure p, and temperature T, the quantities Δx and $\Delta\mu$ are related to the gas phase volume V as[1]

$$\Delta x = \Delta x_0\left(\frac{V^{\text{eff}}}{V}+1\right)^{-1}, \quad \Delta\mu = \Delta\mu_0\left(\frac{V}{V^{\text{eff}}}+1\right)^{-1},$$

$$V^{\text{eff}} = \frac{mkRT^2}{4Mp(d\mu/dx)}. \tag{2}$$

Here Δx_0 and $\Delta\mu_0$ are the values of Δx and $\Delta\mu$ for $V=\infty$ and $V=0$, respectively, k is the Boltzmann constant, R is the gas constant, and M is the molecular mass of the sample substance. The quantities Δx_0 and $\Delta\mu_0$ are related through

$$\Delta x_0 = \frac{\Delta\mu_0}{d\mu/dx}.$$

In our experiment, $m=1$ g, $p=0.1$ atm, $V^{\text{eff}}=40$ cm^3, and $V=0.2$ cm^3. Inserting these values in Eq. (2) yields

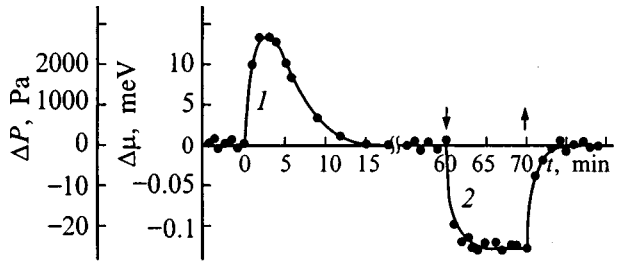

FIG. 1. Increments of oxygen pressure Δp and of the chemical potential of oxygen atoms $\Delta\mu$ in the gas over a PBCO sample plotted as functions of time t, associated with a change of temperature from 604 to 654 °C under noninterrupted gas flow ($V \gg V^{\text{eff}}$) (*1*), and with an application and removal of loading (the down- and up-arrows, respectively) under interrupted gas flow ($V \ll V^{\text{eff}}$) (*2*).

$\Delta x = 0.005\,\Delta x_0$ and $\Delta\mu = 0.995\,\Delta\mu_0$, which means that application of a load, while practically not affecting x, causes an increment of the chemical potential which nearly coincides with the one that would be for $V=0$, i.e. for an isolated sample.

The experimental setup used is described elsewhere.[1] A ZrO_2 crucible, with platinum electrodes deposited on its inner and outer surfaces, serves as a reaction chamber and a solid electrolyte of the pickup. For temperatures above 400 °C, the pickup measures the emf, which is related to the oxygen pressures at the electrodes through the Nernst expression. An increment of the chemical potential of oxygen atoms $\Delta\mu$ causes a change in the emf, $\Delta E = \Delta\mu/2$.

The measurements were performed in the following way. A cylindrical sample prepared by standard ceramic technology was placed in the reaction chamber and heated at the desired temperature in an argon flow with the given partial oxygen pressure. When equilibrating with the gas phase, the sample either released or absorbed oxygen, which could be determined from the pickup readings. On reaching equilibrium, the flow was interrupted, and a uniaxial load of 10^7 Pa was applied to the sample. The increment of chemical potential and that of the oxygen pressure in the gas phase were measured at different temperatures within the 400–850 °C interval.

Figure 1 illustrates a measurement on a PBCO sample performed at 654 °C and an oxygen pressure of 8×10^3 Pa. The figure presents pickup readings as a function of time, which is measured from the instant the heat controller switches from the temperature of the preceding measurement, 604 °C, to 654 °C. During the first 15–20 min following the switching, the oxygen pressure in the flow exceeds the original level because the sample releases oxygen in the course of relaxation to a new equilibrium state. The relaxation time is 3–4 min. The area bounded by the curve is a measure of the amount of released oxygen. The gas flow was interrupted at the 40th min, and the load was applied at the 60th min. One readily sees that the oxygen pressure now decreases, indicating absorption of oxygen by the loaded sample. The load was removed at the 70th min. The oxygen pressure is seen to regain its initial level, i.e. the sample releases the oxygen it had absorbed under load. The relaxation time, as in the case of a temperature variation, is 3–4 min, which implies a ''volume'' nature of the phenomenon. The equilibrium values of Δp and $\Delta\mu$ are -25 Pa and -0.125 meV, respectively. The scatter of these quantities in repeated measurements was within 30%.

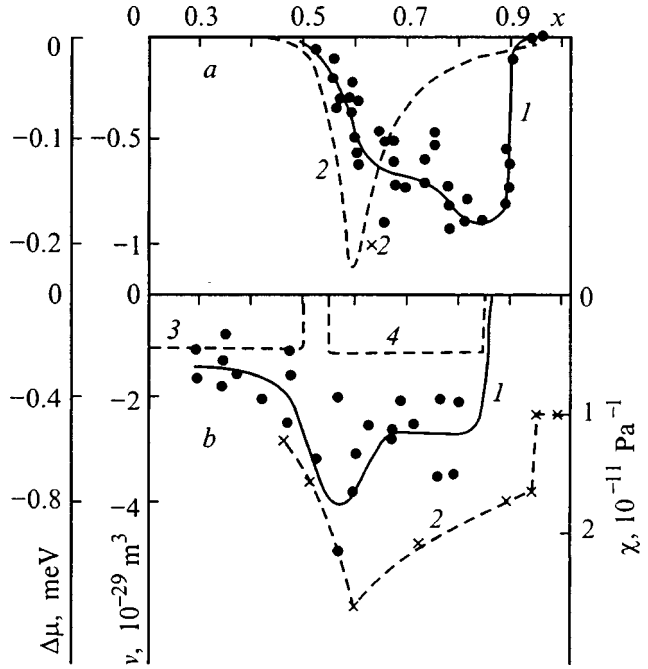

FIG. 2. Load-induced chemical-potential increment $\Delta\mu$ as a function of x obtained for PBCO (*1*) from measurements; (*2*) (a) derived from the experimental $v_{\text{cell}}(x)$ relation[4] using Eq. (3), and (b) load-induced chemical-potential increment $\Delta\mu$ (*1,3,4*) and compressibility χ (*2*) as functions of x obtained for YBCO (*1*) in the present experiment, (*2*) in experiments of Refs. 2 and 3, (*3,4*) by calculation.

Note that application of a load to a sample which had not been loaded before was accompanied by larger increments of the pressure and chemical potential than those presented in Fig. 1. The lower magnitude of the effect in repeated loadings can be assigned to cold work, i.e. to a stressed state of the material which restricts the change in sample volume associated with the removal of a particle.

The values of x corresponding to the measurement temperatures were determined gravimetrically. Figure 2 displays the $\Delta\mu(x)$ relations for PBCO and YBCO (curves *1* in Fig. 2a and 2b, respectively). Both curves lie in the domain of negative $\Delta\mu$. In YBCO, the effect is observed in the tetragonal and orthorhombic phases, with a dip seen at the phase transition point at $x = x_1 \approx 0.55$. In PBCO this effect is observed to occur only in the orthorhombic phase. In both cases, $\Delta\mu$ falls off rapidly to zero as one approaches $x = x_2 \approx 0.85$, and the experimental scatter also practically vanishes, whereas for $x < x_2$ it amounted to 20–40%. It should be pointed out that the large scatter of experimental points for $x < x_2$, rather than being connected with the measurement errors, is a characteristic feature of the materials under study.

Besides the $\Delta\mu(x)$ function obtained by us for YBCO (curve *1*), Fig. 2b shows also the compressibility $\chi(x)$ of YBCO (curve *2*) obtained by x-ray diffraction.[2,3] Note that both curves exhibit a rise within the $x_1 < x < x_2$ interval.

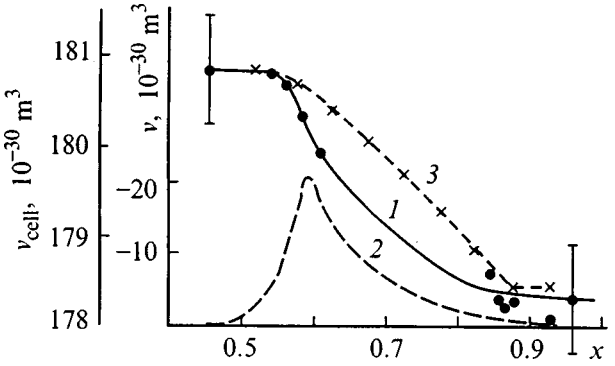

FIG. 3. Unit-cell volume v_{cell} (*1* and *3*) and its derivative dv_{cell}/dx (*2*) as functions of x obtained for PBCO from (*1*, *2*) experiment[4] and (*3*) experimental dependence $v(x)$ (see Fig. 2a).

2. DISCUSSION OF EXPERIMENTAL RESULTS

According to Eq. (1), the interpretation of the phenomenon should reduce to the interpretation of coefficient v. With the loads used in this work, the contribution of deformation to v is very small. This gives us grounds to consider the lattice elements in the calculation of v as incompressible particles. In this approximation, the values of v obtained for a loaded and unloaded sample are the same. The fact that v is an intensive parameter permits one to calculate it as the change in the cell volume v_{cell} induced by the removal from it of one oxygen atom.

For instance, if the dependence of the unit cell volume on x is known, one can use for calculation of v the relation

$$v = dv_{\text{cell}}/dx. \tag{3}$$

The $v_{\text{cell}}(x)$ dependence derived from x-ray diffraction studies[4] of PBCO is presented in Fig. 3 (curve *1*). Also shown is the $v(x)$ function calculated using Eq. (3) (curve *2*). The noticeable change of v_{cell} and, accordingly, the extremum in v are associated with the tetragonal to orthorhombic phase transition of the material. By inserting the $v(x)$ function thus obtained into Eq. (1), one could calculate the corresponding $\Delta\mu_0(x)$ dependence. It is displayed in Fig. 2a (curve *2*) together with the experimental $\Delta\mu(x)$ relation (curve *1*). The effect calculated from x-ray diffraction data is seen to coincide both in sign and order of magnitude with the results of our measurements. A more accurate comparison of these curves would hardly be reasonable in view of the limited accuracy of the x-ray measurements of $v_{\text{cell}}(x)$. At the same time curve *1* permits one to obtain a more accurate relation

$$v_{\text{cell}}(x) = \int_0^x v(x)dx.$$

This relation derived from our experimental results is presented in Fig. 3 (curve *3*).

As can be seen from a comparison of curves *1* and *3* in Fig. 3, curve *1* obtained from x-ray measurements shows the most substantial lattice changes to occur in the vicinity of the ortho-tetra phase transition, while in curve *3* this point does not stand out from among other points within the $x_1 < x < x_2$ interval.

A similar comparison made for YBCO likewise suggests that the effect is connected with the phase transition. At the same time the existence of the effect for $0 < x < 0.5$, far from the transition, implies that some other mechanism is operative here too.

Consider this mechanism. Oxygen exchange between the gas and the sample for $0 < x < 0.5$ can be described by a quasichemical reaction

$$O + 2Cu^{1+} = O^{2-} + 2Cu^{2+}. \tag{4}$$

This actually means that an oxygen atom entering the lattice takes away electrons from two Cu^{1+} ions and changes their valence state to $2+$. Because $Cu^{2+} = Cu^{1+} - e$, reaction (4) can be recast in the form $O = O^{2-} - 2e$, with the corresponding condition of equilibrium

$$\mu = \mu_i - 2\mu_e, \tag{5}$$

where μ_i and μ_e are the chemical potentials of the oxygen ions and electrons, respectively. Taking into account (5), Eq. (1) can now be written

$$\Delta\mu = v_i\Delta\sigma - 2v_e\Delta\sigma, \tag{6}$$

where v_i and v_e are the increments of the sample volume associated with removal of an oxygen ion and an electron, respectively, taken with the opposite sign.

It is known that oxygen absorption by YBCO and, accordingly, the appearance in its lattice of O^{2-} ions decreases rather than increases the sample volume. Considered in the approximation of incompressible particles, this means that an oxygen ion occupies a void in the lattice whose size does not exceed that of the ion. Thus, within this approximation, removal of an oxygen ion should not result in a change of the sample volume, whence it follows that $v_i = 0$.

To estimate v_e, we recall that the electrons involved in formation of an O^{2-} ion are removed from Cu^{1+} ions transforming them to Cu^{2+}. Considering v_e as the increment in the cell volume (taken with the opposite sign) caused by the change in radius of the copper ion as it changes its valence state from $1+$ to $2+$, we obtained $v_e = 0.5 \times 10^{-29}$ m^3. Substituting these values of v_i and v_e into Eq. (6) yields $\Delta\mu = -0.2$ meV (curve *3* in Fig. 2b). This is in agreement both in sign and magnitude with the measured effect.

Consider the mechanism of this effect in the YBCO case for $0.5 < x < 1$. In this region, oxygen absorption is accompanied by hole creation. Because holes are localized at oxygen ions[5] and, thus, are also in lattice voids whose size exceeds that of the ions, one should expect a zero effect throughout the $0.5 < x < 1$ interval. One sees from Fig. 2b, however, that $\Delta\mu = 0$ is observed only for $0.8 < x < 1$.

To explain this disagreement, consider the effect of loading on the tetra-ortho phase transition of the material. This transformation was described[6] in terms of the Ising model as a transition of oxygen atoms in the basal plane from a disordered to an ordered state. The analysis was done for the case of an open system ($V \gg V^{\text{eff}}$). In these conditions, the temperature dependence of the chemical potential μ is governed by the gas phase only. The transition is driven by the decrease in temperature of the sample heated in an oxygen ambient. The phase transition temperature and the corre-

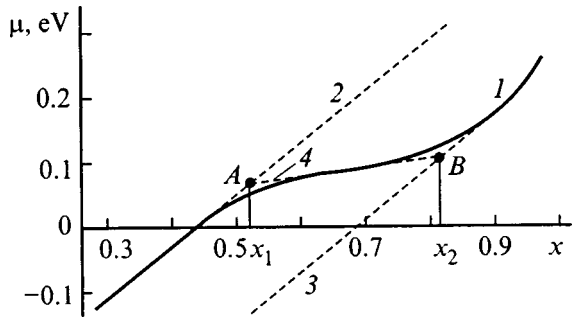

FIG. 4. Dependence of the chemical potential of oxygen atoms in YBCO on x (*1*) calculated from results obtained in the Ising model[6]; (*2*, *3*) obtained by extrapolating the portions of graph *1* relating to the disordered and ordered state, respectively; (*4*) calculated for the phase separation region.

sponding value $x=x_1$ are related to the model parameter u, which is the repulsion energy between neighboring oxygen atoms located in adjacent sublattices.

Our calculation of $\mu(x)$ based on Ref. 6 was done essentially in the lattice gas model. This dependence is displayed in Fig. 4 (curve *1*). To reconcile it with the quantum-mechanical calculations[7] predicting phase separation in YBCO, as well as to explain the discontinuous change in the v coefficient and compressibility χ observed at $x=x_2$ (Fig. 2), we shall assume the smooth portion of the curve between points $A(x_1,\mu_1)$ and $B(x_1,\mu_2)$ to reflect the phase separation. (The positive slope of this portion, which is usually an indication of a single-phase system, can be accounted for here by u being dependent on x.) The portions of the curve to the left of point A and to the right of point B are the x dependences of the chemical potential of the disordered phase, $\mu_{\rm dis}(x)$, and of the ordered one, $\mu_{\rm ord}(x)$. Curves *2* and *3*, which were obtained for $u=0$ and $u=\infty$, respectively, extrapolate these dependences to the $x_1<x<x_2$ region.

The chemical potential acquires here values that are intermediate between $\mu_{\rm dis}$ and $\mu_{\rm ord}$ and depend on the amounts of oxygen in the disordered and ordered phases. Obviously enough, application of a load should result in a redistribution of oxygen between the phases such that the sample volume decreases, i.e. in an increase of the ordered-phase fraction. We neglect the effects not associated with the phase transition by assuming $\mu_{\rm dis}$ and $\mu_{\rm ord}$ to be independent of loading. Then for $x=$const (the condition at which $\Delta\mu$ is measured) an increase in the fraction of the ordered phase should be reflected by a displacement of points A and B down and to the left along lines *2* and *3*. We assume for the sake of simplicity that the displacement of both boundaries of the region is the same and depends linearly on the load. One can then write $x_1(\sigma)=x_1(0)-\alpha\sigma$ and $x_2(\sigma)=x_2(0)-\alpha\sigma$. Here α is the number per cell of oxygen atoms transferred by a unit load to the ordered phase. The chemical potential in the phase-separation region can be presented as a sum of the corresponding partial contributions

$$\mu(x,\sigma)=\mu_{\rm ord}\frac{x-x_1(\sigma)}{x_2-x_1}+\mu_{\rm dis}\frac{x_2(\sigma)-x}{x_2-x_1}. \tag{7}$$

The nearly straight line *4* in Fig. 4 connecting points A and B is a plot of Eq. (7). After differentiation of this relation with respect to σ and comparison of the results with Eq. (1), the increment of the chemical potential in the phase-separation region can be written

$$\Delta\mu=(\mu_{\rm ord}-\mu_{\rm dis})\frac{\alpha}{x_2-x_1}\Delta\sigma=v\Delta\sigma. \tag{8}$$

Here $v=\alpha(\mu_{\rm ord}-\mu_{\rm dis})/(x_2-x_1)$ is the change in sample volume associated with the transfer of an oxygen atom from the disordered to the ordered phase. Thus as one enters the phase-separation region the load-induced increment in the chemical potential jumps from zero to a finite value.

Phase separation in YBCO is an alternation of oxygen-depleted and enriched regions a few lattice constants in size.[7] The interface between solid phases not having a very large lattice mismatch has usually a macroscopic thickness d, within which the lattice constants vary smoothly. If the phase dimensions are much smaller than d, the lattice parameters of one phase practically coincide with those of the other. The dependence of these parameters on x and σ is described by an expression similar to Eq. (7). Accordingly, the deformation of a sample can be written

$$\Delta v_{\rm cell}=(v_{\rm ord}-v_{\rm dis})\frac{\alpha}{x_2-x_1}\Delta\sigma=\alpha v\Delta\sigma. \tag{9}$$

Here $\Delta v_{\rm cell}$ is the absolute volume deformation per cell, and $v_{\rm ord}$ and $v_{\rm dis}$ are the cell volumes in the ordered and disordered phases, respectively. Equation (9) permits one to write the compressibility associated with phase separation in the form

$$\chi_{\rm sep}=\alpha\frac{v}{v_{\rm cell}}. \tag{10}$$

This expression provides an explanation for the similarity between the experimental relationships $\chi(x)$, $\Delta\mu(x)$ and, accordingly, $v(x)$. Using the values of these quantities averaged over the phase-separation regions, $v=2\times10^{-29}$ m^3 and $\chi_{\rm sep}=\chi-\chi(1)=1\times10^{-11}$ Pa^{-1}, we estimated by means of Eq. (10) the coefficient α, which was found to be 9×10^{-11} Pa^{-1}. Inserting it in Eq. (8) yields a calculated relation $\Delta\mu(x)$ (curve *4* in Fig. 2b). As seen from a comparison of curves *4* and *1*, the model accounts for the main experimental results obtained for YBCO and PBCO. At the same time the greater complexity of the experimental curves suggests that the order-disorder transition in these materials has features not accounted for by the model.

Because the increment of chemical potential in the phase separation region is accompanied by a change in volume fractions of these phases, it entails also a displacement of the phase boundaries. In real crystals such a displacement is accompanied by an energy expenditure, which should transfer the material to a state similar to a supercooled liquid. In connection with this, a hysteresis should be observed in the phase separation region. It has indeed been found, and it will be described in our next publication.

The main results of the work can be summed up as follows:

1. Loading YBCO and PBCO samples causes oxygen absorption and, accordingly, a decrease in the chemical potential of oxygen atoms.

2. In the tetragonal phase, the effect is observed only in YBCO. Here it is due to the fact that application of a load (transformed in the lattice into an increment of interatomic force) focuses on the univalent copper atoms while not affecting in any way the oxygen ions. The absence of the effect in PBCO shows that in this material the load-induced forces are distributed differently in the lattice.

3. In the orthorhombic phase, the effect was observed in both YBCO and PBCO within the $0.5<x<0.8$ interval, which is interpreted as a phase separation region. This effect is associated with an increasing fraction of the ordered phase, which has a smaller specific volume and a lower chemical potential of oxygen atoms.

4. In the phase separation region, YBCO and PBCO exhibit a compressibility whose mechanism is associated with the load-induced increase of the fraction of the denser phase. This compressibility is proportional to the load-induced increment of the chemical potential of oxygen atoms.

The authors are grateful to Yu. M. Baĭkov for fruitful discussions and to B. T. Melekh for providing the PBCO samples.

[1] Yu. M. Gerbshteĭn, N. E. Timoshchenko, A. D. Muradov, and A. Zh. Rakhimbekov, Fiz. Tverd. Tela (St. Petersburg) **39**, 599 (1997) [Phys. Solid State **39**, 521 (1997)].
[2] N. N. Sirota and K. Zh. Zhambaĭbekov, Sverkhprovodimost' (KIAE) **7**, 285 (1994).
[3] J. E. Blendell, C. K. Chiang, D. S. Cranmer, S. W. Freiman, E. R. Fuller, J. R. Dresher-Krasika, Ward L. Johnson, H. N. Ledbetter, L. H. Bennett, L. J. Swartzendruber, R. B. Marinenko, R. L. Myklebust, D. S. Bright, and D. E. Newbury, *194th ACS Meeting on the Chemistry of High-Temperature Superconductors* (New Orleans, 1987), p. 240.
[4] M. E. López-Morales, D. Ríos-Jara, J. Tagüeña, R. Escudero, S. La Placa, A. Bezinge, V. Y. Lee, E. M. Engler, and P. M. Grant, Phys. Rev. B **41**, 6655 (1990).
[5] N. Nücker, H. Romberg, X. X. Xi, J. Fink, B. Gegenheimer, and Z. X. Zhao, Phys. Rev. B **39**, 6619 (1989).
[6] H. Bakker, D. O. Welch, and O. W. Lazareth, Jr., Solid State Commun. **64**, 237 (1987).
[7] *Proceedings of the 2nd International Workshop on Phase Separation in Cuprate Superconductors*, edited by E. Sigmund and K. A. Müller (Cottbus, 1993).

Translated by G. Skrebtsov

Josephson and non-Josephson generation — dynamic resistive state in superconducting films

V. F. Khirnyĭ*)

Institute of Single Crystals, Ukrainian Academy of Sciences 310001 Khar'kov, Ukraine
(Submitted August 5, 1998)
Fiz. Tverd. Tela (St. Petersburg) **41**, 577–581 (April 1999)

A model of the dynamic resistive-current state is examined. The model is used to explain the generation of electromagnetic oscillations in thin superconducting films by the existence of phase-slip strips in them. © *1999 American Institute of Physics.* [S1063-7834(99)00404-9]

1. Metastable current states (MSCSs) were discovered in Refs. 1–5. These states appear because of the local nature of the destruction of the superconducting phase in aluminum, indium, or tin films as a result of magnetic Abrikosov vortices moving in a direction transverse to the transport current I and subsequent formation of stationary normal-phase strips along their trajectory.[5–8] In the constant-current regime MSCSs were recorded in the form of straight lines in the current-voltage characteristics (IVCs). In the constant-voltage regime the IVC was N-shaped.[9] Figure 1 shows schematically the IVCs obtained in a constant-current regime (curve *1*) and in a constant-voltage regime (curve *2*). ''Giant Josephson generation'' of electromagnetic oscillations (inset in Fig. 1) in an indium film was observed in the section E–K.[9]

In the present work the conditions under which nonstationary strips of a normal phase appear are investigated and a model of the dynamic resistive-current state, in which Josephson oscillations are generated by the existence of phase-slip strips in the films, is examined. A qualitative and quantitative explanation of the stationary and dynamic processes in film superconductors in the constant-voltage regime are given.

2. It is well known that an Abrikosov vortex possesses a normal-phase core where the order parameter Δ decreases to zero. The radius of the core equals the coherence length ξ of the superconductor. For this reason, when a vortex passes with velocity v_L through a prescribed point in the superconductor in a time $\tau \simeq \xi/v_L$ the quantity Δ at this point at first decreases to zero and then relaxes in a time τ_Δ to its equilibrium value. Depending on the velocity of the vortex, Δ varies over a time $\tau_\Delta < \tau$ or $\tau_\Delta \geqslant \tau$. The time τ_Δ is[10]

$$\tau_\Delta \cong \hbar/\Delta, \tag{1}$$

where $\hbar$ is Planck's constant. The condition $\tau_\Delta < \tau$, under which only a chain of vortices, arranged perpendicularly (or obliquely) to the direction of flow of the transport current, exists in the film, was studied previously in Ref. 11. In what follows, the properties of superconducting films and the behavior of vortices for $\tau_\Delta \geqslant \tau$ are investigated.

In the formation of a chain, vortices move one after another, crossing the film in the transverse direction. In order for the number of vortices in the chain to increase, the current must be increased each time. The electric field arising in the process is[5]

$$E = \Phi_0/\tau_L(I), \tag{2}$$

where Φ_0 is the magnetic flux quantum and $\tau_L(I)$ is the time in which the vortices must traverse the distance between the vortices in the chain so that one vortex exits the film and another enters the film and each vortex occupies the position of the preceding vortex. The velocity of the vortices in the chain depends on the value of E, i.e. it is proportional to the ratio E/B, where $B = \Phi_0 n$ and n is the number of vortices in a chain. On the other hand, according to the condition $\tau_\Delta \geqslant \tau$ and Eq. (1) the velocity of the vortices can be expressed in terms of the parameters of the superconductor, i.e. $V_L \geqslant \xi(T)\Delta(T)/\hbar$. Under isothermal conditions a normal-phase strip of length $l \leqslant \xi$ remains after the moving vortex.[12] In order that the track of each vortex connect with the neighboring vortex and a normal-phase strip intersecting the film crosswise be formed, unrealistically high velocities of vortices are required at temperatures $T \geqslant 0.8T_c$. Hence it follows that a different mechanism plays the main role in the formation of a normal-phase strip intersecting the film along the trajectory of the vortices, specifically, energy dissipation, i.e. heating along the trajectory of the vortices. During such nonisothermal motion of a vortex through the film, a normal-phase strip of length $l > \xi$ remains after the vortex. Otherwise a normal-phase strip crossing the film would not be formed. In what follows, mainly the behavior of vortices only under nonisothermal conditions such that $\tau_\Delta \leqslant \tau_0$, where $\tau_0 = \rho C/A$ is the time in which the heat released during the motion of the vortices is dissipated into the space surrounding the superconductor,[5] is investigated. Here ρ is the density of the sample material, C is the specific heat, $A = (\alpha_1 + \alpha_2)/d$ is the total heat-transfer coefficient, equal to the sum of the coefficients of heat transfer into the substrate α_1 and into the surrounding medium α_2 per unit thickness of the film d.

If the strip is nonstationary in time, it can be called a phase-slip strip. There are three methods for observing the dynamic resistive state. We shall consider them successively:

1) $\tau_L(I) > \tau_0$.

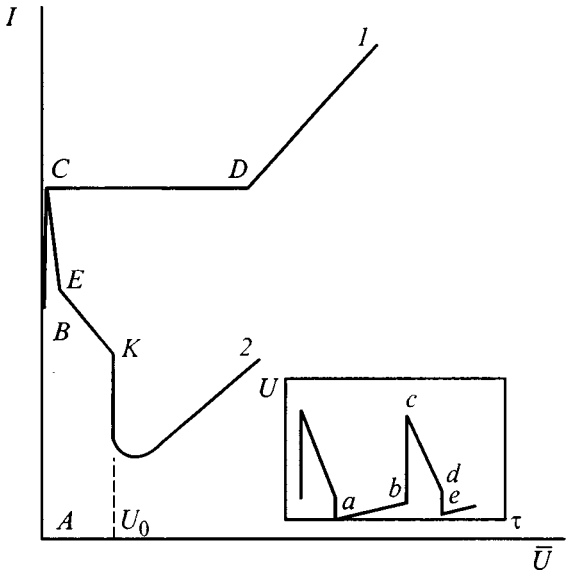

FIG. 1. Schematic form of the IVCs measured in constant-current regimes[1] (*1*), with a voltage source[9] (*2*), or wide superconducting films in a dynamic resistive state. Inset: Oscillogram of voltage pulses of ''giant Josephson generation'' of electromagnetic oscillations.[9]

A normal-phase strip of length $l>\xi$ which remains after a moving vortex can pass to a superconducting state before the next vortex appears at the point considered. As the electric current increases, new vortices enter other locations in the film, where the current and irregularities reduce the Bean–Livingston barrier to zero. The film contains only chains of vortices localized on its irregularities and separated from one another by equilibrium superconducting regions. The IVCs of the samples are broken curves and consist of a series of linear sections with a differential resistance that is a multiple of a definite value R.[13]

2) $\tau_L(I)<\tau_0$.

As the current reaches the value I_{c1}, vortices begin to enter and move in the film (point B in Fig. 1). A further increase of the current (point C in Fig. 1) leads to the development of a temperature instability, since there is still not enough time for the heat released during the motion of the first vortex to dissipate before the second, third, and so on vortices follow it. The local temperature T_L along their trajectory increases, and the temperature instability is completed by avalanche-like destruction of superconductivity accompanied by the appearance of normal-phase strips.[5] Depending on the measurement regimes of the IVCs, their form and the processes leading to the destruction of superconductivity will be different.

a) *Measurement of the IVCs in the constant-current regime.* Since the current is given, a voltage step appears in the IVC (section C–D in the curve *1*, Fig. 1) at the moment the normal-phase strip forms. The superconducting film will pass into a dissipative metastable state with a stationary resistive normal-phase domain pinned at an irregularity in the sample.[5] The strip appears once at a given location in the sample. As the current increases, such domains localize at irregularities in other locations.[1–8]

b) *Measurement of the IVC in the constant-voltage regime.* During the primary formation of the normal-phase strip with current $I_m>I_{c1}$ (point C in Fig. 1), the electric resistance increases from zero to $R\neq 0$. Since the voltage is given, the current flowing through the sample will decrease (section C–E in Fig. 1). Energy dissipation decreases, and this part of the sample cools in time $\sim\tau_0$ and once again passes into an equilibrium superconducting state. For a virtually constant voltage on the film, when the electric current reaches the value I_{c1}, vortices will repeatedly enter the film at the same location (point E in Fig. 1). They will move one after another until a normal-phase strip is formed. In the oscillogram (inset in Fig. 1) this corresponds to the section a–b with the voltage drop on the sample equal to the noise voltage accompanying the motion of the vortices. The minimum time required for any vortex in the chain to traverse the distance separating the vortices at the moment of formation of the normal-phase strip is τ_0. For an indium film $\tau_0 \simeq 10^{-9}$ s the width of the strip is of the order of the heat penetration depth $\lambda_T=(K/A)^{1/2}\simeq 10^{-5}$ m,[5] where K is the thermal conductivity of the sample, scaled to the film thickness. Then, according to Eq. (2) the maximum voltage developing in this case will be 10^{-4} V. This agrees with the data of Ref. 9.

A nonuniform electric field with intensity U appears at the moment the normal-phase strip appears. The voltage U is recorded in the oscillograph in the form of the leading edge of a pulse (section b–c of the oscillogram in the inset in Fig. 1). This voltage consists of several terms, i.e. $U=U_0+U_N+U_n$. The first term, U_0, appears because the electrons in the transport current which move in bound pairs from the region of equilibrium superconductivity, accelerating in the nonuniform electric field over a distance l_0, acquire an additional voltage $\delta\varepsilon=eEl_0$, where e is the electron charge. If $\delta\varepsilon$ is larger than the binding energy $2\varepsilon_0$ of the pair, then an individual electron can be scattered by encountering a defect, and the pair can be ruptured in the process. Here ε_0 is the energy gap of the superconductor. Since $eEl_0=eU_0$, this occurs when $U_0\geqslant 2\varepsilon_0(T)/e$.[5] The second term, U_N, is the voltage drop on the normal-phase strip. The third term, U_n, is the voltage due to the longitudinal electric field that appears in the equilibrium part of the superconductivity located on the side of the normal-phase strip that is arranged in the direction of current flow from the normal region into the superconducting region. The existence of this field was postulated in Ref. 6. Here it is obtained in a natural manner, since the energy of the electrons in the transport current is greater than ε_0. This part of the superconductor over a distance $l_E=l_D(4T/\pi\varepsilon_0)^{0.5}\simeq 10^{-6}-10^{-7}$ m$\ll\lambda_T$ will pass into a nonequilibrium state with the balance of the populations of the ''electron-like'' and ''hole-like'' branches of the electronic excitation energy spectrum destroyed (l_D is the diffusion distance of the quasiparticles). The voltage U_n is very low and can be neglected.

After the normal-phase strip is formed (point C in the inset in Fig. 1), the transport current will drop below I_{c1}. Energy dissipation will likewise decrease and the local temperature along the trjectory of the vortices will reach an equilibrium value in a time τ_0. The region of nonequilibrium superconductivity will also vanish in this time, since it

turned out that τ_0 is of the same order of magnitude as the ''branch mixing'' time τ_Q in an indium film, even though these quantities are associated with different physical processes. One would think that, in the time τ_0, the electric resistance R_N of the normal-phase strip would also decrease to zero. But the nature of the change in the electric resistance of the normal-phase strip $R_N(\tau)$ in time τ will depend on the local temperature and the parameters of the samples. Thus, the pulse duration will be determined by the pairing time τ_R of the quasiparticles with emission of phonons. It equals several microseconds,[14,15] which is of the same order of magnitude as that obtained in Ref. 9 (Fig. 1, section c–d in the inset). More accurately, τ_R is difficult to determine in the present case, since its value depends on the ratio ε_0/kT, in which T should be taken as the temperature T_L of local heating of the strip, which was not determined in Ref. 9. Here k is Boltzmann's constant.

As U decreases, it will reach a minimum value U_0 that can still exist in the superconductor (section d–e in the voltage oscillogram in Fig. 1). This is confirmed by the experiment of Ref. 9. The current flowing through the sample is much lower in magnitude than the critical current and it is insufficient for the strip to remain in the normal state. When the strip passes into the superconducting state, R_N and U drop to zero in time $\sim\tau_\Delta$ (section d–e in the voltage oscillogram in the inset in Fig. 1), and the process leading to the formation and vanishing of the normal-phase strip will repeat with period t_p. Its value can be obtained from the relation determining the average voltage U supplied by the pulse generator, given the maximum amplitude U of the voltage in the pulse and the duty factor

$$\overline{U}=Ut_i/t_p=Ut_i\nu, \tag{3}$$

where ν is the pulse repetition frequency. Conclusions confirmed experimentally in Ref. 9 follow from Eq. (3).

a) $\overline{U}\sim\nu$ with a constant proportionality coefficient, which characterizes oscillations as ''Josephson.'' The function $\varepsilon(\nu)$ has the form of straight lines whose slope decreases with increasing temperature as a result of a decrease of U_0 as T_0 is approached. The intersection of the vertical straight line with them (constant ν regime) gives the temperature dependence $\varepsilon_0(T)$.

b) The lowest frequency of stable generation is inversely proportional to the film width w, since the greater w, the greater t_p and the smaller $\nu_{\min}$ are.

c) The maximum generation frequency is reached for a voltage on the film $\overline{U}=U_0$ (the point K on the IVC, Fig. 1), above which the sample will pass into the normal state. This will be followed by a sharp decrease in the transport current. As the voltage increases further, the working point on the IVC will move along the ascending branch, corresponding to an ohmic dependence.

3) $\tau_L(I)\simeq\tau_0$.

In this case various fluctuations of a thermal or electromagnetic nature will affect the formation of the MSCSs. In the fixed-current regime spontaneous hops (switchings) of the working point on the IVC from the nondissipative section to the MSCS and back or from the section with one value of the differential resistance to a section having a different value are possible (Fig. 2).

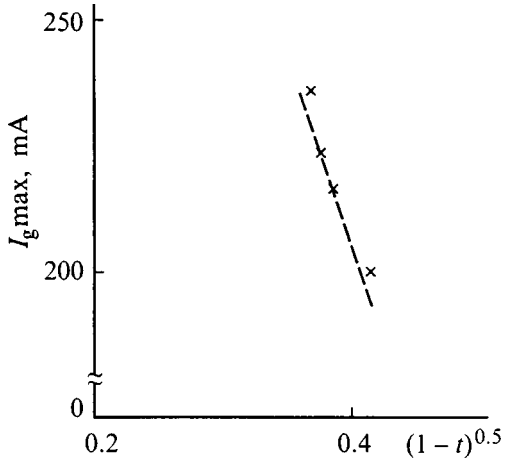

FIG. 2. IVC measured in a constant-current regime with $\tau_L(I)\simeq\tau_0$.

It follows from the condition $\tau_L(I)\simeq\tau_0$ that the vortices must have a minimum velocity $v_L\geqslant\lambda_T/\tau_0\simeq10^5$ m/s $\leqslant v_F$, where v_F is the Fermi velocity, in order for a normal-phase strip to form.

This value is identical to the data presented in many works (see, for example, Ref. 16). It follows from the estimate presented above that Eq. (1) is applicable, since in the present model only fast motion of vortices is considered, so that it is energetically favorable for a vortex to be located in the track of the preceding vortex.

As noted earlier, τ_0 actually depends on the value of the total heat-transfer coefficient A. For this reason, the experimental manifestation of any of the three cases considered above depends mainly on the degree of acoustic matching of the film and substrate, allowing for thermal phonons to escape from the sample. For a metal film–glass interface, it is far from ideal, not only because these two media are acoustically mismatched.[17] Irregularities remaining on the glass surface after polishing scatter thermal phonons very efficiently. Fewer such irregularities remain on sapphire, which is harder than glass.[13] A sapphire substrate made it possible to satisfy the condition $\tau_L(I)>\tau_0$. The second and third cases are very easily realized. This has been indicated in Ref. 13.

Besides the temperature T, the electric current I and the magnetic field H should also influence the generation frequency because of their effect on ε_0. The effect of T,H, and I on ε_0 is qualitatively the same — as they increase, ε_0 decreases and ν increases. However, a parallel magnetic field influences ε_0 in two ways.[18] For film thickness $d<\sqrt{5}\lambda_L(T)$ a second-order phase transition occurs at the critical value of the field and $\varepsilon_0(H)$ decreases monotonically to zero. Here $\lambda_L(T)$ is the London penetration depth of a magnetic field. For $d>\sqrt{5}\lambda_L(T)$ a first-order phase transition is observed and $\varepsilon_0(H)$ decreases to zero abruptly. The generation frequency will show the same behavior.

In strong magnetic fields $\varepsilon_0\neq\Delta$. Specifically, near T_c there is a finite region in the (H,T) plane where $\varepsilon_0\simeq0$ but

$\Delta \neq 0$. For polycrystalline films, gapless superconductivity with $R_N = 0$, similar to that arising when magnetic impurities are added to a superconductor,[19] should exist in it. This assertion is based on the following fact. A film near T_c can be classified as a superconductor in the ''dirty'' limit. The conduction-electron mean-free-path length l_e is very short because of scattering by the boundaries of the crystallites comprising the film, and ξ is large. For example, for an indium film the product $\rho_n l_e = 1.1 \times 10^{-11}\,\Omega \cdot \mathrm{cm}^2$, where ρ_n is the resistivity of the superconducting indium in the normal state. This equality was taken from skin-effect measurements in pure samples.[20] For polycrystalline superconducting films deposited in a moderate vacuum, $\rho_n \simeq 10^{-3}\Omega \cdot \mathrm{cm}$. Then $l_e/\xi(T) \simeq (l_e/\xi_0)^{1/2}(1-t)^{1/2} \simeq 10^{-3} \ll 1$, where $\xi_0 = 4.4 \times 10^{-5}$ cm is the coherence length for indium at $T = 0$ K.[21] It was assumed that $(I-t) = 10^{-2}$, where $t = T/T_c$ is the reduced temperature and T_c is the critical temperature. From Ref. 22 it is known that the electrical conductivity in dynamic regimes of thin films (in the ''dirty'' limit) in a parallel magnetic field is equivalent to that in superconductors with addition of magnetic impurities (first equivalence theorem). If the sample width w exceeds $\lambda_\perp = (2\lambda_L^2(T)/d)$, the effective penetration depth of a magnetic field into a film of thickness d, then the mechanism of the electromagnetic oscillations will be the same but the voltage-drop pulses across the sample will have essentially no trailing edge. Since $U_0 \ll U$, the equality (3) will not hold and the Josephson generation condition will break down. In distinction from ordinary superconductors, in gapless superconductors the screening current I_s caused by the application of a field H is higher than the critical current I_c and $I_s \sim \Delta^2$.[21] Therefore the generation current I_g, by its very nature, will be a screening current and will be larger than I_c in absolute value. The dependence $I_s \sim \Delta^2$ leads to temperature and field dependences of the generation current of the form $I_g(T) \sim (1-t)$ and $I_g(H) \sim (1-H^2/H_c^2)$, while $I_c(T) \sim (1-t)^{3/2}$ and $I_c(H) \sim (1-H^2/H_c^2)^{3/2}$, where H_c is the critical magnetic field. This behavior of I_g has been observed in thin tin films at temperatures from $t = 0.975$ to 0.995.[23] It was assumed that generation was caused by the nonstationary behavior of a phase-slip center, since $w < \lambda_\perp$, and this generation was said to be non-Josephson.

It is known[21] that the dependence of the current density j on the velocity v of condensed pairs possesses a maximum when the velocity v reaches a critical value v_c. In the case studied in Ref. 21, the maximum current $I_{g\max}$ corresponds to the maximum of the non-Josephson generation frequency. Since $v_c \sim (1-t)^{1/2}$, we have $I_{g\max}(T) \sim (1-t)^{1/2}$. Figure 3 shows $I_{g\max}$ versus $(1-t)^{1/2}$, constructed according to Ref. 24. It satisfies the relation presented. The effect of T, H, and I on v_c is qualitatively the same, so that under the action of a magnetic field applied to the sample the maximum of the generation current should shift into the region of weaker and weaker currents, as was observed in Ref. 24. The agreement between the dependences obtained experimentally in Refs. 23 and 24 and those predicted in the present paper presumes the existence of a region of gapless superconductivity near T_c and phase-slip centers in gapless superconductors.

It should be noted that the observation of the influence of the proximity effect on the generation of electromagnetic oscillations in superconducting films would confirm the above-presented estimates and arguments about the existence of a relation between non-Josephson generation and gapless superconductivity.

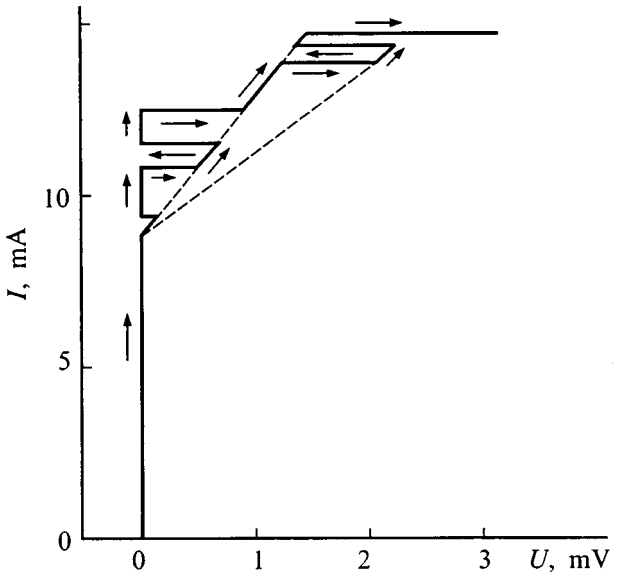

FIG. 3. Current $I_{g\max}$ corresponding to the maximum non-Josephson generation frequency versus the reduced temperature $t = T/T_c$ for a thin tin film. The plot was constructed according to the data of Ref. 22.

3. Thus, using a model in which normal-phase strips periodically form a wide superconducting indium film in a dynamic resistive state a qualitative and quantitative explanation was given for the behavior of IVCs, Josephson generation, and the appearance of a region of nonequilibrium superconductivity. The model is applicable for temperatures at which MSCSs appear, i.e. $t < 0.8$.[1–8] A transition into the resistive state occurs as a result of the penetration of Abrikosov vortices into the sample at high velocities and is characterized by the appearance of normal-phase strips along the trajectory of the vortices. The formation of normal-phase strips is due to the nonisothermal nature of the films, which is due to the poor heat removal from the sample. Phase-slip strips appear in measurements of IVCs in a constant-voltage regime. This distinguishes the model investigated from the model of phase-slip lines, which is applicable for $t > 0.8$.[25,26] According to this model, the motion of the vortices occurs under isothermal conditions, and the superconductor passes into a resistive state without the appearance of normal-phase strips. Isothermal conditions of motion of vortices in films and small deviations of the order parameter Δ from the equilibrium value $\Delta(T)$ at velocities of vortices $v_f \sim v_\tau = (D/\tau_\Delta)^{1/2}$, where $D = \xi^2(T)(1-T/T_c)(6\tau_\varepsilon)^{-1}$, $\tau_\Delta = \pi\Delta(T)\tau_\varepsilon T_c/8(T_c-T)$, and τ_ε is the energy relaxation time constant, were investigated in Refs. 25 and 26. An estimate for $\tau_\varepsilon \simeq 10^{-10}$ gives $v_L \simeq 10^2 v_f$.

In gapless superconductors or films in parallel magnetic fields, generation of electromagnetic oscillations can appear at temperatures close to T_c. The properties of this generation are identical to those of non-Josephson generation,

observed in thin tin or aluminum films near the critical temperature.[23,24]

It should also be noted that, when phase-slip strips form and electromagnetic oscillations are generated in superconducting films, very simple methods can be used to determine the recombination time of quasiparticles into pairs in ordinary and gapless superconductors and the phase diagram for superconductors similar to that predicted in Ref. 21 for an ergodic system.

[a)]E-Mail: root@isc.kharkov.ua

[1] A. A. Galkin, Yu. M. Ivanchenko, and V. F. Khirnyĭ, Fiz. Tverd. Tela (Leningrad) **20**, 1237 (1978) [Sov. Phys. Solid State **20**, 713 (1978)].
[2] Yu. M. Ivanchenko and V. F. Khirnyĭ, Fiz. Nizk. Temp. **4**, 969 (1978) [Sov. J. Low Temp. Phys. **4**, 465 (1978)].
[3] Yu. M. Ivanchenko and V. F. Khirnyĭ, in *Abstracts of Reports at the 20th All-Union Conference on Low-Temperature Physics* (Chernogolovka, 1978).
[4] Yu. M. Ivanchenko, V. F. Khirnyĭ, and P. N. Mikheenko, Zh. Éksp. Teor. Fiz. **77**, 952 (1979) [Sov. Phys. JETP **50**, 479 (1979)].
[5] Yu. M. Ivanchenko, P. N. Mikheenko, and V. F. Khirnyĭ, Zh. Éksp. Teor. Fiz. **80**, 161 (1981) [Sov. Phys. JETP **53**, 86 (1981)].
[6] Yu. M. Ivanchenko and P. N. Mikheenko, Zh. Éksp. Teor. Fiz. **82**, 488 (1982) [Sov. Phys. JETP **55**, 281 (1982)].
[7] Yu. M. Ivanchenko, Yu. V. Medvedev, and P. N. Mikheenko, Fiz. Tverd. Tela (Leningrad) **25**, 763 (1983) [Sov. Phys. Solid State **25**, 436 (1983)].
[8] Yu. M. Ivanchenko and P. N. Mikheenko, Zh. Éksp. Teor. Fiz. **83**, 684 (1982) [Sov. Phys. JETP **56**, 380 (1982)].
[9] Yu. M. Ivanchenko, P. N. Mikheenko, and Ya. I. Yuzhelevskiĭ, JETP Lett. **45**, 618 (1987).
[10] F. J. Rachford, S. A. Wolf, M. Nisenoff, and C. Y. Huang, Phys. Rev. Lett. **35**, 305 (1975).
[11] M. Tinkham, Phys. Rev. Lett. **13**, 804 (1964).
[12] R. P. Huebener, *Magnetic Flux Structures in Superconductors* (Springer–Verlag, Berlin, 1979; Mashinostroenie, Moscow, 1984).
[13] Yu. V. Medvedev and V. F. Khirnyĭ, Fiz. Tverd. Tela (Leningrad) **26**, 1163 (1984) [Sov. Phys. Solid State **26**, 705 (1984)].
[14] H. A. Notarys and J. E. Mercereau, Physica **55**, 424 (1971).
[15] *Tunneling Phenomena in Solids*, edited by E. Burstein and S. Lundquist (Plenum Press, N. Y., 1969; Mir, Moscow, 1973).
[16] A. I. D'yachenko, V. Yu. Tarenkov, and V. V. Stupakov, Zh. Éksp. Teor. Fiz. **82**, 1262 (1982) [Sov. Phys. JETP **55**, 734 (1982)].
[17] S. B. Kaplan, J. Low Temp. Phys. **37**, 343 (1979).
[18] V. L. Ginzburg, Dokl. Akad. Nauk SSSR **83**, 385 (1952); Zh. Éksp. Teor. Fiz. **34**, 113 (1958) [Sov. Phys. JETP **7**, 78 (1958)].
[19] A. A. Abrikosov and L. P. Gor'kov, Zh. Éksp. Teor. Fiz. **39**, 1781 (1960) [Sov. Phys. JETP **12**, 1243 (1961)].
[20] T. Oqushi and Y. Shibuya, J. Phys. Soc. Jpn. **32**, 400 (1972).
[21] P. G. de Gennes, *Superconductivity of Metals and Alloys* (W. A. Benjamin, Inc., N. Y. 1966; Mir, Moscow, 1968).
[22] K. Maki, in *Superconductivity*, edited by R. D. Parks (Marcel Dekker, Inc., N. Y., 1969), Vol. 2, Part 18, pp. 1035–1105.
[23] G. E. Churilov, D. A. Dikin, V. M. Dmitriev, and V. N. Svetlov, Fiz. Nizk. Temp. **15**, 994 (1989) [Sov. J. Low Temp. Phys. **15**, 550 (1989)].
[24] D. A. Dikin, G. E. Shurilov, V. N. Svetlov, and V. M. Dmitriev, Fiz. Nizk. Temp. **14**, 204 (1988) [Sov. J. Low Temp. Phys. **14**, 113 (1988)].
[25] L. I. Glazman, Fiz. Nizk. Temp. **12**, 688 (1975) [Sov. J. Low Temp. Phys. **12**, 389 (1975)].
[26] I. M. Dmitrenko, Fiz. Nizk. Temp. **22**, 849 (1996) [Low Temp. Phys. **22**, 648 (1996)].

Translated by M. E. Alferieff

Effect of normal electrons in superconductors on the current–voltage characteristic of a Josephson junction

V. P. Silin*) and A. V. Studenov

P. N. Lebedev Physics Institute, Russian Academy of Sciences 117924 Moscow, Russia
(Submitted September 11, 1998)
Fiz. Tverd. Tela (St. Petersburg) **41**, 582–587 (April 1999)

It is established that the conductivity of normal electrons in superconductors plays a large role in the current–voltage characteristic of a Josephson junction having a high critical current density, described on the basis of a nonlocal electrodynamics. It is shown in the resistive limit that the normal-electron contribution increases the current through the Josephson junction, while in the capacitive limit it decreases the contribution of Cherenkov resonances. © *1999 American Institute of Physics.* [S1063-7834(99)00504-3]

1. The present work is devoted to the development of a theory of current–voltage characteristics (IVCs) for Josephson junctions (JJs) having a comparatively high critical current density, such that

$$j_c > j_0 = \hbar c^2 (16\pi |e| \lambda^3)^{-1} \sim 10^4 \lambda^{-3}\,[\mathrm{A/cm^2}], \qquad (1)$$

where λ is the London length in microns. When the condition is satisfied, it turns out that JJs can be described on the basis of nonlocal electrodynamics.[1–3] There is an entire series of works on the theory of the IVCs for such JJs.[4–9] In Refs. 4–8 the resistive approximation was used corresponding to the junction capacitance playing a relatively small role compared to the junction conductivity. In Ref. 9 the theory of IVCs of JJs having a comparatively high critical current density was extended to the range of junction parameters such that the capacitance of the junction plays an important role. For a ring-shaped junction in Ref. 9, the excitation of short-wavelength generalized Swihart waves (see, for example, Refs. 2 and 10) is taken into account. The possibility of the existence of such waves is determined completely by the capacitance of the JJ. On the other hand, in Ref. 9 the stationary level of resonance Cherenkov excitation of generalized Swihart waves was determined by the conductivity of the junction. After Ref. 11 was published, it became clear that resistive effects are not taken into account completely in the nonlocal Josephson electrodynamics in Refs. 4–9, since in these works the conductivity of the normal electrons of the superconductors was completely neglected. Such conductivity is obviously negligible only at sufficiently low temperatures at which there are virtually no normal electrons. Later, the conditions under which the role of normal electrons in the description of the IVCs of JJs is decisive were determined. It turns out in the resistive limit, where the conductivity of the normal electrons of superconductors is more important than the conductivity of the contact layer of a JJ, the current through the junction is higher than that obtained in Refs. 4–6. Conversely, the conductivity of the normal electrons decreases the amplitude of the envelope of the excitation resonances of short-wavelength generalized Swihart waves. Finally, the exponential law describing the increase in the contribution of Cherenkov resonances to the current remains the same as the law established in Ref. 9. The latter is associated with the spectral properties of the quasistationary vortex structure, which travels with a low velocity and possesses a nonzero average magnetic field. This structure was found in Ref. 12 and it was used in both Ref. 9 and the present work to describe the vortex state in a JJ.

2. Our starting point is the following integrodifferential equation (compare Ref. 11) for the phase difference φ between the wave functions of cooper pairs on different sides of a junction:

$$\frac{1}{\omega_j^2}\frac{\partial^2\varphi}{\partial t^2} + \frac{\beta}{\omega_j^2}\frac{\partial\varphi}{\partial t} + \sin\varphi = \frac{l}{\pi}\int_{-\infty}^{+\infty}\frac{d\zeta}{\zeta - z}\left(\frac{\partial}{\partial\zeta} + \alpha\frac{\partial^2}{\partial t\,\partial\zeta}\right)\varphi(\zeta,t), \qquad (2)$$

$$\omega_j^2 = \frac{16\pi|e|j_c d}{\hbar\varepsilon}, \quad \beta = \frac{4\pi\sigma}{\varepsilon},$$

$$\alpha = \tau\frac{n_n}{n_s}, \quad l = \frac{\lambda_j^2}{\lambda} = \frac{\hbar c^2}{16\pi|e|j_c\lambda^2}, \qquad (3)$$

where ω_j and λ_j are, respectively, the Josephson frequency and length, β and α characterize the dissipation, σ is the conductivity of the JJ, ε is the permittivity of the material of the nonsuperconducting layer of thickness $2d$ separating identical bulk superconductors, λ is the London length, n_n and n_s are, respectively, the density of normal and superconducting electrons in the superconductor, and τ is the effective free flight time of a normal electron in the superconductor. It is also assumed that $d \ll \lambda$.

The equation (2) holds under the conditions (1) and when the characteristic scale of vortex states of interest to us is small compared to the London length. The achievement made in Ref. 11 is taking account of the last term on the right-hand side of Eq. (2), which is proportional to α.

We shall use the solution $\varphi_0(z)$ of the equation

$$\sin\varphi_0(z)=\frac{l}{\pi}\int_{-\infty}^{+\infty}\frac{d\zeta}{\zeta-z}\frac{d\varphi_0(\zeta)}{d\zeta}. \tag{4}$$

Next we seek the solution of Eq. (2) in the form of a wave traveling with velocity v

$$\varphi(z,t)=\varphi_0(z-vt)+\varphi_1(z-vt),\quad z-vt\equiv s. \tag{5}$$

We assume φ_1 to be a small perturbation compared with φ_0, which makes it possible to linearize the problem. Moreover, we shall employ the approximation $\varphi_1\cos\varphi_0\to\varphi_1$, based on the smallness of this term, which is due to the inequality

$$\frac{v^2}{\omega_j^2}\frac{d^2\varphi_1}{ds^2}\gg\varphi_1. \tag{6}$$

As a result, we obtain the following comparatively simple equation for φ_1

$$\frac{v^2}{\omega_j^2}\frac{d^2\varphi_1}{ds^2}-\frac{\beta v}{\omega_j^2}\frac{d\varphi_1}{ds}+\varphi_1-\frac{1}{\pi}\int_{\infty}^{+\infty}\frac{d\eta}{\eta-s}\left(\frac{d\varphi_1}{d\eta}-\alpha v\frac{d^2\varphi_1}{d\eta^2}\right)=-\frac{v^2}{\omega_j^2}\frac{d^2\varphi_0}{ds^2}+\frac{\beta v}{\omega_j^2}\frac{d\varphi_0}{ds}-av\frac{l}{\pi}\int_{-\infty}^{+\infty}\frac{d\eta}{\eta-s}\frac{d^2\varphi_0(\eta)}{d\eta^2}. \tag{7}$$

As the solution of Eq. (4) we use the result of Ref. 12

$$\varphi_0(s)=\pi+2\tan^{-1}\left(\frac{\tan[s/2L]}{\tanh[a/2]}\right), \tag{8}$$

where $\sinh a=l/L$. This solution is a periodic train of waves which corresponds to a periodic train of magnetic vortices with nonzero average magnetic field

$$H_y(x,s)=-\frac{\Phi_0}{2\pi L}\left\{\frac{\exp[-(\pm x-d)\lambda^{-1}]}{2\lambda+2d}+\frac{L}{2\lambda^2}\left[\frac{\pm x-d}{L}+\sinh^{-1}\frac{l}{L}-\ln\left(2\left[\sqrt{1+\frac{l^2}{L^2}}\cosh\left(\frac{\pm x-d}{L}\right)+\frac{l}{L}\sinh\left(\frac{\pm x-d}{L}\right)-\cos\frac{s}{L}\right]\right)\right]\right\}. \tag{9}$$

The $\pm$ signs correspond to regions on different sides of the junction, and the junction thickness $2d$ is retained for clarity.

According to Eq. (8) we have

$$\frac{d\varphi_0}{ds}=\frac{1}{L}\frac{\sinh a}{\cosh a-\cos(s/L)}=\frac{1}{L}\left(1+2\sum_{n=1}^{\infty}\exp[-na]\cos\frac{ns}{L}\right), \tag{10}$$

$$\frac{d^2\varphi_0}{ds^2}=-\frac{2}{L^2}\sum_{n=1}^{\infty}n\exp[-na]\sin\frac{ns}{L}. \tag{11}$$

Substituting the expressions (10) and (11) into Eq. (7) and using the relations (see, for example, Ref. 13, p. 178)

$$\frac{1}{\pi}\int_{-\infty}^{+\infty}\frac{d\eta}{\eta-s}\sin\frac{n\eta}{L}=\cos\frac{ns}{L},\qquad\frac{1}{\pi}\int_{-\infty}^{+\infty}\frac{d\eta}{\eta-s}\cos\frac{n\eta}{L}=-\sin\frac{ns}{L}, \tag{12}$$

it is easy to show that the solution of Eq. (7) has the form

$$\varphi_1(s)=\varphi_{10}+\sum_{n=1}^{\infty}\left(A_n\cos\frac{ns}{L}+B_n\sin\frac{ns}{L}\right), \tag{13}$$

where

$$\varphi_{10}=(\beta v/\omega_j^2L), \tag{14}$$

$$A_n=\frac{2\exp(-na)\omega_n^2(\beta v/L)[1+(l\alpha\omega_j^2n/\beta L)]}{[\omega_n^2-(nv/L)^2]^2+(\beta vn/L)^2[1+(l\alpha\omega_j^2n/\beta L)]^2}, \tag{15}$$

$$B_n=\frac{2}{n}\exp(-na)\left\{-1+\frac{\omega_n^2[\omega_n^2-(nv/L)^2]}{[\omega_n^2-(nv/L)^2]^2+(\beta vn/L)^2[1+(l\alpha\omega_j^2n/\beta L)]^2}\right\}. \tag{16}$$

Here

$$\omega_n^2=\omega_j^2\left(1+\frac{nl}{L}\right), \tag{17}$$

which corresponds to the spectrum of short-wavelength generalized Swihart waves with wave number n/L. The Cherenkov resonance excitation of harmonics with number n_r is determined by the condition

$$\omega_{n_r}^2\equiv\omega_j^2\left(1+\frac{n_rl}{L}\right)=\frac{n_r^2v_r^2}{L^2}. \tag{18}$$

We have

$$A_{n_r}=\frac{2v_e\exp(-n_ra)}{\beta L[1+(l\alpha\omega_j^2n_r/\beta L)]}, \tag{19}$$

$$B_{n_r}=-\frac{2}{n_r}\exp(-n_ra). \tag{20}$$

Next we assume that l is the characteristic scale of the Abrikosov–Josephson (AJ) vortices and is small compared with the periodicity scale L of the vortex structure. On the other hand, for small values of velocity v of the vortex structure the resonance condition (18) holds for quite large resonance numbers n_r. For this reason, we assume below that

$$n_r\gg(L/l)\gg1. \tag{21}$$

Then, under the condition (1) the inequality $n_r\gg(L/\lambda)$ also holds automatically. Hence the resonance condition (18) can be written in the form

$$n_r=\frac{\omega_j^2 Ll}{v_r^2}. \tag{22}$$

Then we obtain in accordance with Eq. (21)

$$v\ll l\omega_j. \tag{23}$$

For our approach to be applicable the condition

$$\varphi_0\gg\varphi_1. \tag{24}$$

must hold.

According to Eq. (21), the expression (20) obviously corresponds to the condition (24). Therefore the condition (24) reduces to the condition that the quantity (19) is small:

$$\frac{2v_r\exp(-n_rl/L)}{\beta L+l\alpha\omega_j^2 n_r}\ll 1. \tag{25}$$

At the same time for

$$\frac{v_r}{\beta L+l\alpha\omega_j^2 n_r}\gg 1 \tag{26}$$

and $v=v_r$ the inequality

$$\left[\frac{n\beta v}{L}\left(1+\frac{\alpha n\omega_j^2 l}{\beta L}\right)\right]^2\ll\left(\omega_n^2-\frac{n^2v^2}{L^2}\right),\quad n\neq n_r, \tag{27}$$

will be satisfied and the resonance dependences can be assumed to be ''sharp,'' while the nonresonance contribution can be completely eliminated, since it will be negligible.[9]

When the condition (26) holds, the contribution of B_{n_r} (20) to the resonance term can be neglected compared with A_{n_r} (19). Finally, we obtain for $v=v_r$

$$\varphi_{n_r}=\frac{2v_r\exp(-n_rl/L)}{\beta L+\alpha l\omega_j^2 n_r}\cos\frac{n_rs}{L}. \tag{28}$$

It is obvious that on account of the inequality (21) the condition (6) holds for φ_{n_r}.

It is easy to show that near a resonance, i.e. if

$$|v-v_r|<\frac{1}{2}\Delta v_r=\frac{v_r}{4n_r}\ll v_r,$$

where Δv_r is the distance between neighboring resonances (Ref. 19) [*sic*], the condition (27) holds. Then for the contribution to (13) at $n=n_r$ we have

$$\varphi_{n_r}(s)=\frac{2v_r\exp\left(-\frac{n_rl}{L}\right)\left\{(\beta L+l\alpha\omega_j^2 n_r)\cos\frac{n_rs}{L}-[2n_r(v-v_r)]\sin\frac{n_rs}{L}\right\}}{[\beta L+l\alpha\omega_j^2 n_r]^2+[2n_r(v-v_r)]^2}. \tag{29}$$

Since only one resonance appears as each resonance is approached, the expression (29) can be written as a function of the velocity of the moving vortex structure (8). We shall use Eq. (22), and we retain the resonance velocity v_r only in ''sharp'' resonance dependences. Then we have

$$\varphi_1(s)\approx\varphi_{10}+\frac{2v}{L}\exp\left(-\frac{v_0^2}{v^2}\right)$$
$$\times\frac{\left\{\left(\beta+\frac{\alpha\omega_j^2v_0^2}{v^2}\right)\cos\frac{n_rs}{L}-\left[\frac{2v_0\omega_j(v-v_r)}{v^2}\right]\sin\frac{n_rs}{L}\right\}}{[\beta+\alpha\omega_j^2v_0^2/v^2]^2+[2v_0\omega_j(v-v_r)/v^2]^2}. \tag{30}$$

Here $v_0\equiv l\omega_j$ is the characteristic velocity arising in the extremely nonlocal limit of the theory of JJs for high critical current densities.

3. To obtain the IVC we shall examine the energy balance in the JJ through which a constant and spatially uniform current density j flows and in which a slowly varying vortex structure is present. We shall conduct the further analysis in such a way that it is also applicable for a ring-shaped JJ with radius R, where periodic boundary conditions can be used to describe the vortex structure and the perturbation field φ_1.

For a wave structure traveling with velocity v, the rate of change of the energy, determined by the current density j is given by the relation

$$\left(\frac{dE}{dt}\right)_j=\frac{\hbar jv}{2|e|}\int_0^{2\pi R}ds\frac{d\varphi}{ds}. \tag{31}$$

The contribution of the perturbation φ_1 to this expression is zero, and the contribution of the traveling vortex structure (8) is

$$\left(\frac{dE}{dt}\right)_j=\frac{\hbar jv}{2|e|}\frac{\pi R}{L}. \tag{32}$$

If a ring-shaped junction contains m vortices, each carrying one quantum of magnetic flux $\Phi_0=\pi\hbar c/|e|$, then

$$L=R/m. \tag{33}$$

The rate of the dissipative decrease of energy is given by the formula

$$\frac{dE}{dt}=-\frac{\hbar j_c}{2|e|}\int_0^{2\pi R}ds\left\{\frac{\beta v^2}{\omega_j^2}\left(\frac{d\varphi}{ds}\right)^2-\frac{l\alpha v^2}{\pi}\left(\frac{d\varphi}{ds}\right)\int_{-\infty}^{+\infty}\frac{d\eta}{\eta-s}\frac{d^2\varphi}{d\eta^2}\right\}. \tag{34}$$

Correspondingly, we have for the rate of decrease of the energy of the main vortex structure (8)

$$\frac{dE_0}{dt}=-\frac{\hbar j_c}{|e|}\frac{\pi R v^2}{Ll}\left\{\frac{\beta}{\omega_j^2}\cosh a\frac{\alpha}{2}\right\}. \tag{35}$$

Hence we obtain in the limit $l\ll L$

$$\frac{dE_0}{dt}=-\frac{\hbar j_c}{|e|}\frac{\pi R v^2}{Ll}\left[\frac{\beta}{\omega_j^2}+\frac{\alpha}{2}\right]. \tag{36}$$

Finally, for the rate of decrease of the energy of the resonantly excited wave described by Eq. (30) we obtain

$$\frac{dE_1}{dt}=-\frac{\hbar j_c}{|e|}\frac{2\pi R v^2 v_0^2}{L^2}\times\frac{[\beta v^2+\alpha\omega_j^2 v_0^2]\exp(-2v_0^2/v^2)}{[\beta v^2+\alpha\omega_j^2 v_0^2]^2+4\omega_j^2 v_0^2(v-v_r)^2}. \tag{37}$$

The balance of the three contributions to the rate change of the energy (32), (36), and (37) permits writing the following relation between the current density j and the velocity v of the vortex structure (8):

$$\frac{j}{j_c}=\frac{v}{l}\left[\frac{\beta}{\omega_j^2}+\frac{\alpha}{2}\right]+\frac{2v_0^2 v}{L}\times\frac{[\beta v^2+\alpha\omega_j^2 v_0^2]\exp(-2v_0^2/v^2)}{[\beta v^2+\alpha\omega_j^2 v_0^2]^2+4\omega_j^2 v_0^2(v-v_r)^2}. \tag{38}$$

We recall that Eq. (2) is obtained assuming that $\alpha\omega\ll 1$, where ω are the characteristic frequencies of the problem. For the resonance term arising in our analysis this condition assumes the form $\alpha\omega_{n_r}=\alpha l\omega_j^2/\nu_r$ and holds by virtue of the inequality (26).

It is easy to note that the expression (38) holds not only for a ring-shaped JJ but also for the case where the JJ can be regarded as infinite and containing a vortex structure with period $2\pi L$. For this reason, in the analysis below we shall not use the equality (33), which gives in Eq. (38) the dependence on the number of vortices m in the ring, and we shall simply talk about the period of the vortex structure $2\pi L$.

4. The velocity v is related to the static potential difference on the JJ

$$V=-\frac{\hbar}{2|e|}\left\langle\frac{\partial\varphi}{\partial t}\right\rangle, \tag{39}$$

where the averaging is over the time. On averaging a nonzero contribution arises only from φ_0. Therefore

$$V=\frac{\hbar v}{2|e|L}. \tag{40}$$

For this reason it follows from Eq. (38) that

$$\frac{j}{j_c}=V\frac{2|e|L}{\hbar}\left\{\left[\frac{\beta}{\alpha_j^2}+\frac{\alpha}{2}\right]\frac{1}{l}+\frac{2V_0^2[\beta V^2+\alpha\omega_j^2V_0^2]\exp(-2V_0^2/V^2)}{L\{[\beta V^2+\alpha\omega_j^2V_0^2]^2+4\omega_j^2V_0^2[V-V_r]^2\}}\right\}. \tag{41}$$

In this case

$$|V-V_r|<\Delta V_r/2\equiv V_r/4n_r\ll V_r.$$

Here

$$V_0=\frac{\hbar v_0}{2|e|L}=\frac{100}{L}\sqrt{\frac{d}{\lambda\varepsilon}\frac{j_0}{j_c}}[\mu\mathrm{V}], \tag{42}$$

$$V_r=\frac{\hbar v_r}{2|e|L}=\frac{\hbar\omega_j}{2|e|}\sqrt{\frac{l}{n_r l}}=\frac{100}{L}\sqrt{\frac{dL}{\lambda^2\varepsilon n_r}}[\mu\mathrm{V}], \tag{43}$$

where L is in millimeters.

We recall that the resonance contribution to Eq. (38) was obtained assuming that the inequalities (23), (25), and (26) hold for the velocity v of the vortex structure. For this reason, for the resonance contribution we have in Eq. (41) the following conditions for the potential difference V:

$$V\ll V_0, \tag{44}$$

$$\frac{2|e|}{\hbar}\frac{V}{[\beta+\alpha\omega_j^2(V_0/V)^2]}\gg 1, \tag{45}$$

$$\frac{4|e|}{\hbar}\frac{V}{[\beta+\alpha\omega_j^2(V_0/V)^2]}\exp\left(-\frac{V_0^2}{V^2}\right)\ll 1. \tag{46}$$

Neglecting the losses of the resonantly excited waves, which is reasonable for low voltages (see Fig. 1), Eq. (41) gives

$$j=V\frac{2|e|L}{\hbar l}\left[\frac{\beta}{\omega_j^2}+\frac{\alpha}{2}\right]j_c\equiv\frac{V}{R_{\mathrm{eff}}}. \tag{47}$$

The contribution, arising in this case, of the losses in the transitional layer and in the superconductors is additive. Of course, at low temperatures, where α decreases exponentially, the effect we are discussing is small. Conversely, near T_c where

$$\alpha\gg 2\beta/\omega_j^2, \tag{48}$$

the losses in the superconductors due to normal electrons become determining.

As voltage increases, losses to resonantly excited waves become important. The envelope of such resonance contributions is described by the law

$$\frac{j}{j_c}=V\frac{2|e|L}{\hbar}\left\{\left[\frac{\beta}{\omega_j^2}+\frac{\alpha}{2}\right]\frac{1}{l}+\frac{2V_0^2}{L}\frac{\exp(-2V_0^2/V^2)}{[\beta V^2+\alpha\omega_j^2V_0^2]}\right\}. \tag{49}$$

Hence it follows, specifically, that in contrast to the low-voltage limit (47), when the conductivity of normal electrons

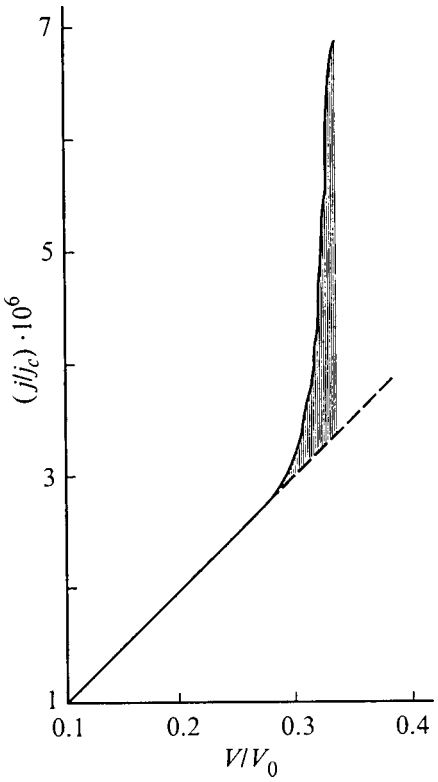

FIG. 1. IVC of a Josephson junction with $(j_c R_\alpha/V_0)=10^7$ ($\sigma_n \sim 10^{10}\ \mathrm{s}^{-1}$), $l/L=10^{-2}$.

decreases the effective resistance R_{eff}, in the region of the nonlinear IVC the normal-electron conductivity decreases the current.

In the limit (48) Eq. (49) assumes the form

$$\frac{j}{j_c}=V\frac{|e|L}{\hbar}\left\{\frac{\alpha}{l}+\frac{4}{\alpha\omega_j^2 L}\exp(-2V_0^2/V^2)\right\} \tag{50}$$

or

$$\frac{j}{j_c}=\frac{V}{R_\alpha j_c}\frac{L}{l}\left\{1+\frac{j_c^2R_\alpha^2}{V_0^2}\frac{l^3}{L^3}\exp\left(-\frac{2V_0^2}{V^2}\right)\right\}, \tag{51}$$

where

$$R_\alpha=\frac{\hbar}{|e|\alpha j_c}. \tag{52}$$

The conditions (44)–(46) give

$$V\ll V_0, \tag{53}$$

$$\frac{j_c R_\alpha V^3 l^2}{2V_0^4 L^2}\gg 1, \tag{54}$$

$$\frac{R_\alpha j_c V^3 l^2}{V_0^4 L^2}\exp\left(-\frac{V_0^2}{V^2}\right)\ll 1. \tag{55}$$

We note that the preexponential factor in Eq. (51) is large compared to one in accordance with Eq. (54) and the conition $l\ll L$.

Figure 1 shows the voltage dependence of the current density in accordance with the envelope (51).

At low voltages the current density is a linear function of the voltage. At high voltages the linear dependence is replaced by a sharp exponential dependence.

5. Let us now discuss the importance of the contribution due to the normal electrons of superconductors to the IVC of a Josephson junction having a high critical current density (41). This contribution is decisive compared to the contribution due to the conductivity of a Josephson junction, if the condition (48) holds. The latter condition can be written, according to Eqs. (3) and (1), as

$$\alpha\gg\frac{2\beta}{\omega_j^2}=\frac{8\pi\sigma\lambda^3}{c^2 d}\left(\frac{j_0}{j_c}\right). \tag{56}$$

Since $\alpha=(n_n/n_s)\tau=(4\pi\sigma_n\lambda^2/c^2)$, where $\sigma_n=e^2 n_n\tau/m$ is the conductivity of the normal electrons in the superconductors, the condition (6) reduces to the inequality

$$\sigma_n\gg\sigma(j_0/j_c)(2\lambda/d). \tag{57}$$

We shall show how the normal electrons influence the superconductor on the linear sections of the IVC (49), which is described by the expression (47).

We note first that the IVCs obtained in Refs. 4–6 and 9, where the contribution of the normal electrons was neglected and the slope of the IVC was determined only by the losses in the transitional layer, are realized for conductivities σ of the Josephson junction that are high enough so that the inequality opposite to Eq. (57) holds.

Conversely, when the contribution due to the normal electrons of the superconductors is important, i.e. when the inequality (57) is satisfied, the IVC [see Eqs. (47) and (51)]

$$j=\frac{V}{R_\alpha}\frac{L}{l} \tag{58}$$

is realized.

It is important to note that the current density corresponding to the IVC (58) is higher than that indicated previously in Refs. 4–6 and 9, where the contribution of the normal electrons was neglected.

We shall now discuss the role of the normal electrons of the superconductors in the description of the nonlinear section of the IVC (49), associated with the resonance excitation of waves. We shall consider the situation where the normal electrons are decisive, i.e. we shall assume that the inequality (57) holds. Then we have, specifically, the IVC (51). We shall show that the conductivity of the normal electrons must be sufficiently small in order for the exponential section of the IVC (51) to appear.

The deviation from linearity in Eq. (51) first appears at voltages

$$V_m\sim V_0/\sqrt{\ln[(j_c R_\alpha/V_0)(l/L)^{3/2}]}. \tag{59}$$

The requirement (53) that V_m be small compared with V_0 obviously holds if V_m satisfies the condition (54), which requires that dissipation be small. Requiring the condition (54) to hold for V_m, we obtain the following inequality for the normal-electron conductivity σ_n:

$$\left(\frac{j_0\lambda}{j_cL}\right)^{3/2}\frac{c}{4\pi\sigma_n\lambda}\sqrt{\frac{\varepsilon L}{d}}\gg\ln^{3/2}\left[\left(\frac{j_0\lambda}{j_cL}\right)\frac{c}{2\pi\sigma_n\lambda}\sqrt{\frac{\varepsilon L}{d}}\right]. \tag{60}$$

Using our assumption (see Eq. (21)) that the characteristic scale l of the AJ vortices is small compared with the period L of the structure, i.e. $l/L=(\lambda j_0/Lj_c)\ll 1$, the following condition for σ_n to be small can be derived from the inequality (60):

$$\sigma_n\ll\frac{c}{4\pi\lambda}\left(\frac{\lambda j_0}{Lj_c}\right)^{3/2}\sqrt{\frac{\varepsilon L}{d}}\Bigg/\ \ln^{3/2}\left(2\sqrt{\frac{Lj_c}{\lambda j_0}}\right). \tag{61}$$

So, for an exponential section to appear in the IVC (51) σ_n must not be too large, as in Eq. (61), and the linear section of the IVC (51) appears when σ_n is large (57). Therefore the IVC (51) obtains for the normal-electron conductivity satisfying the inequality

$$\sigma\frac{j_0}{j_c}\frac{2\lambda}{d}\ll\sigma_n\ll\frac{c}{4\pi\lambda}\left(\frac{\lambda j_0}{Lj_c}\right)^{3/2}\sqrt{\frac{\varepsilon L}{d}}\Bigg/\ \ln^{3/2}\left(2\sqrt{\frac{Lj_c}{\lambda j_0}}\right). \tag{62}$$

The simultaneous satisfaction of the left- and right-hand inequalities in Eq. (62) leads to the following condition for the conductivity σ of a Josephson junction to be small:

$$\sigma\ll\frac{c}{8\pi L}\sqrt{\frac{\varepsilon d j_0}{\lambda j_c}}\Bigg/\ \ln^{3/2}\left(2\sqrt{\frac{Lj_c}{\lambda j_0}}\right). \tag{63}$$

As an illustration, we estimate, following from the inequality (63), the conductivity σ of a Josephson junction for which the IVC (51) is observed. Let $\varepsilon=10$, $d/L=10^{-5}$, $j_c=5j_0$, and $\lambda/L=10^{-2}$. Then we obtain from Eq. (63) (compare Ref. 9)

$$\lambda\sigma\ll 10^9, \tag{64}$$

where σ is measured in s^{-1} and λ in μm.

Summarizing, it has been established for the first time that the conductivity of the normal electrons in superconductors have a decisive influence on the current-voltage characteristics of Josephson junctions having a high critical current density. It should be underscored that this influence holds for very low current densities through the JJ and for very low voltages.

This work was supported by the National Council on High-Temperature Superconductors (project ''AD'' No. 95008) as part of project No. 96-02-1703 of the Russian Fund for Fundamental Research and with the State Support of Leading Scientific Schools (No. 96-15-96750).

*)E-mail: silin@sci.lebedev.ru

[1] G. M. Lapir, K. K. Likharev, L. A. Maslova, and V. K. Semenov, Fiz. Nizk. Temp. **1**, 1235 (1975) [Sov. J. Low Temp. Phys. **1**, 590 (1975)].
[2] Yu. M. Aliev, V. P. Silin, and S. A. Uryupin, Sverkhprovodimost: Fiz., Khim., Tekh. **5**, 228 (1992).
[3] A. Gurevich, Phys. Rev. B **46**, 3187 (1992).
[4] M. Yu. Kupriyanov, K. K. Likharev, and A. K. Semenov, Fiz. Nizk. Temp. **2**, 706 (1976) [Sov. J. Low Temp. Phys. **2**, 346 (1976)].
[5] A. Gurevich, Phys. Rev. B **48**, 12857 (1993).
[6] V. P. Silin, JETP Lett. **60**, 460 (1994).
[7] G. A. Alfimov and V. P. Silin, Zh. Éksp. Teor. Fiz. **108**, 1668 (1995) [JETP **81**, 915 (1995)].
[8] V. P. Silin and S. A. Uryupin, Zh. Éksp. Teor. Fiz. **108**, 2163 (1995) [JETP **81**, 1179 (1995)].
[9] V. P. Silin and A. V. Studenov, Zh. Éksp. Teor. Fiz. **113**, 2148 (1998) [JETP **86**, 117 (1998)].
[10] R. G. Mints, J. Low Temp. Phys. **106**, 183 (1997).
[11] Zh. D. Genchev and V. I. Vas'kivskiĭ, Zh. Éksp. Teor. Fiz. **113**, 955 (1998) [JETP **86**, 521 (1998)].
[12] G. L. Alfimov and V. P. Silin, Zh. Éksp. Teor. Fiz. **106**, 671 (1994) [JETP **79**, 369 (1994)].
[13] *Tables of Integral Transforms (Bateman Manuscript Project)*, edited by A. Erdélyi (McGraw-Hill, N. Y., 1954; Nauka, Moscow, 1970), Vol. 2.

Translated by M. E. Alferieff

Study of $YBa_2Cu_3O_{7-x}$ films at various stages of their growth by medium-energy ion scattering

V. V. Afrosimov, R. N. Il'in, V. I. Sakharov, I. T. Serenkov, and D. V. Yanovskiĭ

A. F. Ioffe Physicotechnical Institute, Russian Academy of Sciences, 194021 St. Petersburg, Russia

S. F. Karmanenko and A. A. Semenov

St. Petersburg State Electrical-Engineering University, 197376 St. Petersburg, Russia
(Submitted September 16, 1998)
Fiz. Tverd. Tela (St. Petersburg) **41**, 588–595 (April 1999)

The initial stages in the formation and growth of yttrium-barium cuprate films have been studied in the course of magnetron sputtering of a ceramic target by combining medium-energy-ion scattering (MEIS) and scanning-electron microscopy. The growth mechanisms of $YBa_2Cu_3O_{7-x}$ films on MgO and substrates having the perovskite structure, $SrTiO_3$ and $LaAlO_3$, at deposition temperatures of 700–780 °C and $(Ar+O_2)$ pressure of ~70 Pa were found to be essentially different. Simulation of MEIS spectra (H^+ or He^+ ions with initial energies of 150–250 keV) and comparison of these results with experimental data revealed that in the first case a film forms from pyramid-shaped islands and, in the second, it grows by a two-dimensional layer-by-layer process starting practically with the first monolayer. For the island mechanism, MEIS permitted determination of the substrate surface coverage and showed the growth of the $YBa_2Cu_3O_{7-x}$ phase to be paralleled by formation of epitaxial nuclei of a Cu_2O phase. After the first, initial stage in the film formation, the second stage, regular growth within reduced thicknesses of 7–15 nm, sets in. This stage is characterized by a practically complete coverage of the substrate and a stable composition. The third stage, regular growth, of an apparently helical nature, was observed to set in at thicknesses above 100 nm. In this stage, the quality of film structure in the bulk and on the surface was found to be somewhat inferior to that of $YBa_2Cu_3O_{7-x}$ single crystals and did not depend on substrate type. [S1063-7834(99)00604-8]

The high-T_c superconductor $YBa_2Cu_3O_{7-x}$ (YBCO) grown in thin films on various insulating substrates remains a basic material of modern cryoelectronics.[1] For this reason, studies of the initial and subsequent stages in the growth of YBCO thin films are not only of basic scientific but of applied interest as well. As follows from investigation of the nature of film growth on various substrates, if the lattice mismatch between the film and the substrate is small enough, the growth starts in a layer-by-layer pattern whereas, if the mismatch is large, islands form[2,3] and the growth pattern may vary depending on the substrate temperature.[3] In the very early stages of the growth, foreign phases, whose concentration varied in a nonmonotonic manner, were observed to nucleate.[4] In later stages, a spiral pattern of growth was revealed in many cases.[5]

The structure of films was studied primarily by electron and atomic-force microscopy. While these methods provide detailed information on specific small parts of film area having dimensions of 10–1000 nm, they are not capable of evaluating macroscopic parts of the film as a whole. Information on the initial stages of growth and the film structure profile averaged over an area of a few mm^2 can be obtained by medium-energy ion scattering (MEIS).[6,7] In contrast to the traditional Rutherford backscattering method, using ions with energies of the order of 10^5 eV and electrostatic analyzers provides a better depth resolution and, as shown in Ref. 6, offers a possibility of studying film growth at thicknesses of up to a few nm.

The objective of this work was to investigate the growth pattern and structural perfection of YBCO films, from their nucleation to thicknesses of a fraction of a μm, depending on the type of substrate and its temperature during the growth, using for this purpose the MEIS and scanning electron microscopy.

1. EXPERIMENTAL TECHNIQUES

The YBCO films were grown by magnetron sputtering of a ceramic target with stoichiometric composition in an $Ar–O_2$ ambient at a pressure of ~70 Pa and substrate temperature 700–780 °C.[8] As substrates one used (100)-oriented plates of MgO, $LaAlO_3$ (LAO), and $SrTiO_3$ (STO) single crystals, and MgO single crystals coated by a $Ba_xSr_{1-x}TiO_3$ layer with $x \approx 0.3$ (BSTO). Two groups of films were prepared, namely, ultrathin, less than 20 nm in thickness, and thin ones, with a thickness of 100–450 nm.

MEIS studies of the films were carried out on the setup described elsewhere.[9] One analyzed the energy distribution of H^+ or He^+ ions with initial energies of 100–200 keV scattered through an angle Θ by interaction of the primary beam with the sample. The analysis was performed with ei-

ther an electrostatic analyzer (ESA) providing a resolution $\Delta E/E=0.005$ at $\Theta=120°$, or a semiconductor detector with $\Delta E=4$ keV at $\Theta=150°$, with the beam operated in a random mode or under channeling conditions along the [001] substrate axis. In these operating modes, one measured the dependence of the yield of scattered ions on their energy, $Y_r(E)$ and $Y_c(E)$, respectively. The measured ratio $\chi(E)=Y_c(E)/Y_r(E)$, called the relative yield, characterized the structural perfection of the samples studied.

For thin films, one determined the superconducting transition temperature T_c from four-probe resistive measurements.

2. SIMULATION OF MEIS SPECTRA

The film thickness and composition, as well as the substrate coverage by the film, were determined by varying the parameters so as to obtain the best fit of the calculated to experimental spectra.[10] The data on the absorption cross sections and straggling were selected from an analysis of a large number of experimental and theoretical works. The film thickness h was calculated as the total number of atoms of the corresponding composition per 1 cm^2 and converted to the linear dimension (in nm) assuming ideal packing.

In studies of ultrathin films, where the effect of energy straggling on the shape of the low-energy tail is small, one can estimate the nonuniformity of film thickness, a particularly essential point when considering the island pattern of growth. A rigorous description of the spectrum requires in this case determination of the shape of the islands and their size distribution.[11] To obtain such experimental information, one has to treat statistically a large array of data acquired in surface studies by tunneling and atomic-force microscopy. The use of these methods permitted one (see, e.g., Refs. 12 and 13) to determine that the nuclei of the YBCO phase on a LAO or MgO substrate may take on various shapes, depending on the actual deposition regime chosen, from a plane monatomic disk to a stepped spiral (screw dislocation). Concurrently obtaining information on the distribution of nuclei according to shape and size over an extended surface area meets with grave difficulties, so that this work made use of a procedure described below based on a normal distribution.

The film surface relief and the shape of formations appearing during island growth conditions were described by setting a surface-area distribution function in thickness of the form

$$f(X)=\frac{dS}{dX}=(2\pi)^{-1/2}\sigma^{-1}\times\exp\left(-\frac{(X-X_0)^2}{2\sigma^2}\right)\left[0.5+G\left(\frac{X_0}{\sigma}\right)\right]^{-1}, \quad (1)$$

where dS is the fraction of surface area corresponding to film portions with a thickness varying from X to $X+dX$, X_0 and σ are variable parameters of the distribution, and function G is defined in the following way:

$$G(z)=(2\pi)^{-1/2}\int_0^z \exp\left(-\frac{x^2}{2}\right)dx. \quad (2)$$

Based on the distribution function (1), one can readily find the average film thickness h over the film-coated portions of the substrate:

$$h=\int_0^\infty Xf(X)dX=X_0+(2\pi)^{-1/2}\sigma\times\exp\left(-\frac{X_0^2}{2\sigma^2}\right)\left[0.5+G\left(\frac{X_0}{\sigma}\right)\right]^{-1}. \quad (3)$$

The parameters X_0 and σ were chosen by simulating the part of the $Y_r(E)$ spectrum corresponding to the film, and the substrate coverage by the film was derived from the ratio of the film to substrate signals in the same spectrum. Next the film was described by the values of the film thickness obtained from Eq. (3) and of the thickness scatter σ. Note that, if the substrate is not fully covered by the film, the spectrum will contain a signal from the uncoated surface, which likewise can be described in a model curve by properly varying the parameters.

Using MEIS in combination with the channeling regime to probe films more than 100 nm thick enabled estimation of the dechanneling rate of the probing beam with increasing depth of its penetration $\chi(\tau)$. The procedure of $\chi(\tau)$ determination from experimental spectra, which permits one to study not only the film but the interface itself, is described elsewhere.[14] In this work one used a simplified technique for most of the films. When simulating the portion of a spectrum corresponding to the film obtained in the channeling mode, $Y_c(E)$, one set $Y_c(\tau)=Y_r(\tau)\chi(\tau)$ for each value of τ. As will be shown in Subsect. IIIB, the dependence of the dechanneling rate on depth can be written

$$\chi(\tau)=\chi_0+D\tau. \quad (4)$$

The parameters χ_0 and D characterizing dechanneling near the surface and in the bulk are variable.

A comparison of the energy widths of thin films in the $Y_c(E)$ and $Y_r(E)$ spectra permitted one to estimate the ratio of stopping powers in the channel, ε_c, and outside it, ε_r, by introducing an effective thickness $h'=\beta h$ ($\beta<1$) for the channeling spectrum. The coefficient β depended on the $\alpha=\varepsilon_c/\varepsilon_r$ ratio and the behavior of the $\varepsilon(E)$ functions and was variable.

3. DISCUSSION

A. Ultrathin films

Five sets of films were prepared for the study of the initial growth stages. The films in each set differed in the substrate but were deposited simultaneously, with the same deposition time $t_d=5$, 15, 30, and 60 min and the same substrate temperature $t_s=700$, 760, and 780 °C.

The quantitative characteristics describing the properties of the ultrathin films are presented in Table I. These are the temperature t_s and material of the substrate, deposition time t_d; the distribution parameters in Eq. (1)—X_0 and σ; film thickness h; coverage C and the minimum yield $\chi_{\min}$ determined from experiment; reduced thickness hC, i.e. the thick-

TABLE I. Parameters of ultrathin films.

No.	Substrate	t_d, min	t_s, °C	X_0, 10^{15} at/cm^2	σ, 10^{15} at/cm^2	h, 10^{15} at/cm^2	h, nm	C, %	hC, nm,	hC/t_d, nm/min	χ_{min}	Notes
1	MgO	5	700	54	50	67	8.9	49	4.4	0.90	1(Cu-0.8)	
2	MgO	5	760	12	30	29	3.9	33	1.3	0.26	1(Cu-0.6)	Excess Cu
3	MgO	15	780	36	50	56	7.5	19	1.4	0.10	0.9(Cu-0.55)	Excess Cu
4	MgO	30	760	16	160	134	18	36	6.5	0.22	0.95	
5	MgO	60	760	110	120	148	19	66	13.0	0.22	0.8	
6	$Ba_xSr_{1-x}TiO_3$	5	700	25	20	29	3.9	90	3.5	0.7	~0.4	
7	$Ba_xSr_{1-x}TiO_3$	5	760	–	–	7.5	1.0	67	0.67	0.13	0.65	Cu deficiency
8	$SrTiO_3$	15	780	24	10	24	3.2	75	2.4	0.16	0.55(0.4)*	
9	$SrTiO_3$	30	760	–	–	60	8.0	90	7.2	0.24	0.52(0.3)*	
10	$LaAlO_3$	30	760	–	–	55	7.3	100	7.3	0.24	0.27	
11	$Ba_xSr_{1-x}TiO_3$	30	760	–	–	52	6.9	100	6.9	0.23	0.12	
12	$LaAlO_3$	60	760	–	–	110	14.6	100	14.6	0.24	0.18	
13	$Ba_xSr_{1-x}TiO_3$	60	760	–	–	110	14.6	100	14.6	0.24	0.17	

Note. Corrected for substrate defects.

ness corresponding to a uniform distribution of the condensed atoms over the substrate surface; and the growth rate hC/t_d.

Figures 1 and 2 display MEIS spectra obtained from films with $t_s = 15$ min on MgO and STO single crystals, respectively (Nos. 3 and 8 in Table I). The $Y_c(E)$ and $Y_r(E)$ were measured with the ESA for 190-keV He^+ ions. The shape of the cation-component peaks depends substantially on the type of the substrate. For the MgO substrate, which has a lattice mismatch with the YBCO film of 8.3%,[15] these peaks exhibit an extended low-energy tail, and the scatter σ prescribed in simulation should be close to the film thickness. This shape of the spectrum is characteristic of the Volmer-Weber mechanism of growth involving formation of three-dimensional stepped islands.[12] The Ba peak obtained with the STO substrate, which is closely lattice-matched to the film (mismatch of ~1.5%, Ref. 15), is nearly symmetric in shape, and the scatter σ, if it is detectable at all, is considerably less than h and close in magnitude to the lattice parameter c. In this case layer-by-layer growth takes place, which implies the two-dimensional mechanism of Frank–van der Merwe. The substrate surface is incompletely covered by the above-mentioned films, which is particularly well seen for the MgO substrate. The incomplete coverage is evidenced by the relatively small film-signal amplitude compared to the signal due to the substrate, as well as by the fact that the substrate signal in the spectrum starts from the point on the energy scale corresponding to the uncoated substrate. Figure 1 presents model spectra corresponding to complete and incomplete (19%) coverage, which illustrate the method used to determine the coverage.

The SEM images of films 4, 9, and 10 (see Table I) are presented in Figs. 3a, 4, and 5. The fraction of the surface area covered by film islands was estimated from a photomicrograph of the YBCO/MgO island structure using the Adobe Photoshop program package. Figure 3b shows a part of the surface of the YBCO/MgO structure constructed using this computer program from the corresponding photomicro-

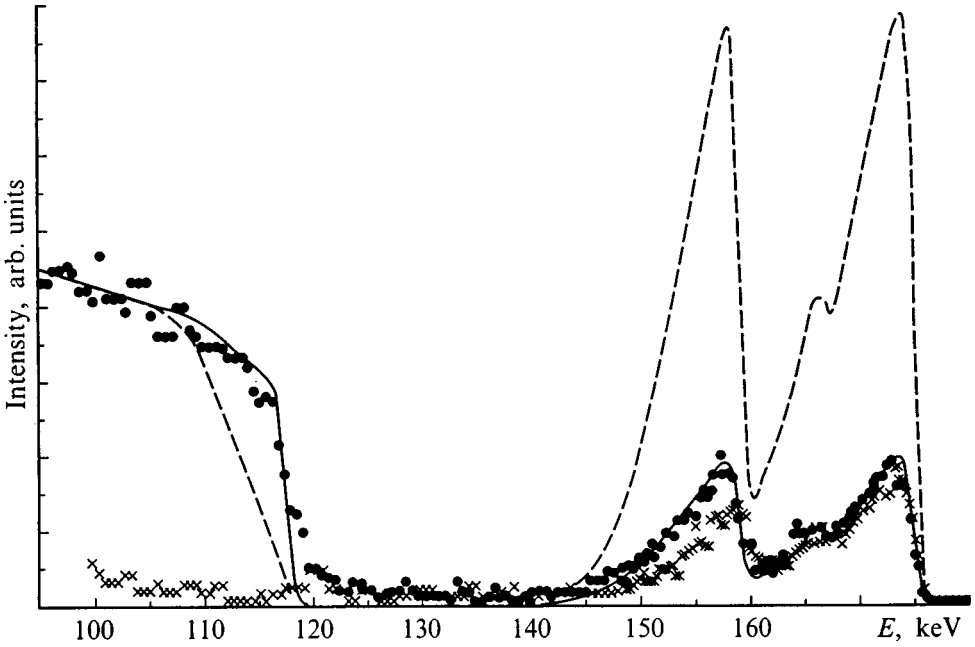

FIG. 1. MEIS spectra of film 3 (MgO substrate). Points and crosses—experiment, random beam orientation and channeling regimes, respectively; solid line—simulation; dashed line—calculation assuming 100% substrate coverage.

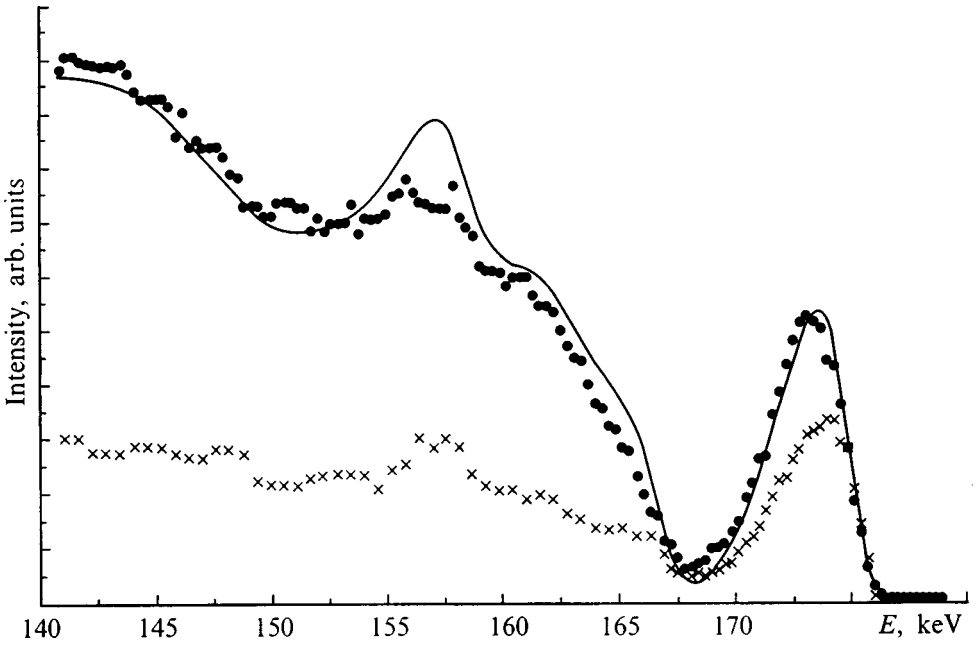

FIG. 2. MEIS spectra of film 8 (STO substrate). Notation same as in Fig. 1.

graph. The fraction of the covered surface area derived from the image thus obtained was found to be 47%. This value agrees satisfactorily with the result obtained by MEIS (36%), if one takes due account of the differences inherent in the two techniques.

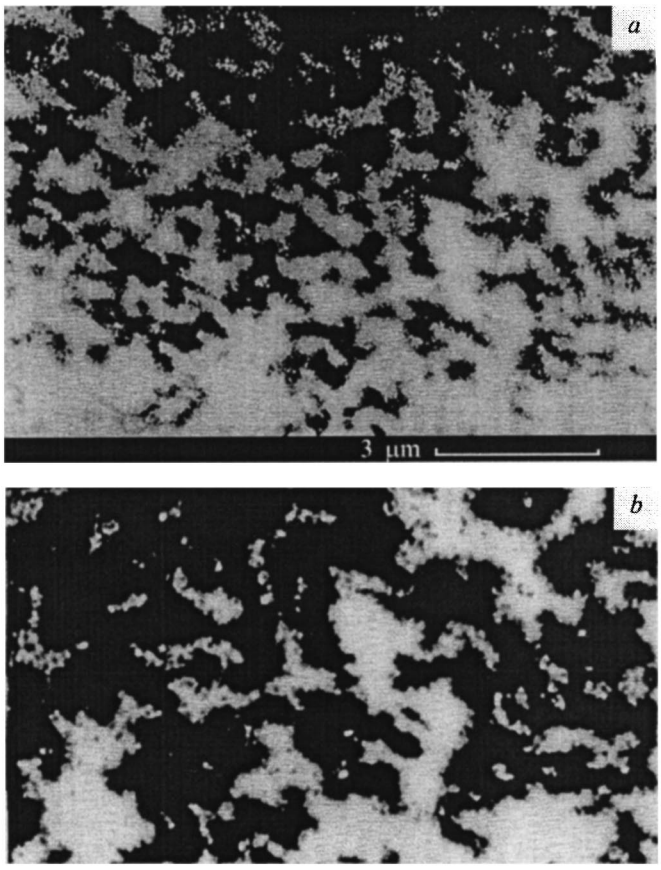

FIG. 3. (a) Photomicrograph and (b) computer-processed image of film 4 (MgO substrate).

Figure 4 shows a photomicrograph of a ~8-nm thick YBCO film on an STO substrate (No. 9, Table I). The presence of numerous scratches provided convincing support of the substrate surface being heavily defected. We readily see that the bright spots and lines occupy less than 1% and lie along macrodefects on the surface, i.e. the scratches are decorated by crystallites of impurity phases. Figure 5 shows an image of the surface of an YBCO film grown in the same run on a LAO substrate, with the outer damaged layer removed. While this YBCO film also contains impurity crystallites, they are distributed randomly and have a lower concentration. The thin YBCO films grown on high-quality perovskite substrates had practically identical surface morphology in that starting from thicknesses on the order of one monolayer the films were continuous and uniform.

A comparison of the spectra and of the parameters obtained in their treatment permits separation of the films in two groups, viz. films on a MgO substrate with a large lattice mismatch, and films on perovskite substrates which have a

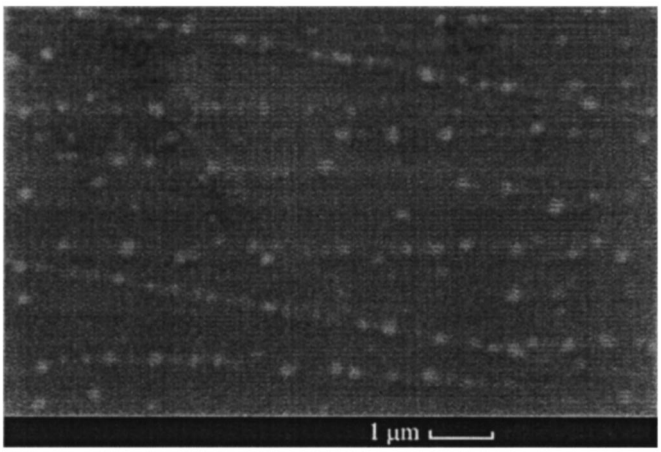

FIG. 4. Photomicrograph of film 9 (STO substrate).

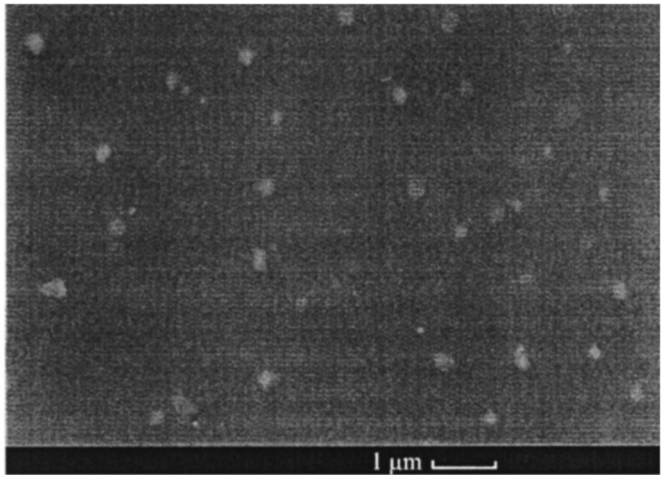

FIG. 5. Photomicrograph of film 10 (LAO substrate).

small mismatch with the YBaCuO lattice (STO, BSTO, and LAO).

1. MgO substrate

The YBCO films on MgO substrates prepared in this work have the following characteristics. The islands cover completely the substrate, starting from an averaged film thickness ~ 20 nm. The nonuniformity in their thickness is substantially in excess of the lattice constant and is approximately equal to their average thickness, which manifests itself in a strong low-energy tailing. All ultrathin films revealed an island pattern of growth accompanied by incomplete coverage of the MgO substrates, which is seen from both MEIS spectra and photomicrographs (Fig. 3a and 3b). Films less than 9 nm in thickness exhibit typically an excess of copper, while thicker ones have a composition closer to stoichiometric. Channeling on the Y-Ba sublattice is practically absent in almost all films, except for the thickest of them (No. 5), although in films 1–3 it can be seen to exist on the Cu-O sublattice ($\chi < 0.8$, Table I), which implies an ordered structure containing only Cu cations. This observation, combined with the substantial copper excess in these films, suggests that Cu_2O nuclei appear, besides other phases, in the initial stages of the growth. (Cu_2O has a cubic lattice with $a = 0.4261$ nm, which is very close to $a = 0.4213$ nm for MgO). The formation of Cu_2O nuclei was earlier revealed by x-ray diffraction.[16]

A comparison of films 1, 2, and 3 permits one to follow the effect of substrate temperature on the growth characteristics. As the temperature increases, the coverage decreases, in full accord with Ref. 12, as does the growth rate because of decreasing supersaturation, and the copper excess increases. Assuming a film to contain only Cu_2O and $YBa_2Cu_3O_7$, the spectra permit a conclusion that the fraction of Cu_2O increases from 10 to 20 at. % as the temperature increases from 760 to 780 °C. The data on channeling indicate that the Cu_2O phase may amount to one half the substrate surface area coated by the film.

An analysis of the films prepared at the same substrate temperature (2, 4, and 5) shows that an increase in deposition time increases proportionally the reduced thickness hC, whereas h increases to thicknesses $\sim 15-20$ nm; after this, the coverage increases with a practically constant thickness, which implies a change in the growth pattern. This is in agreement with the observations[12,17,18] that for film thicknesses not less than $10c$ the islands coalesce, and a crossover takes place from the growth of islands to that of a film by a helical mechanism forming terraces centered on a screw dislocation and having a height of about 1.2 nm.

2. Perovskite substrates

Films grown on small-mismatch substrates have close properties and differ considerably from those on MgO. The scatter in thickness is substantially smaller than in the case of MgO, and noticeably smaller than the thickness itself, which evidences layer-by-layer growth pattern. The coverage for the films obtained in similar conditions is larger than that for films grown on MgO, and is practically complete for t_d over 15 min at all temperatures studied. All films exhibited channeling in the Ba–Y sublattice. The composition of most of the films is close to stoichiometric, although in some films (7 and 8) a copper deficiency is observed, which is seen, in particular, from the deviation of the experimental spectrum from calculations made under the assumption of stoichiometric composition.

The effect of substrate temperature during the film deposition can be inferred from a comparison of films 6 and 7, as well as of 8 and 9. A decrease of temperature brought about an increase in the growth rate and coverage.

A comparison of the film characteristics shows the thinnest of them, No. 7, to have specific characteristics. Its average thickness over the areas where it covers the substrate is 0.94 ± 0.8 nm, which is less than c, the lattice constant of YBCO, which means that it should contain nuclei less than c in height. The thickness of a film with $hC = 0.4$ nm reported in Ref. 6 was also less than c. Besides the small thickness and low growth rate, this film is also copper deficient. It may be conjectured that it is in a nucleation stage, including that of foreign phases, and that the formation of Cu_2O is strongly suppressed by the lattice mismatch. As the growth goes on, the coverage becomes complete, the spread in thickness decreases, the composition approaches stoichiometry, and a regular layer-by-layer growth sets in.

B. Thin films

The thin YBCO films studied in this work varied from 100 to 470 nm in thickness. Deposition on MgO and LAO was at 700 °C and, on $NdGaO_2$, at 760 °C. Table II lists information on the substrate material, temperature and duration of deposition (t_s, t_d), average film growth rate and thickness, as well as on the channeling characteristics, namely, the minimum yield measured after the surface peak, and the simulation parameters χ_0 and D entering Eq. (4). Also given are data on the superconducting transition temperature T_c.

Figures 6 and 7 present spectra obtained in channeling regimes, $Y_c(E)$, and random orientation, $Y_r(E)$, and their ratio $\chi(E)$, both measured and obtained in simulation for

TABLE II. Parameters of thin films.

No.	Substrate	t_d, hour	t_s, °C	T_c, K	h, 10^{15} at/cm^2	h, nm	h/t_d, nm/min	D, 10^{-19} cm^2/at	χ_0	$\chi_{\min}$
14	$LaAlO_3$	2	700	93	800	106	0.88	2.1	0.09	0.13
15	MgO	4	700	93	1230	165	0.69	2.0	0.033	0.10
16	$NdGaO_3$	10	760	92	1350	180	0.3	1.8	0.07	0.15
17	$LaAlO_3$	4	700	93	1600	215	0.9	2.0	0.02	0.10
18	$LaAlO_3$	6	700	94	2300	310	0.86	1.9	0.09	0.17
19	$LaAlO_3$	11	700	93	3500	470	0.71	2.0	0.04	0.08

films on MgO and LAO (films 15 and 14, respectively). The primary proton energy was 230 keV, and the scattering angle $\Theta = 150°$. The $\chi(E)$ relations obtained for the main part of the film were in both cases close to linear. Based on the weak energy dependence of stopping power, relation (4) was assumed to be linear. The satisfactory agreement of a model calculation with experiment confirms such a dependence.

In the case of films grown on a substrate made up of light components, where the low-energy edge of the spectrum is well separated from the substrate spectrum itself, one can study the interface region in more detail. Such a study was made for the YBCO film 15 on a MgO substrate using the technique developed earlier.[14] The $Y_c(E)$ spectra in Figs. 6 and 7 can be divided into five regions. Region I corresponds to the surface peak. Region II, where $\chi(E)$ approaches a linear relation, corresponds to the bulk of the film and exhibits a practically constant dechanneling rate D in Eq. (4). Region III can be identified with the film layers adjacent to the interface, where misfit dislocations can appear. Estimates of the density of the misfit dislocations accompanying coherent growth yielded $n_d \approx 7.5\times10^5$ cm/cm^2 for a dechanneling factor $\sigma_d \approx 0.66$ nm.[14,19] This value of n_d is substantially smaller than could be expected from estimates based on the lattice mismatch (2×10^6 cm/cm^2), which implies predominantly textured growth occurring without misfit dislocations. Region IV corresponds to the substrate layers adjacent to the interface, and region V, to the main part of the film.

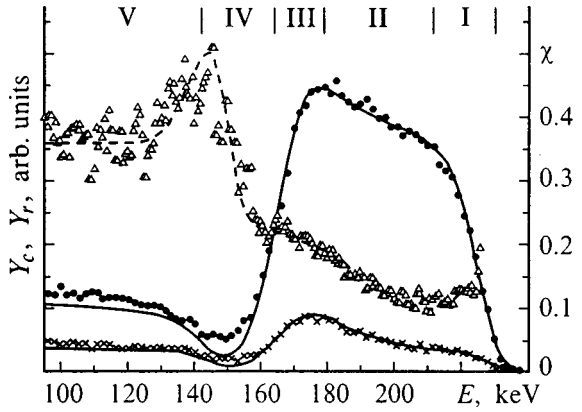

FIG. 6. MEIS spectra and $\chi(E)$ function for film 15 (MgO substrate). Points and crosses—experiment, random orientation and channeling regimes, respectively; triangles—experimental ratios Y_c/Y_r; solid lines—calculated spectra, dashed line—model function $\chi(E)$. $I-V$—spectral regions (see text for explanation).

For other films where separation of the film and substrate regions in the spectrum was difficult to do, only region II was simulated. The technique used was described in Sec. II. A comparison of the spectra obtained in the random and channeling modes permitted one to derive the stopping power ratio α for the channel and outside it for 230-keV protons, which was found to be 0.83 ± 0.06.

The parameters χ_0 obtained in simulation, like the values of $\chi_{\min}$ derived from experiment within the region immediately after the surface peak, at the boundary separating regions I and II, are governed to a considerable extent by the presence of foreign unoriented phases emerging onto the surface, and by crystallite misorientation.[19] Parameter D characterizes the dechanneling rate over the film thickness. For a beam incident normally to the surface, D depends on the concentration of such defects as dislocations whose direction and Burgers vector are nonparallel to the beam, grain boundaries, point defects and stacking faults, in particular, the so-called 2-4-7 and 2-4-8 structures.[20]

The type of a defect can be identified from the energy dependence of the dechanneling rate.[19] For instance, for point defects it is $1/E$, for dislocations—$E^{1/2}$, and for stacking faults there is no such dependence at all. For film 15, one obtained the values of D for different probing-proton energies. It was found that for 96, 127, 181, and 230 keV, $D = 2.2\times10^{-19}$ cm^2/atom, i.e. the dechanneling rate is practically independent of energy, which implies predominance of defects of the type 2-4-7. Strictly speaking, these defects are nor stacking faults, because no new atomic chains appear in the defect plane, and only the type of a chain may change, so that Y–Ba_2 chains are continued by an O_2 chain, or vice versa. Dechanneling at such defects requires an additional

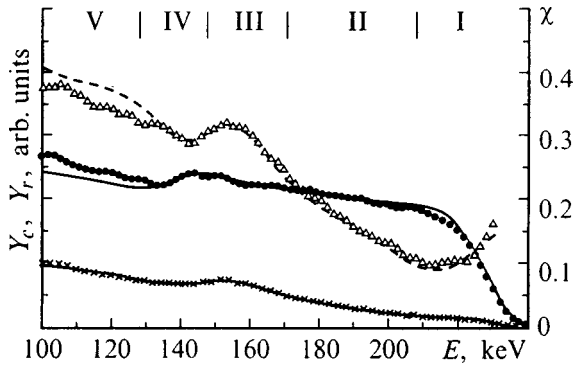

FIG. 7. MEIS spectra and $\chi(E)$ function for film 17 (LAO substrate). Notation same as in Fig. 6.

investigation. Because of a paucity of information on the types of defects present in the films studied, no estimation of the defect concentration in the bulk of the films was carried out. The parameters D and $\chi_{\min}$ obtained can be used to compare the quality of a film with that of good single crystals. For YBCO single crystals, $D=7\times10^{-20}$ cm^2/atom, $\chi_0=0.03$, and the measured value $\chi_{\min}=0.097$.[9] As seen from Table II, almost all films have close values of D, irrespective of the substrate type. This closeness in properties is apparently due to the films deposited on different substrates growing by the same spiral mechanism.[5] The growth rates of thin films are close in magnitude to those of ultrathin ones.

The results obtained can be summed up as follows. We have developed a method of analyzing the structure and composition of thin films based on the measurement and simulation of energy spectra of medium-energy ions scattered through large angles (MEIS), which permits one to derive information on the growth pattern of ultrathin (up to 15 nm) films, defect distribution through the thickness of thin (up to 500 nm) films, and defects at the interface for heavy-element films on light substrates, averaged over a surface area of about 1 mm^2.

This method was combined with SEM to study YBCO films on MgO, $SrTiO_3$, $Ba_xSr_{1-x}TiO_3$, and $LaAlO_3$ substrates in various stages of their growth. In the initial stages, the lattice mismatch between the film and the substrate is essential. Three stages of growth could be discriminated. The first of them, observed with reduced thicknesses of up to 4 nm, is nucleation, which is characterized by incomplete substrate coverage, unstable composition (a Cu_2O impurity on MgO, and Cu deficiency on $Ba_xSr_{1-x}TiO_3$), and a spread in thickness comparable to the thickness itself. The second stage, signaled by the onset of regular island formation on MgO and of layer-by-layer growth on small-mismatch substrates, was observed for reduced thicknesses of 7–15 nm. This stage is characterized by practically complete coverage of the substrate and a stable composition. The third stage, a regular, apparently spiral, growth was seen to occur for thicknesses above 100 nm. The composition obtained here was close to stoichiometric, and the structural quality of a film throughout its thickness and on the surface was slightly inferior to that of YBCO single crystals and did not depend of the actual substrate type.

Support of the Interface-2 Project (Grant 98055) of the State HTSC Program is gratefully acknowledged.

[1] Z.-Y. Shen, *High-Temperature Superconducting Microwave Circuits* (Artech House, Nortwood, 1994).
[2] X.-Y. Zheng, D. H. Lowndes, S. Zhu, J. D. Budai, and R. J. Warmack, Phys. Rev. B **45**, 7584 (1992).
[3] M. Ece, E. G. Gonzalez, H.-U. Habermeir, and B. J. Oral, J. Appl. Phys. **77**, 1646 (1995).
[4] E. K. Gol'man, V. I. Gol'drin, D. A. Plotkin, and S. V. Razumov, Pisma Zh. Tekh. Fiz. **22**, No. 22, 82 (1996) [Tech. Phys. Lett. **22**, 942 (1996)].
[5] D. G. Schlom, D. Anselmetti, J. G. Bednorz, R. F. Broom, A. Catana, T. Frey, Ch. Gerber, H.-J. Güntherodt, H. P. Lang, and J. Mannhart, Z. Phys. B **86**, 163 (1992).
[6] D. Hüttner, U. Günther, O. Meyer, J. Reiner, and G. Linker, Appl. Phys. Lett. **65**, 2863 (1994).
[7] V. V. Afrosimov, G. O. Dzyuba, R. N. Il'in, M. E. Leshchenko, M. N. Panov, V. I. Sakharov, I. T. Serenkov, A. V. Suvorov, and V. V. Tret'yakov, Sverkhprovodimost' **4**, 1767 (1991) [KIAE **4**, 1674 (1991)].
[8] S. F. Karmanenko, V. Yu. Davydov, M. V. Belousov, R. A. Chakalov, G. O. Dzyuba, R. N. Il'in, A. B. Kozyrev, Yu. V. Likholetov, K. F. Njakshev, I. T. Serenkov, and O. G. Vendik, Supercond. Sci. Technol. **6**, 23 (1993).
[9] V. V. Afrosimov, G. O. Dzyuba, R. N. Il'in, M. N. Panov, V. I. Sakharov, I. T. Serenkov, and E. B. Ganza, Zh. Tekh. Fiz. **66**, No. 12, 76 (1996) [Tech. Phys. **41**, 1240 (1996)].
[10] W. K. Chu, J. W. Meyer, and M. A. Nikolett, *Backscattering Spectrometry* (Academic Press, New York, 1978).
[11] M. Zinke-Allmang, Nucl. Instrum. Methods Phys. Res. B **64**, 113 (1992).
[12] N. Savvides and A. Katsaros, Physica C **226**, 23 (1994).
[13] F. J. B. Stork, K. A. Beall, A. Roshko, D. C. DeGroot, D. A. Rudman, R. H. Ono, and J. Krupka, IEEE Trans. Appl. Supercond. **7**, 192 (1997).
[14] V. V. Afrosimov, R. N. Il'in, S. F. Karmanenko, M. N. Panov, V. I. Sakharov, and I. T. Serenkov, Poverkhnost' **8**, 71 (1997).
[15] R. Schulz, M. Simoneau, and J. Lanteigne, Physica C **233**, 113 (1994).
[16] Z. Han, T. I. Selinder, and V. Helmersson, J. Appl. Phys. **75**, 2020 (1994).
[17] S. Zhu, D. H. Lowndes, B. C. Chakoumakos, S. J. Pennycook, X.-Y. Zheng, and R. J. Warmack, Appl. Phys. Lett. **62**, 3363 (1993).
[18] J. R. Sheats and P. Merchant, Appl. Phys. Lett. **62**, 99 (1993).
[19] L. C. Feldman, J. W. Mayer, and S. R. Picraux, *Materials Analysis by Ion Channeling* (Academic, New York, 1982).
[20] R. Ramesh, D. M. Hwang, T. S. Ravi, A. Inam, X. D. Wu, and T. Venkatesan, Physica C **171**, 14 (1990)

Translated by G. Skrebtsov

Role of zinc and nickel impurities in high-temperature superconductors

S. G. Ovchinnikov*

L. V. Kirenskiĭ Institute of Physics, Siberian Branch of the Russian Academy of Sciences 660036 Krasnoyarsk, Russia

(Submitted June 23, 1998; resubmitted October 6, 1998)
Fiz. Tverd. Tela (St. Petersburg) **41**, 596–600 (April 1999)

The local changes produced in the electronic structure and their effect on the physical properties of the superconducting and normal phases when zinc and nickel are substituted for copper are examined on the basis of a multiband p–d model. It is shown that strong electronic correlations suppress the $S=1$ configuration of Ni^{2+} and cause the superposition of the $S=1/2$ and $S=0$ states of nickel. The change in the density of states in p- and n-type systems is studied, and the peculiarity of Zn impurity for p-type systems and Ni impurity for n-type systems is shown. The universal dependence of the T_c on the residual resistance in lightly doped superconductors and deviations from it in optimally doped systems are discussed.
 [S1063-7834(99)00704-2]

It is well known that transition-metal impurities in high-temperature superconductors (copper oxide HTSCs) lead to behavior that is unusual from the standpoint of the BCS theory. Both magnetic and nonmagnetic impurities strongly suppress T_c, and the degree of suppression for p-type HTSCs is greatest for the nonmagnetic impurity Zn and least for the magnetic impurity Ni.[1–3] This effect of Zn is often considered in the literature to be a manifestation of potential scattering in a d-type superconductor.[4–6] The basis for this hypothesis is the appearance of a large residual density of states ($N_{res}(\varepsilon_f)\neq 0$) as a result of nonmagnetic impurities for anisotropic superconductors with an order parameter that possesses zeros on the Fermi surface.[7] The potential and magnetic scattering effects are analyzed in the normal-metal-state model. For HTSCs this approach is hardly applicable for lightly and optimally doped compositions with anomalous metal-phase behavior characterized by strong short-range antiferromagnetic correlations.

A different picture is observed for n-type HTSCs. The magnetic impurities Ni and Co suppress T_c much more strongly than the nonmagnetic impurity Zn in polycrystalline samples $L_{2-x}Ce_xCuO_{4+\delta}$ (L=Pr, Nd, Sm, Eu). This is interpreted to be a manifestation of a gap with S-type symmetry.[8,9] Investigations of $Pr_{2-x}Ce_xCuO_{4+\delta}$ single crystals have shown that Zn does not dissolve in them and substitution of Ni and Co for Cu gives a record (for cuprates) suppression of T_c with $dT_c/dx=-20$ K/at.%, an increase of the residual resistance 450 $\mu\Omega\cdot$cm/at.%, and a change in the sign of the Hall constant.[10]

The residual resistance ρ_{res} in various p-type HTSCs (La-214, Y-123, Bi-2212) correlates with T_c: The increase in ρ_{res} is proportional to the decrease ΔT_c, which suggests that the same mechanism produces both effects. Moreover, the dependence $T_c(\rho_{res})$ in different HTSCs with different Zn impurity concentrations is universal for lightly doped compositions. The universality breaks down for optimally doped compositions.[11]

The effects of the substitution of magnetic and nonmagnetic impurities for copper are being studied in a multielectron multiband p–d model.[12,13] It has been shown that strong electronic correlations suppress the magnetic state $d^8(Ni^{2+})$ with spin $S=1$ and realize quantum-mechanical superposition of the paramagnetic $d^9L(S=1/2)$ and diamagnetic $d^{10}L^2(S=0)$ states.[14]

As a result, the impurity of the formally magnetic Ni^{2+} actually acts as a diamagnetic impurity Zn. This effect is due to the factor u_0^2, expressing the probability of the $d^{10}L^2$ configuration. For this reason, the suppression of the Néel point in lightly doped antiferromagnets satisfies

$$\frac{dT_N}{dx}(\mathrm{Ni}) \Big/ \frac{dT_N}{dx}(\mathrm{Zn}) = u_0^2. \tag{1}$$

In what follows, we shall examine and compare the changes produced in the electronic structure by substitution of Zn and Ni for Cu. For p-type systems Zn impurities act like electronic doping, leading to the formation of additional within-gap states with a_1 symmetry of the deep-impurity-level type, while Ni impurities act like additional hole doping, changing only the intensity of already existing peaks in the density of states of the impurity band with b_1 symmetry. We see in this a microscopic reason why the effects of Zn and Ni are different, because the appearance of Zn impurity levels can result in a strong resonance scattering of the carriers,[15] which does not happen in the case of Ni impurities. Conversely, for n-type superconductors, the substitution of Ni for Cu results in coexistence of electronic and hole states, which is well-known from experiments.

1. FORMATION SCHEME OF THE QUASIPARTICLE BAND STRUCTURE

In the multiband, multielectron p–d model, the Hamiltonian of the CuO_2 layer can be written in the hole representation

$$H=\sum_{i\lambda\sigma}\varepsilon_i^{\lambda}a_{i\lambda\sigma}^{+}a_{i\lambda\sigma}+\sum_{i,j}\sum_{\lambda_1\lambda_2\sigma_1\sigma_2\sigma_3\sigma_4}V_{ij}^{\lambda_1\lambda_2}a_{i\lambda_1\sigma_1}^{+}a_{i\lambda_1\sigma_3}a_{i\lambda_2\sigma_2}^{+}a_{i\lambda_2\sigma_4}+\sum_{\langle i,j\rangle}\sum_{\lambda_1\lambda_2\sigma}t_{ij}^{\lambda_1\lambda_2}a_{i\lambda_1\sigma}^{+}a_{j\lambda_2\sigma}. \quad (2)$$

Here $a_{i\lambda\sigma}$ is an operator annihilating a hole in a Wannier state at the site i (copper or oxygen), in orbital λ, and with spin σ. We took account of two copper orbitals ($d_{x^2-y^2}$ and d_{z^2}) and one p orbital (p_x or p_y) on each oxygen site. Among the Coulomb matrix elements, the intra-atomic Hubbard $U_d(U_p)$ matrix elements for repulsion on one copper (oxygen) orbital with opposite spins, interorbital $V_d(V_p)$ Coulomb and exchange $J_d(J_p)$ matrix elements as well as the interatomic parameters of the Coulomb V_{pd} and exchange J_{pd} copper–oxygen interactions (which, for simplicity, we assume to be the same for all orbitals). The last term in Eq. (1) describes interatomic copper–oxygen hops with the parameters $t_{pd}^{x^2-y^2,x}\equiv T_{pd}$ and $t_{pd}^{z^2x}=T_{pd}/\sqrt{3}$ and oxygen–oxygen hops with the parameter $t_{pp}^{x,y}\equiv t_{pp}$. We denote the charge-transfer energy $\delta=\varepsilon_p-\varepsilon_{d_{x^2-y^2}}$ and the energy splitting of the d level in a uniaxial component of the crystal field as $\Delta_d=\epsilon_{pz^2}-\epsilon_{dx^2-y^2}$.

In the generalized tight-binding method[14] the band structure of the quasiparticles can be calculated, taking account of strong electronic correlations, in two stages: At the first stage the lattice of the CuO_2 layer is divided into elementary cells and the Hamiltonian inside a cell is diagonalized exactly. The cells can be chosen to be either nonoverlapping (CuO_2) or overlapping (CuO_4), and in the latter case the additional problem of constructing the Wannier functions is solved.[16–18] The multielectronic molecular orbitals $m=|n,l\rangle$ (where $n=0,1,2,\ldots$ is the number of holes in a cell, l denotes the collection of all other orbital and spin indices), which are obtained by diagonalizing the Hamiltonian H_0 of a cell, are used to construct the Hubbard operators $X^{pg}=|p\rangle\langle g|$ of this cell.

At the second stage all intercellular hops and interactions are rewritten exactly in the Hubbard–operator representation, and the Hamiltonian (2) assumes the form

$$H=H^{(0)}+H^{(l)}=\sum_{i,m}E_mX_i^{m,m}+\sum_{\langle i,j\rangle}\sum_{m_1,n_1}\sum_{m_2,n_2}T_{m_1n_1}^{m_2n_2}X_i^{m_1n_1}X_j^{n_2m_2}. \quad (3)$$

Here the lattice sites i and j refer only to the centers of the clusters (copper atoms).

Various variants of perturbation theory with respect to the intercellular hops are known for the Hubbard model.[15,19–21] In the strong correlations regime they all lead to a quasiparticle band structure that depends on the temperature and carrier density through the occupation numbers $\langle x^{m,m}\rangle$ of the terms E_m. The latter can be calculated self-consistently using the equation for the chemical potential

$$\Sigma_{nl}n\langle X^{nl;nl}\rangle=n_h, \quad (4)$$

where n_h is the hole density per cell, $n_h=1+x$ for $L_{2-x}Sr_xCuO_4$ and $n_h=1-x$ for $Pr_{2-x}Ce_xCuO_4$.

For us the important states are the ground terms with $n=0,1$, and 2; the vacuum state $|0\rangle$ with $n=0$ corresponds to the $d^{10}p^6$ configuration. The single-hole state with $n=1$ is a superposition of d^9 and $d^{11}L$ configurations. The main term with spin $S=1/2$ and projection $\sigma=\pm1/2$ is

$$|1,\sigma\rangle=u|0;d_{1\sigma};0\rangle-v(|p_x,\sigma;0;0\rangle+|0;0;p_x,\sigma\rangle)/\sqrt{2},$$
$$u^2=(1+\delta/\nu)/2,\quad v^2=1-u^2,\quad \nu^2=\delta^2+8T_{pd}^2. \quad (5)$$

Here $d_1\equiv d_{x^2-y^2}$ and the vector $|\ldots;\ldots;\ldots\rangle$ denotes various multielectronic states of a O–Cu–O cluster.

The two-hole states are a superposition of the configurations d^8,d^9L, and $d^{10}L^2$. We write the ground term in the form

$$|2,S\rangle=u_0|d^{10}L^2\rangle+v_0|d^9L\rangle+w_0|d^8\rangle, \quad (6)$$

where the spin is 0 or 1 (crossover between the singlet $^1A_{lg}$ and the triplet $^3B_{lg}$ is possible).[22] Strong correlations suppress the weight of the d^8 configuration. For the parameters $w_0^2\leqslant 0,1$, which are realistic for oxides, the Zhang–Rice singlet makes the main contribution. In the limit $U_d\to\infty$, neglecting w_0, the coefficients u_0 and v_0 can be written analytically as

$$u_0^2=(1-\Delta_0/\nu_0)^2,\quad v_0^2=1-u_0^2,$$
$$\Delta_0=\delta-V_{pd},\quad \nu_0^2=\Delta_0^2+8T_{pd}^2.$$

Fermi-type quasiparticles in a strongly correlated system can be determined by analogy with the Landau Fermi-liquid theory as local excitations with energy

$$\Omega(n,l_1,l_2)=E(n+1,l_1)-E(n,l_2). \quad (7)$$

Intercluster hops lead to dispersion of these quasiparticles. The single-particle (hole) excitation scheme is shown in Fig. 1, where to simplify the figure only the two lowest terms with $n=1$ and 2 are shown. Here the numbered arrows enumerate different types of holes: A quasiparticle 1 forms an empty conduction band (in the electronic language) and the quasiparticles 2 and 3 form the valence-band top. For both n and p types, there exist hole in-gap states, whose spectral weight is proportional to the carrier density. These holes are denoted by the number 4 for n-type systems and they are described by a superposition of d_{z^2} states of copper and the a_1 molecular orbital of oxygen.[23] For p-type HTSCs the impurity holes are denoted by the number 5 in Fig. 1 and are formed in the ground b_1 orbitals of oxygen.[24]

The spectral weight of quasiparticles is determined by the so-called terminal factor,[25] which for Fermi quasiparticles is the sum of the particles occupying the initial and final states

$$F(l_1,l_2)=\langle X^{n+1,l_1;n+1,l_1}\rangle+\langle X^{n,l_2;n,l_2}\rangle. \quad (8)$$

The occupation numbers themselves are found self-consistently by solving the equation for the chemical poten-

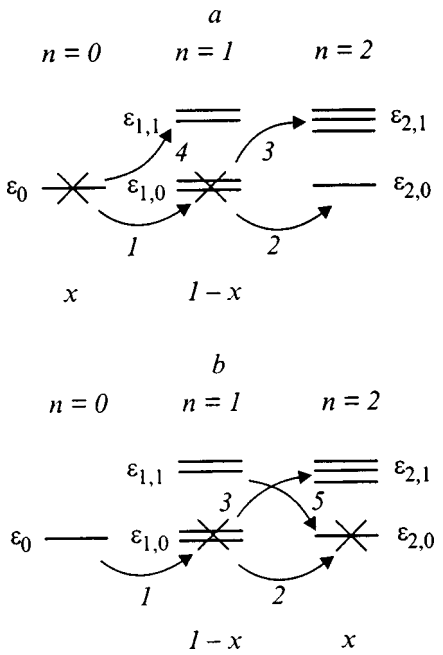

FIG. 1. Scheme of multielectronic terms in various sectors of Hilbert space with $n=0$, 1, and 2 holes per cell. The cross marks indicate partial filling of different terms for *n*-type (a) and *p*-type (b) systems. The numbered arrows show the possible Fermi quasiparticles: *1* — conduction-band bottom; *2*, *3* — singlet and triplet excitations at the valence-band top; *4*, *5* — impurity states for *n*- and *p*-type systems.

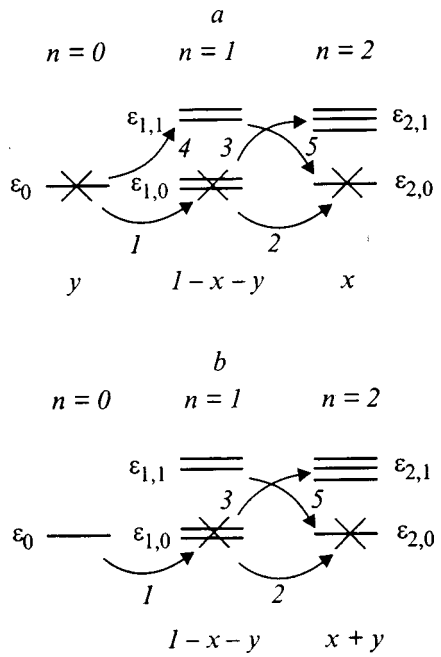

FIG. 2. Change in the quasiparticle spectra in a *p*-type CuO_2 layer due to substitution of zinc (a) and nickel (b) for copper. For Zn there is an additional hole impurity state with a_1 symmetry.

tial (4). These solutions at $T=0$ in the paramagnetic phase for three cases of interest to us — without doping and with *p*- and *n*-type doping — are as follows:

1) undoped system, $n_h=1$,

$$\langle X^{0;0}\rangle=0,\quad \langle X^{1,\sigma;1,\sigma}\rangle=1/2,\quad \langle X^{2,0;2,0}\rangle=0; \tag{9}$$

2) *p*-type doping, $n_h=1+x$,

$$\langle X^{0;0}\rangle=0,\quad \langle X^{1,\sigma;1,\sigma}\rangle=(1-x)/2,\quad \langle X^{2,0;2,0}\rangle=x; \tag{10}$$

3) *n*-type doping, $n_h=1-x$,

$$\langle X^{0;0}\rangle=x,\quad \langle X^{1,\sigma;1,\sigma}\rangle=(1-x)/2,\quad \langle X^{2,0;2,0}\rangle=0. \tag{11}$$

The structure of the solutions is similar in the antiferromagnetic phase with the spin degeneracy lifted in each sublattice.

2. CHANGES IN THE ELECTRONIC STRUCTURE DUE TO SUBSTITUTIONS OF ZINC AND NICKEL FOR COPPER

Each substitution of $Zn^{2+}(d^{10})$ for $Cu^{2+}(d^9)$ decreases the number of holes by one, so that the hole density, for example, in the system $La_{2-x}Sr_xCu_{1-y}Zn_yO_4$ is $n_h=1+x-y$. At the same time the substitution of $Ni^{2+}(d^8)$ for $Cu^{2+}(d^9)$ increases the number of holes, and in the system $La_{2-x}Sr_xCu_{1-y}Ni_yO_4$ the hole density is $n_h=1+x+y$. In other words, from the standpoint of electrical neutrality the substitution of Zn is equivalent to *n*-type doping and the substitution of Ni is equivalent to *p*-type doping. The small spatial radius of impurity states distinguishes them from mobile carriers formed by doping with Ce^{4+} or Sr^{2+}.[14]

In the system $La_{2-x}Sr_xCu_{1-y}Zn_yO_4$ two types of unit cells in the CuO_2 layer can be distinguished: a) a Sr impurity, giving a hole in the cell, where $n_h=2$, lies above or below the cell; b) instead of a CuO_4 square we have ZnO_4 and for this cell $n_h=0$.

Cells where Sr and Zn act simultaneously are unimportant. In the first place such an encounter is unlikely because *x* and *y* are small and in the second place compensation of *p*- and *n*-type doping occurs in such cells.

The change in the density of states in the lightly doped case ($x\ll 1$, $y\ll 1$) can be easily followed in Fig. 2, which shows the quasiparticle scheme for the spatially averaged picture. Here the occupation numbers of the terms are

$$\langle X^{0;0}\rangle=y,\quad \langle X^{1,\sigma;1,\sigma}\rangle=(1-x-y)/2,$$

$$\langle X^{2,0;2,0}\rangle=x. \tag{12}$$

The change in the density of states as a result of within-gap states is

$$\delta N(E)\sim y\,\delta(E-\varepsilon_{1,1}+\varepsilon_0)+x\,\delta(E-\varepsilon_{2,0}+\varepsilon_{1,1}). \tag{13}$$

Here the second term is associated with b_1 impurity states, which merge with the valence-band top as the hole density increases, forming a band responsible for superconductivity. The first term in Eq. (13) is due to holes with a_1 symmetry. These are impurity states, which lie beyond the edge of the ground band with $b_{1=}$ symmetry. According to Ref. 15, the presence of such a state could be the reason for the strong resonance scattering in the unitary limit. Hops between CuO_4 clusters give, as is well known, narrow Hubbard bands with a typical width of less than 0.5 eV.[20] Since the band widths are small, here we neglect the dispersion of the bands and analyze not the entire density of states but only the impurity part, i.e. the part proportional to the hole density.

In the case of Ni substitution for Cu with $n_h = 1 + x + y$, the solution of the self-consistency equation for the chemical potential is

$$\langle X^{0;0}\rangle = 0, \quad \langle X^{1,\sigma;1,\sigma}\rangle = (1-x-y)/2,$$
$$\langle X^{2,0;2,0}\rangle = x + y. \tag{14}$$

In this case, as one can see from Fig. 2b, the electronic structure is formed by the same quasiparticles as in the absence of Ni in Fig. 1b. The main doping-induced change in the density of states is

$$\delta N(E) \sim (x+y)\,\delta(E - \varepsilon_{2,0} + \varepsilon_{1,1}). \tag{15}$$

As a result, the substitution of Ni for Cu leads primarily to a renormalization of the density of states without any qualitative changes to it.

Conversely, in *n*-type superconductors the substitution of Ni for Cu changes the density of states substantially. Let us consider the system $Pr_{2-x}Ce_xCu_{1-y}Ni_yO_4$. The superconductivity and electrical properties of the single crystals have been investigated in Refs. 10, 26, and 27. Here the average Hall density is $h_h = 1 - x + y$. For cells with Cu impurity $h_h = 0$, while for NiO_4 squares $h_h = 2$. The solution of Eq. (4) is

$$\langle X^{0;0}\rangle = x, \quad \langle X^{1,\sigma;1,\sigma}\rangle = (1-x-y)/2,$$
$$\langle X^{2,0;2,0}\rangle = y. \tag{16}$$

Hole quasiparticles are formed by the same excitations as in Fig. 2a. The change in the density of states as a result of the impurity states is

$$\delta N(E) \sim x\,\delta(E - \varepsilon_{1,1} + \varepsilon_0) + y\,\delta(E - \varepsilon_{2,0} + \varepsilon_{1,1}). \tag{17}$$

In this case Ni forms an impurity state with b_1 symmetry. This state is split from the conduction band bottom and can lead to a strong scattering of current carriers. For *n*-type systems Zn impurity plays a passive role, just as Ni for *p*-type systems. Moreover, as shown in Ref. 27, Zn does not dissolve *n*-type single crystals.

3. DISCUSSION

Oxygen nonstoichiometry can also be a source of *p*-type carriers in *n*-type systems even in the absence of Ni. The complicated temperature dependence of the Hall constant $R_H(T)$, which changes sign from negative to positive with decreasing T,[28] indicates the coexistence of two types of carriers. As shown in Ref. 10, the substitution of Ni for Cu destroys the balance between the electrons and holes, and even for $y > 0.7$ at.% the Hall constant becomes positive at all temperatures. Our conclusion that the hole density increases when Ni is substituted is in qualitative agreement with experiment.[10]

Since the residual resistance is formed by carrier scattering at the same impurity levels, it is obvious that the suppression of T_c is proportional to the changes in the residual resistance ρ_{res} and it follows from our calculations for *p*-type HTSCs that $\rho_{res}(\mathrm{Zn}) \gg \rho_{res}(\mathrm{Ni})$. We also wish to comment on the universal dependence $T_c(\rho_{res})$, found for different 214 and 123 systems with Zn substituted for Cu and with different hole densities.[11] It is important that universality occurs for lightly doped systems and breaks down for optimally and heavily doped systems. In lightly doped systems holes are in regions with antiferromagnetic short-range order. The size of these regions is of the order of ξ_{AFM}. Diamagnetic substitution for the Cu^{2+} spin destroys the equivalence of the sublattices and a magnetic moment from the uncompensated sublattice appears near the impurity Zn^{2+}. This moment has been observed experimentally.[29,30] Hole scattering with spin flip by such a defect will suppress superconductivity, just as in the BCS theory.[31] If it is assumed that scattering with spin flip in lightly doped samples is the main mechanism for the suppression of T_c, then we arrive at the two conclusions that 1) both T_c and ρ_{res} are determined by the same parameters so that there is a universal dependence $T_c(\rho_{res})$ and 2) Ni^{2+} impurity gives diamagnetic substitution with probability u_0^2 so that for T_c and ρ_{res} a relation of the form (1) should hold:

$$\frac{dT_c(\mathrm{Ni})}{dx} \Big/ \frac{dT_c(\mathrm{Zn})}{dx} = \rho_{res}(\mathrm{Ni})/\rho_{res}(\mathrm{Zn}) = u_0^2. \tag{18}$$

For optimally and heavily doped systems the situation is more complicated because for them ξ_{AFM} is small and the assumption that spin scattering plays a dominant role is incorrect. Potential scattering Γ_N here predominates over spin scattering Γ_S. The relative contributions of these mechanisms are different for each hole density and the function $T_c(\rho_{res})$ is no linger universal. Analysis of the suppression of $d_{x^2-y^2}$ type superconductivity in Y-123 with Zn substituted for Cu led[32] to the conclusion that $\Gamma_S/\Gamma_N \leqslant 0.1$. Potential scattering by Ni impurities in *p*-type systems is much weaker than for Zn, since it is not of a resonant character. Conversely, in the *n*-type case a resonant character can occur and gives record high suppression of T_c.

In closing, we note that our goal was to relate the observed differences in Zn- and Ni-substituted systems of both *p* and *n* type to the changes occurring in the electronic structure. We showed that, based on a multielectronic approach taking account of strong electronic correlations, differences indeed arise at the microscopic level: For *p*-type systems the Zn impurities form an impurity level with symmetry different from that of the valence band top while Ni impurities do not; for *n*-type systems even the Ni impurity forms a level with symmetry different from that of the conduction-band bottom.

I thank Henri Alloul and Kurt Westerholt for stimulating discussions.

This work was supported by the State Program on High-Temperature Superconductivity (grant No. 95027).

*E-mail: sgo@post.krascience.rssi.ru

[1] J. M. Tarascon, L. H. Greene, P. Barboux, W. R. Mckinnon, G. W. Hull, T. P. Orlando, K. A. Delin, S. Foner, and E. J. Mcniff, Phys. Rev. B **36**, 8393 (1987).
[2] J. Clayhold, N. P. Ong, P. H. Hor, and C. W. Chu, Phys. Rev. B **38**, 7016 (1988).
[3] G. Xiao, M. Z. Cieplak, J. Q. Xiao, and C. L. Chien, Phys. Rev. B **42**, 8752 (1990).
[4] K. Ishida, Y. Kitaoka, N. Ogata, T. Kamino, K. Asayama, J. R. Cooper, and N. Athanassopoulou, J. Phys. Soc. Jpn. **62**, 2803 (1993).

[5] T. Hotta, J. Phys. Soc. Jpn. **62**, 274 (1993).
[6] P. J. Hirschfeld and N. Goldenfeld, Phys. Rev. B **48**, 4219 (1993).
[7] L. P. Gor'kov, JETP Lett. **40**, 1155 (1984).
[8] J. Sugiyama, H. Yoshikawa, H. Hidaka, T. Sakurai, H. Yamauchi, and S. Tanaka, Phys. Rev. B **42**, 803 (1990).
[9] B. Jayaram, H. Chen, and J. Callanway, Phys. Rev. B **52**, 3742 (1995).
[10] M. Brinkmann, H. Bach, and K. Westerholt, Phys. Rev. B **54**, 6680 (1996).
[11] Y. Fukuzumi, K. Mizuhashi, K. Takenaka, and S. Uchida, Phys. Rev. Lett. **76**, 684 (1996).
[12] Yu. B. Gaididei and V. M. Loktev, Phys. Status Solidi B **147**, 307 (1988).
[13] S. G. Ovchinnikov and I. S. Sandalov, Physica C **161**, 607 (1988).
[14] S. G. Ovchinnikov, Fiz. Tverd. Tela (St. Petersburg) **37**, 3645 (1995) [Phys. Solid State **37**, 2007 (1995)].
[15] D. Poilblanc, D. J. Scalapino, and W. Hanke, Phys. Rev. Lett. **72**, 884 (1994).
[16] F. C. Zhang and T. M. Rice, Phys. Rev. B **37**, 3759 (1988).
[17] S. V. Lovtsov and V. Yu. Yushankhai, Physica C **179**, 159 (1991).
[18] R. Raimondi, J. H. Jefferson, and L. F. Feiner, Phys. Rev. B **53**, 8774 (1996).
[19] W. Brenig, Phys. Rep. **251**, 153 (1995).
[20] S. G. Ovchinnikov, Usp. Fiz. Nauk **167**, 1043 (1997).
[21] V. N. Loktev, Fiz. Nizk. Temp. **22**, 3 (1996) [Low Temp. Phys. **22**, 1 (1996)].
[22] V. A. Gavrichkov and S. G. Ovchinnikov, Fiz. Tverd. Tela (St. Petersburg) **40**, 184 (1998) [Phys. Solid State **40**, 163 (1998)].
[23] S. G. Ovchinnikov, Fiz. Tverd. Tela (St. Petersburg) **36**, 2950 (1994) [Phys. Solid State **36**, 1569 (1994)].
[24] S. G. Ovchinnikov, Ferroelectrics **144**, 91 (1993).
[25] R. O. Zaĭtsev, Zh. Éksp. Teor. Fiz. **70**, 1100 (1976) [Sov. Phys. JETP **43**, 575 (1976)].
[26] M. Brinkmann, T. Rex, M. Stief, H. Bach, and K. Westerholt, Physica C **269**, 76 (1996).
[27] M. Brinkmann, T. Rex, H. Bach, and K. Westerholt, J. Cryst. Growth **163**, 369 (1996).
[28] Z. Z. Wang, T. R. Chien, N. P. Ong, J. M. Tarascon, and E. Wang, Phys. Rev. B **43**, 3020 (1991).
[29] G. Xiao, A. Bakhshai, M. Z. Cieplak, Z. Tesanovic, and C. L. Chien, Phys. Rev. B **39**, 315 (1989).
[30] S. T. Ting, P. Pernambuco-Wise, J. E. Crow, and E. Manousakis, Phys. Rev. B **46**, 11772 (1992).
[31] A. A. Abrikosov and L. P. Gor'kov, Zh. Éksp. Teor. Fiz. **39**, 1781 (1960) [Sov. Phys. JETP **12**, 1243 (1961)].
[32] L. S. Borkowski and P. J. Hirschfeld, Phys. Rev. B **49**, 15404 (1994).

Translated by M. E. Alferieff

SEMICONDUCTORS, DIELECTRICS

Metastable optical absorption of relaxed electronic excitations in BeO-Zn crystals

S. V. Gorbunov, K. V. Bautin, and A. V. Kruzhalov

Ural State Technical University, 620002 Ekaterinburg, Russia

V. Yu. Yakovlev

Tomsk Polytechnical University, 634034 Tomsk, Russia

(Submitted July 9, 1998)
Fiz. Tverd. Tela (St. Petersburg) **41**, 601–605 (April 1999)

Spectra of metastable optical absorption and its relaxation kinetics have been studied in zinc-doped BeO crystals by time-resolved pulsed absorption spectroscopy. A comparison of the observed induced optical absorption of self-trapped excitons and small-radius excitons bound to the zinc impurity suggests that their hole components have similar structures and reveals distinctive features of ''forbidden'' optical transitions in the electronic components. Metastable optical absorption in Zn^+ centers has been discovered. It is shown that the small-radius excitons bound to the zinc impurity form in the hole stages of thermally stimulated tunneling recombination processes involving Zn^+ electronic centers. It has been found that the high recombination probability of the electronic and hole centers created in BeO-Zn crystals by an electron beam may be due to the high degree of their spatial correlation. © *1999 American Institute of Physics.* [S1063-7834(99)00804-7]

It is known that doping wide-gap oxides with isovalent impurities affects substantially the recombination and thermally stimulated processes, as well as the relaxation and decay channels of electronic excitations. This gives rise to formation of additional electronic-excitation trapping centers, as well as of luminescence bands associated with electron-hole recombination involving impurity centers[1] and with radiative recombination of impurity-bound large- and small-radius excitons[2].

Studies using a combination of various luminescence techniques revealed that doping beryllium oxide crystals (BeO) with a zinc isovalent impurity results in the appearance in cathodoluminescence spectra of a broad band at 6.0 eV and of an edge luminescence line at 10.21 eV.[3] An analysis of the data obtained suggested[3] coexistence in BeO–Zn of large- and small-radius excitons bound to Zn^{2+} ions, which substitute for beryllium ions in the lattice sites. Besides, thermally-stimulated luminescence (TSL) and EPR spectra of BeO-Zn crystals were found to indicate formation of both electronic (Zn^+ center) and hole trapping centers.[4–7] Thermal ionization of the hole centers produces in TSL spectra primarily a band at 6.0 eV due to zinc-bound excitons and luminescence of self-trapped excitons (STE) of the first, ''low-temperature'' configuration at 6.7 eV. At the same time thermal delocalization of electrons from the Zn^+ centers results in the onset of a 4.9-eV luminescence associated with STEs of the second, ''high-temperature'' configuration.[5] In order to obtain new information on the structure of bound excitons and electronic-excitation localization centers, as well as on the specific features of thermally activated electron-hole processes, a study has been carried out of the metastable optical absorption induced in BeO-Zn crystals by a pulsed accelerated electron beam. A comparison has been made of the transient absorption spectra of bound and self-trapped excitons and of the electronic centers bound to the zinc impurity.

1. SAMPLES AND EQUIPMENT

The BeO-Zn crystals were grown from a sodium-tungstate melt-solution by Maslov using a technique described elsewhere.[8] The charge was doped by adding 2.0 wt.% Zn. The incorporation of the impurity in the BeO lattice was verified by laser-assisted mass spectrography. The Zn impurity content was as high as 350 ppm. This level exceeds by more than an order of magnitude the contents of the residual impurities Li, Na, B, Mg, and Al. The optical measurements in the 1–5-eV region were carried out in the 80–500-K range by pulsed absorption spectroscopy with a ns-range time resolution (7 ns).[9] The spectra were excited by a GIN-600 pulsed electron-beam accelerator ($E=0.2$ MeV, $j=100$ A/cm^2, $t_p=10^{-8}$ s). An additional investigation of optical absorption spectra in polarized light was performed with a quartz Rochon prism.

2. EXPERIMENTAL RESULTS AND DISCUSSION

Electron-pulse-excited luminescence spectra of BeO-Zn crystals exhibit a broad band peaking at 6.0 eV. The 6.0-eV luminescence, which decays exponentially with a characteristic time $\tau=310\ \mu$s remaining constant within the temperature interval from 80 to 400 K, was previously assigned[3] to radiative annihilation of zinc-bound small-radius excitons.

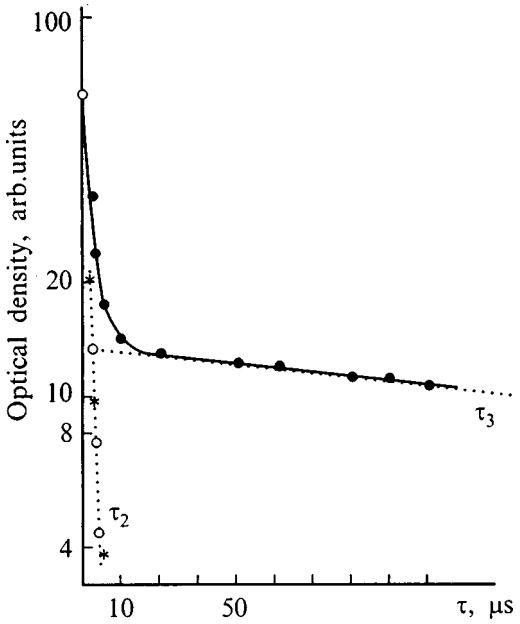

FIG. 1. Relaxation kinetics of optical absorption in BeO-Zn crystals measured at 300 K in the 3.0-eV region.

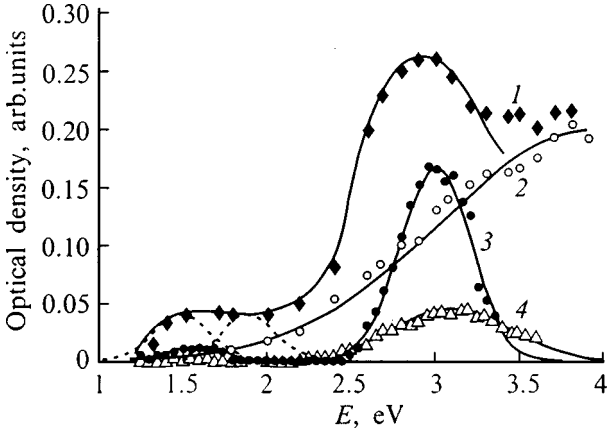

FIG. 2. 300-K transient optical-absorption spectra of (*1,2*) self-trapped excitons and (*3,4*) zinc-bound small-radius excitons measured under the following probing-light polarizations: (*1,3*) $\mathbf{E}\perp\mathbf{C}$ and (*2,4*) $\mathbf{E}\|\mathbf{C}$. Dotted line shows unfolding into Gaussian components.

The observed thermal stability of the 6.0-eV luminescence stimulated a search for similar components in the transient optical absorption of BeO-Zn crystals at 300 K. The relaxation kinetics of the electron-induced absorption within the time interval from the electron pulse termination to 1 ms can be described by superposition of three components with $\tau_1=0.4\,\mu$s, $\tau_2=2\,\mu$s, and $\tau_3=300\,\mu$s (Fig. 1). The first and second components of the transient absorption are characteristic of nominally pure BeO crystals and are due to coexistence of two types of STEs at 300 K.[10] Within the 80–160-K interval, the main contribution to the metastable optical absorption comes from STEs of the low-temperature configuration (STE_1).[11] The corresponding relaxation kinetics are described by an exponential with a time constant $\tau=340\,\mu$s, which is characteristic of triplet states and close to the 6.0-eV luminescence decay time of zinc-bound small-radius excitons.

For $T>160$ K, one observes a shortening of the STE_1 absorption-decay time, which is associated with nonradiative transitions from the triplet state of STE_1 to that of STEs of the second, high-temperature type (STE_2).[12] The shortening of the STE_1 lifetime caused by the thermally activated $STE_1\rightarrow STE_2$ transition accounts for the presence of the first transient-absorption component at 300 K with the time constant $\tau_1=0.4\,\mu$s. The absorption spectrum obtained in polarized light from the STE_1 undergoing a thermally stimulated transition to the STE_2 state through an activation barrier $E_a=240$ meV (Fig. 2) is in agreement with the STE_1 low-temperature spectrum.[11] The difference lies in the lower intensity at 300 K of the short-wavelength 3.9-eV band observed for $\mathbf{E}\|\mathbf{C}$, which is possibly due to the enhanced probability of exciton thermal dissociation under optical excitation of the high-energy states of the STE_1 hole component.

The second stage in the transient-absorption decay kinetics proceeding with a characteristic time $\tau_2=2\,\mu$s is due to STE_2 radiative relaxation.[12] The STE_2 spectrum exhibits a strong shift of the hole band for $\mathbf{E}\perp\mathbf{C}$ to 3.7 eV relative to the STE_1 maximum at 2.9 eV, which is associated[12] with thermally activated hole transfer between the axial and off-axial oxygen-ion sites in the BeO hexagonal lattice. Note that the 1.7-eV bands caused by transitions in the electronic components of both types of STEs[13] are similar in shape and the spectral and polarization characteristics.

The third component in the metastable absorption decay kinetics at 300 K with a characteristic time $\tau_3=(300\pm40)\,\mu$s was observed only in zinc-doped BeO crystals. A combined study of the temperature dependences of the relaxation times of the 6.0-eV luminescence and of the transient-absorption component with τ_3 made for $T>300$ K showed their temperature and decay characteristics to coincide. Thus the third component of the transient optical absorption in BeO-Zn is due to optical transitions in zinc-bound small-radius excitons.

Luminescence studies of pure and zinc-doped BeO crystals revealed a number of features indicating a structural similarity between the zinc-bound excitons and one of the STEs.[3] For instance, the kinetics of the 6.0-eV luminescence decay with a characteristic time constant of 300 μs and of the 6.7-eV luminescence of the low-temperature STE_1 ($\tau=340\,\mu$s) argues for the same triplet nature of the excited states. It was also found that the states of the STE_1 and the zinc-bound small-radius excitons form of those of the free-exciton and zinc-bound large-radius excitons, respectively, as they overcome the nearly equal activation barriers. There are also some differences consisting of a decrease in the degree of polarization and an increase in the thermal stability of the 6.0-eV zinc-bound-exciton luminescence in BeO-Zn.

To establish the structure of zinc-bound excitons, we measured 300-K time-resolved spectra of the metastable optical absorption of BeO-Zn crystals in polarized light. The spectrum of the component due to relaxation of the zinc-bound exciton (Fig. 2) was obtained as the difference between the spectra measured at $t_{del}=50\,\mu$s and $t_{del}=1$ ms. As

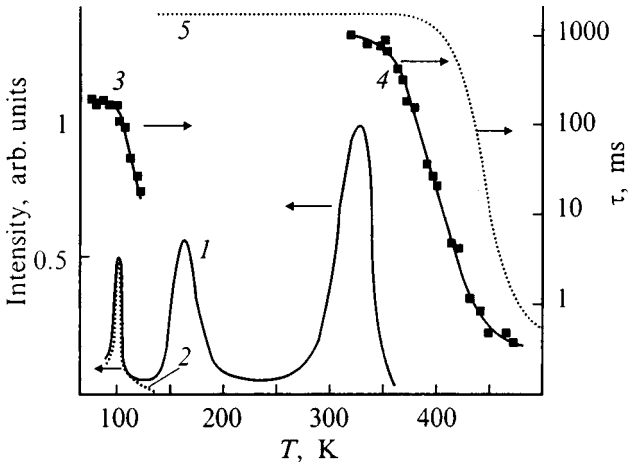

FIG. 3. TSL curves of (*1*) BeO-Zn and (*2*) BeO crystals from Ref. 6, temperature dependences of absorption relaxation times of (*3*) hole and (*4*) electronic Zn^+ centers, and of (*5*) the 6.0-eV luminescence decay time of zinc-bound small-radius excitons in BeO-Zn crystals.

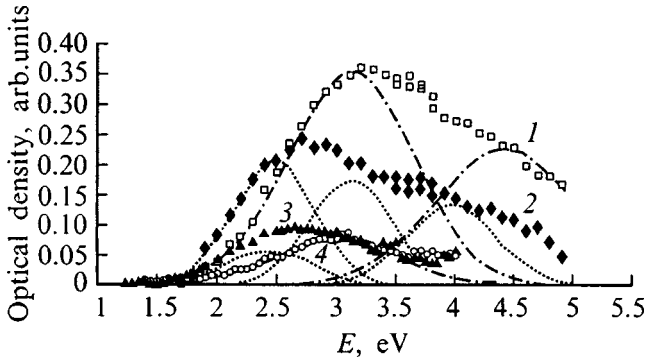

FIG. 4. Spectra of slow transient optical-absorption components in BeO-Zn crystals measured at (*1,2*) 80 K and (*3,4*) 300 K under the following probing-light polarizations: (*2,3*) $\mathbf{E}\perp\mathbf{C}$ and (*1,4*) $\mathbf{E}\|\mathbf{C}$. Dotted and dot-and-dash lines show unfolding into Gaussian components.

seen from Fig. 2, the zinc-bound exciton spectrum for $E>2.5$ eV is close in a number of characteristic features to the STE_1 spectrum. One observes here also small differences due to the shift of the 3.1-eV band by ~ 0.2 eV for $\mathbf{E}\perp\mathbf{C}$, as well as to the intensity ratio and a slight shift of the maxima in the short-wavelength bands for $\mathbf{E}\|\mathbf{C}$. Because the absorption in the UV region of the spectrum can be traced to the STE_1 hole component,[13] one may conclude that the hole cores of the STE_1 and zinc-bound excitons are similar.

At the same time noticeable differences were revealed in the transient-absorption spectrum for $E<2.5$ eV, where optical transitions in the electronic component of STE_1 are quoted[13] to occur. By decomposing the STE_1 spectrum obtained for $\mathbf{E}\perp\mathbf{C}$ into Gaussians we found it to consist of two bands peaking at 1.6 and 1.9 eV (Fig. 2). The absorption intensity due to zinc-bound excitons in this spectral region is lower (by nearly an order of magnitude), making it possible to isolate a weak band near 1.6 eV for $\mathbf{E}\perp\mathbf{C}$ (Fig. 2). It should also be pointed out that a very weak absorption due to zinc-bound excitons is observed in the same spectral interval for $\mathbf{E}\|\mathbf{C}$ as well.

To obtain more information on the structure of zinc-bound excitons in BeO-Zn by time-resolved absorption spectroscopy, we studied the nature and relaxation kinetics of color centers. A comparison of these data with BeO-Zn TSL curves and spectra revealed elementary channels by which zinc-bound excitons form in electron-hole recombination processes.

Decay kinetics studies of the metastable absorption in BeO-Zn crystals performed at 300 K revealed a ''slow'' exponential component with a decay time $\tau\approx 1$ s strongly dependent on the probing-light intensity and temperature. An investigation of the temperature and decay parameters showed the relaxation-time shortening of the centers responsible for this component to obey Mott's law with an activation energy of 0.96 eV (Fig. 3). A comparison of the temperature dependences with TSL and EPR data[4,14] permits a conclusion that this component in the transient absorption decay is associated with thermal delocalization of electrons from the Zn^+ centers. A comprehensive EPR study[4] of this center suggests that it represents essentially an electron trapped in the *s* shell of the Zn^{2+} ion occupying isomorphously the Be^{2+} site in the BeO lattice. The temperature interval within which the Zn^+ center is destroyed is in accord with the TSL peak position at 310 K. The optical characteristics of the Zn^+ center were derived from metastable optical absorption spectra of BeO-Zn crystals measured at 300 K in polarized light with a time delay $t>1$ ms. As seen from Fig. 4, the absorption spectrum of the Zn^+ center consists of two bands, with one of them, peaking at 2.3 eV, polarized perpendicular to the **C** axis, and the other, at 3.1 eV, being isotropic. Cooling BeO-Zn samples to 80 K results in a substantial increase of optical density. For times longer than 1 ms, one clearly distinguishes two exponential stages in color-center destruction kinetics with the times $\tau_1=170$ ms and $\tau_2\approx 3$ s. The polarized spectrum of the transient optical absorption caused by the first slow component in the color-center relaxation kinetics was obtained as a difference between the spectra with $t_{\mathrm{del}}=125$ ms and $t_{\mathrm{del}}=1.5$ s (Fig. 4). By unfolding the spectrum into Gaussian components, one isolated the bands at 2.3 and 3.1 eV characteristic of the Zn^+ centers, as well as additional bands with maxima at 4.0 eV (for $\mathbf{E}\perp\mathbf{C}$) and at 4.5 eV (for $\mathbf{E}\|\mathbf{C}$). By varying the temperature within the 80–120-K interval, one observed a shortening of the decay time of the first component (Fig. 3) with an activation energy $E_a=0.15$ eV. Heating of the sample is accompanied also by the appearance of a TSL peak at 100 K, which is observed in both nominally pure and zinc-doped BeO crystals. As established earlier, the TSL peak at 100 K is due to thermal destruction of the hole trapping centers, which were tentatively assigned to hole self-trapping in BeO.[7] These centers participate effectively in the tunneling luminescence of BeO-Zn crystals. Thus the first, slow relaxation component of induced optical absorption is due to the hole stage in the recombination process. The spectral composition of the TSL peak in BeO-Zn crystals measured at 100 K contains primarily the 6.0-eV luminescence associated with zinc-bound small-radius excitons. The coincidence of the decay kinetics observed in Zn^+ and hole-color-center absorption in the 4.0- and 4.5-eV bands (for $\mathbf{E}\perp\mathbf{C}$ and $\mathbf{E}\|\mathbf{C}$, respectively) suggests that these bands

disappear as a result of the same thermally stimulated tunneling process of hole recombination with the Zn^+ centers, which leads to the formation of zinc-bound excitons. It is essential that after the first, slow component in the relaxation of the absorption induced at 80 K comes to an end, there remain only about 25% of the original number of electronic Zn^+ centers. This evidences a high probability of hole recombination with the Zn^+ centers, which is considerably in excess of that of hole trapping at the Zn^{2+} centers. The idea of the existence of the latter (denoted $[Zn]^+$) was initiated by the appearance of the TSL peak at 160 K, which is present only in BeO-Zn crystals and is due to thermal delocalization of holes.[6,7] It may be conjectured that the second, slow stage in the relaxation kinetics of the induced optical absorption is also associated with the hole stage in the excitation of the recombination luminescence. The spectrum of this luminescence likewise contains a peak at 6.0 eV, which confirms the formation of zinc-bound excitons in the hole recombination with Zn^+ centers. Note that, after the disappearance of the TSL peak at 160 K, 10% of the original (at 80 K) number of Zn^+ centers are destroyed. Measurements of metastable absorption spectra in polarized light made with a time delay of 1.5 s do not permit accurate determination of the contribution of the hole $[Zn]^+$ center absorption to the second, slow component. The growth of the optical density in the short-wavelength UV part of the spectrum indicates that the absorption bands of the $[Zn]^+$ centers lie at energies $E > 3.5$ eV.

Thus one observes in BeO-Zn crystals two low-temperature regions of destruction of various hole centers with the corresponding TSL peaks at 100 and 160 K, which are primarily caused by the formation and radiative annihilation of zinc-bound excitons. It was established that the first peak, at 100 K, is associated with thermally stimulated tunneling annihilation of very closely located hole (possibly, self-trapped) and electronic (Zn^+) centers, with about 75% of the latter produced by the electron beam being destroyed. Such processes, made possible by the high recombination probability of the Tl^0 (Na^0) and V_k centers, were observed to occur earlier in CsI-Tl and CsI-Na crystals and interpreted as due to a high degree of spatial correlation between the radiation-created electronic and hole centers.[15] The second peak at 160 K originates from recombination of more distant hole ($[Zn]^+$) and electronic (Zn^+) pairs.

The closeness of the temperature regions and of the activation energies of the 6-eV luminescence quenching ($E_a = 0.85$ eV) and Zn^+ center destruction ($E_a = 0.96$ eV) suggests that, in order for zinc-bound excitons to form in BeO-Zn in electron-hole processes, an electron must first be trapped near a Zn^{2+} ion. Accepting this scenario, one can now analyze the specific features in the structure of the electronic components of STEs and zinc-bound excitons in BeO. The oscillator strengths of optical transitions in the electronic component of STEs were estimated from the known quantities $f = 0.1-0.2$ for hole centers in alkaline-earth oxides[16] and from a comparison of the parameters of the hole and electronic STE absorption bands in BeO. The value $f \approx 0.05$ obtained indicates that transitions in the electronic component of STEs are strongly forbidden by selection rules. This may be associated with specific features in the electronic structure of BeO. As follows from theoretical calculations made by crystal-cluster,[17] quasi-molecular extended-cell,[18] and pseudopotential[19] methods, the electronic structure of BeO differs from that of alkaline-earth oxides primarily in the substantial contribution (30–40%) the oxygen *s* states provide to conduction-band states. This feature of the partial composition of the conduction-band bottom suggests that optical transitions in the STE electronic component in BeO are actually selection-rule-forbidden $s \rightarrow s$ transitions between one-electron states at the conduction-band minimum, which are derived from the *s* states of beryllium and oxygen. The close-packed würtzite structure of BeO favors strong level splitting and appreciable *s-p* mixing, which results in a partial lifting of the forbiddenness. The lattice of BeO-Zn can suffer strong local strains in the vicinity of the Zn^{2+} ion, because its ionic radius (0.83 Å) is considerably larger than that of Be^{2+} (0.34 Å). The experimentally observed sizable decrease in the intensity of induced absorption in the region of the electronic component of the zinc-bound small-radius exciton evidences a weakening of the optical-transition oscillator strength.

The two absorption bands of the STE_1 electronic component in BeO observed by us at 1.6 and 1.9 eV originate from optical transitions to two excited levels, which are possibly connected with spin-orbit splitting of conduction-band states. A similar two-band pattern is seen also in the optical absorption spectrum of the electronic Zn^+ center. Calculations of the electronic structure of local centers in BeO made with inclusion of spin polarization showed[20] that substitution of Zn^{2+} for Be^{2+} results in a splitting-off of a local level at 1.1 eV below the conduction-band minimum. This value is roughly in accord with the short-wavelength shift of the Zn^+ spectrum with respect to the STE_1 spectrum in BeO.

The authors express gratitude to Ch. B. Lushchik for interest in the work, and to V. Yu. Ivanov and S. V. Kudyakov for fruitful discussions and assistance in experiments.

*E-mail: baut@dpt.ustu.ru

[1] T. N. Kärner, A. F. Malysheva, and V. T. Tazhigulov, Tr. IF AN ÉSSR **55**, 217 (1984).
[2] E. H. Feldbach, Ch. B. Lushchik, and I. L. Kuusmann, JETP Lett. **39**, 61 (1984).
[3] V. Yu. Ivanov, V. A. Pustovarov, S. V. Gorbunov, S. V. Kudyakov, and A. V. Kruzhalov, Fiz. Tverd. Tela (St. Petersburg) **38**, 3333 (1996) [Phys. Solid State **38**, 1818 (1996)].
[4] I. N. Antsygin, V. Yu. Ivanov, and A. V. Kruzhalov, Zh. Tekh. Fiz. **58**, 635 (1988) [Sov. Phys. Tech. Phys. **33**, 386 (1988)].
[5] V. Yu. Ivanov, I. N. Antsygin, S. V. Gorbunov, A. V. Kruzhalov, and V. A. Maslov, Opt. Spektrosk. **64**, 945 (1988) [Opt. Spectrosc. **64**, 564 (1988)].
[6] I. N. Ogorodnikov, A. V. Kruzhalov, and V. A. Maslov, Zh. Prikl. Spektrosk. **49**, 134 (1988).
[7] I. N. Ogorodnikov, V. Yu. Ivanov, and A. V. Kruzhalov, Zh. Prikl. Spektrosk. **54**, 605 (1991).
[8] V. A. Maslov, G. M. Rylov, V. G. Mazurenko, A. V. Kruzhalov, and B. V. Shul'gin, *Abstracts VI Intern. Conference on Crystal Growth* (Moscow, 1980), Vol. 3, p. 268.
[9] B. P. Gritsenko, V. Yu. Yakovlev, G. D. Lyakh, and Yu. N. Safonov, *Abstracts All-Union Conference on Metrology of Fast Processes* (Moscow, 1978), p. 61.

[10] S. V. Gorbunov, S. V. Kudyakov, B. V. Shulgin, and V. Yu. Yakovlev, Radiat. Eff. Defects Solids **135**, 269 (1995).
[11] S. V. Gorbunov, V. Yu. Yakovlev, V. Yu. Ivanov, and A. V. Kruzhalov, Fiz. Tverd. Tela (Leningrad) **32**, 2942 (1990) [Sov. Phys. Solid State **32**, 1708 (1990)].
[12] S. V. Gorbunov, S. V. Kudyakov, V. Yu. Yakovlev, and A. V. Kruzhalov, Fiz. Tverd. Tela (St. Petersburg) **38**, 1298 (1996) [Phys. Solid State **38**, 719 (1996)].
[13] S. V. Gorbunov, S. V. Kudyakov, V. Yu. Yakovlev, and A. V. Kruzhalov, Fiz. Tverd. Tela (St. Petersburg) **38**, 214 (1996) [Phys. Solid State **38**, 119 (1996)].
[14] A. V. Kruzhalov, I. N. Ogorodnikov, and S. V. Kudyakov, Izv. Vyssh. Uchebn. Zaved. Fiz. **39**, No. 11, 76 (1996).
[15] S. A. Chernov and É. D. Aluker, *Trudy Symp. SSD-97* (Ekaterinburg, 1998), p. 30.
[16] B. Henderson and J. E. Wertz, *Defects in Alkaline-Earth Oxides with Applications to Radiation Damage and Catalysis* (Taylor & Francis, London, 1977), p. 159.
[17] V. A. Lobach, I. R. Rubin, A. V. Kruzhalov, B. V. Shul'gin, and V. Yu. Ivanov, Fiz. Tverd. Tela (Leningrad) **29**, 2610 (1987) [Sov. Phys. Solid State **29**, 1506 (1987)].
[18] A. N. Vasil'ev, K. B. Topornin, and R. É. Évarestov, Opt. Spektrosk. **48**, 277 (1980) [Opt. Spectrosc. **48**, 156 (1980)].
[19] I. V. Kityk, V. N. Kolobanov, and V. V. Mikhaĭlin, Vestn. Mosk. Univ., Fiz., Astron. **28**, No. 4, 67 (1987).
[20] A. V. Kruzhalov, V. A. Lobach, I. N. Ogorodnikov, and I. R. Rubin, Zh. Prikl. Spektrosk. **51**, 997 (1989).

Translated by G. Skrebtsov

Propagation of a heat pulse in a bounded conducting medium: thermoelectric detection

Alvaro F. Carballo-Sanchez and Yu. G. Gurevich*)

Centro de Investigacion y de Estudios del I.P.N., Mexico D. F. 07000, Mexico

G. N. Logvinov†) and Yu. V. Drogobitskiĭ

Ternopol' State Pedagogical University 282009 Ternopol', Ukraine

O. Yu. Titov‡)

Department of Physics, Bar-Ilan University Ramat-Gan 52900, Israel
(Submitted May 18, 1998; resubmitted September 3, 1998)
Fiz. Tverd. Tela (St. Petersburg) **41**, 606–611 (April 1999)

The one-dimensional, non-steady thermal field on the surface of a bounded conducting sample arising from the absorption of a square heat pulse of arbitrary duration is calculated. It is shown that the spatial temperature distributions for long and short pulses are fundamentally different: After a short heat pulse is ''switched off'' regions of local heating arise; such regions do not occur in the case of a long pulse. The thermoelectric response is calculated and it is shown that data on the thermal conductivity and thermal diffusivity can be obtained in a single experiment. © *1999 American Institute of Physics.* [S1063-7834(99)00904-1]

Interest in the investigation of diverse properties of materials, specifically, semiconductors, upon excitation of nonsteady-state, thermal processes in them, has increased appreciably in the last few years. Under experimental conditions these processes are excited either using time-modulated continuous high-energy beams or individual energy pulses. In either case, as a rule, laser radiation is used as the source of external excitation.

When the laser radiation is absorbed, its energy is expended partially on heating charge carriers and partially on the production of electron-hole pairs (if the photon energy exceeds the band gap). As a result of the electron-phonon interaction, energetically nonequilibrium carriers transfer energy to phonons, as a result of which transient heat fluxes arise in the current-carrier and phonon subsystems. Nonequilibrium current carriers diffusing into the sample recombine, giving rise to secondary sources of sporadic heating.

In the general case, there are three energetically inequivalent subsystems of quasiparticles under these conditions — electrons, holes, and phonons. If all characteristic times (modulation period or pulse duration of the light flux, lifetimes of the nonequilibrium carriers, and the electron–phonon energy interaction times) are much greater than the characteristic times for establishment of temperature distributions,[1] then all three quasiparticle subsystems should be described by their nonequilibrium temperature.

The detection by some method of thermal response of a material to external radiation enables gathering extensive information about diverse parameters of the material, first and foremost, the thermal, relaxation, and optical properties. At the present time the most widely used methods in the modulated-radiation regime are photothermal methods, based on measurement of the photoacoustic, thermal, piezoelectric, photoluminescence, and other phenomena (see, for example, Refs. 2 and 3).

The detected stationary signal in the general case is produced by all of the processes indicated above, and these processes all operate simultaneously. For this reason, it is quite difficult to distinguish the contribution of each process. In this connection, to study individual energy relaxation processes it seems to us that it is more promising to employ individual heat pulses.

When the energy of a pulse is absorbed, transient relaxation processes arise in the system. Each such process is characterized by its own relaxation time, and the relaxation processes often have different scales. For this reason, each process can, in principle, be studied separately.

The questions associated with the experimental study of transient relaxation processes in semiconductors have been discussed in Refs. 4 and 5. In these works a new method based on measurements of the transient thermo-emf arising in a semiconductor sample after irradiation with a laser pulse is described.

The measurement of the thermo-emf as the output signal in photothermal experiments in semiconductors is very promising because of its simplicity and high measurement accuracy, the absence of intermediate media for converting a signal from one form into another, and the possibility of probing the temperature along the sample.

In the last few years reports have appeared about other pulsed methods. For example, in Ref. 6 diffusivity was measured comparatively simply in various polymer films by measuring the instantaneous values of the pyroelectric responses. However, the measured instantaneous response agrees satisfactorily with the theoretical results only for fairly long pulses. In the words of the authors themselves, this makes the measurements less effective.

Advances in pulsed thermal methods, and the experimental results obtained using such methods, have been a stimulus for constructing an adequate theory of the corre-

sponding thermal processes in semiconductors. The first part of this theory is presented in the present paper.

From a theoretical standpoint, the solution of the problem of transient thermal relaxation processes in semiconductors is too complicated to present in a general form. For this reason, in the present paper we confine ourselves to the simplest model. We shall assume that the nonequilibrium temperatures of all quasiparticles in the experimental sample are the same and the absorption of an energy pulse occurs at the surface. Such a model can be realized, for example, in semiconductors with *n*- or *p*-type conductivity with a sufficiently strong electron-phonon energy interaction with the semiconductor in close contact with a metal film that absorbs the incident radiation and transforms it into heat. We note that the model formulated is exact for describing the propagation of a heat pulse in metals and opaque dielectrics.

1. CALCULATION OF THE NON-STEADY-STATE THERMAL FIELD $T(x)$

In the absence of interior heat sources the heat flux density $\mathbf{Q}$ at local temperature $T(r,t)$, where r is the radius vector and t is the time, are ordinarily related with one another by the well-known Fourier relation

$$\mathbf{Q}=-\kappa\nabla T, \tag{1}$$

where κ is the thermal conductivity.

The heat-conduction equation itself, reflecting the law of conservation of energy, is parabolic and in one dimension it has the form

$$\frac{\partial T}{\partial t}=D\frac{\partial^2 T}{\partial x^2}, \tag{2}$$

where $D=\dfrac{\kappa}{\rho c}$ is the thermal diffusivity and ρ is the density and c the specific heat of the material.

We note that there are many works (see, for example, Refs. 7 and 8) where it is asserted that Eq. (2) presumes an infinite heat propagation velocity and therefore is incorrect in the general case. The authors indicated propose taking account of the finiteness of this velocity by modifying the relation (1) as

$$\mathbf{Q}+\tilde{\tau}\frac{\partial \mathbf{Q}}{\partial t}=-\kappa\nabla T, \tag{3}$$

which together with the law of conservation of energy leads to a ''telegraph-type'' heat-conduction equation

$$\frac{\partial T}{\partial t}+\tilde{\tau}\frac{\partial^2 T}{\partial t^2}=D\frac{\partial^2 T}{\partial x^2}. \tag{4}$$

Here $\tilde{\tau}$ is a parameter with the dimension of time.

However, the physical meaning of the parameter $\tilde{\tau}$ is not indicated in any work devoted to the discussion of this question. It is merely indicated that $\tilde{\tau}$ is a relaxation time associated with the properties of the material. As $\tilde{\tau}$ approaches zero, Eq. (4) transforms into Eq. (2). This means that if the pulse duration τ or the characteristic modulation time is greater than $\tilde{\tau}$, Eq. (2) can be used; if the indicated times are shorter than or of the order of $\tilde{\tau}$, Eq. (4) must be used. From our standpoint, however, the last assertion is incorrect, since the relaxation time $\tilde{\tau}$ can only be the time required to establish the temperature in the system. Therefore if the pulse duration or modulation period is less than or of the order of $\tilde{\tau}$, there is not enough time for the temperature to become established in the sample and the thermal processes cannot be described in terms of the temperature.

Let a square heat pulse of duration τ and intensity Q_0 be incident on the left-hand surface $x=0$ of a uniform and isotropic sample in the form of a parallelepiped with unit cross-sectional area. The right-hand surface $x=l$ is in contact with the surrounding medium at fixed temperature T_0. The lateral faces of the sample are assumed to be thermally insulated.

In the general case the heat flux through the surface $x=l$ should be determined by the Newtonian boundary condition

$$Q(x=l)=h[T(x=l)-T_0],$$

where h is a parameter that determines the intensity of heat transfer between the sample and the surrounding medium and $T(x=l)$ is the sample temperature at the point $x=l$.

In the limits $h\to 0$ and $h\to\infty$ the relation written down above determines, respectively, the adiabatic $[Q(x=l)=0]$ and isothermal $[T(x=l)=T_0]$ contacts. We note that in the problem at hand the adiabatic boundary condition is incompatible with the boundary condition on the surface $x=0$. This follows from the fact that after the heat pulse has passed $(t>\tau)$ the heat flux from the left is zero, and therefore it can flow out only through the surface $x=l$, which is impossible in the case of an adiabatic boundary condition.

The second limiting case of an isothermal contact is completely compatible with the boundary condition on the surface $x=0$ for any moment in time. This is the case studied in the present paper.

To determine the temperature field $T(x,t)$ produced by the incident heat pulse we divide the entire time interval into two subintervals

a) $0<t\leqslant\tau$,

b) $t>\tau$.

Next, we assume that the intensity Q_0 and hence the change in temperature in the sample are sufficiently small so that all transport constants depend only on the temperature T_0 and therefore the initial Eq. (2) is assumed to be linear.

According to the formulation of the problem, in the interval $0<t\leqslant\tau$ the boundary and initial conditions for Eq. (2) are

$$\left.\frac{\partial T}{\partial x}\right|_{x=0}=-\frac{Q_0}{\kappa}, \tag{5}$$

$$T(x,t)|_{x=l}=T_0, \tag{6}$$

$$T(x,t)|_{t=0}=T_0. \tag{7}$$

The general solution of Eq. (2) with the boundary and initial conditions (5)–(7) is

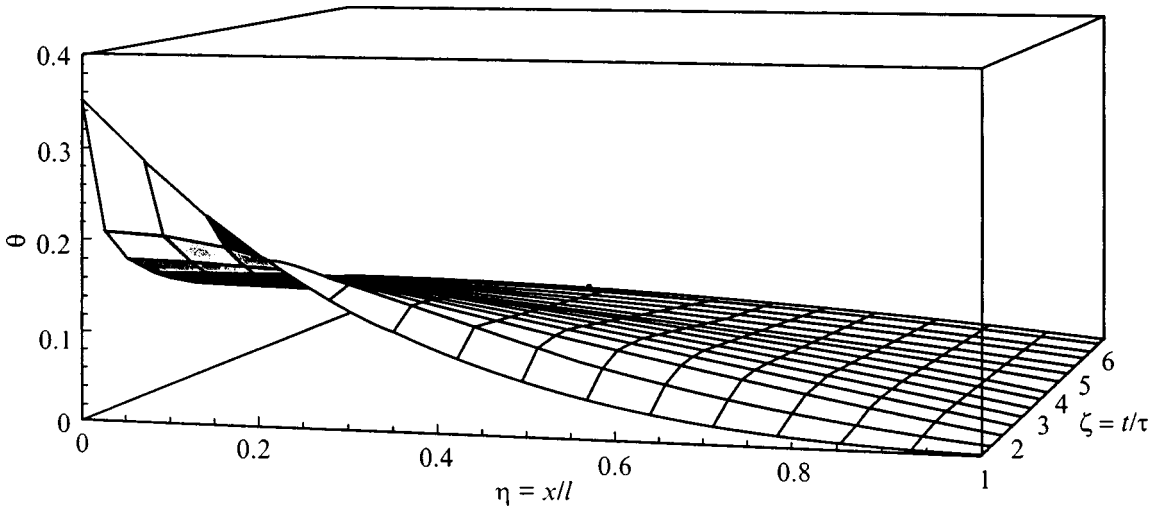

FIG. 1. Two-dimensional dependence of the function $\Theta(\eta, \zeta)$ for a short pulse ($\tau = 0.1\tau_0$) after the pulse is switched off.

$$T(x,t) = T_0 + \frac{Q_0}{\kappa}(l-x) - \frac{8l}{\pi^2}\frac{Q_0}{\kappa}\sum_{k=0}^{\infty}\frac{\cos\left[(2k+1)\dfrac{\pi x}{2l}\right]}{(2k+1)^2} \times \exp\left[-(2k+1)^2\frac{\pi^2 D}{4l^2}t\right]. \quad (8)$$

We note that the solution (8) corresponds to the establishment of a static temperature distribution after the heat flux is switched on.[9]

At time $t = \tau$ the heat influx into the sample stops and the solution (8) for this moment in time serves as the initial condition for Eq. (2) for the interval $t > \tau$. The boundary conditions for this time interval are

$$\left.\frac{\partial T}{\partial x}\right|_{x=0} = 0, \quad (9)$$

$$T(x,t)|_{x=l} = T_0. \quad (10)$$

In this case the solution is described by the function

$$T(x,t) = T_0 + \frac{8l}{\pi^2}\frac{Q_0}{\kappa}\sum_{k=0}^{\infty}\frac{\cos\left[(2k+1)\dfrac{\pi x}{2l}\right]}{(2k+1)^2} \times \left\{\exp\left[(2k+1)^2\frac{\pi^2 D}{4l^2}\tau\right] - 1\right\} \times \exp\left[-(2k+1)^2\frac{\pi^2 D}{4l^2}t\right]. \quad (11)$$

A criterion for linearity of Eq. (2) can be derived from the expression (8). The coordinate dependence of the transport constants κ, ρ, and c can be neglected, if $T(x,t) - T_0 \ll T_0$, i.e. the intensity of the incident pulse must satisfy the relation

$$Q_0 \ll \frac{\kappa T_0}{l}. \quad (12)$$

2. ANALYSIS OF THE TEMPERATURE DISTRIBUTIONS

It is evident from the results (8) and (11) obtained above that the character of the temperature distribution depends on the parameter $\tau_0 = (4l^2/\pi^2 D)$, which has the dimensions of time. Physically, this is the macroscopic relaxation time of a temperature fluctuation arising in the entire volume of the sample under the influence of a thermal perturbation.

As follows from Eqs. (8) and (11), the ratio of the times τ and τ_0 greatly influences the character of the coordinate- and time-dependences of the temperature. Since these parameters are independent, both the situation $\tau \gg \tau_0$ (long pulses) and $\tau \ll \tau_0$ (short pulses) can be realized. We note that for fixed physical parameters of the material the pulse duration criterion depends strongly on the geometric dimensions of the sample (in this case, the sample length).

The characteristic two-dimensional dependence of the function $\Theta(\eta,\zeta) = (\kappa/Q_0 l)[T(\eta,\zeta) - T_0]$, where $\eta = (x/l)$ and $\zeta = (t/\tau)$, is displaed for a short pulse in Fig. 1. It is clearly seen that in this case the function $\Theta(\eta,\zeta)$ and hence also the function $T(x,t)$ are nonlinear with respect to both arguments. Moreover, the function is nonmonotonic as a function of the variable t. It is obvious that this feature should be reflected in the characteristics of the thermoelectric signal that has appeared in the sample.

For long pulses, the sample is heated up exponentially rapidly (in a time $\sim\tau_0$) and it stays in a nearly steady state for a long time ($\sim\tau$). After the heat pulse is ''switched off,'' the temperature $T(x,t)$ approaches its equilibrium value T_0 exponentially rapidly (likewise in a time $\sim\tau_0$). For $\tau_0 < t$, the temperature is a linear function of the coordinates to a high degree of accuracy. The heating and relaxation processes are accompanied by monotonic increase and decrease of temperature in time at everywhere in the sample.

A different picture is observed for a short pulse ($\tau \ll \tau_0$) passing through the sample (Figs. 2 and 3). In this case there are no quasistationary states in the heating process

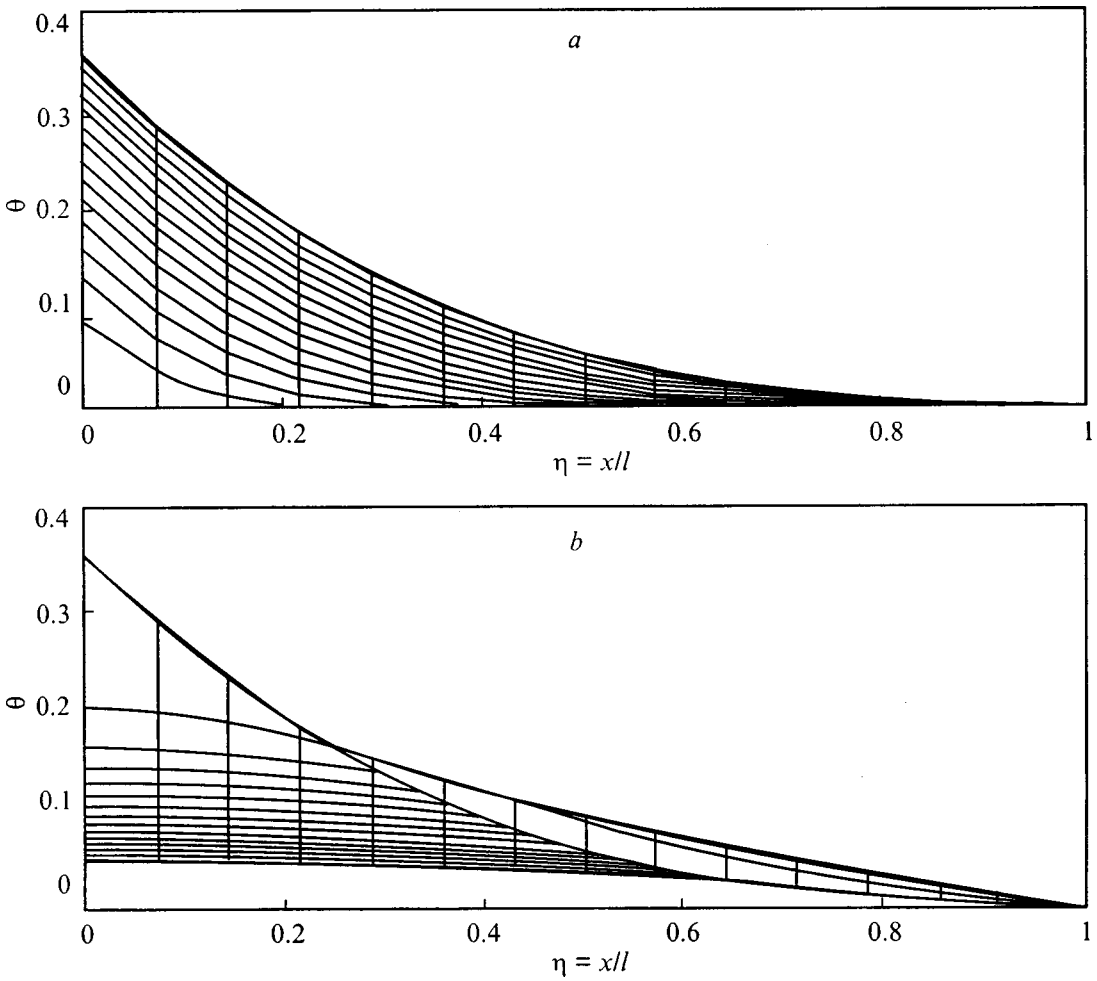

FIG. 2. Dynamics of the spatial distribution functions $\Theta(\eta, \zeta)$ for a short pulse ($\tau = 0.1\tau_0$). a — In the time interval $0 < t \leqslant \tau$; b — in the time interval $t > \tau$.

$(0 < t \leqslant \tau)$, and the spatial temperature distribution is strongly nonlinear at each moment in time (Fig. 2a). For $\tau/\tau_0 \ll 1$ the series (11) determining the relaxation process converges slowly and each harmonic can be matched with its own relaxation time $\tau_k = (\tau_0/(2k+1)^2)$. Since $\tau_k < \tau_0$, each subsequent harmonic decays more rapidly than the preceding one, and therefore the entire relaxation process in the sample after the pulse is switched off is characterized by the time τ_0 (Fig. 3).

A substantial departure from the preceding case is the presence of spatial regions where a time-nonmonotonic behavior of temperature is observed during the relaxation of the

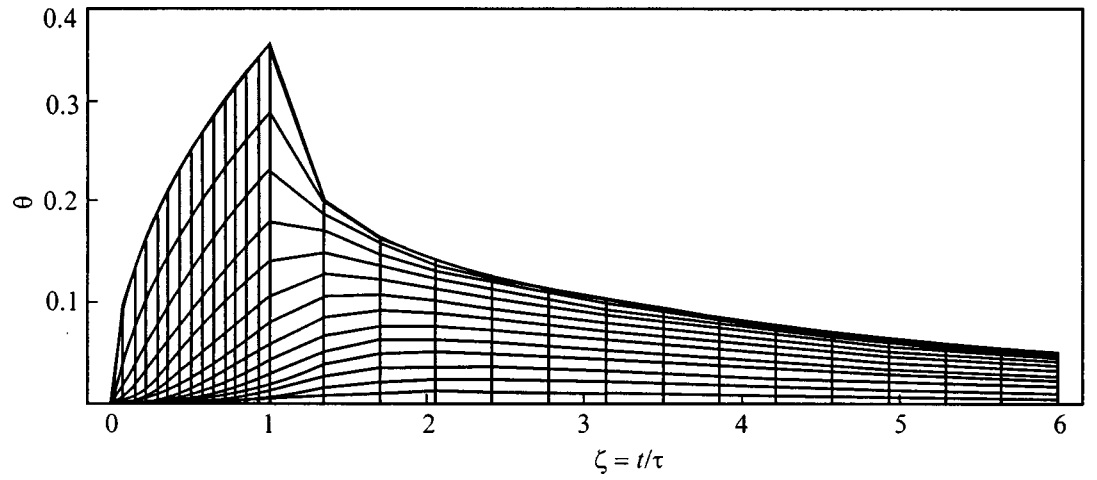

FIG. 3. $\Theta(\eta, \zeta)$ versus the dimensionless parameter $\zeta = t/\tau$ at various points in the sample for a short pulse ($\tau = 0.1\tau_0$).

thermal perturbation (Fig. 2b). Physically, this behavior can be understood as follows. Let us distinguish a layer in the sample lying between the planes $x=0$ and $x'=(\pi/2)\sqrt{D\tau}$. For $\tau<\tau_0$ (x' lies between 0 and 1), there is enough time for a quasi-steady temperature distribution to be established in this layer during the heat pulse. For this reason, after the pulse is ''switched off'' the function $T(x,t)$ in this layer will behave qualitatively, for all times $t>\tau$, just as in the entire sample for a long pulse ($\tau>\tau_0$), i.e. it will remain monotonic, being a linear function of the coordinates at $t=\tau$. For $x>x'$ the temperature gradient is no longer constant, as a result of which the inflowing heat fluxes in any layer with surfaces $x>x'$ exceed the outgoing fluxes and local heating occurs throughout the entire thermal relaxation process.

It is obvious that, at the point $x>x'$, the temperature is maximum at the time

$$t''=\tau+\frac{4}{\pi^2}\frac{(x''-x')^2}{D}. \tag{13}$$

If $x'\geqslant 1(\tau>\tau_0$, long pulse), obviously, there are no regions of local heating, since there is enough time during the action of the pulse for a quasi-steady temperature distribution to be established in the entire sample.

3. CALCULATION OF THE THERMOELECTRIC RESPONSE

It is well known that a spatial nonuniformity in the temperature in a closed inhomogeneous circuit leads to the appearance of a thermo-emf in the circuit. This effect is most easily seen in semiconductors because of the large value of the differential thermopower α compared to other conducting materials[10] and the strong temperature dependence of the chemical potential of the charge carriers. Under open-circuit conditions, the thermo-emf measured between the end surfaces of a sample is

$$E(t)=-\int_0^l \alpha\frac{dT(x,t)}{dx}dx=\alpha[T(x=0,t)-T_0]. \tag{14}$$

Taking into consideration the initial conditions of the problem and using the expressions (8) in (11), it is easy to obtain

$$E(t)=\alpha\frac{Q_0 l}{\kappa}\frac{8}{\pi^2}\sum_{k=0}^{\infty}\frac{\exp\left(-(2k+1)^2\dfrac{t}{\tau_0}\right)}{(2k+1)^2}+\Theta(t-\tau)\times\alpha\frac{Q_0 l}{\kappa}\left\{1-\frac{8}{\pi^2}\sum_{k=0}^{\infty}\frac{\exp\left(-(2k+1)^2\dfrac{t-\tau}{\tau_0}\right)}{(2k+1)^2}\right\}, \tag{15}$$

where $\Theta(t-\tau)=\{^{0,\ t\leqslant\tau}_{1,\ t>\tau}$ is the Heaviside function.[11] The thermo-emf calculated per unit heat flux $\varepsilon(t)=(E(t)/Q_0)[(\mu V/Q_0)\times 10^{-3}]$ for different ratios of τ and τ_0 is presented in Fig. 4 (the parameters of Si were used in the calculations: $\alpha=0.4(\mu\text{V/K})$,[12] $\kappa=0.96(\text{W/cm}\cdot\text{K})$,[13] $T_0=300$ K, $\tau=10^{-8}$ s, $l=1$ cm).

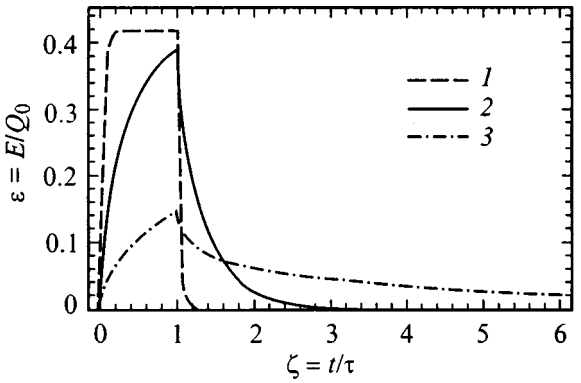

FIG. 4. Thermoelectric response for heat pulses of various durations. τ: *1* — $10\tau_0$, *2* — τ_0; *3* — $0.1\tau_0$.

A characteristic feature of the graphs is the presence of sharp peaks of the thermo-emf for short- and intermediate-duration heat pulses. For long pulses, the sharp peaks degenerate into a horizontal plateau, in complete agreement with physical notions. For $\tau\gg\tau_0$, the problems are similar to finding the thermo-emf for a continuously acting external perturbation.

The graph clearly show that the maximum values of the thermoelectric responses increase with the pulse duration. Their relaxation times (when relation (12) is satisfied) remain unchanged.

Measurement of the relaxation time of the thermoelectric response and of the maximum amplitude of the response makes it possible to determine important thermal parameters, such as the thermal diffusivity D and the thermal conductivity κ, in a single experiment.

As indicated above, for $t>\tau$, the temperature in the section $x=0$ and together with it the thermo-emf are monotonically decreasing functions of time. However, if the thermo-emf is measured between the points $x''>x'$ and $x>l$, then for short pulses ($\tau<\tau_0$) a peak appears in the time dependence of the thermo-emf. The coordinate of this peak is determined not by the time $t=\tau$ but rather by relation (13) (Fig. 5). This makes it possible to determine D directly and much more accurately (than in the preceding case).

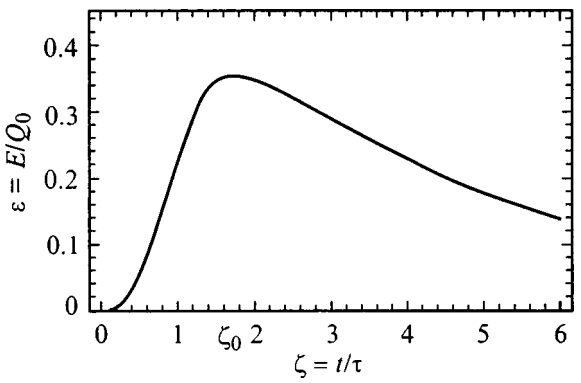

FIG. 5. Thermoelectric response to a short pulse ($\tau=0.1\tau_0$) with the thermo-emf measured between the sections $x=x''$ and $x=l$; $\zeta_0=1+((x''-x')^2/D\tau)$.

One of us (G. N. L.) thanks Dr. Gerardo Gonzales de la Cruz and Dr. Yu. G. Gurevich as well as colleagues in the Department of Solid-State Physics at CINVESTAV (Mexico) for their hospitality.

*)E-Mail: gurevich@fis.cinvestav.mx
†)E-Mail: logvinov@ecolab.ternopil.ua
‡)E-Mail: titovo@biu.ac.il

[1] F. G. Bass, V. S. Bochkov, and Yu. G. Gurevich, *Electrons and Phonons in Bounded Semiconductors* (Nauka, Moscow, 1984).
[2] A. Rosencwaig and A. Gersho, J. Appl. Phys. **47**, 64 (1976).
[3] A. Mandelis, *Photoacoustic and Thermal Waves Phenomena in Semiconductors* (North-Holland, Amsterdam, 1987).
[4] M. Sasaki, H. Negishi, and M. Inoue, J. Appl. Phys. **59**, 796 (1986).
[5] V. A. Kolbachinski, Z. M. Dashevskii, M. Inoue, M. Sasaki, H. Negishi, W. X. Gao, P. Lostak, J. Horak, and A. De Visser, Phys. Rev. B **52**, 10915 (1995).
[6] S. Bauer and A. S. De Reggi, J. Appl. Phys. **80**, 6124 (1996).
[7] D. D. Joseph and L. Presiosi, Rev. Mod. Phys. **61**, 41 (1989).
[8] M. A. Olivares-Robles and L. S. Carsia-Colin, J. Non-Equilib. Thermodyn. **21**, 361 (1996).
[9] H. S. Carslaw and J. C. Jaeger, *Conduction of Heat in Solid* (Clarendon Press, Oxford, 1947).
[10] A. F. Ioffe, *Semiconductor Thermoelements* (Soviet Academy of Sciences Press, Moscow, 1960).
[11] G. Korn and T. Korn, *Mathematical Handbook for Scientists and Engineers* (McGraw-Hill, N. Y., 1961; Nauka, Moscow, 1973).
[12] T. H. Gebal and C. W. Hull, Phys. Rev. **98**, 940 (1955).
[13] P. I. Baranskiĭ, V. P. Klachkov, and I. V. Potykevich, *Handbook of Semiconductor Electronics* (Naukova dumka, Kiev, 1975).

Translated by M. E. Alferieff

X-ray microanalysis of quaternary semiconductor solid solutions and its application to the (SnTe-SnSe):In system

V. A. Moshnikov, A. V. Moshnikov, and A. I. Rumyantseva

St. Petersburg State Electrical Engineering University, 197376 St. Petersburg, Russia

S. A. Nemov

St. Petersburg State Technical University, 195251 St. Petersburg, Russia

R. V. Parfen'ev and A. V. Chernyaev

A. F. Ioffe Physicotechnical Institute, Russian Academy of Sciences, 194021 St. Petersburg, Russia
(Submitted September 3, 1998)
Fiz. Tverd. Tela (St. Petersburg) **41**, 612–617 (April 1999)

A reliable technique of local chemical characterization of multicomponent semiconductor solid solutions has been developed, and the possibility of its application to the SnTe-SnSe quaternary solid solutions doped with 16 at. % In verified. The behavior of the electrical resistivity of samples of these solid solutions at low temperatures, 0.4–4.2 K, has been studied. The critical temperature T_c and the second critical magnetic field H_{c2} of the superconducting transition and their dependences on the solid-solution composition have been determined. The superconducting transition at $T_c \approx 2-3$ K is due to hole filling of the In-impurity resonance states, and the observed variation of the superconducting transition parameters with increasing Se content in the solid solution is related to the extrema in the valence band and the In band of resonance states shifting with respect to one another. © *1999 American Institute of Physics.* [S1063-7834(99)01004-7]

The II-VI compounds have both scientific and practical interest due to their unusual properties when doped with Group-III elements, in this case, In-doped SnTe-based solid solutions. The In impurity atoms form in the energy spectrum of SnTe and of the solid solutions $Sn_{1-x}Ge_xTe$ ($x \leqslant 0.2$) and $Sn_{1-x}Pb_xTe$ ($x \leqslant 0.4$) (Refs. 1 and 2, respectively) a band of quasilocal (resonance) states within the valence band. The position of the impurity band and its broadening depend essentially on the doping level, N_{In}, i.e. the concentration of In introduced into the crystal, and the solid-solution composition. The existence of the band of In quasilocal states with a high DOS, $g_{In} \propto N_{In}$, gives rise to a number of new physical phenomena, such as pinning of the hole Fermi level ε_F and resonant hole scattering into the In band.[2,3] In-doped SnTe, in particular, exhibits anomalous temperature and concentration dependences of the main kinetic coefficients and low Hall mobilities [$R\sigma \lesssim 100\,\mathrm{cm^2/(V\cdot s)}$]. The filling of impurity resonance states is closely connected with the onset of superconductivity with superconducting transition temperatures fairly high for semiconductors (the helium temperature region) and critical magnetic fields of the order of 10–30 kOe.[3–5] It should be pointed out that T_c and H_{c2} in SnTe without the In impurity are an order of magnitude lower.[6] Therefore SnTe:In-based solid solutions may hold promise as materials for low-temperature bolometers to operate in the helium temperature region. Besides, the close connection between the existence of resonance impurity states and the associated superconductivity permits one to use investigation of the superconducting properties of such materials as a method of probing the resonance impurity states. Accurate determination of the superconducting parameters and development of bolometric transducers is possible, however, only on highly homogeneous bulk samples and films without second-phase inclusions. One has therefore to perform a high-precision analysis of the composition of samples of the solid solutions studied.

One of the most promising methods of quantitative chemical characterization of substances at present is x-ray microanalysis. This method has as obvious merits a high localization of measurements (1–3 μm), a sensitivity of $5 \times 10^{18}\,\mathrm{cm^{-3}}$, as well as the practically nondestructive action of the electron microprobe on the sample surface.

The objective of this work was to develop a reliable technique of local chemical characterization of quaternary semiconductor solid solutions and to check the possibility of applying this technique to the (SnTe-SnSe):In solid-solution system.

1. SAMPLES

Samples, whose composition could be described by the chemical formula $Sn_{0.84}In_{0.16}Se_yTe_{1-y}$ ($y = 0.02$, 0.04, 0.08, 0.12, 0.16), were prepared by metal-ceramic technique. The ingots were produced by melting the starting semiconductor-grade compositions in vacuum. After the ingots were ground to a powder (grain size $d \leqslant 0.1$ mm), it was hot-pressed at 350 °C. The samples were subsequently annealed in vacuum at 600 °C for 100 h. X-ray microanalysis did not reveal any trace of a second phase up to a Se content $y = 0.16$.

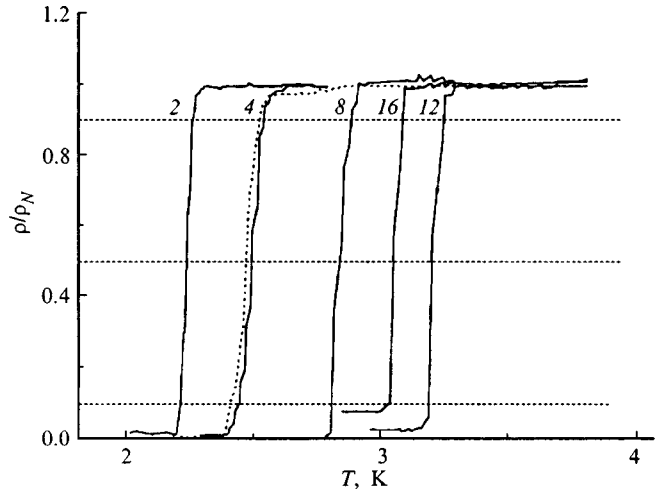

FIG. 1. Superconducting transition in $Sn_{0.84}In_{0.16}Se_yTe_{1-y}$ solid solutions. The figures indicate Se content in at. %. Critical temperature T_c(K) and (transition width ΔT_c(K)): *2*—2.23 (0.03), *4*—2.49 (0.09), *8*—2.83 (0.06), *12*—3.17 (0.04), *16*—3.05 (0.04). Normal-state resistivity of samples, ρ_N (m$\Omega\cdot$cm): *2*—6.70, *4*—14.56, *8*—0.68, *12*—1.10, *16*—0.34. Dashed line shows the superconducting transition in a $Sn_{0.84}In_{0.16}Te$ sample ($T_c = 2.46$ K, $\Delta T_c = 0.10$ K).

Studies of the superconducting properties of these solid solutions showed that the resistivity jump observed at the superconducting transition (Fig. 1) is sharp, without any steps or breaks, which indicates the absence of superconducting phases of a different composition. The curves illustrating the magnetic-field-induced breakdown of the superconducting state follow a similar behavior (Fig. 2). The small widths of the superconducting transition in temperature $\Delta T_c \ll T_c$ (Fig. 1) and in magnetic field ΔH_{c2} (Fig. 2) imply a good quality of the samples and their high volume homogeneity. The transition widths in temperature and magnetic field were determined as the differences in temperature (or magnetic field) at the levels $\rho = 0.9\rho_N$ and $\rho = 0.1\rho_N$ (ρ_N is the sample resistivity in normal state). The superconducting parameters themselves, T_c and H_{c2}, were derived from the condition $\rho = 0.5\rho_N$. It should be pointed out that the sample which did not contain Se at all exhibited approximately the same values of these quantities. The drop in the resistivity of the samples practically to zero (the zero level was determined by switching off the current through the sample) evidences the absence in them of a nonsuperconducting phase.

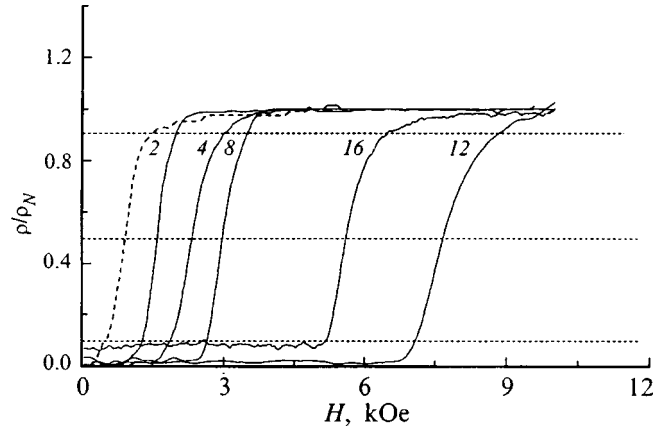

FIG. 2. Superconducting transition in a magnetic field in $Sn_{0.84}In_{0.16}Se_yTe_{1-y}$ solid solutions. The figures indicate Se content in at. %. The second critical magnetic field H_{c2}, Oe (transition width in magnetic field, ΔH_{c2}, Oe): *2*—1550 (600), *4*—2300 (1080), *8*—3050 (970), *12*—5450 (1770), *16*—7675 (1120). The experimental curves were obtained at 2.31 K on samples *2* and *4*, and at 2.41 K on samples *8*, *12*, *16*. Dashed line presents the corresponding dependence for a $Sn_{0.84}In_{0.16}Te$ sample measured at $T = 2.35$ K ($H_{c2} = 900$ Oe, $\Delta H_{c2} = 1000$ Oe).

Considering the appreciable In content in the samples, one could expect segregation of this component in the form of a separate phase. The difference of the superconducting-transition parameters for In [for pure In, $T_c = 3.405$ K, and the critical magnetic field at zero temperature $H_{c2}(0) = 285$ Oe (Ref. 7)] from those observed in our solid solutions (see Figs. 1 and 2) shows, however, that it is in the $Sn_{0.84}In_{0.16}Se_yTe_{1-y}$ solid solution that the transition occurs.

Note that the bulk nature of superconductivity in $Sn_{1-x}In_xTe$ was established from measurements[8] of the specific heat $C(T)$.

2. METHOD OF X-RAY SPECTRAL MICROANALYSIS OF QUATERNARY SOLID SOLUTIONS

A variety of methods are used for treatment of experimental analytic information (the intensity of characteristic x-ray radiation, CXR): the method of α coefficients, ZAF correction, Monte Carlo etc.[9–12] The methods based on the Monte Carlo model are used to simulate the CXR distribution in a sample, derive the exact position of emission in longitudinal and transverse directions, and estimate the emergent CXR intensity. In calculations one usually prescribes the sample composition, number of layers, and their geometry. The algorithm employed in experimental data treatment and determination of the composition directly in the course of measurements is conventionally based on ZAF models, where the functions introduced to account for the CXR generation and absorption, as well as for the fluorescence excited by the CXR or bremsstrahlung spectrum are calculated separately.[13] Calculation of the corrections requires prescribing hypothetical compositions with subsequent correction of the inserted values after comparison with experimental data. Several algorithms for this procedure were developed. The iterations are most frequently done by Wegstein's method[14]. In any case, the iterations are completed after the sum of the concentrations of all components becomes close to unity.

Because of experimental and calculational errors, the validity of such an approach in the case of solid solutions becomes questionable; indeed, the results may come into conflict with the purely physicochemical requirement of the existence of semiconducting solid solutions in quasibinary slices. Besides, there exists an uncertainty in selection of an appropriate calculational algorithm because of a large number of ZAF correction procedures which are capable of providing a satisfactory agreement for a particular narrow class of materials. Moreover, the limitations inherent in the diffusion model of Archard-Mulvey which underlies the ZAF

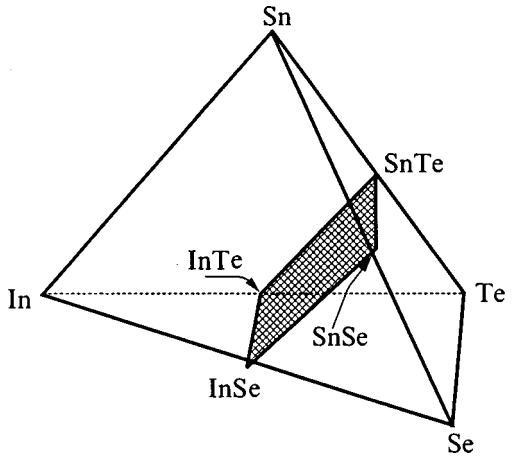

FIG. 3. Quasibinary cut plane for the Sn-In-Se-Te system.

method should result in an increase in error as one crosses over to materials with an ever larger number of components.

Semiconducting solid solutions crystallize in quasibinary cuts. This property permits one to use calibration graphs for ternary solid solutions ($A_xA^*_{1-x}B$ or $AB_xB^*_{1-x}$), as well as offers a possibility of finding an optimum algorithm. A graphic-analytical method (method of isohypses) based on data available on binary systems has been proposed for microanalysis of multicomponent samples.[15] For some quaternary solid solutions this method yields quite satisfactory results, while for others it was found to entail large errors.

Theoretically this is attributed to the fact that the isohypse method is based on looking for the crossing point of the surfaces (or straight lines in the case of ternary systems) meeting the condition of constant CXR intensity.[16] The crossing of such straight lines (isohypses) corresponding to the experimental CXR intensities for the analytes yields a configurative point for the composition one is looking for. Linear interpolation indicates essentially that one neglects the deviation of the linear CXR dependence on mass concentration in this stage of calculations.

In quaternary systems, semiconducting solid solutions lie in planes passing through the configurative points corresponding to binary compounds (Fig. 3). The cross section will be planar, however, only in the tetrahedron constructed using molar (rather than mass) concentrations. Besides, the CXR intensities are nonlinear functions of concentration, and therefore application of a linear approximation proves quite frequently to be too rough.

The essence of the technique been proposed lies in lifting the requirement of linearity inherent in the isohypse method by calculating equal-intensity lines in a nonlinear approximation. In this way one removes also the limitations due to the contradiction between the planarity of the quaternary-system cut underlying the construction of the tetrahedron in atomic fractions and the dependence of $I_{i\,\mathrm{sam}}/I_{i\,\mathrm{ref}}$ on mass concentration, where $I_{i\,\mathrm{sam}}$ and $I_{i\,\mathrm{ref}}$ are the CXR intensities of the ith component excited by the electron microprobe in the sample and the reference, respectively.

The technique is based on nonlinear interpolation procedures and is applicable to ternary and quaternary systems, as well as to solid solutions containing a larger number of components. The algorithm used includes the following steps:

1. Deriving the nonlinearity coefficient C_i from the $I_{i\,\mathrm{sam}}/I_{i\,\mathrm{ref}}=F_i$ relation for a ternary system $A_{1-x}B_xC$:

$$F_i=xI_i^{\mathrm{AC}}/I_i+(1-x)I_i^{\mathrm{BC}}/I_i+C_i^{\mathrm{AC-BC}}x(1-x);$$

2. Calculation of F_i for each ith component in a multicomponent system;

3. Determination of the composition corresponding to the crossing point of the family of F_i lines.

The $F_i(x,y)=I_{i\,\mathrm{sam}}/I_{i\,\mathrm{ref}}$ relation for a quaternary system $A_xB_{1-x}C_yD_{1-y}$ can be written as

$$F_i(x,y)=F_{i4}+[F_{i3}-F_{i4}]x+[F_{i2}-F_{i4}]y+[F_{i1}+F_{i4}-F_{i2}-F_{i3}]xy-[C_{i24}+\{C_{i13}-C_{i24}\}x]y[1-y]-[C_{i34}+\{C_{i12}-C_{i34}\}y]x[1-x],$$

with the indices 1, 2, 3 and 4 assigned to the binary compounds AC, BC, AD, and BD, respectively.

For quaternary systems of the kind $A_xB_yC_{1-x-y}D$ and $AB_xC_yD_{1-x-y}$

$$F_{i3}(x,y)=F_{i3}+(F_{i1}-F_{i3})x+(F_{i2}-F_{i3})y-C_{i12}xy-C_{i13}x(1-x-y)-C_{i23}y(1-x-y),$$

with the indices 1, 2 and 3 assigned to the binary compounds AD, BD, and CD, respectively (for $A_xB_yC_{1-x-y}D$), and 1, 2, and 3 for AD, BD, and CD (for $AB_xC_yD_{1-x-y}$).

For a five-component system of the kind $A_xB_{1-x}C_yD_zE_{1-x-y}$, nonlinear interpolation yields the following expression for $F_i(x,y,z)$:

$$F_i(x,y,z)=x[yF_{i1}+zF_{i3}+wF_{i5}-C_{i13}xz-C_{i15}yw-C_{i35}zw]+(1-x)[yF_{i2}+zF_{i4}+wF_{i6}-C_{i24}yz-C_{i26}yw-C_{i46}zw]-x(1-x)[yC_{i12}+zC_{i34}+wC_{i56}],\quad \text{where } w=1-y-z,$$

with the binary compounds AC, BC, AD, BD, AE, and BE being identified by the indices 1, 2, 3, 4, 5, and 6, respectively.

The F_i functions for systems with a still larger number of components can be calculated in a similar way.

Table I lists the coefficients of nonlinearity for the basic ternary solid solutions of the four-component solid solution $Sn_{1-x}In_xSe_yTe_{1-y}$, whose relative intensities are presented graphically in Fig. 4. The correction functions to account for the generation effect (the atomic number) were calculated

TABLE I. Nonlinearity coefficients C_1 for basic ternary solid solutions in the Sn-In-Se-Te system.

	System			
Element	SnSe-InSe	SnTe-SnSe	SnTe-InTe	InTe-InSe
Sn	1.138×10^{-2}	2.1×10^{-3}	9.712×10^{-3}	0
In	1.142×10^{-2}	0	8.342×10^{-3}	3.306×10^{-3}
Te	0	3.957×10^{-2}	4.326×10^{-2}	1.116×10^{-2}
Se	8.6×10^{-5}	8.114×10^{-2}	0	8.167×10^{-2}

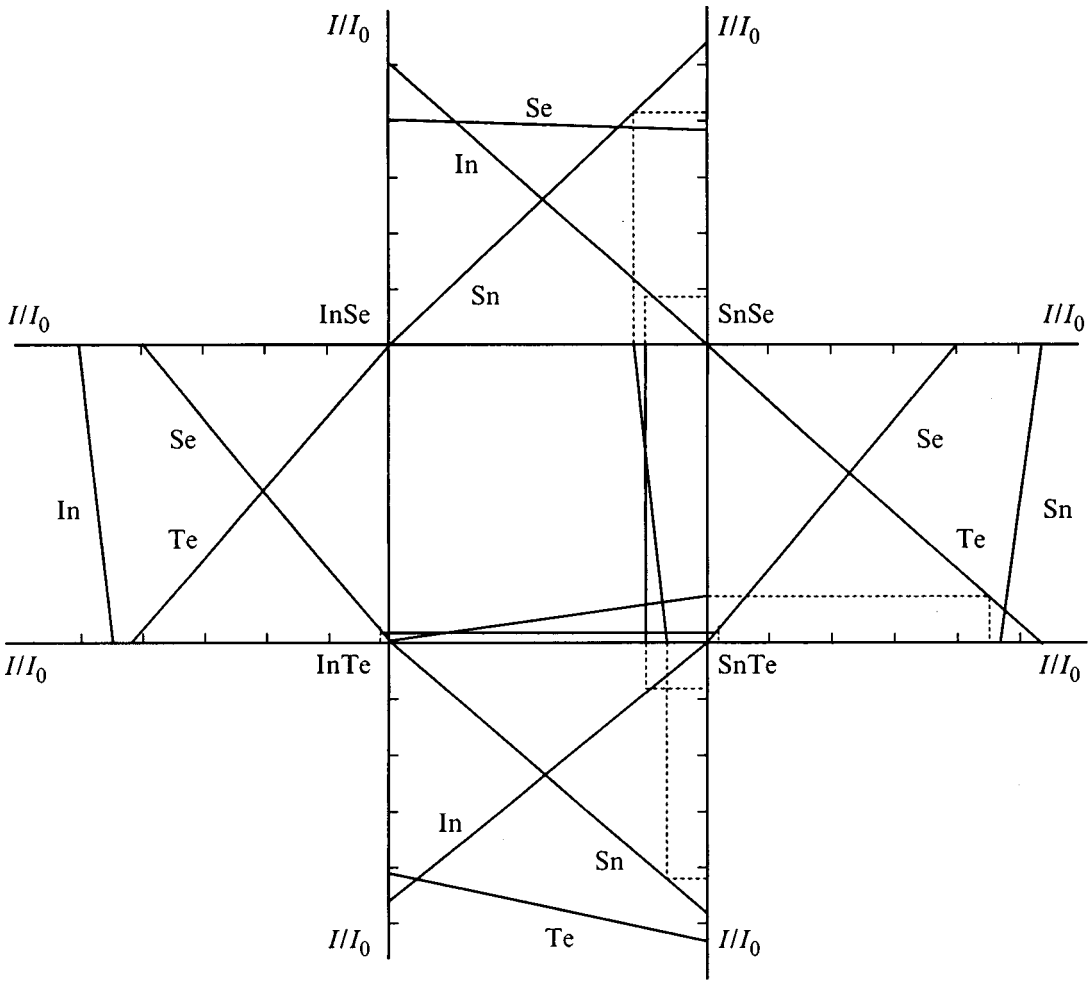

FIG. 4. Graphic-analytic method of compositional analysis of the (SnTe-SnSe):In quaternary system.

using the Duncumb-Shields relation, and for the absorption, from the Philibert expression with Lenard's constant, which was modified by Heinrich, and the secondary-fluorescence correction was introduced with the use of the Reed-Long theoretical relation. The x-ray takeoff angle θ was 18°, and the accelerating voltage, 20 kV.

The difficulty in experimental verification of the proposed algorithm consisted in the need to compare calculations with experimental data obtained on multicomponent samples which were prepared in accordance with the requirements imposed on reference standards. In $Sn_{1-x}In_xSe_yTe_{1-y}$, one may expect both inhomogeneities in the x and y compositions, and precipitation of excess components in the form of microinclusions. The measurements were performed on a Cameca instrument, the accelerating voltage was also 20 kV, and the CXR takeoff angle was 18°.

The composition of $Sn_{0.84}In_{0.16}Se_yTe_{1-y}$ can be preliminarily analyzed using calibration graphs (the graphic-analytic method). Figure 4 illustrates application of this method to the Sn-In-Se-Te system. To find the composition $x(y)$, the experimental CXR intensities of each element are plotted on the corresponding axes and projected on the sides of the square, and isohypses are drawn. It should be pointed out that if the concentrations of all components of the solid solution were determined accurately, the configurational point inside the square will actually be the intersection of two straight lines at the $x(y)$ point. The presence of experimental errors results in a misfit quadrangle, and because the x-ray statistics obey a Poisson distribution, experimental data for elements present in lower concentrations (In, Se) are more reliable. The charge compositions and the results of data treatment obtained by the proposed technique based on the parabolic interpolation procedures are given in Table II.

As seen from Table II, the initial charge compositions and the measurements made on the samples are in a good agreement.

3. SUPERCONDUCTING PROPERTIES OF SAMPLES

The temperature dependence of sample resistivity $\rho(T)$ was measured within a temperature interval of 0.4 to 4.2 K in

TABLE II. Compositions of the samples studied.

Original charge		Experimental results	
x	y	x	y
0.16	0.02	0.1610	0.0205
0.16	0.04	0.1600	0.0402
0.16	0.08	0.1600	0.0803
0.16	0.12	0.1600	0.1201
0.16	0.16	0.1600	0.1600

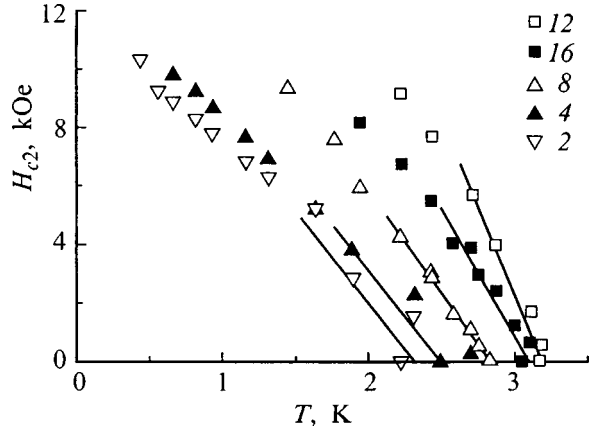

FIG. 5. Temperature dependences of the second critical magnetic field $H_{c2}(T)$ in $Sn_{0.84}In_{0.16}Se_yTe_{1-y}$ solid-solution samples. The figures relate to Se content in at. %.

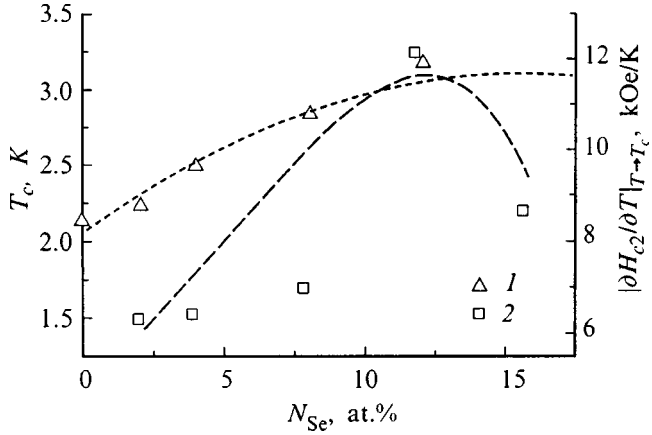

FIG. 6. (*1*) Superconducting transition temperature T_c and (*2*) modulus of the derivative of the second critical magnetic field with respect to temperature at the superconducting transition, $|\partial H_{c2}/\partial T|_{T\to T_c}$, as functions of composition y for samples of the $Sn_{0.84}In_{0.16}Se_yTe_{1-y}$ solid solutions.

zero field and in magnetic fields H of up to 10 kOe (Fig. 1). The derivatives $|\partial H_{c2}/\partial T|_{T\to T_c}$ for each sample were found from the corresponding $H_{c2}(T)$ experimental relations displayed in Fig. 5. As seen from the temperature dependences $\rho(T)$ in Fig. 1, the superconducting transition in the $Sn_{0.84}In_{0.16}Se_yTe_{1-y}$ solid solutions studied ($y=0.02-0.16$) is observed to occur in the 2–3-K interval. Such high values of T_c were characteristic also of the $Sn_{1-x}Ge_xTe$:In and $Sn_{1-x}Pb_xTe$:In solid solutions studied earlier,[1,3,5] where it was found that the onset of superconductivity in these compounds is governed by the hole filling of the In-impurity resonance states. Therefore one can associate observation of the superconducting transition with the existence of In resonance states in the valence band of the $Sn_{0.84}In_{0.16}Se_yTe_{1-y}$ solid solutions studied by us. Unfortunately, the band structure of the SnTe-SnSe solid solutions, as far as we know, has not been investigated. Therefore we used for the estimation data[17] on the band structure of SnTe. Using the Hall data for the hole concentration ($p\sim10^{21}\,cm^{-3}$) and the results quoted in Ref. 17, we came to the conclusion that the Fermi level ε_F in the samples studied lies in the Σ zone approximately 0.3 eV below the top of the main valence-band extremum (at the L point of the Brillouin zone). As mentioned above, the band of In resonance states is located at about the same energies, $\varepsilon_{In}\approx\varepsilon_F$.

The technique of x-ray microanalysis of four-component materials developed here provided reliable characterization of the samples studied. This permitted us to investigate the dependence of the superconducting transition parameters on Se content in the solid solution (see Fig. 6). Taking into account the complex valence-band structure of SnTe (the presence of extrema at the L, Σ, and Δ points of the Brillouin zone),[17] the observed nonmonotonic dependence of critical temperature $T_c(y)$ on the amount of Se can be associated with a mutual shift of the valence-band extrema and of the In impurity band with increasing Se content in the $Sn_{1-x}In_xSe_yTe_{1-y}$ ($y=0.16$) solid solution.

Thus we have proposed a technique of x-ray microanalysis of multicomponent semiconducting solid solutions based on nonlinear interpolation procedures. This technique is capable of improving appreciably the accuracy of composition determination of quaternary solid solutions as was verified on samples of the $Sn_{0.84}In_{0.16}Se_yTe_{1-y}$ ($y=0.02-0.16$) system. It was also shown that nonlinear interpolation (parabolic approximation) permits analysis not only of quaternary but of quinternary solid solutions as well.

Knowledge of the composition of the samples studied made it possible to establish the dependence of the superconducting transition parameters on Se content in $SnSe_yTe_{1-y}$:In solid solutions for a fixed In impurity content (0.16 at. %).

Support of the ''Integration'' program (Project 75 of 1997) and, partially, of the Russian Fund for Fundamental Research (Grant 96-02-17848) is gratefully acknowledged.

[1] A. V. Berezin, M. K. Zhitinskaya, S. A. Nemov, R. V. Parfen'ev, and D. V. Shamshur, Fiz. Tverd. Tela (Leningrad) **34**, 1216 (1992) [Sov. Phys. Solid State **34**, 643 (1992)].
[2] V. I. Kaĭdanov and Yu. I. Ravich, Usp. Fiz. Nauk **145**, 51 (1985) [Sov. Phys. Usp. **28**, 31 (1985)].
[3] G. S. Bushmarina, I. A. Drabkin, V. V. Kompaniets, R. V. Parfen'ev, D. V. Shamshur, and M. A. Shakhov, Fiz. Tverd. Tela (Leningrad) **28**, 1094 (1986) [Sov. Phys. Solid State **28**, 612 (1986)].
[4] V. I. Kaĭdanov, S. A. Nemov, and Yu. I. Ravich, Fiz. Tekh. Poluprovodn. **26**, 201 (1992) [Sov. Phys. Semicond. **26**, 113 (1992)].
[5] R. V. Parfeniev, D. V. Shamshur, M. A. Shakhov, and Zb. Chrapkiewicz, J. Alloys Compd. **219**, 313 (1995).
[6] R. A. Hein and P. H. E. Meier, Phys. Rev. **179**, 497 (1969).
[7] H. R. O'Neal and N. E. Phillips, Phys. Rev. **137**, A748 (1965).
[8] T. Nakajima, M. Isino, H. Miyauchi, and E. Kanda, J. Phys. Soc. Jpn. **34**, 282 (1973).
[9] S. G. Konnikov and A. F. Sidorov, *Electron Microprobe Studies of Semiconductor Materials and Devices* [in Russian] (Énergiya, Moscow, 1978).
[10] *Quantitative Electron Probe Microanalysis*, edited by V. D. Scott and G. Love (Wiley, New York, 1983; Mir, Moscow, 1986).

[11] L. A. Pavlova and L. F. Paradina, *X-Ray Spectral Microanalysis and its Application to Mineralogy* [in Russian] (Yakutsk Scientific Center, Yakutsk, 1990).
[12] V. P. Afonin and V. I. Lebed', *Monte Carlo Method in X-Ray Spectral Microanalysis* [in Russian] (Nauka, Novosibirsk, 1989).
[13] V. A. Moshnikov and D. A. Yas'kov, *X-Ray Spectral Microanalysis in the Physical Chemistry of Semiconductors* [in Russian] (LÉTI, Leningrad, 1986).
[14] S. J. B. Reed, *Electron Microprobe Analysis* (Cambridge University Press, Cambridge, 1993; Mir, Moscow, 1979).
[15] A. I. Zaslavskiĭ, T. T. Dedegkaev, and A. F. Sidorov, *Graphic-Analytic Microprobe Analysis of Ternary Systems. Equipment and Methods of X-Ray Analysis* [in Russian] [Mashinostroenie (Leningrad) **17**, 163 (1975)].
[16] R. Assenov, V. Moshnikov, B. Patarov, and D. Yaskov, Cryst. Res. Technol. **22**, 1289 (1987).
[17] G. S. Bushmarina, I. A. Drabkin, M. A. Kvantov, and O. E. Kvyatkovskiĭ, Fiz. Tverd. Tela (Leningrad) **32**, 2869 (1990) [Sov. Phys. Solid State **32**, 1666 (1990)].

Translated by G. Skrebtsov

A vibronic-structure analysis of optical spectra in ZnO:Ni^{3+} crystals by localized-vibration simulation

A. N. Kislov, V. G. Mazurenko, and A. N. Varaksin

Ural State Technical University, 620002 Ekaterinburg, Russia
(Submitted June 2, 1998)
Fiz. Tverd. Tela (St. Petersburg) **41**, 618–622 (April 1999)

A theoretical study is reported of the vibrations associated with a Ni^{3+} impurity charged with respect to the ZnO lattice. The calculations were made by a recursive method in terms of the shell model for vibrations with different symmetries. The vibronic structure observed in the spectra of $d-d$ intracenter transitions in the Ni^{3+} impurity has been interpreted using model calculations. © *1999 American Institute of Physics.* [S1063-7834(99)01104-1]

The broad utilization of II–VI semiconductor compounds doped by $3d$ transition metals has initiated a systematic investigation of their physical properties. In this connection, studies of the $3d$-shell vibronic states may provide important relevant information. It can be obtained experimentally by measuring absorption or luminescence spectra. In the cases where the number of electrons in the $3d$ shell does not change, one observes intracenter $d-d$ vibronic transitions. Optical spectra of the transitions between vibronic states caused by electron interaction with electromagnetic field have mostly vibronic replicas originating from creation or annihilation of phonons in the crystal. The shape of a vibronic replica can be used to reconstruct the phonon spectrum of the doped crystal which includes information on the electron-phonon coupling of the transition.[1] Analysis of spectroscopic data relies primarily on theoretic studies of such vibronic transitions. Obtaining quantitative characteristics by rigorous application of quantum-mechanical theory usually entails formidable mathematical difficulties, even if reasonable approximations are made. A phenomenological approach is frequently employed to simulate various properties of the dopant ion. Such an approach to lattice dynamics can, in particular, form a basis for a quantitative treatment of the phonon-wing profile in the spectrum of a doped crystal. At the same time interpretation of the vibronic structure is approached, as a rule, by comparing it with the vibrational spectrum of an ideal crystal[2–4] without taking into account the impurity-induced defect vibrations, which is particularly important in the case of a charged impurity. While this approach can be justified as a rough approximation, in a general case it is not rigorous.[2] The recursive method[5] appears promising for use in numerical simulation of the vibrational spectrum of a crystal with a defect. It was found to be one of the few methods applicable to ionic crystals, where long-range Coulomb interaction with charged defects plays an essential role.

In the present work, the recursive method is employed to simulate the vibrational spectrum of the ionic-covalent crystal ZnO doped by a nickel impurity Ni^{3+} ($3d^7$), which is charged relative to the lattice, with subsequent use of this calculation to analyze the phonon wing of the zero-phonon line in the emission spectrum of ZnO:Ni produced in the intracenter $d-d$ transition $\Gamma_1-{}^4T_2(F)\rightarrow\Gamma_2-{}^4A_2(F)$ for the Ni^{3+} impurity.[4]

1. METHOD OF CALCULATION AND RESULTS

One of the consequences of the harmonic approximation in lattice dynamics consists in that the displacement from its equilibrium position of any atom in a crystal is a complex vibrational process representing a superposition of all possible normal modes of the crystal of different frequencies ν. The frequency distribution of the normal-vibration contribution is determined by a function called the local density of states (LDOS) of phonons. This quantity is usually employed when analyzing various physical processes involving phonons. The phonon LDOS is related to the imaginary part of the diagonal element of the one-particle Green's function Fourier transform, which, in its turn, is determined by the dynamic crystal matrix in real space.[6] The essence of the recursive method, as applied to lattice dynamics, lies in using the Lanzos recurrence relation to construct an orthogonal set of vectors starting from the initial displacement vector of a given atom. In each stage of the vector construction process, an ever increasing number of atoms surrounding the original atom become involved. Each new vector carries information on atomic displacements which contribute to the preceding displacement vector. The dynamic matrix transforms in the basis of these vectors to the tridiagonal form, and the diagonal element of the Green's function acquires the form of an easily calculable continuous fraction.

Rigorous inclusion of Coulomb long-range interaction is essential in the calculation of the dynamic matrix of ionic crystals, particularly of those containing a charged impurity. This requires construction of a cluster of sufficiently large size and account for interactions among all atoms. A study showed that the required accuracy of calculations taking explicitly into account Coulomb long-range interaction can be reached for a cluster of 1000–1500 atoms.[7] The sparse-matrix technique permits presently shell-model lattice-dynamics simulation of clusters having up to 1000 atoms.

Interpretation of impurity optical spectra can be simplified considerably by invoking the point-symmetry properties

TABLE I. Parameters of the short-range part of the interaction potential in ZnO.

Interacting ions	A_{ij} (eV)	ρ_{ij} (Å)	C_{ij} (eV·Å^{-6})
$Zn^{+2}-Zn^{+2}$	890	0.3	0
$Zn^{+2}-O^{-2}$	1934	0.2792	0
$O^{-2}-O^{-2}$	88760	0.149	0

of defects. Indeed, an electron of the impurity interacts only with vibrations of symmetry Γ, whose displacements transform according to the irreducible representation of the impurity point-symmetry group contained in the symmetric product $[\Gamma_a^2]$ for the irreducible representation of the wave function of electronic state (a). This makes working with symmetrized ion displacements more convenient. In this case the contribution to the normal-mode frequency distribution is characterized by a symmetrized phonon LDOS (SLDOS), which is determined by projecting normal crystal modes onto the displacement of symmetry Γ.

When a defect is incorporated in the crystal, crystal vibrations become distorted because of the corresponding change in the force constants and mass. If the change is strong, defect-induced vibrations (resonance or pseudolocal, gap, or local) set in. Using phonon SLDOS for an ideal, $G_\Gamma^0(\nu)$, and doped, $G_\Gamma(\nu)$, crystal permits one to isolate vibrations of this kind. The maxima in the $G_\Gamma(\nu)$ spectrum which do not coincide with those in $G_\Gamma^0(\nu)$ determine the oscillation frequency of Γ symmetry associated with the defect. Taking into account defect-related vibrations is essential for proper interpretation of the vibrational spectral structure of a doped crystal.

Adequate description of the interaction among atoms of the crystal matrix, as well as among the impurity and the remaining atoms of the crystal is a major problem in numerical simulation of the lattice dynamics of crystals containing impurities. Calculations of the structure and other characteristics of many oxides make use presently of an approach[8–10] in which the atoms are assumed to interact via a pairwise, central-force potential, and the atomic polarizability is taken account of within the shell model. In this phenomenological model, the interaction potential between the ions and the shells is presented as a sum of a short- and a Coulomb long-range term. The short-range part consists of the well-known Born-Mayer term describing the repulsion of ions originating from the overlap of their electronic shells and of a term responsible for the dipole-dipole ion interaction, and the Coulomb part assumes the point-like nature of ions.

The literature describing this model presently has no data on the interaction potentials for zinc oxide, which crystallizes in the hexagonal würtzite structure, that would describe adequately its vibrational properties. We have used here, for the ZnO crystal, ion interaction potentials whose parameters for the short-range part were determined using the well-known empirical interaction potential of the Ni^{2+} ion, with an electronic structure close to that of Zn^{2+}, and of the oxygen ion O^{2-}. We obtained the required set of parameters (Table I) by fitting the parameters of the short-range potentials proposed[10] for a NiO crystal to experimental frequencies measured[11] in the high-symmetry directions of the Brillouin zone of the ZnO crystal. Note that when choosing the parameters within the molecular statics method[12] we took into account the lattice stability with respect to the lattice constants $a=3.25$ Å and $c=5.21$ Å. We also calculated the binding energy of the defect-free ZnO lattice, -41.2 eV, which is in a good agreement with the experimental value of -42.2 eV (Ref. 9), as well as the static and high-frequency dielectric constants, 6.0 and 3.7, which were found to differ somewhat from the experimental values of 8.5 and 4.1 (Ref. 13), respectively. In this and other calculations, one took into account the short-range interionic potential including second-nearest neighbors.

In an ideal ZnO crystal, the four oxygen ions nearest to the zinc ion form a distorted tetrahedron, in which the bond length between Zn^{2+} and O^{2-} along the hexagonal axis C is 1.99 Å, and that between Zn^{2+} and the other three O^{2-} ions is 1.975 Å. Substitution of nickel for zinc shifts the equilibrium positions of the neighboring ions. The calculation of the static lattice distortion by a Ni^{3+} impurity due to the change in the Coulomb part of the force constants was carried out in the molecular statics approximation without compensation of the excess charge. The minimum of the total crystal energy was determined by the gradient method. The calculations showed that the nearest neighbors of the Ni^{3+} impurity move closer to it. The equilibrium position of the O^{2-} ion on the C axis shifts by 0.246 Å, and the other three nearest-neighbor O^{2-} ions shift by 0.24 Å. The calculations reveal also a strong damping of the lattice distortions. The equilibrium-position shifts of ions in the next coordination sphere are already an order of magnitude smaller than those for the four O^{2-} ions so that one may neglect them. The formation energy of the lattice in the equilibrium configuration distorted by the Ni^{3+} substitutional impurity and calculated in the above way was found to be -30.3 eV.

The electrons localized at an impurity interact most strongly with atomic vibrations primarily of the first coordination spheres. Because of the elastic interaction among atoms, these vibrations, rather than being normal, represent actually a wave packet of all normal vibrations of the crystal, and the relevant information is contained in the phonon SLDOS $G_\Gamma(\nu)$ projected onto the first coordination-sphere region.

We chose as initial vectors for the recursive method symmetrized displacements which are normal coordinates for the region near a nickel impurity bounded by the first coordination sphere of four O^{2-} ions. The Ni^{3+} substitutional impurity occupies in the ZnO crystal the site with point symmetry group C_{3v}. A group-theoretical analysis yielded nine symmetrized displacements, namely, $4A_1$, A_2, and $5E$, and for them the phonon SLDOS were calculated.

For illustration, Fig. 1 shows the calculated vibrational SLDOS projected on a displacement of symmetry A_1 of a Zn^{2+} ion in ZnO, and of Ni^{3+} ion in ZnO:Ni^{3+}. We see the creation of a resonance vibration at a frequency $\nu_{Ni}(A_1)=8.2$ THz and of a gap vibration at $\nu_{Ni}(A_1)=11.2$ THz in which the impurity itself is involved. Calculations predict also that the vibrational motion of symmetry A_1 of the O^{2-} ion lying on the C axis should produce a Ni^{3+}-induced gap

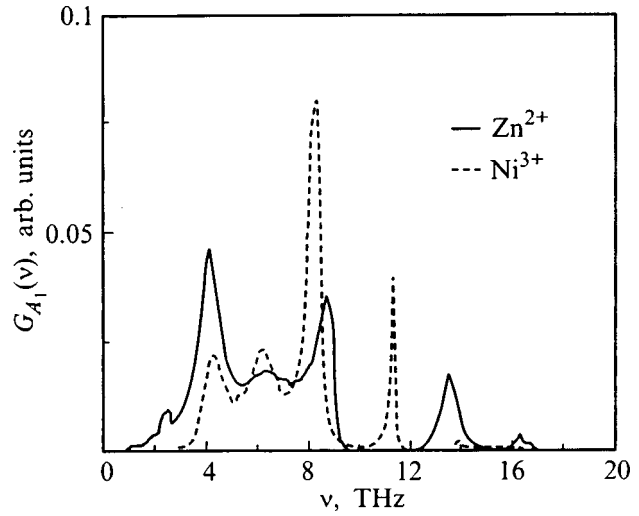

FIG. 1. Calculated phonon SLDOS projected on A_1-type displacement of the Zn^{2+} ion in ZnO and of the Ni^{3+} ion in ZnO:Ni^{3+}.

vibration at a frequency $\nu_O(A_1)=11.2$ THz. Figure 2 presents a frequency distribution of normal vibrations projected on symmetrized A_1 and E displacements of all ions in the first coordination sphere in the ZnO:Ni^{3+} crystal. The SLDOS of phonons of symmetry E exhibits a strong peak lying in the gap, whose position determines the O^{2-} gap vibration frequency $\nu_0\ (E)=10.0$ THz.

2. DISCUSSION

In a general case, the profile of an impurity-center optical spectrum is determined by the intensity of all possible vibronic transitions from the corresponding electronic state of the impurity, and the shape of the vibronic satellite of the zero-phonon line is determined by the vibrational states of the system in the initial (a) and final (b) electronic states. Using the Condon approximation and assuming the elastic constants not to change in an electronic transition, the shape

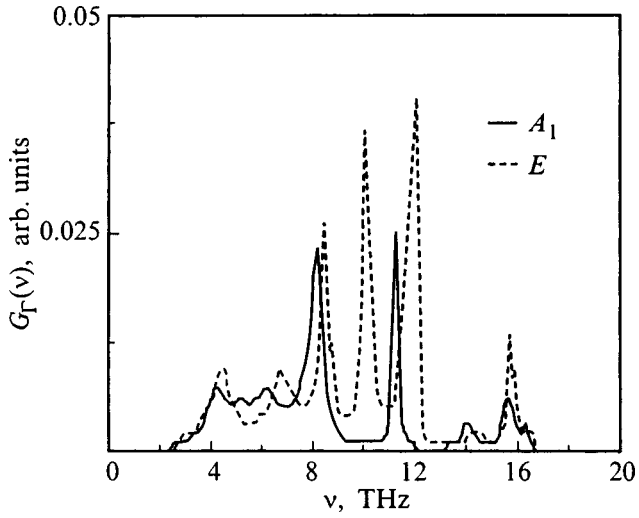

FIG. 2. Phonon SLDOS projected on ion displacements of symmetries A_1 and E in the defect-containing region bounded by the first coordination sphere in the ZnO:Ni^{3+} crystal.

of the vibronic satellite associated with one-phonon processes can be written in terms of the frequency function of the linear part of the expansion in normal coordinates of the electron-phonon coupling of the transition, and of the phonon DOS of the crystal with the impurity in the initial state.[2,14] Such an approach permits consideration of systems characterized by weak electron-phonon coupling and a small perturbation of the crystal vibrational states in an electronic transition. The low-temperature spectra of such systems have predominantly one-phonon wings. As an illustration may serve the Ni^{3+} spectrum emitted in the intracenter $d-d$ transition $\Gamma_1-{}^4T_2(F)\rightarrow\Gamma_2-{}^4A_2(F)$ in ZnO:Ni, which was measured at 4.2 K.[4]

Symmetry selection rules allow electronic transitions induced by a perturbation f from the initial (a) to the final (b) state if the irreducible representation Γ_a describing the wave-function symmetry of state (a) is contained in the direct product of the irreducible representations $\Gamma_f\otimes\Gamma_b$ by which the perturbation operator f and the wave function of state (b) transform. According to these rules, the transition under consideration is forbidden in the electric-dipole approximation. The reason for this lies in that the Ni^{3+} ion is in a field of symmetry C_{3v}, and for π-polarized radiation ($\mathbf{E}\|C$), where $\mathbf{E}$ is the electric vector of the radiation, the electric-dipole moment operator f transforms according to a Γ_1-type irreducible representation, and for σ-polarized radiation ($\mathbf{E}\perp C$), to a Γ_3-type one. The electric-dipole transition becomes allowed due to the spin-orbit coupling, which splits each energy level of states Γ_1 and Γ_2 into two spin-degenerate sublevels Γ_4 and $\Gamma_{5,6}$ described by a double point group $\check{C}_{3v}$. In this case the transition takes place from the spin-orbit component $\Gamma_{5,6}$ of the $\Gamma_1-{}^4T_2(F)$ level. Now the $\Gamma_{5,6}-\Gamma_1-{}^4T_2(F)\rightarrow\Gamma_{6,5}-\Gamma_2-{}^4A_2(F)$ transition is allowed for π-polarized radiation, and $\Gamma_{5,6}-\Gamma_1-{}^4T_2(F)\rightarrow\Gamma_4-\Gamma_2-{}^4A_2(F)$, for σ-polarized one.

Note the small energy separation between the spin-orbit components of each of the Γ_1 and Γ_2 levels and their spin degeneracy. This results in a mixing between the spin-orbit-split electronic levels with E-symmetry ionic displacements, which are dipole active in the Jahn-Teller pseudoeffect and effect, respectively. These phenomena affect, however, only the fine structure of the phonon wing, whose inclusion presupposes precise knowledge of the eigenvalue of the electronic Schrödinger equation for different ion configurations and solution of this equation for ions taking into account the nonadiabaticity term. This is, in its turn, a formidable problem. In this connection we shall disregard the Jahn-Teller effect and pseudoeffect in our analysis of emission spectra.

According to group-theoretical rules, the vibrations coupled to an electronic transition, which is induced by a perturbation operator f, from an electronic state with Γ_a to that with Γ_b possess the symmetry of the irreducible representation belonging to the direct product $\Gamma_a\otimes\Gamma_f\otimes\Gamma_b$. Therefore the zero-phonon line produced in a $\Gamma_{5,6}\rightarrow\Gamma_{6,5}$-type electronic intracenter transition in the Ni^{3+} impurity ion is accompanied by a phonon wing consisting of vibrations of symmetry A_1. In a $\Gamma_{5,6}\rightarrow\Gamma_4$-type transition, vibrations of symmetry A_1 and E contribute to the vibronic satellite. The resolution in the emission spectrum presented

TABLE II. Frequency positions of strong peaks in the phonon wing of the emission spectrum and SLDOS for the ZnO:Ni^{3+} crystal (in THz).

Calculation		
$G_\Gamma^0(\nu)$	$G_\Gamma(\nu)$	Experiment (Ref. 4)
4.1 (A_1 and E)	4.2 (A_1 and E)	3.2
6.5 (A_1 and E)	6.3 (A_1 and E)	–
8.7 (A_1 and E)	8.3 (A_1 and E)	7.5
–	10.0 (E)	9.9
–	11.2 (A_1)	–
–	12.0 (E)	12.3
14.0 (A_1 and E)	–	13.8
16.2 (A_1 and E)	15.6 (A_1 and E)	15.0

in Ref. 4 and dominated by one-phonon processes involving phonon creation is not high enough to permit isolation of the phonon contributions due to each of these transitions from the vibrational background. Therefore the phonon wing of the emission spectrum contains all A_1 and E vibrations, which complicates its analysis.

Table II lists the frequencies of the strongest peaks in the vibrational background, which are reckoned from the zero-phonon line. Also shown for vibrations of the A_1 and E symmetry are the frequency positions of the features observed in the calculated SLDOS $G_\Gamma(\nu)$ and $G_\Gamma^0(\nu)$ projected on the first coordination sphere surrounding the Ni^{3+} substitutional impurity in the ZnO:Ni crystal, and the Zn^{2+} ion in an ideal ZnO crystal, respectively. A comparison of the vibronic structure in the optical spectrum with the calculated SLDOS reveals a good correlation between the positions of the strong peaks for $G_\Gamma(\nu)$ only. Note the feature in the phonon wing of the emission spectrum at a frequency equal to that of the calculated gap vibration of symmetry E, which is induced by the Ni^{3+} impurity. Calculations predict a peak at the frequency of the gap vibration of symmetry A_1, which is absent in the vibrational background. This may be accounted for by an insufficiently strong vibronic structure intensity to permit its detection. To the peak in the phonon wing at 13.8 THz corresponds a weak structure in the calculated SLDOS. Its appearance in the experimental spectrum appears to be due either to the linear part in the electron-phonon coupling of the electronic transition being frequency dependent, or to electron interaction with vibrations which do not feel strongly the influence of the impurity.

The assignment of lines in Ref. 4 was based on a comparison of their positions with those of the critical points in the dispersion curves, at which one observes Van Hove singularities in the total phonon DOS of an ideal ZnO crystal. In view of the fact that the shape of the vibronic satellite of the zero-phonon line is dominated by local dynamics of a doped crystal, we do not believe this approach to be rigorous enough. Calculations show that the Ni^{3+} impurity, which carries a positive charge relative to the neutral lattice of the ZnO crystal, affects considerably the shape of vibrations of the neighboring ions.

Thus we have studied the change in the local lattice dynamics of a doped ZnO:Ni^{3+} crystal for vibrations of different symmetries. An analysis of the vibrational background of the zero-phonon line in the Ni^{3+} impurity spectrum emitted in a $d-d$ intracenter transition in the ZnO:Ni^{3+} crystal, performed with due account of symmetry considerations, leads one to a conclusion that the structure of this background is described qualitatively well by the phonon SLDOS obtained in a numerical simulation of a crystal containing a charged Ni^{3+} impurity.

The authors express their gratitude to V. I. Sokolov for fruitful discussions.

Support of the Russian Fund for Fundamental Research (Grants 96-02-16278a and 96-02-19785) is gratefully acknowledged.

[1] R. I. Personov, I. S. Osad'ko, É. D. Godyaev, and E. I. Al'shits, Fiz. Tverd. Tela (Leningrad) **13**, 2653 (1971) [Sov. Phys. Solid State **13**, 2224 (1971)].
[2] I. V. Ignat'ev and V. V. Ovsyankin, in *Spectroscopy of Crystals* [in Russian] (Nauka, Leningrad, 1983).
[3] S. V. Mel'nichuk, V. I. Sokolov, T. P. Surkova, and V. M. Chernov, Fiz. Tverd. Tela (Leningrad) **33**, 3247 (1991) [Sov. Phys. Solid State **33**, 1833 (1991)].
[4] H.-J. Schulz and M. Thiede, Phys. Rev. B **35**, 18 (1987).
[5] R. Haydock, V. Heine, and M. J. Kelly, J. Phys. C **5**, 2845 (1972).
[6] J. Hafner, Helv. Phys. Acta **56**, 257 (1983).
[7] A. N. Kislov, Cand. Phys. Math. Sci. Thesis (Ekaterinburg, 1992).
[8] M. J. L. Sangster and A. M. Stoneham, Philos. Mag. B **43**, 597 (1981).
[9] G. V. Lewis and C. R. A. Catlow, J. Phys. C **18**, 1149 (1985).
[10] A. M. Stoneham and M. J. L. Sangster, Philos. Mag. B **52**, 597 (1985).
[11] A. W. Hewat, Solid State Commun. **8**, 187 (1970).
[12] Yu. N. Kolmogorov and A. N. Varaksin (Available from VINITI No. 2395, 1989).
[13] I. P. Kuz'mina and V. A. Nikitenko, *Zinc Oxide: Preparation and Optical Properties* [in Russian] (Nauka, Moscow, 1984).
[14] A. Maradudin, *Theoretical and Experimental Aspects of the Effects of Point Defects and Disorder on the Vibrations of Crystals* (Academic Press, New York, 1966; Mir, Moscow, 1968).

Translated by G. Skrebtsov

Primary acoustic echo during excitation of a paramagnetic crystal by picosecond elastic video pulses

V. Yu. Man'kov

Astrakhan' State Technical University 414025 Astrakhan', Russia

S. V. Sazonov

Kaliningrad State Technical University 236000 Kaliningrad, Russia

(Submitted August 19, 1998)
Fiz. Tverd. Tela (St. Petersburg) **41**, 623–628 (April 1999)

The primary acoustic echo formed during excitation of a paramagnetic crystal with effective spin $S=1$ by two transverse picosecond elastic video pulses is investigated theoretically. Both exciting video pulses are applied perpendicular to the external magnetic field. It is shown that the primary acoustic echo in the general case consists of six longitudinal and transverse signals at the frequencies of the transitions within a Zeeman triplet. The optimal parameters of the exciting video pulses for the appearance of different echo signals are determined. © *1999 American Institute of Physics.* [S1063-7834(99)01204-6]

Soon after femtosecond optical video pulses were generated under laboratory conditions (signals containing of the order of one period of the oscillations),[1–3] there appeared the possibility of generating subnanosecond and picosecond acoustic (elastic) video pulses.[4,5] The observation of the spin-phonon interaction[6,7] in crystals with paramagnetic impurities gave an impetus to search for acoustic effects similar to nonstationary coherent phenomena in optics and magnetic radio spectroscopy.[8] Thus, soon after the photon echo,[9,10] the phonon (spin-acoustic) echo was predicted theoretically[11] and then observed.[8] In the latter case the paramagnetic crystal was excited by a sequence of resonant hypersonic pulses, giving rise to quantum transitions between Zeeman sublevels of paramagnetic ions.

The photon echo generated by a sequence of extremely short optical pulses (ESP-echo) exhibits a number of features as compared with the standard resonance effect.[12–15] It is natural to conjecture that the acoustic echo formed by excitation of a paramagnetic crystal by a sequence of elastic video pulses (acoustic ESP echo) will also have at least as many features.

The present paper is devoted to a theoretical investigation of the acoustic echo formed during excitation of a paramagnetic crystal, consisting of effective spins $S=1$, by two elastic video pulses. As a specific example of such a medium, we have in mind a cubic MgO single crystal with iron-group paramagnetic-ion impurities strongly coupled to phonons.[16]

1. FORMULATION OF THE PROBLEM

Let the paramagnetic cubic crystal be in an external magnetic field $\mathbf{B}_0$, parallel to a four-fold principal axis (Z axis). Both exciting elastic video pulses are transverse and are applied to the crystal perpendicular to B_0 (Voigt geometry). We assume that the video pulses propagate parallel to the X axis, which is also the other four-fold principal axis. The polarization plane of the video pulses makes an arbitrary angle α with $\mathbf{B}_0$. Accordingly, we shall represent the Hamiltonian $\hat{H}$ of the system ''paramagnetic ions + acoustic phonons'' in the form

$$\hat{H}=\int (\hat{\mathscr{H}}_s+\hat{\mathscr{H}}_{ph}+\hat{\mathscr{H}}^{int})d^3\mathbf{r}, \tag{1}$$

where $\hat{\mathscr{H}}_s$, $\hat{\mathscr{H}}_{ph}$, and $\hat{\mathscr{H}}^{int}$ are, respectively, the density of the Hamiltonians of the spin system, the phonon field, and their interaction, respectively. Here[16]

$$\hat{\mathscr{H}}_s=\sum_j \hbar\omega_{0j}\hat{S}_z^{(j)}\delta(\mathbf{r}-\mathbf{r}_j), \tag{2}$$

$$\hat{\mathscr{H}}_{ph}=\frac{\hat{p}_x^2+\hat{p}_y^2+\hat{p}_z^2}{2\rho}+\frac{1}{2}\rho a_\perp^2 \times\left[\left(\frac{\partial\hat{U}_y}{\partial x}\right)^2+\left(\frac{\partial\hat{U}_x}{\partial x}\right)^2\right]+\frac{1}{2}\rho a_\parallel^2\left(\frac{\partial\hat{U}_x}{\partial x}\right)^2, \tag{3}$$

$$\hat{\mathscr{H}}^{int}=\sum_j\left[\frac{3}{2}G_{11}(\hat{S}_x^{(j)})^2\frac{\partial\hat{U}_x}{\partial x}+G_{44}(\hat{S}_x^{(j)}\hat{S}_y^{(j)}+\hat{S}_y^{(j)}\hat{S}_x^{(j)})\frac{\partial\hat{U}_y}{\partial x}+G_{44}(\hat{S}_x^{(j)}\hat{S}_z^{(j)}+\hat{S}_z^{(j)}\hat{S}_x^{(j)})\frac{\partial\hat{U}_z}{\partial x}\right]\delta(\mathbf{r}-\mathbf{r}_j). \tag{4}$$

Here $\hbar$ is Plank's constant, ω_{0j} is the transition frequency between neighboring Zeeman sublevels of a spin triplet, $\hat{S}_x^{(i)}$,$\hat{S}_y^{(j)}$, and $\hat{S}_z^{(j)}$ are 3×3 spin matrices for $S=1$, $\delta(\mathbf{r}-\mathbf{r}_j)$ is a Dirac δ function, $\hat{p}_x$,$\hat{p}_y$, and $\hat{p}_z$ are the Cartesian components of the momentum density operator of the elastic medium, $\hat{U}_x$,$\hat{U}_y$, and $\hat{U}_z$ are operators of the elastic displacements of the crystal, ρ is the average density of the medium,

$a_\perp(a_\parallel)$ is the velocity of transverse (longitudinal) sound, and G_{ij} and G_{44} are the spin-elastic coupling constants. The integration in Eq. (1) extends over the entire volume of the sample, and the summation in Eqs. (2) and (4) extends over all paramagnetic ions with spin $S=1$.

We shall make several remarks concerning Eq. (4). As the duration of the acoustic video pulse decreases, the effects due to the spatial nonlocality of the spin-phonon coupling can become substantial, since the video pulse no longer ''sees'' the crystal as a continuous medium.[5,17–19] The spatial size of pulses with duration $t_p\sim 10$ ps is $l\sim at_p\sim 10^{-5}$ cm (a is the sound velocity in the crystal). The lattice constant, however, is $h\sim 10^{-7}$ cm. Since $l\gg h$, here the spatial dispersion of the spin-phonon interaction can be neglected. Moreover, picosecond elastic video pulses are quite strong, and the pressure P_s within them reaches 0.1 GPa.[4,5] The relative deformations corresponding to such pressures are $\varepsilon\sim 10^{-3}$.[17] In this case terms quadratic in the components of the strain tensor must be present in the spin-phonon coupling Hamiltonian.[20] In the present paper we shall assume that the pulses are not so strong, and for this reason anharmonicity in the spin-phonon coupling can be neglected.

According to Eq. (2), the Zeeman spectrum of a paramagnetic ion is equally spaced.

On account of the high power of the acoustic video pulses we shall assume below that the semiclassical approach is valid. In this approach the material equations for the spin dynamics are quantum-mechanical and have the form of the Liouville equation for the density operator $\hat{\rho}$

$$\frac{\partial\hat{\rho}}{\partial t}=\frac{i}{\hbar}[\hat{H}_s+\hat{H}^{int},\hat{\rho}], \tag{5}$$

where $\hat{H}_s=\int\hat{\mathscr{H}}_s d^3\mathbf{r}$, $\hat{H}^{int}=\int\hat{\mathscr{N}}^{int}d^3\mathbf{r}$, and the displacement operators $\hat{U}_x$, $\hat{U}_y$, and $\hat{U}_z$ in Eq. (4) are replaced by c-number functions U_x, U_y, and U_z.

Here we assume that the propagation time of an elastic video pulse through the sample is shorter than the irreversible phase relaxation time, and therefore we shall neglect the latter.

We obtain the equations for the displacements of the elastic field using the classical Hamiltonian equations

$$\frac{\partial\mathbf{U}}{\partial t}=\frac{\delta H}{\delta p},\qquad \frac{\partial\mathbf{p}}{\partial t}=-\frac{\delta H}{\partial\mathbf{U}}, \tag{6}$$

where $H=\langle H\rangle$, $\langle\ldots\rangle$ is the quantum-averaging operation, $\mathbf{U}=(U_x,U_y,U_z)$ and $\mathbf{p}=(p_x,p_y,p_z)$.

Using Eqs. (1)–(4) and (6) we obtain

$$\frac{\partial^2\varepsilon_{xx}}{\partial t^2}-a_\parallel^2\frac{\partial^2\varepsilon_{xx}}{\partial x^2}=\frac{3}{2}\frac{G_{11}}{\rho}\frac{\partial}{\partial x^2}\sum_j\langle(\hat{S}_x^{(j)})^2\rangle\delta(\mathbf{r}-\mathbf{r}_j), \tag{7}$$

$$\frac{\partial^2\varepsilon_{yx}}{\partial t^2}-a_\perp^2\frac{\partial^2\varepsilon_{yx}}{\partial x^2}=\frac{G_{44}}{\rho}\frac{\partial}{\partial x^2}\times\sum_j\langle\hat{S}_y^{(j)}\hat{S}_x^{(j)}+\hat{S}_x^{(j)}\hat{S}_y^{(j)}\rangle\delta(\mathbf{r}-\mathbf{r}_j), \tag{8}$$

$$\frac{\partial^2\varepsilon_{zx}}{\partial t^2}-a_\perp^2\frac{\partial^2\varepsilon_{zx}}{\partial x^2}=\frac{G_{44}}{\rho}\frac{\partial}{\partial x^2}\times\sum_j\langle\hat{S}_z^{(j)}\hat{S}_x^{(j)}+\hat{S}_x^{(j)}\hat{S}_z^{(j)}\rangle\delta(\mathbf{r}-\mathbf{r}_j), \tag{9}$$

where $\varepsilon_{xx}=\partial U_x/\partial x$, $\varepsilon_{yx}=\partial U_y/\partial y$, and $\varepsilon_{zx}=\partial U_z/\partial x$ are the components of the strain tensor of the elastic medium.

Echo-type effects are nonlinearly parametric, which means that in the system of material equations (5) the field of the elastic pulses is assumed to be given, i.e. the back effect of the absorbing spins on the field of the exciting pulses can be neglected. The induction and echo signals are calculated using Eqs. (7)–(9) in the approximation of fixed right-hand sides. In this connection we note that Eq. (4) contains the term $\sim(\hat{S}_x^{(j)})^2\partial\hat{U}_x/\partial x$ describing the interaction of an effective spin with the longitudinal component of the field of the elastic strains. Even though the excitation is accomplished only by the transverse video pulses, because $G_{11}\neq 0$ the longitudinal component of the elastic field can appear in the induction and echo signals (see Eq. (7)). To calculate the excitation of the spins we shall set $\varepsilon_{xx}=0$.

2. SOLUTION OF THE MATERIAL AND WAVE EQUATIONS. ANALYSIS OF THE ECHO SIGNALS

To investigate the excitation of the spin system we shall assume, following Refs. 15, 21, and 22, that the duration t_p of the exciting video pulses is so short that

$$\mu\equiv 2\omega_0 t_p\ll 1. \tag{10}$$

Taking $\omega_0\sim 10^{10}$ s^{-1},[8] we arrive at the conclusion that video pulses $t_p\sim 10$ ps satisfy the inequality (10). To zeroth order in the small parameter μ we set $\hat{H}_s=0$ in Eq. (5). Then the equation describing the excitation process has the form

$$\frac{\partial\hat{\rho}}{\partial t}=\frac{i}{\hbar}[\hat{H}^{int},\hat{\rho}]. \tag{11}$$

If the condition[23]

$$\left[\hat{H}^{int}(t),\int_{t_0}^{t}\hat{H}^{int}(t')dt'\right]=0 \tag{12}$$

is satisfied, where t_0 is the time at which the video pulse is applied, the solution of Eq. (11) can be represented in the form

$$\hat{\rho}(t)=\exp(i\hat{\Theta})\hat{\rho}(t_0)\exp(-i\hat{\Theta}). \tag{13}$$

Here $\hat{\rho}(t_0)$ is the density matrix of the medium before the application of an elastic video pulse, $\hat{\Theta}=1/\hbar\int_{t_0}^{t}\hat{H}^{int}(t')dt'$.

Condition (12) holds, for example, if the exciting video pulses are linearly polarized.[24]

We shall write the operator $\hat{\Theta}$ in the matrix representation

$$\hat{\Theta}=\begin{pmatrix} 0 & \frac{\Theta_{zx}}{\sqrt{2}} & -i\Theta_{yx} \\ \frac{\Theta_{zx}}{\sqrt{2}} & 0 & -\frac{\Theta_{zx}}{\sqrt{2}} \\ i\Theta_{yx} & -\frac{\Theta_{zx}}{\sqrt{2}} & 0 \end{pmatrix}, \tag{14}$$

where $\Theta_{zx}=G_{44}/\hbar\int_{t_0}^{t}\varepsilon_{zx}dt'$ and $\Theta_{yz}=G_{44}/\hbar\int_{t_0}^{t}\varepsilon_{yx}dt'$.

To calculate $\exp(\pm i\hat{\Theta})$ in Eq. (13) we employ Sylvester's relation[25]

$$e^{\pm i\hat{\Theta}}=\sum_{r=1}^{3} e^{\pm i\lambda_r}\frac{\Pi_{s\neq r}(\hat{\Theta}-\lambda_s\hat{I})}{\Pi_{s\neq r}(\lambda_r-\lambda_s)}, \tag{15}$$

where $\lambda_r (r=1,2,3)$ are the eigenvalues of the matrix $\hat{\Theta}$ and $\hat{I}$ is the unit matrix.

Then for the matrix (14) we have

$$e^{\pm i\hat{\Theta}}=\left(\hat{I}-\frac{\hat{\Theta}^2}{\Theta^2}\right)+\frac{\hat{\Theta}^2}{\Theta^2}\cos\Theta\pm i\frac{\hat{\Theta}}{\Theta}\sin\Theta, \tag{16}$$

where $\Theta=G_{44}/\hbar\int_{t_0}^{t}\varepsilon_{\perp}dt'$. The components ε_{zx} and ε_{yx} of the strain tensor are related with $\varepsilon_{\perp}$ by the relations

$$\varepsilon_{zx}=\varepsilon_{\perp}\cos\alpha, \quad \varepsilon_{yx}=\varepsilon_{\perp}\sin\alpha. \tag{17}$$

Substituting the expression (16) into Eq. (13) we find an expression for the density operator $\hat{\rho}(t)$ during the periods of the pulsed actions.

To calculate the induction and echo signals during the periods after the application of the video pulses, we shall set, as is ordinarily done, $\hat{H}^{int}=0$ in Eq. (5) and then integrate over the detunings in the inhomogeneously broadened contour for allowed transitions.

As calculations show, two elastic video pulses with the corresponding parameters α_1,Θ_1,t_{p1} and α_2,Θ_2,t_{p2} acting on thermodynamically equivalent paramagnets generate acoustic echo signals at the times $3\tau/2+t_{p1}+t_{p2}$ — at the frequency $2\omega_0$ with strain components ε_{xx} ($(3\tau/2)_{xx}$-echo) and ε_{yx} ($(3\tau/2)_{yx}$-echo), $2\tau+t_{p1}+t_{p2}$ at frequency ω_0 with the component ε_{zx} ($(2\tau)_{zx}$-echo) and at the frequency $2\omega_0$ with the components ε_{xx} ((2τ)-echo) and ε_{yx} ($(2\tau)_{yx}$-echo), and $3\tau+t_{p1}+t_{p2}$ — at the frequency ω_0 with elastic component ε_{zx} ($(3\tau)_{zx}$-echo). We present below expressions for the components of the strain tensor at the moments when echo signals appear for temperatures of the medium $T\ll\hbar\omega_0/k_B$ (k_B is Boltzmann's constant), for which before any action on the medium $\rho_{11}\approx 1$, $\rho_2\approx\rho_{33}\approx 0$. These relations were found on the basis of Eqs. (7)–(9) and have the form

$$\frac{3\tau}{2}+t_{p1}+t_{p2}: \quad \varepsilon_{xx}^{(2\omega_0)}=\frac{3G_{11}A_{xx}^{(3\tau/2)}}{2\rho a_{\parallel}^2},$$

$$A_{xx}^{(3\tau/2)}=\langle(\hat{S}_x^{(j)})^2\rangle\left(t=\frac{3}{2}\tau+t_{p1}+t_{p2}\right)$$
$$=(b_1-c_1)[(d_2+f_2)(b_2+c_2)a_1-(c_2-b_2)\times(d_2-f_2)(d_1+f_1)],$$

$$\varepsilon_{yx}^{(2\omega_0)}=\frac{G_{44}A_{yx}^{(3\tau/2)}}{\rho a_{\perp}^2},$$

$$A_{yx}^{(3\tau/2)}=\langle\hat{S}_y^{(j)}\hat{S}_x^{(j)}+\hat{S}_x^{(j)}\hat{S}_y^{(j)}\rangle\times\left(t=\frac{3}{2}\tau+t_{p1}+t_{p2}\right)=2A_{xx}^{(3\tau/2)}; \tag{18}$$

$$2\tau+t_{p1}+t_{p2}: \quad \varepsilon_{xx}^{(2\omega_0)}=\frac{3G_{11}A_{xx}^{(2\tau)}}{2\rho a_{\parallel}^2},$$

$$A_{xx}^{(2\tau)}=\langle(\hat{S}_x^{(j)})^2\rangle(t=2\tau+t_{p1}+t_{p2})$$
$$=a_1(d_1+f_1)(d_2^2-f_2^2),$$

$$\varepsilon_{yx}^{(2\omega_0)}=\frac{G_{44}A_{yx}^{(2\tau)}}{\rho a_{\perp}^2},$$

$$A_{yx}^{(2\tau)}=\langle\hat{S}_y^{(j)}\hat{S}_x^{(j)}+\hat{S}_x^{(j)}\hat{S}_y^{(j)}\rangle(t=2\tau+t_{p1}+t_{p2})=2A_{xx}^{(2\tau)};$$

$$\varepsilon_{zx}^{(\omega_0)}=\frac{G_{44}A_{zx}^{(2\tau)}}{\rho a_{\perp}^2},$$

$$A_{zx}^{(2\tau)}=\langle\hat{S}_z^{(j)}\hat{S}_x^{(j)}+\hat{S}_x^{(j)}\hat{S}_z^{(j)}\rangle(t=2\tau+t_{p1}+t_{p2})$$
$$=\sqrt{2}(b_1-c_1)[(c_2^2-b_2^2)(d_1+f_1)-(d_2+f_2)g_2a_1-(d_2-f_2)g_2(d_1+f_1)-(b_2^2-c_2^2)a_1]; \tag{19}$$

$$3\tau+t_{p1}+t_{p2}: \quad \varepsilon_{zx}^{(\omega_0)}=\frac{G_{44}A_{zx}^{(3\tau)}}{\rho a_{\perp}^2},$$

$$A_{zx}^{(3\tau)}=\langle\hat{S}_z^{(j)}\hat{S}_x^{(j)}+\hat{S}_x^{(j)}\hat{S}_z^{(j)}\rangle(t=3\tau+t_{p1}+t_{p2})$$
$$=\sqrt{2}a_1(d_1+f_1)[(d_2+f_2)(b_2+c_2)-(b_2-c_2)(d_2-f_2)]. \tag{20}$$

Here

$$a_{1,2}=\cos^2\alpha_{1,2}\cos^2\frac{\Theta_{1,2}}{2}+\sin^2\alpha_{1,2}\cos\Theta_{1,2},$$

$$b_{1,2}=\frac{1}{\sqrt{2}}\sin 2\,\alpha_{1,2}\sin^2\frac{\Theta_{1,2}}{2},$$

$$c_{1,2}=\frac{1}{\sqrt{2}}\cos\alpha_{1,2}\sin\Theta_{1,2},$$

$$d_{1,2}=\cos^2\alpha_{1,2}\sin^2\frac{\Theta_{1,2}}{2},$$

$$f_{1,2}=\sin\alpha_{1,2}\sin\Theta_{1,2},$$

$$g_{1,2}=\sin^2\alpha_{1,2}+\cos^2\alpha_{1,2}\cos\Theta_{1,2}. \tag{21}$$

TABLE I. Optimal values of the controlling parameters and the dimensionless intensities of the echo responses.

$[A_{\xi\nu}^{(t_e)}]^2$:	Optimal parameters for					
	$(3\tau/2)_{xx}$ echo $\alpha_1=-16.3°$, $\Theta_1=0.35\pi$, $\alpha_2=144.7°$, $\Theta_2=0.67\pi$	$(3\tau/2)_{yx}$ echo $\alpha_1=-16.3°$, $\Theta_1=0.35\pi$, $\alpha_2=144.7°$, $\Theta_2=0.67\pi$	$(2\tau)_{xx}$ echo $\alpha_1=90°$, $\Theta_1=3/4\pi$, $\alpha_2=90°$, $\Theta_2=1/2\pi$	$(2\tau)_{yx}$ echo $\alpha_1=90°$, $\Theta_1=3/4\pi$, $\alpha_2=90°$, $\Theta_2=1/2\pi$	$(2\tau)_{zx}$ echo $\alpha_1=45°$, $\Theta_1=0.39\pi$, $\alpha_2=90°$, $\Theta_2=1/2\pi$	$(3\tau)_{zx}$ echo $\alpha_1=-90°$, $\Theta_1=3/4\pi$, $\alpha_2=35.2°$, $\Theta_2=0.67\pi$
$[A_{xx}^{(3\tau/2)}]^2$	1/4	1/4	0	0	0	0
$[A_{yx}^{(3\tau/2)}]^2$	1	1	0	0	0	0
$[A_{xx}^{(2\tau)}]^2$	0	0	1/4	1/4	1/16	0
$[A_{yx}^{(2\tau)}]^2$	0	0	1	1	1/4	0
$[A_{zx}^{(2\tau)}]^2$	0	0	0	0	2	0
$[A_{zx}^{(3\tau)}]^2$	1/4	1/4	0	0	0	1/4

The subscripts 1 and 2 denote that the parameters so labeled belong to the first and second video pulse, respectively. The expressions for the echo responses at arbitrary temperatures ($\rho_{23},\rho_{33}\neq 0$) are too complicated to present here.

Thus, the effect of two transverse elastic video pulses satisfying Eq. (10) on a $S=1$ spin system in a direction perpendicular to $\mathbf{B}_0$ is to produce four transverse echo signals ε_{zx} and ε_{yx}, at the frequencies ω_0 and $2\omega_0$, respectively, and two longitudinal echoes ε_{xx} at the frequency $2\omega_0$.

The echo pulses ε_{zx}-polarized in the plane of the magnetic field $\mathbf{B}_0$ are caused by spontaneous transitions with $\Delta m=-1$ (m — magnetic quantum number), and therefore they arise at the frequency ω_0 between the nearest sublevels of a Zeeman triplet. The echo signals ε_{yx}, polarized in a plane normal to $\mathbf{B}_0$, and also the longitudinal echo signals ε_{xx} are due to transitions between the extreme levels of a Zeeman triplet of frequency $2\omega_0$, for which $\Delta m=-2$.

The presence among the echo signals of an acoustic echo of pulses of different polarization (including longitudinal) is, possibly, the main distinction from the photon echo case under excitation of the medium by extremely short pulses.[15]

The spatial size I of an acoustic video pulse of duration $\tau_p\sim 10$ ps is of the order of 10^{-5} cm, which is much shorter than the characteristic size L of a paramagnetic sample. In this connection it is necessary to take account of effects due to the propagation of an echo signal inside the sample.[8] Without going into complicated mathematical calculations, we shall confine ourselves to estimating the influence of propagation. The total magnetization and, with it, the components of the strain tensor will decrease due to the compensation of the contributions from regions of the sample where the hypersound wave of an echo signal has opposite phases. As a result, the intensity of the echo response is $(2\pi a/\omega_0 L)^2$ times lower than for thin samples, when propagation effects can be neglected.[8] The second important aspect of the propagation effects in our problem is the fact that, when the sample is excited by transverse video pulses, the spin system responds with, besides transverse, longitudinal echo signals, which have different propagation velocities — $a_\perp$ and $a_\parallel$, respectively. As a result, the detection time of a longitudinal echo pulse ε_{xx} by a pickup placed at the end of the sample far from the source shifts relative to the transverse echo signal by the time $\Delta t=L(1/a_\parallel-1/a_\perp)$. For example, a transverse echo pulse ε_{yx} at the frequency $2\omega_0$ arises at the time $t_{yx}=3\tau/2+t_{p1}+t_{p2}$. Then the longitudinal echo signal ε_{xx} at the same frequency can be detected at the moment $t_{yx}+\Delta t$. The same is true near the time $2\tau+t_{p1}+t_{p2}$, where a longitudinal pulse should also be detected together with a transverse pulse.

If the paramagnetic sample is so long that $L|a_\parallel^{-1}-a_p^{-1}|\gtrsim\tau$, echo signals, which we conventionally refer to the times $3\tau/2+t_{p1}+t_{p2}$, $2\tau+t_{p1}+t_{p2}$, and $3\tau+t_{p1}+t_{p2}$, can overlap on account of the difference of the velocities of the longitudinal and transverse sound or a change in the order in which they are detected. For example, if $a_\perp>a_\parallel$ and $L(a_\parallel^{-1}-a_\perp^{-1})>\tau$, then the last detected echo signal will be not the transverse pulse ε_{zx} at the frequency ω_0 but rather a longitudinal signal ε_{xx} at the frequency $2\omega_0$, which we conventionally refer to the time $2\tau+t_{p1}+t_{p2}$.

We shall find the optimal values of the parameters $\Theta_{1,2}$ and $\alpha_{1,2}$ (controlling parameters) for which the intensity of the echo signal of interest to us is maximum. The intensities of the echo signals of the longitudinal and two transverse components can be expressed in terms of the corresponding strains as

$$I_{xx}=\frac{1}{2}\rho a_\parallel^2\varepsilon_{xx}^2,$$

$$I_{yx}=\frac{1}{2}\rho a_\perp^2\varepsilon_{yx}^2,$$

$$I_{zx}=\frac{1}{2}\rho a_\perp^2\varepsilon_{zx}^2. \tag{22}$$

It follows from Eqs. (18)–(21) that this problem reduces to finding the extrema of the corresponding responses as functions of the variables Θ_1, α_1, Θ_2, and α_2.

It is convenient to represent the computational results in the form of a table. The headings of the columns contain the sets of optimal values of the parameters α_k and Θ_k ($k=1,2$) for a given type of echo signal, and the columns themselves consist of the quantities $[A_{\xi\nu}^{(t_e)}]^2$ (where $\xi=x,\ y,\ z$; $\nu=x$; $t_e=3\tau/2,\ 2\tau,\ 3\tau$) for all echo signals with the given parameters.

It is evident from Table I that, for example, for

$\alpha_1=90°$, $\Theta_1=3\pi/4$, $\alpha_2=90°$, and $\Theta_2=\pi/2$ two echo signals arise: $(2\tau)_{xx}$-echo and $(2\tau)_{yx}$-echo. The parameters $[A_{xx}^{(2\tau)}]^2$ and $[A_{yx}^{(2\tau)}]^2$ assume the values 1/4 and 1, respectively. The indicated values of $\alpha_1,\Theta_1,\alpha_2$, and Θ_2 are optimal for both echo signals. It is interesting to note that the $(3\tau)_{zx}$-echo signal at the frequency ω_0 and polarized in a direction $\mathbf{B}_0$ appears most clearly (optimally) if neither the first nor second exciting transverse video pulse is polarized in the direction of the external magnetic field (see Table I). All other echo signals are completely absent.

Thus, by varying the values of the controlling parameters it is possible to vary not only the intensity of various two-pulse (primary) echo signals but also the number of such signals itself. This circumstance opens up quite good possibilities for applications of the acoustic ESP echo in various systems for real-time information processing.

The investigation performed in this work shows that the primary acoustic echo caused by the excitation of a paramagnetic crystal by two elastic video pulses satisfying Eq. (10) is formed by several signals in contrast to the corresponding resonance effect. In our case $(S=1)$ six primary-echo signals at the frequencies ω_0 and $2\omega_0$ appear. Despite the fact that the exciting pulses are transverse, the echo signals contain both transverse and longitudinal components of the strain tensor of the medium. The intensity of the acoustic echo depends largely on the spin-phonon coupling constants G_{11} and G_{44}. For example, for the paramagnetic Fe^{2+} ions in a MgO crystal matrix $G_{11}=650\ \mathrm{cm}^{-1}$ and $G_{44}=380\ \mathrm{cm}^{-1}$.[6] Hence, and also from Eqs. (18)–(21), it is evident that the intensities of the longitudinal echo signals can often exceed the corresponding intensities of the transverse echo responses. The appearance of elastic echo signals having various polarizations distinguishes the acoustic ESP echo from the corresponding optical effect in isotropic media,[15] for which the polarization of the echo signals is the same as the polarization of the exciting video pulses. Transitions between the Zeeman sublevels can be caused not only by a spin-phonon but also by magnetic-dipole and electric-quadrupole interactions, so that not only acoustic but also electromagnetic signals can appear among the echo responses of a medium excited by elastic pulses.[20] The inverse effect, where the excitation of a crystal by magnetic pulses engenders elastic echo responses,[20] is also possible. Switching from monochromatic exciting pulses to video signals, it becomes necessary to investigate the characteristic features of echo effects for cases where a paramagnetic crystal is excited by a combined sequence of acoustic and electromagnetic video pulses. In this connection we note that some nonlinear parametric effects due to the magnetic-dipole interaction of electromagnetic video pulses have been investigated in Refs. 26–29.

In the present paper we considered one of the simplest geometries of the proposed experiment, in which both exciting video pulses are applied in a direction perpendicular to the external magnetic field. Correspondingly, acoustic-echo signals are ''emitted'' in the same direction. It is of great interest to investigate the spatiotemporal characteristics of an acoustic echo in the case of a crystal excited by elastic video pulses applied at different angles with respect to $\mathbf{B}_0$. In this case, similarly to how this occurs in the case of multifrequency photon echo,[15] one should expect not only temporal differences between the primary acoustic echo signals but also differences in their propagation directions. It seems to us that this could engender interest in theoretical and experimental investigations of acoustic echo effects accompanying the excitation of crystals by various sequences of elastic and electromagnetic video pulses.

[1] D. H. Auston, K. P. Cheung, J. A. Valdmanis, and D. A. Kleinmann, Phys. Rev. Lett. **53**, 1555 (1984).
[2] J. T. Darrow, B. B. Hu, X. C. Chang, and D. H. Auston, Opt. Lett. **15**, 323 (1990).
[3] P. C. Becker, H. L. Fragnito, J. Y. Bigot, C. H. Brito-Crus, and C. V. Shank, Phys. Rev. Lett. **63**, 505 (1989).
[4] S. A. Akhmanov, V. A. Vysloukh, and A. S. Chirkin, *Optics of Femtosecond Laser Pulses* (Nauka, Moscow, 1988).
[5] S. A. Akhmanov, and V. É. Gusev, Usp. Fiz. Nauk **162**, 3 (1992) [Sov. Phys. Usp. **35**, 153 (1992)].
[6] A. Kastler, Experientia **8**, 1 (1952).
[7] S. A. Al'tshuler, Dokl. Akad. Nauk **85**(6), 1235 (1952).
[8] V. A. Golenishchev-Kutuzov, V. V. Samartsev, and B. M. Khabibullin, *Pulsed Optical and Acoustical Coherent Spectroscopy* (Nauka, Moscow, 1988).
[9] U. Kh. Kopvillem and V. R. Nagibarov, Fiz. Met. Metalloved. **15**(2), 313 (1963).
[10] N. A. Kurnit and J. D. Abella, Phys. Rev. Lett. **6**, 567 (1964).
[11] V. R. Nagibarov and U. Kh. Kopvillem, Zh. Éksp. Teor. Fiz. **52**, 936 (1967) [Sov. Phys. JETP **25**, 618 (1967)].
[12] V. Yu. Man'kov, A. Yu. Parkhomenko, and S. V. Sazonov, Kvant. Elektron. (Moscow) **24**(10), 934 (1997).
[13] V. Yu. Man'kov, A. Yu. Parkhomenko, and S. V. Sazonov, Izv. Ross. Akad. Nauk, Ser. Fiz. **62**(2), 287 (1998).
[14] V. Yu. Man'kov, A. Yu. Parkhomenko, and S. V. Sazonov, Proc. SPIE **3239**, 5 (1997).
[15] A. Yu. Parkhomenko and S. V. Sazonov, JETP Lett. **67**, 934 (1998).
[16] J. Tucker and V. Rampton, *Microwave Ultrasonics in Solid State Physics* (North-Holland, Amsterdam, 1972; Mir, Moscow, 1975).
[17] S. V. Sazonov, J. Phys.: Condens. Matter **4**, 6485 (1992).
[18] S. V. Sazonov, Izv. Vyssh. Uchebn. Zaved. Fiz. **36**(4), 94 (1993).
[19] S. V. Sazonov, J. Phys.: Condens. Matter **6**, 6295 (1994).
[20] S. A. Al'tshuler and B. M. Kozyrev, *Electronic Paramagnetic Resonance* (Nauka, Moscow, 1972).
[21] É. M. Belenov and A. V. Nazarkin, JETP Lett. **51**, 288 (1990).
[22] É. M. Belenov, A. V. Nazarkin, and V. A. Ushchapovskiĭ, Zh. Éksp. Teor. Fiz. **100**, 762 (1991) [Sov. Phys. JETP **73**, 442 (1991)].
[23] I. A. Lappo-Danilevskiĭ, *Application of Matrix Functions to the Theory of Linear Systems of Ordinary Differential Equations* (Gostekhizdat, Moscow, 1957).
[24] S. V. Sazonov, Izv. Ross. Akad. Nauk, Ser. Fiz. **58**(8), 129 (1994).
[25] U. Kh. Kopvillem and S. V. Prants, *Polarization Echo* (Nauka, Moscow, 1985).
[26] I. Nakata, J. Phys. Soc. Jpn. **60**(2), 77 (1991).
[27] S. V. Sazonov, Kvant. Elektron. (Moscow) **20**, 135 (1993).
[28] S. V. Sazonov and E. V. Trifonov, Zh. Éksp. Teor. Fiz. **103**, 1521 (1993) [JETP **76**, 744 (1992)].
[29] S. V. Sazonov, J. Phys.: Condens. Matter **7**, 175 (1995).

Translated by M. E. Alferieff

Investigation of the specific heat of bismuth tellurite in the temperature range 100–370 K

K. V. Domoratskiĭ and L. Ya. Sadovskaya

Dnepropetrovsk State University, 320625 Dnepropetrovsk, Ukraine

V. M. Rizak and V. A. Stefanovich

Uzhgorod State University, 294000 Uzhgorod, Ukraine

(Submitted September 18, 1998)
Fiz. Tverd. Tela (St. Petersburg) **41**, 629–631 (April 1999)

The temperature dependence of the specific heat C_p of bismuth tellurite is measured. The experimental data are compared with the results of a calculation that takes account of the Debye and Einstein mechanisms of the specific heat.
[S1063-7834(99)01304-0]

Bismuth tellurite is a comparatively new nonlinear optical material of practical interest.[1–7] Bi_2TeO_5 crystals have orthorhombic C_{2v}^{15} symmetry, room-temperature lattice parameters $a=11.602$ Å, $b=16.461$ Å, and $c=5.523$ Å and $Z=8$ formula units.[2] According to Ref. 3, a second-order phase transition to a centrosymmetric phase occurs in the crystal at $T\sim 1050$ K. The optical and electrical properties of bismuth tellurite crystals have been studied in a series of works.[4,5] Its promising photorefractive properties are noted.[1,6,7] However, there is no information on the thermodynamic parameters of the material. The present paper contains the results of measuring the specific heat (C_p) of Bi_2TeO_5 in the temperature interval 100–370 K, the change in the thermodynamic functions calculated according to it, and a discussion of the results, taking account of the characteristic features of this crystal.

The experimental samples are variable-composition crystals at the center of the phase diagram of $Bi_2O_3-TeO_2$.[8] Bismuth tellurite single crystals with the composition Bi_2TeO_5 and of high optical quality were grown by the Czochralski method from a melt of the initial, especially pure grade, components Bi_2O_3 and TeO_2 in the ratio 47 and 53 mole%, respectively. Small single crystals with a total mass of 4.05 g were used in this work. The measurements of $C_p(T)$ were performed under adiabatic conditions in an automated vacuum calorimeter. The basic features of the operation of this instrument are described in Ref. 9. The experimental values of the specific heat were obtained in a heating regime with discrete heat input every 1.5 K. To ensure thermal equilibrium, the time to reach each point was at least 20–25 min. The error in the C_p measurements did not exceed 1%.

Figure 1a shows the temperature dependence of the molar specific heat of bismuth tellurite crystals. In the experimental temperature range C_p increases monotonically with temperature. At ~ 325 K the atomic molar specific heat reaches its classical value, corresponding to the Dulong–Petit law, and then increases slightly, approaching saturation (Fig. 1b). The specific heat curve was smoothed by the least-squares method. The computed values of C_p and the corresponding computed changes in the thermodynamic functions are presented in Table I.

An important parameter in the study of the specific heat is the Debye temperature Θ_D. Since there are no low-temperature experimental data on $C_p(T)$, Θ_D was calculated in terms of the root-mean-cube of the sound velocity $\langle v\rangle$[10–12] according to the expression

$$\Theta_D=\frac{h}{k}\left(\frac{3}{4\pi V}\right)^{1/3}\left[\sum_{i=1}^{3}\int\{\nu_i(\Theta,\varphi)\}^{-3}d\Omega\right]^{-1/3}, \qquad (1)$$

where h and k are, respectively, the Planck and Boltzmann constants, V is the unit-cell volume, $\nu_i(\Theta,\varphi)$ is the sound velocity vector (for $i=1$ the longitudinal and for $i=2$ and 3 the transverse components of the vector are integrated), and Ω is the solid angle. In the case of an orthorhombic crystal the root-mean-cube velocity was estimated to a first approximation according to the expression

$$\langle v\rangle=\left[\frac{1}{9}\left(\frac{1}{v_{11}^3}+\frac{1}{v_{22}^3}+\frac{1}{v_{33}^3}+\frac{2}{v_{12}^3}+\frac{2}{v_{13}^3}+\frac{2}{v_{23}^3}\right)\right]^{-1/3}, \qquad (2)$$

v_{ij} $(i,j=1,2,3)$ are the components of the velocity vector of the longitudinal and transverse phonons in the crystal (the first index corresponds to the direction of propagation and the second index corresponds to the direction of polarization). The following values of the components of the sound velocity vector were calculated using the values obtained in Ref. 13 for the room-temperature elastic constants in bismuth tellurite:

$$v_{11}=3377 \text{ m/s}, \quad v_{12}=1957 \text{ m/s}, \quad v_{13}=1841 \text{ m/s},$$

$$v_{22}=3657 \text{ m/s}, \quad v_{23}=2064 \text{ m/s}, \quad v_{33}=3351 \text{ m/s},$$

Averaging over the crystallographic directions and types of phonons gives $\langle v\rangle=2472$ m/s. The corresponding Debye temperature is $\Theta_{Dv}=72$ K.

The good agreement with the experimental data examining the specific heat in the Debye model is obtained only for the case when the acoustic modes make the main contribu-

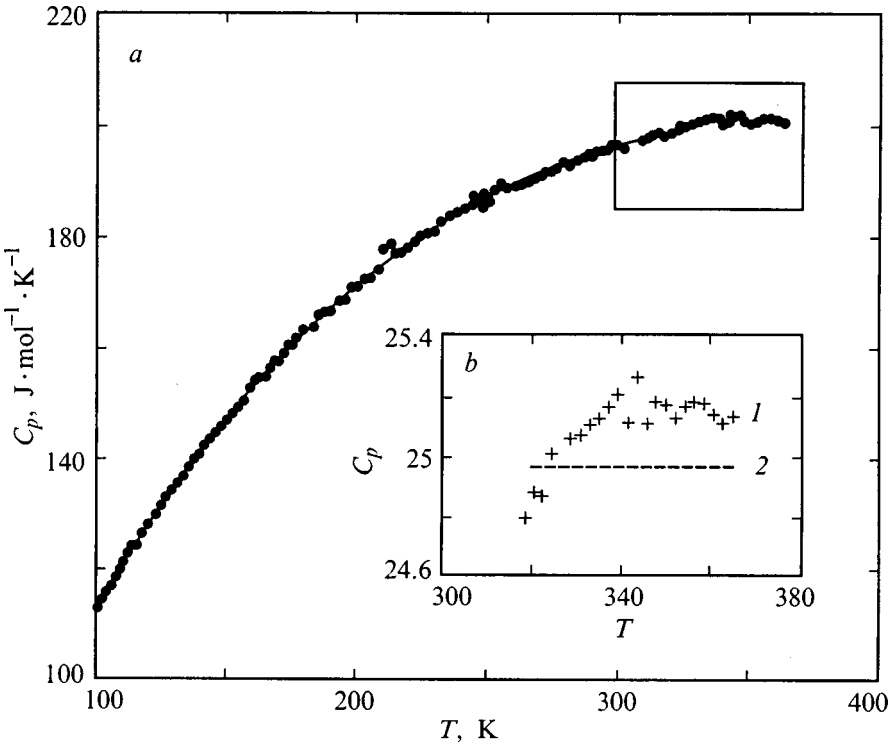

FIG. 1. Temperature variation of the molar specific heat C_p in bismuth tellurite (temperature range 100–370 K) (a). The deviation of the atomic specific heat of bismuth tellurite (*1*) in the temperature range 330–370 K from the classical Dulong–Petit law (*2*) (b).

tion to the specific heat, since this model is intended for a substance with $N=1$ atoms per unit cell. For a Bi_2TeO_5 single crystal there are $N=64$ atoms per unit cell , so that the contribution of not only three acoustic modes but also 189 $(3N-3)$ optical modes was taken into account.

Besides the Debye model, the Einstein model of specific heat was also used to match theory and experiment. Data on the vibrational spectra of the optical modes in bismuth tellurite were required to use the Einstein model. To this end, the Raman scattering (RS) spectra were measured in a Bi_2TeO_5 single-crystal sample in the form of a $7.4\times9.6\times4.4$ mm^3 parallelepiped cut along the principal crystallographic directions. The faces of the sample were polished. Using a He–Ne laser, the room-temperature RS spectra were obtained for all possibilities of the irreducible representations $(A1, A2, B1, B2)$ in the given space group.

The molar specific heat was obtained as follows:

$$C=C_D+C_E, \tag{3}$$

where C_D is the Debye contribution to the specific heat obtained from the Debye function $D(\Theta/T)$ by substituting the value of Θ_D computed above, C_E is the contribution of the Einstein component to the specific heat calculated from the expression

$$C_E=\frac{1}{z}\sum_{j}^{3N-3} a_j RE(h\nu_j/kT), \tag{3'}$$

TABLE I. Smoothed values of the molar specific heat and the corresponding computed thermodynamic functions (T, K; C_p, ΔS, $\Delta\Phi$, J·mole^{-1}K^{-1}; ΔH, J·mole^{-1}).

T, K	C_p	$S(T)-S(100\text{ K})$	$H(T)-H(100\text{ K})$	$\Phi(T)-\Phi(100\text{ K})$
100	113.1	0.0	0	0.00
120	128.0	18.4	3949	36.34
140	141.1	35.5	7420	68.89
160	152.6	50.5	10470	98.11
180	162.5	63.5	13090	124.40
200	171.0	74.5	15340	148.10
220	178.2	83.9	17250	169.40
240	184.2	91.8	18840	188.40
260	189.2	98.3	20170	205.40
280	193.2	103.5	21230	220.60
300	196.3	107.6	22050	234.00
320	198.7	110.7	22680	246.00
340	200.6	113.2	23190	256.70
360	201.9	114.9	23530	266.10

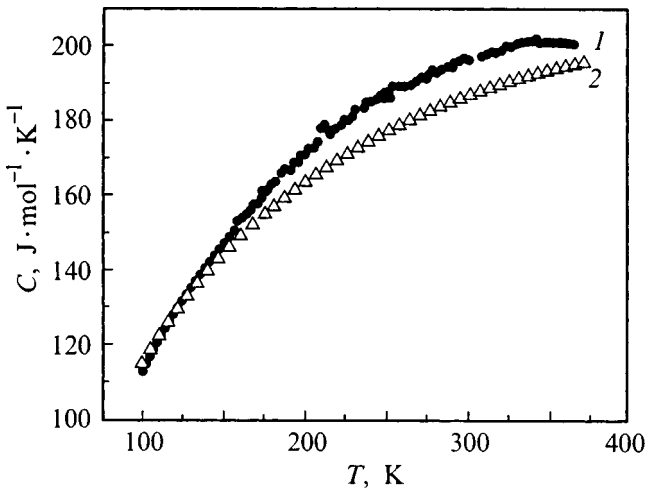

FIG. 2. Experimental (*1*) and computed (*2*) temperature dependences of the specific heat of bismuth tellurite.

where R is the gas constant, T is the absolute temperature, $E(h\nu_i/kT)$ is the Einstein function (the contribution to the specific heat of the optical modes), corresponding to the characteristic frequency ν_j of the RS spectra,[11] a_j is the weighting factor introduced, since not all modes are resolved in the RS spectra, and z is the number of molecules per unit cell of the Bi_2TeO_5 single crystal.

Figure 2 shows the molar specific heat obtained experimentally and computed theoretically. The discrepancy between the calculations and the experimental data could be due to the fact that the dispersion of the optical modes was neglected in the analysis and, moreover, the calculations were performed in the harmonic approximation, while in real crystals the atomic vibrations are anharmonic.

We thank A. Yu. Kudzin and E. D. Solgatova for assistance and active paraticipation in the discussion of the results obtained.

[1] I. Foldvari, H. Liu, and R. C. Powell, SPIE Proc. **1626**, 9 (1992).
[2] D. Mercurio, M. El. Farissi, B. Frit, and P. Goursat, Mater. Chem. Phys. **9**, 467 (1983).
[3] S. Yu. Stefanovich, L. Ya. Sadovskaya, and A. M. Antonenko, Fiz. Tverd. Tela (Leningrad) **33**, 2215 (1991) [Sov. Phys. Solid State **33**, 1249 (1991)].
[4] G. Magdula, L. Kovacs, A. Peter, and E. Hartmann, Opt. Mater. **1**, 161 (1992).
[5] V. P. Avremenko, A. Yu. Kudzin, S. P. Reprentcheva, L. Ya. Sadovskaya, and G. Kh. Sokolianskii, Ferroelectrics **82**, 173 (1988).
[6] I. Foldvari, A. Peter, L. A. Kappers, O. R. Gilliam, and R. Capelletti, J. Mater. Sci. **27**, 750 (1992).
[7] I. Foldvari, H. Liu, R. C. Powell, and A. Peter, J. Appl. Phys. **71**, 5465 (1992).
[8] B. Frit, M. James, G. Peres, and P. Hagenmuller, Rev. Chim. Miner. **8**, 453 (1971).
[9] V. M. Malyshev and G. A. Mil'ner, Prib. Tekh. Éksp., No. 6, 195 (1986).
[10] P. P. Pavinskiĭ, *Introduction to the Theory of Solids* (Leningrad, 1979).
[11] L. A. Girifalco, *Statistical Physics of Materials* (Wiley, N. Y., 1973; Mir, Moscow, 1975).
[12] D. D. Betts, A. B. Bhatia, and G. K. Norton, Phys. Rev. **104**, 43 (1956).
[13] A. M. Antonenko, V. M. Gorbatenko, L. Ya. Sadovskaya, and S. Yu. Ermakov, Fiz. Tverd. Tela (St. Petersburg) **38**, 938 (1996) [Phys. Solid State **38**, 518 (1996)].

Translated by M. E. Alferieff

Nonunidirectional two-beam interaction in photorefractive bismuth silicate in an alternating electric field

V. Yu. Krasnoperov, R. V. Litvinov, and S. M. Shandarov

Tomsk State University of Control Systems and Radioelectronics 634050 Tomsk, Russia
(Submitted September 28, 1998)
Fiz. Tverd. Tela (St. Petersburg) **41**, 632–637 (April 1999)

The effective nonunidirectional energy exchange between like-polarized light beams is investigated experimentally on a photorefractive grating formed by diffusion drift in a bismuth silicate crystal placed in an alternating external electric field. © *1999 American Institute of Physics.* [S1063-7834(99)01404-5]

The two-beam interaction of light waves in photorefractive crystals is the subject of intense research.[1–7] The analysis presented in Refs. 3 and 4 of two-wave interaction shows that steady energy transfer on a photorefractive grating formed by diffusion drift always occurs in one direction, which depends only on the orientation of the lattice vector **K** relative to the crystal-physical coordinate system. Nonunidirected, i.e. always directed from the strong to the weak beam (or from the weak to the strong beam), energy transfer occurs with the interaction of light beams on an amplitude grating[7] or on a photorefractive grating formed by intermode interaction as a result of the photogalvanic effect in birefringent crystals.[5]

The analysis of the solution of the equations of coupled waves performed in Ref. 8 for the case of a nonlocal photorefractive response has demonstrated the possibility of efficient steady nonunidirected energy transfer with two-wave interaction on a photorefractive grating having vectors $\mathbf{K}\|[\bar{1}10]$ and $\mathbf{K}\|[\bar{1}11]$ that is formed in cubic crystals in an alternating external electric field. It was shown that such energy transfer can be due to a dominant contribution of the so-called self-diffraction gyration effect[9,10] to the two-wave gain.

In the present work the effective steady nonunidirectional energy transfer accompanying the interaction of like-polarized waves on a photorefractive grating formed in a cadmium oxide doped bismuth silicate crystal is investigated experimentally and theoretically.

1. EXPERIMENT

The standard arrangement of a symmetric two-beam interaction at wavelength $\lambda_0=633$ nm (Fig. 1) in a cadmium-doped sample of the photorefractive crystal $B_{12}SiO_{20}$: CdO with dimensions $10.1\times8.1\times7.9$ mm^3 along the crystallographic directions $[110]\times[001]\times[\bar{1}10]$ was used in the experiments. We note that this sample was used previously[11] to investigate the generation of subharmonics of the fundamental photorefractive grating. Its absorption coefficient was $\alpha=0.1$ cm^{-1}; the electrooptic constant measured with constant mechanical stresses $r_{41}^T=-2.9\times10^{-12}$ mV; the specific counterclockwise rotation (looking toward the beam) is $\rho=22.1$ deg/mm. The frequency and amplitude of the external voltage applied to copper electrodes, which were clamped to the lateral faces of the crystal (Fig. 1), were $f=300$ Hz and $U_m=8$ kV. The period of the interference grating was $\Lambda=20\mu$m. For maximum contrast (modulation coefficient) of the interference pattern at the entrance face of the crystal $m(0)=1$ ($m(0)=2\sqrt{I_S(0)I_P(0)}/(I_S(0)+I_P(0))$) the total intensity of the light beams with intensities $I_S(0)$ and $I_P(0)$ incident on the crystal was $I_0=8$ mV/cm^2. The intensities $I_{S,P}(d)$ of the light beams at the exit from the crystal was measured with a photodiode (Fig. 1). The investigation of the kinetics of the light-beam intensities showed that the interaction becomes steady after 900 s have elapsed. The efficiency of energy transfer between the beams according to the measured values of the light beam intensities was determined in terms of the two-beam gain[2]

$$\Gamma=\frac{1}{d}\ln\left(\frac{I_S(d)I_P(0)}{I_S(0)I_P(d)}\right). \tag{1}$$

The gain will be positive if energy is transferred, as a result of the interaction, from the beam $I_P(d)$ to the beam $I_S(d)$ and negative when energy is transferred in the opposite direction.

Figure 2 shows the measured gain Γ versus the contrast of the interference pattern on the entrance face of the crystal, which was decreased relative to its maximum value $m(0)=1$ ($I_S(0)=I_P(0)$) by attenuation of the beam $I_S(0)$ or the beam $I_P(0)$ with light filters, is displayed in Fig. 2 for waves linearly polarized perpendicular to the photorefractive-grating vector **K**, oriented along the $[\bar{1}10]$ axis of the crystal. As one can see from the figure, for $I_S(0)\leqslant I_P(0)$ energy transfer is always directed from the beam I_P to the beam I_S. However, for $I_S(0)>I_P(0)$ the direction of transfer changes when $m(0)<0.95$, and transfer occurs from the beam I_S to the weaker beam I_P.

For $m(0)=0.02$ the two-wave gain Γ was measured as a function of the angle θ between the plane of incidence of the light beams on the crystal (Fig. 1), which was also the (001) plane of the crystal (lattice vector in the direction $[\bar{1}10]$), and the polarization plane of these beams. These dependences for the cases $I_S(0)<I_P(0)$ and $I_S(0)>I_P(0)$ are presented in Fig. 3. The method used to calculate the theoretical curves *1* and *2* presented here is described in the next sec-

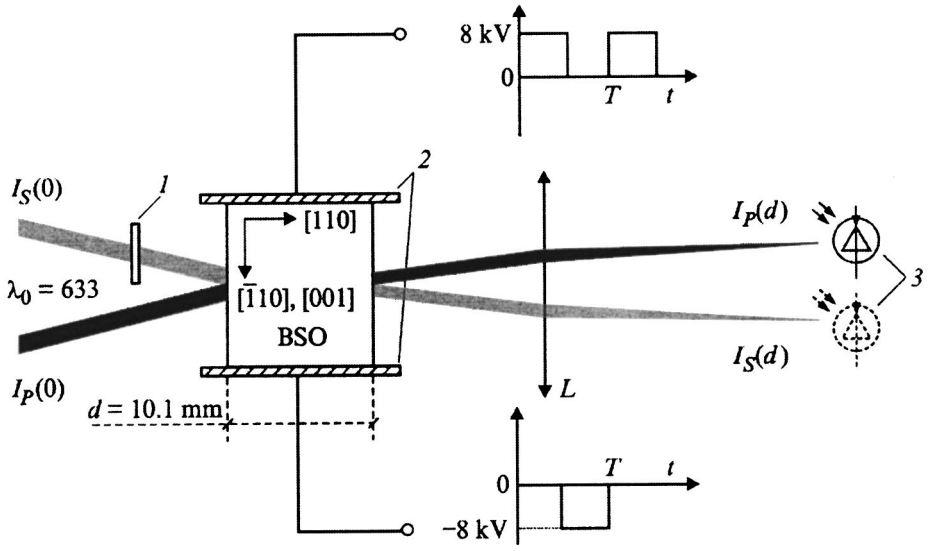

FIG. 1. Experimental arrangement. *1* — Light filter, *2* — copper electrodes, *3* — Fd-24.

tion. As follows from Eq. (1), for $m(d) \ll 1$ the gain Γ is approximately $\Gamma' = \ln(I_S(d)/I'_S(0))/d$ in the first case and $\Gamma'' = \ln(I''_P(0)/I_P(d))/d$ in the second case.

In both cases, for simple exponential intensification (attenuation) of the beam I_S and, in the absence of nonunidirectional energy transfer, the beam I_P attenuates (intensifies) and the dependences $\Gamma(\theta)$ for them should be the same. As one can see from Fig. 3, this does not happen. It can be inferred that this is due to the positive nonunidirectional addition of energy to the weak beam. It follows from the dependences presented that the nonunidirectional energy transfer under the present experimental conditions results in intensification of the weak beam for all values of the angle θ. We note that this is not so in general. Specifically, when the external voltage decreases, the dependences presented in Fig. 3 shift toward one another, right up to complete merging at $U_m = 0$. The maximum and minimum gains will be equal in absolute magnitude and opposite in sign.

The measurements of Γ for waves linearly polarized perpendicular to the photorefractive lattice vector **K** oriented, like the external field, along the [001] axis showed that, in this case, the two-beam interaction is characterized by the standard, for photorefractive lattices,[2,4] unidirectional energy transfer. However, the efficiency of such transfer for $m(0) = 0.02$ was different for the cases $I_S(0) < I_P(0)$ and $I_S(0) > I_P(0)$ and, correspondingly, $\Gamma = 5.5$ and 2.8 cm^{-1}. This confirms the existence of a mechanism of nonunidirectional energy transfer for the vector **K** directed along the [001] axis of the crystal.

As follows from the results of Ref. 7, such energy transfer in a two-beam interaction process is possible as a result of the formation of an amplitude grating in addition to a photorefractive grating. The contribution of the first grating to the two-wave gain is nonunidirectional and does not depend on the orientation of the vector **K** relative to the crystal-physical coordinate system. It is shown in Refs. 3 and 4 that, in the low-contrast regime ($m(d) \ll 1$) with a two-wave interaction on a photorefractive grating, the numerical value of the two-wave gain changes sign under a symmetric interchange (Fig. 1) of the intensities of the waves incident on the crystal. If this is taken as a basis and the contribution of the amplitude grating to Γ is assumed to be additive,[7] the amplitude of the absorption coefficient $\Delta\alpha$ of the grating can be determined from the measurements described above. For $m(0) = 0.02$ it should assume the value $\Delta\alpha = 3.4$ cm^{-1} for $\mathbf{K} \| [\bar{1}10]$ and $\Delta\alpha = 1.4$ cm^{-1} for $\mathbf{K} \| [001]$. These values are an order of magnitude greater than the measured value of the absorption coefficient of the crystal. In this case a sub-

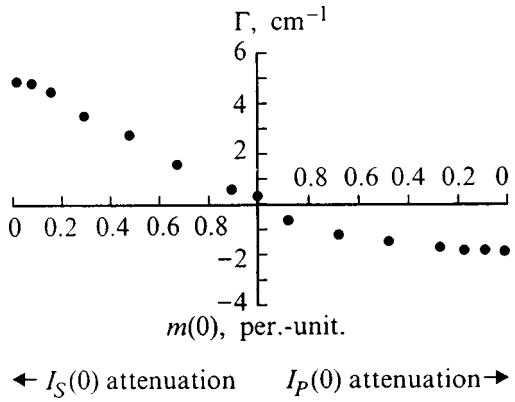

FIG. 2. Two-beam gain versus the modulation coefficient of the interference pattern on the entrance face of the crystal.

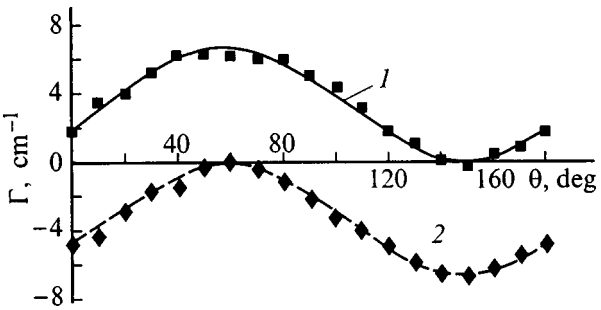

FIG. 3. Two-beam gain versus the angle between the plane of incidence (001) of the light beams incident on the crystal and the polarization plane of these beams for $m(0) = 0.02$: *1* — $I_S(0) < I_P(0)$; *2* — $I_S(0) > I_P(0)$.

stantial photoinduced absorption of light should be observed. Such absorption could be due to the presence of not only deep donor levels but also shallow traps in the crystal.[12] The difference in the photoionization cross sections with photogeneration of electrons from donor and trap centers can lead to the formation of an amplitude grating. However, the absorption coefficient was ~ 0.1 cm^{-1} and did not change when the crystal was illuminated by beams with intensity ranging from 0.3 to 100 mW/cm^2.

To determine the possible contribution of the amplitude grating to the above-described nonunidirectional energy transfer we performed measurements of the symmetric interaction efficiency for two waves incident on the (001) face. In this case the lattice vector **K**, just as the external field, was oriented along the [110] axis of the crystal, and the ratio of the beam intensities was $I_P(0)/I_S(0)=1000$. The polarization of the incident beams was chosen to be orthogonal to the vector **K**. As is well known,[2] for such a geometry the efficiency of two-beam interaction by a photorefractive grating formed in crystals with 23 symmetry is zero. Therefore energy transfer between the beams is possible only because of their interaction on the amplitude grating. The efficiency of such an interaction does not depend on the geometry of the experiment or on the orientation of the lattice vector **K** relative to the crystal-physical coordinate system. The measured value of the two-beam gain was $\Gamma=\Delta\alpha=0.025$ cm^{-1}. This value is much smaller than the value that we obtained for the efficiency of nonunidirectional energy transfer. It was nonzero because of the inaccurate orientation of the sample relative to the (001) crystal plane.

2. MODEL OF NONUNIDIRECTIONAL ENERGY TRANSFER ACCOMPANYING A TWO-WAVE INTERACTION ON A PHOTOREFRACTIVE GRATING WITH VECTOR $\mathbf{K}\parallel[\bar{1}10]$

To devise a theoretical interpretation of the experimental results obtained above we shall use a mode approach to the analysis of the two-wave interaction in photorefractive crystals.[8,13] We shall represent the light field of the signal and pump waves as a superposition of the characteristic waves of the crystal. The vector diagram of such a two-wave interaction by a photorefractive grating with vector $\mathbf{K}\parallel[\bar{1}10]$ is presented in Fig. 4.

For this orientation of the vector **K** and small absorption $\alpha\lambda_0/4\pi$, circular $\rho\lambda_0/2\pi$ and linear $\sigma n_0=n_0^3 r_{41}^T E_0/2$ birefringence of the same order of magnitude (n_0 is the refractive index, $E_0=U_m/L$, and L is the transverse size of the crystal), the expressions for the refractive indices $n_{1,2}$ of the characteristic waves and the corresponding characteristic polarization vectors $\mathbf{e}_1$ and $\mathbf{e}_2$ can be obtained from the general relations presented in Ref. 8. In the approximation of small angles $2\theta_{in}$ the refractive indices and polarization vectors of the characteristic waves corresponding to the same wave surface can be assumed to be the same as those for the characteristic waves propagating along the OX axis

$$\dot{n}_{1,2}=n_0-i\frac{\alpha\lambda_0}{4\pi}\pm\frac{\rho\lambda_0}{2\pi}\sqrt{1+\xi^2}, \tag{2}$$

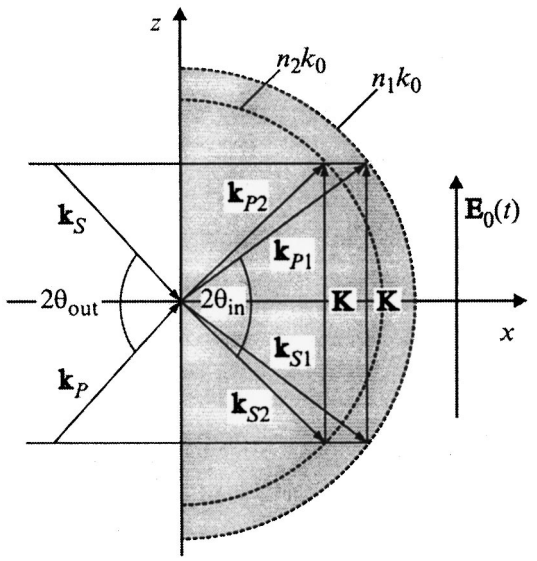

FIG. 4. Vector diagram of a two-wave interaction on a photorefractive grating with vector $\mathbf{K}\parallel[\bar{1}10]$ in a cubic crystal placed in an external electric field $\mathbf{E}_0(t)\parallel\mathbf{K}$.

$$\mathbf{e}_1=\frac{1+i\xi}{\sqrt{1+\xi^2}}\frac{\mathbf{y}^0}{\sqrt{2}}+\frac{i\mathbf{z}^0}{\sqrt{2}}, \tag{3}$$

$$\mathbf{e}_2=\frac{\mathbf{y}^0}{\sqrt{2}}-\frac{\xi+i}{\sqrt{1+\xi^2}}\frac{\mathbf{z}^0}{\sqrt{2}}, \tag{4}$$

where $\xi=\pi n_0^3 r_{41}^T E_0/\rho\lambda_0$ and $\mathbf{y}^0=\mathbf{z}^0\times\mathbf{x}^0$, where $\mathbf{x}^0$ and $\mathbf{z}^0$ are the unit vectors of the coordinate system.

For incident waves with scalar amplitudes $E_{S,P}$ and linear polarization vectors making angles $\theta_{S,P}$ with the plane of incidence, the amplitudes of the characteristic waves excited in the crystal at the boundary $x=0$ are determined by the expressions

$$C_{S1,P1}(0)=\frac{\tau E_{S,P}}{\sqrt{2}}\left\{\sin(\theta_{S,P})\frac{1-i\xi}{\sqrt{1+\xi^2}}-i\cos(\theta_{S,P})\right\}, \tag{5}$$

$$C_{S2,P2}(0)=\frac{\tau E_{S,P}}{\sqrt{2}}\left\{\sin(\theta_{S,P})+\cos(\theta_{S,P})\frac{1-\xi}{\sqrt{1+\xi^2}}\right\}, \tag{6}$$

where τ is the coefficient of Fresnel losses.

For the orientation of the lattice vector $\mathbf{K}\parallel[\bar{1}10]$ and in the approximation of inexhaustible pumping, for $I_S(0)\ll I_P(0)$ the equations for the amplitudes of the coupled waves[8] can be represented in the form

$$\frac{dC_{S1}(x)}{dx}=\frac{\Gamma_{St}}{2I_0}(C_{S1}(x)C_{P1}^*(0)+C_{S2}(x)C_{P2}^*(0))\times\left\{\frac{\xi C_{P1}(0)}{\sqrt{1+\xi^2}}-\frac{\xi+i}{1+\xi^2}C_{P2}(0)\exp[i\Delta kx]\right\}, \tag{7}$$

$$\frac{dC_{S2}(x)}{dx}=-\frac{\Gamma_{st}}{2I_0}(C_{S1}(x)C_{P1}^{*}(0)+C_{S2}(x)C_{P2}^{*}(0))\times\left\{\frac{\xi-i}{1+\xi^2}C_{P1}(0)\exp[-i\Delta kx]+\frac{\xi C_{P2}(0)}{\sqrt{1+\xi^2}}\right\},\tag{8}$$

where $\Gamma_{st}=2\pi n_0^3 r_{41}^T E_1^{sc}/\lambda_0$ includes the photoelastic contribution,[14] $\Delta k=(\dot{n}_1-\dot{n}_2)2\pi/\lambda_0=2\rho\sqrt{1+\xi^2}$, $I_0=|C_{S1(0)}|^2+|C_{S2}(0)|^2+|C_{P1}(0)|^2+|C_{P2}(0)|^2\approx|C_{P1}(0)|^2+|C_{P2}(0)|^2$, and E_1^{sc} is the effective amplitude of the space-charge field which depends on the photorefractive parameters of the crystal, the period of the grating, and the amplitude and temporal shape of the external electric field.[15,16]

For like-polarized waves incident on the crystal ($\theta_S=\theta_P=\theta$) the vector amplitude of the resulting light field of the signal wave at a distance x from the crystal boundary can be obtained in the form[8]

$$\mathbf{E}_S(x)=\left\{\mathbf{E}_{\parallel}^{S}(x)\exp\left[\frac{\Gamma_{st}x}{2}\eta(x)\right]+\mathbf{E}_{\perp}^{S}(x)\Gamma_{st}\mathcal{J}_S(x)\right\}\times\exp[-\alpha x].\tag{9}$$

Here

$$\mathbf{E}_{\parallel}^{S}(x)=C_{S1}(0)\mathbf{e}_1+C_{S2}(0)\mathbf{e}_2\exp[i\Delta kx],\tag{10}$$

$$\mathbf{E}_{\perp}^{S}(x)=C_{S2}^{*}(0)\mathbf{e}_1-C_{S1}^{*}(0)\mathbf{e}_2\exp[i\Delta kx],\tag{11}$$

$$\eta(x)=\frac{\xi^2+\mathrm{sinc}(2\rho x\sqrt{1+\xi^2})}{1+\xi^2}\sin(2\theta)-\rho x\,\mathrm{sinc}^2(\rho x\sqrt{1+\xi^2})\cos(2\theta),\tag{12}$$

$$\mathcal{J}_S(x)=\frac{1}{2(1+\xi^2)}\int_0^x[\xi+i\xi^2\cos(2\theta)+i\sqrt{1+\xi^2}\times\sin(2\theta)\sin(2\rho x'\sqrt{1+\xi^2})-(\xi-i\cos(2\theta))\cos(2\rho x'\sqrt{1+\xi^2})]\times\exp\left(\frac{\Gamma_{st}x'}{2}\eta(x')\right)dx',\tag{13}$$

where $\mathrm{sinc}\,(x)=\sin(x)/x$.

Thus, after interacting with the reference wave in a crystal of thickness $x=d$ the light field of the signal wave can be represented as a superposition of elliptically polarized light fields $\mathbf{E}_{\parallel}^{S}(d)$ and $\mathbf{E}_{\perp}^{S}(d)$. It is easy to show from Eqs. (10), (11), (3), and (4) that these fields satisfy the orthogonality condition $\mathbf{E}_{\parallel}^{S}(d)\cdot\mathbf{E}_{\perp}^{S*}(d)=0$. The polarization structure $\mathbf{E}_{\parallel}^{S}(0)$ of the first component corresponds to the signal wave in the absence of a photorefractive interaction (no pump wave). In the presence of pumping the intensity of this component $I_{\parallel}^{S}(d)=I_S(0)\exp[\Gamma_{st}d\eta(d)]$ can increase or decrease, depending on the sign of the exponent. This is characteristic for an ordinary two-beam interaction.

The intensity of the light field component $I_{\perp}^{S}(x)=I_S(0)\Gamma_{st}^2|\mathcal{J}_S(x)|^2$ orthogonal to the signal wave (in the absence of an interaction) determines the contribution of the self-diffraction gyration effect[8–10] to the total intensity $I_S(d)=I_{\parallel}^{S}(d)+I_{\perp}^{S}(d)$ of the signal beam at the exit from the crystal. The contribution of this component always increases the intensity of the weaker signal beam as a result of power transfer from the stronger pump wave. The orthogonally polarized component of the light field appears with the interaction, on account of diffraction with a change of the polarization state (the processes $\mathbf{k}_{S1}=\mathbf{k}_{P2}-\mathbf{K}+\Delta\mathbf{k}$ and $\mathbf{k}_{S2}=\mathbf{k}_{P1}-\mathbf{K}-\Delta\mathbf{k}$ in Fig. 4), on the photorefractive grating formed by the initial pump and signal waves (the processes $\mathbf{K}=\mathbf{k}_{P1}-\mathbf{k}_{S1}$ and $\mathbf{K}=\mathbf{k}_{P2}-\mathbf{k}_{S2}$), and its efficiency is high because of the short length of the detuning vector $\Delta\mathbf{k}$.

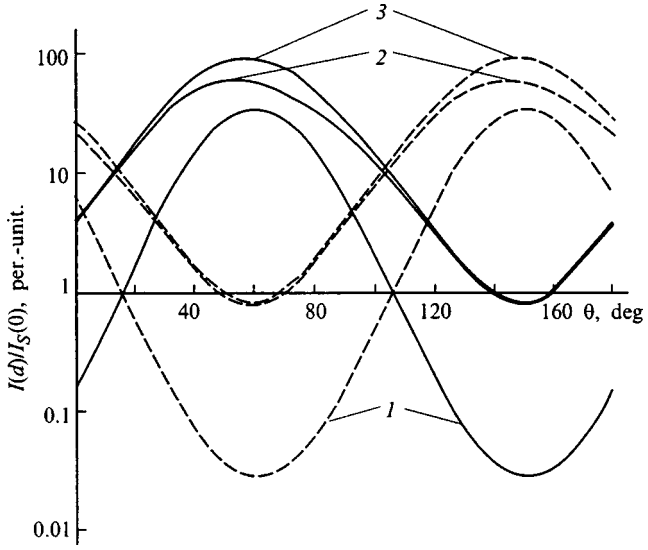

FIG. 5. Relative gain (attenuation) of the intensity $I_{\parallel}(d)/I_S(0)$ (curves *1*) and $I_{\perp}(d)/I_S(0)$ (curves *2*) of the components of the light field and of the total intensity $I_{\parallel}(d)+I_{\perp}(d)/I_S(0)$ (curves *3*) at the exit from the crystal versus the angle θ between the incidence plane and the polarization vector of the incident waves. $\Gamma_{st}=+10\ \mathrm{cm}^{-1}$ — solid curves, $\Gamma_{st}=-10\ \mathrm{cm}^{-1}$ — dashed curves.

The relations for the vector amplitude $\mathbf{E}_P(x)$ of the pump wave for $I_P(0)\ll I_S(0)$ can be obtained from Eqs. (9)–(13) by replacing the indices $S1$ and $S2$ by $P1$ and $P2$ and changing the sign of the terms containing Γ_{st} from plus to minus. Therefore, the intensity of the weak pump wave at the crystal exit is determined as $I_P(d)=I_P(0)\exp[-\Gamma_{st}d\eta(d)]+I_P(0)\Gamma_{st}^2|\mathcal{J}_P(d)|^2$.

Figure 5 shows the relative gain (attenuation) of the intensities $I_{\parallel}^{S}(d)/I_S(0)$ and $I_{\perp}^{S}(d)/I_S(0)$ of the components of the light field of the signal wave and the total intensity $I(d)/I_S(0)=(I_{\parallel}^{S}(d)+I_{\perp}^{S}(d))/I_S(0)$ at the exit of the $Bi_{12}SiO_{20}$ crystal versus the angle θ between the plane of incidence and the polarization vector of the incident waves. The solid curves correspond to a positive coupling constant $\Gamma_{st}=+10\ \mathrm{cm}^{-1}$ and the dashed curves correspond to a negative constant $\Gamma_{st}=-10\ \mathrm{cm}^{-1}$. The values of the other physical parameters of the model employed corresponded to the above-described experimental conditions. It follows from the curves shown that, for the light-field component with intensity $I_{\parallel}^{S}(d)/I_S(0)$ (curves *1*), intensification is replaced by attenuation with a change in sign of the coupling constant. The amplification efficiency equals the attenuation efficiency. For the case at hand, for all values of the angle θ the

contribution of the self-diffraction gyration effect (curves *2*) to the total intensity of the light field of the signal wave (curves *3*) is much larger than the standard photorefractive intensification. For most values of θ the orthogonal component of the light field of the signal wave intensifies ($I_{\perp}^{S}(d)/I_S(0)>1$).

The relations (2)–(6) and (9)–(13) make it possible to write an analytic expression for the two-wave gain (1) in the form

$$\Gamma_{th}(x)=\Gamma_{st}\eta(x)$$
$$+\frac{1}{x}\ln(1+|\mathcal{J}_S(x)|^2\Gamma_{st}^2\exp(-\Gamma_{st}x\,\eta(x))) \qquad (14)$$

in the approximation of an inexhaustible pump for $I_S(0)\ll I_P(0)$ and

$$\Gamma_{th}(x)=\Gamma_{st}\eta(x)$$
$$-\frac{1}{x}\ln(1+|\mathcal{J}_P(x)|^2\Gamma_{st}^2\exp(\Gamma_{st}x\,\eta(x))), \qquad (15)$$

for $I_S(0)\gg I_P(0)$.

The second term in these expressions describes the contribution of self-diffraction gyration. Its sign remains unchanged under a 180° rotation of the lattice vector. If this term is greater in magnitude than the first term, then the sign of $\Gamma_{th}(x)$ will be positive irrespective of the sign of Γ_{st}. This condition of nonunidirectional energy transfer can hold, other parameters remaining the same, both for all values of the interaction length x and for values of x greater than some value x_Γ. [8] The first case, for values of the angle between the polarization vector of the waves incident on the crystal and their plane of incidence $\theta=0$ and $\theta=90°$, occurs when

$$|\Gamma_{st}|\geqslant|4\rho|, \qquad (16)$$

and the second case occurs when this inequality does not hold. The greater the departure from this inequality, the greater the interaction length x_Γ at which nonunidirectional energy transfer will appear is. In the experiments the quantity x_Γ is limited by the dimensions of the sample. For this reason, it is possible to observe nonunidirectional energy transfer in a $Bi_{12}SiO_{20}$ crystal at wavelength $\lambda=633$ nm with the parameter Γ_{st} increasing (due to an increase in the local component of the space-charge field) to values comparable to $4\rho=15.5\ \mathrm{cm}^{-1}$.

3. COMPARISON OF EXPERIMENTAL RESULTS WITH NUMERICAL CALCULATIONS

The theoretical curves $\Gamma(\theta)$ presented in Fig. 3 for the case $I_S(0)<I_P(0)$ (curves *1*) and $I_S(0)>I_P(0)$ (curve *2*) were calculated using Eqs. (14) and (15). In the calculations, the value $\Gamma_{st}=15.3\ \mathrm{cm}^{-1}$ was used for the coupling constant of the interacting waves, obtained by a least-squares fit of the theoretical dependence $\Gamma_{th}(\theta)$ to the experimental data $\Gamma(\theta)$. The use of the material constants obtained in Ref. 11 for a $Bi_{12}SiO_{20}$: CdO crystal, neglecting nonunidirectional energy transfer, to estimate the parameter Γ_{st} using well-known relations for the photorefractive response of a medium with a one-level band model[15,16] gives 29.4 cm^{-1}. The latter satisfies the condition (17). The result of the calculation of the coupling constant for the $Bi_{12}SiO_{20}$: CdO crystal, taking account of the presence of shallow traps and, using the expressions presented in Ref. 17 and the parameters measured here, is $\Gamma_{st}=15.1\ \mathrm{cm}^{-1}$, which is in good agreement with the value obtained in the present work. We note that the value $\Gamma_{st}=15.3\ \mathrm{cm}^{-1}$ does not satisfy the inequality (16) ($4\rho=15.5\ \mathrm{cm}^{-1}$), but a calculation of the spatial dependence $\Gamma_{th}(x)$ using Eq. (15) gives the threshold value $x_\Gamma=0.45$ cm, which is less than the thickness of the experimental sample.

In summary, it was shown in this work that efficient nonunidirectional energy transfer in a two-beam interaction on a photorefractive grating with vector $\mathbf{K}\|[\bar{1}10]$ formed by diffusion-drift mechanism in a $Bi_{12}SiO_{20}$: CdO crystal in an alternating electric field is possible.

This work was partially supported by the Krasnoyarsk affiliate of the firm ''Stek'' (Tomsk).

[1] A. Ashkin, G. D. Boyd, and J. M. Driedzic, Appl. Phys. Lett. **9**, 72 (1966).
[2] M. P. Petrov, S. I. Stepanov, and A. V. Khomenko, *Photoerefractive Crystals in Coherent Optics* (Nauka, St. Petersburg, 1992).
[3] B. I. Sturman, Zh. Tekh. Fiz. **48**(5), 1010 (1978) [Sov. Phys. Tech. Phys. **23**, 589 (1978)].
[4] V. I. Vinetskiĭ, N. V. Kukhtarev, S. G. Odulov, and M. S. Soskin, Usp. Fiz. Nauk **129**, 113 (1979) [Sov. Phys. Usp. **22**, 742 (1979)].
[5] B. I. Sturman and V. M. Fridkin, *Photogalvanic Effect in Media without a Center of Symmetry and Related Phenomena* (Nauka, Moscow, 1992).
[6] A. V. Alekseev-Popov, A. V. Knyaz'kov, and A. S. Saĭkin, Pis'ma Zh. Tekh. Fiz. **9**(18), 1108 (1983) [Sov. Tech. Phys. Lett. **9**, 475 (1983)].
[7] K. Shcherbin, S. Odoulov, R. Litvinov, E. Shandarov, and S. Shandarov, J. Opt. Soc. Am. B **13**, 2268 (1996).
[8] R. V. Litvinov and S. M. Shandarov, Opt. Spektrosk. **83**, 334 (1997).
[9] N. V. Kukhtarev, M. S. Brodin, and V. I. Volkov, Fiz. Tverd. Tela (Leningrad) **30**, 2757 (1988) [Sov. Phys. Solid State **30**, 1588 (1988)].
[10] N. V. Kukhtarev, B. D. Pavlik, V. V. Sorokina, and T. I. Semenets, Kvant. Élektron. **13**, 326 (1986) [Sov. J. Quantum Electron. **16**, 216 (1986)].
[11] R. V. Litvinov, S. M. Shandarov, D. V. Yakimov, A. V. Reshet'ko, S. N. Pitchenko, Yu. F. Kargin, and V. V. Volkov, Zh. Tekh. Fiz. **67**(12), 31 (1997) [Tech. Phys. **42**, 1400 (1997)].
[12] P. Taybati and T. Mangereften, J. Opt. Soc. Am. B **8**, 1053 (1991).
[13] D. J. Webb, A. Kiebling, B. I. Sturman, E. Shamonina, and K. H. Ringhofer, Opt. Commun. **108**, 31 (1994).
[14] S. I. Stepanov, N. D. Khat'kov, and S. M. Shandarov, Fiz. Tverd. Tela (Leningrad) **29**, 3054 (1987) [Sov. Phys. Solid State **29**, 1754 (1987)].
[15] S. I. Stepanov, in *Optical Holography with Writing in Three-Dimensional Media*, edited by Yu. N. Denisyuk (Nauka, Leningrad, 1986).
[16] S. I. Stepanov and M. P. Petrov, Opt. Commun. **53**, 292 (1985).
[17] O. V. Kobozev, S. M. Shandarov, R. V. Litvinov, Yu. F. Kargin, and V. V. Volkov, Fiz. Tverd. Tela (St. Petersburg) **40**, 2037 (1998) [Phys. Solid State **40**, 1844 (1998)].

Translated by M. E. Alferieff

DEFECTS, DISLOCATIONS, PHYSICS OF STRENGTH

Superionic conductivity of the heterovalent solid solutions $R_{1-x}M_xF_{3-x}$ (R=REE, M=Ca, Ba) with tysonite-type structure

N. I. Sorokin, E. A. Krivandina, Z. I. Zhmurova, and B. P. Sobolev

Institute of Crystallography, Russian Academy of Sciences 117333 Moscow, Russia

M. V. Fominykh and V. V. Fistul'

Moscow Academy of Fine Chemical Technology 117571 Moscow, Russia

(Submitted September 15, 1998)
Fiz. Tverd. Tela (St. Petersburg) **41**, 638–640 (April 1999)

The fluorine-ion conductivity of anion-deficient solid solutions $R_{1-x}Ca_xF_{3-x}$ and $R_{1-x}Ba_xF_{3-x}$ having the tysonite (LaF_3) structure was investigated by the impedance spectroscopy method. $R_{1-x}Ca_xF_{3-x}$ (R=La, Pr, Nd, Sm, Gd, Tb, Dy, Ho) and $R_{1-x}Ba_xF_{3-x}$ (R=La, Pr, Nd) single crystals were grown from the melt by the Bridgman–Stockbarger method. The electrophysical measurements were performed in the frequency range $5-5\times10^5$ and temperature range 300–700 K. The temperature dependences of the electrical conductivity for the crystals studied is determined by the migration of fluorine anions along various structural positions. It is shown that, from the standpoint of increasing the conductivity of tysonite matrices RF_3 (R=La, Pr, Nd), doping by CaF_2 and BaF_2 is less promising than SrF_2. © *1999 American Institute of Physics.*
[S1063-7834(99)01504-X]

In the group of inorganic fluorides possessing tysonite-type structure (LaF_3), anion-deficient nonstoichiometric phases $R_{1-x}M_xF_{3-x}$ (R is a rare-earth element (REE), M=Ca, Sr, Ba), which are heterovalent solid solutions with a variable number of atoms per unit cell, are of special interest. $R_{1-x}M_xF_{3-x}$ crystals are middle-temperature superionic conductors with conduction along the fluorine anions, while the contribution of the electronic conductivity can be neglected compared to the fluorine ion conductivity.[1–5] Charge compensation by substitution of divalent cations for trivalent REE ions is accompanied by the formation of fluorine vacancies in the anionic sublattice. Fluorine ion transport in tysonite crystals occurs by a vacancy mechanism and is very sensitive to breakdown of stoichiometry.

It is known[6–9] that the behavior of the temperature dependences of the electrical conductivity for anion-deficient tysonite solid solutions $R_{1-x}M_xF_{3-x}$ is determined by the structure and dynamical disordering of the fluorine sublattice. For $T<T_c$ (T_c is the disordering temperature of the fluorine sublattice) fluorine-ion transport with participation of V_F^+ vacancies occurs within a uniform fluorine subsystem $F_1(g)$, where g denotes the type of crystallographic site in the $P\bar{3}c1$ space group.[10] Exchange of mobile vacancies between the uniform $F_1(g)$ and combined $F_2(g)$ and $F_3(a)$ subsystems of the fluorine atoms starts near $T\simeq T_c$. For $T>T_c$ transport of fluorine vacancies completely encompasses the anionic sublattice, including the $F_1(g)$ and $F_2(d)+F_3(a)$ sites.

In previous work[4,5,11,12] we studied the electrophysical characteristics of tysonite single crystals $R_{1-x}Sr_xF_{3-x}$ (R=La–Yb, Y), $R_{1-x}Ca_xF_{3-x}$ (R=Ho, Er, Tm), and $La_{0.95}(Ba_{1-x}Sr_x)_{0.05}F_{2.95}$ ($0\leqslant x\leqslant 1$). In the present work the study of the variation of the superionic conductivity in the family of tysonite nonstoichiometric phases $R_{1-x}M_xF_{3-x}$ with M=Ca, Ba was continued to search for the compositions having the highest fluorine conductivity.

1. EXPERIMENTAL PROCEDURE

Single crystals of the solid solutions were grown in a helium atmosphere by the Bridgman–Stockbarger method in a KRF-1 growth system (the system was designed and built by the Special Design Office of the Institute of Crystallography of the Russian Academy of Sciences). The initial reagents were especially pure grade BaF_2, LaF_2, and PrF_3, and the other RF_3 compounds were chemically pure grade. Oxygen impurity was removed from the compounds by preliminary fluoridation in the melt. The fluoridizing agent was especially pure grade PbF_2, 5 mass% of which was added to the charge.

The following solid solutions were obtained: $La_{0.95}Ca_{0.05}F_{2.95}$, $Pr_{0.95}Ca_{0.05}F_{2.95}$, $Nd_{1-x}Ca_xF_{3-x}$ ($x=0.01$, 0.05, 0.10, 0.15), $Sm_{0.94}Ca_{0.06}F_{2.94}$, $Gd_{0.84}Ca_{0.16}F_{2.84}$, $Tb_{0.8}Ca_{0.2}F_{2.8}$, $Dy_{0.78}Ca_{0.22}F_{2.78}$, $Ho_{0.77}Ca_{0.23}F_{2.77}$, $La_{0.95}Ba_{0.05}F_{2.95}$, $Pr_{0.95}Ba_{0.05}F_{2.95}$ and $Nd_{0.95}Ba_{0.05}F_{2.95}$ — ~10 mm in diameter and 15–25 mm long crystals (the compositions are indicated according to the charge). The graphite crucibles were lowered with a velocity of 5.2 ± 0.2 mm/h.

TABLE I. The values of T_c, A, and $\Delta H_{m,v}$ for $R_{1-x}Ca_xF_{3-x}$ and $R_{1-x}Ba_xF_{3-x}$ single crystals having tysonite type structure.

		$T<T_c$		$T<T_c$	
Crystal	T_c^*, K	log (A, S·cm^{-1}·K)	$\Delta H_{m,v}$, eV	log (A, S·cm^{-1}·K)	$\Delta H_{m,v}$, eV
$La_{0.95}Ca_{0.05}F_{2.95}$	440	5.28 (8)**	0.435 (5)	3.72 (6)	0.298 (7)
$Pr_{0.95}Ca_{0.05}F_{2.95}$	440	5.00 (9)	0.378 (6)	3.64 (7)	0.260 (7)
$Nd_{0.99}Ca_{0.01}F_{2.99}$	445	4.9 (1)	0.423 (7)	3.04 (7)	0.258 (7)
$Nd_{0.95}Ca_{0.05}F_{2.95}$	440	4.24 (3)	0.324 (2)	3.45 (6)	0.264 (7)
$Nd_{0.90}Ca_{0.10}F_{2.90}$	460	5.9 (1)	0.47 (1)	3.92 (9)	0.29 (1)
$Sm_{0.94}Ca_{0.06}F_{2.94}$	460	5.4 (3)	0.42 (2)	3.30 (5)	0.228 (6)
$Gd_{0.84}Ca_{0.16}F_{2.84}$	575	6.89 (7)	0.661 (6)	5.04 (8)	0.45 (1)
$Tb_{0.80}Ca_{0.20}F_{2.80}$	570	6.64 (6)	0.681 (6)	5.28 (4)	0.527 (5)
$Dy_{0.78}Ca_{0.22}F_{2.78}$	–	5.85 (3)	0.670 (3)	–	–
	($T<685$ K)				
$Ho_{0.77}Ca_{0.23}F_{2.77}$	–	5.91 (6)	0.694 (5)	–	–
	($T<685$ K)				
$La_{0.95}Ba_{0.05}F_{2.95}$	430	4.49 (7)	0.356 (5)	3.65 (6)	0.284 (6)
$Pr_{0.95}Ba_{0.05}F_{2.95}$	465	4.50 (5)	0.371 (4)	3.72 (6)	0.299 (7)
$Nd_{0.95}Ba_{0.05}F_{2.95}$	470	4.79 (4)	0.409 (3)	3.64 (5)	0.301 (6)

Note. *The values of T_c were calculated from the formula $T_c=(\Delta H_1-\Delta H_2)/k(\ln A_1-\ln A_2)$. **The standard deviations of the values are presented in parentheses.

X-ray diffraction was used to confirm that the crystals grown had tysonite-type structure.

The samples used for conductivity measurements were 12 mm in diameter and ~5 mm high cylinders. The electrical conductivity σ was determined from the impedance spectra of the electrochemical cells C—$R_{1-x}M_xF_{3-x}$—C with graphite electrodes. The impedance measurements were performed in the frequency ranges $5-5\times10^5$ Hz and temperatures 300–700 K in a $\sim10^{-1}$ Pa vacuum. A detailed description of the measuring apparatus and the method for determining the bulk resistance of the crystals are presented in Refs. 4 and 13. The error in measuring the bulk resistance was less than 5%. All electrophysical investigations were performed on unoriented single-crystal samples assuming pseudoisotropic behavior of σ, which was satisfied quite strictly for concentrated solid solutions $R_{1-x}M_xF_{3-x}$ ($x\geqslant0.05$) with the same defect structure as tysonite.[12,14]

2. RESULTS AND DISCUSSION

A kink near the temperature T_c (the values of T_c are indicated in Table I) is observed in the temperature dependences of the fluorine-ion conductivity for all $R_{1-x}Ca_xF_{3-x}$ and $R_{1-x}Ba_xF_{3-x}$ crystals investigated except $Dy_{0.78}Ca_{0.22}F_{2.78}$. In the temperature range below and above T_c the temperature dependences $\sigma(T)$ satisfied the Arrhenius–Frenkel equation

$$\sigma T=A\exp[-\Delta H_{m,v}/kT],$$

where $\Delta H_{m,v}$ is the activation enthalpy of the migration of anionic vacancies. The values of the preexponential factor A and the enthalpy $\Delta H_{m,v}$ are summarized in Table I.

We shall now analyze the change in the characteristics of the fluorine-ion transport in the series of solid solutions studied $R_{1-x}M_xF_{3-x}$ (M=Ca, Ba). The maximum electric conductivity σ_{max} in the solid solutions $Nd_{1-x}Ca_xF_{3-x}$ was observed for the composition with $x_0=0.05$. The latter quantity agrees well with the values $x_0=0.03-0.07$,[2,12,14–16] found for the solid solutions $R_{1-x}Sr_xF_{3-x}$ (R=La, Ce, Pr, Nd) and $R_{1-x}Ba_xF_{3-x}$ (R=La, Ce). For $R_{1-x}Ca_xF_{3-x}$ crystals, as the ionic radius of the cation R^{3+} decreases from La^{3+} to Ho^{3+}, an increase of the CaF_2 content (the index of the breakdown of stoichiometry is x) results in a diminishment of the fluorine-ion transport as a result of an intensification of ion-ion interactions of the defects. This completely confirms the results of our investigations of the transport properties of the solid solutions $R_{1-x}Sr_xF_{3-x}$ (R=La–Yb, Y)[5] and $R_{1-x}Ca_xF_{3-x}$ (R=Ho, Er, Tm).[11]

In the group of tysonite solid solutions investigated, the values of the fluorine-ion conductivity for $R_{0.95}M_{0.05}F_{2.95}$ (R=La, Pr, Nd; M=Ca, Ba) and $Sm_{0.94}Ca_{0.06}F_{2.94}$ single crystals are $2\times10^{-5}-1\times10^{-4}$ S·cm^{-1} at 293 K. This fact recommends them as anionic solid electrolytes, suitable for use in F_2 and HF gas analyzers, in fluoride-selective membranes, and in electrochemical fluorine generator.

Figure 1 shows the variation of the isothermal conductivity as a function of the ionic radius $r_{M^{2+}}$ in the series of

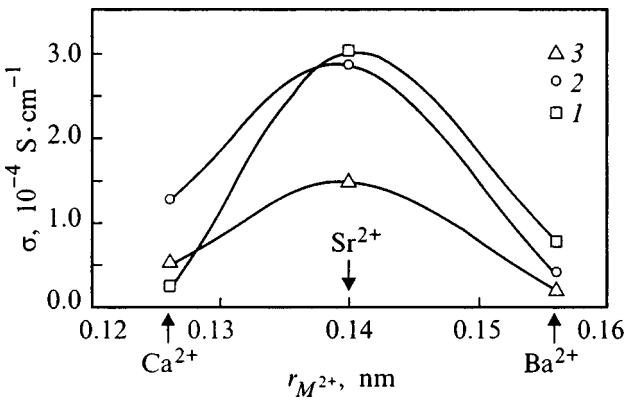

FIG. 1. Variation of the conductivity at 293 K as a function of the ionic radius $r_{M^{2+}}$ in the series of solid solutions $La_{0.95}M_{0.05}F_{2.95}$ (*1*), $Pr_{0.95}M_{0.05}F_{2.95}$ (*2*), and $Nd_{0.95}M_{0.05}F_{2.95}$ (*3*), M=Ca, Sr, Ba.

solid solutions $La_{0.95}M_{0.05}F_{2.95}$, $Pr_{0.95}M_{0.05}F_{2.95}$, $Nd_{0.95}M_{0.05}F_{2.95}$ (M=Ca, Sr, Ba). The ionic radii are given according to the Shannon system with $r_{F^-}=0.119$ nm.[17] It is evident that in studying the superionic transport for individual tysonite matrices RF_3 (R=La, Pr, Nd) doping by SrF_2 is preferable to CaF_2 and BaF_2.

The existence of a conductivity maximum in a number of two-component solid solutions $La_{0.95}M_{0.05}F_{2.95}$, $Pr_{0.95}M_{0.05}F_{2.95}$, and $Nd_{0.95}M_{0.05}F_{2.95}$ with M=Sr makes it desirable to investigate the electrical conductivity of ternary solid solutions of the type $La_{0.95}(M_{1-x}M'_x)_{0.05}F_{2.95}$ to optimize anionic transport. Optimal geometric matching of the doping cations $M^{2+}+M'^{2+}$ and the matrix cation R^{3+} will be observed when the average ionic radius of the impurity cations is as close as possible to the ionic radius r_{dop}($r_{dop}=(1-x)r_{M^{2+}}+xr_{M'^{2+}}$) of the rare-earth cation.

In Ref. 12 we investigated a family of ternary solid solutions $La_{0.95}(Ba'_{1-x}Sr_x)_{0.05}F_{2.95}$ ($0\leqslant x\leqslant 1$), where $r_{Sr^{2+}}=0.140$ nm, $r_{Ba^{2+}}=0.156$ nm, and $r_{La^{3+}}=0.130$ nm. However, for these solid solutions $r_{La^{3+}}=0.130$ nm does not fall into the range of variation of the average ionic radius r_{dop} of the impurity cations: The values of r_{dop} vary from 0.14 to 0.156 nm. The investigations of anionic transport in tysonite crystals must be continued using the solid solutions $La_{0.95}(Ca_{1-x}Sr_x)_{0.05F_{2.95}}$ ($0\leqslant x\leqslant 1$), since $r_{Ca^{2+}}=0.126$ nm and the range of variation of r_{dop} from 0.126 to 0.14 nm contains the value $r_{La^{3+}}=0.130$ nm.

[1] L. E. Nagel and V. O'Keeffe, in *Ion Transport in Solids*, edited by W. Van Gool (North Holland, Amsterdam, 1973), p. 165.

[2] T. Takahashi, H. Iwahara, and T. Ishikawa, J. Electrochem. Soc. **124**, 280 (1977).

[3] A. Roos and J. Schoonman, Solid State Ionics **13**, 205 (1984).

[4] N. I. Sorokin and B. P. Sobolev, Kristallografiya **39**(5), 889 (1994) [Crystallogr. Rep. **39**, 810 (1994)].

[5] N. I. Sorokin, M. V. Fominykh, E. A. Krivandina, Z. I. Zhmurova, and B. P. Sobolev, Kristallografiya **41**, 310 (1996) [Crystallogr. Rep. **41**, 292 (1996)].

[6] L. P. Otroshchenko, V. B. Aleksandrov, B. A. Maksimov, V. I. Simonov, and B. P. Sobolev, Kristallografiya **30**, 658 (1985) [Crystallogr. Rep. **30**, 383 (1985)].

[7] S. F. Radaev, E. A. Krivandina, L. A. Muradyan, B. A. Maksimov, N. N. Bydanov, V. A. Sarin, B. P. Sobolev, and V. I. Simonov, Kristallografiya **36**, 369 (1991) [Crystallogr. Rep. **31**, 195 (1991)].

[8] A. I. Lifshits, V. M. Buznik, P. P. Fedorov, and B. P. Sovolev, Izv. Akad. Nauk SSSR, Neorg. Mater. **18**, 135 (1982).

[9] A. F. Aalders, A. Polman, A. F. M. Arts, and H. W. de Wijn, Solid State Ionics **9–10**, 539 (1983).

[10] *International Tables for Crystallography* edited by T. Hahn (Dordrecht, 1983).

[11] N. I. Sorokin, I. I. Buchinskaya, and B. P. Sobolev, Kristallografiya **40**, 1039 (1995) [Crystallogr. Rep. **40**, 964 (1995)].

[12] N. I. Sorokin, M. V. Fominykh, E. A. Krivandina, Z. I. Zhmurova, O. I. Lyamina, and B. P. Sobolev, Fiz. Tverd. Tela (St. Petersburg) **40**, 658 (1998) [Phys. Solid State **40**, 604 (1998)].

[13] A. K. Ivanov-Shits, N. I. Sorokin, P. P. Fedorov, and B. P. Sorokin, Fiz. Tverd. Tela (Leningrad) **25**, 1748 (1983) [Sov. Phys. Solid State **25**, 1007 (1983)].

[14] A. Roos and F. C. M. van Pol, R. Keim, J. Schoonman, Solid State Ionics **13**, 191 (1984).

[15] I. V. Murin, O. V. Glumov, and Yu. V. Amelin, Zh. Prikl. Khim. **53**(7), 1474 (1980).

[16] H. Geiger, G. Shon, and H. Strok, Solid State Ionics **13**, 205 (1985).

[17] R. D. Shannon, Acta Cryst. A **32**, 751 (1976).

Translated by M. E. Alferieff

Characteristics of the elastic strain of a Ge(111) surface under a mechanical load

V. E. Korsukov, S. A. Knyazev, A. S. Luk'yanenko, and V. A. Obidov

A. F. Ioffe Physicotechnical Institute, Russian Academy of Sciences 194021 St. Petersburg, Russia
(Submitted May 15, 1998; resubmitted September 18, 1998)
Fiz. Tverd. Tela (St. Petersburg) **41**, 641–644 (April 1999)

Estimates are obtained for various components of the elastic strain in a Ge(111) surface layer under isotropic lateral tension. Agreement with the reversible components of surface thinning, derived from energy shifts in the volume and surface plasma peaks, suggests that the latter have an elastic character. It is conjectured that the anomalously high strain in a thin surface layer is due to the partially quasielastic variation of the relief of strained semiconductor surfaces. © *1999 American Institute of Physics.* [S1063-7834(99)01604-4]

A number of substantial mechanical effects were discovered in Refs. 1–6, devoted to studying the effect of a mechanical load on the structure of the Ge(111) face, as well as in other works.[7–9] We divide these effects into two groups — reversible and irreversible relative to the load. In the present paper we shall examine the effects of a mechanical action on the Ge(111) face. The choice of the object of investigation — a germanium surface — is dictated by the following problem: Semiconductor crystals are characterized by a wide region of elasticity, so that using the loading method that we have developed it was possible to achieve substantial loads $\sigma \sim 1$ GPa and higher without macroscopic damage to the sample. A substantial reversible component of the mechanical action on the surface was observed in the process. We believe that this effect is due to (mainly) the elastic deformation of the surface. The relation between the reversible mechanical effects and the elastic strain of the Ge(111) surface is obvious from general considerations, but thus far it has not been established quantitatively sufficiently systematically.

The aim of the present work is to fill this lacuna. Here estimates are obtained for the elastic strain in a surface layer on the Ge(111) face on the basis of the macroscopic theory of elasticity, and they are compared with the reversible components of the thinning, derived from the energy shifts of volume and surface plasmons as a function of the load, as well as with LEED (low-energy electron diffraction) data.[10]

1. EXPERIMENTAL PROCEDURE AND RESULTS

The effect of a mechanical load on the surface atomic layers of the Ge(111) face was studied using specially developed loading methods, which make it possible to obtain well-reproducible states of isotropic lateral stretching of the layers in a wide range of loads $0<\sigma<2$ GPa. The samples consisted of circular 20 mm in diameter and 0.2 mm thick Ge wafers cut from a single-crystal blank, so that their flat surface deviated from the crystallographic (111) plane by not more than 0.5° (vicinal angle); this angle was monitored using x-ray diffraction. The surface studied was prepared by the conventional method, combining mechanical and chemical polishing, as well as sputtering of the surface with Ar^+ ions and annealing in an ultrahigh vacuum.[1,2,6] The loading apparatus was equipped with a number of heating elements, making it possible to anneal the samples efficiently directly in the vacuum chamber of the spectrometer at any stage of the experiment.

Two loading schemes were used in our experiments (Figs. 1a and 1b). The top surface of the sample was rested against a stationary outer ring-shaped support 1 and the bottom surface of the sample was pressed with the force F of either a ring-shaped die (scheme *a*) or sphere 3 (scheme *b*). The central regions of the top surface were investigated (these regions are hatched in the figure).

A characteristic feature of the loading schemes employed is that the edges of the samples are free, unclamped edges, which made it possible to eliminate edge effects during loading and to increase the resulting stresses at the center of the sample.[11]

The scheme *a* made it possible to produce at the center of the sample surface a biaxial centrosymmetric tension.[11] The largest stress reached in our experiments using this scheme exceeded 1 GPa. This scheme was used to perform the basic measurements of the LEED and EELS electron

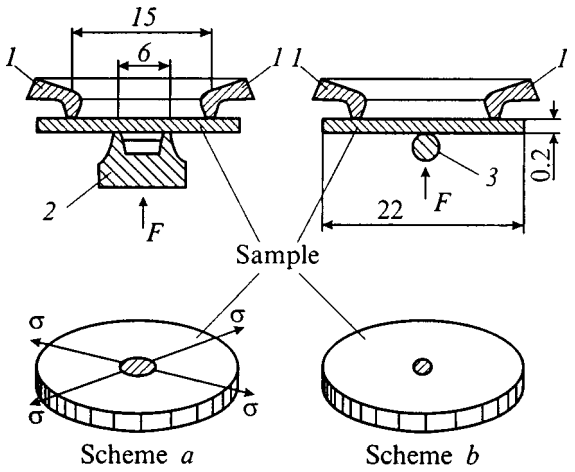

FIG. 1. Loading schemes: *1* — exterior ring-shaped support, *2* — ring-shaped die, *3* — spherical die, F — applied force, σ — tensile stress.

energy-loss spectroscopy) spectra and to calibrate the stress measurements performed with scheme *b*.

It should be noted that the concept of a mechanical stress is applicable and can be calculated well not only in the interior but also at the surface layers, whose thickness is much larger than interatomic distances. Good agreement between the computed stresses and the stresses measured experimentally using x-ray diffraction in reflection from a Si(111) surface has been shown precisely for such layers in Refs. 12 and 13.

In Refs. 12 and 13 a method was proposed for measuring the stresses in the near-surface Ge and Si layers by Raman spectroscopy in reflection from a surface. The stresses were estimated according to the shift and splitting of the *LO* and *TO* phonon frequencies. In our experiments we employed calculations and both experimental methods, as in Ref. 13, to determine the stresses.

In scheme *b*, a large stress gradient is obtained at the center of the sample. The highest value of the stress σ exceeded 2 GPa for Ge(111). The estimate was made according to the calibration in scheme *a*. It should be noted that the stresses are also difficult to calculate in a thicker surface layer scheme *b*, but they can be measured according to the shift and splitting of the *LO* and *TO* phonons as a function of the load by Raman spectroscopy in reflection from a Si surface.[13]

The EELS results on reversible and irreversible thinnings[14] are presented in Figs. 2a and 2b, where ε_1^s and ε_1^b are the reversible thinnings of the layers 1 and 3 nm, while ε_2^s and ε_2^b are the irreversible thinnings of the layers 1 and 3 nm, respectively. The separation of the thinnings into reversible and irreversible components was made by recording the positions of the plasma peaks (for the initial sample, loaded to a load σ_i and after unloading).[14] In addition, in the loading scheme *a* σ_i varied in the range $0<\sigma_i<1$ GPa. Figure 2b will not be discussed in the present paper. In what follows, we shall consider only the reversible components of the thinnings ε_1^s and ε_1^b. To compare these quantities with the elastic strain of the surface we shall use a macroscopic approximation to estimate the various components of the elastic strain in 3 and 1 nm layers.

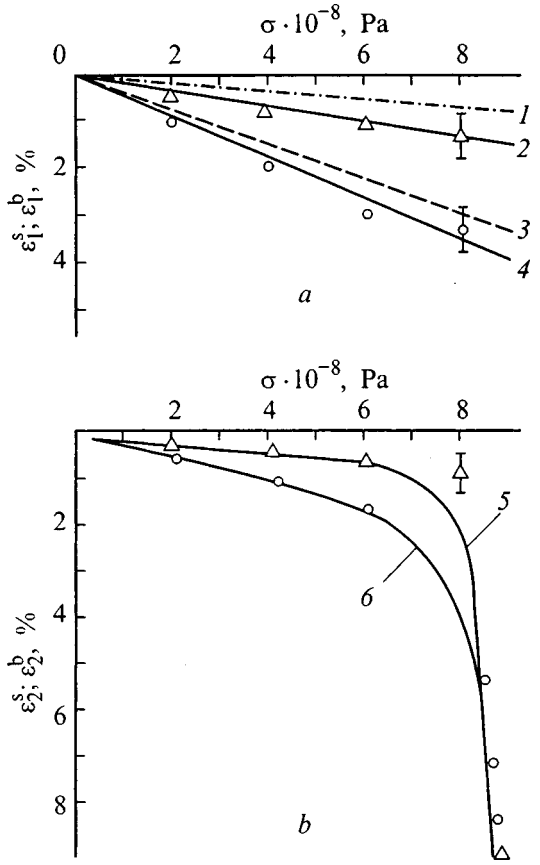

FIG. 2. Reversible ε_1^b and ε_1^b (a) and irreversible ε_2^b and ε_2^b (b) thinnings of the 1 and 3 nm thick surface layers versus the stress σ in Ge(111): *1* — computed quasielastic strain for a 3 nm thick layer, *2* — ε_1^b — reversible thinning of the 3 nm thick layer, *3* — computed quasielastic strain for the 1 nm thick layer, *4* — ε_1^s — reversible thinning of the 1 nm thick layer (a), *5* — ε_2^b — irreversible thinning of the 3 nm thick layer, *6* — ε_2^s — irreversible thinning of the 1 nm thick layer (b).

2. ELASTIC DEFORMATION OF GE(111) SURFACE LAYERS. MACROSCOPIC APPROXIMATION

We start by estimating the strain in the thicker, 3 nm surface layer, which includes of the order of 10 atomic monolayers. The static relaxation of the crystal lattice (change in the geometric parameters of the unit cell), as well as the difference of the interatomic interaction parameters on the surface from their values in the interior are substantial for the thinner layer. We shall employ here the interior values of the corresponding parameters. We are interested in the elastic strain ε_v^b of the interior of a unit cell in the layer of interest. Evidently, this strain should be compared to the thinning ε_1^b determined from the shift of the bulk plasmon. In the macroscopic approximation

$$\varepsilon_v^b \equiv \delta V/V = \varepsilon_{xx}+\varepsilon_{yy}+\varepsilon_{zz} \equiv \mathrm{Tr}\hat{\varepsilon}, \tag{1}$$

where $\varepsilon_{xx}, \varepsilon_{yy}$, and ε_{zz} are the components of the strain tensor ε and $\mathrm{Tr}\hat{\varepsilon}$ is the trace of the strain tensor. For crystals with a cubic unit cell we fine

$$\varepsilon_v^b = (S_{11}+2S_{12})\,\mathrm{Tr}\,\hat{\sigma}, \tag{2}$$

where S_{11} and S_{12} are elastic compliance constants and $\mathrm{Tr}\hat{\sigma}$ is the trace of the stress tensor. For isotropic lateral stretching $\mathrm{Tr}\hat{\sigma}=2\sigma$, where σ are the stresses in sections perpendicular to the surface plane. We shall calculate the elastic compliance constants s_{11} and s_{12} using the tabulated values of the elastic stiffness constants C_{11} and C_{12} and the relation[15]

$$(S_{11}+2S_{12}) = (C_{11}+2C_{12})^{-1}. \tag{3}$$

Thus, we obtain in the macroscopic approximation

$$\varepsilon_v^b[\%] = 2(C_{11}+2C_{12})^{-1}\sigma = 8.4\times10^{-10}\,\sigma\,[\mathrm{Pa}]. \tag{4}$$

This linear dependence is displayed in Fig. 2a (dashed line). Within the limits of error, it is identical to $\varepsilon_1^b(\sigma)$, which justifies our conclusion that the thinning $\varepsilon_1^b(\sigma)$ measured according to the shift of the bulk plasmon is the elastic strain in a 3 nm thick surface layer. The somewhat higher experi-

mentally observed value of the thinning ε_1^b can be explained by the influence of surface effects in the strain. These effects are discussed below.

Let us now examine the elastic strain in the thinner, 1 nm layer. As follows from Fig. 2a, here the thinning $\varepsilon_1^s(\sigma)$ measured according to the shift of the surface-plasmon energy is approximately three times larger than the elastic strain in the interior of the crystal. To explain this difference it must be assumed that the values of the lattice structure and elastic constants on the surface differ from the values in the interior of the crystal. In the present case, even though the thickness of the layer decreased by only a factor of 3 on passing from $\varepsilon_1^b(\sigma)$ to $\varepsilon_1^s(\sigma)$ (this is several interplanar distances), we assume that surface effects start to play a role in the structure and dynamics of the lattice.

In the first place, the cubic symmetry of the unit cell breaks down because of static relaxation,[16] so that the number of elastic constants is no longer limited to the triplet C_{11}, C_{12}, and C_{44}. [15] In the second place, the values of these elastic constants are different from the values in the interior. These differences are all maximum on the surface itself and decrease exponentially in a direction into the interior of the crystal. We now average the elastic characteristics of the lattice over the thinner 1 nm layer, where once again we employ the macroscopic approximation.

The very fact that the elastic properties of the lattice at the surface differ from those in the interior of the crystal is well established and is unquestioned. In the present case it is necessary to explain the much higher strain of the cell volume in the 1 nm layer than in the interior of the crystal. To analyze this effect we shall also employ the results of Ref. 10, where the mechanical strain of the Ge(111) surface was studied by LEED. This method makes it possible to specify the strain of the uppermost (1–2 lattice constants) surface layer, specifically, to determine the strain components which are parallel $\varepsilon_{\parallel}^s$ and perpendicular $\varepsilon_{\perp}^s$ to the surface plane. The accuracy with which the parallel strain is determined by LEED is low. However, according to the results of Ref. 10, it can be asserted that it does not exceed 0.5% at the maximum attainable load $\sigma \sim 300$ MPa. There are no grounds for expecting that the parallel strain on the surface exceeds the interior value. For this reason, we shall assume that it equals the computed value of the linear strain in the interior. For $\sigma = 300$ MPa

$$\varepsilon_{\parallel}^s \cong \varepsilon_{\parallel}^b \cong 0.25\% \tag{5}$$

Then the strain $\varepsilon_{\perp}^s$ is of special interest. In Ref. 10, a positive (anomalous) value $\varepsilon_{\perp}^s \sim 0.5\%$ was obtained. In Ref. 10 it is shown that the indicated strain anomaly is possible without lattice instability. However, it must be independently confirmed in order to ascertain the result reliably. We note in Ref. 7 that such a strain anomaly was not observed on the Si(110) face. We see confirmation of the observed anomaly in the characteristic features, being discussed here, of the strain on the Ge(111) surface, presented in Fig. 2a, and our problem now is to find correspondence between the results of these independent experiments. A correspondence is established by the following strain estimates. In the interior of the crystal the strain component $\varepsilon_{\perp}^b$ normal to the surface plane can be estimated, taking account of Eqs. (4) and (5). For $\sigma = 300$ MPa

$$\varepsilon_{\perp}^b \cong \varepsilon_v^b - 2\varepsilon_{\parallel}^b \sim -0.25\%. \tag{6}$$

This corresponds to the normal Poisson effect — compression of the crystal in a direction perpendicular to the load plane. On the surface itself this strain component, according to Ref. 10, has the opposite sign and is twice as large in magnitude. Then we obtain the desired estimate of the strain ε_v^s (for $\sigma = 300$ MPa)

$$\varepsilon_v^s \cong 2\varepsilon_{\parallel}^s + \varepsilon_{\perp}^s \sim 1\%. \tag{7}$$

Within the limits of error, this estimate agrees with the experimental value of the thinning ε_1^s obtained from the shift of the surface-plasmon energy. Therefore, the experimental results presented in Fig. 2a agree with those of Ref. 10 and, considered together, they give a fairly complete picture of the strain in the Ge(111) surface layers under lateral mechanical tension of this surface.

The good agreement between the above-obtained estimates of the strains ε_v^s and ε_v^b and the experimentally measured thinnings ε_1^s and ε_1^b in the 1 and 3 nm surface layers reinforces the conclusion that these effects have an elastic character.

To explain the high value of the thinning ε_1^s in the 1 nm layer the anomalous character of the strains $\varepsilon_{\perp}^s$ was taken into account — an effect observed earlier by LEED[10] and termed an anomalous Poisson effect. We believe that additional confirmation is thereby also obtained for this effect. The question of the nature of this effect remains open. Since the anomalous character of the strain $\varepsilon_{\perp}^s$ refers to the uppermost atomic layer, it can be inferred that there is a definite relation between this strain and the change in the electronic structure as well as the change in the surface relief in a mechanical force field.[8,17] Indeed, in Ref. 9 a mechanical load was found to produce a system of atomic steps on the Si(001) surface. In Ref. 9 it was shown that the atomic steps serve as boundaries of domains with alternating superstructures (21) and (12). An external load is observed to change the relative fraction of the areas of the domains (12) and (21), depending on the sign of the applied load. This transition occurs as a result of the shifts of the domain walls. When one of the superstructures vanishes, the width of the terrace doubles, and the boundary between them transforms from a monatomic to a diatomic step. These effects are all quasireversible relative to the applied load.

We believe that the anomalously high value of the strain which we observed in the thinnest surface layer is due to the indicated variations of the relief of the Ge(111) face and is of a partially quasielastic character. However, the relation between the quasielastic variation of the relief and the elastic deformation of the Ge(111) face requires additional discussion.

[1] V. E. Korsukov, S. A. Knyazev, A. S. Luk'yanenko, R. R. Nazarov, B. A. Obidov, E. V. Stepin, and V. N. Svetlov, Fiz. Tverd. Tela (St. Petersburg) **38**, 113 (1996) [Phys. Solid State **38**, 61 (1996)].
[2] R. R. Nazarov, V. E. Korsukov, A. S. Luk'yanenko, and M. Shematov, Poverkhnost', No. 1, 97 (1990).
[3] V. E. Korsukov, A. S. Luk'yanenko, P. V. Patrievskiĭ, and V. N. Svetlov, Poverkhnost', No. 5, 27 (1987).
[4] V. E. Korsukov, in *The Physics of Strength and Plasticity*, edited by S. N. Zhurkov (Nauka, Leningrad, 1986).
[5] V. E. Korsukov, A. S. Luk'yanenko, R. R. Nazarov, P. V. Patrievskiĭ, and Ya. E. Chiviksin, Poverkhnost' **2**, 69 (1988).
[6] V. E. Korsukov, S. A. Knyazev, A. S. Luk'yanenko, R. R. Nazarov, P. V. Patrievskiĭ, and M. Shermatov, Fiz. Tverd. Tela (Leningrad) **30**, 2380 (1988) [Sov. Phys. Solid State **30**, 1373 (1988)].
[7] B. A. Nesterenko, A. V. Broviĭ, and A. I. Sorokovykh, Poverkhnost', No. 5, 81 (1986).
[8] K. Cho, J. D. Joannopopulos, and A. N. Berker, Phys. Rev. B **53**, 1002 (1996).
[9] B. S. Swartzentruber, Y. M. Mo, M. B. Webb, and M. G. Lagally, J. Vac. Sci. Technol. A **8**, 210 (1990).
[10] A. S. Luk'yanenko, *Author's Abstract of Candidate's Dissertation* (Leningrad, 1988).
[11] F. F. Bitman, Ya. S. Uflyand, and B. S. Ioffe, Prikl. Mekh. Tekh. Fiz. **6**(5), 122 (1970).
[12] I. I. Novak, V. V. Baptizmanskiĭ, and Yu. F. Titovets, Opt. Spektrosk. **49**, 322 (1980) [Opt. Spectrosc. **49**, 174 (1980)].
[13] I. I. Novak, V. V. Baptizmanskiĭ, and L. V. Zhoga, Opt. Spektrosk. **43**, 252 (1977) [Opt. Spectrosc. **43**, 145 (1977)].
[14] V. Korsukov, A. Lukyanenko, and B. Obidov, Surf. Rev. Lett. **6**, 5, (1998).
[15] C. Kittel, *Introduction to Solid State Physics* (Wiley, N. Y., 1976; Nauka, Moscow, 1978).
[16] B. A. Nesterenko and O. V. Snitko, Fiz. Tverd. Tela (Leningrad) **6**, 2913 (1964) [Sov. Phys. Solid State **6**, 2321 (1964)].
[17] B. A. Nesterenko, A. V. Broviĭ, and A. I. Sorokovykh, Poverkhnost', No. 8, 81 (1986).

Translated by M. E. Alferieff

MAGNETISM AND FERROELECTRICITY

Latent paramagnetism in $CsFeCl_3$

Yu. D. Zavorotnev*)

Donetsk Physicotechnical Institute, Ukrainian Academy of Sciences 340114 Donetsk, Ukraine
(Submitted June 2, 1998)
Fiz. Tverd. Tela (St. Petersburg) **41**, 645–646 (April 1999)

It is shown that latent paramagnetism can occur in a lattice having a hexagonal arrangement of magnetic spins. This state is characterized by the fact that the effective exchange interaction on the two sublattices vanishes and the corresponding ions become paramagnetic. The appearance of such a state explains the nonequidistant spacing of the jumps in the magnetization in $CsFeCl_3$. © *1999 American Institute of Physics.* [S1063-7834(99)01704-9]

$CsFeCl_3$ crystals possess D_{6h}^4 symmetry.[1] The magnetic Fe^{2+} ions form a regular hexagonal structure in the XOY plane and each ion is surrounded by an octahedron consisting of six Cl^- ions. These octahedra determine the crystal field acting on an Fe^{2+} ion and single-ion easy-plane anisotropy. Two magnetization jumps occur in $CsFeCl_3$ — in magnetic fields 9.6 and 31.2 MA/m.[2] These jumps are due to the crossing of the ground state by the excited levels in a magnetic field. The first jump is 2/3 of the maximum magnetization (Fig. 1). Our investigations showed that, if all ions are crystallographically equivalent, then the jumps will be equidistant, since the g factor is the same for all energy levels. Hence the conclusion follows that a phase transition should occur in the region of the first jump and the Fe^{2+} ions should become nonequivalent.

According to the experimental data of Ref. 1, a magnetic cell contains ions of the second coordination sphere and there are 26 Fe^{2+} ions, which can be divided into three subgroups in the two planes. Two ions in the first subgroup are at the centers of hexagons, and 12 ions in the second group lie on lines connecting the centers to the centers of the lateral sides. All other ions (third subgroup) are located at the vertices. It is obvious that the ions of one subgroup will not pass into those of another subgroup under any of the operations of the D_{6h} symmetry group. For this reason, in the calculations below, the third subgroup will be neglected. Its possible configurations will coincide with the states of the second subgroup when translational invariance is also taken into account. The dimension D of the obtained permutation representation is 14, and

$$D=2A_{1g}+2B_{1g}+E_{1g}+E_{2g}+A_{1u}+B_{1u}+E_{1u}+E_{2u}. \tag{1}$$

The states of the ions in the first subgroup can be described by only two irreducible ferromagnetism (FM) and antiferromagnetism vectors. Of all the possible configurations of the second subsystem we shall consider only those that are characterized by the irreducible vectors

$$\mathbf{B}_1=1/(2\sqrt{2})(\mathbf{s}_1-\mathbf{s}_3-\mathbf{s}_4+\mathbf{s}_6+\mathbf{s}_8-\mathbf{s}_{10}-\mathbf{s}_{11}+\mathbf{s}_{13}),$$

$$\mathbf{B}_2=1/(2\sqrt{2})(\mathbf{s}_1-\mathbf{s}_2-\mathbf{s}_5+\mathbf{s}_6+\mathbf{s}_8-\mathbf{s}_9-\mathbf{s}_{12}+\mathbf{s}_{13}),$$

$$\mathbf{A}_1=1/(2\sqrt{2})(\mathbf{s}_1-\mathbf{s}_3+\mathbf{s}_4-\mathbf{s}_6+\mathbf{s}_8-\mathbf{s}_{10}+\mathbf{s}_{11}-\mathbf{s}_{13}),$$

$$\mathbf{A}_2=1/(2\sqrt{2})(\mathbf{s}_1-\mathbf{s}_2+\mathbf{s}_5-\mathbf{s}_6+\mathbf{s}_8-\mathbf{s}_9+\mathbf{s}_{12}-\mathbf{s}_{13}). \tag{2}$$

Here $\mathbf{s}_i$ $(i=1-14)$ are the spins of the i-th ion (Fig. 2). These vectors transform according to the irreducible representations E_{2g}, E_{2g}, E_{1u}, and E_{1u}, respectively. Ferromagnetic ordering occurs between the planes.

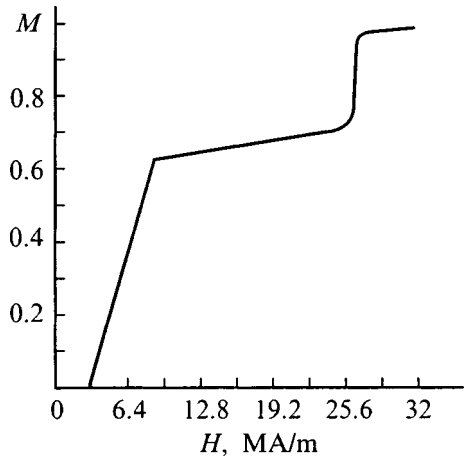

FIG. 1. Magnetization curve for $CsFeCl_3$.

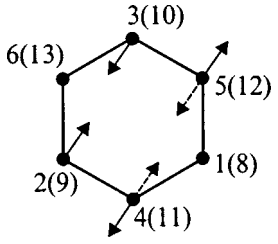

FIG. 2. Configuration with ''hidden'' paramagnetism. The numbers in parentheses are the numbers of the ions in the second plane.

Two situations with $\mathbf{B}_1 \neq 0$ and $\mathbf{B}_2 \neq 0$ are possible: 1) The spins of the neighboring ions make an angle $2\pi/3$ with one another, and $\mathbf{s}_1+\mathbf{s}_4=\mathbf{s}_3+\mathbf{s}_6, \mathbf{s}_1+\mathbf{s}_5=\mathbf{s}_2+\mathbf{s}_6$. This configuration occurs in $CsFeCl_3$ at $H=0$. 2) $\mathbf{s}_1=\mathbf{s}_6=\mathbf{s}_8=\mathbf{s}_{13}=0$, $\mathbf{s}_3=\mathbf{s}_4=-\mathbf{s}_2=-\mathbf{s}_5$ (Fig. 2, solid arrows). This configuration contains, according to Gufan's definition,[3] latent paramagnetism (PM), since the central spins of the ions 1, 6, 8, and 13 are zero and the exchange interaction on the corresponding sublattices is completely compensated. The symmetry of the spin subsystem is lowered to C_{2v}, and the twofold axis is parallel to the line connecting the ions 1 and 6. Taking account of the relativistic interactions showed that the states can be of the easy-plane or easy-axis type.

If $\mathbf{A}_1 \neq 0$ and $\mathbf{A}_2 \neq 0$, then two cases are possible here: 1) The spins of neighboring ions make angles $\pi/3$. 2) The state with latent PM (Fig. 2, broken arrows).

The following mechanism of magnetization of the compound $CsFeCl_3$ can be inferred from what we have said above. According to neutron diffraction investigations, a 120-degree ordering ($\mathbf{B}_1 \neq 0, \mathbf{B}_2 \neq 0$) and FM interaction between the planes occur at the initial temperature. When a field is imposed, the ions in the second group pass into a state with latent PM ($\mathbf{B}_1 \neq 0, \mathbf{B}_2 \neq 0$). The magnetic energy of these two states in the absence of a magnetic field is the same. However, if the anisotropy on the paramagnetic ions changes to easy-axis anisotropy, then for $H \neq 0$ the configuration with latent PM is energetically more favorable. The ions in the first group likewise should become paramagnetic with easy-axis anisotropy. For field intensities 9.6 MA/m $< H <$ 31.2 MA/m the magnetization of each PM is $2\mu_B$ and the magnetization of the magnetic ions is $1\mu_B$. Since three ions in the plane are paramagnetic and six are magnetic, the magnetization per ion is

$$M_z = (1 \times 6/9 + 2 \times 3/9)\mu_B = 2/3 \times 2\mu_B .$$

Hence it follows that the first jump is 2/3 of the maximum magnetization $(2\mu_B)$.

*)E-mail: zavorot@host.dipt.donetsk.ua

[1] M. Steiner, Solid State Commun. **38**, 1179 (1981).
[2] Naoshi Suzuki and Yukio Tagawa Physica B **155**, 375 (1989).
[3] Yu. M. Gufan, E. I. Kut'in, V. L. Lorman, A. M. Prokhorov, and E. G. Rudashevskiĭ, JETP Lett. **46**, 287 (1987).

Translated by M. E. Alferieff

Effect of conduction electrons on the law of approach to saturation of a metallic ferromagnet with surface pinning of the magnetic moment

Yu. I. Man'kov*)

L. V. Kirenskiĭ Institute of Physics, Siberian Branch of the Russian Academy of Sciences, 660036 Krasnoyarsk, Russia
(Submitted July 14, 1998)
Fiz. Tverd. Tela (St. Petersburg) **41**, 647–653 (April 1999)

The effect of conduction electrons on the magnetization curve of a metallic ferromagnet with surface pinning of the magnetic moment is investigated theoretically. The electronic contribution is due to the rearrangement of the discrete spectrum of charge carriers trapped by the nonuniform magnetic induction of such a ferromagnet, and it is a kind of diamagnetic effect that appreciably decreases the volume-averaged magnetization of the ferromagnet. A power-law dependence $H^{-3/4}$ on the external magnetic field H is obtained according to the law of magnetization approach to saturation. This dependence is due to the contribution of the conduction electrons. © *1999 American Institute of Physics.* [S1063-7834(99)01804-3]

The effect of surface pinning of the magnetic moment of a ferromagnet on its physical properties continuously attracts investigators. The behavior of the magnetic subsystem of such materials,[1–23] specifically, the magnetization processes in a ferromagnet, is unique because of the nonuniform distribution of the magnetic moment over the thickness of the sample and is characterized by two main features: first, the displacement of the magnetization curve and — for irreversible magnetization reversal — of the hysteresis loop of the ferromagnet and, second, the law of approach to saturation.

Much less attention has been devoted to the investigation of the effect of surface pinning of the magnetic moment (surface anisotropy) on other subsystems of the ferromagnet. Nuclear magnetic resonance[7] and the electrical properties[24,25] of such materials have been studied. As far as I know, however, the interaction of the magnetic and any other subsystem has never been studied in ferromagnets with surface anisotropy. At the same time such an effect could be substantial, if the high-energy subsystem of the ferromagnet, for example, the electronic subsystem, is modified by surface pinning of the magnetic moment. In the present paper the effect of changes produced in the conduction-electron spectrum by a nonuniform magnetic induction of a ferromagnet with surface pinning of the magnetic moment on the magnetization curve of the ferromagnet is examined.

The restructuring of the discrete spectrum of the electrons in a magnetic field, due to the nonuniformity of the material or the magnetic field itself, is well known. It occurs near the surface of a normal metal (magnetic surface levels),[26] in a domain wall of a metallic ferromagnet,[27] or for electrons trapped by the domain structure of the ferromagnet.[28,29] The magnetic surface levels lead, as is well known,[30,31] to an additional contribution to the thermodynamic potential of a metallic sample and change its diamagnetic properties. In a ferromagnet the conduction electrons localized in a domain wall increase its energy and width.[32] The mechanism of these effects is common to systems with a nonuniform distribution of the magnetic induction. It consists in the fact that, for a magnetic uniformity much smaller in size than the electron cyclotron radius, some electrons are influenced by an effective potential which is much narrower than in the case of a uniform magnetic field. As a result, the electronic subsystem of a metallic ferromagnet acquires an additional energy.

In a ferromagnet with surface pinning of the magnetic moment the size of the magnetic nonuniformity or the width of the transitional region where the magnetic moment vector turns depends on the external magnetic field (see, for example, Refs. 1 and 5), so that the conduction electrons should influence mainly the magnetization curve of the metallic ferromagnet. In the present paper the electronic contribution to the law of magnetization approach to saturation is determined.

1. MAGNETIZATION DISTRIBUTION

Let us consider an isotropic metallic ferromagnet with a magnetic subsystem whose free energy has the form

$$\mathcal{F}_m = \int_V \left[\frac{1}{2} \alpha \left(\frac{\partial \mathbf{M}}{\partial \mathbf{r}} \right)^2 - \mathbf{M} \cdot \mathbf{H} \right] d\mathbf{r}. \tag{1}$$

Here $\mathbf{M}$ is the magnetization vector, $M \equiv |\mathbf{M}|$, V is the volume of the sample, $\mathbf{H}$ is the external magnetic field, and α is the exchange parameter. Let us consider a flat ferromagnetic layer of thickness d, where the magnetization vector $\mathbf{M}$ is pinned on one surface (bottom face in Fig. 1) and free on the other. In such samples, for magnetization in a magnetic field $\mathbf{H}$ directed opposite to the vector $\mathbf{M}$ fixed on the surface, there arises a magnetization distribution that is nonuniform over the thickness of the layer. The solution of the magnetostatic problem with the boundary conditions $M_z|_{y=0} = -M$ and $(\partial M_z/\partial y)|_{y=d} = 0$ has the form[1,2,5]

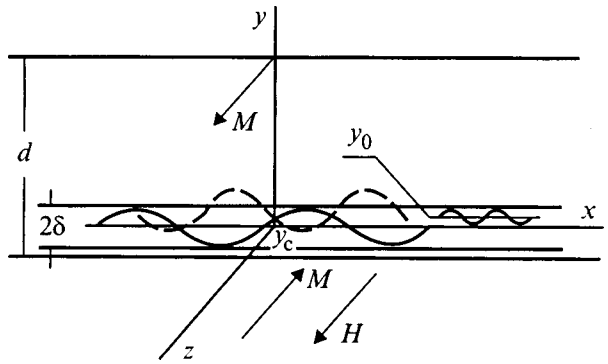

FIG. 1. Geometry of the problem and coordinate system. The wavy lines show the trajectories of the trapped electrons.

$$\frac{M_z}{M}=\begin{cases}-1+2k^2\mathrm{sn}^2[(h/\alpha)^{1/2}y], & h\geqslant h_u,\\ -1, & h<h_u.\end{cases} \tag{2}$$

Here, similarly to Ref. 5, the coordinate y is measured from the bottom face of the sample. The component $M_y=0$, just as in a Bloch domain wall, while M_x is determined by the relation $M_x^2+M_z^2=M^2$. In the expression (2) $h=H/M$, where $H=|\mathbf{H}|$; $h_u=(\pi/2)^2\alpha/d^2$ is the critical field or the field in which the magnetization curve is displaced. It is greatest for $d<10^{-6}$ cm, for which for typical values of α in metallic ferromagnets $\alpha/d^2\geqslant 1$. As d increases, the field h_u appreciably decreases ($h_u\propto d^{-2}$), becoming negligibly small at $d\approx 10^{-3}$ cm (for $\alpha=5\times 10^{-12}$ cm^2 the field $h_u\approx 10^{-5}$). The modulus k of the complete elliptic integral of the first kind $\mathbf{K}(k)$ as a function of the magnetic field can be found from the equation

$$\mathbf{K}^2(k)=hd^2/\alpha\sim h/h_u. \tag{3}$$

The magnetic field corresponding to the saturation region of the magnetization curve is determined in the present model by the condition $h\gg h_u$. In this limit the expression (2) assumes the form

$$\frac{M_z}{M}\approx -1+2\tanh^2\left[\frac{y}{\sqrt{2}\delta}\right]. \tag{4}$$

Here

$$\delta=\sqrt{\frac{\alpha}{2h}}. \tag{5}$$

is the half-width of the transitional region near the surface of the sample $y=0$, the main location where the magnetization vector turns ($\delta\ll d$).

Since **M** depends only on the coordinate y, the average magnetization $\langle M\rangle$ of the layer accompanying magnetization-reversal along the z axis is given by the expression

$$\langle M\rangle=\frac{1}{d}\int_0^d M_z dy. \tag{6}$$

Carrying out the integration with M_z in the form (4) we obtain the law of variation of the magnetization of a ferromagnet in an external magnetic field

$$\frac{\Delta M}{M}=\frac{2\sqrt{2}\delta}{d}\tanh\frac{d}{\sqrt{2}\delta}. \tag{7}$$

Thus, if the exponentially small difference of the hyperbolic tangent in Eq. (7) from 1 is neglected, then one can see that the change in the magnetization $\Delta M\equiv M-\langle M\rangle$ is proportional to the width δ of the transitional region, where the vector **M** turns. In accordance with the definition of δ (5) we obtain for the relative change in the magnetization of a ferromagnet with surface anisotropy the characteristic magnetic field dependence

$$\frac{\Delta M}{M}=\frac{2}{d}\sqrt{\frac{\alpha}{h}}\propto\frac{1}{d\sqrt{H}}. \tag{8}$$

Hence for $d=10^{-3}$ cm and $h=10^{-3}$ follows the estimate $\Delta M/M\approx 0.15$, i.e. for such a sample thickness the deviation of the average magnetization $\langle M\rangle$ from M is quite large (in contrast to h_u), which is due to the inverse proportionality of $\Delta M/M$ to d. In this case the satisfaction of the law (8) becomes the best evidence of the existence of surface pinning of a magnetic moment in a ferromagnetic layer.

If M_z in the form of the exact expression (2) is substituted into Eq. (6), then, as shown in Ref. 11, $\Delta M/M=2\mathbf{E}(k)/\mathbf{K}(k)$, where $\mathbf{E}(k)$ is a complete elliptic integral of the second kind. Hence we obtain once again the expression (8) for $h\gg h_u$. Experimentally, the dependence $\Delta M/M\propto 1/\sqrt{H}$ has been observed, for example, in Ref. 2, where thin ferromagnetic films on a magnetically hard substrate were investigated.

It should be noted that the $1/\sqrt{H}$ dependence in the law of approach of the magnetization to saturation holds in bulk samples, where it is due to the point localization of stresses,[33] and in amorphous ferromagnets with spatial fluctuations of the anisotropy constant.[34] In both cases the coefficient of $1/\sqrt{H}$ is independent of the sample thickness.

2. CONDUCTION ELECTRONS

We shall describe a charged quasiparticle of the electronic subsystem of the ferromagnet by the Hamiltonian

$$\mathcal{H}_s=\varepsilon_s\left(\mathbf{P}-\frac{e}{c}\mathbf{A}(\mathbf{r})\right), \tag{9}$$

where **P** is the canonical momentum of the quasiparticle with charge e in the band s. We assume an arbitrary dispersion law for charge carriers. The vector potential **A** can be expressed in terms of the magnetic induction vector of the ferromagnet $\mathbf{B}=\nabla\times\mathbf{A}$, the coordinate dependence of whose components is determined by the magnetization distribution in the sample ($\mathbf{B}(\mathbf{r})=\mathbf{H}+4\pi\mathbf{M}(\mathbf{r})$). If $\mathbf{B}(\mathbf{r})\equiv\mathbf{B}(y)$, as in our problem, then the vector potential can be written in the form

$$A_x=-\int_0^y B_z(y')dy',\quad A_y=0,\quad A_z=\int_0^y B_x(y')dy'. \tag{10}$$

Hence follows the Landau gauge in the case of a uniformly magnetized sample. For **A** in the form (10) the Hamiltonian $\mathcal{H}_s$ is independent of x and z (cyclic variables). Therefore the

momentum components P_x and P_z of the quasiparticles are conserved in the motion. Carrying out the semiclassical quantization procedure we obtain the condition for quantization of the quasiparticle energy in the form

$$S(P_x,P_z,\mathcal{E})=2\pi\frac{|e|B}{c}\hbar(n+\gamma), \tag{11}$$

where

$$\frac{|e|B}{c}\oint p_y dy=S(P_x,P_z,\mathcal{E}). \tag{12}$$

Here $\mathcal{E}$ is the quasiparticle energy, $B=4\pi M$, $\mathbf{P}=(P_x,p_y,P_z)$, $n=1,2,3,\ldots,0\leqslant\gamma\leqslant 1$, and $\hbar$ is Planck's constant divided by 2π.

A nonuniform induction $\mathbf{B}(y)$ does not affect different groups of charge carriers in the same way. Its nonuniformity has virtually no effect on quasiparticle trajectories far from the transitional region but, when $\delta\ll R$, where R is the average radius of a charge-carrier orbit in the field B, the transitional region is crossed at not too acute an angle. For such carriers $S(P_x,P_z,\mathcal{E})\approx S(P_z,\mathcal{E})$ and their spectrum is virtually identical to that in a uniform magnetic field. The rearrangement of the spectrum is maximal for quasiparticles moving inside the transitional region (Fig. 1). Let us examine their dynamics in greater detail.

For $h\gg h_u$ the projection M_z of the magnetization vector is given by the expression (4). Then B_z vanishes at the point $y=y_c\equiv u_c(\alpha/h)^{1/2}$, where $u_c=\tanh^{-1}(1/2-h/8\pi)^{1/2}$. One can see that this point exists only for $h<4\pi$. If $h\ll 4\pi$, then $y_c\sim\delta$ and, moreover, this approximation makes it possible to set $B\approx 4\pi M$. Only such values of the magnetic field will be considered below.

Taking as the origin on the y axis the point y_c, as shown in Fig. 1, we obtain for the components of the magnetic induction vector taking account of only the first term in the expansion near this point

$$B_x\approx B,\quad B_y=0,\quad B_z\approx By'/\delta, \tag{13}$$

where $y'=y-y_c$. To investigate the electronic subsystem we shall assume that this expansion holds in the entire transitional region $-\delta<y'<\delta$ and that outside this region the induction in the sample is uniform, i.e. according to Fig. 1, $B_z\approx\mp 4\pi M$ below and above the transitional region. For $\delta\ll R$ the function $\varepsilon_s(\mathbf{P}-e\mathbf{A}(\mathbf{r}))/c)$ in Eq. (9) can be expanded in a power series near the point $\mathbf{p}_0=(P_x,p_{y0},P_z)$, where p_{y0} is determined by the equation $v_y=0$. We note that, depending on the orientation and form of the Fermi surface, there may be no such point in the band s or there can be several such points. Let us consider the electronic band where there is one such point. To simplify the calculations we drop the index s. Simple transformations yield

$$\varepsilon(\mathbf{p})=\varepsilon_0+\frac{1}{2m_y}(p_y-p_{y0})^2+\frac{1}{2}m_y\omega_1^2(y'-y_0)^2, \tag{14}$$

where $\mathbf{p}=\mathbf{P}-e\mathbf{A}(\mathbf{r})/c$, $\varepsilon_0=\varepsilon(\mathbf{p}_0)$, $y_0=v_{z0}\delta/v_{x0}$, $|y_0|<\delta$, and v_{x0}, u_{z0}, and m_y are the components of the velocity and the effective mass of the conduction electrons near the point $\mathbf{p}_0$,

$$\omega_1=(eBv_{x0}/c\,\delta m_y)^{1/2}. \tag{15}$$

In what follows we shall be interested in the particles undergoing finite motion in the transitional region. For them ω_1 is real and it is the frequency of the motion in the transitional region. From expression (15) follows $ev_{x0}/m_y>0$, which determines the position of this group of carriers on the isoenergy surface. According to Eq. (14), the cross-sectional area corresponding to quasiparticles in the transitional region of the ferromagnet has the form

$$S(\mathcal{E},P_x,P_z)=2\pi(\mathcal{E}-\varepsilon_0)\sqrt{\frac{m_y eB\delta}{v_{x0}c}}. \tag{16}$$

Hence, using the quantization condition (11), we obtain for the charge-carrier spectrum the expression

$$\mathcal{E}_n(P_x,P_z)=\varepsilon_0+\hbar\left(n+\frac{1}{2}\right)\omega_1. \tag{17}$$

Since the Hamiltonian (14) describes a harmonic oscillator whose semiclassical spectrum is identical to the quantum spectrum, the quantity γ appearing in Eq. (11) is set equal to 1/2.

Equations (17) and (15) apply to the case of a ferromagnet with an arbitrary isoenergy surface the expressions for the electron spectrum in the transitional region, and the electron frequencies obtained previously in Ref. 24 for a spherical Fermi surface, as well as the expressions for the spectrum and frequency of electrons trapped by a domain wall.[27] In the latter case $\delta=\sqrt{\alpha/\beta}$, where β is the uniaxial anisotropy constant.

It is convenient to represent the frequency ω_1 in the form

$$\omega_1=\omega_B\sqrt{R_x/\delta}, \tag{18}$$

where $\omega_B=|eB/m_y c|$, $R_x=m_y v_{x0}c/eB$ is the radius of curvature of the electron trajectory at the point where $v_y=0$ and is determined by the radius of curvature $m_y v_{x0}$ of the isoenergy surface in a plane passing through the p_y axis and the velocity vector $\mathbf{v}$. In the case of a quadratic and isotropic electron dispersion law, R_x is the cyclotron radius of electrons with velocity v_{x0} and ω_B is the cyclotron frequency in the magnetic field B.

In multiband ferromagnets, there exists a set of generally different frequencies ω_{1s}. The index s then enumerates the sections of isoenergy surfaces in bands corresponding to trapped electrons.

In the foregoing discussion we neglected the conduction-electron spin. This is valid if $\hbar v_y/\delta\ll I_{sd}$, which means that the electron spin adiabatically follows the magnetization during the motion of an electron in the transitional layer. In a metallic ferromagnet the s–d exchange integral is $I_{sd}\sim 10^{-13}$ erg. Then the latter inequality can hold for $\delta\sim 10^{-4}$ cm, even if the electron Fermi velocity $v_F\sim 10^8$ cm/s is taken for v_y.

Finally, we note that, using in Eq. (1) the linear approximation (13) for M_z and then determining the parameter δ from the condition that the free energy $\mathcal{F}_m$ is minimum, gives an expression for $\Delta M/M$ that differs from the exact expression (8) by the numerical factor ≈ 0.9. This correspon-

dence of the relation obtained on the basis of an approximate description to the exact result can be explained by the fact that the average magnetization $\langle M\rangle$, being an integral characteristic, is insensitive to the details of the magnetization distribution.

3. THERMODYNAMIC POTENTIAL OF THE ELECTRONIC SUBSYSTEM

We write the thermodynamic potential of the conduction-electron gas in the form

$$\Omega=-2T\frac{L_xL_z}{(2\pi\hbar)^2}\times\sum_n\int_{S>0}dP_xdP_z\,\ln\left[1+\exp\frac{\zeta-\mathcal{E}_n(P_x,P_z)}{T}\right], \tag{19}$$

where $\mathcal{E}_n(P_x,P_z)$ is determined from the condition (11); L_x and L_z are the dimensions of the sample in the xz plane; and, ζ is the chemical potential. We shall use the Poisson equation to carry out the summation in Eq. (19). We make the substitution

$$dn=\frac{c}{2\pi\hbar eB}\frac{\partial S}{\partial\mathcal{E}}\,d\mathcal{E}, \tag{20}$$

in the integral over n arising in the process, and integrating over $\mathcal{E}$ by parts we obtain

$$\Omega=-2\frac{L_xL_z}{(2\pi\hbar)^3}\int_0^\infty d\mathcal{E}f(\mathcal{E})\int_0^{\mathcal{E}}d\mathcal{E}'\times\int_{S>0}dP_xdP_z\frac{\partial S(\mathcal{E}',P_z,P_x)}{\partial\mathcal{E}'}\times\left\{1+2\mathrm{Re}\sum_{l=1}^\infty\exp\left[il\frac{c}{eB\hbar}S(\mathcal{E}',P_x,P_z)-i2\pi l\gamma\right]\right\}. \tag{21}$$

Here $f(\mathcal{E})=\{1+\exp[(\mathcal{E}-\zeta)/T]\}^{-1}$ is the Fermi distribution function. The first term in braces in Eq. (21) gives, after integrating, the thermodynamic potential Ω_0 of a free-electron gas, which is independent of the magnetic induction.[35]

We shall integrate the second term in braces in Eq. (21) by the stationary-phase method. Since the oscillation effects are of no interest to us in what follows, we take account of the contributions (21) only of the boundaries of the region of integration. For electrons, which move wholly or mainly outside the transitional region, the function S is essentially independent of P_x: $S(\mathcal{E}',P_z,P_x)\approx S(\mathcal{E}',P_z)$. In this case the peaks of the region of integration over P_z contribute to Eq. (21). The corresponding term Ω_L in the thermodynamic potential Ω describes, just as in a uniformly magnetized sample, the diamagnetism of the electron gas.[35] For us, however, the contribution of trapped electrons to the thermodynamic potential is of greatest interest. This contribution determines the peak region of the integration over P_x in Eq. (21), which we denote by $P_m(\mathcal{E},P_z)$. Here it is important that, as P_x approaches P_m, the spectrum of any trapped electrons is described by Eq. (17). For example, for the trajectory shown by the dashed line in Fig. 1, the limiting trajectory is the trajectory shown by the wavy line near $y_0\neq 0$. Thus, using Eq. (16) for S and performing the standard calculations,[35–37] we obtain for the thermodynamic potential of the electron gas in a ferromagnet with surface pinning of the magnetic moment

$$\Omega=\Omega_0+\Omega_L+\frac{L_xL_z}{\sqrt{\delta}}\sum_s G_s, \tag{22}$$

where

$$G_s=\frac{1}{24(2\pi)^2\hbar}\int_0^\infty d\mathcal{E}\int_{y_0<\delta}dP_z\frac{f(\mathcal{E})}{\sqrt{R_{xs}(\mathcal{E},P_z,P_{ms})}}. \tag{23}$$

Here the radius of curvature R_x of the electronic trajectory is taken at the point $P_x=P_m$. The potential Ω_L in Eq. (22), generally speaking, has a factor $1-\mathrm{const}(\delta/d)\sqrt{\delta/R}$, where the quantity being subtracted is proportional to the number of trapped electrons. However, the δ-dependent part of Ω_L is several orders of magnitude smaller than the last term in Eq. (22), so that it can be ignored.

In summary, the part of the thermodynamic potential that depends on the width of the transitional region is inversely proportional to $\sqrt{\delta}$, i.e. the free energy of the electronic subsystem will decrease as δ increases. This behavior of the thermodynamic quantities is due to the fact that the spacing between the energy levels in the electron spectrum (17) in the transitional region will decrease with increasing δ.

Given the dispersion law of the conduction electrons, G_s can be calculated. Here we estimate this parameter making the assumption that the ferromagnet is a single-band magnet with an ellipsoidal isoenergy surface

$$\varepsilon(\mathbf{p})=\frac{(P_x-e/cA_x)^2}{2m_x}+\frac{p_y^2}{2m_y}+\frac{(P_z-e/cA_z)^2}{2m_z}. \tag{24}$$

Then $\varepsilon_0=P_x^2/2m_x+P_z^2/2m_z$, $v_{z0}=P_z/m_z$, and $P_m=\sqrt{2m_x\varepsilon-m_xP_z^2/m_z}$. Performing the integration in Eq. (23) with $u_{x0}=P_m/m_x$, we have for G_s the expression

$$G=\frac{1}{15(2\pi)^2}\left(\frac{eB}{c}\right)^{1/2}\frac{\zeta}{\hbar}(2\zeta m_x)^{1/4}\left(\frac{m_z}{m_y}\right)^{1/2}I. \tag{25}$$

Here the index s has been dropped [a single term appears instead of the sum over s in Eq. (22)]

$$I=\sqrt{2}[2E(\lambda,1/\sqrt{2})-F(\lambda,1/\sqrt{2})],$$

where F and E are elliptic integrals of the first and second kinds and $\lambda=\cos^{-1}[m_x/(m_x+m_z)]^{1/4}$. The limits of integration over P_x were determined from the condition $y_0=\delta$, i.e. it was assumed that the expansion (14) holds in the entire transitional region. For $m_x\ll m_z$ the parameter $I\approx\sqrt{2}[2\mathbf{E}(1/\sqrt{2})-\mathbf{K}(1/\sqrt{2})]\approx 1.2$. In the limit $m_x\gg m_z$ we have $I\approx(m_z/m_x)^{1/2}\ll 1$. Therefore G is greater when $m_y\ll m_x\ll m_z$, which corresponds to a Fermi surface that is

oblate in the p_y direction and prolate in the direction p_z in the $p_z p_x$ plane. Finally, for a spherical Fermi surface ($m_x = m_y = m_z = m_0$)

$$G = \frac{0.74}{15(2\pi)^2\hbar}\zeta m_0 \omega_B \sqrt{R}, \tag{26}$$

which, to within a constant, is identical to the coefficient of $1/\sqrt{\delta}$ in the electronic contribution to the free energy of a ferromagnet with a domain wall.[32]

4. EQUILIBRIUM WIDTH OF THE TRANSITION REGION AND THE MAGNETIZATION CURVE

In accordance with expression (22), an increase in δ is energetically favorable for the electronic subsystem. The increase in magnetic energy due to the deviation of δ from the equilibrium value (5), determined only by the magnetic subsystem of the ferromagnet, will be compensated by a decrease in the energy of the electronic subsystem. In other words, a new equilibrium width of the transition region arises. We shall calculate it, assuming that the distribution (4) of the magnetic moment is valid for a metallic ferromagnet with surface pinning of the magnetic moment, where δ is now an unknown parameter to be determined from the condition of a minimum of the free energy.

Substituting the expression (4) into Eq. (1) and integrating over the volume of the sample we obtain for the free energy of the isotropic metallic ferromagnet, using Eq. (22),

$$\mathcal{F} = -VMH + Vn_0\zeta + \Omega_0 + \Omega_L + L_x L_z \times \left[2M_0^2 \left(\frac{\alpha}{\sqrt{2\delta}} + \sqrt{2} h \delta \right) + \frac{1}{\sqrt{\delta}} \sum_s G_s \right]. \tag{27}$$

Here the surface energy density (the expression in brackets) is singled out. It is convenient to represent it in the form

$$F_w = 2M^2 \left(\frac{\alpha}{\sqrt{2\delta}} + \sqrt{2} h \delta + \frac{g}{\sqrt{\delta}} \right), \tag{28}$$

where $g = (1/2M^2)\Sigma_s G_s$. From the condition of a minimum of the function $F_w(\delta)$ we obtain the equation

$$\delta^2 - \frac{g}{2\sqrt{2h}}\sqrt{\delta} - \frac{\alpha}{2h} = 0, \tag{29}$$

whose solution determines the equilibrium value of the width of the transitional region. Allowing g in Eq. (29) to approach zero, the solution of the equation gives for δ the expression (5). For finite g the solution of Eq. (29) was obtained numerically. For small values of g, when the effect of the electronic subsystem can be treated as a perturbation, the solution of this equation can be written in the simple analytic form

$$\delta = \left(\frac{\alpha}{2h} \right)^{1/2} \left[1 + \frac{1}{2} \left(\frac{h_c}{h} \right)^{1/4} \right], \quad h_1 \ll h \ll h_2. \tag{30}$$

Here $h_c = g^4/8\alpha^3$ is the characteristic field, $h_1 = \max\{h_u, h_c\}$, and h_2 is the upper limit of the admissable values of the magnetic field, determined by the smallest of the limiting fields. Now there is only one limit on the magnetic field ($h \ll 4\pi$); a second limit will be obtained below. Comparing Eq. (30) with the numerical solution of Eq. (29) shows that this expression is a good approximation when $h \approx h_c$. Formally Eq. (9) possesses a solution for $h \ll h_c$ also (if, of course, $h_c \gg h_u$), but then there arises the question of the applicability of the expression (4) for describing the magnetization distribution in the sample.

Since, as follows from expression (7), the equilibrium value of δ determines the field-dependence of the magnetization, we have

$$\frac{\Delta M}{M} = \frac{2}{d} \left(\frac{\alpha}{h} \right)^{1/2} \left[1 + \frac{1}{2} \left(\frac{h_c}{h} \right)^{1/4} \right], \quad h_1 \ll h \ll h_2. \tag{31}$$

In the derivation of Eq. (31) we neglected in Eq. (7) the exponentially small deviation of the hyperbolic tangent from 1. If the law of approach of the magnetization to saturation is rewritten in a different form, which is also often used, representing $\langle M \rangle$ as a power-law function of H, then

$$\frac{\langle M \rangle}{M} = 1 - \frac{a^{1/2}}{H_{3/4}} - \frac{a^{3/4}}{H_{3/4}}. \tag{32}$$

The coefficients a_i can be expressed in terms of the physical parameters appearing in Eq. (31).

Graphically, the magnetization curve can be represented more clearly in the coordinates M' and $h^{-1/4}$, where

$$M' \equiv \frac{\Delta M d}{2M} \left(\frac{h}{\alpha} \right)^{1/2}. \tag{33}$$

In the absence of an electronic contribution to the magnetization of the ferromagnet the function $M'(h^{-1/4}) = 1$. Figure 2 (solid line) shows the dependence of M' on $h^{-1/4}$, following from the numerical solution of Eq. (29) with $g = 1.7 \times 10^{-9}$ cm$^{3/2}$. This value of g for an ellipsoidal Fermi surface can be obtained from Eq. (25) with $(m_x/m_y)^{1/2} \approx 10$, $\zeta = 7$ eV, $M = 500$ Gs, and m_x is equal to the free-electron mass. Here $h_c \approx 8 \times 10^{-3}$, which is three orders of magnitude greater than h_u with sample thickness $d = 10^{-3}$ cm. The dashed line in Fig. 2 shows the dependence following from the approximate relation (31). The slope angle of the straight line with respect to the abscissa is proportional to g. One can see that $\Delta M/M$ can be approximated well by Eq. (31) right up to $h \approx h_c$.

The results presented above can be extended to the case of a uniaxial ferromagnet with easy axis along z. We shall assume that a nonuniform distribution of the magnetization, for which the expression (4) holds, has been produced in a such sample. Then h can be replaced by $h_\pm = \beta \pm h$ in Eq. (5) as well as in all subsequent expressions. We use the $+$ sign when the vector **H** is directed opposite to the vector **M** pinned on the surface, as shown in Fig. 1, and we use the $-$ sign when **H** is parallel to **M**. In other words, the expression (31) with h in it replaced by $h_\pm$ describes a section of the hysteresis loop of the ferromagnet. The inequalities (31) remain valid when h is replaced by $h_\pm$ in them.

Thus, the restructuring of the conduction-electron spectrum in a nonuniform magnetic induction of a ferromagnet with surface pinning of the magnetic moment contributes to the magnetization process in such a material. The magneti-

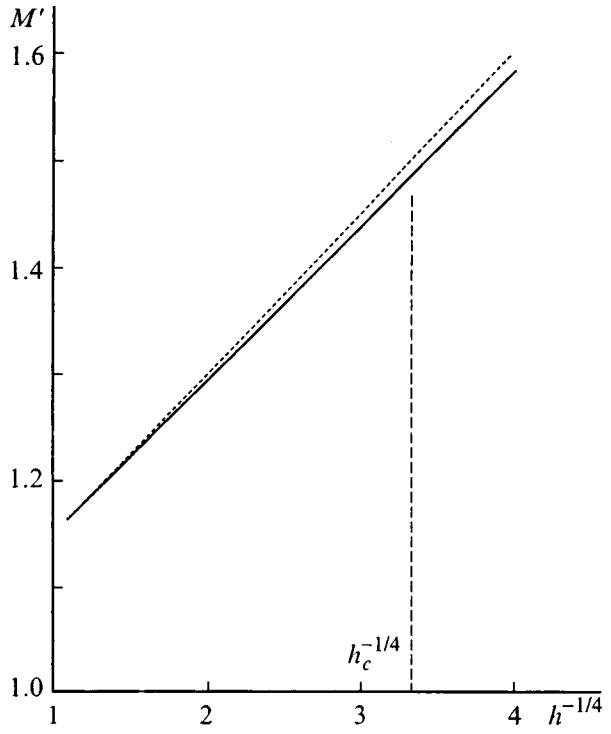

FIG. 2. Dependence of relative change in magnetization on the external magnetic field. The solid line was constructed using the numerical solution of Eq. (29) for δ; the dashed line corresponds to the expression (31).

zation curve becomes smoother, and its modification by the conduction electrons is greatest in weak magnetic fields, where $\Delta M/M$ is relatively large (Eq. (31)). This fact could facilitate experimental observation of the effect.

The results presented in this paper were obtained for a magnetic field in the interval $h_1 \ll h \ll 4\pi$, where the limits were discussed above. We note another limit on the magnetic field . This limit is due to the condition $\delta \gg \lambda_y$, where λ_y is the localization length of the wave function of a trapped electron. In accordance with Eq. (14) this inequality has the form

$$\delta \gg \sqrt{\frac{\hbar}{m_y \omega_1}} \tag{34}$$

or, taking account of the δ-dependence of ω_1,

$$\delta \gg R_x \left(\frac{\hbar}{m \omega_B} \right)^{2/3}. \tag{35}$$

Using the values of the physical parameters presented above for obtaining estimates gives $\delta \gg 10^{-6}$ cm. The inequalities determining the range of δ can be represented as a condition on the magnetic field

$$h \ll h_w = \frac{\alpha}{2R_x^2} \left(\frac{\zeta}{\hbar \omega_B} \right)^{4/3}. \tag{36}$$

According to this equation $h_w \approx 10$. Thus the limiting field entering in Eqs. (30) and (31) is determined by the expression $h_2 = \min\{h_w, 4\pi\}$. There is a limit on the external magnetic field that is due to the finite magnitude of the field of surface pinning of the magnetization. However, its value in the case, for example, of a film on an antiferromagnetic substrate reaches several tens of kilooersteds and certainly exceeds all characteristic fields.

Let us now examine the effect of scattering of the trapped electrons by impurities. If $l_y \gg \lambda_y$, where l_y is the electron mean free path length in the direction of the y axis ($l_y = v_y \tau$; τ is the electron free travel time), electron collisions do not change any of the results presented above. In other words, the spacing between the levels in the spectrum (17) should satisfy the condition $\omega_1 \gg 1/\tau$. For $h \approx 10^{-2}$ this inequality holds if the free path length $l = v_F \tau \approx 10^{-3}$ cm. Such values of l are characteristic for pure ferromagnets at low temperature.

The slope angle of the dashed line in Fig. 2 is proportional to the quantity g, determined in terms of the electronic parameters of the ferromagnet. Thus it is possible to determine the characteristics of local sections of the Fermi surface by means of magnetic measurements. However, at first even a simple observation of the electronic contribution to the magnetization curve would be of definite interest, since there are still no experimental proofs of the existence of electrons trapped by a domain wall or by the transition region in a ferromagnet with surface pinning of the magnetic moment.

For nickel $g \approx 10^{-10}$ cm$^{3/2}$ (the values of the exchange constant, magnetization, and chemical potential of this material were used above for estimates). Then, for sample thickness $d = 10^{-3}$ cm, the increase in $\Delta M/M$ due to trapped electrons is approximately 20% in a field $h = 10^{-3}$. The contribution to the magnetization $\langle M \rangle$, i.e., the value of the last term in Eq. (32), is approximately 0.03. For comparison, we note that Landau diamagnetism produces a relative decrease of the magnetization M of the order of 10^{-6}.

The results obtained here qualitatively describe also the magnetization curve of flat samples with antiparallel surface pinning of the magnetic field on opposite faces. Therefore it can be inferred that the effects studied can be intensified by producing a multilayer system having alternating layers of a ferromagnet and a material giving strong surface pinning.

I thank V. A. Ignatchenko for a discussion of the results obtained in this work.

*)E-mail: theor@iph.krasnoyarsk.su

[1] A. Aharoni, E. H. Frei, and S. Shtrikman, J. Appl. Phys. **30**, 1956 (1959).
[2] E. Goto, N. Hagshi, T. Miyashita, and K. Nakagawa, J. Appl. Phys. **36**, 2951 (1965).
[3] A. A. Glazer, A. P. Potapov, R. I. Tagirov, and Ya. S. Shur, Fiz. Tverd. Tela (Leningrad) **8**, 3022 (1966) [Sov. Phys. Solid State **8**, 2413 (1966)].
[4] B. P. Khrustalev, A. S. Mel'nik, and N. M. Salanskiĭ, Zh. Éksp. Teor. Fiz. **56**, 435 (1969) [Sov. Phys. JETP **29**, 238 (1969)].
[5] Yu. V. Zakharov and V. A. Ignatchenko, Zh. Éksp. Teor. Fiz. **59**, 951 (1970) [Sov. Phys. JETP **32**, 517 (1971)].
[6] N. M. Salansky and M. Sh. Erukhimov, Thin Solid Films **6**, 129 (1970).
[7] V. G. Bar'yakhtar, V. F. Klepikov, and V. L. Sobolev, Fiz. Tverd. Tela (Leningrad) **13**, 1454 (1971) [Sov. Phys. Solid State **13**, 1212 (1971)].
[8] V. G. Bar'yakhtar, V. F. Klepikov, and V. L. Sobolev, Fiz. Tverd. Tela (Leningrad) **13**, 3517 (1971) [Sov. Phys. Solid State **13**, 2973 (1971)].
[9] Yu. V. Zakharov and E. A. Khlebopros, Zh. Éksp. Teor. Fiz. **73**, 1101 (1977) [Sov. Phys. JETP **46**, 584 (1977)].
[10] D. I. Sementsov and V. A. Syabro, Fiz. Nizk. Temp. **4**, 1279 (1978) [Sov. J. Low Temp. Phys. **4**, 602 (1978)].

[11] Yu. V. Zakharov and E. A. Khlebopros, Fiz. Tverd. Tela (Leningrad) **22**(12), 3651 (1980) [Sov. Phys. Solid State **22**, 2137 (1980)].
[12] M. Sh. Erukhimov, V. A. Seredkin, and V. Yu. Yakovchuk, Fiz. Met. Metalloved. **52**, 57 (1981).
[13] V. A. Seredkin, G. I. Frolov, and V. Yu. Yakovchuk Fiz. Met. Metalloved. **63**, 457 (1987).
[14] A. Aharoni, J. Appl. Phys. **61**, 3302 (1987).
[15] D. L. Mils, Phys. Rev. B **40**, 11153 (1989).
[16] E. V. Babkin, Fiz. Tverd. Tela (Leningrad) **31**(6), 181 (1989) [Sov. Phys. Solid State **31**, 1578 (1989)].
[17] E. V. Babkin and Kh. O. Urinov, Fiz. Tverd. Tela (Leningrad) **32**, 2623 (1990) [Sov. Phys. Solid State **32**, 1522 (1990)].
[18] M. Sh. Erukhmov and G. M. Erukhimov, Fiz. Tverd. Tela (Leningrad) **33**, 1403 (1991) [Sov. Phys. Solid State **33**, 790 (1991)].
[19] R. Krishman, M. Porte, and M. Tessier, J. Magn. Magn. Mater. **103**, 47 (1992).
[20] Yu. V. Zakharov, Dokl. Akad. Nauk SSSR **344**, 328 (1995) [Phys. Dokl. **40**, 464 (1995)].
[21] Yu. I. Bespyatykh, A. D. Bordman, I. E. Dikshteĭn, and S. A. Nikitov, Fiz. Tverd. Tela (St. Petersburg) **38**, 295 (1996) [Phys. Solid State **38**, 166 (1996)].
[22] H. N. Bertram and D. L. Paul, J. Appl. Phys. **82**, 2439 (1997).
[23] B. N. Fillipov, L. G. Korzunin, and E. V. Rebryakova, Fiz. Met. Metalloved. **84**, 42 (1997).
[24] Yu. I. Man'kov, Fiz. Tverd. Tela (Leningrad) **23**, 2508 (1981) [Sov. Phys. Solid State **23**, 1473 (1981)].
[25] Yu. I. Man'kov, Fiz. Met. Metalloved. **68**, 640 (1989); Fiz. Tverd. Tela (Leningrad) **32**, 1208 (1990) [Sov. Phys. Solid State **32**, 707 (1990)]; Fiz. Tverd. Tela (St. Petersburg) **36**, 3634 (1994) [Phys. Solid State **36**, 1923 (1994)].
[26] M. S. Khaĭkin, Zh. Éksp. Teor. Fiz. **39**, 212 (1960) [Sov. Phys. JETP **12**, 152 (1961)]; Usp. Fiz. Nauk **96**, 409 (1968) [Sov. Phys. Usp. **11**, 785 (1969)].
[27] R. G. Mints, JETP Lett. **9**, 387 (1969).
[28] F. G. Bass and V. L. Fal'ko, Fiz. Nizk. Temp. **6**, 60 (1980) [Sov. J. Low Temp. Phys. **6**, 29 (1980)].
[29] Yu. V. Zakharov and L. S. Titov, Solid State Commun. **53**, 447 (1985).
[30] L. A. Fal'kovskiĭ, JETP Lett. **11**, 111 (1970).
[31] S. S. Nedorezov, JETP Lett. **14**, 415 (1971).
[32] Yu. I. Man'kov, R. G. Khlebopros, and Yu. V. Zakharov, Fiz. Tverd. Tela (Leningrad) **17**, 352 (1975) [Sov. Phys. Solid State **17**, 222 (1975)]; Fiz. Met. Metalloved. **39**, 461 (1975).
[33] S. V. Vonsovskiĭ, *Magnetism* (Wiley, N. Y., 1974; Nauka, Moscow, 1971), p. 838.
[34] V. A. Ignatchenko, R. S. Iskhakov, and G. V. Popov, Zh. Éksp. Teor. Fiz. **82**, 1518 (1982) [Sov. Phys. JETP **55**, 878 (1982)].
[35] I. M. Lifshits and A. M. Kosevich, Zh. Éksp. Teor. Fiz. **29**, 730 (1955) [Sov. Phys. JETP **2**, 636 (1956)].
[36] A. M. Kosevich and I. M. Lifshits, Zh. Éksp. Teor. Fiz. **29**, 743 (1955) [Sov. Phys. JETP **2**, 646 (1956)].
[37] D. Shoenberg, *Magnetic Oscillations in Metals* (Cambridge University Press, N. Y., 1984; Mir, Moscow, 1986).

Translated by M. E. Alferieff

Effect of a magnetoelastic interaction on the rate of transient processes in iron borate single crystals

O. S. Kolotov

M. V. Lomonosov Moscow State University, 119899 Moscow, Russia
(Submitted July 14, 1998)
Fiz. Tverd. Tela (St. Petersburg) **41**, 654–655 (April 1999)

A semiempirical relation between the rate of transient processes in iron borate single crystals and the amplitude of the magnetic field and intensity of the magnetoelastic oscillations is proposed. Experimental data confirming the applicability of the expression to real pulsed magnetization-reversal curves are presented. © *1999 American Institute of Physics.* [S1063-7834(99)01904-8]

It has been shown[1–3] that magnetoelastic interaction is one of the factors determining the duration of the transient processes in iron borate ($FeBO_3$) single crystals. The excitation of pulsed magnetoelastic oscillations leads to additional dissipation of energy and associated retardation of the transient process. It has been found[2,3] that the efficiency of the magnetoelastic interaction decreases for process durations $\tau \leqslant 13-17$ ns. As a result, the rate of change of the magnetization increases rapidly, and kinks appear in the pulsed magnetization-reversal curves showing the reciprocal of the magnetization-reversal time τ^{-1} versus the amplitude H_s of the pulsed magnetic field. On the whole, the data accumulated thus far give only a qualitative understanding of the role of the magnetoelastic interaction. Here, to obtain quantitative information, a semiempirical expression approximating the rate τ^{-1} of the transient process versus the field H_s and intensity of the magnetoelastic oscillations is proposed.

To derive the expression of interest to us we shall employ the fact that most pulsed processes in $FeBO_3$ are associated with the rotation of the magnetization.[3–5] We shall assume that the energy acquired by the sample from the magnetic field is absorbed by the magnetic subsystem of the crystal and expended on the excitation of magnetoelastic oscillations. Correspondingly, we have for the energy density

$$\Delta \mathbf{M} \cdot \mathbf{H}_s = \Delta E_m + \Delta E_{me}, \tag{1}$$

where $\Delta \mathbf{M}$ is the change in magnetization during the transient process. To estimate the density of the energy losses ΔE_m in the magnetic subsystem we shall employ an expression for the dissipation function $\dot{w}_m$. For a weak ferromagnet[6,7]

$$\dot{w}_m = \frac{M_0 \alpha}{2\gamma} \left(\frac{d\mathbf{l}}{dt} \right)^2, \tag{2}$$

where α is the Gilbert damping constant, $\mathbf{l} = \mathbf{L}/M_0 = (\mathbf{M}_1 - \mathbf{M}_2)/M_0$ is the normalized antiferromagnetism vector, $\mathbf{M}_1$ and $\mathbf{M}_2$ are the sublattice magnetizations and M_0 is their absolute value, and γ is the gyromagnetic ratio.

Since the planar anisotropy is large,[8] it can be assumed that the vector $\mathbf{l}$ remains in the plane of the single crystal. Then

$$\dot{w}_m \cong \alpha M_0 \dot{\varphi}^2 / 2\gamma, \tag{2a}$$

where φ is the azimuthal angle. Let us assume that the instantaneous rate of change $\dot{\varphi}$ of this angle is its average rate of change during the transient process. Then the energy losses in the magnetic subsystem are

$$\Delta E_m = \dot{w}_m \tau. \tag{3}$$

We shall also assume that the energy losses to excitation of magnetoelastic oscillations are

$$\Delta E_{me} = kA^2, \tag{4}$$

where the coefficient of proportionality k depends on the elastic and magnetoelastic constants of the material and also the method used to determine the intensity A of the magnetoelastic oscillations.

It follows from expressions (1)–(4) that

$$\tau^{-1} = aH_s - bA^2, \tag{5}$$

where

$$a = \frac{2\gamma M_s (\cos\eta_2 - \cos\eta_1)}{\alpha M_0 (\eta_2 - \eta_1)^2},$$

$a = ak$, and η_1 and η_2 are the angles between the initial and final positions of the magnetization vector $\mathbf{M}_s$ of the sample and the field $\mathbf{H}_s$.

Since the information about the elastic and magnetoelastic properties of iron borate are incomplete and there are no data on the value of the damping constant α in the frequency range $\sim 10-100$ MHz, corresponding to the $\sim 3-30$ ns process that we are investigating,[8] it is difficult to calculate the coefficients a and b. However, the experimental values of the coefficients discussed can be used to obtain quantitative information about the degree of the effect of the magnetoelastic oscillations. It is obvious that the possibility itself of determining these quantities from experiment is due to the applicability of expression (5) to actual transient processes.

In the present work we studied two processes: 180° and 90° pulsed magnetization-reversal. The investigations were performed using an induction setup with resolution time ~ 1 ns.[9] The magnetization-reversal time τ, as usual, was as-

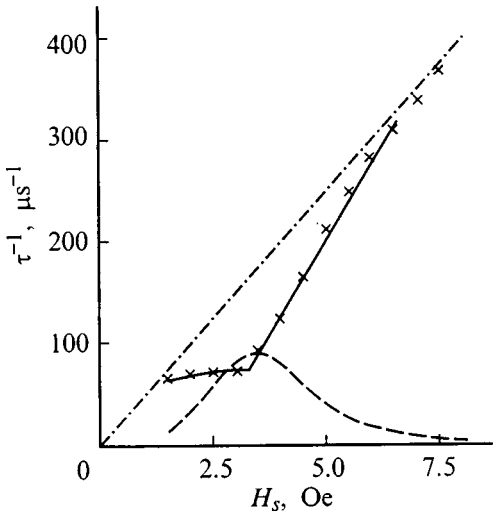

FIG. 1. Solid line represents experimental pulsed magnetization-reversal curve. The dot-dash line is the limiting function $\tau^{-1}(H_s)$ for $A=0$. Dashed curve shows bA^2 dependence on the field H_s. The crosses indicate the values of $\tau^{-1}=aH_s-bA^2$.

sumed to equal the interval between the moments when the voltage of the longitudinal magnetization-reversal signal was 0.1 of its amplitude. The intensity A of the magnetoelastic oscillations was determined according to the amplitude of the oscillations of the signal.[1–3] A batch of six single crystals ranging in thickness from 22 to 110 μm was investigated. The results obtained are illustrated here for a sample with the following parameters: thickness 45 μm, technical saturation field 1.4 Oe, and period of magnetoelastic oscillations 22 ns.

If expression (5) does indeed approximate the real dependences, then the values of the coefficients a and b can be found from a system of two equations obtained for two different fields H_s and the corresponding experimental values of τ^{-1} and A^2. An example of the application of expression (5) to actual processes is presented in Fig. 1. Here the solid line represents the experimentally obtained curve $\tau^{-1}(H_s)$ with 90° pulsed magnetization-reversal. The crosses show the values calculated using expression (5) with $a=50(\mu\text{s Oe})^{-1}$ and $b=3(\mu\text{s})^{-1}(\text{mV})^{-2}$ which fall near the real pulsed magnetization-reversal curve.

Similar data were also obtained for other samples investigated. Thus, despite a number of simplifying assumptions used in its derivation, expression (5) approximates quite well the real pulsed magnetization-reversal curves. Using the experimental values of the coefficient b, it is possible to obtain a clearer picture of the effect of magnetoelastic oscillations on the rate of transient processes. To this end, the dependence of bA^2 on the field H_s is shown in Fig. 1 (dashed line). The dot-dash straight line, representing the function $\tau^{-1}=aH_s$, characterizes the rate of magnetization-reversal in the absence of a magnetoelastic interaction. Comparing the curves presented shows clearly that the appearance of magnetoelastic oscillations leads to strong retardation of the transient process. Instead of the straight line with the switching constant $S_{w0}=1/a$ (equal to 0.02 Oe μs for the sample under study), two sections are observed on the pulsed magnetization-reversal curve. On the first section the switching coefficient S_{w1} (0.14 Oe μs) is much larger and on the second section S_{w1} (0.013 Oe μs) is much smaller than S_{w0}. The strongest retardation is observed near the kink in the curve $\tau^{-1}(H_s)$. Here the magnetization-reversal rate decreases by up to a factor of 1.5–2.5 (for different samples).

It is obvious that the straight line $\tau^{-1}=aH_s$ should approximate the magnetization-reversal rate for sufficiently strong fields, when $A\to 0$. This means that in fields $H_s\sim 8-10$ Oe a knee should appear in the pulsed magnetization-reversal curves. Such a knee is indeed observed. However, since the magnetization-reversal times at which this happens are comparable to the time resolution of the apparatus, the time resoluton of the apparatus must be improved in order to identify this knee more reliably.

In conclusion, we note that using the experimental values of the coefficient a and the published data on M_s, M_0, and γ it is possible to estimate the Gilbert damping constant corresponding to the processes improved here. The values of α found in this manner are close to 0.01.

I thank L. I. Antonov, V. A. Pogozhev, and G. V. Smirnov for valuable discussions and A. P. Krasnozhon for a discussion and assistance in performing the experiment.

[1] O. S. Kolotov, En Han Kim, A. P. Krasnozhon, and V. A. Pogozhev, JETP Lett. **58**, 53 (1993).
[2] O. S. Kolotov, En Han Kim, A. P. Krasnozhon, and V. A. Pogozhev, Fiz. Tverd. Tela (St. Petersburg) **36**, 231 (1994) [Phys. Solid State **36**, 127 (1994)].
[3] O. S. Kolotov, A. P. Krasnozhon, and V. A. Pogozhev, Fiz. Tverd. Tela (St. Petersburg) **38**, 1017 (1996) [Phys. Solid State **38**, 565 (1996)].
[4] O. S. Kolotov, En Han Kim, and V. A. Pogozhev, Fiz. Tverd. Tela (St. Petersburg) **36**, 515 (1994) [Phys. Solid State **36**, 284 (1994)].
[5] O. S. Kolotov, En Han Kim, and V. A. Pogozhev, Vestn. Mosk. Univ., Fiz., Astron. **6**, 57 (1996).
[6] A. K. Zvezdin and A. A. Mukhin, Zh. Éksp. Teor. Fiz. **102**, 577 (1992) [Sov. Phys. JETP **75**, 306 (1992)].
[7] V. G. Bar'yakhtar, M. V. Chetkin, B. A. Ivanov, and S. N. Gadetskii, Springer Tracts Mod. Phys. **129**, No. 1 (1994).
[8] R. Diehl, W. Jantz, B. I. Nolang, and W. Wettling, Curr. Top. Mater. Sci. **11**, 241 (1984).
[9] O. S. Kolotov, V. A. Pogozhev, and R. V. Telesnin, *Methods and Apparatus for Investigating the Impulse Properties of Thin Magnetic Films* (Moscow State University Press, Moscow, 1970).

Translated by M. E. Alferieff

Nonlinear Kerr effect in magnetic crystals

A. D. Petrenko

*Donetsk State Technical University, 340000 Donetsk, Ukraine**

(Submitted July 17, 1998)
Fiz. Tverd. Tela (St. Petersburg) **41**, 656–659 (April 1999)

The reflection of an intense light wave from the boundary of a semiinfinite magnetic crystal is investigated theoretically. Expressions are obtained for the rotation angle of the polarization ellipse and the degree of ellipticity of the reflected wave as a function of the polarization of the incident radiation. The physical wave-interaction mechanisms that give rise to this effect are established. © *1999 American Institute of Physics.* [S1063-7834(99)02004-3]

The optical Kerr effect — deformation of the polarization ellipse and rotation of the major axis of the ellipse on reflection from a magnetized sample — is well known in the linear optics of magnetic media.[1] In strong light fields, the polarization of the reflected light evidently will depend on the intensity of the light. This corresponds to the nonlinear Kerr effect. The experimental study of this phenomenon can be used for the spectroscopy of opaque crystals as well as for studying the near-surface states of such crystals. Specifically, in media with isotropic linear characteristics the anisotropy of the nonlinear response starts to play a large role, which could be a source of unique information about the fine details of the crystal structure.[2]

The experimental investigations of the induced Faraday and Kerr effects in CsI_3 and CuCl crystals[3] have demonstrated the possibility of ''in reflection'' spectroscopy for exciton diagnostics.

The present paper investigates theoretically the nonlinear Kerr effect arising on reflection of a monochromatic light wave with arbitrary elliptical polarization from the boundary of a semiinfinite magnetic crystal. The case of normal incidence in the direction of magnetization of the crystal (polar effect) is studied.

1. FIELD OF THE REFLECTED WAVE

The polarization characteristics of the reflected light wave — the azimuth Φ of the polarization ellipse and the degree of ellipticity B — can be found if the electric field vector of the wave, which is determined by solving the corresponding boundary value problem, is known.

Let the $z=0$ plane be the interface of the two media — vacuum–nonlinear crystal and let the Oz axis be oriented in the [001] direction. Then the electric field $\mathbf{E}=(E_x,E_y,0)$ of the wave in the crystal is determined from the wave equation

$$\frac{d^2\mathbf{E}(z)}{dz^2}+\frac{\omega^2}{c^2}(\mathbf{D}^{\mathrm{L}}(z)+\mathbf{D}^{\mathrm{NL}}(z))=0, \tag{1}$$

where $\mathbf{D}^{\mathrm{L}}=\hat{\varepsilon}\mathbf{E}$ and $\mathbf{D}^{\mathrm{NL}}=\hat{\chi}\mathbf{EEE}$ are the linear and nonlinear parts of the electric induction vector, respectively.

For simplicity we shall confine our attention to the case where the magnetic field or spontaneous magnetization of the crystal are directed along the high-symmetry axis Oz of the crystal, since the investigation of the effect in crystals with a lower symmetry does not present any fundamental difficulties and does not change the essential features but does lead to much more complicated results. The transverse linear permittivity tensor has the form

$$\hat{\varepsilon}=\begin{pmatrix} \varepsilon & i\varepsilon' \\ -i\varepsilon' & \varepsilon \end{pmatrix} \tag{2}$$

Here $\varepsilon=\varepsilon_{xx}^{(0)}=\varepsilon_{yy}^{(0)}, i\varepsilon'=\varepsilon_{xy}^{(m)}$, and the tensor $\hat{\varepsilon}=\hat{\varepsilon}^{(0)}+\hat{\varepsilon}^{(m)}$ is represented as a sum of purely optical $\hat{\varepsilon}^{(0)}$ and magnetooptical $\hat{\varepsilon}^{(m)}$ parts.

For crystals with weak nonlinearity Eq. (1) can be solved in the fixed-field approximation, where the vector $\mathbf{D}^{\mathrm{NL}}(z)$ is assumed to be known and is determined by the field $\mathbf{E}^0(z)$ — the solution of the corresponding linear problem.

In the circular variables $E_\pm(z)=E_x(z)\pm iE_y(z)$ the system of equations (1) acquires the form

$$\left[\frac{d^2}{dz^2}+\frac{\omega^2}{c^2}(\varepsilon\pm\varepsilon')\right]E_\pm(z)=-\frac{\omega^2}{c^2}D_\pm^{\mathrm{NL}}(z). \tag{3}$$

Setting $D_\pm^{\mathrm{NL}}(z)=0$ in Eq. (3), we find the field in the linear crystal

$$E_\pm^0(z)=E_\pm^0(0)\exp(ik_\pm z). \tag{4}$$

Here $k_\pm=(\omega/c)\sqrt{\varepsilon\pm\varepsilon'}$ are the wave numbers of the normal circularly polarized waves and $E_\pm^0(0)$ are the amplitudes of the transmitted waves, determined by solving the linear boundary-value problem.

We shall assume that the wave incident on the crystal has arbitrary elliptical polarization, and

$$\mathbf{E}^i(z)=(a_1e^{i\varphi_1}\mathbf{e}_x+a_2e^{i\varphi_2}\mathbf{e}_y)\exp(ikz), \tag{5}$$

where $\mathbf{e}_{x,y}$ are the unit vectors along the Ox and Oy axes. We shall represent the field $\mathbf{E}^R(z)$ of the reflected wave and the field $\mathbf{E}^T(z)$ of the wave transmitted into the crystal in the form

$$\mathbf{E}^R(z)=(E_x^R\mathbf{e}_x+E_y^R\mathbf{e}_y)e^{-ikz}, \tag{6}$$

$$\mathbf{E}^T(z)=\frac{1}{2}(E_+^T(z)e^{ik_+z}+E_-^Te^{ik_-z})\mathbf{e}_x$$

$$-\frac{1}{2}(E_+^T(z)e^{ik_+z}+E_-^Te^{ik_-z})\mathbf{e}_y. \quad (7)$$

The amplitudes of the waves $E_\pm^T(0), E_\pm^R=E_x^R\pm iE_y^R$ are determined from the system of equations[4]

$$E_\pm^T(0)-E_\pm^R=a_\pm,$$

$$k_\pm E_\pm^T(0)=kE_\pm^R=ka_\pm+iS_\pm \quad (8)$$

and are

$$E_\pm^R=E_\pm^{0R}+\delta E_\pm^R, \quad (9)$$

$$E_\pm^T(0)=E_\pm^{0T}+\delta E_\pm^T. \quad (10)$$

In these expressions $a_\pm=a_1e^{i\varphi_1}\pm ia_2e^{i\varphi_2}$,

$$E_\pm^{0R}=r_\pm a_\pm, \quad (11)$$

$$E_\pm^{0T}=t_\pm a_\pm \quad (12)$$

are the amplitudes of the reflected and transmitted waves obtained by solving the linear problem, $r_\pm=(k-k_\pm)/(k+k_\pm)$ and $t_\pm=2k/(k+k_\pm)$ are, respectively, the linear reflection and refraction coefficients

$$\delta E_\pm^R=\delta E_\pm^T=\frac{iS_\pm}{k+k_\pm} \quad (13)$$

are the corrections to the amplitudes due to the self-action of light in the crystal,

$$S_\pm=\left.\frac{dE_\pm^T(z)}{dz}\right|_{z=0}. \quad (14)$$

The field amplitudes $E_\pm^T(z)$ of the wave transmitted into the nonlinear crystal can be found from Eq. (1), where the nonlinear induction vector must be set equal to

$$\mathbf{D}^{\mathrm{NL}}(z)=4\pi\hat{\chi}\mathbf{E}^{0T}(z)\mathbf{E}^{0T}(z)\mathbf{E}^{0T}(z). \quad (15)$$

Here the electric field vector $\mathbf{E}^{0T}$ is determined by Eqs. (4) and (12) and possesses circular components

$$E_\pm^0(z)=t_\pm A_\pm\exp(ik_\pm z+i\delta_\pm), \quad (16)$$

where

$$A_\pm=\sqrt{a_1^2+a_2^2-2a_1a_2\sin(\varphi_2-\varphi_1)}, \quad (17)$$

$$\delta_\pm=a\tan\left(\frac{a_1\sin\varphi_1\pm a_2\cos\varphi_2}{a_1\cos\varphi_1\mp a_2\sin\varphi_2}\right), \quad (18)$$

and $\beta=(1/2)(\delta_+-\delta_-)$ determines the angle between the major axis of the polarization ellipse and the abscissa.

Like the permittivity tensor of the crystal, we shall represent the cubic nonlinear susceptibility $\hat{\chi}$ as a sum of the optical and magnetooptical parts $\hat{\chi}=\hat{\chi}^{(0)}+\chi^{(m)}$. In the problem at hand the following components of the susceptibility will be nonzero:

$$\chi_1=\chi_{xxxx}^{(0)}=\chi_{yyyy}^{(0)},\quad \chi_2=\chi_{xxyy}^{(0)}=\chi_{yyxx}^{(0)},$$

$$\chi_3=\chi_{xyxy}^{(0)}=\chi_{yxxy}^{(0)},\quad \chi_4=\chi_{xyxy}^{(0)}=\chi_{yxyx}^{(0)},$$

$$i\eta_1=-\chi_{yyyx}^{(m)}=\chi_{xxxy}^{(m)},\quad i\eta_2=-\chi_{yxxx}^{(m)}=\chi_{xxyx}^{(m)},$$

$$i\eta_3=-\chi_{yxyy}^{(m)}=\chi_{xyxx}^{(m)},\quad i\eta_4=-\chi_{xyyy}^{(m)}=\chi_{yxxx}^{(m)}.$$

Calculating the vector $\mathbf{D}^{\mathrm{NL}}(z)$ and substituting it into Eq. (1) we obtain expressions for the field of the wave in the nonlinear crystal[4] and for $S_\pm$

$$S_\pm=\frac{i\pi\omega^2t_\pm A_\pm e^{i\delta_\pm}}{4c^2k_\pm}\Big[2A_\mp^2t_\mp^2[\chi_1+\chi_3\pm(\eta_2-\eta_4)]$$

$$+A_\pm^2t_\pm^2[\chi_1+\chi_2-\chi_3+\chi_4\mp(\eta_1-\eta_2-\eta_3+\eta_4)]$$

$$+2\frac{k_\pm}{k_\mp}A_\mp^2t_\mp^2e^{\mp4i\beta}[\chi_1-\chi_2-\chi_3-\chi_4$$

$$\mp(\eta_1+\eta_2+\eta_3+\eta_4)]\Big]. \quad (19)$$

2. POLARIZATION OF THE REFLECTED WAVE

The azimuth of the polarization ellipse and the degree of ellipticity of the wave reflected from the nonlinear crystal can be found using the relations

$$\tan 2\Phi=\frac{\mathrm{Im}\,(E_+^RE_-^{R*})}{\mathrm{Re}\,(E_+^RE_-^{R*})}, \quad (20)$$

$$B=\frac{|E_+^R|^2-|E_-^R|^2}{|E_+^R|^2+|E_-^R|^2}. \quad (21)$$

For our case of weakly nonlinear crystals $|\delta E_\pm^R|\ll|E_\pm^{0R}|$, and therefore we can set $\Phi=\beta+\Phi^{\mathrm{L}}+\Phi^{\mathrm{NL}}$ and $B=B^{\mathrm{L}}+B^{\mathrm{NL}}$. Moreover, for simplicity we shall confine our attention to media with weak magnetization ($\varepsilon'\ll\varepsilon$). Then we obtain for the polarization characteristics of the wave reflected from a linear crystal

$$\Phi^{\mathrm{L}}=-\frac{\mathrm{Im}\,\varepsilon'}{\sqrt{\varepsilon}(\varepsilon-1)}, \quad (22)$$

$$B^{\mathrm{L}}=B_0+(1-B_0^2)\frac{\mathrm{Re}\,\varepsilon'}{\sqrt{\varepsilon}(\varepsilon-1)}, \quad (23)$$

where

$$B_0=\frac{A_+^2-A_-^2}{A_+^2+A_-^2} \quad (24)$$

is the degree of ellipticity of the incident wave.

The nonlinear corrections to the rotation angle of the polarization ellipse and the degree of ellipticity of the reflected wave are determined by the expressions

$$\Phi^{\mathrm{NL}}=\frac{1}{2r_+r_-A_+A_-}\Big[\mathrm{Re}\left(\frac{E_-^{0R}S_+^*}{k+k_+}-\frac{E_+^{0R}S_-^*}{k+k_-}\right)\cos2\beta$$

$$-\mathrm{Im}\left(\frac{E_-^{0R}S_+^*}{k+k_+}-\frac{E_+^{0R}S_-^*}{k+k_-}\right)\sin2\beta\Big], \quad (25)$$

$$B^{\mathrm{NL}}=\frac{4}{(|E_+^{0R}|^2+|E_-^{0R}|^2)^2}\times\mathrm{Im}\left(\frac{|E_+^{0R}|^2E_-^{0R}S_-^*}{k+k_-}-\frac{|E_-^{0R}|^2E_+^{0R}S_+^*}{k+k_+}\right). \quad (26)$$

Substituting the values of $S_\pm$ from Eq. (19) into Eqs. (25) and (26) we find, up to higher-order infinitesimals, an expression for the nonlinear optical rotation angle of the reflected light wave in the form of a sum of five terms

$$\Phi^{\mathrm{NL}}=\sum_{i=1}^{5}\Phi_i, \quad (27)$$

corresponding to different physical mechanisms of the interaction of the waves in the crystal.

The first term was obtained in Ref. 4. It is associated with the anisotropy of the nonlinear optical susceptibility of the crystal and is given by

$$\Phi_1=2KI_0\,\mathrm{Re}\,(\chi_1-\chi_2-\chi_3-\chi_4)\sin 4\beta, \quad (28)$$

where

$$K=\frac{8\pi^2k^6}{ck_0(k^2-k_0^2)^2(k+k_0)}$$

and $I_0=(c/4\pi)(A_+^2+A_-^2)$ is the intensity of the incident light.

The angle

$$\Phi_2=KI_0\,\mathrm{Im}\,[\eta_1+\eta_2+\eta_3-3\eta_4+2(\eta_1+\eta_2+\eta_3+\eta_4)\cos 4\beta] \quad (29)$$

is due to the nonlinear absorption of light as a result of a magnetooptic interaction in the crystal.

The other terms in Eq. (27) are all associated with the finite ellipticity of the incident radiation. Specifically, the angle Φ_3 describes the combined effect of linear magnetic gyrotropy and the nonlinear optical interaction of the waves

$$\Phi_3=\frac{\omega^2\mathrm{Re}\,\varepsilon'}{c^2k_0^2}\frac{(2k_0+k)}{(k+k_0)}KI_0B_0\times\mathrm{Re}\,(\chi_1-\chi_2-\chi_3-\chi_4)\sin 4\beta. \quad (30)$$

In transmitted light the nonlinear Faraday effect is associated with the imaginary part of the nonlinear magnetooptic susceptibility,[5] while in the reflected light this mechanism gives rise to rotation described by the angle

$$\Phi_4=-2KI_0B_0\,\mathrm{Re}\,(\eta_1+\eta_2+\eta_3+\eta_4)\sin 4\beta. \quad (31)$$

Finally, the angle Φ_5 is the analog of the Maker–Terhune–Savage effect[6] ''in reflection'' and is determined by the expression

$$\Phi_5=KI_0B_0\,\mathrm{Im}\,[\chi_1-\chi_2+3\chi_3+\chi_4-2(\chi_1-\chi_2-\chi_3-\chi_4)\cos 4\beta]. \quad (32)$$

In experiments with linearly polarized light, the real radiation possesses finite ellipticity $B_0\geqslant 10^{-2}$,[7] so that the terms $\Phi_3-\Phi_5$ must be assumed to be different from zero for a linearly polarized incident wave also.

To estimate the relative contributions of different wave-interaction mechanisms to the effect we set $\mathrm{Re}\,\chi/\mathrm{Im}\,\chi\sim\mathrm{Re}\,\eta/\mathrm{Im}\,\eta=\mu$, $\mathrm{Re}\,\eta/\mathrm{Re}\,\chi\sim\mathrm{Re}\,\varepsilon'\sim\alpha_{\mathrm{F}}/k$, where α_F is the specific linear Faraday rotation. Comparing Eqs. (28)–(32) gives $\Phi_1/\Phi_2\sim\mu k/\alpha_{\mathrm{F}}$, $\Phi_3/\Phi_2\sim B_0\mu$, $\Phi_4\sim\Phi_3$, $\Phi_5/\Phi_2\sim B_0k/\alpha_{\mathrm{F}}$. For ferromagnetic crystals $\alpha_{\mathrm{F}}\sim 10^3$ cm^{-1}. Setting also $\mu\sim 10^2$, $k\sim 10^5$ cm^{-1}, and $B_0\sim 10^{-2}$ we find that the angles $\Phi_2-\Phi_5$ are of the same order of magnitude, and the purely optical rotation Φ_1 is approximately four orders of magnitude greater. In media with an isotropic nonlinear response the latter is identically zero.

On the basis of the estimates made above, we shall retain the largest terms in Eq. (26). As a result, we obtain an expression for the nonlinear degree of ellipticity of the reflected wave in the form

$$B^{\mathrm{NL}}=-\frac{2k^5cA_+^2A_-^2}{(k+k_0)(k^2-k_0^2)^2k_0I_0}\times\mathrm{Re}\left\{(k-k_0)[B_0(-\chi_1+\chi_2-3\chi_3+\chi_4)-2B_0(\chi_1-\chi_2-\chi_3-\chi_4)\cos 4\beta-(\eta_1+3\eta_2+\eta_3-3\eta_4)-2(\eta_1+\eta_2+\eta_3+\eta_4)\cos 4\beta]-\frac{k\varepsilon'}{\sqrt{\varepsilon}k_0(k+k_0)}[(2kk_0+k^2-5k_0^2)\times(\chi_1+\chi_2-\chi_3+\chi_4)+2(k^2-2kk_0-k_0^2)(\chi_1+\chi_3)+2(k_0^2-k^2-2kk_0)(\chi_1-\chi_2-\chi_3-\chi_4)\cos 4\beta]\right\}. \quad (33)$$

Therefore the nonlinear ellipticity depends not on the total intensity of the radiation but rather on the intensities of its circular components.

The extensive use of magnetic crystals in quantum electronics and nonlinear optics raises the question of investigating nonlinear magnetooptic susceptibilities. From this standpoint, the rotation of the polarization of the transmitted light is a quite complicated effect,[5] which requires a more careful interpretation of the corresponding experiments.[8] As has been shown, measurements of the polarization state of the reflected wave can substantially supplement the information obtained from ''in transmission'' measurements. Specifically, this can be accomplished by measuring the nonlinear optical rotation angle as a function of the orientation of the azimuth of the polarization ellipse of the incident radiation. This is especially true for media with strong absorption, where investigations in reflected light are more effective or the only types of measurements that are possible.

*E-mail: info@dgtu.donetsk.ua

[1] R. V. Pisarev, in *The Physics of Magnetic Semiconductors* (Nauka, Leningrad, 1974).
[2] S. A. Akhmanov, V. I. Emel'yanov, and N. I. Koroteev, Usp. Fiz. Nauk **147**, 675 (1985) [Sov. Phys. Usp. **28**, 1084 (1985)].

[3] G. E. Jellisson and D. H. Lowndes, Appl. Opt. **24**, 2948 (1985).
[4] A. D. Petrenko and G. I. Trush, Kristallografiya **37**, 159 (1992) [Sov. Phys. Crystallogr. **37**, 84 (1992)].
[5] Ş. B. Borisov, I. L. Lyubchanskiĭ, A. D. Petrenko, and G. I. Trush, Zh. Éksp. Teor. Fiz. **105**, 524 (1994) [JETP **78**, 279 (1994)].
[6] P. D. Maker, R. W. Terhune, and C. M. Savage, Phys. Rev. Lett. **12**, 507 (1964).
[7] S. A. Bakhramov, A. T. Berdikulov, A. M. Kokhkharov, V. V. Tikhonenko, and P. K. Khabilulaev, Dokl. Akad. Nauk SSSR **309**, 607 (1989) [Sov. Phys. Dokl. **34**, 1018 (1989)].
[8] J. Frey, R. Frey, C. Flytzanis, and R. Triboulet, J. Opt. Soc. Am. B **9**, 132 (1992).

Translated by M. E. Alferieff

Effect of noncrystallographic magnetic anisotropy on magnetization reversal in multilayer magnetic films

M. I. Kurkin and D. Z. Khusainov

Institute of Metal Physics, Ural Division of the Russian Academy of Sciences, 620219 Ekaterinburg, Russia
(Submitted June 2, 1998; resubmitted September 14, 1998)
Fiz. Tverd. Tela (St. Petersburg) **41**, 660–664 (April 1999)

A study has been carried out of the magnetization of a layered system consisting of two exchange-coupled easy-axis ferromagnetic layers separated by a nonmagnetic spacer and having mutually perpendicular anisotropy axes. It is shown that the magnetization of such a system can undergo stepwise decrease with increasing magnetic field. The field dependence of the magnetization has a bifurcation point. The magnetization orientation can exhibit jumps in excess of 90° depending on the angle of magnetic-field orientation. © *1999 American Institute of Physics.* [S1063-7834(99)02104-8]

This paper discusses the magnetic properties of special magnetic films, in which the magnetic layers are, first, separated by nonferromagnetic (Cu, Cr,...) spacers and, second, the spacer thicknesses are small enough that the exchange coupling between adjacent layers exceeds the interactions responsible for the magnetic anisotropy,[1] i.e.

$$H_E > H_A, \tag{1}$$

where H_E is the effective interlayer exchange interaction field, and H_A is the magnetic anisotropy field. We assume here that the magnetic anisotropy is of a noncrystallographic nature, because the effect of crystallographic anisotropy was already investigated earlier[2,3]. The nature of the noncrystallographic anisotropy may be associated with the influence of the substrate or with the growth kinetics of individual layers, and its contribution in weakly anisotropic magnets may even turn out to be dominant.[4]

One of the features inherent in noncrystallographic magnetic anisotropy consists in that one can orient in a desired way the easy magnetization axes of different film layers. If the exchange coupling between these layers is weak, $H_E \ll H_A$, the total moment of such films is determined by competition between two factors, namely, the magnetic anisotropy field H_A and the external magnetic field H. In this case the magnetization of the films will be described by monotonically rising curves.[4]

In our case of $H_E > H_A$, the film moment will be the result of an interplay among three fields, H_A, H, and H_E. Their combined action produces more possible versions than can be expected with two factors so that the magnetization curves may exhibit declining portions under certain conditions. They will reflect a decrease of the projection of magnetization M on the direction of magnetic field H with increasing H (as is the case with diamagnetic substances).

The possible appearance of declining portions in the magnetization curves of weak ferromagnets was already pointed out.[5] This situation can be realized if the Dzyaloshinsky interaction responsible for weak ferromagnetism generates at the same time a magnetic anisotropy, in which case it will act as the third factor in a competition between H and the antiferromagnetic exchange field H_E to produce the resultant magnetization.

1. BASIC RELATIONS

The simplest system which can have a declining portion in the magnetization curve consists of two ferromagnetic layers with magnetizations $\mathbf{M}_1$ and $\mathbf{M}_2$ separated by a nonferromagnetic spacer. The layers are coupled through antiferromagnetic interaction

$$F_{ex} = H_E(\mathbf{M}_1\mathbf{M}_2)/M_0, \tag{2}$$

where H_E is the effective exchange field ($H_E > 0$), and $M_0 = |\mathbf{M}_1| = |\mathbf{M}_2|$. In each layer there is uniaxial magnetic anisotropy with an easy magnetization axis. The directions of the axes are given by unit vectors $\mathbf{c}_1$ and $\mathbf{c}_2$ ($|\mathbf{c}_1| = |\mathbf{c}_2| = 1$):

$$F_A = -H_A(\mathbf{M}_0\mathbf{c}_1)^2/M_0 - H_A(\mathbf{M}_0\mathbf{c}_2)^2/M_0, \tag{3}$$

where H_A is the effective magnetic-anisotropy field. For $\mathbf{c}_1 \| \mathbf{c}_2$, the film under consideration does not differ in magnetic properties from the well-studied uniaxial antiferromagnet.[5] Features of the type of declining portions appear in magnetization curves when the $\mathbf{c}_1$ and $\mathbf{c}_2$ axes are misoriented. We shall limit ourselves here to the $\mathbf{c}_1 \perp \mathbf{c}_2$ case, where these features are most strongly pronounced.

To describe properly the magnetization and magnetization reversal processes in the three-layer film under study, one has to take into account the interaction with the external magnetic field $\mathbf{H}$, which can be presented in the form

$$F_Z = -(\mathbf{M}_1 + \mathbf{M}_2)\cdot\mathbf{H}. \tag{4}$$

Although we assume the $\mathbf{c}_1$, $\mathbf{c}_2$, and $\mathbf{H}$ vectors to lie in the film plane, nevertheless under certain conditions (under hard-axis magnetization) the $\mathbf{M}_1$ and $\mathbf{M}_2$ vectors can deflect from this plane. We disregard these possibilities by assuming the $\mathbf{M}_1$ and $\mathbf{M}_2$ vectors to be confined to the film plane by a strong demagnetizing field $4\pi M_0 \gg H_E$.

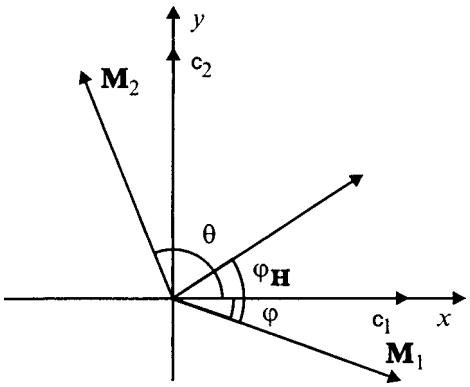

FIG. 1. Mutual orientation of the external magnetic field **H**, magnetizations $\mathbf{M}_1$ and $\mathbf{M}_2$, and easy magnetization axes $\mathbf{c}_1$ and $\mathbf{c}_2$.

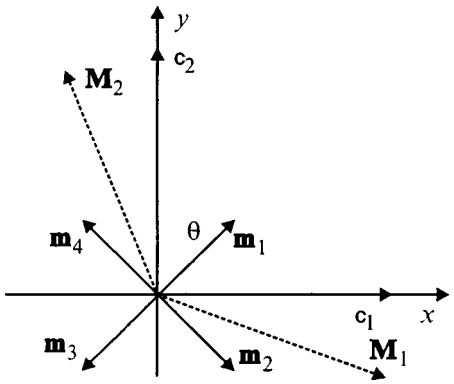

FIG. 2. Possible orientations of net magnetization vectors $\mathbf{m}_1$, $\mathbf{m}_2$, $\mathbf{m}_3$, and $\mathbf{m}_4$ in zero field. Dashed lines depict the magnetization vectors $\mathbf{M}_1$ and $\mathbf{M}_2$ which add to produce the $\mathbf{m}_1=\mathbf{M}_1+\mathbf{M}_2$ vector.

The equilibrium orientations of the magnetic moments $\mathbf{M}_1$ and $\mathbf{M}_2$ are given by angles θ and φ (Fig. 1), which can be found by minimizing the total energy

$$F=F_{ex}+F_A+F_Z. \tag{5}$$

In view of Eqs. (2)–(4), the conditions of the minimum can be written

$$\partial F/\partial\theta=-H_E\sin\theta-\frac{1}{2}H_A\sin 2(\theta-\varphi)$$
$$-H\sin(\varphi_H+\varphi-\theta)=0, \tag{6}$$

$$\partial F/\partial\varphi=\frac{1}{2}H_A[\sin 2\varphi+\sin 2(\theta-\varphi)]$$
$$+H[\sin(\varphi_H+\varphi)+\sin(\varphi_H+\varphi-\theta)]. \tag{7}$$

For $H=0$, to the minimum in F correspond four roots of Eqs. (6) and (7)

$$\varphi_{1,2}=(\pm\pi/4-\delta\theta/2),\quad \varphi_{3,4}=\pm(3\pi/4+\delta\theta/2),$$
$$\theta=\pi-\delta\theta,$$
$$\tan(\delta\theta)=H_A/2H_E. \tag{8}$$

They describe canted $\mathbf{M}_1$ and $\mathbf{M}_2$ structures with the total moment

$$m=2M_0\sin(\delta\theta/2)=M_0H_A/2H_E, \tag{9}$$

which is the result of competing interactions F_{ex} (2) and F_A (3). The orientation of vectors $\mathbf{m}_1$, $\mathbf{m}_2$, $\mathbf{m}_3$, and $\mathbf{m}_4$ corresponding to the four roots of Eq. (8) is shown in Fig. 2. The dashed lines in the figure specify vectors $\mathbf{M}_1$ and $\mathbf{M}_2$ which add to yield vector $\mathbf{m}_1=\mathbf{M}_1+\mathbf{M}_2$. The orientations of $\mathbf{M}_1$ and $\mathbf{M}_2$ for the three other vectors, $\mathbf{m}_2$, $\mathbf{m}_3$, and $\mathbf{m}_4$, are not shown to avoid burdening the figure with unnecessary details.

The second effect due to competition between F_{ex} (2) and F_A (3) is the weakening of the effective magnetic-anisotropy field F_A^{eff} acting on vectors **m** (9) compared to the field F_A acting on $\mathbf{M}_1$ and $\mathbf{M}_2$. To calculate field F_A^{eff}, one has to express angle θ through φ using (6) for $H=0$ and insert the relations thus obtained in Eq. (5). For $H_A\ll H_E$, which is the lowest approximation with respect to H_A/H_E, this substitution yields

$$F(\varphi)=-H_EM_0-H_AM_0/2-M_0(H_A^2/8H_E)\sin^2(2\varphi). \tag{10}$$

The last term in Eq. (10) refers to the effective magnetic anisotropy of the film under study. It is periodic with respect to φ with a period of $\pi/2$ [rather than π, as is the case with other orientations of $\mathbf{c}_1$ and $\mathbf{c}_2$], and its effective field

$$H_A^{\text{eff}}=H_A^2/2H_E \tag{11}$$

is $H_A/2H_E$ times lower than the field F_A determining the moment m (9).

2. MAGNETIZATION CURVES

The existence of four roots of Eqs. (6) and (7) for $H=0$ implies that the film under study can have a domain structure with domains of four types. As will be shown later, however, the film can be transferred to a single-domain state by magnetizing it to saturation along one of the **m** vectors (Fig. 2). It is the processes of magnetization reversal in such a single-domain film that we are going to consider in this Section.

These processes are described by the solutions of Eqs. (6) and (7) obtained for $H\neq 0$. The form of these solutions depends essentially on the orientation of **H** with respect to the c_1 axis (Fig. 1). Figure 3 displays magnetization reversal curves corresponding to the angles $\varphi_H=\pi/4$ (solid line) and $\varphi=-\pi/4$ (dashed line). One immediately sees the following characteristic features in these curves:

1. The presence of self-crossing points 1 and 1'.

This implies the existence of two different states with the same $\mathbf{m}(H)=\mathbf{M}_1+\mathbf{M}_2$ vectors. In one of them, the $\mathbf{M}_1$ and $\mathbf{M}_2$ vectors are oriented along the easy axes, $\mathbf{M}_1\|\mathbf{c}_1$ and $\mathbf{M}_2\|\mathbf{c}_2$, which corresponds to the minimum in F_A (3), and in the other, they are aligned with the hard-magnetization axes, $\mathbf{M}_1\perp\mathbf{c}_1$ and $\mathbf{M}_2\perp\mathbf{c}_2$, the situation corresponding to the maximum in F_A. In both cases, the magnetic anisotropy does not affect the magnitude of the moment m, and with respect to the other two interactions, F_{ex} (2) and F_z (4), these two orientations are completely equivalent (see Fig. 1 for $\varphi_H=\pi/4$, $\varphi=0$, and $\theta=\pi/2$).

2. The presence of declining portions in fields $H=H_2$ and $H=H_{2'}$.

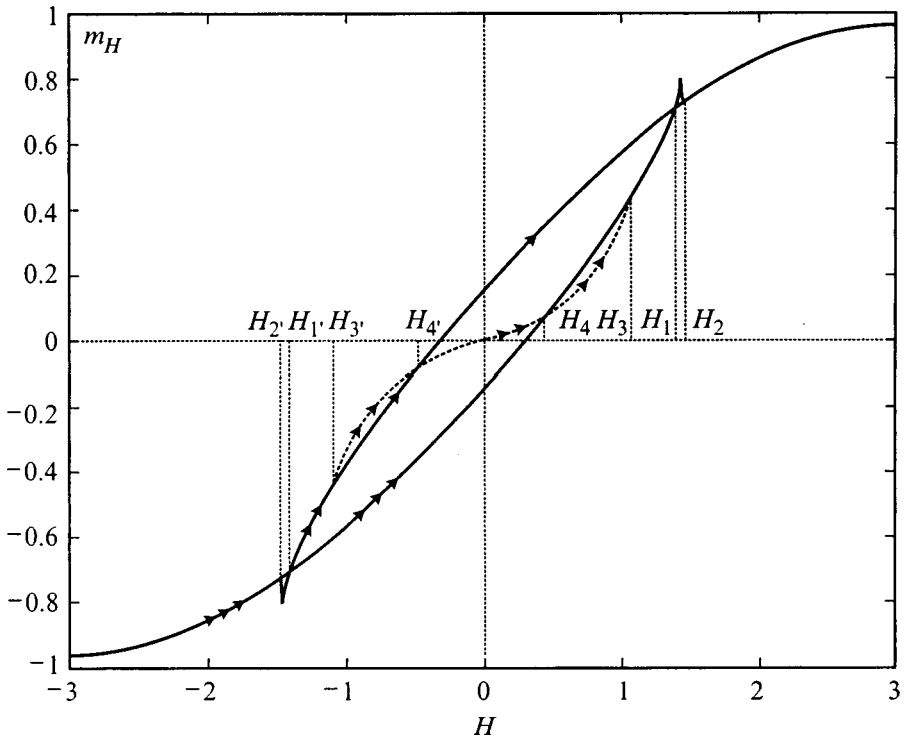

FIG. 3. Dependence of the magnetization projection on magnetic field on the field (the magnetization is expressed in units of magnetic moment $2M_0$, and the field, in units of H_E) in the case where the field orientation $\varphi_H=\pi/4$ and $-\pi/4$, and the anisotropy parameter $H_A/H_E=0.6$. The solid portion of the curve relates to the field oriented at an angle $\varphi_H=\pi/4$, and in the case of $\varphi_H=-\pi/4$ a dashed portion appears provided sample magnetization starts with fields $H<H_3$.

For $|H|<|H_2|=|H_{2'}|$, there exist two stable configurations of vectors $\mathbf{M}_1$ and $\mathbf{M}_2$ with respect to $\mathbf{H}$ (Fig. 4). In one of them, the angle between $\mathbf{M}_1$ and its easy axis $\mathbf{c}_1$ is larger than that between $\mathbf{M}_1$ and its hard axis $\mathbf{c}_2$, i.e. $(\mathbf{M}_1\mathbf{c}_1)<(\mathbf{M}_1\mathbf{c}_2)$ and, similarly, $(\mathbf{M}_2\mathbf{c}_2)<(\mathbf{M}_2\mathbf{c}_1)$. When in this state, the magnetic anisotropy favors an increase in the projections of $\mathbf{M}_1$ and $\mathbf{M}_2$ on the $\mathbf{H}$ field. In the second state with $(\mathbf{M}_1\mathbf{c}_1)>(\mathbf{M}_1\mathbf{c}_2)$ and $(\mathbf{M}_2\mathbf{c}_2)>(\mathbf{M}_2\mathbf{c}_1)$, which lies lower in energy than the first one, the magnetic anisotropy together with the exchange coupling F_{ex} (2) impedes alignment of $\mathbf{M}_1$ and $\mathbf{M}_2$ with H. As a result, the total moment $\mathbf{m}=|\mathbf{M}_1+\mathbf{M}_2|$ in the first state turns out to be larger than that in the second one.

For $H=|H_2|$, the first state with a higher energy loses stability, and the system jumps over into the second, lower state with a smaller $m=|\mathbf{M}_1+\mathbf{M}_2|$.

3. The presence of a branching point 3 corresponding to a second-order phase transition.

Point 3 is the merging point of the magnetization curves of two different states, with $\mathbf{m}(0)\uparrow\downarrow\mathbf{H}$ (solid line in Fig. 3) and with $\mathbf{m}(0)\perp\mathbf{H}$ (dashed line in Fig. 3). In the course of magnetization reversal from the $\mathbf{m}(0)\uparrow\downarrow\mathbf{H}$ state, the H field changes the angle between $\mathbf{M}_1$ and $\mathbf{M}_2$. In the second case, $\mathbf{m}(0)\perp\mathbf{H}$, magnetization reversal occurs in two stages. First the magnetic moment turns in the (x,y) plane to become aligned with the H field, while changing little in magnitude (the dashed portion of the magnetization curve in Fig. 3). This process comes to an end at $H=H_3$ $[\mathbf{m}(H_3)\|\mathbf{H}]$, after which the system forgets its initial state, and further magnetization occurs as in the $\mathbf{m}(0)\uparrow\downarrow\mathbf{H}$ case.

For $H>0$, the curves in Fig. 3 depict the magnetization of the various domains corresponding to the four solutions of Eqs. (6) and (7) (for $H=0$). The upper branch of the hysteresis loop corresponds to magnetization of the domains with $\mathbf{m}(0)\uparrow\uparrow\mathbf{H}$, the lower one, to that of the $\mathbf{m}\uparrow\downarrow\mathbf{H}$ domains, and the dashed curve, to the $\mathbf{m}(0)\perp\mathbf{H}$ domains. For $H>H_2$ only one curve is seen to be left, i.e. the film becomes single domain (if it was a multidomain one for $H=0$).

Consider now the film magnetization reversal processes corresponding to changes in $m_H(H)$ with decreasing field H. If H is lowered starting from $H>H_2$, the behavior of $m_H(H)$ will follow that of the upper hysteresis-loop branch in Fig. 3. Repeated magnetization (i.e. the variation of $m_H(H)$ with increasing H) depends on the point on this branch from which H will start to increase. If it does it from a value $H<H_2=-H_2$, the magnetization reversal will follow the lower branch of the loop (triple arrow). If this point lies within $H_{2'}<H<H_{3'}$, then up to $H=H_{3'}$ the quantity $m_H(H)$ will follow the upper branch of the hysteresis loop, to transfer subsequently (after the $H=H_{3'}$ point) to the lower branch by the dashed line (double arrow in Fig. 3).

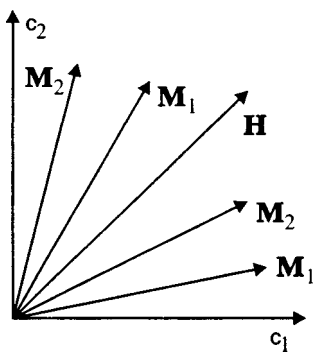

FIG. 4. Two possible configurations of $\mathbf{M}_1$ and $\mathbf{M}_2$ vectors for fields $H<H_2$.

Finally, if H is lowered starting from a value $H>H_{3'}=-H_3$, $m_H(H)$ will remain on the upper branch of the loop, so that the magnetization reversal will avoid hysteresis (single arrow).

In conclusion to this Section, a note concerning the dependence of $m_H(H)$ on the angle between the $\mathbf{c}_1$ and $\mathbf{c}_2$ axes is appropriate (Fig. 1). As already mentioned, the features in the magnetization reversal curves discussed are maximum for $\mathbf{c}_1 \perp \mathbf{c}_2$. As the angle between $\mathbf{c}_1$ and $\mathbf{c}_2$ decreases, points 1 and 2 (1' and 2') on these curves approach one another and, hence, the jump in $m_H(H)$ occurring at $H=H_2$ and $H=H_{2'}$ decreases. For $\mathbf{c}_1 \| \mathbf{c}_2$, the three-layer film considered here does not differ in magnetic properties from an easy-axis antiferromagnet if H lies in the film plane. If a film is magnetized normal to its surface, one has to take into account the demagnetizing field $4\pi M_0$ which was neglected in our calculations.

4. Magnetization curves in a rotating magnetic field.

We have presented above the results of calculations of the $m_H(H)$ quantities made for two orientations of H ($\varphi_H=\pm\pi/4$). Because the magnetization reversal curves obtained for other values of φ_H differ substantially, we analyzed also the orientation dependences of two magnetic characteristics, namely, of the net film moment $m=|\mathbf{M}_1+\mathbf{M}_2|$ and of its projection m_H on the magnetic field vector. It is these characteristics that were chosen for the analysis, because they are usually studied by various experimental methods. The quantity m_H can be most conveniently determined from magnetic measurements, while m can be derived also from magnetoresistance data.

The results of the calculations displayed graphically in Fig. 5 correspond to the ratio $H_A/H_E=0.6$. Along the horizontal axis is plotted the angle φ'_H, which, in contrast to φ_H, is reckoned from the equilibrium orientation $m(0)$ rather than from the $\mathbf{c}_1$ axis. The values of the field H for which the angular dependences $m(H,\varphi'_H)$ and $m_H(H,\varphi'_H)$ were calculated are specified in the caption to Fig. 5. For $H/H_E \ll 1$, we have $m(H,\varphi'_H) \cong m(0)$ and $m_H(H,\varphi'_H) \propto \cos(\varphi'_H)$ (in Fig. 5 this case is not presented). As H increases, the minimum in the $m_H(H,\varphi'_H)$ curve splits at $\varphi'_H=\pi$ into two minima, at $\varphi'_H \approx 2$ and $\varphi'_H \approx 4$, and a maximum appears at $\varphi'_H \approx \pi$ (Fig. 5). As H increases still further, a similar maximum forms in the $m(H,\varphi'_H)$ dependence as well. The behavior of $m_H(H,\varphi'_H)$ and $m(H,\varphi'_H)$ undergoes a qualitative change at $H=H_A$, where the minima at $\varphi'_H \approx 2$ and $\varphi'_H \approx 4$ are replaced by jumps corresponding to reorientation of the $\mathbf{m}=\mathbf{M}_1+\mathbf{M}_2$ vector to a new equilibrium state (Fig. 5b). The magnitude of these jumps, δm and δm_H, depends on the H_A/H_E ratio. In the case under study, $H_A/H_E=0.6$, we obtain $\delta m \approx \delta m_H \approx 0.25\,(2M_0)$, where $2M_0$ is the magnetic moment of a saturated film. This means that the magnetoresistance of a film exhibiting a giant magnetoresistance $\Delta\rho=\rho(0)-\rho(2H_E)$ will undergo a substantial change

$$\delta\rho/\Delta\rho = \delta m/2M_0 \approx 0.25. \tag{12}$$

However as H_A/H_E decreases, the $\delta\rho/\Delta\rho$ ratio decreases too. For instance, for $H_A/H_E=0.2$ we obtained $\delta\rho/\Delta\rho \approx 0.1$.

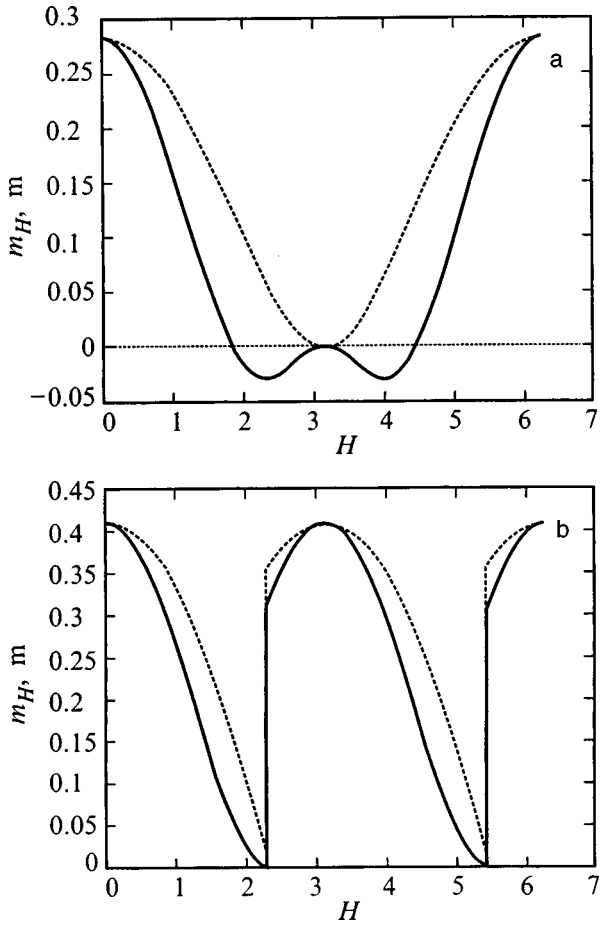

FIG. 5. Dependence of the magnetization projection m_H (solid line) on magnetic field and of the modulus of magnetization m (dashed line) on angle φ'_H between the field H and equilibrium magnetization $m(0)$ (the magnetization is expressed in units of magnetic moment $2M_0$, the anisotropy parameter $H_A/H_E=0.6$). (a) $H/H_E=0.3$, (b) $H/H_E=0.6$.

For $H>H_A$, the jumps in m and m_H occurring at $\varphi'_H \approx 2$ and ≈ 4 are retained within the field interval $H_A \leqslant H \leqslant 2H_A$ while decreasing in magnitude. Finally, for $H>H_E$ the $m(H,\varphi'_H)$ and $m_H(H,\varphi'_H)$ dependences transform to $m(H,\varphi'_H) \approx 2M_0 + k\cos(\varphi'_H)$ and $m_H(H,\varphi'_H) \approx 2M_0 + k_H\cos(\varphi'_H)$, with the coefficients of proportionality k and k_H vanishing at $H=2H_E$.

The authors owe sincere gratitude to N. G. Bebenin for stimulating discussions.

Support of the Russian Fund for Fundamental Research (Grant 96-02-16489) is gratefully acknowledged.

[1] R. E. Camley and R. L. Stamps, J. Phys.: Condens. Matter **5**, 3727 (1993).
[2] B. Dieny, J. P. Gavigan, and J. P. Rebouillat, J. Phys.: Condens. Matter **2**, 159 (1990).
[3] B. Heinrich and J. F. Cochran, Adv. Phys. **42**, 523 (1993).
[4] *The Properties of Single-Crystal Films of Magnetically Ordered Substances* [in Russian] (Kirenskiĭ Inst., Krasnoyarsk, 1978).
[5] E. A. Turov, *Physical Properties of Magnetically Ordered Crystals* [in Russian] (AN SSSR, Moscow, 1963).

Translated by G. Skrebtsov

Inhomogeneous magnetostriction states in uniaxial ferromagnetic films

Yu. I. Bespyatykh and I. E. Dikshteĭn

Institute of Radio Engineering and Electronics, Russian Academy of Sciences, 141120 Fryazino, Moscow District, Russia

(Submitted September 21, 1998)
Fiz. Tverd. Tela (St. Petersburg) **41**, 665–671 (April 1999)

Surface magnetoelastic Love waves and nonuniform distributions of the magnetization and elastic strains are investigated in a uniaxial ferromagnetic film on a massive nonmagnetic substrate in a tangential external magnetic field. A new inhomogeneous phase is predicted having spatial modulation of the order parameter, arising from magnetostrictive coupling of the magnetization with lattice strains near the interface of the magnetoelastic and elastic media. It is shown that, at some critical magnetic field H_c, different from the orientational transition field in an isolated sample, a magnetoelastic Love wave propagating parallel to the magnetization vector in the film plane becomes unstable. The frequency and group velocity of the wave vanish at wave number $k=k_c\neq 0$ and the wave freezes, forming a domain structure localized in the film and adjoining substrate. © *1999 American Institute of Physics.* [S1063-7834(99)02204-2]

The magnetoelastic interaction plays an important role in the formation of the static and dynamic properties of magnetically ordered crystals. Besides the well-known and widely used magnetoacoustic resonance, there is also the large effect of this interaction on quasistatic magnetization-reversal processes, domain structure, the nonlinear dynamics of magnets, and so on.[1,2] Although the magnetoelastic interaction in magnetic crystals is relatively weak, under certain conditions it leads to effects such as the anomalous decrease of the elastic moduli and change in the dispersion laws of volume and surface magnetoelastic waves near orientational phase transitions.[3–7] The velocity of a Rayleigh wave near the transition point decreases, and the penetration depth of the wave into the crystal increases.[6] New types of waves arise as a result of the magnetoelastic interaction. For example, a shear volume elastic wave in a ferromagnetic crystal with magnetostriction and dipole interaction with certain directions of the external magnetic field transforms into a surface wave.[8] Surface Rayleigh elastic waves,[9–11] Love waves,[12,13] and Stoneley waves[14] can decay, because of the coupling with the magnetic subsystem, by radiation of spin waves into the interior volume of the crystal. Recently, new types of self-localized surface waves have been predicted in magnets.[15] The existence of these waves is entirely due to the magnetoelastic interaction and the nonlinearity of the magnetic subsystem. The investigation of the magnetoelastic-wave spectra makes it possible to determine the type of soft mode by which a phase transition occurs. For example, in thin isolated magnetic films the flexuarl mode is the soft mode.[16]

In the present paper an example of the anomalous behavior of magnetoelastic Love waves in a uniaxial magnetic film on a nonmagnetic substrate is studied. The inhomogeneous magnetostrictional states of the system, which are formed because of the possibility of the energy of long-range fields of magnetoelastic stresses decreasing as a result of stress localization near the film–substrate boundary at a depth of the order of the period of the domain structure, are investigated.

1. FORMULATION OF THE PROBLEM. BASIC EQUATIONS

The appearance of a magnetostrictive superstructure follows from the following simple considerations. If the magnetoelastic interaction constants are small, then under certain conditions the elastic strains and stresses in the system can be assumed to be small and the energy F of the system can be written in the form

$$F=F_m+F_e+F_{me}=\int dv(f_m+f_e+f_{me}), \tag{1}$$

where F_m is the magnetic energy, F_e is the elastic energy of the lattice, F_{me} is the magnetoelastic interaction energy, the elastic energy density f_e is a positive-definite quadratic form

$$F_e\geqslant 0, \tag{2}$$

and the magnetoelastic energy density f_{me} is linear in the strains u_{ik}.

In general, the energy F of the system in the metastable states is minimum, so that the distribution of the magnetization $\mathbf{M}$ and elastic displacements $\mathbf{u}$ in the structure satisfy the equations

$$[\mathbf{M}\times\mathbf{H}_{\text{eff}}]=0, \quad \delta F/\delta\mathbf{u}=\delta(F_e+F_{me})/\delta\mathbf{u}=0, \tag{3}$$

where $\mathbf{H}_{\text{eff}}$ is the effective magnetic field

$$\mathbf{H}_{\text{eff}}=-\delta F/\delta\mathbf{M}=-\delta(F_m+F_{me})/\delta\mathbf{M}. \tag{4}$$

Using the second equation from Eqs. (3) and taking account of the uniformity of f_e and f_{me} with respect to the displacements, it is easy to obtain the relation

$$2F_e+F_{me}=0, \tag{5}$$

whence, together with Eq. (2), follow the conditions

$$F_e+F_{me}=F_{me}/2, \quad F_{me}\leqslant 0. \tag{6}$$

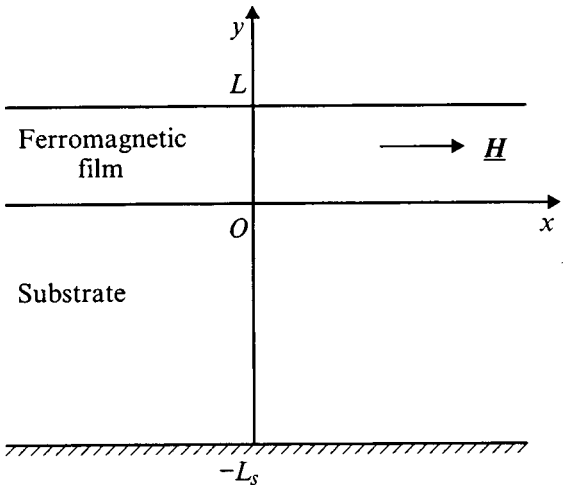

FIG. 1. Geometry of the layer-structure ferromagnetic film–nonmagnetic substrate.

The equal signs in Eqs. (2) and (6) hold only if there are no elastic strains in the system. Hence it follows that, for a given magnetization distribution in the absence of external elastic stresses, the interaction of the magnetic and elastic subsystems can decrease the total energy of the system. The second equation from the equations of state (3) makes it possible in this case to express the displacement uniquely in terms of the magnetization and to switch to the effective magnetic energy, which depends only on the magnetization. The additional contribution from the elastic subsystem to the magnetic energy is negative and nonlocal even when a local approximation is used for the elastic and magnetoelastic energy. If there are no strains and no dipole field in a homogeneous magnetic state (for example, in the film–substrate layered system, where the massive substrate prevents deformation of the film), the magnetoelastic contribution to the energy can lead to instability of the homogeneous phase and the appearance of domain structure. This is also possible under conditions such that domains do not exist at all in a purely magnetic system.

As an example of such behavior of the system, we shall consider the orientational phase transition and the spectrum of magnetoelastic excitations in the layered structure ferromagnetic film–nonmagnetic substrate. Let the magnet possess uniaxial magnetic symmetry, and let the symmetry axis be the easy magnetization axis and oriented parallel to the film plane. It is assumed that the stresses due to the mismatch of the lattice constants of the magnetic material and substrate simply renormalize the anisotropy field and the elastic and magnetoelastic moduli. Moreover, let the substrate be quite massive and its bottom side clamped. This will allow us to assume in what follows the displacements in both direction perpendicular to the unperturbed film surface and in the film plane to be small. The system is placed in a tangential external magnetic field which is perpendicular to the anisotropy axis of the magnet. The geometry of the structure is presented in Fig. 1.

The energy F of the system is

$$F=F_{\text{film}}+F_{\text{subs}}, \tag{7}$$

where the energy of the film F_{film} has the form (1) with

$$F_m=\int_{V_f} dv\left\{-\mathbf{H}\cdot\mathbf{M}-\frac{1}{2}\mathbf{H}_D\cdot\mathbf{M}-\frac{\beta}{2}M_z^2 + \frac{\alpha}{2}\frac{\partial\mathbf{M}}{\partial x_i}\cdot\frac{\partial\mathbf{M}}{\partial x_i}\right\}, \tag{8}$$

$$F_e=\frac{1}{2}\int_{V_f} dv\, C_{ijkl}^{(f)}u_{ij}^{(f)}u_{kl}^{(f)}, \tag{9}$$

$$F_{me}=B\int_{V_f} dv[M_x^2u_{xx}^{(f)}+M_y^2u_{yy}^{(f)}+M_z^2u_{zz}^{(f)}+2(M_xM_yu_{zy}^{(f)} + M_yM_zu_{yz}^{(f)}+M_xM_zu_{xz}^{(f)})], \tag{10}$$

and the energy of the substrate F_{subs} is clearly elastic

$$F_{\text{subs}}=\frac{1}{2}\int_{V_s} dv\, C_{ijkl}^{(s)}u_{ij}^{(s)}u_{kl}^{(s)}. \tag{11}$$

Here $\mathbf{H}\parallel\mathbf{n}_x$ is the external magnetic field, $\mathbf{H}_D=\nabla\Phi$ is the dipole field, $\mathbf{M}$ is the magnetization, $\beta>0$ is the uniaxial anisotropy constant, α is the inhomogeneous exchange constant, B is the magnetostriction constant of the ferromagnetic film, $C_{ijkl}^{(f)}$ and $C_{ijkl}^{(s)}$ are the elastic moduli, $u_{ik}^{(f)}=(\partial u_i^{(f)}/\partial x_k+\partial u_k^{(f)}/\partial x_i)/2$, $u_{ik}^{(s)}=(\partial u_i^{(s)}/\partial x_k+\partial u_k^{(s)}/\partial x_k)/2$ are strain tensors, and v_f and v_s are the volumes of the magnetic film and substrate, respectively. The elastic anharmonicities and nonlinearity of the strain tensor are neglected, since they lead to a neglible renormalization of the elastic and magnetoelastic moduli of the film and substrate.[4] For simplicity, we shall confine our attention to the isotropic approximation for the magnetostriction energy of the film and substrate.

The dependence of the magnetization $\mathbf{M}$ and elastic displacements $\mathbf{u}^{(f,s)}$ in the system on the time t is described by the equations

$$\frac{\partial\mathbf{M}}{\partial t}=-g[\mathbf{M}\times\mathbf{H}_{\text{eff}}],\quad \rho^{(f,s)}\frac{\partial^2u_i^{(f,s)}}{\partial t^2}=\frac{\partial}{\partial x_k}\left(\frac{\delta F}{\delta\sigma_{ik}^{(f,s)}}\right), \tag{12}$$

where $g>0$ is the gyromagnetic ratio and $\rho^{(f)}$ and $\rho^{(s)}$ are the densities of the film and substrate, respectively. Let $\mathbf{h}=\mathbf{H}/M_0,\mathbf{h}_D=\mathbf{H}_D/M_0,\mathbf{m}=\mathbf{M}/M_0,\varphi=\Phi/M_0$, and $\omega_0=gM_0$.

The potential φ of the dipole field and the normal component of the magnetic induction $b_y=h_{Dy}+4\pi m_y$ are continuous on the surfaces $y=0$ and $y=L$ of the magnetic film, and the derivative $\partial\mathbf{m}/\partial y$ of the magnetization also vanishes there. In addition, at the ferromagnet–vacuum boundary $y=L$

$$\begin{aligned}&\sigma_{xy}^{(f)}=2C_{44}u_{xy}^{(f)}+BM_0^2m_xm_y=0,\\ &\sigma_{yy}^{(f)}=(C_{11}-2C_{44})(u_{xx}^{(f)}+u_{yy}^{(f)}+u_{zz}^{(f)})+2C_{44}u_{yy}^{(f)}\\ &\qquad+BM_0^2m_y^2=0,\\ &\sigma_{yz}^{(f)}=2C_{44}u_{yz}^{(f)}+BM_0^2m_ym_z=0,\end{aligned} \tag{13}$$

and at the ferromagnet–substrate boundary $y=0$

$$\sigma_{xy}^{(f)}=2C_{44}^{(f)}u_{xy}^{(f)}+BM_0^2m_xm_y$$
$$=2C_{44}^{(s)}u_{xy}^{(s)}+BM_0^2m_xm_y=\sigma_{xy}^{(s)},$$

$$\sigma_{yy}^{(f)}=(C_{11}^{(f)}-2C_{44}^{(f)})(u_{xx}^{(f)}+u_{yy}^{(f)}+u_{zz}^{(f)})+2C_{44}^{(f)}u_{yy}^{(f)}+BM_0^2m_y^2$$
$$=(C_{11}^{(s)}-2C_{44}^{(s)})(u_{xx}^{(s)}+u_{yy}^{(s)}+u_{zz}^{(s)})+2C_{44}^{(s)}u_{yy}^{(s)}$$
$$=\sigma_{yy}^{(s)},$$

$$\sigma_{yz}^{(f)}=2C_{44}^{(f)}u_{yz}^{(f)}+BM_0^2m_ym_z$$
$$=2C_{44}^{(s)}u_{yz}^{(s)}+BM_0^2m_ym_z=\sigma_{yz}^{(s)},\quad \mathbf{u}^{(f)}=\mathbf{u}^{(s)}. \tag{14}$$

We shall analyze the character of the variation of the low-frequency region of the spectrum of the magnetoelastic waves and of the ground state of the system as a function of the external field.

2. SPECTRUM OF LOW-FREQUENCY MAGNETOELASTIC EXCITATIONS AND THE LINE OF INSTABILITY OF THE HOMOGENEOUS PHASES

First, we shall consider a state of the system that is homogeneous in the coordinates x and z. The magnetization and elastic strains in the film and substrate can be functions only of the coordinate y. Then we find from Eqs. (12)–(14) the nonzero components of the strain tensor of the film

$$u_{xy}^{(f)}=-(h_{me}/2B)m_xm_y,\quad u_{yy}^{(f)}=-(h_{me}/B)m_y^2,$$

$$u_{yz}^{(f)}=-(h_{me}/2B)m_ym_z, \tag{15}$$

where $h_{ne}=B^2M_0^2/C_{44}^{(f)}$. After these expressions are substituted in Eqs. (9)–(10) the sum of the elastic energy and magnetostriction energy becomes

$$F_e+F_{me}=-\frac{1}{2}M_0^2h_{me}S\int_0^L dy\left(1-\frac{C_{11}^{(f)}-C_{44}^{(f)}}{C_{11}^{(f)}}m_y^2\right)m_y^2, \tag{16}$$

where S is the surface area of the structure in the xz plane. According to relation (16), the coupling of the magnetic and elastic subsystems leads to an effective uniaxial magnetic anisotropy of the easy-axis type with the axis oriented in the direction of the normal to the interface between the media. Since the magnetostriction constants in ferromagnets are small ($h_{me}\ll 4\pi$), the effective anisotropy constant is small.

We shall express the components of the normalized magnetization **m** in terms of the polar ϑ angle and the azimuthal ψ angle as

$$n_x=\cos\vartheta,\quad m_y=\sin\vartheta\sin\phi,\quad m_z=\sin\vartheta\cos\phi. \tag{17}$$

In the new variables the total energy of the system is

$$F=M_0^2S\int_0^L dy\left\{-h\cos\vartheta+2\pi\sin^2\vartheta\sin^2\phi\right.$$
$$-\frac{\beta}{2}\sin^2\vartheta\cos^2\phi+\frac{\alpha}{2}\left[\left(\frac{d\vartheta}{dy}\right)^2+\sin^2\vartheta\left(\frac{d\phi}{dy}\right)^2\right]$$
$$\left.-\frac{h_{me}}{2}\left[1+\frac{(C_{44}^{(f)}-C_{11}^{(f)}}{C_{11}^{(f)}}\sin^2\vartheta\sin^2\phi\right]\sin^2\vartheta\sin^2\phi\right\}. \tag{18}$$

Minimizing the energy (18) with respect to ϑ and ϕ and solving the equation of state, we obtain the following homogeneous phases of the system: a collinear phase $\mathbf{m}\|\mathbf{H}$ and two angular phases with magnetization parallel to the film plane ($\phi=0$)

$$\vartheta=\vartheta_0=\begin{cases}0, & h>\beta\\ \cos^{-1}(h/\beta), & 0<h<\beta\end{cases}. \tag{19}$$

For all of these states there are no elastic strains.

To determine the region of stability of the collinear phase relative to small magnetoelastic perturbations we shall find the spectrum of low-frequency excitations in the system. First, we shall examine the propagation of magnetoelastic waves in a direction parallel to the external field ($k_z=0$). Since the domain walls formed in this case are not magnetically charged and there is no dipole field in them, such excitations have the highest instability threshold with respect to the field **H** and the strongest magnetoelastic coupling.

Let the variable components of the magnetization $\tilde{\mathbf{m}}$ and displacements $\tilde{\mathbf{u}}^{(f)}$ depend on the coordinates and time as $\exp[i(k_xx+k_yy-\omega t)]$. Then the following relations between the Fourier amplitudes $\tilde{\mathbf{m}}$ and $\tilde{\mathbf{u}}^{(f)}$ (the indices **k** and ω for the amplitudes are dropped here and below) follow from the equations of motion (12):

$$\varphi=\frac{4\pi ik_y}{k^2}\tilde{m}_y,\quad \tilde{u}_z^{(f)}=\frac{ik_xBM_0^2\tilde{m}_z}{(C_{44}^{(f)}k^2-\rho^{(f)}\omega^2)},$$

$$\tilde{m}_z=i\Omega\tilde{m}_y\left\{\alpha k^2+h-\beta-\frac{k_x^2B^2M_0^2}{(C_{44}^{(f)}k^2-\rho^{(f)}\omega^2)}\right\}^{-1},$$

$$\tilde{u}_x^{(f)}=\frac{ik_yBM_0^2[C_{11}^{(f)}(k_y^2-k_x^2)+2C_{44}^{(f)}k_x^2-\rho^{(f)}\omega^2]}{(C_{11}^{(f)}k^2-\rho^{(f)}\omega^2)(C_{44}^{(f)}k^2-\rho^{(f)}\omega^2)}\tilde{m}_y,$$

$$\tilde{u}_y^{(f)}=\frac{ik_xBM_0^2[C_{11}^{(f)}(k_x^2-k_y^2)+2C_{44}^{(f)}k_y^2-\rho^{(f)}\omega^2]}{(C_{11}^{(f)}k^2-\rho^{(f)}\omega^2)(C_{44}^{(f)}k^2-\rho^{(f)}\omega^2)}\tilde{m}_y, \tag{20}$$

where $k^2=k_x^2+k_y^2$ and $\Omega=\omega/\omega_0$. Substituting the expressions (20) into the second equation of the system (12), eliminating the denominator and equating to zero the coefficient of $\tilde{m}_y$, we obtain a dispersion relation for the magnetoelastic waves with $\mathbf{k}\perp\mathbf{n}_z$ in an infinite ferromagnetic film

$$[(\alpha k^2+h+4\pi k_y^2/k^2)(\alpha k^2+h-\beta)-\Omega^2]$$
$$\times(k^2S_l^{(f)^2}\omega^2)(k^2S_t^{(f)^2}-\omega^2)^2=h_{me}S_t^{(f)^2}\{k_x^2(\alpha k^2$$
$$+h+4\pi k_y^2/k^2)(k^2S_l^{(f)^2}-\omega^2)(k^2S_t^{(f)^2}-\omega^2)$$
$$+[(\alpha k^2+h-\beta)(k^2S_t^{(f)^2}-\omega^2)-h_{me}k_x^2S_t^{(f)^2}]$$
$$\times[(k_x^2-k_y^2)^2S_l^{(f)^2}+4k_x^2k_y^2S_t^{(f)^2}-\omega^2k^2]\}, \quad (21)$$

where $S_l^{(f)}=(C_{11}^{(f)}/\rho^{(f)})^{1/2}$ and $S_t^{(f)}=(C_{44}^{(f)}/\rho^{(f)})^{1/2}$ are the phase velocities of the longitudinal and transverse elastic waves in the ferromagnet, respectively. At low frequencies Eq. (21) becomes

$$\Omega^2\left(k^2S_t^{(f)^2}+h_{me}\frac{\omega_0^2}{k^2S_t^{(f)^2}}\frac{k_x^2}{k^2}\Delta_R\right)=\Delta_L\Delta_R, \quad (22)$$

$$\Delta_L=\alpha k^2+h-\beta-h_{me}\frac{k_x^2}{k^2}, \quad (23)$$

$$\Delta_R=\left\{\alpha k^2+h+\frac{4\pi k_y^2}{k^2}-\frac{h_{me}}{k^4S_l^{(f)^2}}[(k_x^2-k_y^2)^2S_l^{(f)^2}\right.$$
$$\left.+4k_x^2k_y^2S_t^{(f)^2}]\right\}k^2S_t^{(f)^2}. \quad (24)$$

At $\omega=0$ the system of equations (12)–(14) separates into two independent subsystems. The condition $\Delta_t=0$ is the characteristic equation for magnetoelastic disturbances with polarization $\tilde{m}_z$, $\tilde{u}_z^{(f)}$, and the condition $\Delta_R=0$ is the characteristic equation for magnetoelastic disturbances with polarization $\tilde{m}_y,\tilde{u}_x^{(f)},\tilde{u}_y^{(f)}$, and φ.

Let us examine in greater detail the spectrum of low-frequency magnetoelastic excitations in the film–substrate system in the case that the uniaxial anisotropy of the magnetic film is quite large $\beta\gg4\pi$. In external fields $h-\beta\leqslant h_{me}\ll4\pi\ll\beta\sim h$ we obtain

$$|\tilde{h}_{Dy}|=4\pi k_y^2|\tilde{m}_y|/k^2\ll h|\tilde{m}_y|,$$
$$|B(k_x\tilde{u}_y^{(f)}+k_y\tilde{u}_x^{(f)})|\sim h_{me}|\tilde{m}_y|\ll h|\tilde{m}_y|. \quad (25)$$

In these approximations

$$\tilde{m}_y\cong-i\Omega\tilde{m}_z/h, \quad (26)$$

and therefore we can set $\varphi=\tilde{u}_{x,y}^{(f,s)}=0$. Then the solution of the equations of motion (12), (20), (21), and (26) can satisfy only the boundary conditions

$$\partial\tilde{m}_z/\partial y=0,\quad \partial\tilde{u}_z^{(f)}/\partial y=0 \quad \text{at } y=L, \quad (27)$$
$$\partial\tilde{m}_z/\partial y=0,\quad C_{44}^{(f)}\partial\tilde{u}_z^{(f)}/\partial y=C_{44}^{(s)}\partial\tilde{u}_z^{(s)}/\partial y,$$
$$\tilde{u}_z^{(f)}=\tilde{u}_z^{(s)} \quad \text{at } y=0. \quad (28)$$

Its form is as follows:

$$\tilde{m}_z=A[\eta_1(y)+\eta_2(y)]\exp[i(k_xx-\omega t)],$$
$$\tilde{u}_z^{(f)}=A[\gamma_1(y)+\gamma_2(y)]\exp[i(k_xx-\omega t)],$$
$$\tilde{u}_z^{(s)}=A[\cot(q_1L)+\gamma_3\cot(q_2L)]\exp[q_3y+i(k_xx-\omega t)], \quad (29)$$

where

$$\eta_{1,2}(y)=-i\gamma_{1,2}(y)[-\rho^{(f)}\omega^2+C_{44}^{(f)}(k_x^2$$
$$\pm q_{1,2}^2)]/(k_xBM_0^2),$$
$$\gamma_1=\cos[q_1(L-y)]/\sin(q_1L),$$
$$\gamma_2=\gamma_3\cosh(q_2(L-y)]/\sinh(q_2L),$$
$$\gamma_3=\frac{q_1}{q_2}\frac{S_t^{(f)^2}(k_x^2+q_1^2)-\omega^2}{S_t^{(f)^2}(k_x^2-q_2^2)-\omega^2},$$
$$q_{1,2}^2=[(Q_+^2+4\alpha^{-1}h_{me}C_{44}^{(f)^2}k_x^2)^{1/2}\pm Q_-]/(2C_{44}^{(f)})\mp k_x^2,$$
$$Q_\pm=\rho^{(f)}\omega^2\pm C_{44}^{(f)}[h(h-\beta)-\Omega^2]/(\alpha h),$$
$$q_3=(k_x^2-\rho^{(s)}\omega^2/C_{44}^{(s)})^{1/2}.$$

Substituting the expressions (29) into Eqs. (27) and (28), we find the dispersion relation for magnetoelastic waves in the form

$$\frac{C_{44}^{(f)}}{C_{44}^{(s)}}\left[\frac{q_1}{q_2}-\gamma_3\left(\frac{q_2}{q_3}+\frac{C_{44}^{(s)}}{C_{44}^{(f)}}\cot(q_2L)\right)\right]\tan(q_1L)=1. \quad (30)$$

For simplicity, we shall assume that the densities and elastic moduli of the film and substrate are identical ($\rho^{(f)}=\rho^{(s)}=\rho, C_{11}^{(f)}=C_{11}^{(s)}=C_{11}, C_{44}^{(f)}=C_{44}^{(s)}=C_{44}^{(s)}=C_{44}$), and we shall analyze the solutions of Eq. (30) for two limiting particular cases: thick $L\gg L^*\equiv a(H_E/H_{me})^{1/2}$ ($H_E=M_0\sqrt{\alpha}/a$ and $H_{me}=h_{me}M_0$ are the exchange and magnetostriction fields, respectively) and thin $L\ll L^*$ magnetic films.

For thick films $L\gg L^*$ and wave numbers $k_x\sim k_c\equiv[\pi/(2LL^*)]^{1/2}$ the dispersion of the low-frequency Love waves can be described by

$$\omega_m^2=S_t^2\{[(H-H_A-H_{me})/(H_{me}+L^{*^2}k_x^2]k_x^2$$
$$+(2m-1)^2\pi^2/(4L^2)\},$$
$$(m=1,2,3,\ldots), \quad (31)$$

where $H_A=\beta M_0$ is the anisotropy field. Each new mode (new surface Love wave) arises for $q_1=(2m-1)\pi/(2L)$. The mode with $m=1$ is soft. Using the condition

$$\omega=0,\quad \partial\omega/\partial k_x=0, \quad (32)$$

we determine the critical field

$$H_c=H_A+H_{me}-2H_Ea^2k_c^2 \quad (33)$$

in which the collinear phase becomes unstable with respect to small magnetoelastic disturbances, and the spatial scales of the critical mode are determined by the equalities

$$d_c=2\pi/k_c,\quad k_c=(\pi/2LL^*)^{1/2},$$
$$q_1\cong\pi/(2L),\quad q_3\cong k_c,\quad q_2\cong(2L^*)^{-1}\gg k_c. \quad (34)$$

As the film thickness increases, the critical field H_c approaches H_A+H_{me}, i.e. the film becomes essentially free,

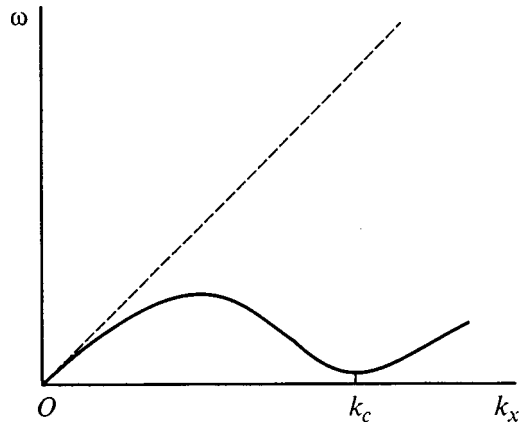

FIG. 2. Qualitative form of the low-frequency region of the spectrum of magnetoelastic waves in a uniaxial ferromagnetic film on an elastic nonmagnetic substrate for $H \cong H_c$. The dashed straight line corresponds to the volume shear mode.

and the superstructure period d_c and the penetration depth of the elastic stresses into the film and substrate increase.

For thin films $L \ll L^*$ and wave numbers $k_x \sim k_c \equiv L/(2D^{*2})$ the dispersion relation for low-frequency Love waves has the form

$$\omega^2 = S_t^2[H - H_A + H_E a^2 k_x (k_x - 2k_c)]/ [H_E a^2 (1 + S_t^2/V_s^2)], \tag{35}$$

where $S_1 = (C_{44}/\rho)^{1/2}$ and $V_s = g(\alpha M_0 H)^{1/2}$.

Using the condition (32) we find the values of the critical field and parameters of the critical perturbation as

$$H_c = H_A + H_E a^2 k_e^2, \tag{36}$$

$$d_c = 2\pi/k_c = 4\pi L^{*^2}/L,$$

$$q_{1,2} = [L/(2L^{*^3})]^{1/2}[1 \mp 3L/(8L^*)]. \tag{37}$$

As the film thickness decreases, the field H_c approaches the transition field from the collinear into the angular corner phase H_A of the clamped sample, i.e. the substrate increasingly impedes the elastic strain of the film. The period d_c and penetration depth $q_3^{-1} \sim d_c(2\pi)$ of the surface solution into the substrate increase. The parameters of the magnetostriction superstructure in a two-dimensional ferromagnetic film on a thick substrate can be obtained from Eqs. (36) and (37) by the substitution $L \to a$.

We note that relation (30) gives the exact values of the critical field and parameters of the critical mode for any value of the anisotropy constant β, since for $\omega = 0$ the variables in the system of equations (12)–(14) separate.

In the long-wavelength limit ($|k_x L| \ll 1$) the dispersion of the Love waves is described by

$$\omega = S_t |k_x| (1 - k_x^2 L^2/2). \tag{38}$$

Just as in the case of an isotropic nonmagnetic film, the penetration depth of a wave into the substrate is $q_3^{-1} \sim (k_x^2 L)^{-1}$. The spectrum of magnetoelastic Love waves in a thin uniaxial ferromagnetic film on an elastic substrate in an external field $H \cong H_c$ is displayed in Fig. 2.

It follows from the dispersion relation (30) that an inhomogeneous magnetoelastic state does not arise in the limiting cases where the bottom side of the magnetic film is free ($C_{44}^{(s)} = 0$) and completely clamped ($C_{44}^{(\infty)} = \infty$).

Static perturbations with components of the inhomogeneous magnetization $\tilde{m}_y$ and displacements $\tilde{u}_x$ and $\tilde{u}_y$ are stable, since they are related to the rotation of the magnetization in the ''hard'' plane

For magnetoelastic waves propagating perpendicular to the external field, the variables of the system of equations (12)–(14) separate. The surface mode with components $\tilde{u}_y$ and $\tilde{u}_z$ is not coupled with the magnetization and is of no interest to us. It is easy to show that at $H = H_c$ the frequency of the low-frequency magnetoelastic Love wave with nonzero $\tilde{m}_y, \tilde{m}_z, \tilde{u}_x$, and φ does not vanish. Specifically, for thick films its dispersion relation has the form

$$\omega^2 \left\{ \frac{1}{\omega_0^2} + \frac{1}{k^2 S_t^2} \left[2\Delta_L + h_{me} \left(\alpha k^2 + h - \beta \frac{k_y^2}{k^2} \right) \right] \right\} = \Delta_L,$$

$$\Delta_L = (\alpha k^2 + h - \beta + 4\pi - h_{me})(\alpha k^2 + h) - (4\pi - h_{me})\beta(k_y^2/k^2),$$

$$k_y = \pi/2L. \tag{39}$$

Stabilization of the Love wave is a consequence of an increase in energy of the demagnetizing field.

To determine the stability region of the angular phases (19) the complete linearized system of equations and boundary conditions (12)–(14) must be solved. However, it can be proved that the magnetoelastic Love wave whose wave vector is parallel to the magnetization in the angular phase and nonzero inhomogenuous components of the magnetization and displacements $\tilde{m}_x, \tilde{m}_z, \tilde{u}_x$, and $\tilde{u}_z$ possesses the lowest instability threshold. Just as the Love wave (29) and (30), it does not produce a dipole field. The instability field H_c' of the angular phase relative to the appearance of an inhomogeneous state and the wave number k_c' of the critical mode are determined from the following relations: For thick ferromagnetic films ($L \gg L^*$)

$$H_c'^2 \cong H_A[H_A - H_{me} + 2\pi^2 a^2 H_E/(LL^*\beta^{1/2})],$$

$$k_c'^2 \cong \pi^2/(LL^*), \tag{40}$$

and for thin ferromagnetic films ($L \ll L^*$)

$$H_c'^2 \cong H_A(H_A - \pi^2 H_{me} L^2/L^{*^2}), \quad k_c' \cong 2\pi^2 L/L^{*^2}. \tag{41}$$

As $L \to 0$, the instability field of the angular phase approaches the anisotropy field H_A.

The general form of the phase diagram of a uniaxial ferromagnetic film with magnetostriction on a semiinfinite nonmagnetic substrate is presented in the coordinates (L,H) in Fig. 3. Qualitatively, it is similar to the phase diagram of an isolated uniaxial ferromagnetic film with easy axis perpendicular to its extended surface, in the absence of magnetoelastic interactions.[17–19] The domain phase has the lowest energy in the entire range of fields and film thicknesses in the diagram to the left of the line of second-order phase transitions $H_c(L)$ from the collinear to the domain phase, while

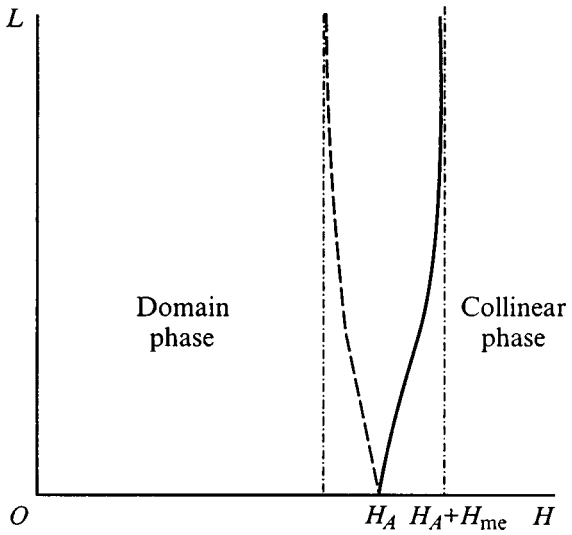

FIG. 3. Phase diagram of a uniaxial ferromagnetic film on an elastic nonmagnetic substrate: solid curve is the line of instability of the collinear phase, dashed curve represents instability line of the angular phase.

the angular phases are metastable in the range from zero field to the instability line $H_c'(L)$. The existence of domain structure in a wide range of fields and film thicknesses is due to the infinite thickness of the substrate.

For finite substrate thickness $L_s \gg L$, the domain structure becomes energetically unfavorable when the domain size D exceeds the substrate thickness ($D > L_s$). The substrate thickness plays the role of the screening length of the field of the elastic strains, similarly to the London penetration depth of the field in a uniaxial ferromagnetic film with a superconducting coating.[18,19] As a result, the angular phase is absolutely stable in thin films, and a direct transition in the field from the collinear to the angular phase is possible.

3. DISCUSSION AND CONCLUSIONS

It was shown that the magnetoelastic interaction does not reduce to renormalization of the anisotropy constants of the magnetic film. The long-range character of the magnetoelastic stresses in the layered system ferromagnetic-film–nonmagnetic-substrate in an external magnetic field leads to the appearance of magnetoelastic domains in external fields close to the transition field of the collinear to the homogeneous angular phase transition.

The domain formation mechanism described above can be important even for magnetic materials with weak magnetostriction. For iron-yttrium garnet at room temperature $M_0 = 140$ G, $\alpha = 3.8 \times 10^{-11}$ cm^2, $\rho = 5.17$ g/cm^3, $C_{44} \sim 10^{12}$ dynes/cm^3, $BM_0^2 \sim 10^7$ ergs/cm^3, whence $h_{me} \sim 2 \times 10^{-3}$ and $L^* \sim 10^{-4}$ cm. Near the instability point of the collinear phase $H = H_c$, the domain size $D/2 \sim 150\ \mu$m for $L \sim 10^{-5}$ cm and $D/2 \sim 20\ \mu$m for $L \sim 20\ \mu$m. According to the experimental data, the domain sizes in thick iron–yttrium garnet films on gallium-gadolinium garnet substrates in weak tangential external fields are of this order of magnitude. Approximately the same values of h_{me} are obtained for lithium ferrite and iron, For hexagonal cobalt they are an order of magnitude higher. Of course, such estimates for materials with cubic and hexagonal symmetry are only qualitative. Quantitative estimates require special analysis.

It can be concluded on the basis of the considerations presented above that such inhomogeneous states can also occur in other materials where subsystems interact with one another, for example, in antiferromagnetic and superconducting films grown on a massive elastic substrate.

This work was supported by the Russian Fund for Fundamental Research (Projects Nos. 96-02-17283a and 96-02-16082).

[1] S. V. Vonsovskiĭ, *Magnetism* (Wiley, N. Y., 1974; Nauka, Moscow, 1971).
[2] V. V. Lemanov, *The Physics of Magnetic Dielectrics* (Nauka, Leningrad, 1974).
[3] I. E. Dikshteĭn, E. A. Turov, and V. G. Shavrov, in *Dynamic and Kinetic Properties of Magnetic Systems* (Moscow, 1986).
[4] V. I. Ozhogin and V. L. Preobrazhenskiĭ, Zh. Éksp. Teor. Fiz. **73**, 988 (1977) [Sov. Phys. JETP **46**, 523 (19977)]; Usp. Fiz. Nauk **155**, 593 (1988) [Sov. Phys. Usp. **31**, 713 (1988)]; J. Magn. Magn. Mater. **100**, 544 (1991).
[5] Yu. V. Gulyaev, I. E. Dikshteĭn, and V. G. Shavrov, Usp. Fiz. Nauk **40**, 701 (1997).
[6] S. V. Gerus and V. V. Tarasenko, Fiz. Tverd. Tela (Leningrad) **17**, 2247 (1976) [Sov. Phys. Solid State **17**, 1487 (1976)].
[7] V. G. Bar'yakhtar and R. A. Turov, in *Spin Waves and Magnetic Excitations 2*, edited by A. S. Borovik-Romanov and S. K. Sinha (North–Holland, Amsterdam, 1988), Chap 7.
[8] J. P. Parekh, Electron. Lett. **5**, 322 (1969); ibid. **5**, 540 (1969).
[9] B. N. Filippov and L. G. Onoprienko, Fiz. Met. Metalloved. **30**, 1121 (1970).
[10] J. P. Parekh and H. I. Bertoni, Appl. Phys. Lett. **20**, 362 (1972).
[11] R. Q. Scott and D. L. Mills, Phys. Rev. B **15**, 3545 (1977).
[12] H. Mattheus and Van De Vaart, Appl. Phys. Lett. **15**, 373 (1969).
[13] R. E. Camley, J. Appl. Phys. **50**, 5272 (1979).
[14] R. E. Camley and A. A. Maradudin, Appl. Phys. Lett. **38**, 610 (1981).
[15] I. E. Dikshtein and Sung-Ho Suck Salk, Phys. Rev. B **53**, 14 957 (1996).
[16] I. E. Dikshteĭn, Fiz. Tverd. Tela (Leningrad) **31**(3), 175 (1989) [Sov. Phys. Solid State **31**, 447 (1989)].
[17] V. G. Bar'yakhtar and B. A. Ivanov, Zh. Éksp. Teor. Fiz. **72**, 1504 (1977) [Sov. Phys. JETP **45**, 789 (1977)].
[18] Yu. I. Bespyatykh, V. Vasilevskiĭ, É. G. Lokk, and V. D. Khariton, Fiz. Tverd. Tela (St. Petersburg) **40**, 1068 (1998) [Phys. Solid State **40**, 975 (1998)].
[19] Yu. I. Bespyatykh, E. H. Lokk, S. A. Nikitov, and W. Wasilevski, J. Magn. Magn. Mater. (1998), at press.

Translated by M. E. Alferieff

Magnetic structure of a $RbDy(WO_4)_2$ single crystal

V. P. D'yakonov* and É. E. Zubov

Donetsk Physicotechnical Institute, Ukrainian National Academy of Sciences, 340114 Donetsk, Ukraine

A. A. Pavlyuk

Institute of Inorganic Chemistry, Russian Academy of Sciences, Siberian Branch, 630095 Novosibirsk, Russia

M. T. Borowiec and H. Szymczak

Institute of Physics, Polish Academy of Sciences, 02-668 Warsaw, Poland
(Submitted June 29, 1998; resubmitted September 28, 1998)
Fiz. Tverd. Tela (St. Petersburg) **41**, 672–676 (April 1999)

The results of measuring the temperature and field dependences of the magnetization of a $RbDy(WO_4)_2$ single crystal in the temperature range from 4.2 to 50 K and in magnetic fields up to 1.6 T are presented. The energies of the exchange and dipole-dipole interactions are estimated. The magnetic structure of the ground state is determined. © *1999 American Institute of Physics.* [S1063-7834(99)02304-7]

Rubidium dysprosium tungstate $RbDy(WO_4)_2$ is a member of the family of double tungstates containing alkali-metal (M) and rare-earth (R) cations $M^+R^{3+}(WO_4)_2$. We know of only one publication devoted to the study of $RbDy(WO_4)_2$. An antiferromagnetic (AFM) phase transition with a Néel temperature $T_N = 0.818$ K was established in it on the basis of specific-heat measurements.[1] The low symmetry of the crystal environment of the Dy^{3+} ion is responsible for the fairly strong anisotropy of the magnetic properties of $RbDy(WO_4)_2$. Taking into account the low magnetic-ordering temperature, we can theorize that the role of the dipole-dipole interactions will be very significant in establishing the long-range order. Magnetic investigations of $RbDy(WO_4)_2$ are also prompted by a desire to establish the magnetic structure of the ground state.

This paper presents the results of measurements of the magnetization as a function of temperature and magnetic field strength in a $RbDy(WO_4)_2$ single crystal.

1. SAMPLES AND EXPERIMENT

The outward appearance of the $RbDy(WO_4)_2$ crystal is shown in Fig. 1. The crystallographic (a, b, and c) and fixed magnetic (x, y, and z) axes are indicated in the figure.

Rubidium dysprosium tungstate crystals have a monoclinic α-$KY(WO_4)_2$ structure with C_{2h}^6 symmetry.[2,3] The lattice parameters are $a = 8.14$ Å, $b = 10.45$ Å, and $c = 7.57$ Å with the monoclinic angle $\beta = 94°$. The Dy^{3+} ion has local C_2 symmetry. The unit cell contains dysprosium ions in two chains parallel to the a axis. The chains are shifted relative to each other by half a period along the b and c axes.

The magnetic measurements of the $RbDy(WO_4)_2$ single crystal were performed on a PAR Model 450 vibrating sample magnetometer at temperatures between 4.2 and 50 K and in magnetic fields up to 1.6 T. The direction of the applied field was chosen in the *ab*, *bc*, and *ac* planes. The dimensions of the samples were roughly $1.2 \times 1.4 \times 5$ mm. The samples were oriented along one of the crystallographic directions.

2. EXPERIMENTAL RESULTS

The angular dependence of the magnetization of the Rb $Dy(WO_4)_2$ single crystal shows that only the b crystallographic axis coincides with one of the principal directions of the susceptibility tensor (the y axis). The other two directions (the z and x axes) lie in the *ac* plane and deviate by $\varphi = 12°$ from the c and a crystallographic axes, respectively (Fig. 1).

The dependences of the magnetization M on magnetic field and temperature are shown in Figs. 2a and b. At 4.2 K magnetic saturation is not achieved up to $H = 1.6$ T. As can be seen from Fig. 2a, the difference in magnetization along the c and b directions in the *bc* plane is insignificant. Strong magnetization anisotropy was observed in the *ac* and *ab* crystallographic planes. Plots of the temperature dependence of the magnetization along the z and x axes in the *ac* plane measured in a magnetic field are shown in Figs. 3a and b. The function $M(T)$ depends on the orientation and strength of the magnetic field. The M_x component of the magnetization is more than an order of magnitude smaller than M_z (Fig. 3a). As can be seen from the inset in Fig. 3a, the plot of $1/M(T)$ has inflection points inflection near 6 and 16 K. The inflection points on the $M(T)$ curves are less pronounced. The plots of $1/M(T)$ are linear with respect to temperature and have different slopes above and below the inflection points.

Since the measurements were performed on long thin samples with a small demagnetizing factor, the point of intersection of the $1/M_i(T)$ curve with the temperature axis specifies the Curie temperature ϑ_i. It is presumed in analogy

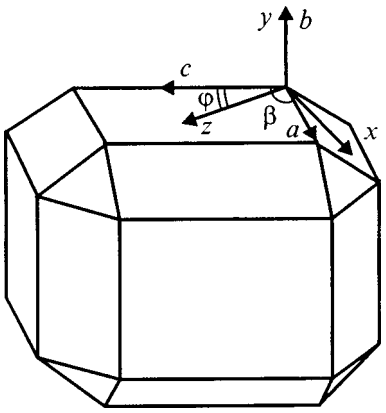

FIG. 1. External appearance of the $RbDy(WO_4)_2$ crystal: *a*, *b*, *c* — crystallographic axes; *x*, *y*, *z* — magnetic axes; $\beta=94°$ and $\varphi=12°$.

to $KDy(WO_4)_2$ (Ref. 4) that the features found on the $1/M(T)$ curves of the $RbDy(WO_4)_2$ single crystal are each due to a structural phase transition (SPT).

It was found that the magnetic field strongly influences the $1/M(T)$ curve. This is naturally reflected in the value of the Curie temperature ϑ. This temperature is known to be independent of the magnetic field strength. In the present case, the influence of the magnetic field on the $1/M(T)$ curve and on the value of ϑ evidently reflects changes in the electronic spectrum of the ground state of the Dy^{3+} ions during the structural phase transition in the magnetic field.

The susceptibility can be described in an approximation by the Curie–Weiss law

$$M_i/H=\chi_i=\frac{C_i}{T-\vartheta_i},$$

where $C_i=N_A(\mu_B g_i)^2 S(S+1)/3k$, N_A is Avogadro's number, μ_B is the Bohr magneton, S is the effective spin, which equals 1/2, and k is Boltzmann's constant.

The parameters C_i, ϑ_i, and g_i for $RbDy(WO_4)_2$ were calculated as a result of an analysis of the experimental data (Table I). The temperature range in which the influence of excited levels can be neglected was considered in the analysis. According to Table I, the g factors along the principal crystallographic directions above and below T_{spt1} differ less than do the Curie temperatures ϑ_2 and ϑ_1, probably due to changes in the exchange parameters accompanying the structural transitions.

The magnetic-field dependence of the Curie temperature was also established. As the magnetic field becomes stronger, the Curie temperature ϑ_2 increases. The variation of ϑ_2 is probably caused by the magnetostriction effects in the rare-earth magnet investigated.

Let us estimate the parameters of the exchange interaction along three different directions. The expression for the Curie temperature ϑ_α in an arbitrary direction α has the form

$$\vartheta_\alpha=-\frac{-2S(S+1)}{3k}(J_\alpha^0+E_\alpha^0), \qquad (1)$$

where $J_\alpha^0/k=zJ_\alpha/k$, $z=6$ is the number of nearest neighbors, J_α is the parameter of the exchange interaction between a pair of magnetic ions in the α direction, $E_\alpha^0=L_{\alpha1}/k+L_{\alpha2}/k$ is the contribution of the dipole-dipole interaction, and $L_{\alpha1}/k$ is the contribution of the magnetic-dipole interaction with a Lorentz sphere of radius $R=200$ Å.

The lattice sums $L_{\alpha1}$ have the following values:

$$L_{a1}/k=-0.209\text{K}, \quad L_{b1}/k=0.192\text{K},$$

$$L_{c1}/k=1.47\text{K}(T>T_{spt1});$$

$$L_{a1}/k=-0.128\text{K}, \quad L_{b1}/k=0.138\text{K},$$

$$L_{c1}/k=1.07\text{K}(T<T_{spt1}).$$

Also, $L_{\alpha2}$ is the contribution of the magnetic-dipole interaction associated with the Lorentz term and the demagnetizing field:

$$L_{\alpha2}/k=(-4\Pi/3+4\Pi N)C_{\alpha N}, \qquad (2)$$

where $C_{\alpha N}=4(m_B g_\alpha)^2/kabc$ and $N=0.079$ is the demagnetizing factor.

Performing the summation, we obtained the following values of the constants along the principal crystallographic directions:

$$L_{a2}/k=-0.335\text{K}, \quad L_{b2}/k=-2.67\text{K},$$

$$L_{c2}/k=-2.67\text{K}(T>T_{spt1});$$

$$L_{a1}/k=-0.206\text{K}, \quad L_{b1}/k=-1.92\text{K},$$

$$L_{c1}/k=-1.95\text{K}(T<T_{spt1}).$$

The total contribution E_α^0 of the dipole-dipole interaction to the magnitude of ϑ_α has the form

$$E_a^0/k=-0.54\text{K}, \quad E_b^0/k=-2.48\text{K},$$

$$E_c^0/k=-1.2\text{K}(T>T_{spt1});$$

$$E_a^0/k=-0.33\text{K}, \quad E_b^0/k=-1.78\text{K},$$

$$E_c^0/k=-0.87\text{K}(T<T_{spt1}).$$

Assuming that the exchange parameters for all the nearest neighbors are equal in magnitude, we calculated the exchange parameter J_α^0 on the basis of (1) and the experimental values of ϑ_α. The results are listed in Table II.

It can be seen from the data presented that the contribution of the dipole-dipole interactions to the spin-spin interactions at $T>T_{spt1}$ is insignificant. At $T<T_{spt1}$ the value of the dipole-dipole energy is greatest along the b direction (in the direction perpendicular to the DyW_2O_8 planes) and smallest along the a direction (along the chains of Dy^{3+} ions). Although exchange is largest along the a axis at $T>T_{spt1}$, its role in the formation of the long-range order decreases at $T<T_{spt1}$, since the contribution of the dipole-dipole interactions becomes significant in that case.

It can be stated on the basis of the data in Table II that exchange is essentially isotropic at $T<T_{spt1}$.

Let us now determine the magnetic structure of the ground state in $RbDy(WO_4)_2$ at low temperature ($T<T_{spt1}$). The ground-state energies of various magnetic

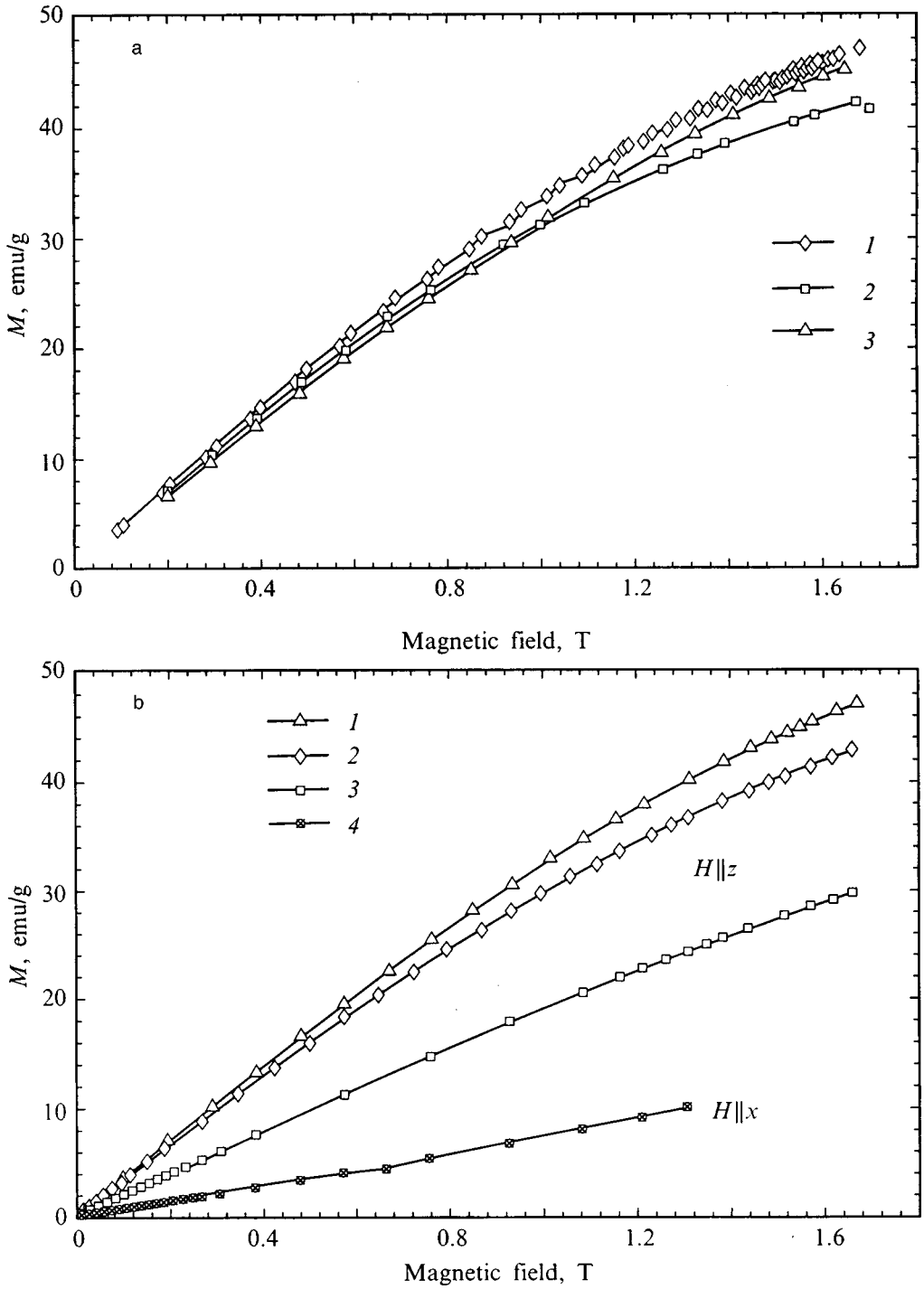

FIG. 2. Field dependence of the magnetization as a function of the angle φ between the c axis and the direction of H in the bc plane (a) at $T=4.2$ K for $\varphi=0°$ (*1*), 45° (*2*), and 90° (*3*) and its temperature dependence (with a field in zx plane) for $H\|z$ at 4.2 K (*1*), 4.9 K (*2*), and 9.5 K (*3*) and for $H\|x$ at 4.2 K (*4*) (b).

structures of Bravais lattices with one magnetically active ion were estimated by the method developed in Ref. 5.

The calculation was performed using the usual expression for the dipole energy

$$E_{\text{dip}}=\sum_{ij}\left[\frac{\mathbf{m}_i\cdot\mathbf{m}_j}{r_{ij}^3}-3\frac{(\mathbf{m}_i\cdot\mathbf{r}_{ij})(\mathbf{m}_j\cdot\mathbf{r}_{ij})}{r_{ij}^5}\right],$$

where m_i is the magnetic moment, which can be stated in terms of the spin components S_i^α by means of the relation

$$m_i^\alpha=\mu_b g_\alpha S_i^\alpha \quad (\alpha=x,y,z),$$

and $\mathbf{r}_{ij}$ is the radius vector joining the ith and jth lattice points.

The values of the g factors listed in Table I for $T<T_{\text{spt1}}$ were used in the calculations.

The determination of the ground state calls for a search for the magnetic structure having the lowest energy for the magnetic moment $\mathbf{m}_i$ in the field of surrounding magnetic

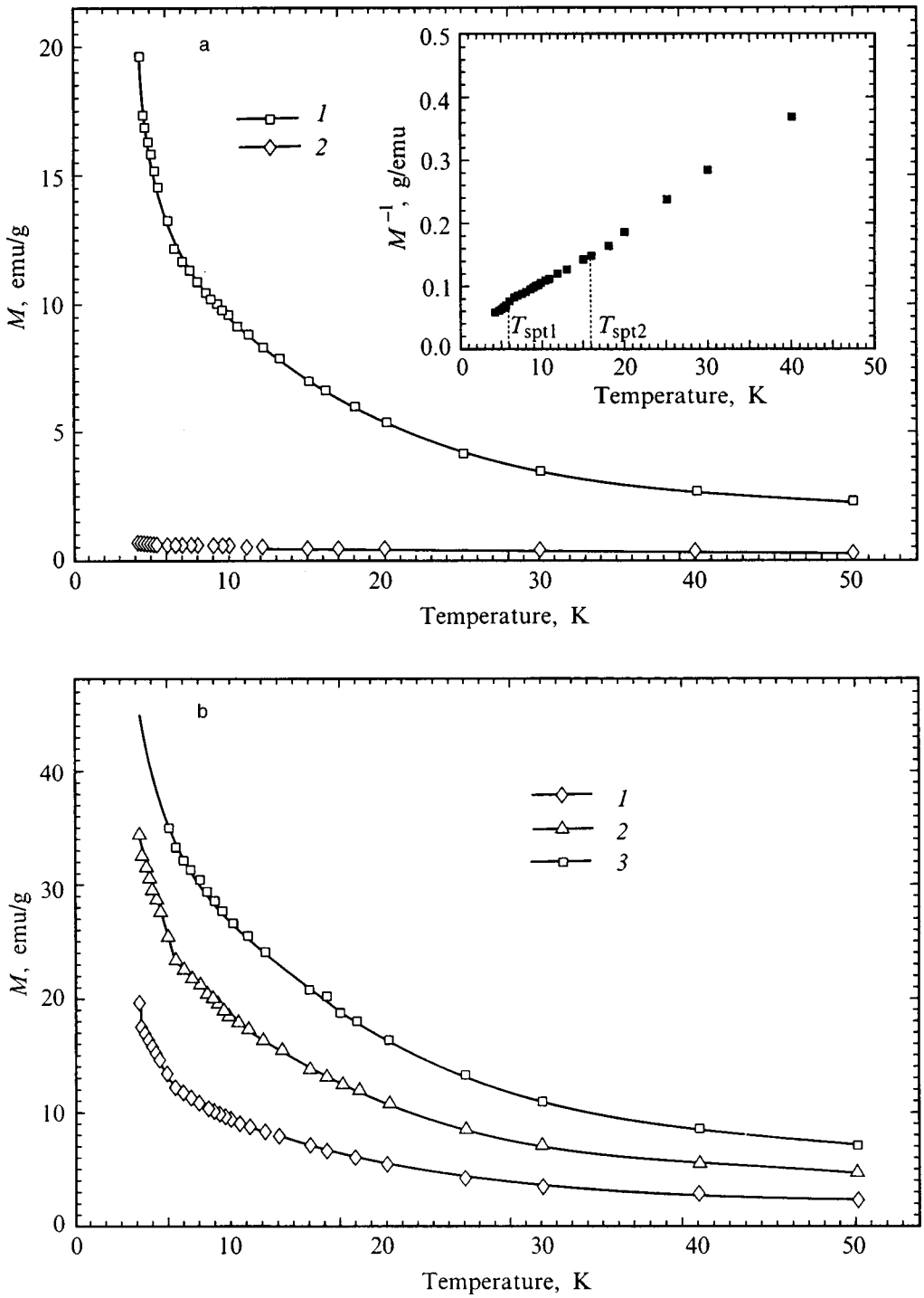

FIG. 3. Temperature dependences of the magnetization measured with a magnetic field of strength $H=0.5$ T oriented along the z (*1*) and x (*2*) axes (a) (inset — temperature dependence of the reciprocal of the magnetization along the z axis) and with magnetic fields of various strengths [$H=0.5$ T (*1*), 1.0 T (*2*), and 1.5 T (*3*)] oriented along the z axis (b).

moments coupled by dipole-dipole and exchange interactions.

A numerical analysis of the lattice sums based on the theory in Ref. 5 was performed for a sphere of radius $R=200$ Å. It was found that an AFM structure with a checkerboard array has the lowest energy. We have the following values of the energy E_α^0 for three directions of the antiferromagnetic vector: $E_a^0=-4.1$ K, $E_b^0=-5.9$ K, $E_c^0=-5$ K. Thus, the magnetic structure of crystalline $RbDy(WO_4)_2$ has the form of a system of antiferromagnetically ordered magnetic moments of Dy^{3+} ions directed collinearly to the b axis.

Thus, the temperature and field dependences of the magnetization of a $RbDy(WO_4)_2$ single crystal over broad ranges of temperatures ($T=4.2-50$ K) and magnetic fields (up to 1.6 T) have been investigated in this work. Strong magnetization anisotropy in the *ac* and *ab* planes has been established. The magnetic axes have been determined using the

TABLE I. Curie temperature ϑ, g factor, and Curie constant C obtained from the experimental data with application of a field along the principal crystallographic directions.

	$T_{spt2}>T>T_{spt1}$			$T<T_{spt1}$		
Direction	ϑ_2, K	C, cm^3/mole	g_i	ϑ_1, K	C, cm^3/mole	g_i
Along the *a* axis (*ab* plane)				−2	1.5	4
Along the *c* axis (*bc* plane)	−4.7	19.4	14.4	−1.7	14.1	12.3
Along the *b* axis (*bc* plane)	−4.3	19.3	14.4	−1.5	14.1	12.2
Along the *z* axis (*ac* plane)	−4.7	20.6	14.8	−0.7	13.4	11.9

angular dependences of $M(H)$. The inflection points on the $1/M(T)$ curve are associated with the occurrence of two structural phase transitions in the crystal investigated. The changes in the Curie temperature, as well as the g factors, upon structural phase transition, points to a strong correlation between the magnetic properties and the crystal and electronic structures. The exchange and dipole-dipole energies have been estimated. It has been shown that the exchange interactions between the Dy^{3+} ions along the principal crystallographic directions are antiferromagnetic and essentially isotropic. The dipole-dipole interactions along the *b* axis make the largest contribution to the total energy of the spin interactions. The magnetic structure of the ground state of the $RbDy(WO_4)_2$ single crystal has been established on the basis of an analysis of experimental data and the results of calculations of the dipole-dipole interactions. It has the form of a system of antiferromagnetically ordered Dy^{3+} ions with an antiferromagnetic vector along the *b* axis.

TABLE II. Exchange interaction parameter J_α along the principal crystallographic directions.

	$-J_a^0/k$	$-J_b^0$	$-J_c^0$
$T>T_{spt1}$	17.7	11.1	10.6
$T<T_{spt1}$	4.3	4.8	4.3

M. T. Borowiec and H. Szymczak thank the Polish State Committee for Science (KBN) for its partial support of this research (Project No. 2PO3807108).

*E-mail: dyakonov@host.dipt.donetsk.ua

[1] M. T. Borowiec, V. Dyakonov, A. Jedrzejczak, V. Markovich, A. Pavlyuk, H. Szymczak, E. Zubov, and M. Zaleski, J. Low Temp. Phys. **110**, 1003 (1998).
[2] V. K. Trunov and V. K. Rybakov, J. Inorg. Chem. **19**, 636 (1974).
[3] P. V. Klevtsov and R. F. Klevtsova, J. Struct. Chem. **18**, 339 (1978).
[4] M. T. Borowiec, V. Dyakonov, E. Zubov, E. Khatsko, and H. Szymczak, J. Phys. I (Paris) **7**, 1639 (1997).
[5] T. H. Niemeyer, Physica (Amsterdam) **57**, 281 (1972).

Translated by P. Shelnitz

Synthesis and magnetic properties of $Cu_3B_2O_6$ single crystals

G. A. Petrakovskiĭ,* K. A. Sablina, A. M. Vorotynov, O. A. Bayukov, A. F. Bovina, and G. V. Bondarenko

L. V. Kirenskiĭ Institute of Physics, Russian Academy of Sciences, Siberian Branch, 660036 Krasnoyarsk, Russia

R. Szymczak, M. Baran, and H. Szymczak

Institute of Physics, Polish Academy of Sciences, 02-668 Warsaw, Poland
(Submitted May 5, 1998; resubmitted October 1, 1998)
Fiz. Tverd. Tela (St. Petersburg) **41**, 677–679 (April 1999)

The temperature dependence of the magnetic susceptibility of $Cu_3B_2O_6$ single crystals grown by spontaneous crystallization from a melt consisting of a mixture of CuO and B_2O_3 and the behavior of their magnetization are investigated in magnetic fields up to 55 kOe. A broad susceptibility maximum is observed near 39 K, and a sharp drop in susceptibility is observed at $T<10$ K. The paramagnetic Néel temperatures for all orientations of the magnetic field in the crystal investigated are negative, attesting to the predominantly antiferromagnetic character of the exchange interactions. The effective magnetic moment of the Cu^{2+} ion is anisotropic and lies in the range from $1.054\mu_B$ to $1.545\mu_B$. The magnetization depends linearly on magnetic field at $T>10$ K, whereas at temperatures below 10 K a discontinuity is observed at fields of the order of 40 kOe. At room temperature, electron magnetic resonance characterized by an almost isotropic g factor ($g=2.165$) is detected at 36.22 GHz. The exchange interactions in $Cu_3B_2O_6$ are analyzed on the basis of the Goodenough–Kanamori rules. The possibility of the establishment of a singlet magnetic state in the crystal is analyzed. [S1063-7834(99)02404-1]

The main reason for the great interest of researchers in oxide compounds of copper is the high-temperature superconductivity observed in some of them. In particular, it is important to understand the mechanisms which shape the magnetic state, especially the singlet ground state, in such compounds.[1–3] For example, in crystalline $CuGeO_3$ the mechanism which shapes the singlet state is probably associated with a spin-lattice interaction and competition between exchange interactions, while in ladder systems it is a purely quantum fluctuation effect.

This paper is the first to present the results of an experimental investigation of the magnetic susceptibility, magnetization, and electron magnetic resonance of $Cu_3B_2O_6$ single crystals.

1. SYNTHESIS AND CRYSTAL STRUCTURE OF $Cu_3B_2O_6$

Single crystals of $Cu_3B_2O_6$ were grown by spontaneous crystallization from a solution in a melt on the basis of the results of the physicochemical investigation of the ternary $Li_2O–CuO–B_2O_3$ system in Ref. 4. The mixture of the starting materials CuO and B_2O_3 containing 70 mol % CuO and 30 mol % B_2O_3 was placed in a platinum crucible and heated to 1200°C. Crystallization took place as the temperature was lowered at the rate of 2 deg/h to 900°C. The crystals were extracted by mechanical means and had the form of oblique prisms of dark green color with dimensions up to $3\times3\times3$ mm^3.

X-ray fluorescence analysis confirmed the chemical formula $Cu_3B_2O_6$ and the absence of foreign phases. X-ray diffraction analysis of the crystals obtained showed that they belong to the triclinic system with space group $P1$ and the unit cell parameters $a=3.344$ Å, $b=19.757$ Å, $c=19.587$ Å, $\alpha=88.91°$, $\beta=70.05°$, and $\gamma=69.93°$, in agreement with the data in Ref. 5. It can be seen from the crystal structure shown in Fig. 1 that the magnetic Cu^{2+} ions are coordinated in octahedral, square, and pyramidal environments of oxygen ions. The mean Cu–O distances within a layer in the bc plane and between layers are equal to 1.95 and 2.90 Å, respectively, clearly suggesting a quasi-two-dimensional magnetic state. An analysis of the exchange interactions on the basis of the Goodenough–Kanamori rules[6] shows that there are two types of exchange interactions in the system: 135° antiferromagnetic Cu–O–Cu interactions with an energy of the order of 100 K and 90° ferromagnetic interactions with an energy of the order of 10 K. The dominant type of exchange is antiferromagnetic according to the results of the magnetic-susceptibility measurements. The following fragments of Cu^{2+} ions can be identified in the structure of $Cu_3B_2O_6$: chains of four copper ions in an octahedral oxygen environment; chains of four copper ions, two of which have an octahedral environment while the other two have a square environment; pairs of copper ions, one of which has an octahedral environment while the other has a pyramidal environment; groups of copper ions in an octahedral environment; and, finally, copper ions in a square environment. All of these groups of copper ions are coupled predominantly by

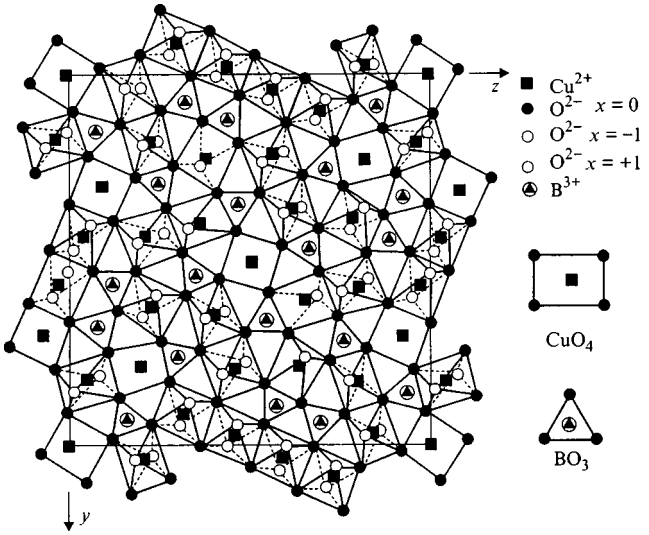

FIG. 1. Crystal structure of $Cu_3B_2O_6$.

negative exchange interactions to form two-dimensional layers in the bc plane.

2. MAGNETIC PROPERTIES

The static magnetic properties of the crystals were investigated on SQUID and vibrating sample magnetometers in fields up to 50 kOe at temperatures between 2 and 300 K. The results of the SQUID measurements of the temperature dependence of the magnetic susceptibility determined in an arbitrary direction in the bc plane of the crystal in 6- and 20-kOe fields are shown in Fig. 2. The presence of a broad susceptibility maximum at a temperature of about 39 K, the sharp drop in susceptibility at temperatures below 10 K, and the identity of the results of the measurements in 6- and 20-kOe fields are noteworthy. The high-temperature behavior of the susceptibility is described by the Curie–Weiss law with the parameters $\Theta=-422$ K and $\mu_{\text{eff}}=1/06\mu_B$. Deviations from the Curie–Weiss law are observed at temperatures below 150 K. The results of the magnetic-susceptibility measurements performed on the vibrating sample magnetometer for two mutually perpendicular directions of the external magnetic field in the bc plane and in a direction perpendicular to that plane are shown in Fig. 3. The measurements were performed in a 14.14-kOe magnetic field. The asymptotic

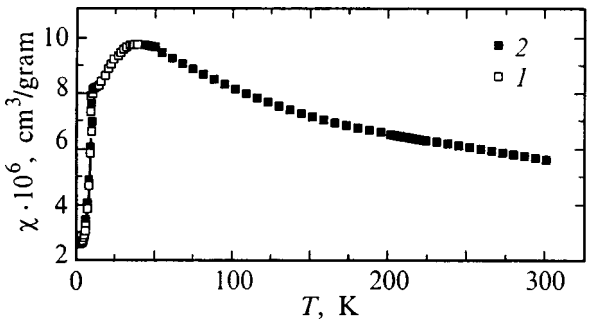

FIG. 2. Temperature dependence of the magnetic susceptibility of a $Cu_3B_2O_6$ single crystal measured in a SQUID magnetometer for $H||(bc)$: *1* — $H=6$ kOe, *2* — $H=20$ kOe, solid curve — Eq. (1)

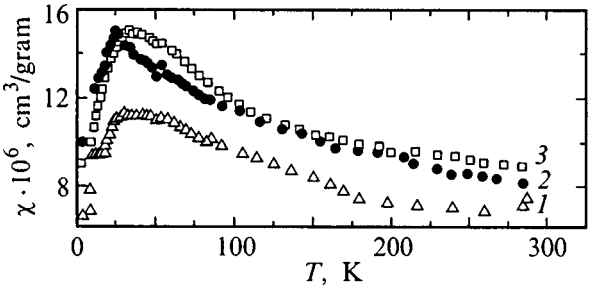

FIG. 3. Temperature dependence of the magnetic susceptibility of a $Cu_3B_2O_6$ single crystal measured in a vibrating sample magnetometer: *1*, *2* — magnetic field in two mutually perpendicular directions in the bc plane, *3* — $H\perp(bc)$.

Néel temperatures and effective magnetic moments corresponding to these three orientations of the magnetic field have the following values: $\Theta_1=-335$, $\Theta_2=-400$, $\Theta_3=-691$, $\mu_{\text{ef1}}=1.054$, $\mu_{\text{ef2}}=1.247$, and $\mu_{\text{ef3}}=1.545\mu_B$. As can be seen from Fig. 3, a low-temperature drop in the magnetic susceptibility is observed for all three orientations of the magnetic field. We note that fairly strong anisotropy of the susceptibility is observed in the (bc) plane of the crystal. Just this anisotropy may be responsible for the difference between the results of the magnetic-susceptibility measurements in Figs. 2 and 3. The sharp drop in the susceptibility χ (Fig. 2) observed when the temperature was lowered below 10 K is described by the dependence

$$\chi=A+B\exp(-\Delta/T) \tag{1}$$

with the parameters $A=2.66\times10^{-6}\text{cm}^3/\text{g}$, $B=1.4\times10^{-4}\text{cm}^3/\text{g}$, and $\Delta=33.3$ K. Such a dependence is characteristic of systems having a singlet ground state separated from the excited states by an energy gap Δ. Estimates show that the residual low-temperature susceptibility A can be attributed to the Van Vleck paramagnetic contribution. The singlet ground magnetic state can be either a result of a collective phase transition (such as a spin-Peierls state) or a state of cluster formations.[7,8]

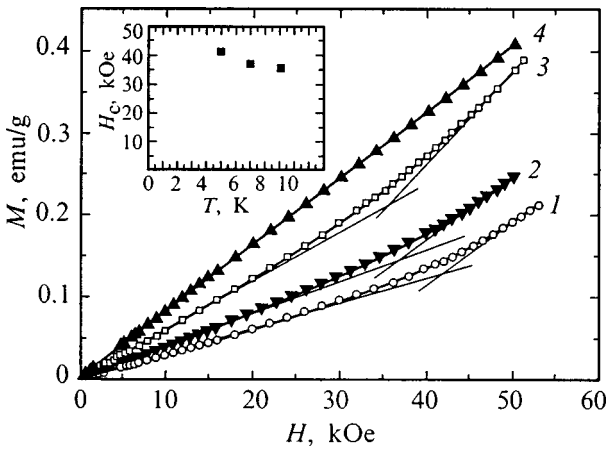

FIG. 4. Field dependences of the magnetization of a $Cu_3B_2O_6$ single crystal (orientation of the field as in Fig. 2) at various temperatures: *1*, *2*, *3*, *4*: — 5, 7, 9, and 12 K respectively. Inset — temperature dependence of the field corresponding to the discontinuity (see text).

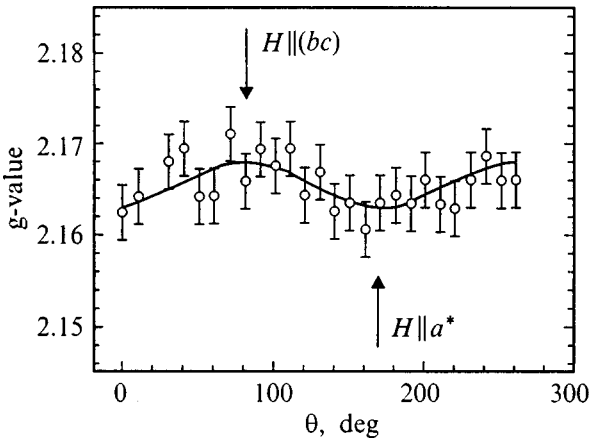

FIG. 5. Angular dependence of the g factor of the magnetic resonance line at room temperature for $Cu_3B_2O_6$, $\nu = 36.22$ GHz; a^* — magnetic field perpendicular to the bc plane of the crystal.

The field dependences of the magnetization of $Cu_3B_2O_6$ for the same orientation of the magnetic field as in Fig. 2 and various temperatures are shown in Fig. 4. At temperatures below 12 K the field dependence of the magnetization becomes nonlinear. The characteristic field corresponding to the magnetization discontinuity depends on temperature. This dependence is shown in the inset in Fig. 4; the field corresponding to the discontinuity was obtained by extrapolating the linear segments on the magnetization curves to the point where they intersect.

We also performed preliminary measurements of the electron magnetic resonance of a $Cu_3B_2O_6$ single crystal at a frequency of 36.22 GHz and a temperature of 300 K. Measurements performed for different orientations of the magnetic field showed that there is resonant absorption line, whose position depends weakly on orientation and is determined by an almost isotropic g factor roughly equal to 2.165 (Fig. 5).

Thus, the principal results of our investigation are the discovery of a low-temperature drop in magnetic susceptibility, a nonlinear dependence of the magnetization at temperatures below 10 K, and electron magnetic resonance. The exchange interactions of the Cu^{+2} ions in crystalline $Cu_3B_2O_6$ are predominantly antiferromagnetic. The crystal structure suggests an in-plane magnetic state with a probable ground-state singlet separated from the excited states by an energy gap. Additional experimental studies are needed to establish a more detailed picture of the magnetic state of the crystal investigated.

We thank A. I. Pankrats for some useful discussions.

This research was carried out with financial support from the Krasnoyarsk Territorial Science Foundation (Grant No. 7F0195).

*E-mail: gap@cc.krascience.rssi.ru

[1] N. Motoyama, H. Eisaki, and S. Uchida, Phys. Rev. Lett. **76**, 3212 (1996).
[2] T. Barnes and J. Riera, Phys. Rev. B **51**, 6817 (1994).
[3] Y. Ueda, J. Phys. Soc. Jpn. **65**, 3142 (1996).
[4] G. K. Abdullaev, P. F. Rza-Zade, and Kh. S. Mamedov, Zh. Neorg. Khim. **27**, 1837 (1982).
[5] H. Behm, Z. Kristallogr. **150**, 251 (1981); H. Behm, Z. Kristallogr. B **154**, 251 (1981).
[6] J. B. Goodenough, *Magnetism and the Chemical Bond* (Interscience, New York, 1963; Metallurgiya, Moscow 1968).
[7] B. C. Tsukerblat and M. I. Belinskiĭ, *Magnetochemistry and Radio-Frequency Spectroscopy of Exchange Clusters* [in Russian] (Shiintsa, Kishinev, 1983).
[8] E. Pytte, Phys. Rev. B **10**, 4637 (1974).

Translated by P. Shelnitz

LATTICE DYNAMICS. PHASE TRANSITIONS

Nonequilibrium phase transition in quenched samples of $Fe_{0.1}TiTe_2$

A. N. Titov* and T. B. Popova

Ural State University, 620083, Ekaterinburg, Russia

S. G. Titova

Institute of Metallurgy, Russian Academy of Sciences, Ural Branch, 620016 Ekaterinburg, Russia
(Submitted May 11, 1998)
Fiz. Tverd. Tela (St. Petersburg) **41**, 680–683 (April 1999)

The influence of the heat treatment of $Fe_{0.1}TiTe_2$ samples on the appearance of thermally induced ''levitation'' is investigated. It is postulated that this phenomenon is most probably caused by undamped fluctuations of the electric charge on the surface of particles of the material.
 [S1063-7834(99)02504-6]

New intercalates based on the titanium dichalcogenides M_xTiX_2 (M=Ag, Fe, Co; X=Se, Te) exhibit several unusual phase transitions, which are accompanied by a change in the conductivity type from metallic to thermally activated.[1–4] Special interest has been aroused by the discovery of thermally induced ''levitation'' in these materials,[5] which is observed as continuous motion (hopping, swinging, rotation about an axis, and hovering without support on the ampul walls) of particles of these materials within an evacuated ampul in the temperature range 100−500 °C. The motion of crystals upon phase transitions is not unique and has previously been observed in many materials (see, for example, Ref. 6). Such behavior has traditionally been attributed to sharp changes in the dimensions of the crystals upon a martensitic phase transition or a phase transformations associated with the Jahn–Teller effect. However, this explanation is not convincing in the case of M_xTiX_2, since the motion of crystals of these materials is observed over a broad temperature range and is not restricted in time. Two possible causes of ''levitation'' were suggested in Ref. 5: fluctuations of the dimensions of the crystals due to the formation and dissociation of covalent Ti–M–Ti complexes or fluctuations of the electrostatic surface charge due to a pyroelectric effect. The hypothesis that there is a pyroelectric effect is unconvincing because of the high conductivity of the materials under consideration (1−100 S/cm). This paper is devoted to an investigation of the typical ''levitating'' material $Fe_{0.1}TiTe_2$ for the purpose of obtaining additional information regarding this unusual phenomenon.

The samples of $Fe_{0.1}TiTe_2$ were prepared by the thermal intercalation of powered iron, produced by reducing iron carbonyl in a hydrogen atmosphere, in $TiTe_2$ preliminarily obtained by ampul synthesis from the elements (Ti of 99.95% purity and Te with a purity no less than 99.5%). The $TiTe_2$ synthesis temperature was 950 °C, while the intercalation temperature was 800 °C. The lower value of the intercalation temperature in comparison to the $TiTe_2$ synthesis temperature was used to prevent the mixing of titanium and iron atoms, which has been observed, for example, for the Fe_xTiSe_2 system.[7]

The phase composition of the samples was monitored by x-ray diffraction analysis at room temperature (DRON-UM-1 diffractometer, Cu $K\alpha$ radiation). The temperature dependence of the crystal-lattice parameters was determined on samples quenched from the respective temperatures. The accuracy of the determination of the unit-cell periods was $\Delta a/a=3\times10^{-4}$ and $\Delta c/c=5\times10^{-4}$, respectively. The conductivity σ was measured by a four-point probe on cold-pressed samples of rectangular shape. The experimental procedure was described in detail in Ref. 8.

The phase transitions were detected by differential thermal analysis (DTA) combined with thermogravimetric analysis (TG). The measurements were performed on a Q-1500 derivatograph in a dynamic regime with a heating rate of 5 K/min using powdered $Fe_{0.1}TiTe_2$ samples. Samples weighing ~1 g, which were single-phase according to x-ray diffraction analysis, were placed in special evacuated Pyrex ampuls of small dimensions fitting derivatograph arm. This enabled us to avoid, not only oxidation of the samples in air, but also variation of their composition during the experiments, as well as to perform all the derivatographic measurements for a given composition on the same samples and to avoid errors associated with the inaccuracy of determining the composition when the influence of various heat treatments on the phase composition was investigated. To standardize the original state before rapid cooling, the sample was heated to 550 °C, held at that temperature for about an hour, and slowly cooled together with the furnace over the course of roughly 6 h. For rapid cooling, the ampul with the sample was placed in a furnace heated to the respective temperature, held at that temperature for 10 min, and then withdrawn and forcibly cooled in a jet of air with sprayed drops of water at the rate of ~30 K/s.

The main experimental results are presented in Figs. 1–4. It is clearly seen that the DTA curve of the sample quenched from 350 °C exhibits an endothermic effect at

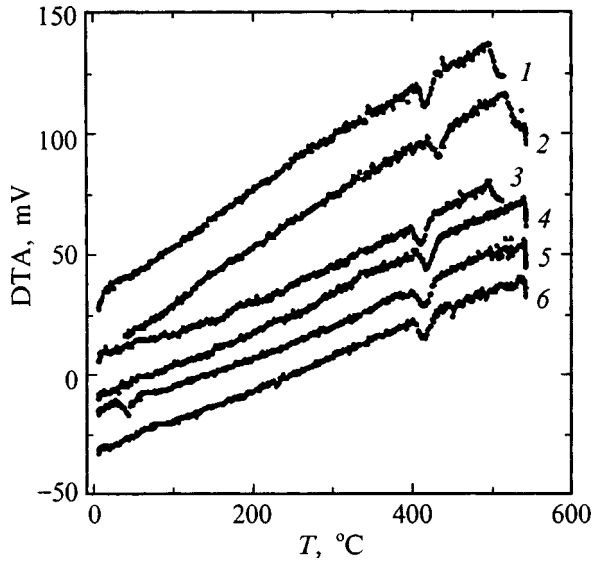

FIG. 1. Temperature dependences of the DTA signal for $Fe_{0.1}TiTe_2$ subjected to various heat treatments: *1* — slow cooling; *2* — quenching from 600 °C; *3* — quenching from 550 °C; *4* — quenching from 450 °C; *5* — quenching from 350°C; *6* — holding at 350°C for a week followed by rapid cooling by the standard method.

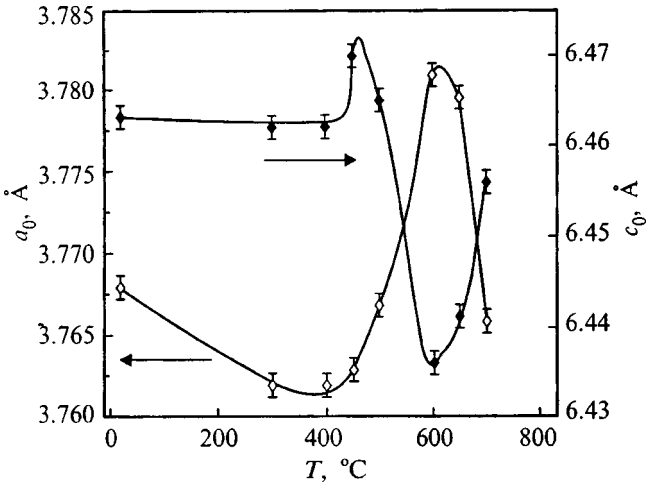

FIG. 3. Values of the crystallographic parameters of the hexagonal $Fe_{0.1}TiTe_2$ lattice for quenched samples as a function of the temperature before quenching.

67°C, which is not observed following the other heat treatments (Fig. 1). This effect can attest to a first-order phase transition with a heat of 4.8 kJ/mol. The TG curve of this sample exhibited a large spread of readings of the derivatograph balance from the temperature of the endothermic effect up to 450°C (Fig. 2). This instability of the TG signal was not observed in samples rapidly cooled from other temperatures and was detected just for the case of quencing from 350°C. We believe that such anomalous behavior of the TG signal can be produced only by the mobility of particles in the sample, since any movement of the lattice (even chaotic) leads to variation of the moment of the force exerted by the sample on the derivatograph arm. Thus, the thermogravimetric curve can be regarded as a record of the motion of particles in a temperature range.

The dependence of the crystallographic parameters of the $Fe_{0.1}TiTe_2$ samples quenched from various temperatures (Fig. 3) demonstrates the absence of appreciable changes in the respective temperature range. Therefore, it seems more justified to postulate that ''levitation'' is due to an electrostatic process rather than an abrupt change in volume. To test this hypothesis, $Fe_{0.1}TiTe_2$ single crystals prepared in accordance with the method described in Ref. 5 were placed in an ampul, whose bottom was partially covered by a highly conductive tantalum foil. Upon heating, motion of the crystals was observed only above the insulating surface of the ampul, while there was no motion above the conducting surface. This allowed us to attribute the ''levitation'' to the interaction of fluctuations of the surface charge of the particles of the material with the induced charge of the dielectric sub-

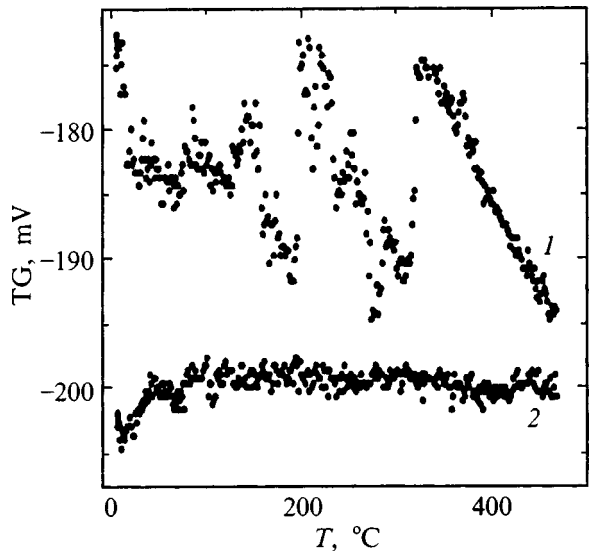

FIG. 2. Typical dependences of the readings of the derivatograph balance (the TG signal) for ''levitating'' (*1*) and ordinary (*2*) samples.

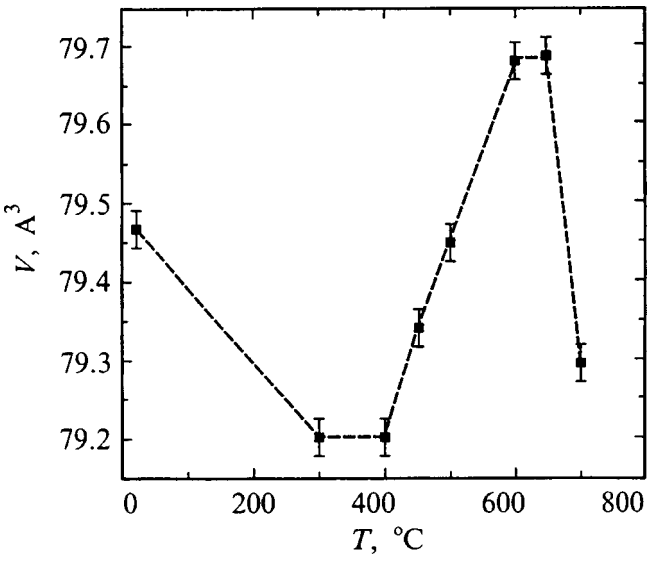

FIG. 4. Unit-cell volume of $Fe_{0.1}TiTe_2$ calculated from values of the crystallographic parameters as a function of the temperature prior to quenching.

strate. To test this hypothesis, we measured the electric charge on the (001) faces of an $Fe_{0.1}TiTe_2$ single crystal during heating. For this purpose, the short-circuit current of conductors connected to the various faces of the crystals was measured, and the potential of the faces was determined directly. The accuracies of the measurements were 1 μA and 1 μV, respectively. Neither method detected the appearance of a permanent surface charge.

The formation of macroscopic surface charges probably requires the presence of ferroelectric domains, whose restructuring with variation of the temperature can lead to fluctuations of the incompletely compensated charge. Such an explanation, however, can be reconciled with the fairly high conductivity of $Fe_{0.1}TiTe_2$ (Fig. 4) only under the additional assumption of high anisotropy of the electrical properties.

The possibility of the appearance of a state with domain fluctuations (switchings) was examined theoretically in a recent paper.[9] It was shown therein that a similar situation can be observed near the phase-transition point from the high-susceptibility phase to the distorted phase, which has a double-well potential. A microscopic mixture of nuclei of these phases has a triple-well potential.

The maintenance of the form of the x-ray diffraction pattern after the samples are quenched points to the absence of phases which appear or decay during quenching. It can be theorized that such phases are present as fragments with a short correlation length and are consequently inaccessible to x-ray analysis. The decrease in c_0 upon the intercalation of iron in $TiTe_2$ (Ref. 10) and the simultaneous decrease in conductivity[5] indicate that intercalation leads to the formation of covalent Ti–Fe–Ti centers, which tie the layers of the matrix lattice together. This situation has been observed in many compounds of the type M_xTiX_2 (M = Ag, Ti, Fe, Co, Ni; X = Se, Te).[10–12] The thermally activated temperature dependence of the conductivity of a slowly cooled sample (Fig. 5) indicates that all the electrons introduced with iron are localized at Ti–Fe–Ti centers. Taking into account that iron exists in the divalent state in Fe_xTiTe_2 (Ref. 10), such a center can be described as $Ti^{3+}-Fe^{2+}-Ti^{3+}$ in the approximation of ionic bonding. It can be theorized that these centers dissociate upon heating, releasing free electrons to the conduction band. The increase in conductivity with increasing temperature agrees well with this hypothesis. However, the lack of an increase in c_0 and even some decrease in the unit-cell volume upon heating provide evidence that dissociation takes place not according to the scheme $Ti^{3+}-Fe-Ti^{3+}\rightarrow Ti^{4+}-Fe-Ti^{4+}+2e$ (e is a free electron), but according to the scheme $Ti^{3+}-Fe-Ti^{3+}\rightarrow Ti^{3+}-Fe-Ti^{4+}+1e$, which leads to maintenance of the covalent bonds tying the layers of the matrix lattice together. A $Ti^{3+}-Fe-Ti^{3+}$ (''2'') center, like a $Ti^{4+}-Fe-Ti^{4+}$ (''0'') center, has a single-well potential, while a $Ti^{3+}-Fe-Ti^{4+}$ (''1'') center has a double-well potential. Thus, a mixture of regions of the crystal lattice where centers of types ''1'' and ''2'' dominate can satisfy the conditions for the existence of domain fluctuations.[9] Therefore, a center of type ''1'' has a dipole moment oriented along a normal to the basal plane of the lattice. The cause of the association of centers in domains may be minimization of the energy of the elastic lattice distortions associated with each type of center. The fact that the rapidly cooled samples have a higher conductivity compared with the slowly cooled (equilibrium) sample can be evidence that rapid cooling fixes a state of the sample with a mixture of centers, leaving some of the electrons free. Dissociation of the centers is probably associated with kinetic hindrances, and the achievement of an equilibrium state requires a long time. In fact, samples held for a week at 350 °C exhibited an absence of ''levitation'' (see Fig. 1). It was shown in Ref. 9 that fluctuations can appear only in a very narrow range of values of the interaction parameters. Such conditions are probably created in part of a rapidly cooled sample as a result of the nonequilibrium process. The similarity of the results of rapid cooling from all temperatures below 600 °C is indicated by the identical slope of the temperature dependences of the DTA signal, which attests to a similar value for the specific heat of these samples. Thus, a temperature of 350 °C, from which quenching leads to ''levitation,'' is not characteristic; we were able to realize conditions for domain fluctuations under this rapid-cooling regime.

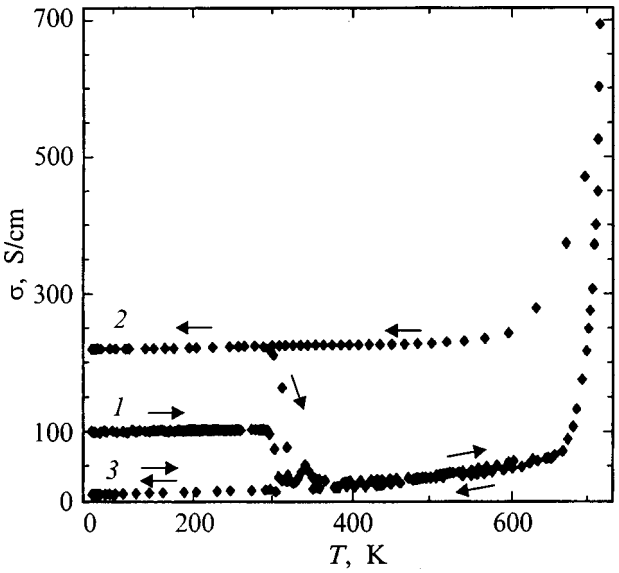

FIG. 5. Temperature dependence of the conductivity of $Fe_{0.1}TiTe_2$ for a sample after various heat treatments: *1* — quenching from 300 °C; *2* — quenching (dynamic regime) from 450 °C; *3* —slow cooling. The direction of the temperature variation is indicated by the arrows next to each curve.

Under all the types of heat treatment the characteristic feature of the DTA curves is the presence of an endothermic effect at 440 °C, whose magnitude differs somewhat for different temperatures at the onset of rapid cooling and amounts to less than 1 J/g. The temperature of this effect is close to the melting point of tellurium, which can segregate as an impurity during heat treatment. Such a thermal effect can be caused by the presence of ~5 wt. % tellurium. This impurity was detected in the x-ray diffraction experiments, but in such cases they revealed an increase in the unit-cell volume of the $Fe_{0.1}TiTe_2$ samples quenched from temperatures above 440 °C, which attests to a possible connection between this endothermic effect and the phase transformation in $Fe_{0.1}TiTe_2$ itself.

In conclusion, we thank Kh. M. Bikkin and A. S.

Moskvin for a useful discussion of the results and their interpretation, as well as P. G. Bruce and Dr. J. T. S. Irvine (St. Andrews University) for providing valuable data.

This work was performed with partial support from the Russian Foundation for Basic Research (Grant No. 97-03-33615a).

*E-mail: alexander.titov@usu.ru

[1] A. N. Titov, Fiz. Tverd. Tela (St. Petersburg) **38**, 3126 (1996) [Phys. Solid State **38**, 1709 (1996)].
[2] A. N. Titov, Neorg. Mater. **33**, 534 (1997).
[3] A. N. Titov and S. G. Titova, J. Alloys Compd. **256**, 13 (1997).
[4] V. G. Pleshchev, A. N. Titov, and A. V. Kuranov, Fiz. Tverd. Tela (St. Petersburg) **39**, 1618 (1997) [Phys. Solid State **39**, 1442 (1997)].
[5] A. N. Titov, Fiz. Met. Metalloved. **81**(6), 75 (1996).
[6] O. Grottaz, F. Kubel, and H. Schmid, J. Mater. Chem. **7**, 143 (1997).
[7] G. Galvarin, J. R. Gavarri, M. A. Buhannic, P. Colombet, and M. Danot, Rev. Phys. Appl. **22**, 1131 (1987).
[8] L. S. Krasavin, M. V. Spitsyn, and A. V. Titov, Fiz. Tverd. Tela (St. Petersburg) **39**, 61 (1997) [Phys. Solid State **39**, 52 (1997)].
[9] V. S. Vikhnin and O. A. Zaĭtsev, Fiz. Tverd. Tela (St. Petersburg) **39**, 547 (1997) [Phys. Solid State **39**, 476 (1997)].
[10] V. G. Pleshchev, A. N. Titov, S. G. Titova, and A. V. Kuranov, Neorg. Mater. **33**(11) (1997).
[11] O. U. Pankratova, L. E. Grigor'eva, R. A. Zvinchuk, and A. V. Suvorov, Zh. Neorg. Khim. **38**, 410 (1993).
[12] Y. Arnaud, M. Chevreton, A. Ahouanjianou, M. Danot, and J. Rouxel, J. Solid State Chem. **17**, 9 (1976).

Translated by P. Shelnitz

Electronic structure and instability of Ni_2MnGa

O. I. Velikokhatnyĭ and I. I. Naumov

Institute of the Physics of Strength and Materials Sciences, Siberian Branch of the Russian Academy of Sciences, 634021 Tomsk, Russia

(Submitted July 9, 1998)
Fiz. Tverd. Tela (St. Petersburg) **41**, 684–690 (April 1999)

The nature of the magnetic and structural phase transitions in the Heusler alloy Ni_2MnGa is studied by numerical calculations of the electronic structure, generalized susceptibility, and various Fermi-surface cross sections. © *1999 American Institute of Physics.* [S1063-7834(99)02604-0]

1. Recent years have witnessed considerable interest in the Ni_2MnGa alloy exhibiting a remarkable variety of phase transformations under cooling and loading (magnetic ordering, phonon mode softening, transitions to incommensurate long-period structures, martensitic transformations etc.).[1–15] Phase transformations and pretransition states are responsible for many of the unusual properties of this alloy, in particular, the shape-memory effect. It is essential that, unlike other alloys with similar characteristics, the shape memory in Ni_2MnGa can be controlled by an external magnetic field (martensitic transformations take place in the ferromagnetic state).[2,7,12,13,15] This and some other aspects give one grounds to classify Ni_2MnGa among the very promising, so-called smart materials.[16]

The Ni_2MnGa compound undergoes during cooling the following sequence of phase transformations[1,3,9,11,14]

$$\beta \xrightarrow{380\ \mathrm{K}} \beta_{\mathrm{FM}} \xrightarrow{260\ \mathrm{K}} \mathrm{PM} \xrightarrow{200\ \mathrm{K}} \mathrm{M},$$

where β is the high-temperature nonmagnetic phase with cubic symmetry (the Heusler structure or $L2_1$), β_{FM} is the ferromagnetic phase with the same structure ($L2_1$), PM is the premartensitic phase with a tripled period along the [110] direction, and M is the martensitic tetragonal phase with an incommensurate lattice modulation along the same direction. The $\beta_{\mathrm{FM}} \rightarrow$ PM transition consists actually in condensation of transverse acoustic phonons $TA_2[\xi\xi 0]$ with $\xi = 1/3$ (a first-order, but very close to second-order transition).[8,9,11,14] It might seem that this condensation would create a homogeneous strain in the original cubic lattice. At the same time the original Bragg reflections reveal neither splitting nor shear[9,11,14] so that, on the whole, the PM phase remains cubic.

Significantly, the ''preparation'' of the system for the $\beta_{\mathrm{FM}} \rightarrow$ PM transition starts not in the ferromagnetic phase β_{FM} but rather in the high-temperature nonmagnetic β phase. In the latter phase, the transverse phonon mode $TA_2[\xi\xi 0]$ exhibits an anomaly at $\xi \approx 1/3$ already for $T \geqslant 400$ K, which becomes a dip as the temperature is lowered.[9,11] Ferromagnetic ordering (the $\beta \rightarrow \beta_{\mathrm{FM}}$ transition) in no way stops the process of dip formation in TA_2 so that, at $T_I = 260$ K, as already mentioned, phonons with $\mathbf{q} = \pi/a[1/3,1/3,1/3]$ condense to initiate the transition from β_{FM} to the tripled premartensitic PM phase. It should be pointed out that besides the short-wavelength TA_2 phonons, the elastic modulus $C' = (C_{11} - C_{12})/2$, which is genetically connected with the long-wavelength behavior of the same TA_2 mode in the long-wavelength limit, also shows an anomalous temperature dependence. Moreover, the C_{44} and C_{11} moduli exhibit a softening with decreasing temperature as well.

The martensite transformation PM→M ($T_m \approx 200$ K) consists both an appreciable tetragonal lattice distortion ($a = 5.920$ Å and $c = 5.566$ Å, $c/a \approx 0.94$, Ref. 1) and of a periodic shear of the (110) planes along $[1\bar{1}0]$. It had been believed that the modulation period in the $(110)[1\bar{1}0]$ system is commensurate and equal to five (110) spacings (with no shear at each fifth plane).[2–7,10] More precise measurements revealed, however, that the period is in actual fact incommensurate and is characterized by a wave vector $\pi/a\,[0.43,0.43,0]$.[11] We shall refer in what follows to this martensitic structure as M(5) to indicate that the period of its lattice modulation is approximately five interplanar distances.

The martensite transformation temperature T_m and the structure of the martensitic phase are extremely sensitive to a deviation of the alloy from stoichiometry. For instance, when excess Ga was substituted primarily for Ni in the $Ni_{47.6}Mn_{25.7}Ga_{26.7}$, the T_m temperature could not be reached by cooling down to 4.2 K.[14] On the other hand, the $Ni_{52}Mn_{25}Ga_{23}$ alloy where, conversely, excess Ni was introduced in place of Ga, transforms not to M(5) but rather to a bcc monoclinic structure with $a = 6.14$ Å, $b = 5.78$ Å, $c = 5.51$ Å, and $\gamma = 90.5°$.[10] Similar to the PM and M(5) phases, it is characterized by a transverse static-displacement wave of atoms having a wave vector normal to the (110) plane. We shall refer subsequently to this structure as M(7) because its wavelength is equal to seven distances between these planes.

Martensitic transformations in the alloy under study can be driven not only by a change in temperature but by a load application above T_m as well. For instance, compression along [100] initiates the PM → M(5) transition; note that the c axis in the M(5) martensitic structure is parallel to the direction of compression, and the modulation vector, perpendicular to it.[3,6,10] [110] compression induces a sequence of transitions: PM → M(5) → M(7) → T, where T is a tetrago-

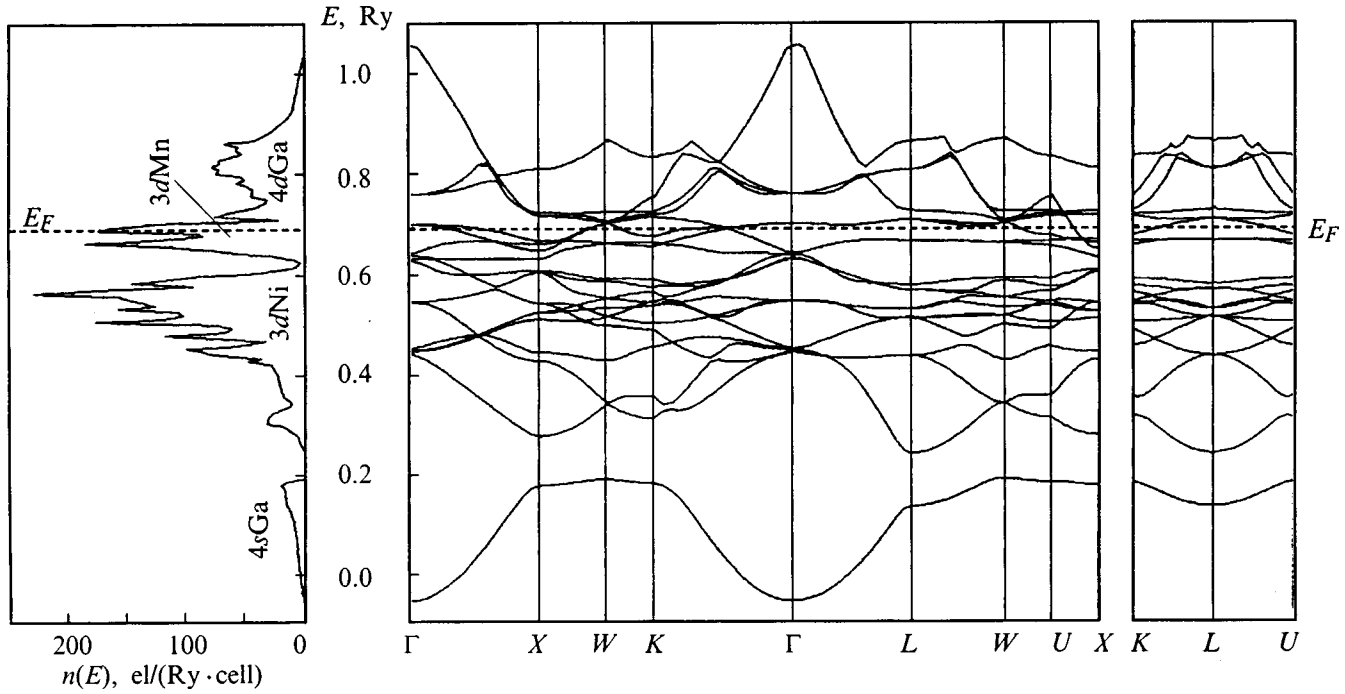

FIG. 1. Electron energy spectrum $\varepsilon_\lambda(\mathbf{k})$ and density of states $n(\varepsilon)$ of the paramagnetic β phase of Ni_2MnGa. The electronic states providing a dominant contribution to the total $n(\varepsilon)$ are identified.

nal structure with $a=b=5.22$ Å and $c=6.44$ Å.[4–7,10] Unlike M(5), it exhibits a tetragonal ratio c/a larger than unity ($c/a=1.234$) and is not modulated. Tension along [100] initiates the same transformation sequence PM → M(5) → M(7) → T; but the c axis in M(5) is now perpendicular to the direction of tension (in contrast to the [001] compression), and the modulation vector has a projection on this direction.[4,10] In the M(7) structure, the largest parameter a is oriented along the tension axis, and the direction of the lattice modulation, similar to the case of M(5), has a projection on this axis. In nonstoichiometric alloys the stress-induced phase transitions may follow another sequence.[10]

Because a lowering of temperature and applied loads give rise to increasingly complex structures, it appears reasonable to consider first the factors responsible for instabilities in the most symmetric, high-temperature phases β and β_{FM}. We are not aware of any similar attempts based on *ab initio* electronic structure calculations. At the same time it is *a priori* obvious that, for instance, transitions to long-period martensitic structures M(5) and M(7) cannot be accounted for by a simple model of short-range forces and should instead be related to long-range interaction, which depends essentially on local geometry of the Fermi surface. It is this situation that is observed in nonmagnetic β alloys exhibiting the shape-memory effect (TiNi, CuZn, Ni-Al etc.), where the formation of long-period lattices is unambiguously associated with nesting parts of the Fermi surface.[17–21] It would be reasonable to expect the same to apply to the Ni_2MnGa alloy.

In this connection the objective of this work was to investigate the driving force of the ferromagnetic ordering (i.e. of the $\beta \rightarrow \beta_{FM}$ transition) and to make a comprehensive analysis of the Fermi surface geometry in the β and β_{FM} phases, including a search for its superposing portions capable of initiating transitions to the three-layer (PM), five-layer [M(5)], and seven-layer [M(7)] structures. Self-consistent calculations of the electron-energy spectrum $\varepsilon_\lambda(\mathbf{k})$, density of electronic states $n(\varepsilon_F)$, generalized electronic susceptibility

$$\chi(\mathbf{q})=\frac{2\Omega}{(2\pi)^3}\int d\mathbf{k}\sum_{\lambda,\lambda'}\frac{f(\varepsilon_\lambda(\mathbf{k}))[1-f(\varepsilon_{\lambda'}(\mathbf{k}+\mathbf{q}))]}{\varepsilon_{\lambda'}(\mathbf{k}+\mathbf{q})-\varepsilon_\lambda(\mathbf{k})}, \tag{1}$$

and of various Fermi surface cross sections in the β and β_{FM} phases were carried out. We used the full-potential spin-polarized LMTO method[22] within the local-spin-density approximation. The exchange correlation potential was of the Barth-Hedin type.[23] The basis set included the $4s$,$4p$, and $4d$ Ga orbitals, while the strongly localized $3d$ orbitals of this element were assigned to core states. The lattice parameter chosen was 5.825 Å,[1] and integration over occupied states was performed by the tetrahedral method;[24] the self-consistent calculation of the spectrum $\varepsilon_\lambda(\mathbf{k})$ was performed over 72 reference points in the irreducible part of the Brillouin zone, and that of $\chi(\mathbf{q})$, over 490 points. The calculation of $\chi(\mathbf{q})$ included only the energy bands crossing the Fermi level and governing the behavior of this quantity [bands 15 and 16 in the nonmagnetic phase β, and bands 13 and 14 for the spin-up (+) states and 17,18,19 for the spin-down (–) states in the β_{FM} phase]. It should be pointed out that, in the case of the ferromagnetic phase β_{FM}, we calculated the $\chi=\chi^{++}+\chi^{--}$ susceptibility determined by inter- and intra-band electronic transitions without spin reversal, because it is its features that may indicate the possibility of charge-density wave and long-period structure formation and

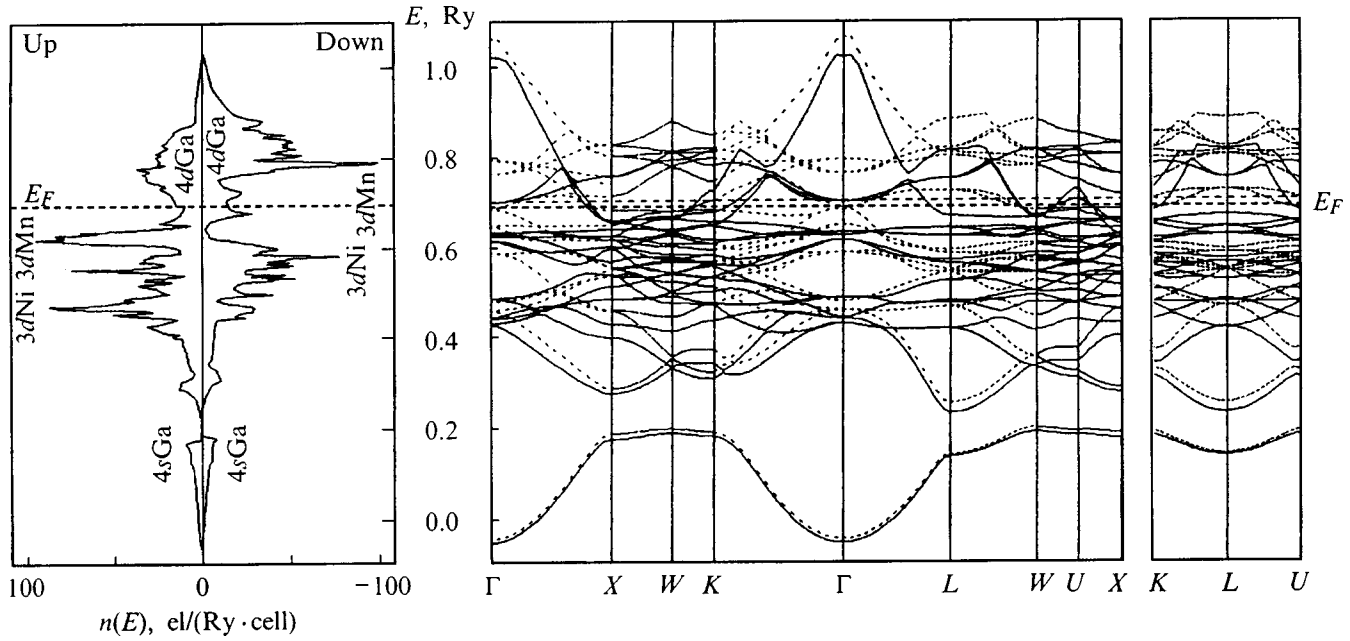

FIG. 2. Electron energy spectrum $\varepsilon_\lambda(\mathbf{k})$ and density of states $n(\varepsilon)$ of the ferromagnetic β phase of Ni_2MnGa. The electronic states providing a dominant contribution to the total $n(\varepsilon)$ for both spin orientations are identified.

of the appearance of anomalies in phonon frequency dispersion curves[25,26] (within the ferromagnetic matrix). As for the χ^{+-} susceptibility associated with spin-flip transitions, it was of no interest to us here, because it is related to excitation of spin waves (magnons) with comparatively long wavelengths.[25,26]

2. Figure 1 presents the electron energy spectrum $\varepsilon_\lambda(\mathbf{k})$ and density of states $n(\varepsilon)$ for the paramagnetic β phase of Ni_2MnGa. Note the separation of the d band of the alloy into two subbands, with the lower-energy one (lying ~ 0.6 Ry below ε_F) related genetically to Ni, and the high-energy one (in the region of ε_F), to Mn. An analysis shows that the wave functions corresponding to the lower subband are fairly diffuse, i.e. are of the bonding nature. By contrast, the upper subband is characterized by strongly localized wave functions of the antibonding type. The corresponding sharp peak in $n(\varepsilon)$ is at the ε_F level, and $n(\varepsilon_F)$ assumes a very high value of 175 states/Ry·cell (44 states/Ry·atom).

The valence band extends to ~ 0.45 Ry (6.0 eV) below the Fermi level. This value correlates well with the valence-band widths measured in other manganese-based Heusler alloys, namely, Co_2MnSn (5 eV), Cu_2MnAl (6 eV), and Pd_2MnSn (7 eV).[27]

Ferromagnetic ordering affects the band structure of Ni_2MnGa in the following way (compare Figs. 1 and 2). First, the sharp boundary dividing the d band into two subbands disappears, which implies enhanced hybridization of the Ni and Mn $3d$ wave functions. Second, the density of states at Fermi level $n(\varepsilon_F)$ decreases (by about five times!), an effect caused by the Mn d states with oppositely oriented spins which are widely spaced in the Fermi-level region.

The latter factor accounts also for the strong Mn magnetic moment of $\sim 3.49\,\mu_B$. At the same time the magnetic moment at the Ni and Ga atoms is small, 0.33 and $-0.05\,\mu_B$, respectively. This adds up to a moment of 4.10 μ_B per cell, which is in excellent agreement with the experimental value[1] of 4.17 μ_B. The conclusion[1] that the Ni magnetic moment does not apparently exceed 0.3 μ_B is also in accord with our calculations (as already mentioned, we obtained 0.33 μ_B for the Ni moment).

The change in the electronic structure of Ni_2MnGa with the onset of ferromagnetic order is the same as in pure Fe, Co, and Ni.[28] One has therefore grounds to maintain that the ferromagnetism of Ni_2MnGa has the Stoner nature, i.e. it originates from exchange interaction between band electrons.[25,26] Indeed, the Fermi level in nonmagnetic Ni_2MnGa, as already mentioned, coincides with a sharp and strong DOS peak, and the Stoner parameter $I n(\varepsilon_F)$ (I is the exchange interaction constant) should be large. We believe that this parameter is large enough so that the Stoner criterion for ferromagnetism, $I n(\varepsilon_F) \geqslant 1$,[25] is upheld.

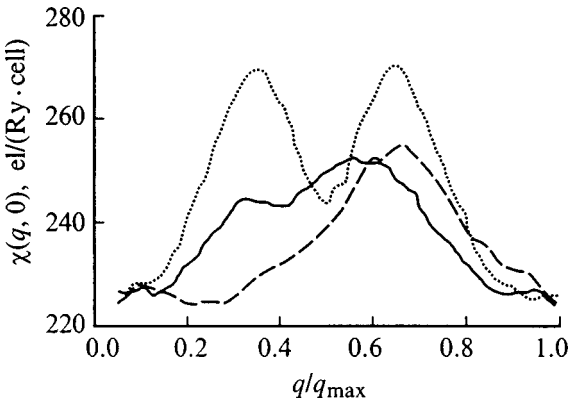

FIG. 3. Static generalized susceptibility $\chi(\mathbf{q})$ of the paramagnetic β phase calculated along the high-symmetry directions in the Brillouin zone of a $B2$ structure. Solid line — along ⟨110⟩, dashed line — along ⟨100⟩, dotted line — along ⟨111⟩.

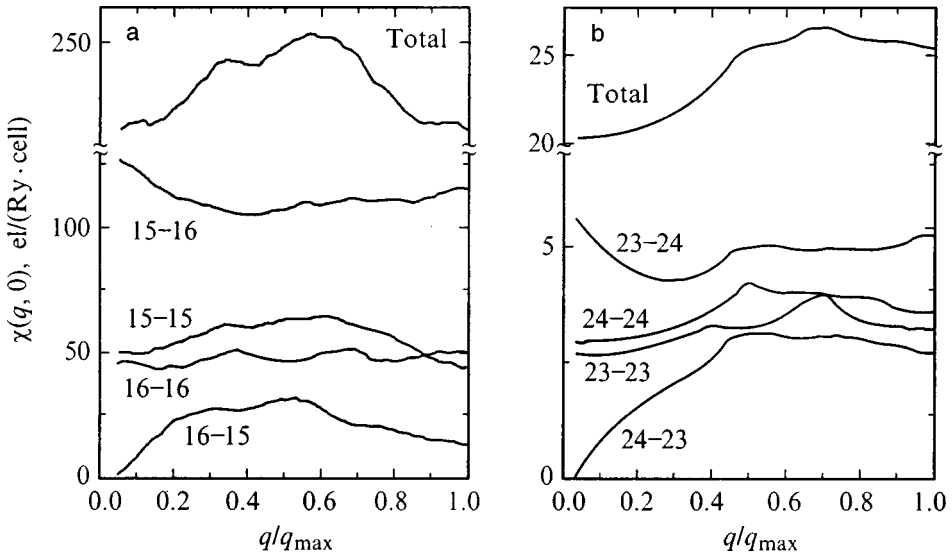

FIG. 4. Generalized susceptibility $\chi(\mathbf{q})$ and the principal partial contributions calculated along the $\langle 110\rangle$ direction in the Brillouin zone of a $B2$ structure for (a) paramagnetic β phase of Ni_2MnGa and (b) high-temperature β phase of $AuCuZn_2$.

In accordance with the picture of itinerant ferromagnetism for this alloy, magnetic interaction should produce spin splitting of the d bands such that in the spin-down bands the Fermi level lies in the region of comparatively small $n(\varepsilon)$ where it separates the bonding and antibonding states. At the same time the spin-up d orbitals are nearly filled. In these conditions, while the electron kinetic energy increases, the gain in the exchange energy compensates this effect completely to make the ferromagnetic state preferable to the paramagnetic one.

By our calculations, the total energy of the ferromagnetic state is lower than that of the paramagnetic one by 0.025 Ry/atom. Using the estimate $k_B T_C \approx (E_{\mathrm{FM}} - E_{\mathrm{AFM}})$, we obtain $T_C = 394$ K, which exceeds nearly ten times the true transition temperature ($T_C \sim 380$ K). The strong overestimate of T_C obtained within Stoner theory is quite typical,[26] it is in no way a consequence of a rough theoretical approach, but rather indicates that this theory cannot be applied to description of high-temperature magnetic properties. Indeed, by Stoner theory all magnetic moments vanish above the Curie temperature T_C. In actual fact, however, only the average magnetization of a system becomes zero above T_C, while localized spin moments and elementary excitations in the form of spin waves can exist.[25,26] It is the inclusion of the latter that can radically change the above estimate.

3. Figure 3 shows the static generalized susceptibility of the paramagnetic phase β calculated along the high-symmetry directions $\langle 100\rangle$, $\langle 110\rangle$, and $\langle 111\rangle$ for the Brillouin zone of a $B2$ structure, which is twice that of an $L2_1$ structure; this is done for conveniency of comparison with experiment, because it is for the wave vectors confined within the first Brillouin zone of a $B2$ structure that the measurements of phonon frequencies ω^2 of the Ni_2MnGa alloy were made.[9,11] As seen from Fig. 3, $\chi(\mathbf{q})$ displays maxima along all the above directions for wave vectors $\sim 2/3\, q_{\max}$, where $q_{\max}$ is the zone edge point. The double-humped $\langle 111\rangle$ curve centered about the midpoint is actually the result of the above-mentioned artificial doubling of the Brillouin zone. An analysis shows that all $2/3\, q_{\max}$ vectors can be identified with the corresponding superposing parts of the Fermi surface.

It appears essential that the local $\chi(\mathbf{q})$ maximum in the $\langle 110\rangle$ direction coincides with the position of the anomaly in the $TA_2[\xi\xi 0]$ branch. This maximum is due to the $15 \rightarrow 15$ and $16 \rightarrow 16$ transitions between the superposing parts of the Fermi surface. This suggests that the anomaly in $TA_2[\xi\xi 0]$ observed in the paramagnetic β phase could be, at least partially, of the Kohn nature.

It is of interest to compare the Ni_2MnGa alloy under study with the $AuCuZn_2$ alloy, which likewise has a Heusler structure, demonstrates also a $TA_2[\xi\xi 0]$ anomaly, and undergoes a transition to the tripled ($9R$) structure.[29] As evident from Figs. 4a and 4b, in these two systems the $\chi(\mathbf{q})$ curves themselves and their partial components exhibit a similar behavior along the $\langle 110\rangle$ direction. Indeed, the global maximum in $\chi(\mathbf{q})$ corresponds in both cases to $\xi = 2/3$ (in the case of $AuCuZn_2$, it is the only maximum altogether). It appears essential that, in contrast to $AuCuZn_2$, in Ni_2MnGa the $\chi(\mathbf{q})$ relation has also a local maximum at $\xi = 1/3$. As already mentioned, it is for this wave vector that one observes a phonon anomaly in Ni_2MnGa.[9,11] At the same time in $AuCuZn_2$ the phonon anomaly is seen to exist at $\xi = 2/3$ rather than at $\xi = 1/3$,[29] i.e. at a wave vector corresponding to the only maximum in $\chi(\mathbf{q})$, and this is what suggests its having the Kohn nature.

That the phonon anomaly in Ni_2MnGa occurs at the local rather than global $\chi(\mathbf{q})$ maximum suggests that the electronic factor plays a secondary, yet quite substantial, part in its formation (unlike $AuCuZn_2$, where it is dominant). By the theory of Gooding and Krumhansl,[30] the dips in the $TA_2[\xi\xi 0]$ curves in the β phases are accounted for by anharmonic effects. Such dips form not for any wave vector but only for $\mathbf{q} = 2\pi/an[1,1,1]$, where n is an integer (for Ni_2MnGa, $n = 6$). Thus in Ni_2MnGa the anharmonic and the electronic factor can act in the same direction and produce the anomaly observed at $\xi = 1/3$.

4. In the ferromagnetic phase, the $\chi(\mathbf{q})$ susceptibility ($\mathbf{q} \| [110]$) exhibits two fairly sharp peaks at the incommen-

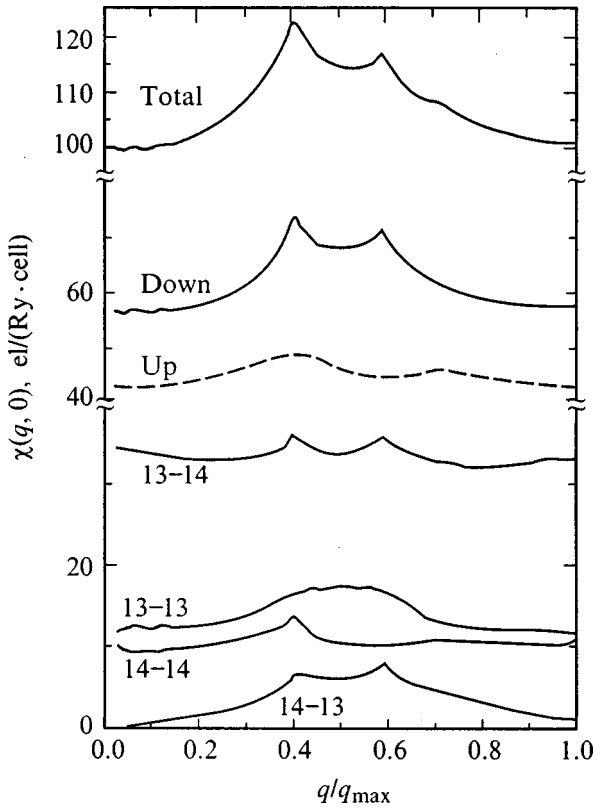

FIG. 5. Generalized susceptibility $\chi(\mathbf{q})$ for the ferromagnetic β phase of Ni_2MnGa calculated along the $\langle 100 \rangle$ direction (upper curve). Also shown are the total contributions to $\chi(\mathbf{q})$ due to spin-up transitions (dashed line) and spin-down transitions (solid line). The figures refer to the partial contributions due to transitions between spin-down states.

surate vectors $\mathbf{q}_1 \approx \pi/a\,[0.42,0.42,0]$ and $\mathbf{q}_2 \approx \pi/a[0.59,0.59,0]$, to which the closest commensurate vectors are $\mathbf{k}_1 = \pi/a\,[2/5,2/5,0]$ and $\mathbf{k}_2 = \pi/a\,[4/7,4/7,0]$, accordingly (Fig. 5). As seen from the figure, the maximum in $\chi(\mathbf{q})$ at $\mathbf{q}=\mathbf{q}_1$ derives from electronic transitions between the spin-down states $13\rightarrow 14$, $14\rightarrow 13$, and $14\rightarrow 14$. As for the $\chi(\mathbf{q})$ maximum at $\mathbf{q}=\mathbf{q}_2$, it is due only to the $13\rightarrow 14$ and $14\rightarrow 13$ transitions. The $13\rightarrow 14$ and $14\rightarrow 13$ contributions at $\mathbf{q}=\mathbf{q}_1$ and $\mathbf{q}=\mathbf{q}_2$ are specific in that they are related to the nesting hole ($13h$) and electronic ($14e$) parts of the Fermi surface separated by the above vectors (see Fig. 6a and 4b). Remarkably, the contribution to $\chi(\mathbf{q})$ of the $14\rightarrow 14$ intraband transitions is maximum also at $\mathbf{q}=\mathbf{q}_1$, as a result of which the total susceptibility for this wave vector is higher than that for $\mathbf{q}=\mathbf{q}_2$. The specific feature of the $14\rightarrow 14$ contribution at $\mathbf{q}=\mathbf{q}_1$ is due to the flattened parts of the Fermi surface in the 14th band, which is clearly seen from the Fermi-surface cross sections presented in Fig. 6b and 6c. It appears remarkable that vector $\mathbf{q}_1$ practically coincides with the wave vector $\pi/a\,[0.43,0.43,0]$ characterizing lattice modulation in the M(5) structure. One can thus maintain that the $\beta_{FM}\rightarrow$ M(5) transition is of the Peierls type, although it is possibly not accompanied by complete softening of the phonon modes (in Ni_2MnGa, the $TA_2\,[\xi,\xi,0]$ branch as a whole lies low). In view of this, the tetragonal distortion of the M(5) phase may be considered as resulting from lattice accommodation (secondary-order parameter) to the onset of atomic displacement waves throughout the $[110][1\bar{1}1]$ system (the primary, true order parameter).

Furthermore, the $\chi(\mathbf{q})$ peak at $\mathbf{q}=\mathbf{q}_2$ indicates a tendency to form within the β_{FM} phase of a structure whose period along [110] would exceed sevenfold the original one. It appears reasonable to identify this structure with the experimentally observed M(7). One does not observe here, however, a one-to-one correspondence with the M(5) case, and the problem can be formulated as follows.

Atomic displacements in the M(5) and M(7) phases were approximated in Refs. 4 and 10 by superposition of commensurate sine waves whose amplitudes were chosen from the best-fit condition between the measured and calculated x-ray intensities. It was found that, in the M(5) case, the displacement of each (110)-type jth plane in the structure can be well fitted by the expression $A\sin(k_1 j)+B\sin(2k_1 j)+C\sin(3k_1 j)$ with $A=-0.06$, $B=0.002$, $C=-0.007$, and $\mathbf{k}_1=\pi/a\,[2/5,2/5,0]$. Because $|A|$ is substantially larger than B and $|C|$, the displacements in a five-layer structure are determined by a wave with a vector close to $\mathbf{q}_1$, which produces the maximum in $\chi(\mathbf{q})$. For the M(7) seven-layer phase, the situation is different. In this structure, the displacement of the jth plane is well described by a sum $A\sin[(k_2/2)j]+B\sin(k_2 j)$ with $A=0.083$, $B=-0.027$, and $\mathbf{k}_2=\pi/a\,[4/7,4/7,0]$. Here likewise $A>|B|$, and the leading contribution is due not to the vector $\mathbf{k}_2$ but rather to $\mathbf{k}_2/2$, i.e. to about one half the nesting vector $\mathbf{q}_2$. This implies that, in contrast to M(5), in the M(7) structure the nesting properties of the Fermi surface are related to the lattice modulation in a more complex way.

In view of the specific features in $\chi(\mathbf{q})$ the M(7) structure, as M(5), should also be incommensurate. Experimental papers consider it, however, as commensurate.[4,10] In this connection it appears appropriate to repeat that the M(5) phase was also believed to be commensurate for a long time, and that only high-precision measurements revealed its incommensurate nature. We are of the opinion that the question of whether lattice modulations in the M(7) martensitic structure are commensurate or not requires further experimental investigation.

The original feature in $\chi(\mathbf{q})$ observed at $\xi=1/3$ apparently disappears under ferromagnetic ordering (Fig. 5). Thus no nesting-associated reasons for $TA_2\,[\xi\xi 0]$ softening for this wave vector exist in the β_{FM} phase any longer. Because in actual fact, as already mentioned, the softening process does not stop, its driving forces are in no way related to nesting and/or flattened portions of the Fermi surface. As suggested above, they are apparently of an anharmonic nature.[30]

5. Thus the transition from paramagnetic to ferromagnetic state in Ni_2MnGa is most likely of the Stoner type and is due to a very high density of states at the Fermi level in the paramagnetic phase. This phase is characterized also by the existence of nesting portions in the Fermi surface, which are separated by vector $\mathbf{q}=\pi/a\,[1/3,1/3,1/3]$. Besides other factors, these portions may also contribute to softening of the transverse acoustic branch $TA_2\,[\xi\xi 0]$ for the above vector (by producing a Kohn-type anomaly). The ferromagnetic

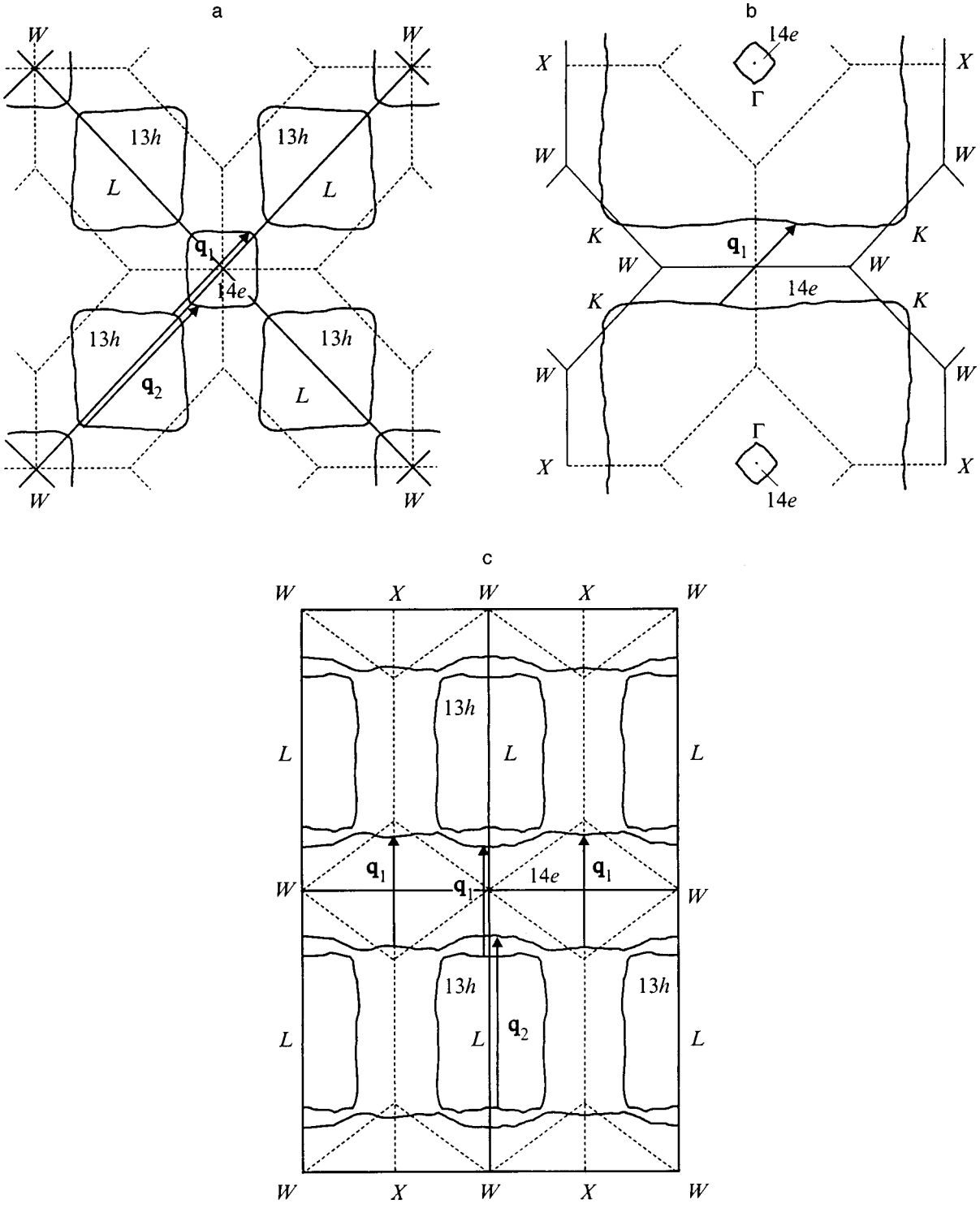

FIG. 6. Portions of the Fermi surface cross sections drawn in the repeated-band diagram of the Ni_2MnGa ferromagnetic β phase for spin-down states. (a) Section in $k_z=0.5$ plane; (b) $k_z=0$; (c) $k_z+k_y=1$. $\mathbf{q}_1$ and $\mathbf{q}_2$ are nesting vectors.

phase is characterized by two sharp peaks in $\chi(\mathbf{q})$ ($\mathbf{q}\|[110]$) at $\mathbf{q}_1\approx\pi/a\,[0.42,0.42,0]$ and $\mathbf{q}_2\approx\pi/a\,[0.56,0.56,0]$ related to Fermi surface nesting. While nesting of the first type may give rise to the experimentally observed five-layer martensitic structure M(5), that of the second type could account (but possibly with not as high a confidence) for the seven-layer martensitic M(7).

[1] P. J. Webster, K. R. A. Ziebeck, S. L. Town, and M. S. Peak, Philos. Mag. B **49**, 295 (1984).
[2] A. N. Vasil'ev, V. V. Kokorin, Yu. I. Savchenko, and V. A. Chernenko, Zh. Éksp. Teor. Fiz. **98**, 1437 (1990) [Sov. Phys. JETP **71**, 803 (1990)].
[3] I. K. Zasimchuk, V. V. Kokorin, V. V. Martynov, A. V. Tkachenko, and V. A. Chernenko, Fiz. Met. Metalloved. No. 6, 110 (1990).
[4] V. V. Kokorin and V. V. Martynov, Fiz. Met. Metalloved. No. 9, 106 (1991).

[5] V. V. Kokorin, V. V. Martynov, and V. A. Chernenko, Fiz. Tverd. Tela (Leningrad) **33**, 1250 (1991) [Sov. Phys. Solid State **33**, 708 (1991)].
[6] V. V. Martynov and V. V. Kokorin, J. Phys. B **2**, 739 (1992).
[7] A. N. Vasil'ev, A. Keiper, V. V. Kokorin, V. A. Chernenko, T. Takagi, and J. Tani, JETP Lett. **58**, 306 (1993).
[8] G. Fritsch, V. V. Kokorin, and A. Kempf, J. Phys.: Condens. Matter **6**, L107 (1994).
[9] A. Zheludev, S. M. Shapiro, P. Wochner, A. Schwartz, M. Wall, and L. E. Tanner, Phys. Rev. B **51**, 11310 (1995).
[10] V. V. Martynov, J. Phys. III **5**, C8-91 (1995).
[11] A. Zheludev, S. M. Shapiro, P. Wochner, A. Schwartz, M. Wall, and L. E. Tanner, J. Phys. III **5**, C8-1139 (1995).
[12] V. V. Kokorin, V. A. Chernenko, A. N. Vasil'ev, S. M. Konoplyuk, and E. A. Khapalyuk, Fiz. Tverd. Tela (St. Petersburg) **37**, 3718 (1995) [Phys. Solid State **37**, 2049 (1995)].
[13] A. N. Vasil'ev, S. A. Klestov, V. V. Kokorin, R. Z. Levitin, V. V. Snegirev, and V. A. Chernenko, Zh. Éksp. Teor. Fiz. **109**, 973 (1996) [JETP **82**, 524 (1996)].
[14] V. V. Kokorin, V. A. Chernenko, J. Pons, E. Cesari, and S. Segui, Fiz. Tverd. Tela (St. Petersburg) **39**, 557 (1997) [Phys. Solid State **39**, 485 (1997)].
[15] S. M. Konoplyuk and Yu. P. Stetskiv, Metall. Nov. Tekhnol. **19**, 54 (1997).
[16] R. E. Newnham, MRS Bull. **18**, No. 4, 24 (1993).
[17] G.-L. Zhao, T. C. Leung, B. N. Harmon, M. Keil, M. Müllner, and W. Weber, Phys. Rev. B **40**, 7999 (1989).
[18] I. I. Naumov, O. I. Velikokhatnyĭ, and V. Z. Bashirov, JETP Lett. **54**, 573 (1991).
[19] O. I. Velikokhatnyĭ, I. I. Naumov, and V. Z. Bashirov, Fiz. Met. Metalloved. No. 12, 30 (1992).
[20] G. L. Zhao and B. N. Harmon, Phys. Rev. B **42**, 2818 (1992).
[21] I. I. Naumov and O. I. Velikokhatnyi, J. Phys.: Condens. Matter **9**, 10339 (1997).
[22] S. Yu. Savrasov and D. Yu. Savrasov, Phys. Rev. B **46**, 12181 (1992).
[23] U. Barth and L. Hedin, J. Phys. C **5**, 1629 (1972).
[24] J. Rath and A. J. Freeman, Phys. Rev. B **11**, 2109 (1975).
[25] T. Moriya, J. Magn. Magn. Mater. **14**, 1 (1979).
[26] R. M. White, *Quantum Theory of Magnetism* (Springer, Berlin, 1983; Mir, Moscow, 1985).
[27] P. Mohn, P. Blaha, and K. Schwarz, J. Magn. Magn. Mater. **140-144**, 183 (1995).
[28] *Handbook of the Band Structure of Elemental Solids*, edited by D. A. Papaconstantopoulos (Plenum, New York, 1986).
[29] M. Mori, Y. Yamada, and G. Shirane, Solid State Commun. **17**, 127 (1975).
[30] R. J. Gooding and J. A. Krumhansl, Phys. Rev. B **39**, 1535 (1989).

Translated by G. Skrebtsov

Study of Mn^{2+} EPR spectra in the incommensurate phase of Rb_2ZnCl_4

M. P. Trubitsyn

Dnepropetrovsk State University, 320625 Dnepropetrovsk, Ukraine
(Submitted August 19, 1998)
Fiz. Tverd. Tela (St. Petersburg) **41**, 691–694 (April 1999)

An EPR study of Mn^{2+} centers in the incommensurate phase of rubidium tetrachlorozincate crystals is reported. It is shown that the temperature dependence of the high-field hyperfine line group $M_S=3/2\leftrightarrow 5/2$ can be described in terms of a simple ''local'' model.[1] The data obtained support the nonclassical type of critical behavior in Rb_2ZnCl_4 crystals corresponding to the three-dimensional Heisenberg model for a two-component order parameter. © *1999 American Institute of Physics.* [S1063-7834(99)02704-5]

Experimental methods capable of providing information on local properties of a crystal structure occupy a special place in studies of incommensurate (IC) modulated phases. In particular, the specifically inhomogeneous broadening of magnetic-resonance lines made it possible to confirm and, for a number of crystals, to establish the onset of an incommensurate modulation of the structure. It is known that, below the transition point T_i from the high-temperature to the IC phase, the loss of translational periodicity results in a transformation of single resonance lines into an inhomogeneously broadened spectrum bounded by singular peaks. The singular shape of the spectrum reflects the dependence of the resonance position on the incommensurate displacement field U. As a reasonable approximation in the high-temperature region of the IC phase may serve the one-harmonic model, by which structural distortions can be presented as $U=\rho\cos\varphi(z)$, with the amplitude ρ assumed to be spatially independent, and the phase φ, to depend linearly on the coordinate z along the modulation axis, $\varphi=q_iz+\varphi_0$. In this case the resonant fields near T_i can be expanded[1]

$$H_R=H_0+aU+\frac{1}{2}bU^2+\ldots$$

$$=H_0+A\Delta T^{\beta}\cos\varphi+\frac{1}{2}B\Delta T^{2\beta}\cos^2\varphi;$$

$$\Delta T=(T_i-T),\quad \rho\sim\Delta T^{\beta},\quad A\sim a,\quad B\sim b, \qquad (1)$$

where H_0 corresponds to the resonance-line position in the high-temperature phase, and the expansion coefficients depend on the localization of active centers in the unit cell and on the magnetic field orientation relative to the crystallographic axes. This approach, first proposed by Blinc and coworkers, explained the main features of magnetic resonance spectra in the IC phase and stimulated experimental research. The results obtained could not, however, always be described in terms of expansion (1). A variety of considerations were put forward for their interpretation. It was proposed to take into account ''nonlocal effects,''[2] which can become manifest if the distances to neighboring atoms making a dominant contribution to the crystal field at the active center are comparable to the wavelength of the structural modulation. The dephasing in atomic displacements in the active-center environment generated in this case requires taking into account the symmetric and the antisymmetric harmonic of the modulation wave.[2] In their analysis of NMR data, the authors of Ref. 3 assumed the need to include higher-order components in the Fourier expansion of the incommensurate displacement field U.

This work reports on a study of Mn^{2+} EPR spectra of Rb_2ZnCl_4 crystals, which undergo at transition at $T_i=303$ K from the paraelectric phase (space group $Pnam$) to an IC phase modulated along the **a** axis[4]. The measurements were performed on an X-band radiospectrometer equipped with a liquid-nitrogen cryostat. During spectrum recording, the temperature was stabilized to better than 0.1 K.

The spectrum contained the high-field hyperfine sextet $M_S=3/2\leftrightarrow 5/2$, which exhibits the highest sensitivity to structural changes below T_i. At the same time the significant resonance-line splitting in the IC phase permitted studies only within a limited temperature interval adjoining T_i, because further cooling resulted in a superposition of neighboring hyperfine groups. The measurements were carried out in an external magnetic field $\mathbf{H}\|\mathbf{a}$ and for **H** deviating from the **a** axis by 3.5 and 7° in the (**ac**) plane. It is known that above T_i the Mn^{2+} centers lie in the (**ab**) mirror plane, which is locally disrupted in the IC phase. Hence in the $\mathbf{H}\|\mathbf{a}$ orientation the coefficients of the linear term in expansion (1) vanish. If **H** does not lie in the (**ab**) plane, the parameters a and A in Eq. (1) are already nonzero and, in a first approximation, are proportional to the sine of the doubled deflection angle. Thus by varying properly the **H** deflection angle from the **a** axis, one can change the relative magnitude of the coefficients of the linear and quadratic terms in expansion (1), which permits one to verify the applicability of the models proposed in Refs. 1–3.

The position of the resonance lines above the transition point was determined by approximating the experimental profile with a convolution of a Lorentzian with a Gaussian. Below T_i a single center was assumed to be described by a Lorentzian, whose position, according to Eq. (1), depends on the phase of the incommensurate displacement wave

$$\int_0^{2\pi} L\{[H-H_R(\varphi)]/\delta H(\varphi)\}d\varphi.$$

It should be noted that the dependence of the local width δH on phase φ was also taken into account when describing the spectral shape in the IC phase.

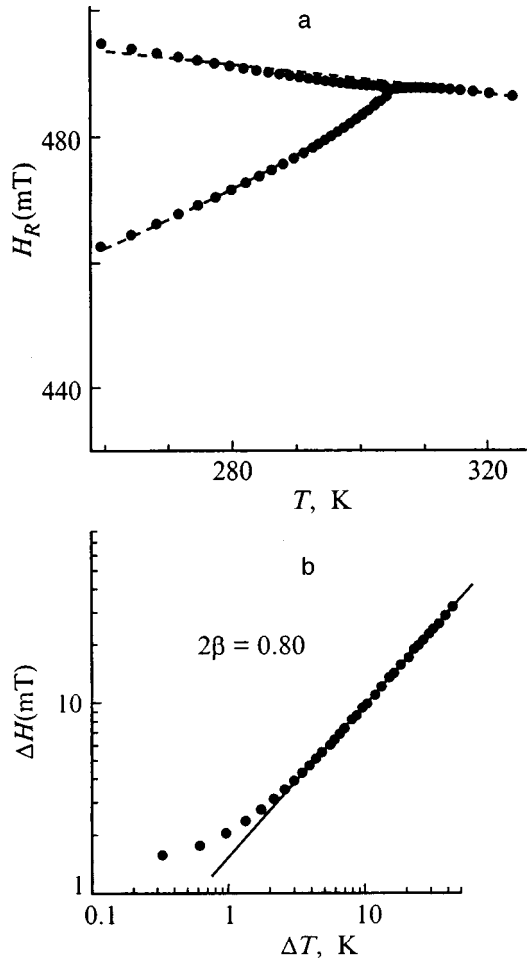

FIG. 1. (a) Temperature dependence of the resonance fields for the low-field component $m_J=5/2$ of the $M_S=3/2\leftrightarrow 5/2$ hyperfine sextet measured for $\mathbf{H}\|\mathbf{a}$. The dashed lines are plots of Eq. (2) with the parameters given in the text. (b) The splitting between the singularities plotted as a function of $\Delta T=T_i-T$ on a log-log scale.

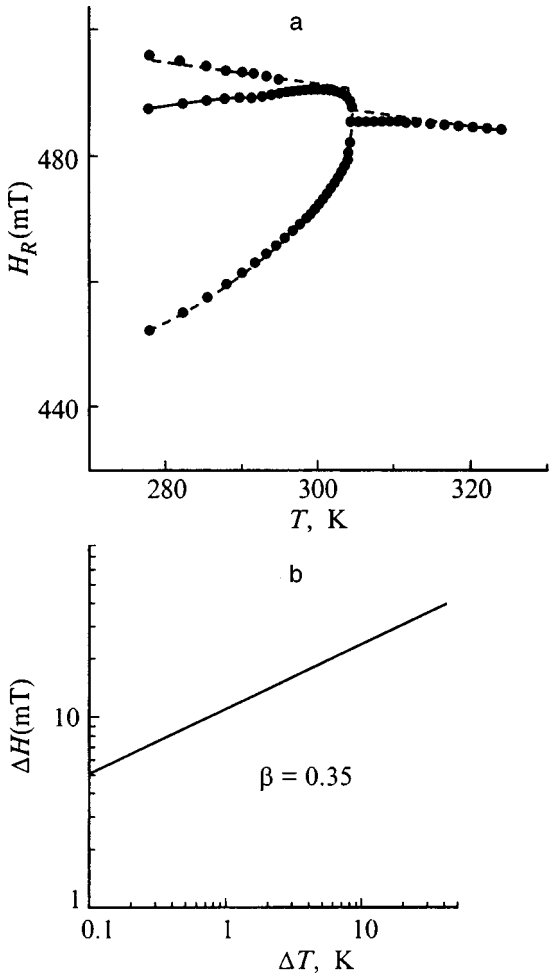

FIG. 2. (a) Temperature dependences of the resonance fields for the $\angle\mathbf{H},\mathbf{a}=3.5°$ and $\mathbf{H}\perp\mathbf{b}$ orientations. The dashed lines are plots of Eqs. (3a) and (3b). (b) Temperature dependence of the distance between the singularities split by the linear term in expansion (1).

The temperature dependences of the position of the low-field hyperfine component ($m_J=5/2$) for $T>T_i$, and of the corresponding singularities for $T<T_i$, are shown in Fig. 1a for the main orientation $\mathbf{H}\|\mathbf{a}$. One readily sees in the paraphase a slight thermal drift (~ -0.11 mT/K) of the resonance line, which below $T_i=304.44$ K splits into a singular spectrum described by the quadratic term in expansion (1). The positions of the singularities are determined by the condition $dH_R/d\varphi=0$ and, according to Eq. (1), can be written

$$H_{Q1}=H_0, \quad (\varphi=\pm\pi/2),$$

$$H_{Q2}=H_0+\frac{1}{2}B\Delta T^{2\beta}, \quad (\varphi=0,\pi). \tag{2}$$

The position of the singularity H_{Q1} corresponds to the line drift in the paraphase extrapolated to the IC phase, whereas the singular peak H_{Q2} shifts relative to H_0 proportional to the squared incommensurate-wave amplitude. The temperature dependence of the splitting between the singularities which, according to Eq. (2), is equal to $\Delta H=H_{Q2}-H_{Q1}=\frac{1}{2}B\Delta T^{2\beta}$, is shown in Fig. 1b on a log-log scale. One readily sees that for $T_i-T\geqslant 3.5$ K the experimental points can be fitted by a straight line with a slope $2\beta=0.80\pm 0.01$. The dashed lines in Fig. 1a display calculated relations obtained using Eq. (2) with a parameter $B_1=-3.28$ mT$\cdot$K$^{-2\beta}$ ($A_1=0$) and the above value of index β. We see that the experimental relations can be satisfactorily described in terms of the ''local'' expansion (1). The deviations from the theoretical curves seen to exist near T_i can be assigned[6,7] to fluctuation contributions.

Figure 2a presents temperature dependences of the resonance fields measured for the magnetic field orientations $\angle\mathbf{H},\mathbf{a}=3.5°$ and $\mathbf{H}\perp\mathbf{b}$. One of the singular peaks in the IC phase is seen to split into two under cooling, and below $T\sim 297$ K three singularities are observed. For this orientation, the linear term in Eq. (1) is no longer symmetry forbidden, and immediately below T_i it causes splitting of the resonance line into two singularities, whose positions are given by the following expressions

$$H_{L1}=H_0+A\Delta T^{\beta}+\frac{1}{2}B\Delta T^{2\beta} \quad (\varphi=0),$$

$$H_{L2}=H_0-A\Delta T^{\beta}+\frac{1}{2}B\Delta T^{2\beta} \quad (\varphi=\pi). \tag{3a}$$

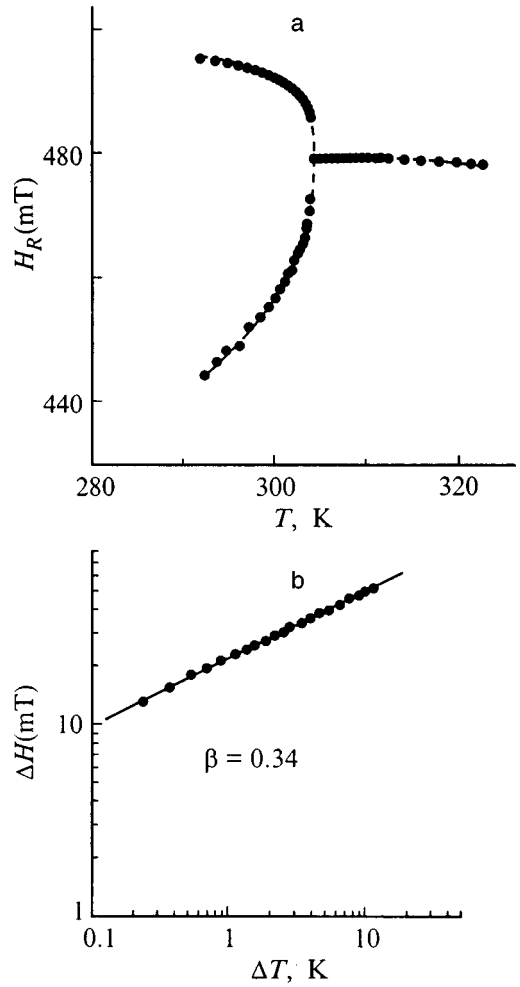

FIG. 3. (a) Temperature dependences of the resonance fields for the $\angle \mathbf{H},\mathbf{a}=7°$ and $\mathbf{H}\perp\mathbf{b}$ orientations. The dashed lines are plots of Eq. (3a). (b) Temperature dependence of the singular splitting plotted on a log-log scale.

As the temperature decreases, the quadratic term ($\propto \Delta T^{2\beta}$) grows faster than the linear one ($\propto \Delta T^{\beta}$) does, and at $T=T_i-(A/|B|)^{1/\beta}$, the singularity H_{L1} ($B<0$) or H_{L2} ($B>0$) splits in two. The position of the third peak is temperature independent and can be written

$$H_{LQ}=H_0-A^2/(2B), \tag{3b}$$

Figure 2b plots the distance between the H_{L1} and H_{L2} singularities split by the linear term as a function of ΔT on a log-log scale. The slope of this relation obtained by least-squares fitting is $\beta=0.35\pm0.01$ within the total temperature range covered. The dashed lines in Fig. 2a are plots of Eqs. (3a) and (3b) calculated with the parameters $A_2=5.32$ mT·K$^{-\beta}$ and $B_2=-3.62$ mT·K$^{-2\beta}$.

As the deflection angle of field **H** from the **a** axis increases to 7° (Fig. 3a), the linear term in Eq. (1) becomes dominant. In the temperature range covered, one observes two singularities whose positions can be described by Eq. (3a). The index of the order parameter derived from the temperature dependence of the singular splitting for the given orientation is $\beta=0.34\pm0.01$ (Fig. 3b). The dashed lines in Fig. 3a are plots of Eqs. (3a) calculated with the parameters $A_3=10.86$ mT·K$^{-\beta}$ and $B_3=-4.02$ mT·K$^{-2\beta}$.

As seen from the above data, the temperature dependence of resonance fields for the $M_S=3/2\leftrightarrow5/2$ hyperfine group in the high-temperature region of the IC phase of Rb_2ZnCl_4 crystals is satisfactorily described by expansion (1) based on a simple local model.[1] The behavior of the high-field singularity when measured in the main orientation, $\mathbf{H}\|\mathbf{a}$ (Fig. 1a), suggests that the ''nonlocality'' of interaction may play a noticeable part at lower temperatures. It is known that the crystal field at Mn^{2+} centers is dominated by their nearest neighbors, namely, the Cl^- ions,[5] which are separated in phase by not more than $\sim2°$ in the modulation wave immediately below T_i,[4] and still less upon further cooling. Therefore the original physical meaning of the ''nonlocality'' of interaction[2] no longer appears appropriate in the case under study. Superposition of rotational vibrations and twisting of the $ZnCl_4$ tetrahedra in the incommensurate distortion wave propagating through the crystal structure[8] seems to be a more likely reason for the appearance of the nonlocal terms in expansion (1).

The magnitude of index β obtained in tilted-field orientations agrees to a fairly high accuracy with the theoretical value of 0.35 from the three-dimensional two-component Heisenberg model[9]. The value of 2β obtained for the case of quadratic coupling of resonance fields with the order parameter ($\mathbf{H}\|\mathbf{a}$ in Fig. 1) exceeds the doubled values of β derived in measurements of the singular splitting induced by linear coupling ($\angle\mathbf{H},\mathbf{a}=3.5$ and 7° in Figs. 2 and 3). This discrepancy may be due to secondary order parameters having a pattern of critical behavior different from that of the primary lattice distortion. Their contribution to singular splitting in the case of quadratic coupling of resonance fields with the order parameter may affect the magnitude of the critical indices.[9–11] In accordance with the analysis made in Ref. 9, this manifestation of the secondary order parameters provides supportive evidence for a nonclassical nature of the critical properties of rubidium tetrachlorozincate crystals and puts an end to the earlier attempts[12,13] of describing the available experimental data, which were based on Landau theory.

[1] R. Blinc, Phys. Rep. **79**, 331 (1981).
[2] R. Blinc, J. Seliger, and S. Žumer, J. Phys. C **18**, 2313 (1985).
[3] J. M. Perez-Mato, R. Walisch, and J. Petersson, Phys. Rev. B **35**, 6529 (1987).
[4] K. Gesi and M. Iizumi, J. Phys. Soc. Jpn. **46**, 697 (1979).
[5] M. Pezeril, J. Emery, and J. C. Fayet, J. Plasma Phys. **41**, L-499 (1980).
[6] A. Kaziba, M. Pezeril, J. Emery, and J. C. Fayet, J. Plasma Phys. **46**, L-387 (1985).
[7] M. P. Trubitsyn and V. V. Savchenko, Ferroelectrics **134**, 259 (1992).
[8] J. Emery, S. Hubert, and J. C. Fayet, J. Plasma Phys. **45**, L-693 (1984).
[9] R. A. Cowley and A. D. Bruce, J. Phys. C **11**, 3577 (1978).
[10] A. D. Bruce and R. A. Cowley, *Structural Phase Transitions* (Taylor & Francis, London, 1981; Mir, Moscow, 1984).
[11] R. Walisch, J. M. Perez-Mato, and J. Petersson, Phys. Rev. B **40**, 10747 (1989).
[12] J. Petersson and E. Schneider, Ferroelectrics **53**, 297 (1984).
[13] J. J. L. Horikz, A. F. M. Arts, and H. W. de Wijn, Phys. Rev. B **37**, 7209 (1988).

Translated by G. Skrebtsov

Spontaneous graphitization and thermal disintegration of diamond at $T>2000$ K

V. D. Andreev*)

Institute of Superhard Materials, Ukrainian Academy of Sciences, 254074 Kiev, Ukraine
(Submitted September 1, 1998)
Fiz. Tverd. Tela (St. Petersburg) **41**, 695–701 (April 1999)

A theoretical description of the mechanism and kinetics of the graphitization of diamond taking place with two sharply differing activation energies and accompanied by explosive disintegration of the graphitized diamond crystals is obtained in the approximation of a model interatomic interaction potential. © *1999 American Institute of Physics.*
[S1063-7834(99)02804-X]

It is known from experiments involving the heating of diamond to temperatures above $T>2000$ K in a vacuum or an inert medium[1–3] that the explosive disintegration and spontaneous graphitization of diamond crystals take place under such conditions. These purely outward manifestations of the behavior of diamond are reflected quantitatively in the plotting of the specific heat $c_p(T)$, which begins to rise at $T>2000$ K with a deviation from the ''Debye'' form.[4–6] In addition, the investigations of the graphitization of diamond powders performed in Ref. 3 in the temperature range 1900−2200 K showed that the Arrhenius plot (Fig. 1) in $\ln C_g$ vs T^{-1} coordinates (C_g is the graphite content in the sample after isochoric anneals of diamond for $\Delta t=30$ min) exhibits two linear segments with different slopes, which correspond to the activation energies $E_{ac1}=336\pm21$ kJ/mol (at $T<2000$ K) and $E_{ac2}=42\pm8$ kJ/mol (at $T>2000$ K).

Thus, it turns out that the activation energy for spontaneous graphitization accompanied by explosive thermal disintegration is ~42 kJ/mol and differs significantly from the activation energy for graphitization according to a diffusive mechanism, which is equal to ~350 kJ/mol (Ref. 3).

This raises the problem of the theoretical description of the graphitization kinetics of diamond for an unusual sequence of activation energies E_{ac1} and E_{ac2} on the temperature scale: the graphitization process with the lower activation energy E_{ac2} begins and proceeds at higher temperatures than the process with the higher value E_{ac1}. It should be noted here that kinetic reactions of this kind are known: the oxidation of diamond, which also takes place with two different activation energies, the smaller of which corresponds to higher temperatures, can serve as an experimental analog.[2,3]

1. INTERATOMIC INTERACTION POTENTIAL IN A DIAMOND LATTICE

The model-potential method was found to be most preferable for the analysis and theoretical description of the thermodynamic behavior of diamond in the temperature range where the diamond-graphite phase transformation accompanied by disintegration of the lattice takes place. The physicomechanical properties of a diamond lattice with purely covalent interatomic bonds can be described to a fairly high accuracy using the model potential of the interatomic interactions between two nearest-neighbor carbon atoms[7]

$$U(r)=U_0\frac{nm}{n-m}\left[\frac{1}{n}\left(\frac{r_0}{r}\right)^n-\frac{1}{m}\left(\frac{r_0}{r}\right)^m\right], \tag{1}$$

where $n=4$, $m=6$, $U_0=-356.7$ kJ/mol is the bond energy determined from the experimental value of the diamond lattice energy $E_{lat}=-\frac{1}{2}\cdot 4U_0=713.4$ kJ/mol, and $r_0=0.154$ nm is the equilibrium interatomic distance determined from the experimental (x-ray diffraction) value of the lattice constant for diamond $a=4/\sqrt{3}\,r_0=0.3567$ nm. The force of the interatomic interactions can be determined from the potential (1) as

$$F(r)=-dU/dr. \tag{2}$$

The correspondence of the potential (1) to the mechanical properties of the diamond lattice was tested on the basis of experimental data on the bulk compressibility of diamond: using the parameters of the diamond lattice and replacing the interatomic distances r in (1)–(2) by the specific volume $V=1/\rho$ (here ρ is the density) so that r_0 becomes the volume $V_0=1/\rho_0=0.28475$ cm^2/g ($\rho_0=3.51$ cm^3), we obtain (Fig. 2) the potential $U(V)$

$$U(V)=U_0\frac{nm}{n-m}\left[-\frac{1}{m}\left(\frac{V_0}{V}\right)^{m/3}+\frac{1}{n}\left(\frac{V_0}{V}\right)^{n/3}\right],\ \text{kJ/mol}, \tag{3}$$

as well as the zero-temperature isotherm $p(V)=-U(V)/dV$ in the form

$$p(V)=0.53\frac{U_0}{V}\left[\left(\frac{V_0}{V}\right)^2-\left(\frac{V_0}{V}\right)^{4/3}\right],\ \text{GPa}, \tag{4}$$

where 0.53 is a factor needed for the change in dimensions. From (4) we find the bulk elastic modulus

$$K_0=V_0\,dp(V_0)/dV. \tag{5}$$

A comparison of the data on the cold compression of diamond[8–10] with the isotherm (4) is presented in Fig. 3. The experimental value of the bulk elastic modulus determined by the most accurate methods, i.e., using ultrasound, Brillouin scattering, and Raman spectroscopy,[10–13] is equal to

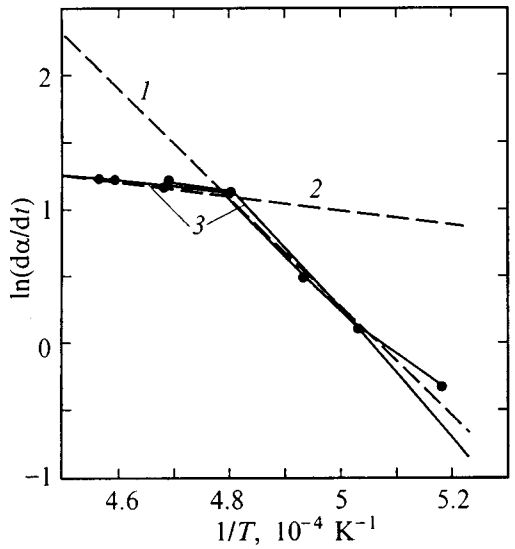

FIG. 1. Arrhenius plots for the graphitization rates of diamond with the activation energies $E_{ac1}=336$ kJ/mol (curve *1*) and $E_{ac2}=42$ kJ/mol (curve *2*). Curve *3* was calculated using Eq. (13). The experimental data were borrowed from Ref. 3.

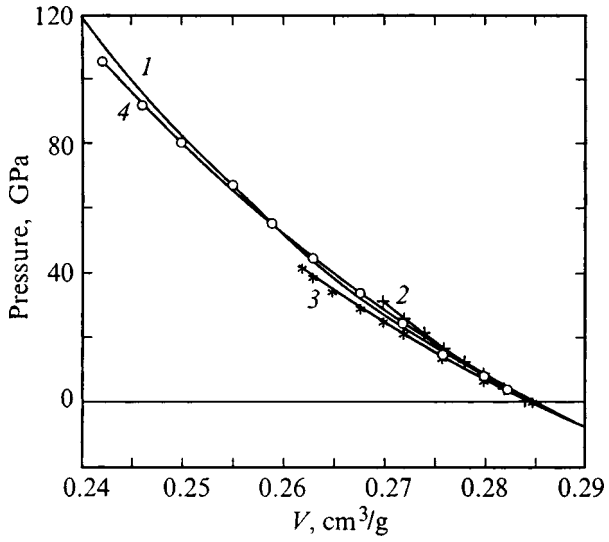

FIG. 3. Zero-temperature compression isotherm (curve *1*) calculated from Eq. (4) in comparison to experimental data: *2* — hydrostatic compression in a high-pressure solid-alloy machine,[8] *3* — hydrostatic compression on a diamond anvil,[10] *4* — shock compression.[9]

$K_0=442-444$ GPa for diamond. Accordingly, the value of K_0 determined from the equation for the zero-temperature isotherm (4) equals $K_0=443.01$ GPa.

The good agreement between the calculation and the experimental data permits the use of the potential (1) as a first approximation for analyzing the behavior of carbon atoms in a diamond lattice with sufficient reliability without taking into account many-particle interatomic interactions.

2. FORCE BARRIER TO OVERCOMING THE ''ULTIMATE STRENGTH'' OF AN INTERATOMIC BOND DUE TO INTERATOMIC INTERACTIONS, ENERGY, AND TEMPERATURE IN A DIAMOND LATTICE

It follows from Eqs. (1)–(2) that the interatomic attractive force $F(r)$ reaches a maximum $F(r_{bar})=F_{max}$, which is called the ''ultimate strength'' of an interatomic bond, at a certain distance $r=r_{bar}>r_0$ ($r_{bar}\approx 1.2r_0$ is the barrier distance). In this case an interatomic bond is a special type of spring with ''reversible'' elasticity:[14] as it is stretched, the restoring force $F(r)$ at first increases and then, after passing through the barrier F_{max}, decreases despite further stretching (Fig. 4).

This property of the bonds suggests that, in the case under consideration, the atoms can be located in stable and unstable positions of dynamic (vibrational) equilibrium with an identical restoring force $F<F_{max}$ but different values of the energy increment: $\Delta U_1<\Delta U_{bar}$ and $\Delta U_2>\Delta U_{bar}$ [here the quantity $\Delta U_{bar}=U(r_{bar})-U_0$ corresponds to the energy increment when the force barrier F_{max} is achieved at the distance r_{bar}]. In the former case the dynamic equilibrium of the system is stable (the restoring force increases when additional energy is imparted to the system), and in the latter case it is unstable and leads to rupture of the bond: when

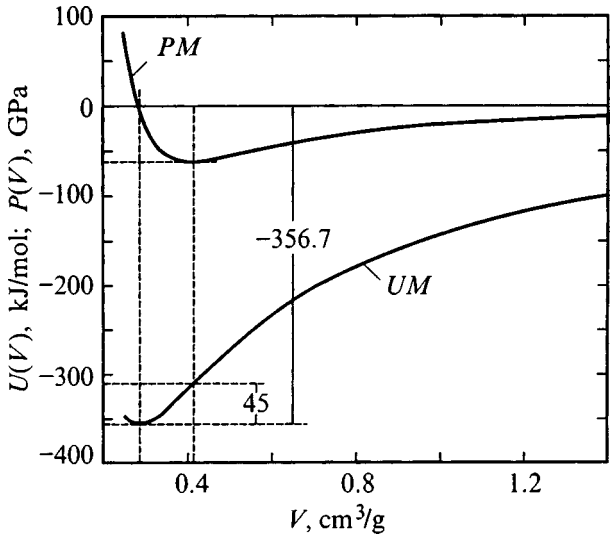

FIG. 2. Plots of $U(V)$ and $P(V)$ for diamond.

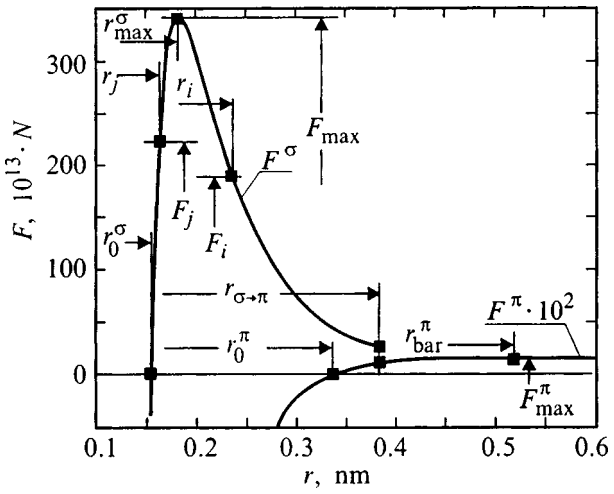

FIG. 4. Covalent (for diamond) and van der Waals (for graphite) interaction forces between carbon atoms.

additional energy is imparted to the system, the deviation of the atoms from their equilibrium positions increases, and the restoring force decreases. The bond ruptures if the energy increment ΔU in the system reaches a value $\Delta U > U_0$, i.e., when an energy $\Delta Q = \Delta U - E_0$ exceeding the bond dissociation energy D_0 is imparted to the system, i.e., under the condition $\Delta Q > D_0$.

The bond dissociation energy equals[15] $D_0 = -U_0 - E_0 \approx 339.4$ kJ/mol, where $U_0 = -356.7$ kJ/mol, $E_0 = \frac{9}{8} R\theta_D \approx 17.3$ kJ/mol is the energy of the zero-point vibrations in the diamond lattice, and $\theta_D = 1850$ K is the Debye temperature of diamond. The threshold value of the energy imparted to the system that suffices to overcome the ''ultimate strength'' of an interatomic bond equals $\Delta U_{\text{bar}} = 45$ kJ/mol (Fig. 2).

If the energy imparted to the system ΔU is thermal, i.e., if $\Delta U = \Delta Q$, then, according to the experimental data in Refs. 4–6 on the heat content of diamond, the threshold value ΔQ_{bar} will correspond to the temperature

$$T_{\text{bar}} = 2350 \text{ K}, \tag{6}$$

in agreement with the experimental values of the temperature $T > 2000$ K for the onset of the spontaneous graphitization and explosive disintegration of diamond, which has the following values for diamonds with different defect densities: ~2100 K for crystals of ASM 28/20 synthetic diamond powder,[3] ~2200 K for crystals of technical-grade natural diamond,[1], and ~2300 K for crystals of high-quality natural diamond.[16]

3. RUPTURE OF INTERATOMIC BONDS IN A DIAMOND LATTICE

In multiply bonded systems of atoms (chains, networks, and lattices), where the motion of a large number of atoms under the action of the imparted energy is stochastic, rather than synchronized, the energy increment ΔU is distributed among all n bonds as $\overline{\Delta U_n} = 1/n\,\Delta U$ on the average. Then the energy increment for each specific interatomic bond is $\Delta U_n = \overline{U_n} \pm \delta U_n$, where δU_n is the fluctuational part of the energy per bond. For the system as a whole $\Sigma_n \delta U_n = 0$.

The fluctuation of the energy ΔU_n in the interatomic bonds relative to the mean value $\overline{\Delta U_n}$ causes the maximum deviations r_n of the atoms from one another for the nth bond to also differ from one another by a certain amount δr_n, i.e., $r_n = \overline{r_n} \pm \delta r_n$, where $\overline{r_n}$ is the mean value of the maximum deviation of the atoms from one another corresponding to $\overline{\Delta U_n}$. This, in turn, entails fluctuations of the attractive restoring forces F_n corresponding to the maximum interatomic distances r_n, i.e.,

$$F_n = \overline{F_n} \pm \delta F_n. \tag{7}$$

If the energy increment in the lattice satisfies the condition $\overline{\Delta U_n} \ll \Delta U_{\text{bar}}$ in the interatomic bonds, the condition for attractive interatomic forces will be satisfied at the small distances $r_n \ll r_{\text{bar}}$:

$$F_n = \overline{F_n} \pm \delta F_n < F_{\max}, \quad r_0 < r_n \ll r_{\text{bar}}. \tag{8}$$

This condition ensures preservation of the interatomic bonds in the lattice during anharmonic vibrations corresponding to the potential (1).

If the energy increment distributed among n bonds $\overline{\Delta U_n}$ reaches a value $\overline{\Delta U_n} \approx \Delta U_{\text{bar}}$, then $\overline{F_n} \approx F_{\max}$, and because of the fluctuations (7) conditions can arise for i and j bonds under which the attractive interatomic restoring forces in these bonds will have the following values as a consequence of the ''reversible'' elasticity (Fig. 4):

$$F_i = \overline{F_n} + \delta F_n(+\delta r_n) < F_{\max}, \quad r_n > r_{\text{bar}}, \tag{9}$$

$$F_j = \overline{F_n} + \delta F_n(-\delta r_n) < F_{\max}, \quad r_0 < r_n < r_{\text{bar}}. \tag{10}$$

In this case different relationships between the forces F_i and F_j can be realized, viz., $F_i = F_j$, $F_i < F_j$, and $F_i > F_j$. For two neighboring bonds, any of these relationships characterizes an unstable state of the system as a whole and leads to the same behavior pattern in those bonds: a j bond, which is loaded by the force F_j ($r_j < r_{\text{bar}}$) tends to a more advantageous energy state, in which $\Delta U_j = \Delta r_j F_j$ tends to zero as the deviation of the atoms from their equilibrium positions decreases, i.e., as $\Delta r_j \to 0$. The force F_i ($r_i > r_{\text{bar}}$) of an i bond will not oppose the shortening of the adjacent j bond, since the corresponding increase in the length of the i bond (by $+\Delta r_i$) caused by this shortening (by $-\Delta r_j$) will decrease, rather than increase, the strain resistance force because of the ''reversible'' elasticity. As a result, the energy of the i bond will increase by the quantity ΔU_i, which is equal to the energy ΔU_j released when the j bond is unloaded.

It can be shown by direct calculations that similar unloading will occur in all the interatomic bonds which are in the state of the force loading (10) and join atoms to one another in bonded chains, networks, or lattices. The energy ΔU_j of each unloaded bond will be ''transferred'' to the elongating i bond and accumulate in the latter until the bond energy U_0 is overcome, i.e., until a state $\Sigma_1^n \Delta U_j > U_0$ is reached, where $n \leqslant j$ is the number of unloaded bonds ''transferring'' unloading energy to the i bond being broken. For example, for a diamond lattice in a state in which the energy ΔU is distributed between the bonds as $\overline{\Delta U_n} \approx \Delta U_{\text{bar}} = 45$ kJ/mol, the barrier due to the bond energy $U_0 = 356.7$ kJ/mol can be overcome when the disintegration process involves $U_0 : \Delta U_{\text{bar}} \cong 8$ bonds, one of which is broken, while the others are unloaded (transfer their elongation energy to the bond being cleaved).

If the number of bonds unloaded per bond ruptured under the condition $\overline{\Delta U_n} \approx \Delta U_{\text{bar}}$ is much greater than eight, i.e., if $N = n/8 \gg 1$ and, therefore, $\Sigma_1^n \Delta U_j = NU_0$, then after breaking the i bond the remainder $(N-1)U_0 \gg U_0$ of the energy ''transferred'' is partially converted into the kinetic energy of the two atoms being detached from one another, which transfer part of this energy in the form of an unloading wave to the neighboring j bonds ($r_j < r_{\text{bar}}$), thereby bringing the latter into the state of the i bonds ($r_i > r_{\text{bar}}$), which are predisposed to breaking. After this, the rupture of the i bonds described above will be repeated in the form of a

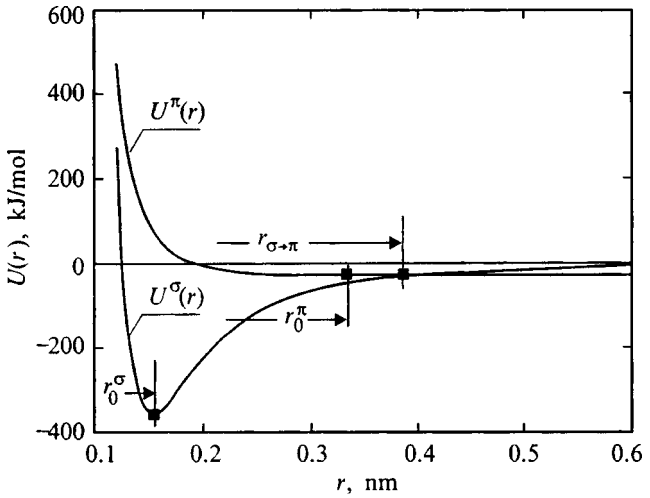

FIG. 5. Potentials of covalent (for diamond) and van der Waals (for graphite) bonds between carbon atoms.

chain reaction along a rupture line or plane until $\sim N$ bonds are broken at a rate not exceeding the propagation rate of elastic Rayleigh waves.

The number of i bonds ($r_i > r_{\text{bar}}$), i.e., potentially broken bonds in the lattice, and, therefore, the degree of destruction of its integrity will clearly depend on the energy imparted to the lattice ΔU and on the magnitude of the local fluctuations. Therefore, the degree of disintegration can vary from the onset of the appearance of lattice defects in the form of individual broken bonds to the complete separation of the entire crystal into individual fragments, which, in turn, will break into even smaller parts when additional energy is imparted to the system.

4. SPONTANEOUS GRAPHITIZATION MECHANISM IN DIAMOND

In the picture of the rupture of interatomic bonds considered above, the barrier due to the dissociation energy D_0 can be overcome only when $r_i \to \infty$, i.e., when the distance between the atoms being detached from each other actually increases to macroscopic values. In a diamond lattice this process is accompanied by a transition of the carbon atoms being separated from the sp^3 state to the sp^2 state with a corresponding change in the type of bonding: from a purely covalent 4σ bond system to a $(3\sigma+\pi)$ bond system containing a weak van der Waals π bond in addition to the strong covalent bonds.

Figures 4 and 5 show plots of the interatomic interaction potentials and forces for a covalent bond in diamond and a van der Waals bond in graphite. The latter corresponds to a potential[7] of the form

$$U^{\pi}(r) = -Ar^{-6} + C\exp(-\beta r), \tag{11}$$

where $A = 1499$ kJ/mol$\cdot 10^{-6}$nm^6, $C = 33.4$ kJ/mol, and $\beta = 0.7254$ nm^{-1}.

It can be seen from Fig. 5 that the potential for covalent bonds (1) intersects the potential for van der Waals bonds (11) at the interatomic distance $r = r_{\sigma\to\pi} \approx 2.5 r_0$, at which it is energetically advantageous for the atoms moving apart to go over to the lower potential curve, i.e., to the potential curve for van der Waals bonds.

On the plot of the interatomic forces (Fig. 4) this point corresponds to a jump from the covalent bonding curve to the van der Waals force curve, i.e., the atom undergoes a transition at this point from an unstable state of ''reversible'' elasticity relative to the equilibrium position at the point $r_0 = r_0^{\sigma} = 0.154$ nm to a state of ordinary elasticity (the increase in bond length is accompanied by an increase in the stretching resistance force), i.e., to a state of stable vibrations relative to the new equilibrium position at the point $r_0^{\pi} = 0.335$ nm.

The subsequent behavior of the bond being broken is determined by the difference between the energy stored in a σ bond when it is elongated by $r_{\sigma\to\pi}$ and the energy of a π bond stretched to the same point. From (1) and (11) we obtain $\Delta U^{\sigma}(r_{\sigma\to\pi}) = U^{\sigma}(r_{\sigma\to\pi}) - U_0^{\sigma} \cong 332$ kJ/mol and $\Delta U^{\pi}(r_{\sigma\to\pi}) = U^{\pi}(r_{\sigma\to\pi}) - U_0^{\pi} \cong 0.2$ kJ/mol, where $U_0^{\sigma} - U_0 = -356.7$ kJ/mol, $U_0^{\pi} \cong -25.1$ kJ/mol (Ref. 7), and $U^{\sigma}(r_{\sigma\to\pi}) = U^{\pi}(r_{\sigma\to\pi}) \approx -24.9$ kJ/mol (Fig. 5). A $sp^3 \to sp^2$ transformation of the excited state of the carbon atoms being separated, accompanied by emission of the excess energy equal to the difference between the energies of these states ($\sim$70 kJ/mol, Ref. 7), takes place at this stage. Therefore, after an atom goes over to the π bond, its energy is almost an order of magnitude larger than the dissociation energy of that bond. After the ''ultimate strength'' $F_{\max}^{\pi}$ of the van der Waals π bond has been overcome at an interatomic distance $r_{\text{bar}}^{\pi} \cong 0.52$ nm (Fig. 4), this excess energy leads to rupture of the bond, and the remainder of the elastic energy is transformed into kinetic energy, which, as was shown above, is transferred to neighboring atoms.

The validity of the scheme just presented for the destruction of the 4σ bond system of a diamond lattice, with a transition to the $(3\sigma+\pi)$ bond system of a graphite lattice, is quantitatively confirmed by the rupture of C–C single bonds in individual hydrocarbon molecules, in which the bonds between the carbon atoms, as in the diamond lattice, are created by valence electrons occupying hybrid sp^3 orbitals:[14] when such a C–C σ bond is stretched (the original equilibrium distance between the centers of carbon atoms is 0.154 nm, which coincides with the interatomic distances in the diamond lattice), it ceases to bind the bonded atoms when its elongation $\Delta r = r - r_0$ roughly reaches a value >0.3 nm. This elongation corresponds to an interatomic distance $r \approx 0.5$ nm, which actually coincides with the value of r_{bar}^{π} given above. In this case free radicals (i.e., ends of ruptured bonds), which can be detected by ESR, form. After a σ bond is broken, the unpaired electron of each carbon atom passes into a π orbital as a result of the $sp^3 \to sp^2$ transformation, and the remaining electrons occupy σ orbitals, thereby forming a $(3\sigma+\pi)$ bond system.

Thus, the rupture of one bond in a diamond lattice and a $sp^3 \to sp^2$ transformation of the carbon atoms being detached from each other leads (Fig. 6) to the transformation of an eight-atom group of a diamond lattice into two planar

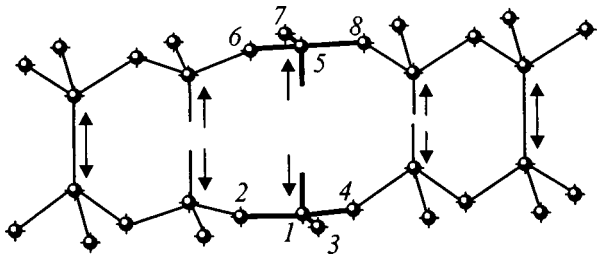

FIG. 6. Scheme of the rupture and $sp^3 \rightarrow sp^2$ transformation of interatomic bonds during spontaneous graphitization.

four-atom fragments of a graphite lattice located on opposite cleavage surfaces.

The subsequent spreading of bond cleavage accompanied by the transition of carbon atoms from the sp^3 the sp^2 state accounts for the experimentally observed spontaneous graphitization process with the explosive disintegration of diamond crystals when they are heated to $T>2000$ K, as well as the fact that fragments of the crystals broken up in such a process consist of diamond, whose surface is coated by graphite.

It is noteworthy that the mechanism of the phase transformation just described with alteration of the type of bonding [4σ to $(3\sigma+\pi)$ bonding], which is accompanied by explosive disintegration of the crystal, should be characteristic only of a lattice with purely covalent interatomic bonds. The presence of an ionic component in the interatomic interaction, as, for example, in the BN lattice, causes overcoming of the ''ultimate strength'' of a covalent bond not to be accompanied by spontaneous disintegration of the lattice, since the atoms are held by the remaining ionic component of the interatomic bond.

5. EQUATION FOR THE RATE OF SPONTANEOUS GRAPHITIZATION

The essential coincidence between the theoretical quantities D_0, ΔQ_{bar}, and T_{bar} and the experimental values of the activation energies and the threshold temperature associated with the kinetics of the graphitization of diamond, provide grounds to assume that experimental kinetic dependences of spontaneous graphitization can be explained theoretically on the basis of the mechanisms for the thermal disintegration and spontaneous graphitization of diamond established in the preceding sections.

As we know, the Arrhenius equation for the rate of formation of a new phase has the form

$$d\alpha/dt = A_0 \exp(-E_{\text{ac}}/RT), \tag{12}$$

where α is the concentration of the new phase; A_0 is the rate constant of the reaction, which, in a first approximation, depends on temperature and equals the maximum possible value of the rate (12) of a reaction taking place according to a specific mechanism of interaction and reorganization of the atoms; E_{ac} is the activation energy or the energy barrier which must be overcome for the reaction to occur according to (12); R is the universal gas constant; T is the temperature; and $\exp(-E_{\text{ac}}/RT)$ is the Boltzmann factor, which reflects the Maxwellian probability of overcoming the barrier E_{ac} as a result of energy fluctuations at an assigned temperature T.

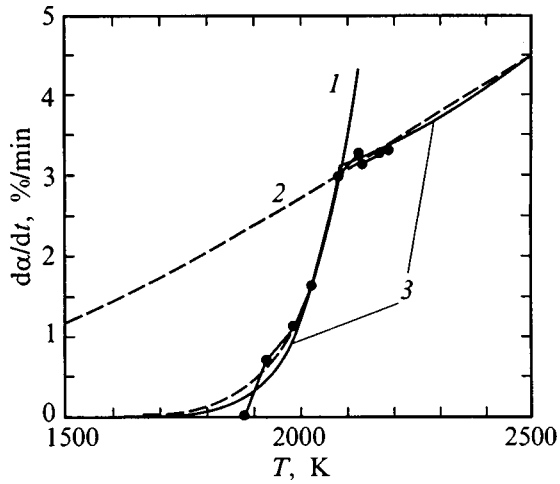

FIG. 7. Graphs of the graphitization rate of diamond calculated from the Arrhenius equation (12) for the activation energies $E_{\text{ac1}}=336$ kJ/mol (curve *1*) and $E_{\text{ac2}}=42$ kJ/mol (curve *2*). Curve *3* was calculated from Eq. (13). The experimental data were taken from Ref. 3.

Figure 7 presents experimental data on the graphitization of diamond[3] and approximate plots of the reaction rates calculated from Eq. (12) using the values of E_{ac1} and E_{ac2}. The reaction rate constants fitted to the experimental data have the values $A_{01}=8\times10^8$%/min$=1.33\times10^5$ s^{-1} and $A_{02}=34$%/min$=5.7\times10^{-3}$ s^{-1}, i.e., they differ by approximately seven orders of magnitude. As we know, according to the theory of absolute reaction rates, the limiting value of the rate constant for most crystals is of the order of $A_0 \approx kT/h \approx 10^{13}$ s^{-1} (Ref. 15).

It can easily be seen from Fig. 7 that Eq. (12) cannot be used to explain why the smaller activation energy E_{ac2} ''triggers'' spontaneous graphitization only at a very high temperature (>2000 K), but does not ''activate'' this mechanism at lower temperatures, while graphitization with the activation energy $E_{\text{ac1}}>E_{\text{ac2}}$ takes place in the temperature range below 2000 K, but does not take place at higher temperatures. Therefore, the cause of the phenomenon under consideration should be sought only in the atomic mechanism of spontaneous graphitization, which has two barriers, viz., the energy barrier due to bond dissociation energy D_0 and the force barrier due to the ''ultimate strength'' of the bond $F_{\max}$, which activates the spontaneous graphitization mechanism. As was shown above, the latter barrier corresponds to a certain threshold energy ΔQ_{bar} and a certain temperature T_{bar}.

In the absence of the second barrier, the reaction kinetics should be described by the Arrhenius equation (12) associated with the probability of overcoming the barrier due to the dissociation energy, i.e., $E_{\text{ac1}}=D_0$. The introduction of the probability of overcoming the second barrier $E_{\text{ac2}}=\Delta Q_{\text{bar}}$ into the rate equation is possible when the fluctuational nature of the spontaneous graphitization mechanism is taken into account. In fact, the interatomic bond length increment $\Delta r=r-r_0$ can be mapped to the lattice energy increment ΔU and, accordingly, to the temperature, i.e., $\Delta r \Leftrightarrow T$. Then,

fluctuations of an interatomic bond length $r_n=\overline{r_n}\pm\delta r_n$ will correspond to fluctuations of the local temperature $T_n=T\pm\delta T_n$ of the respective bond, where T is the mean value of the temperature, which is equivalent to the parametric value of the lattice temperature. Therefore, the temperature T in the Arrhenius kinetic equation (12) should be replaced by a certain fluctuational value $T(W)$ of the local bond temperature, which is functionally dependent on the probability W of overcoming the barrier due to the ''ultimate strength'' of the bond $F_{\max}$, i.e., on the probability of achieving the threshold energy ΔQ_{bar} at an assigned value of the lattice temperature T. In this case the Arrhenius equation for the graphitization process, which takes into account the two activation barriers $E_{\text{ac1}}=D_0$ and $E_{\text{ac2}}=\Delta Q_{\text{bar}}$, should have the form

$$d\alpha/dt=A_0\exp[-D_0/RT(W)]. \tag{13}$$

The fluctuational temperature $T(W)$, which depends on the parametric value of the lattice temperature T and on the Boltzmann probability factor W for overcoming the barrier ΔQ_{bar}, will be defined as[2]

$$T(W)=T\exp\left[\frac{3}{8RT}(\Delta H^0(T)-|\Delta Q_{\text{bar}}-\Delta H^0(T)|)\right]. \tag{14}$$

The solution of Eq. (13) using (14) requires knowledge of the heat-content function of diamond $\Delta H^0(T)\int_0^T c_p\,dT$. Approximation of the experimental data[4–6] by a tenth-degree polynomial was employed in the present work.

Equation (13) was solved by a numerical method using the MATLAB 5.2 software for the value of the dissociation energy $D_0=339.4$ kJ/mol and for the values fitted to the experimental data[3] for the barrier ($\Delta Q_{\text{bar}}=38.45$ kJ/mol) and the reaction rate constant ($A_0=1.55\times10^4$%/min $=2.58\ \text{s}^{-1}$).

The calculated results are presented in the form of curve *3* in Fig. 1 [in $\ln(d\alpha/dt)$ vs T^{-1} coordinates] and in Fig. 7 (in $d\alpha/dt$ vs T coordinates), from which it is seen that Eq. (13) correctly describes the character of the variation of the graphitization rate as a function of temperature. At $T<1900$ K, graphitization is essentially beyond the sensitivity of the experimental method, and its rate begins to increase only at $T>1900$ K. This increase continues until the threshold temperature T_{bar} is achieved, after which the plot of the graphitization rate has a discontinuity. If it is taken into account that the solution was obtained on the basis of an interatomic interaction potential of the form $U\sim r^{-4}-r^{-6}$, which is known to incorporate a definite inaccuracy, and that the spread of the experimental data upon high-temperature graphitization amounts to 10–20%, the theoretical description of the graphitization process obtained using Eq. (13) can be considered faithful to the real process to a high degree.

Thus, spontaneous graphitization, which is accompanied by the explosive disintegration of a diamond crystal, is a process that takes place in accordance with Eq. (13) at temperatures exceeding the threshold value T_{bar}, beyond the ''accuracy limits'' of interatomic bonds in the diamond lattice. Since there is a force barrier in each interatomic interaction (the ''ultimate strength'' of the bond), which determines the threshold value of the energy needed to overcome this barrier $\Delta Q_{\text{bar}}\Leftrightarrow T_{\text{bar}}$, the graphitization process takes place, as it were, with two sharply different activation energies and corresponding reaction rate constants, although it is, in fact, described by Eq. (13) with a single rate constant A_0 and dissociation energy D_0 for the entire process, i.e., it is described by a single (without matching) curve.

*)E-mail: andreyev@andr.kiev.ua

1)Unpublished data supplied to the author by Prof. A. V. Bochko (Institute of Problems in Materials Science, Ukrainian National Academy of Sciences).

2)The temperature $T(W)$ can be defined in the following manner. As was shown above, the rupture of a single bond according to the ''energy-transfer'' mechanism involves eight atoms: the two on the ends of the bond being cleaved and the three atoms bonded directly to each of the two preceding atoms, i.e., a standard eight-atom group of a diamond lattice, in which the central bond is cleaved. The value of the threshold energy $\Delta Q_{\text{bar}}=\Delta U_{\text{bar}}-E_0$ per atom corresponds to the energy $\Delta Q_{\text{bar}}/N_0$ (here N_0 is Avogadro's number). When the three degrees of freedom of atomic motion are taken into account, the mean energy of an atom sufficient to overcome the force barrier $F_{\max}$ will be equal to $3\Delta Q_{\text{bar}}/N_0$. To overcome this barrier in one bond in an eight-atom group according to the ''energy-transfer'' mechanism, it is sufficient to impart the mean energy $\Delta Q^*_{\text{bar}}=\frac{1}{8}(3\Delta Q_{\text{bar}}/N_0)$ to each atom of this group. The thermal energy of an atom ΔQ^* (after subtraction of the energy of the zero-point vibrations E_0) in the eight-atom group under consideration at the temperature T and zero pressure will be specified by the enthalpy $\Delta H^0(T)\int_0^T c_p\,dT$ as $\Delta Q^*=\frac{1}{8}(3\Delta H^0(T)/N_0)$. Then the energy for passage through one barrier ΔQ_{bar} at T in both the forward, high-temperature direction at $\Delta Q<\Delta Q_{\text{bar}}$ and in the reverse, low-temperature direction at $\Delta Q>\Delta Q_{\text{bar}}$ will be equal to the absolute value of the difference $\Delta Q^*_{\text{bar}}-\Delta Q^*$, i.e., the activation energy of the spontaneous graphitization process at T will be equal to $E^*_{\text{ac}}3/8N_0\,|\Delta Q_{\text{bar}}-\Delta H^0(T)|$, and, therefore, the Boltzmann probability factor for the activation energy E^*_{ac} will have the form $C\exp(-E^*_{\text{ac}}/kT)C\exp(\frac{3}{8}|\Delta Q_{\text{bar}}-\Delta H^0(T)|/R)$. The normalization condition for the expression obtained is elimination of the influence of the Boltzmann factor when $\Delta Q_{\text{bar}}=0$, i.e., $C\exp(-\frac{3}{8}|\Delta Q_{\text{bar}}-\Delta H^0(T)|/R)_{\Delta Q_{\text{bar}}=0}=1$, whence the value of the normalization factor will be $C\exp(\frac{3}{8}\Delta H^0(T)/R)$. Then the normalized Boltzmann factor will have the form

$$W=\exp\left[\frac{3}{8RT}(\Delta H^0(T)-|\Delta Q_{\text{bar}}-\Delta H^0(T)|)\right].$$

[1] M. Seal, Phys. Status Solidi **3**, 658 (1963).
[2] T. Evans, ''Changes produced by high temperature treatment of diamond'' in *The Properties of Diamond* (Academic Press, 1979), pp. 403–424.
[3] V. D. Andreev, Yu. I. Sozin, and T. D. Ositinskaya, Sverkhtverd. Mater. **4**, 36 (1995).
[4] V. R. Malik and L. P. Efimovich, Sverkhtverd. Mater. **3**, 27 (1983).
[5] *Thermodynamic Properties of Individual Substances* [in Russian], edited by V. P. Glushko (Nauka, Moscow, 1978), Vol. 2, Part 1.
[6] *Physical Properties of Diamond* [in Russian], edited by N. V. Novikov (Naukova Dumka, Kiev, 1987).
[7] V. D. Andreev and V. R. Malik, Sverkhtverd. Mater. **2**, 5 (1987).
[8] R. W. Lynch and H. G. Drickamer, J. Chem. Phys. **44**, 181 (1966).
[9] M. N. Pavlovskiĭ, Fiz. Tverd. Tela (Leningrad) **13**, 893 (1971) [Sov. Phys. Solid State **13**, 741 (1971)].
[10] I. V. Aleksandrov, A. F. Goncharov, A. N. Zisman, and S. M. Stishov, Zh. Éksp. Teor. Fiz. **93**, 680 (1987) [Sov. Phys. JETP **66**, 384 (1987)].
[11] S. Fahy and S. G. Louie, Phys. Rev. B **36**, 3373 (1987).
[12] H. J. McSkimin and P. Andreatch Jr., J. Appl. Phys. **43**, 2944 (1972).
[13] M. H. Grimsditch and A. K. Ramdas, Phys. Rev. B **11**, 3139 (1975).
[14] V. R. Regel', A. I. Slutsker, and É. E. Tomashevskiĭ, *Kinetic Nature of the Strength of Solid Solutions* [in Russian] (Nauka, Moscow, 1974).
[15] L. D. Landau and E. M. Lifshitz, *Statistical Physics, Vol. 1*, 3rd. ed. (Pergamon Press, Oxford–New York, 1980; Nauka, Moscow, 1976).
[16] H. Eyring and F. W. Cagle, Z. Electrochem. **56**, 480 (1952).

Translated by P. Shelnitz

Photoinduced phase transition in Ag_3AsS_3 crystals

Yu. P. Gololobov

Ukrainian Transportation University, 252010 Kiev, Ukraine
(Submitted April 7, 1998; resubmitted September 14, 1998)
Fiz. Tverd. Tela (St. Petersburg) **41**, 702–704 (April 1999)

It is shown that the illumination of samples leads to the appearance of anomalies in the temperature dependences of the propagation velocity of longitudinal ultrasonic waves along the principal crystallographic directions of proustite (Ag_3AsS_3) at $T\sim 150$ K. The features discovered are associated with a photoinduced phase transition caused by restructuring of the cation sublattice of proustite. © *1999 American Institute of Physics.* [S1063-7834(99)02904-4]

The unique physical phenomena discovered in proustite crystals include a photoinduced phase transition, i.e., a phase transition which occurs at a definite temperature only in the presence of light. An hypothesis regarding the occurrence of such a phase transition in Ag_3AsS_3 was first advanced in Ref. 1 by Smolenskiĭ *et al.*, who concluded in their further studies that a photoinduced phase transition takes place in proustite at $T\sim 200$ K.[2–4] At the same time, other investigators, using the same experimental methods, did not detect any signs of the occurrence of this phase transition.[5,6] Thus, the question of the occurrence and nature of the photoinduced phase transition in Ag_3AsS_3 remained open.

For this reason we decided to study thoroughly the temperature dependences of the gap width (E_g) and the velocity of longitudinal ultrasonic waves propagating along the principal crystallographic directions in proustite crystals. The proposed investigative methods are known to be extremely sensitive to the occurrence of phase transitions. In addition, the latter method permits the direct comparison of investigations of darkened and illuminated samples, i.e., provides a possibility, in principle, to ascertain whether a phase transition is, in fact, photoinduced.

Oriented samples cut from synthetic proustite single crystals grown by the Bridgman–Stockbarger method were investigated. The *X*, *Y*, and *Z* axes were selected in the usual manner for crystals of trigonal symmetry.[1] The gap width was determined by the method previously used to measure E_g in an isomorphous analog of proustite, viz., crystalline Ag_3AsS_3.[7] The relative changes in the propagation velocity of longitudinal ultrasonic waves at $f=11$ MHz were recorded using the method described in Ref. 8, and the error in the determination of $\Delta V/V$ did not exceed 0.01%. The measurements were performed in a dynamic regime, but the variation rate of the temperature did not exceed 1.5 K/min. The temperature was measured in the range 100–240 K using a copper-constantan thermocouple, one of whose junctions was fastened directly to the sample. The accuracy of the temperature measurements was ± 0.5 K. An LG-78 helium-neon laser served as the light source.

Figure 1 presents plots of the temperature dependence of the gap width of proustite crystals for the cases of light polarized parallel (curve *1*) and perpendicular (curve *2*) to the *C* axis. As can be seen, clearly expressed discontinuities are observed on both plots at $T\sim 150$ K, while $\partial E_g/\partial T$ undergoes a jump characteristic of a second-order phase transition [in the case of $E\| C$, $\Delta(\partial E_g/\partial T)=4.1\times 10^{-4}$ eV/K, and in the case of $E\perp C$, $\Delta(\partial E_g/\partial T)=2.1\times 10^{-4}$ eV/K]. The temperature dependences of the relative change in velocity $\Delta V/V$ obtained for the *Z*, *Y*, and *X* directions are shown in Figs. 2 and 3. In the case of the darkened samples the plots of $\Delta V/V=f(T)$ coincide with the dependences previously obtained in Ref. 9. When the samples are illuminated, anomalies are observed on the temperature dependences of the velocity for all three directions at $T\sim 150$ K (see curves *2* and *5*), the most significant of them being the velocity jump typical of a phase transition for piezoelectrically active ultrasonic waves propagating along the *C* axis of the proustite crystals. Thus, illumination of the samples leads to the appearance of anomalies, providing evidence of the occurrence of a photoinduced phase transition in the proustite crystals.

In the case of piezoelectrically active ultrasonic waves propagating along the *Y* and *Z* directions, the smoother variation of $\Delta V/V$ with temperature for the illuminated samples is noteworthy. This is due apparently to the screening of the piezoelectric field by light-generated free charges. In fact, measurements of the conductivity σ of the illuminated proustite samples at $T=100$ K showed that $\sigma_y=9.1\times 10^{-2}$ S/m and $\sigma_z=2.3\times 10^{-3}$ S/m at 11 MHz. Thus, in the presence of light, the screening condition $\omega_c>\omega$ ($\omega_c=\sigma/\varepsilon\varepsilon_0$ is the Maxwell relaxation frequency, and $\omega=2\pi f$ is the circular frequency of the ultrasonic waves) is satisfied for ultrasonic waves propagating along the *Y* direction and is not satisfied for a *Z*-cut crystal. Therefore, at $T=100$ K it can be assumed that $V_y=V_0(1+K_{22}^2)^{1/2}$, where V_0 is the ultrasonic wave velocity along the *Y* axis of the illuminated proustite crystals and V_y is the velocity in unilluminated crystals. This makes it possible to estimate the electromechanical coupling coefficient K_{22} from the difference $\Delta V/V$ for such samples (see Fig. 3). It follows from the calculations that $K_{22}=0.14$ for proustite at $T=100$ K. With consideration of the temperature difference, this value agrees fairly well with the values $K_{22}=0.10-0.11$ determined by other independent methods.[10,11]

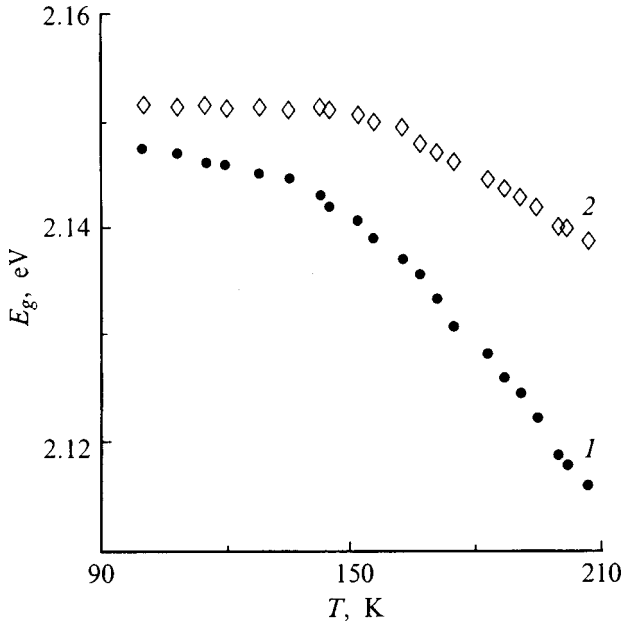

FIG. 1. Temperature dependence of the gap width of proustite crystals for allowed direct transitions: *1* — $E\|C$, *2* — $E\perp C$.

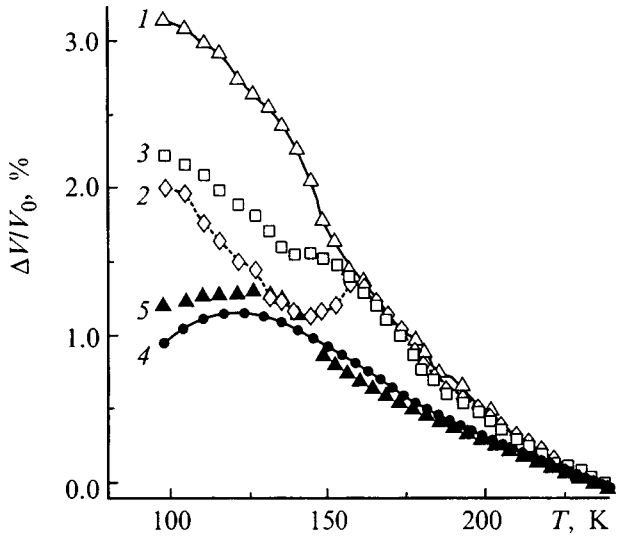

FIG. 3. Temperature dependence of the propagation velocity of ultrasonic waves along the Y (*1–3*) and X (*4*, *5*) axes of a proustite crystal: *1* — without illumination; *2* — freshly prepared sample under illumination; *3* — third of continuous cycles with illumination; *4* — without illumination; *5* — with illumination.

Several features of the anomalous behavior of the dependences investigated at $T\sim150$ K should be noted. It was discovered that the magnitude and character of the anomalies detected depend on the history of the sample. For example, Fig. 3 shows the temperature dependences of the ultrasonic wave velocity for a *Y*-cut crystal from a freshly prepared sample and for the same sample after two cooling-heating cycles (curves *2* and *3*). As can be seen, the thermal cycling of the illuminated samples leads to smoothing of the original velocity jump to a ''step,'' which is faithfully reproduced in repeated measurements.

In addition, it was discovered that proustite crystals have photostructural memory not only near the ferroelectric phase transition ($T_c=28$ K), but also at higher temperatures. For example, if the heating of a proustite sample from 100 to 300 K in the presence of laser illumination is followed 1 h later by a repeated cooling-heating cycle for the same, but now thoroughly darkened sample, the velocity jump at $T\sim150$ K still appears, but it is appreciably smaller in magnitude (see Fig. 1). However, after the sample is stored for 24 h at room temperature, its properties are restored, and the usual temperature dependence of the ultrasonic wave velocity for darkened samples is again observed. The effect observed is probably a manifestation of photostructural memory due to the appearance of a new system of defects under the action of light, which differs from the system of defects appearing during the thermal cycling of darkened samples.

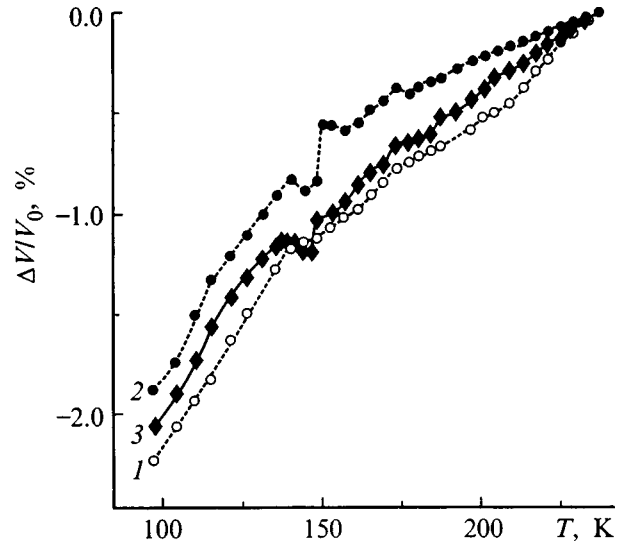

FIG. 2. Temperature dependences of the propagation velocity of ultrasonic waves along the *Z* axis of a proustite crystal: *1* — without illumination; *2* — with illumination; *3* — without illumination 1 h after heating with illumination.

Thus, the data obtained confirm the occurrence of a photoinduced phase transition in proustite crystals, but, according to our data, this phase transition occurs at $T\sim150$ K, rather than at the temperature of 200 K previously cited in Ref. 1. In this context we recall that Smolenskiĭ *et al.*[1] reliably detected splitting of an *E* mode when the temperature was raised to $T\sim150$ K, while the value of 200 K was established when the experimentally obtained dependences were extrapolated to higher temperatures. The occurrence of the phase transition specifically at $T\sim150$ K is also supported by the humps in the temperature dependences of the frequencies of acoustic phonons discovered at that temperature,[2] the anomalous behavior of the frequencies of the lines in the Raman spectrum,[12] and the temperature-induced quenching of the residual conductivity.[13] As for the nature of the photoinduced phase transition, it is most probably associated with disordering of the silver sublattice. Since the illumination of Ag_3AsS_3 crystals leads to disordering of the Ag^+ ions predominantly in the left-handed helical $(AgS)_\infty$ chains, and a rise in temperature is accompanied by the disordering prim-arily of the right-handed helical chains,[14] the simultaneous action of light and heat can be

accompanied by defect-formation processes associated with restructuring of the entire proustite cation sublattice.

[1] G. A. Smolenskiĭ, I. G. Siniĭ, E. G. Kuz'minov, and A. A. Godovikov, Fiz. Tverd. Tela (Leningrad) **21**, 2332 (1979) [Sov. Phys. Solid State **21**, 1343 (1979)].
[2] G. A. Smolenskiĭ, I. G. Siniĭ, S. D. Prokhorova, A. A. Godovikov, R. Laĭkho, T. Levola, and E. Karaemyaki, Fiz. Tverd. Tela (Leningrad) **23**, 2017 (1981) [Sov. Phys. Solid State **23**, 1178 (1981)].
[3] G. A. Smolenskiĭ, I. G. Siniĭ, S. D. Prokhorova, E. G. Kuz'minov, and A. A. Godovikov, Kristallografiya **27**, 140 (1982) [Sov. Phys. Crystallogr. **27**, 82 (1982)].
[4] L. A. Kot, S. D. Prokhorova, Yu. M. Sandler, I. G. Siniĭ, and I. N. Flerov, Fiz. Tverd. Tela (Leningrad) **25**, 1535 (1983) [Sov. Phys. Solid State **25**, 884 (1983)].
[5] P. J. S. Ewen, W. Taylor, and G. L. Paul, J. Phys. C: Solid State Phys. **16**, 6475 (1983).
[6] L. A. Rebane and K. E. Haller, Fiz. Tverd. Tela (Leningrad) **25**, 1789 (1983) [Sov. Phys. Solid State **25**, 1030 (1983)].
[7] D. F. Baĭsa, D. D. Kolendritskiĭ, M. I. Goloveĭ, I. Yu. Roman, and A. I. Kovalenko, Fiz. Tverd. Tela (Leningrad) **30**, 573 (1988) [Sov. Phys. Solid State **30**, 327 (1988)].
[8] A. D. Belyaev, Yu. P. Gololobov, and V. F. Machulin, Defektoskopiya No. **6**, 92 (1984).
[9] A. D. Belyaev, Yu. P. Gololobov, V. F. Machulin, and E. G. Miselyuk, Fiz. Tverd. Tela (Leningrad) **26**, 1349 (1984) [Sov. Phys. Solid State **26**, 820 (1984)].
[10] Ya. M. Olikh, Phys. Status Solidi A **80**, K81 (1983).
[11] A. D. Belyaev, N. A. Borovoĭ, Yu. P. Gololobov, V. F. Machulin, and E. G. Miselyuk, Fiz. Tverd. Tela (Leningrad) **26**, 1890 (1984) [Sov. Phys. Solid State **26**, 1146 (1984)].
[12] L. A. Rebane and K. E. Haller, Fiz. Tverd. Tela (Leningrad) **24**, 2351 (1982) [Sov. Phys. Solid State **24**, 1335 (1982)].
[13] A. N. Babushkin, V. B. Zlokazov, L. Ya. Kobelev, and A. B. Shaĭkin, Paper deposited in the All-Union Institute of Scientific and Technical Information of the Academy of Sciences of the USSR (VINITI), No. 1117–79, 8 pp., Izv. Vyssh. Uchebn. Zaved., Fiz. (1979).
[14] N. A. Borovoĭ, Yu. P. Gololobov, and I. N. Salivonov, Fiz. Tverd. Tela (St. Petersburg) **41**, (1999) [Phys. Solid State **41**, (1999)] (in press).

Translated by P. Shelnitz

LOW-DIMENSIONAL SYSTEMS, SURFACE PHYSICS

Effect of dissipation on the properties of surface polaritons in GaAs/AlGaAs heterojunctions in a quantizing magnetic field

N. N. Beletskiĭ and S. A. Borisenko

Institute of Radiophysics and Electronics, National Academy of Sciences of Ukraine, 310085 Kharkov, Ukraine

(Submitted July 9, 1998)
Fiz. Tverd. Tela (St. Petersburg) **41**, 705–711 (April 1999)

A study is reported of nonradiative surface and bulk polaritons in GaAs/$Al_xGa_{1-x}As$ real heterojunctions under conditions favoring integer-quantum Hall effect (IQHE) and in the presence of dissipation in a two-dimensional electron layer. The conditions of their existence, the spectrum, and damping have been determined. It is shown that under IQHE conditions all aspects of surface and bulk polaritons are quantized. It is found that, as the wave number is varied, surface and bulk polaritons can transform continuously into one another. The possibilities of experimental observation of nonradiative polaritons are discussed. © *1999 American Institute of Physics.* [S1063-7834(99)03004-X]

1. Surface polaritons at the boundaries of two-dimensional electron systems (2DES) acted upon by an external magnetic field recently have been attracting considerable attention.[1–5] Of particular interest is the strong-magnetic-field case, where integer quantum Hall effect (IQHE) occurs in 2D-electron systems.[6,7] Under these conditions, the high-frequency 2DES-conductivity tensor components are quantized, i.e. they change discontinuously with varying magnetic field. This makes all characteristics of surface polaritons quantized too. The properties of surface polaritons under IQHE conditions were studied for a single[6] and a double[7] 2DES. It was shown[6,7] that the group velocity of surface polaritons in the IQHE regime undergoes jumps proportional to the fine-structure constant $\alpha = e^2/c\hbar$, where e is the electronic charge, c is the velocity of light, and $\hbar = h/2\pi$ (h is the Planck constant).

At the same time, the properties of surface polaritons were studied in Ref. 6 under the assumption that the plane occupied by the 2DES is embedded in a homogeneous medium with permittivity ε. In actual fact, the real structure of the GaAs/$Al_xGa_{1-x}As$ heterojunction simulated by a 2D electron layer is more complex. Indeed, a doped $Al_xGa_{1-x}As$ layer has a finite thickness. As a result, the electrons making up a 2DES are sandwiched between GaAs (this layer forms the substrate, and it may be considered infinitely thick) and the $Al_xGa_{1-x}As$ layer, which is in contact with vacuum (or air). Besides, it was pointed out[8,9] that $Al_xGa_{1-x}As$ and GaAs have different dielectric permittivities, and their ratio was set to 0.95. The above factors can produce qualitatively new features in the propagation of surface polaritons along a real GaAs/$Al_xGa_{1-x}As$ heterojunction. Besides, under real conditions one should take into account dissipation in the 2DES. This dissipation can give rise not only to a quantitative change in the surface-polariton spectrum, but also in appearance of new types of nonradiative polaritons (both surface and bulk), whose electromagnetic field dies out exponentially away from both interfaces of the $Al_xGa_{1-x}As$ layer.

This work studies nonradiative polaritons in real GaAs/$Al_xGa_{1-x}As$ heterojunctions in the IQHE regime. The effect of the $Al_xGa_{1-x}As$ layer thickness and of the energy dissipation in the 2DES on the conditions of existence, spectrum, and damping of nonradiative polaritons were investigated. It is shown that besides the surface polaritons pinned to the GaAs-$Al_xGa_{1-x}As$ interface there may exist another type of surface polaritons, which are localized at the $Al_xGa_{1-x}As$-vacuum/air interface (the Brewster modes). It was found that besides these two types of surface polaritons, a GaAs/$Al_xGa_{1-x}As$ heterojunction is capable of supporting propagation of bulk polaritons of various orders, which have one or several energy-flow maxima in the $Al_xGa_{1-x}As$ layer. It is pointed out that in the IQHE conditions all characteristics of surface and bulk polaritons are quantized. It was established that surface and bulk polaritons can transform into one another in a continuous manner with variation of the wave number.

2. Consider the structure shown in Fig. 1 as a model of the GaAs/$Al_xGa_{1-x}As$ heterojunction. It consists of two semi-bounded media, *1* ($z>d$) and *3* ($z<0$), with dielectric permittivities ε_1 and ε_3, respectively. A semiconductor layer with thickness d (medium *2*) and a dielectric permittivity ε_2 is sandwiched between these media. Let medium *2* be the $Al_xGa_{1-x}As$ semiconductor, and medium *3*, the GaAs semiconductor. These two semiconductors produce a 2D electron system at the $z=0$ interface. The external quantizing magnetic field **B** is directed along the z axis perpendicular to the 2DES. We assume the polaritons in this structure to be nonradiative, i.e. that their electromagnetic fields in media *1* and *3* decay exponentially with increasing distance from the interfaces of layer *2* into either medium. Without loss of

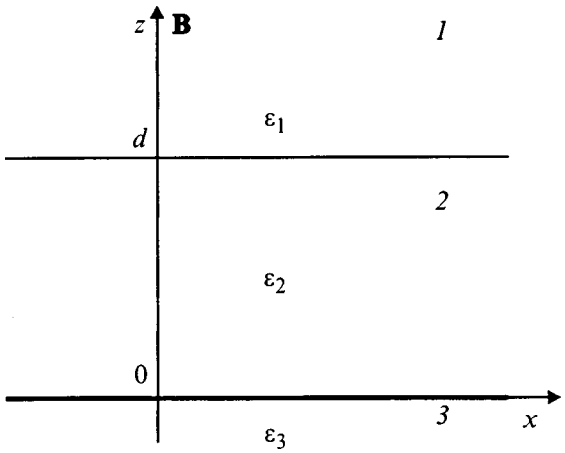

FIG. 1. Geometry of the GaAs/Al_xGa_{1-x}As heterojunction. Semibounded medium *1* is vacuum/air with dielectric permittivity $\varepsilon_1=1$, medium *2* is an Al_xGa_{1-x}As semiconductor slab with a thickness d and dielectric permittivity $\varepsilon_2=12.0$, and semibounded medium *3* is GaAs semiconductor with dielectric permittivity $\varepsilon_3=12.9$.

generality, we assume the nonradiative polaritons to propagate along the x axis. The dependence of all electromagnetic fields on coordinate x and time t will be described by the relation $\exp[i(kx-\omega t)]$, where k is the wave number, and ω is the wave frequency.

To derive the dispersion relation describing propagation of nonradiative polaritons in a GaAs/Al_xGa_{1-x}As heterojunction, one has to take into account two types of waves, TE and TM. This is due to the existence of a surface current at the $z=0$ 2DES interface, which acts on both TE and TM waves.[10] We assume further that at the $z=d$ interface the tangential components of the electric, **E**, and magnetic, **H**, fields of nonradiative waves are continuous, while at $z=0$ the tangential components of the magnetic field undergo a discontinuity

$$H_{x,2}^{(s)}=H_{x,3}^{(s)}=\frac{4\pi}{c}(\sigma_{xx}E_y^{(s)}-\sigma_{xy}E_x^{(s)}), \tag{1a}$$

$$H_{y,2}^{(s)}=H_{y,3}^{(s)}=-\frac{4\pi}{c}(\sigma_{xx}E_x^{(s)}+\sigma_{xy}E_y^{(s)}). \tag{1b}$$

Here $\sigma_{ij}(\omega)$ are components of the 2DES conductivity tensor, and the superscript s indicates that the electric and magnetic fields in Eqs. (1a) and (1b) are calculated at the $z=0$ interface. We assume that the spatial dispersion of the 2DES conductivity tensor may be neglected, i.e. that $kl\ll 1$, where $l=(c\hbar/eB)^{1/2}$ is the magnetic length. Then the nonvanishing 2DES conductivity tensor components can be written[6,7]

$$\sigma_{xx}=\frac{2e^2}{h}\frac{N\gamma}{1+\gamma^2}, \tag{2a}$$

$$\sigma_{xy}=\frac{2e^2}{h}\frac{N}{1+\gamma^2}. \tag{2b}$$

In Equations (2a) and (2b), $\gamma=(\nu-i\omega)/\Omega$, where $\Omega=eB/mc$ is the electron cyclotron frequency, ν is the electron-momentum relaxation frequency, and $N=\pi l^2 n$ is the Landau level filling factor, which takes on integer values ($N=1,2,\ldots$) equal to the number of completely filled Landau levels lying below the Fermi level (n is the electron density in the 2DES).[6,7]

Using the above boundary conditions, one readily finds the following dispersion relation describing propagation of nonradiative polaritons in the heterojunction under study

$$A_1A_2+(4\pi\sigma_{xy}/c)^2p_2p_3B_1B_2=0, \tag{3}$$

where

$$A_1=[p_3\varepsilon_2-p_2\varepsilon_3-(i4\pi p_2p_3\sigma_{xx}/\omega)](p_2\varepsilon_1-p_1\varepsilon_2)+\exp(2p_2d)[p_3\varepsilon_2+p_2\varepsilon_3+(i4\pi p_2p_3\sigma_{xx}/\omega)]\times(p_2\varepsilon_1+p_1\varepsilon_2), \tag{4}$$

$$A_2=[p_2-p_3+(i4\pi\omega\sigma_{xx}/c^2)](p_2-p_1)-\exp(2p_2d)\times[p_2+p_3-(i4\pi\omega\sigma_{xx}/c^2)](p_2+p_1), \tag{5}$$

$$B_1=p_2-p_1+\exp(2p_2d)(p_2+p_1), \tag{6}$$

$$B_2=p_2\varepsilon_1-p_1\varepsilon_2-\exp(2p_2d)(p_1\varepsilon_2+p_2\varepsilon_1). \tag{7}$$

Here the variables

$$p_i=\sqrt{k^2-\frac{\omega^2}{c^2}\varepsilon_i}, \quad i=1,2,3 \tag{8}$$

represent transverse wave numbers describing distribution of the electromagnetic field of nonradiative polaritons along the z axis.

Because the polaritons are nonradiative, the following conditions should hold:

$$\mathrm{Re}\,p_1>0, \quad \mathrm{Re}\,p_3>0. \tag{9}$$

If $\varepsilon_2=\varepsilon_3$, then, in the limit as $d\to\infty$, the dispersion relation (3) coincides with that for surface polaritons in a 2DES embedded in a homogeneous medium with permittivity ε_2.[6,7]

3. Consider now the results of a numerical solution of dispersion relation (3) with inclusion of dissipation in the 2DES. We shall assume the wave number k to be a real, and the frequency $\omega=\omega'+i\omega''$, a complex quantity. For conveniency of the numerical solution of (3), we introduce the following dimensionless quantities: $\xi'=\omega'/\Omega$, $\xi''=\omega''/\Omega$, $\zeta=ck/\Omega$, $\chi=z\Omega/c$, $\delta=d\Omega/c$, and $\Gamma=\nu/\Omega$. All calculations were carried out for a GaAs/Al_xGa_{1-x}As heterojunction with $\varepsilon_2=12.0$ and $\varepsilon_3=12.9$. The Al_xGa_{1-x}As layer (medium *2*) was assumed to be in contact with air/vacuum with permittivity $\varepsilon_1=1.0$ (medium *1*).

Figure 2 presents a $\xi'(\zeta)$ spectrum and damping $\xi''(\zeta)$ for the $\delta=0.1$ case calculated for three Landau level filling factors N. Dashed line *4* corresponds to the light line, and in the absence of dissipation ($\Gamma=0$) separates the regions of radiative and nonradiative polaritons. Dispersion curves *1°–3°* correspond to zero dissipation, and for the above values of N they start at the light line *4*.

As seen from Fig. 2, the presence of dissipation in a 2DES broadens the existence region of nonradiative polaritons; indeed, they exist for all values of ζ. To the right of light line *4*, the dispersion curves change little compared to the nondissipative case. In this region the electromagnetic

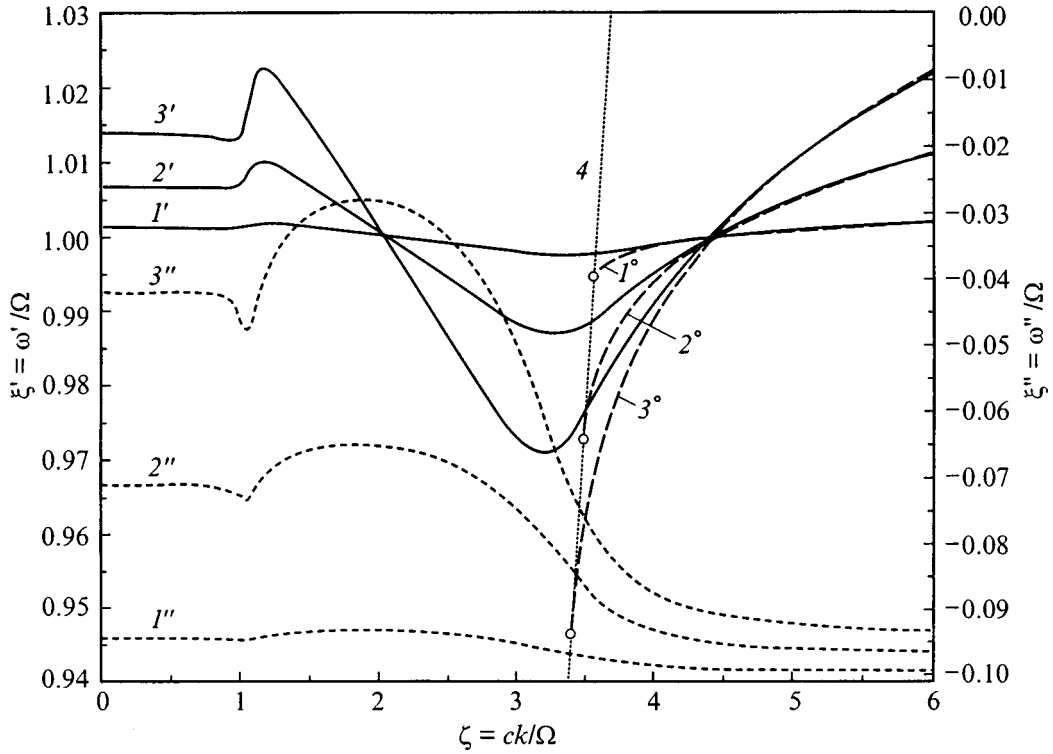

FIG. 2. Spectrum $\xi'(\zeta)$ ($1'$–$3'$) and damping $\xi''(\zeta)$ ($1''$–$3''$) of nonradiative polaritons in a GaAs/$Al_xGa_{1-x}As$ heterojunction in the case of $\delta=0.1$ and $\Gamma=0.1$ calculated for various N: *1* — 1, *2* — 5, *3* — 10. Dashed line *4* is the light line for GaAs ($\xi'=\zeta/\sqrt{\varepsilon_3}$). Dashed lines *1°*–*3°* are dispersion curves for the case of no dissipation present.

field of nonradiative polaritons decays exponentially away from the 2DES interface ($z=0$), which means that they are surface polaritons. As one approaches light line *4*, the dispersion curves $\xi'(\zeta)$ deflect upward from their nondissipative counterparts to continue nonmonotonically up to the ordinate axis ($\zeta=0$). It was already pointed out[6,7] that near the cyclotron resonance ($\xi\approx1$) the dispersion curves cross roughly at the same point. Examining Fig. 2, it is seen that taking into account dissipation in the 2DES gives rise to the appearance of two points of intersection of the dispersion curves, with one of them being to the left, and the other, to the right of the light line *4*. Having crossed these points, the dependence of the frequency ξ' of nonradiative polaritons on N (for a fixed ζ) reverses its nature. Indeed, to the left of the first intersection of the dispersion curves the polariton frequency ξ' increases with N, while, for wave numbers ζ between the two crossing points of the dispersion curves, it decreases with increasing N. Finally, to the right of the second intersection point the wave frequency ξ' again grows with increasing N. Note that, within the region of wave numbers ζ lying to the left of the first dispersion-curve, crossing the $\xi'(\zeta)$ curve gives a region where $\partial\xi'/\partial\zeta>0$. The extent of this region grows with increasing N. We believe that the portion of the dispersion curve with $\partial\xi'/\partial\zeta>0$ is associated with generation of surface polaritons of the type of Brewster modes at the $z=d$ interface. The possible formation of TM-type Brewster modes at the interface between two dissipative media with positive real parts of the dielectric permittivities was pointed out earlier.[2,4] Our case is specific in that the surface polaritons of the Brewster-mode type have mixed polarization, and their appearance at the $z=d$ interface is due to dissipation in the 2D electron system located at the $z=0$ interface. As evident from Fig. 2, Brewster modes are generated at the $z=d$ interface if $\zeta\approx\sqrt{\varepsilon_1}=1$.

Figure 3 shows the variation of the spectrum $\xi'(\zeta)$ and of the damping $\xi''(\zeta)$ of nonradiative polaritons with Γ. One readily sees that the dispersion curves $\xi'(\zeta)$ for small Γ ($\Gamma=0.01-0.03$) have a spectrum endpoint $p_3'=0$ lying to the left of light line *5*. At this point, the electromagnetic field of nonradiative polaritons becomes delocalized and their damping vanishes, $\xi''=0$. As Γ increases, and the endpoint of the nonradiative polariton spectrum shifts to the left to reach the ordinate axis $\zeta=0$ for $\Gamma=0.05$. The $\zeta=0$ point corresponds to surface oscillations of the electromagnetic field which are circularly polarized in the 2DES plane ($E_{x2}/E_{y2}=i$, $H_{x2}/H_{y2}=i$), and whose frequency depends on δ.

Consider now the effect of the $Al_xGa_{1-x}As$ layer thickness on the spectrum and damping of nonradiative polaritons. Figure 4 presents the spectrum $\xi'(\zeta)$ and damping $\xi''(\zeta)$ for various values of δ. Examining Fig. 4 we see that the dispersion curves $\xi'(\zeta)$ can contain several regions with a positive derivative $\partial\xi'/\partial\zeta$. For small values of δ ($\delta=0.1$), curve *1'* has two such portions, with one of them lying to the left of the light line 5, and the other, to the right of it. The first region is associated with the formation of the Brewster mode at the $z=d$ interface, and the second, with the creation of a surface polariton at $z=0$. As δ increases,

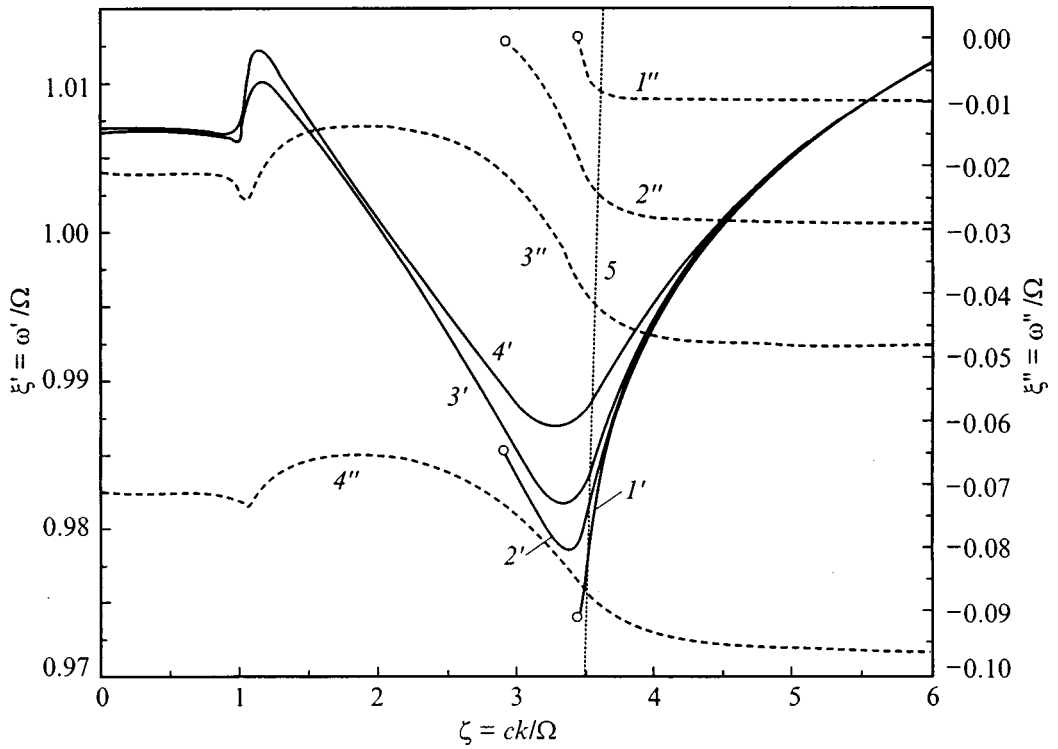

FIG. 3. Spectrum $\xi'(\zeta)$ (solid lines *1′–4′*) and damping $\xi''(\zeta)$ (dotted lines *1″–4″*) of nonradiative polaritons in a GaAs/$Al_xGa_{1-x}As$ heterojunction in the case of $\delta=0.1$ and $N=5$ calculated for various Γ: *1* — 0.01, *2* — 0.03, *3* — 0.05, *4* — 0.1. Dashed line *5* is the light line for GaAs ($\xi'=\zeta/\sqrt{\varepsilon_3}$).

two regions with a positive derivative $\partial\xi'/\partial\zeta$ appear in the dispersion curves $\xi'(\zeta)$ to the left of the light line *5* (curves *2*' and *3*' in Fig. 4). The first of them, as already mentioned, originates from Brewster mode formation at $z=d$, and the second, from the creation of a first-order bulk polariton. The x component of the average energy flux $\mathbf{S}(z)=(c/8\pi)\mathrm{Re}[\mathbf{EH}^*]$ of this polariton has one maximum within the $Al_xGa_{1-x}As$ layer. As δ increases still more, a third region with a positive derivative $\partial\xi'/\partial\zeta$ appears in the dispersion curve $\xi'(\zeta)$ to the left of the light line *5* (disper-

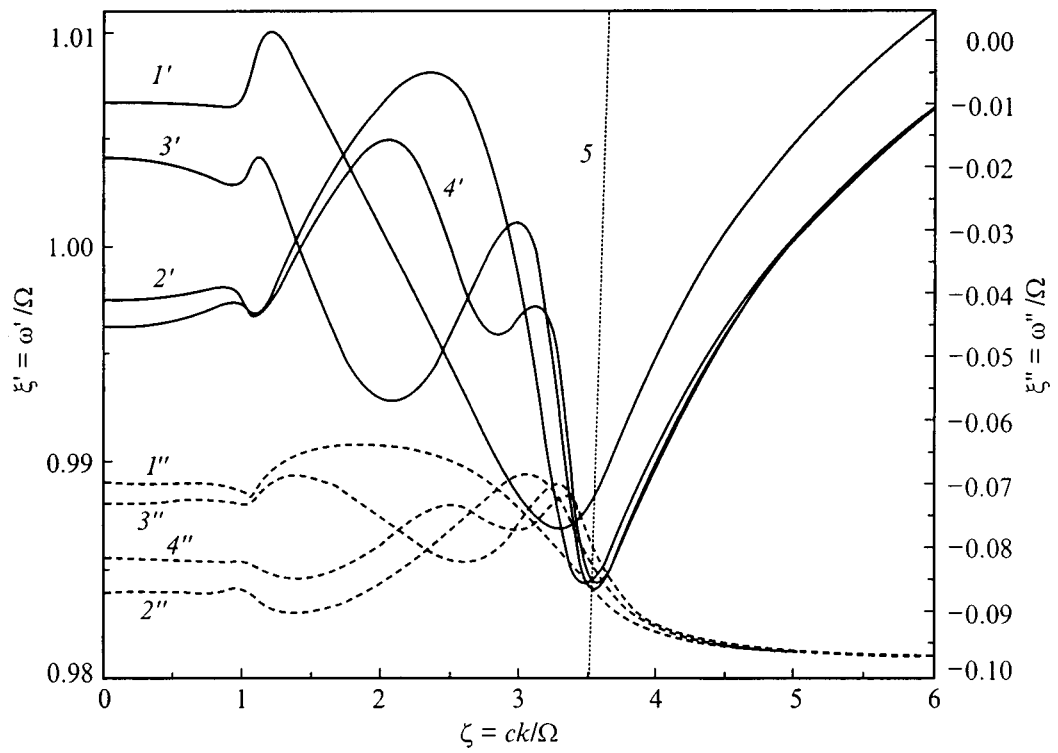

FIG. 4. Spectrum $\xi'(\zeta)$ (solid lines *1′–4′*) and damping $\xi''(\zeta)$ (dotted lines *1″–4″*) of nonradiative polaritons in a GaAs/$Al_xGa_{1-x}As$ heterojunction in the case of $\Gamma=0.1$ and $N=5$ calculated for various δ: *1* — 0.1, *2* — 0.5, *3* — 1.0, *4* — 1.5. Dashed line 5 is the light line for GaAs ($\xi'=\zeta/\sqrt{\varepsilon_3}$).

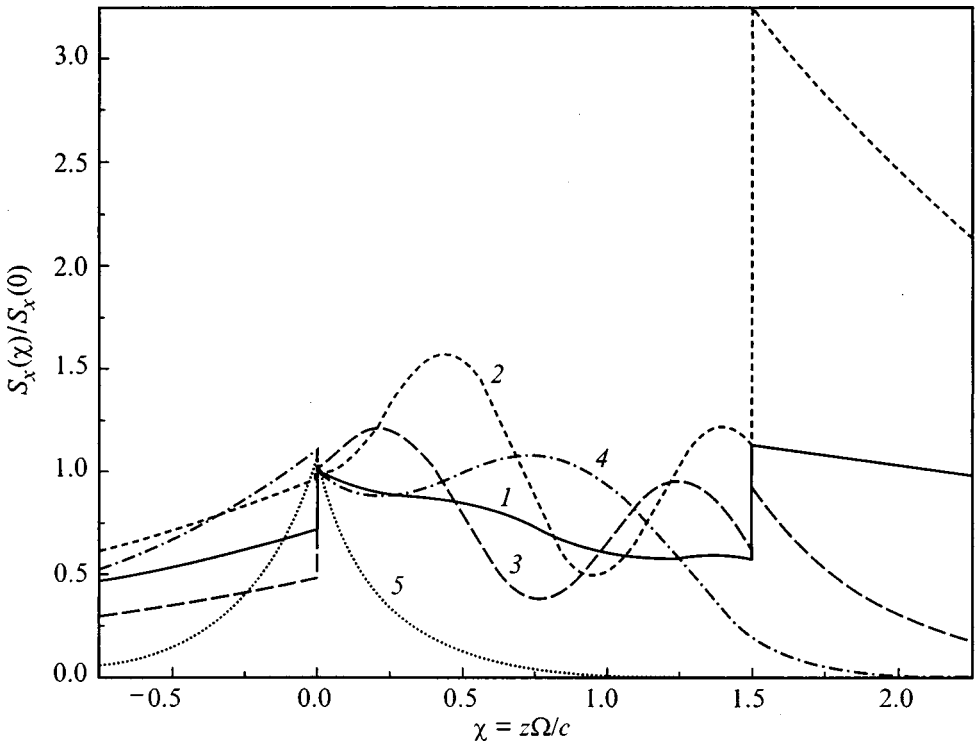

FIG. 5. $S_x(\chi)/S_x(0)$ relations for the case of $N=5$, $\Gamma=0.1$, $\delta=1.5$ calculated for various ζ: *1* — 0.5, *2* — 0.99, *3* — 1.5, *4* — 3.0, *5* — 4.0.

sion curve *4'*). This region can be assigned to the creation of a second-order bulk polariton, for which the $S_x(z)$ relation has two maxima within the $Al_xGa_{1-x}As$ layer.

Figure 5 displays the $S_x(\chi)/S_x(0)$ relation ($\chi=z\Omega/c$ is a dimensionless coordinate in the z direction) for the case of $N=5$, $\Gamma=0.1$, and $\delta=1.5$ constructed for various values of ζ. For small ζ ($\zeta=0.5$, curve *1*) the $S_x(\chi)$ distribution through the layer thickness is practically uniform. Note that the fraction of the energy flow propagated in medium *1* in the x direction is slightly larger than that in medium *3*. Energy transport in medium *1* increases substantially in the vicinity of the $\zeta=1$ point. Curve *2* in Fig. 5 refers to $\zeta=0.99$, which corresponds to the first point of the maximum in dispersion curve *4* of Fig. 4.This case reflects Brewster mode excitation at the $z=d$ interface. As ζ increases still further, the fraction of the energy flux propagating in medium *1* in the x direction decreases, and that in the $Al_xGa_{1-x}As$ layer (medium *2*), increases. For $\zeta=1.5$, nonradiative polaritons have two maxima in the $S_x(\chi)$ relation within the $Al_xGa_{1-x}As$ layer (curve *3*). This situation corresponds to excitation of second-order bulk polaritons in the $GaAs/Al_xGa_{1-x}As$ heterojunction. Further increase of ζ results in a gradual transformation of the second-order bulk polariton into a first-order bulk polariton ($\zeta=3.0$, curve *4*). This polariton produces only one maximum in $S_x(\chi)$ within the $Al_xGa_{1-x}As$ layer. Note that the formation of bulk polaritons of the first and second order brings about the appearance of local minima in the $\xi''(\zeta)$ relations (dashed curves *2''–4''* in Fig. 4). The reason for this lies in that the fraction of the energy flow propagated by bulk polaritons in the x direction within the $Al_xGa_{1-x}As$ layer is larger than that at its $z=0$ interface, which dissipates the wave energy. Finally, if ζ is to the right of the light line ($\zeta=4$, curve *5*), surface polaritons producing a maximum in energy flow at the $z=0$ interface are created in the $GaAs/Al_xGa_{1-x}As$ heterojunction. The damping of surface polaritons increases monotonically with ζ to approach its maximum value $\xi''=-\Gamma$.

It is of interest to analyze the dependence of the frequency and damping of surface electromagnetic oscillations ($\zeta=0$) on the quantity δ. Figure 6 shows the $\xi'(\delta)$ and $\xi''(\delta)$ relations for the case of $\zeta=0$, $N=5$ and for different values of Γ. For $\delta\to 0$ we obtain a 2DES sandwiched between media with dielectric permittivities ε_1 and ε_3. As follows from Eq. (3), $\xi'=1$, and $\xi''=-\Gamma+4\alpha N/(\sqrt{\varepsilon_1}+\sqrt{\varepsilon_3})$. Because ξ'' must be negative, surface electromagnetic oscillations can exist if $\Gamma>4\alpha N/(\sqrt{\varepsilon_1}+\sqrt{\varepsilon_3})$. For finite δ, the $\xi'(\delta)$ and $\xi''(\delta)$ relations are oscillating functions whose amplitude decreases with increasing δ. Finally, for $\delta\to\infty$ we come to a 2DES adjoining media with dielectric permittivities ε_2 and ε_3. For this case we have $\xi'=1$, $\xi''=-\Gamma+4\alpha N/(\sqrt{\varepsilon_2}+\sqrt{\varepsilon_3})$. Because $\varepsilon_2>\varepsilon_1$, the conditions of excitation of surface electromagnetic oscillations in the $\delta\to\infty$ case are less rigorous than those for $\delta\to 0$ (for the same value of N). Thus if Γ lies within

$$\frac{4\alpha N}{\sqrt{\varepsilon_1}+\sqrt{\varepsilon_3}}>\Gamma>\frac{4\alpha N}{\sqrt{\varepsilon_2}+\sqrt{\varepsilon_3}}, \tag{10}$$

there exists a critical value of δ below which surface electromagnetic oscillations cannot be generated.

Thus various types of fast and slow nonradiative polaritons can exist in $GaAs/Al_xGa_{1-x}As$ heterojunctions. They can be used for contactless probing of a heterojunction, namely, determination of the Landau-level filling factor, of the thickness of the $Al_xGa_{1-x}As$ layer, and of the electron-momentum relaxation frequency. In view of the discontinuous change in the parameters of nonradiative polaritons, they

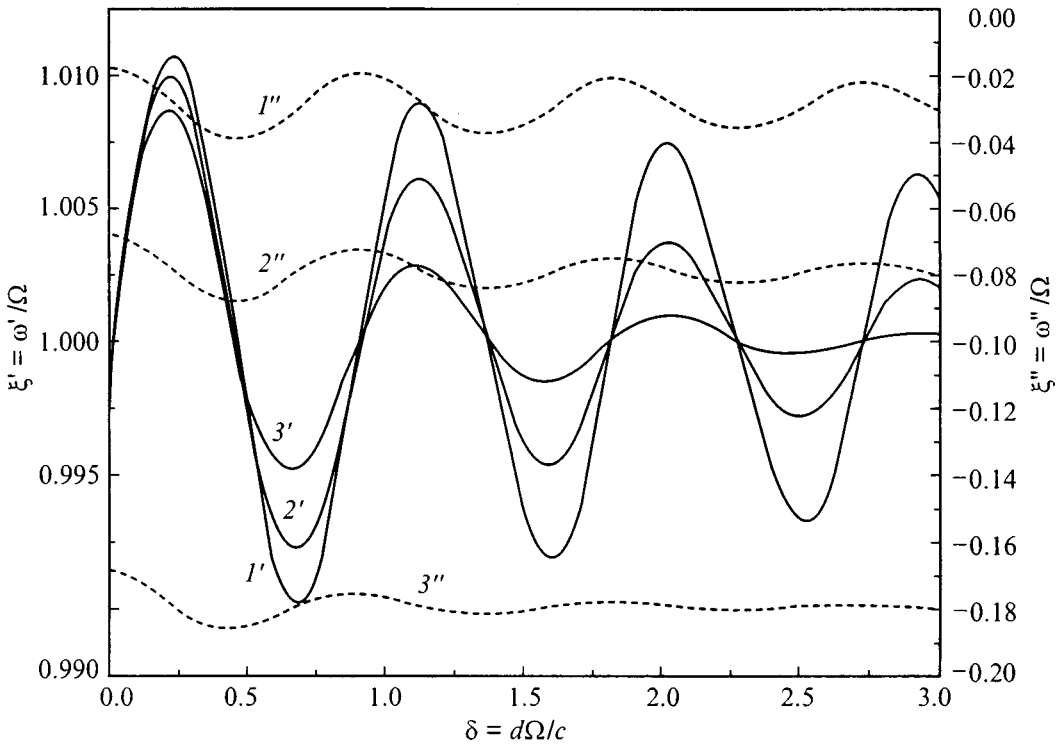

FIG. 6. $\xi'(\delta)$ and $\xi''(\delta)$ relations (curves *1′–3′* and *1″–3″*, respectively) for surface electromagnetic oscillations ($\zeta=0$) calculated for the $N=5$ case and for different values of Γ: *1* — 0.05, *2* — 0.1, *3* — 0.2.

can be of interest for potential device applications in semiconductor nanoelectronics.

We note in conclusion that nonradiative polaritons in semiconductors can be studied by various experimental methods, including disrupted total internal reflection[1,2] and inelastic light scattering[11]. The latter method permits excitation of slow surface polaritons with wave numbers $k\sim 2\times 10^5$ cm^{-1}. For such values of k the phase velocity of surface polaritons will be of the order of 0.01 c.

*)E-mail: beletski@ire.kharkov.ua

[1] *Surface Polaritons: Electromagnetic Waves at Surfaces and Interfaces*, Modern Problems in Condensed Matter Sciences, Vol. 1, edited by V. M. Agranovich and D. L. Mills (North-Holland, Amsterdam, 1982).
[2] *Electromagnetic Surface Modes*, edited by A. D. Boardman (Wiley, New York, 1982), p. 776.
[3] T. Ando, B. Fowler, and F. Stern, Rev. Mod. Phys. **54**, 437 (1982).
[4] R. S. Brazis, Litov. Fiz. Sb. **21**, No. 4, 73 (1981).
[5] Yu. A. Kosevich, A. M. Kosevich, and J. C. Granada, Phys. Lett. A **127**, 52 (1988).
[6] I. E. Aronov and N. N. Beletskii, J. Phys.: Condens. Matter **8**, 4919 (1996).
[7] I. E. Aronov, N. N. Beletskii, G. P. Berman, and A. R. Bishop, Phys. Rev. B **56**, 10392 (1997).
[8] N. C. Constantinou and M. G. Cottam, J. Phys. C **19**, 739 (1986).
[9] R. F. Wallis and J. J. Quinn, Phys. Rev. B **38**, 4205 (1988).
[10] M. Nakayama, J. Phys. Soc. Jpn. **36**, 393 (1974).
[11] L. L. Sohn, A. Pinczuk, B. S. Dennis, L. N. Pfeiffer, and K. W. West, Solid State Commun. **93**, 897 (1995).

Translated by G. Skrebtsov

Solitons in two- and three-dimensional crystals at Fermi resonance of optical modes

O. A. Dubovskiĭ and A. V. Orlov

Institute of Physics and Power Engineering, State Scientific Center of the Russian Federation, 249020 Obninsk, Russia

(Submitted July 20, 1998)
Fiz. Tverd. Tela (St. Petersburg) **41**, 712–716 (April 1999)

It is shown that soliton excitations of the peak, crater, and dark types, previously found by authors only in one-dimensional crystals, exist in two- and three-dimensional crystal systems of the superlattice type at Fermi resonance of modes of adjoining crystals. An analytical solution for the central part of soliton envelopes is presented. A numerical calculation gives results coinciding with the analytical solution in the central part of the solitons and demonstrates the presence of oscillations of the envelopes on the wings of peak and crater solitons in two- and three-dimensional crystals, which are not observed in one-dimensional crystals. © *1999 American Institute of Physics.* [S1063-7834(99)03104-4]

Experimental and theoretical investigations have been conducted of nonlinear optical modes in organic superlattices with programmed alternation of monolayers of organic molecules and new technologies have been developed for fabricating multilayer superlattices for nonlinear optical devices,[1–3] which may be used eventually to create an optical computer. In Refs. 4–6 attention was focused on the important role of the Fermi resonance of optical modes in contacting crystal planes, under which the energy $\hbar\omega_C$ of an exciton in one of the planes is close to the total energy $2\hbar\omega_B$ of two excitons in the neighboring plane. It was shown in Refs. 6–9 that, in such superlattice-type systems of the specific mixed $BB+C$, exciton excitations can propagate along the interface (they are known as Fermi-resonance interface modes or FRIM's).[6] These quantum and classical FRIM's are responsible for the bistability[7] and, possibly, the generation of nonlinear soliton excitations, i.e., many-particle complexes of FRIM states.[8–10] In addition, soliton solutions having smooth monotonic envelopes of the familiar hyperbolic cosine type were obtained in Refs. 8–10 for model one-dimensional crystal systems under the assumption of smoothness of the soliton envelopes, which makes it possible to use the corresponding nonlinear second-order differential equations. It was shown in our previous investigations[11,12] of FRIM-type soliton excitations in one-dimensional closed crystal chains with increasing length that soliton excitations of the type which was previously found in Refs. 8–10 by solving the corresponding nonlinear second-order differential equations comprise a separate element of a whole class of soliton excitations, having different types of symmetric[11] and antisymmetric[12] envelopes. It was shown in Refs. 11 and 12 that, in contrast to Refs. 8–10, the carrier frequency of a soliton is not a fixed quantity and can vary with a certain threshold in response to a corresponding change in the envelope. The results of Refs. 11 and 12 were subsequently used in Refs. 13 and 14 in a more thorough investigation of solitons of the various types found in Refs. 11 and 12 using the corresponding nonlinear second-order differential equations. The heightened interest in the soliton excitations found in Refs. 11 and 12 calls for a more detailed study of these excitations in real crystal systems that can be investigated experimentally, i.e., on two-dimensional interfaces, in planar superlattices,[10], in three-dimensional crystals with Fermi resonance of monomers,[15] etc. We note that Fermi resonance can also have a significant influence on the spectra of optical and acoustic multiphonon modes in light metals such as beryllium.[16]

This paper examines FRIM-type nonlinear excitations in actual two-dimensional (2D) and three-dimensional (3D) crystal systems. We shall consider, first, 2D systems consisting of two monolayers of molecules of types B and C in contact in a superlattice at Fermi resonance of optical excitations in these molecules or a topologically similar monolayer of organic molecules, in each of which there is Fermi resonance of intramolecular optical modes and, second, crystals of similar organic molecules. When the results of Refs. 11 and 12, which were obtained for 1D crystals, are developed further, it will be shown that several types of soliton excitations having fundamentally different types of envelopes also exist in 2D and crystal systems. Solitons of the so-called ''peak'' (p) type have a maximum at the center of the envelope and an ensuing decline of the envelope to zero with increasing distance toward the soliton wings. Solitons of the ''crater'' (c) type have a relative minimum at the center, then maxima on nearby lattice points, and a decline of the envelope to zero with increasing distance from the soliton center. ''Dark'' (d) solitons have an absolute minimum at the soliton center and an asymptotic increase with oscillations as the final asymptotic limit is approached on the wings. In addition, a fine structure can be observed on the wings of solitons of the p and c types for 2D and 3D systems, in contrast to the solitons found in Refs. 11 and 12 for 1D systems. We note that the dependence of the envelopes on the carrier frequency of the modes and the detuning from Fermi resonance were also investigated. The calculations showed that as the carrier frequency approaches the band of single-particle excitations and the detuning from Fermi resonance decreases, the amplitude of the solitons decreases,

their width increases, and a macroscopic description is possible with the use of the corresponding nonlinear second-order differential equations. Such a description may be of great interest in connection with the appearance of several new studies in this area[13,14] and the initial work on some interesting experiments.

The Hamiltonian H of a crystal system consisting of two contacting two-dimensional monolayers of molecules of types B and C or a three-dimensional crystal of monomers in the form of molecules with Fermi resonance of intramolecular modes has the form

$$H=H_C+H_B+H_{\text{int}}, \tag{1}$$

where H_C and H_B are the Hamiltonians of free excitons of the C and B types:

$$H_C=\sum_{\mathbf{n}} \hbar\omega_C c_{\mathbf{n}}^{+}c_{\mathbf{n}}+\sum_{\mathbf{nm}} V_{\mathbf{nm}}^{(c)}c_{\mathbf{n}}^{+}c_{\mathbf{m}},$$

$$H_B=\sum_{\mathbf{n}} \hbar\omega_B b_{\mathbf{n}}^{+}b_{\mathbf{n}}+\sum_{\mathbf{nm}} V_{\mathbf{nm}}^{(b)}b_{\mathbf{n}}^{+}b_{\mathbf{m}}. \tag{2}$$

In (2) $\mathbf{n}=(n_x,n_y)$ for 2D systems, and $\mathbf{n}=(n_x,n_y,n_z)$ for systems; b^{+}, c^{+}, b, and c are the Bose exciton creation and annihilation operators, and $V_{\mathbf{nm}}^{(c,b)}$ are the matrix elements of the intermolecular interaction operators, which specify the translational motion of c and b excitons. The Hamiltonian H_{int} of the third-order anharmonic $C+BB$ interaction in (1), which defines Fermi resonance, has the form

$$H_{\text{int}}=\Gamma\sum_{\mathbf{n}} [(b_{\mathbf{n}}^{+})^2c_{\mathbf{n}}+c_{\mathbf{n}}^{+}(b_{\mathbf{n}})^2], \tag{3}$$

where Γ is a constant of that interaction. A detailed discussion of a Hamiltonian like H_{int} is given in Ref. 6.

The Heisenberg equations for the operators $b_{\mathbf{n}}$ and $c_{\mathbf{n}}$

$$i\hbar\frac{db_{\mathbf{n}}}{dt}=-[H,b_{\mathbf{n}}], \quad i\hbar\frac{dc_{\mathbf{n}}}{dt}=-[H,c_{\mathbf{n}}] \tag{4}$$

in the case of the interaction of nearest neighbors with consideration of (1)–(3) have the following form:

$$i\hbar\frac{db_{\mathbf{n}}}{dt}=\hbar\omega_B b_{\mathbf{n}}+V_B\sum_{\mathbf{l}} b_{\mathbf{n+l}}+2\Gamma b_{\mathbf{n}}^{+}c_{\mathbf{n}}, \tag{5a}$$

$$i\hbar\frac{dc_{\mathbf{n}}}{dt}=\hbar\omega_C c_{\mathbf{n}}+V_C\sum_{\mathbf{l}} c_{\mathbf{n+l}}+\Gamma b_{\mathbf{n}}^{2}, \tag{5b}$$

$$V_{\mathbf{nm}}^{(b,c)}=V_{B,C}\delta_{\mathbf{n,m+l}}. \tag{5c}$$

Nonlinear optical excitations with large occupation numbers upon strong laser pumping are usually described using a quasiclassical approximation, within which all the operators in (5) are replaced by their mean values $\langle b_{\mathbf{n}}\rangle\equiv B_{\mathbf{n}}$ and $\langle c_{\mathbf{n}}\rangle\equiv C_{\mathbf{n}}$, where $B_{\mathbf{n}}$ and $C_{\mathbf{n}}$ are the amplitudes of the modes.[6–12] We shall seek solutions of the system of equations for $B_{\mathbf{n}}$ and $C_{\mathbf{n}}$ corresponding to (5) with the time dependences $B_{\mathbf{n}}=B_{\mathbf{n}}\exp(-i(\omega/2)t)$ and $C_{\mathbf{n}}=C_{\mathbf{n}}\exp(-i\omega t)$ for the real amplitudes $B_{\mathbf{n}}$ and $C_{\mathbf{n}}$, where ω is the carrier frequency. When these time dependences are used, the system of equations for $B_{\mathbf{n}}$ and $C_{\mathbf{n}}$ has the form

$$\frac{\hbar\omega}{2}B_{\mathbf{n}}=\hbar\omega_B B_{\mathbf{n}}+V_B\sum_{\mathbf{l}} B_{\mathbf{n+l}}+2\Gamma B_{\mathbf{n}}C_{\mathbf{n}}, \tag{6a}$$

$$\hbar\omega C_{\mathbf{n}}=\hbar\omega_C C_{\mathbf{n}}+V_C\sum_{\mathbf{l}} C_{\mathbf{n+l}}+\Gamma B_{\mathbf{n}}^{2}. \tag{6b}$$

It is not difficult to see that the solutions of the system of equations (6) $B_{\mathbf{n}},C_{\mathbf{n}}$ depend on the parameters Γ and $\hbar$ as scaling factors; therefore, it is natural to introduce the quantities $b_{\mathbf{n}}=(\Gamma/\hbar)B_{\mathbf{n}}$ and $c_{\mathbf{n}}=(\Gamma/\hbar)C_{\mathbf{n}}$, which have the dimensions of frequency. The system of equations corresponding to (6) for these quantities has the form

$$\frac{\omega}{2}b_{\mathbf{n}}=\omega_B b_{\mathbf{n}}+\frac{V_B}{\hbar}\sum_{\mathbf{l}} b_{\mathbf{n+l}}+2b_{\mathbf{n}}c_{\mathbf{n}}, \tag{7a}$$

$$\omega c_{\mathbf{n}}=\omega_C c_{\mathbf{n}}+\frac{V_C}{\hbar}\sum_{\mathbf{l}} c_{\mathbf{n+l}}+b_{\mathbf{n}}^{2}. \tag{7b}$$

A soliton solution of the system of equations (5) with an envelope of the familiar form, viz., an inverse hyperbolic cosine, was found analytically for a one-dimensional system in Refs. 8–10. Solitons of a localized type, i.e., ''standing'' solitons, with a zero velocity of the soliton maximum ($v=0$) and traveling solitons with $v\neq 0$ were found. As a consequence of the *a priori* assumed smoothness of the envelopes and the proportionality of the B and C amplitudes, the carrier frequencies and the soliton velocities turned out to be fixed quantities specified by the parameters appearing in (1)–(3). It will be shown below that several solitons of different types can propagate in the two- and three-dimensional crystals considered. The localized ''standing'' solitons were considered first.

The azimuthally and spherically symmetric soliton solutions were investigated in the first stage. Accordingly, square and cubic clusters with a designated central lattice point and increasing odd integer numbers of lattice points $N=N_2$ and $N=N_3$ for 2D and 3D systems, respectively, were systematically considered. For 2D systems $N_2=5,9,13,21,\ldots$, and for 3D systems $N_3=7,19,27,\ldots$, in accordance with the algorithm for creating circles and spheres near the central lattice point with successively increasing radii. In this case the radial dependence of the amplitudes is fixed by the single index r according to the distance from the central lattice point. For 2D systems the numbering $b_0\equiv b_{0,0}$, $b_1\equiv b_{0,\pm 1}\equiv b_{\pm 1,0}$, $b_2\equiv b_{\pm 1,\pm 1}$, $b_3\equiv b_{\pm 2,0}\equiv b_{0,\pm 2}$, $b_4\equiv b_{\pm 2,\pm 1}\equiv b_{\pm 1,\pm 2}$ was henceforth used in accordance with this principle. For systems the numbering $b_0\equiv b_{0,0,0}$, $b_1\equiv b_{\pm 1,0,0}\equiv b_{0,\pm 1,0}\equiv b_{0,0,\pm 1}$, $b_2\equiv b_{0,\pm 1,\pm 1}\equiv b_{\pm 1,0,\pm 1}\equiv b_{\pm 1,\pm 1,0}$, etc. was used. The corresponding radius vectors of these lattice points are $r_0=0$, $r_1=a$, $r_2=\sqrt{2}a$, $r_3=2a,\ldots$ for a 2D system and $r_0=0$, $r_1=a$, $r_2=\sqrt{2}a$, $r_3=\sqrt{3}a$, etc. for a system, where a is the lattice constant. The quantities r_i can be regarded as the radii of the corresponding coordination circles (2D) or spheres (3D).

In order to single out the principal analytical features of the envelopes of the soliton excitations, let us consider a 2D system with the smallest possible number of lattice points $N_2=5$. The equations (7) for b_n and c_n have the following form:

$$\left(\frac{\omega}{2}-\omega_B\right)b_0-4\frac{V_B}{\hbar}b_1=2b_0c_0,\ \ (\omega-\omega_C)c_0-4\frac{V_C}{\hbar}c_1=b_0^2, \tag{8a}$$

$$\left(\frac{\omega}{2}-\omega_B\right)b_1-\frac{V_B}{\hbar}b_0=2b_1c_1,\ \ (\omega-\omega_C)c_1-\frac{V_C}{\hbar}c_0=b_1^2. \tag{8b}$$

This system of equations has exact analytical solutions. To simplify the analysis we set $V_A\equiv V_B\equiv\hbar V$. Expressing $c=c(b)$ from the first equalities in (8a) and (8b) as a function of b, after substitution into the second equalities in (8a) and (8b) we obtain two nonlinear coupled equations for b_0 and b_1

$$2b_0^2=(\omega-\omega_C)\left(\frac{\omega}{2}-\omega_B\right)-V(\omega-\omega_C)\frac{4}{x}-4V\left(\frac{\omega}{2}-\omega_B\right)+4V^2x, \tag{9a}$$

$$2b_1^2=(\omega-\omega_C)\left(\frac{\omega}{2}-\omega_B\right)-V(\omega-\omega_C)x-4V\left(\frac{\omega}{2}-\omega_B\right)+4V^2\frac{1}{x}, \tag{9b}$$

where $x\equiv b_0/b_1$ is the ratio between the amplitudes. After dividing (9a) by (9b), for x we obtain the fourth-order equation

$$V(\omega-\omega_C)x^4-(\omega-\omega_C-4V)\left(\frac{\omega}{2}-\omega_B\right)x^3+(\omega-\omega_C-4V)\times\left(\frac{\omega}{2}-\omega_B\right)x-4V(\omega-\omega_C)=0. \tag{10}$$

This equation has the exact analytical solutions $x=x_i(\omega)$ with a complex dependence of $x_i(\omega)$. However, approximating solutions can be found for soliton solutions with strong localization of the excitations. For peak solitons with $x\gg1$ only the first two terms in the equation must be taken into account. As a result, for $x=x_p$ we obtain the following expression:

$$x_p=\frac{(\omega-\omega_C-4V)\left(\frac{\omega}{2}-\omega_B\right)}{V(\omega-\omega_C)}>1. \tag{11}$$

For a dark soliton with $x\ll1$, only the last two terms must be taken into account in the equation, and, accordingly, for $x=x_d$ we obtain

$$x_d=\frac{4V(\omega-\omega_C)}{(\omega-\omega_C-4V)\left(\frac{\omega}{2}-\omega_B\right)}<1. \tag{12}$$

Finally, for solitons of the crater type with $x\approx1$ all the terms must be taken into account, but an expansion in the small deviation δ of the value of x from unity can be written, where $x=1+\delta$ and $\delta\ll1$. As a result for $x=x_c$ we obtain the following relation

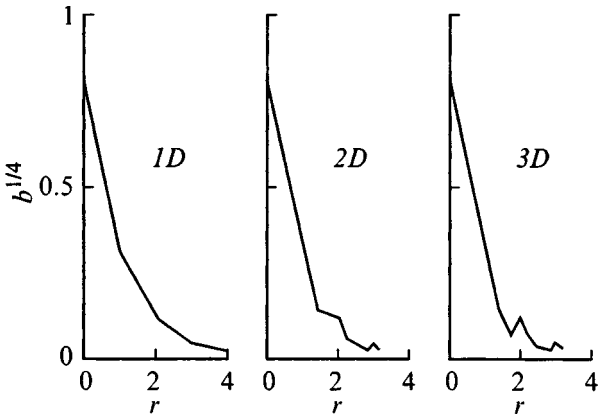

FIG. 1. Radial dependences of the envelopes of peak solitons in 1D, 2D, and 3D crystal systems.

$$\delta=\frac{3V(\omega-\omega_C)}{4V(\omega-\omega_C)-2(\omega-\omega_C-4V)\left(\frac{\omega}{2}-\omega_B\right)}<1,$$

$$x_c=1+\delta. \tag{13}$$

The inequalities in the relations (11)–(13) define the region for the existence of solitons and the corresponding thresholds. The values of b_0 and b_1 for solitons of all three types are obtained from the relations (7) when the values of x_p, x_d, and x_c found by solving (9) are used. The calculations analogous to (8)–(13) for a system with the minimal number of lattice points $N_3=7$ gives the same relations for amplitudes with small numerical corrections. As further calculations showed, as N is increased, only growth of the wings of these solitons with the base values b_0 and b_1 thus obtained occurs. At the same time, it will be noted below that the soliton wings in 2D and 3D systems exhibit some definite nonmonotonicity with slow decay and local maxima, which is not observed for 1D solitons.[11,12]

The analytical calculations of the soliton envelopes for systems with $N_2>5$ and $N_3>7$ are fairly complicated; therefore, numerical calculations of the solutions of the system of nonlinear equations for $b_{\mathbf{n}}$ obtained from (7) after the substitution of $c_{\mathbf{n}}=c_{\mathbf{n}}(b_{\{m\}})$ as functions of $b_{\mathbf{n}}$ and the nearby $b_{\mathbf{m}}$ into (7b) were performed for such systems on a Pentium computer. The equations themselves are not presented here because of the cumbersome nonlinear relationship between $c_{\mathbf{n}}$ and different b_m. Parallel calculations were performed for 1D, 2D, and 3D systems. In the 1D system corresponding to a one-dimensional cluster the calculations were performed to the 7th lattice point, which is at a distance of 7a from the central lattice point, in the 2D system they were performed to the 8th coordination circle, and in the system they were performed to the 10th coordination sphere. Figures 1, 2, and 3 present only the central parts of the envelopes up to $n=4$ for the 1D system for purposes of comparison with the 2D and 3D systems. A different number of coordination spheres and circles was used to trace the oscillations on the soliton wings for different values of r.

Figures 1, 2, and 3 present the results of calculations of the radial dependence of the envelopes of b_r for solitons of

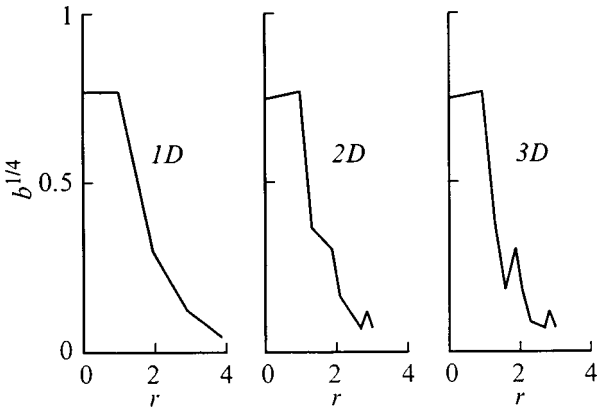

FIG. 2. Radial dependences of the envelopes of crater solitons in 1D, 2D, and 3D crystal systems.

the *p* (peak) type (Fig. 1), *c* (crater) type (Fig. 2), and *d* (dark) type (Fig. 3). We note that the values of the radius *r* for systems of different dimensionality differ: in a 1D system $r=r_i=ia$, in a 2D system $r=r_{ij}=(i^2+j^2)^{1/2}a$, and in a system $r=r_{ijk}=(i^2+j^2+k^2)^{1/2}a$, where the indices *i*, *j*, and *k* label the lattice points in the crystal. Since for some of the dependences of b_r obtained the values of the function for different *r* in the range $0\leqslant r\leqslant 7$ differ by 5–10 order of magnitude, for visual perception of the results the dependence of $(b_r)^{1/4}$ on *r*, which monotonically depicts b_r with relative raising of small values of the function and relative lowering of large values of the function, is presented in Figs. 1, 2, and 3. All the frequency characteristics were expressed in units of ω_C. The values of the parameters were chosen close to the real optical parameters $V_B/\hbar\omega_C=V_C/\hbar\omega_C=0.01$ and $\omega_B/\omega_C=0.4$ used in Refs. 4 and 9–12. It was noted in Refs. 11 and 12 that the carrier frequency ω in 1D systems has threshold values, above which solitons of a different type appear. A similar situation is observed in 2D and 3D crystals. For the parameters used, the lowest threshold values of the carrier frequency $\omega=\omega_0$, at which *d* and *c* solitons appear, correspond to $\omega_0/\omega_C\cong 1.02$ in the 1D system, $\omega_0/\omega_C\cong 1.14$ in the 2D system, and $\omega_0/\omega_C\cong 1.54$ in the 3D system. The value $\omega/\omega_C=1.7$ was selected for a simultaneous graphical representation of the 1D, 2D, and 3D systems. It can be seen in Fig. 1 that, unlike the envelope for the 1D system, the envelopes of *p* solitons for the 2D and systems exhibit local maxima and slowing of the decline at definite values of *r*. These values of *r* correspond to the points on the crystallographic axes $(i,0)$ and $(0,i)$, where $i=2,3,\ldots$ in the 2D system. In the 3D system local maxima are observed at the points $(i,j,0)$, $(i,0,j)$, and $(0,i,j)$, where $i,j=2,3,\ldots$. The values of the envelopes at the points $(i,0)$ and $(0,i)$ of the 2D system $b_r=b_{i,0}=b_{0,i}$ and the values at the points $(i,0,0)$, $(0,i,0)$, and $(0,0,i)$ of the 3D system $b_r=b_{i00}=b_{0i0}=b_{00i}$ are close to the envelope values $b_r=b_i$ in the 1D system. The envelope values $b_r=b_{ij0}=b_{i0j}=b_{0ij}$ in the system are close to the values $b_r=b_{ij}$ in the 2D system. The latter are associated with the extremely small value $V/\hbar\omega_C=0.01$ for typical systems, the large difference between ω and ω_C, and the large detuning from Fermi resonance $\omega_C-2\omega_B$; however, at large *V*, small differences between ω and ω_C, and small detunings from Fermi resonance these values differ more significantly. The qualitative analytical calculations performed showed that the aforementioned local maxima and slowing of the decline on the envelopes appear because, for example, in the 2D system a molecule having $r=6$ interacts with the molecule of the lower coordination circle having $r=3$ and, accordingly, its amplitude is increased compared to the amplitude of the molecule having $r=5$, which interacts with the molecule having $r=4$. Similar situations are observed in other cases in 2D and 3D crystals.

Figure 2, which plots the envelopes of *c* solitons, reveals that, at $r=0$, the values of the amplitudes at the center for the 1D, 2D, and 3D systems are related by the law $b_0>b_{00}>b_{000}$ (with the former numbering). Beginning at the next coordination circle or sphere with $r=1$, i.e., on the descending portions of the plots of b_r, the behavior of the envelopes of *c* solitons have the same features as the envelopes of *p* solitons. However, the oscillations on the soliton wings have greater amplitudes than in Fig. 1.

Figure 3, which plots the envelopes of *d* solitons, reveals that, at $r=0$, the values of the envelopes increase in the order $b_0<b_{00}<b_{000}$, whereas at $r=1$ these values obey the opposite relationship $b_1>b_{10}>b_{100}$. On the portion of the dependence for $r>1$, the plots of the envelopes of *d* solitons have a minimum and then asymptotically approach a constant finite value. Thus, 2D and 3D systems obey the same law that was noted in a 1D system in Ref. 11.

We also note that the numerical values of the envelopes of *p*, *c*, and *d* solitons obtained in 2D system at the central point, and the first coordination circle, coincide to within a small error with the values obtained from the analytical relations (10)–(13), simultaneously confirming the applicability of both the numerical programs used and the analytical procedures for the corresponding expansions.

We note that the radial dependences of b_r give only a rough visual picture of the actual structuring along the crystallographic directions in the naturally richer spatial dependence of the amplitudes of the modes in 2D and 3D crystal lattices. The already developed investigations of the azimuthal dependence of soliton envelopes[13,14] and the experimental studies that have been started in this area are of in-

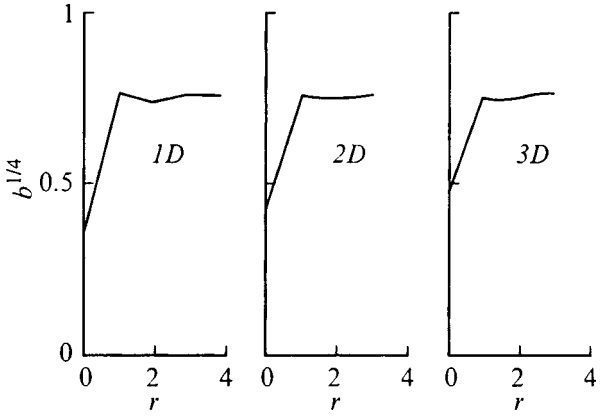

FIG. 3. Radial dependences of the envelopes of dark solitons in 1D, 2D, and 3D crystal systems.

terest. In this paper attention was focused on peak, crater, and dark solitons. Similar investigations should be undertaken for solitons of the qualitatively different types that were first explored in our previous studies.[11,12]

In conclusion, we express our sincere thanks to V. M. Agranovich for some useful remarks.

This work was performed with support from the Russian state scientific-technical program ''Crucial Areas in the Physics of Condensed Media'' in the area of ''Neutron Studies of Matter.'' O.A.D. thanks Volkswagen Stiftung for its partial support in the form of Grant I/69928.

[1] F. F. So, S. R. Forrest, Y. Q. Shy, and W. H. Steier, Appl. Phys. Lett. **56**, 674 (1990).
[2] F. F. So and S. R. Forrest, Phys. Rev. Lett. **66**, 2649 (1991).
[3] V. M. Agranovich, Mol. Cryst. Liq. Cryst. **230**, 13 (1993).
[4] V. M. Agranovich, R. D. Atanasov, and G. F. Bassani, Chem. Phys. Lett. **199**, 621 (1992).
[5] V. M. Agranovich, Phys. Scr. T **49**, 699 (1993).
[6] V. M. Agranovich and O. A. Dubovsky, Chem. Phys. Lett. **210**, 458 (1993).
[7] V. M. Agranovich and J. B. Page, Phys. Lett. A **183**, 651 (1993).
[8] V. M. Agranovich and A. M. Kamchatnov, JETP Lett. **59**, 424 (1994).
[9] V. M. Agranovich, O. A. Dubovsky, and A. M. Kamchatnov, J. Phys. Chem. **98**, 13 607 (1994).
[10] V. M. Agranovich, S. A. Darmanyan, O. A. Dubovsky, A. M. Kamchatnov, E. I. Ogievetsky, P. Reineker, and T. Neidlinger, Phys. Rev. B **53**, 15 451 (1996).
[11] O. A. Dubovskiĭ and A. V. Orlov, Fiz. Tverd. Tela (St. Petersburg) **38**, 1221 (1996) [Phys. Solid State **38**, 675 (1996)].
[12] O. A. Dubovskiĭ and A. V. Orlov, Fiz. Tverd. Tela (St. Petersburg) **38**, 1931 (1996) [Phys. Solid State **38**, 1067 (1996)].
[13] S. Darmanyan, A. Kobyakov, and F. Lederer, Phys. Rev. E **57**, 957 (1998).
[14] V. M. Agranovich, S. A. Darmanyan, K. I. Grigorishin, A. M. Kamchatnov, T. Neidlinger, and P. Reineker, Phys. Rev. B **57**, 2461 (1998).
[15] V. M. Agranovich and I. I. Lalov, Usp. Fiz. Nauk **146**, 267 (1985) [Sov. Phys. Usp. **28**, 484 (1985)].
[16] O. A. Dubovskiĭ and A. V. Orlov, Fiz. Tverd. Tela (St. Petersburg) **39**, 542 (1997) [Phys. Solid State **39**, 472 (1997)].

Translated by P. Shelnitz

Specific features in the temperature dependence of photoluminescence from CdTe/ZnTe size-quantized islands and ultrathin quantum wells

V. V. Zaĭtsev,*) V. S. Bagaev, and E. E. Onishchenko

P. N. Lebedev Physical Institute, Russian Academy of Sciences, 117924 Moscow, Russia
(Submitted August 24, 1998)
Fiz. Tverd. Tela (St. Petersburg) **41**, 717–724 (April 1999)

A study has been carried out of the temperature dependences of luminescence spectra on a large number of CdTe/ZnTe structures differing in average thickness, $\langle L_z \rangle = 0.25-4$ monolayers (ML), and CdTe layer geometry (continuous, island type). The influence of geometric features in the structure of ultrathin layers on linewidth, the extent of lateral localization of excitons, their binding energy, and exciton-phonon coupling is discussed. It is shown that in island structures there is practically no lateral exciton migration. The exciton-phonon coupling constant in a submonolayer structure has been determined, $\Gamma_{ph} = 53$ meV, and it is shown that in structures with larger average thicknesses Γ_{ph} is considerably smaller. Substantial lateral exciton migration was observed to occur in a quantum well with $\langle L_z \rangle = 4$ ML, and interaction with acoustic phonons was found to play a noticeable part in transport processes. It has been established that the depth of the exciton level in a quantum well and structural features of an ultrathin layer significantly affect the temperature dependences of integrated photoluminescence intensity.
 [S1063-7834(99)03204-9]

1. Studies of structures containing submonolayers or a small number of monolayers of one semiconductor embedded in the matrix of another has recently been attracting increasing interest.[1–10] One succeeds in obtaining in this case perfect ultrathin quantum wells and quantum dots with a large number of semiconductors characterized by considerable lattice mismatch. As shown earlier,[2,3] such structures grown by MBE on CdTe- and ZnTe-based compounds, whose lattice mismatch is 6%, have a high quantum yield of exciton emission at 5 K within a broad interval in the visible (extending from the green to red wavelengths), depending on the actual thickness of the CdTe ultrathin layer. Our structures differed not only in average thickness but in geometry as well, namely, continuous or island type. In the latter case, the structures represent actually an ensemble of quantum islands lying in the same plane. This situation was of particular interest for us, because, as shown by our calculations, the wave-function overlap of neighboring islands in the lateral direction is small, permitting one to consider a set of islands as a quasi-isolated quantum-dot ensemble.

Investigation of emission spectra of such structures at different temperatures is of interest from more than one viewpoint. On the one hand, an analysis of the exciton-emission line shape, linewidth and position makes it possible in some cases to draw a conclusion concerning exciton-phonon coupling, as well as on the presence or absence of lateral migration. On the other hand, experimental relations of the integrated photoluminescence intensity offer quite frequently a possibility to reveal the major mechanism responsible for the weakening of the emission with increasing temperature.

Following preliminary information on the samples and on the experimental techniques used, we are going to discuss in Section III the specific features of quantum-island structures. The experimental results obtained from submonolayer structures and structures with $\langle L_z \rangle \geqslant 1$ ML, and their discussion are presented in Sections IV and V, respectively.

2. The structures under study were MBE grown on GaAs(001) substrates and represented $\sim 1\ \mu$m thick ZnTe films, with CdTe ultrathin layers or submonolayers embedded in the latter at a distance of 50 nm from the surface; the average growth thickness $\langle L_z \rangle$, the position of the excitonic transition $E_{\rm ex}$, the depth of the level ε (relative to the free-exciton position in ZnTe), and the line FWHM, Γ, of these embedded CdTe layers measured at 5 K are listed in Table I. In structure W3, the CdTe ultrathin layers are separated by ZnTe layers 50 nm thick, and in W4 and W5, 10 nm thick. In the W1 structure, two submonolayers are separated by a 5-ML thick ZnTe layer. High-resolution TEM images[4] showed $\langle L_z \rangle < 4$-ML thick layers to represent actually a system of isolated CdTe islands. Their lateral dimensions do not exceed 3 and 6 nm, and thickness, 3 and 5 ML for layers with an average thickness of 1 and 3 ML, respectively. Their in-plane spacings are of the order of 10–20 nm. In the W4 structure containing $\langle L_z \rangle = 4$-ML CdTe formations the islands coalesce to form a layer with varying local thickness.

Photoluminescence spectra were measured within a temperature range from 5 to 150 K. An argon laser operating on single lines provided optical excitation (the exciting photon energy in our experiments was 2.541 eV). The spectra were analyzed with a double-grating monochromator with a resolution not worse than 0.01 nm. The PM tube output was fed into a narrow-band amplifier with a lock-in detector. The experiment was computer controlled and processed in CAMAC format. The luminescence studied at different temperatures included measurement of the linewidth $\Gamma(T)$, line shift

TABLE I. Luminescence line characteristics of the CdTe/ZnTe structures for $T=5$ K.

Average CdTe layer thickness, ML (sample)	Line position, eV	Level depth, meV	Γ, meV
0.25 (W1)	2.3425	38.5	3.0
1 (W4)	2.3095	71.5	11.5
1.2 (W3)	2.2680	113.0	15.5
1.6 (W3)	2.2325	148.5	21.5
2 (W3)	2.1715	209.5	26.0
2 (W2)	2.1700	211.0	23.0
3 (W4)	2.1230	258.0	25.0
2 (W5)	2.1115	269.5	37.0
3 (W5)	1.9675	413.5	26.0
4 (W4)	1.9220	459.0	22.5

$\Delta(T)$, and integrated photoluminescence intensity $I(T)$.

3. Prior to considering the experimental results, consider some features of the energy spectra of excitons and the pattern of their spatial localization, which are determined by the small thickness of the CdTe layers and their geometry. Of major interest are the island structures, because, as this will be shown below, the exciton wave functions may exhibit appreciable lateral localization in this case. As a result, a set of islands may be considered as a quasi-isolated ensemble of quantum dots. Besides, for some island dimensions the exciton binding energy E_B may become higher than that in the case of continuous layers, with a corresponding weakening of exciton coupling with optic phonons, which accounts for the intrinsic level broadening with increasing temperature.

We start the consideration of the above problems with a discussion of the band model of the CdTe/ZnTe structures. Specifically, the potential jump in the valence band is dominated here by the strains generated by the lattice mismatch between the two materials. If they are disregarded, the so-called chemical potential jump in the valence band, according to both theoretical calculations and experiments,[11] is small and is not over 10% of the band offset ΔE_g between the materials of the heteropair. Thus the main part of ΔE_g (if one neglects the strains, $\Delta E_g \approx 0.8$ eV) falls on the conduction band, which accounts for a large potential well ΔE_c for electrons. It is the quantization of the light particle that explains the extremely broad spectral range of emission lines observed[2–4] in our structures.

The above features in the CdTe/ZnTe band diagram suggest that the energy spectrum of excitons and their localization in island structures should be determined primarily by electrons. Therefore we shall start with the calculational technique used and the results bearing on the energy and wave functions of electrons in the cylindrical-island model, setting aside for a while the discussion of excitonic effects.

Because the thickness of an island L_z is considerably smaller than its lateral dimension, the Schrödinger equation can be solved approximately. We write the electron wave function in the form $\psi(x,y,z)=\psi_1(z)\psi_2(x,y)$, as this was done, for instance, in Ref. 12. This reduces the problem to solving a one-dimensional Schrödinger equation for a square quantum well of thickness L_z having a potential $U(z)=\Delta E_c\theta(|z|-L_z/2)$, and a two-dimensional equation with a potential $U(\rho)=[\Delta E_c-E_e(L_z)]\theta(\rho-R)$, where z and ρ are, respectively, the coordinates normal to the island plane and the distances reckoned from the center of a cylindrical island of radius R, $\theta(x)$ is the Heaviside function, and $E_e(L_z)$ is the electron energy, which is the solution of the one-dimensional problem and is reckoned from the bottom of the one-dimensional well. The islands will be considered isolated, and the validity of this assumption will be borne out by the subsequent analysis.

The one-dimensional problem is specific in that the well layer thickness is small, which makes the envelope method inapplicable. It turned out, however, that this approximation gives good agreement with both experiment and theoretical calculations made within the empirical tight-binding method. The relevant points were already discussed by us before.[2,3] The theoretical works analyzed in these papers can be complemented by a recent publication[13] where a study of an InAs monolayer in GaAs also revealed a close similarity between the results obtained by the two above-mentioned methods for excitons consisting of an electron and a heavy hole, and a difference for the *e-lh* exciton. Note that the emission measured in our structures is due to excitons of the first type.[2–4] Calculations made using well-known relations[14] show that the exciton transition energies $E_{ex}(L_z)$, as well as $E_e(L_z)$, decrease approximately linearly with increasing thickness within the interval $L_z=1-4$ ML with close values of dE_{ex}/dL_z and dE_e/dL_z, which were found to be about 100 meV/ML.

The contribution due to lateral quantization is found from the solution of the two-dimensional Schrödinger equation, which for the ground state can be written

$$\left[\frac{d^2}{d\rho^2}+\frac{1}{\rho}\frac{d}{d\rho}+\frac{2m_e^*}{\hbar^2}(E-U(\rho))\right]\psi_2(\rho)=0, \tag{1}$$

where $U(\rho)=U_\rho\theta(\rho-R)$, $U_\rho=U_\rho(L_z)$ is the potential well depth, and

$$\psi_2(\rho)=\begin{cases} c_1J_0(k_1\rho) & \rho<R, \quad k_1=\sqrt{\dfrac{2m_e^*E}{\hbar^2}}, \\ c_2J_1(k_2\rho) & \rho>R, \quad k_2=\sqrt{\dfrac{2m_e^*(U_\rho-E)}{\hbar^2}}. \end{cases} \tag{2}$$

The condition of continuity of ψ_2 and ψ_2' at $\rho=R$ yields an equation for the lateral quantization energy E

$$k_2J_0(k_1R)K_1(k_2R)=k_1J_1(k_1R)K_0(k_2R), \tag{3}$$

where J_0 and J_1 are Bessel functions of the first kind, and K_0 and K_1 are the modified Hankel functions.

Because the depth of a two-dimensional well $U_\rho(L_z)=[\Delta E_c-E_e(L_z)]\approx 0.1n-0.05$ eV (where $n=1,\ldots,4$ for $L_z=1,\ldots,4$ ML, respectively) is quite large, the contribution of lateral quantization for small island radii turns out to be substantial. Figure 1a presents numerical results characterizing the effect of the lateral dimensions of a cylindrical island on electron energy. One immediately sees that the electron energy (in the figure it is normalized to the well depth) can differ appreciably from that in the planar-well case for

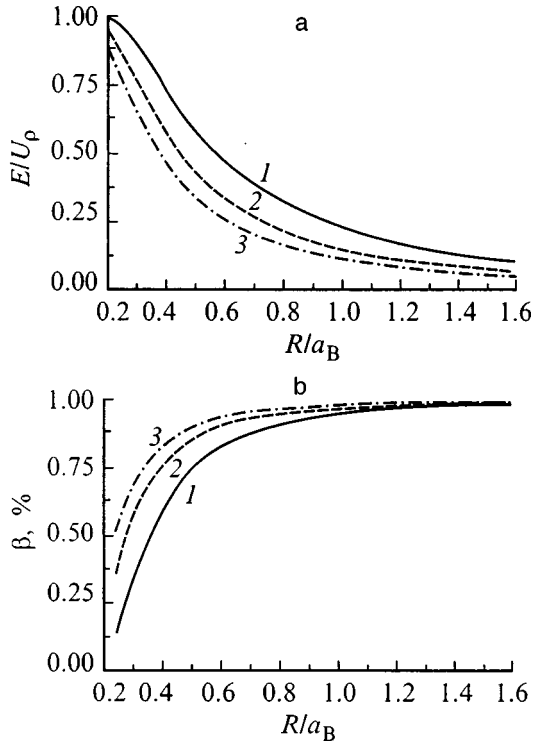

FIG. 1. (a) Lateral quantization energy (normalized to well depth U_ρ) and (b) extent of lateral localization plotted as functions of island radius for island thickness L_z(ML): *1*—2, *2*—3, *3*—4.

$R/a_B > 0.3$, which corresponds to real island dimensions (a_B, the exciton Bohr radius in ZnTe, is 5 nm), with the difference increasing with thickness L_z. Table II lists electron-hole transition energies calculated for CdTe layers with $\langle L_z \rangle = 1-2$ ML. The calculations used the island sizes determined by electron microscopy. Shown for comparison are the results of a planar-layer model calculation, which in real conditions would correspond to continuous layers (quantum wells) with thickness fluctuations whose lateral size is much less than the exciton Bohr radius. One sees that the calculations made within the cylindrical island model agree much better with experimental data.

Figure 1b presents data characterizing wave-function localization inside an island. The degree of lateral localization $\beta = 2\pi \int |\psi_2(\rho)|^2 \theta(R-\rho)\rho d\rho$ increases with L_z and remains appreciable for all L_z and real R. The latter suggests that the islands may be considered isolated. An upper estimate of the overlap integrals, made with account of the real island sizes and separations, shows that corrections to the electron energies due to wave-function overlap are indeed small. Because of the spread in exciton energies, whose statistics remain unknown, it would be difficult to make a rigorous evaluation of the exciton tunneling-transition probabilities between islands. There are grounds to believe that, because such calculations must take into account participation of acoustical phonons, the probability of transitions should be small compared to that of recombination.

TABLE II. Calculated positions of electron-hole transitions (without including of the exciton binding energy) for CdTe layers of average thickness 1–2 ML.

Average layer thickness, ML	1.0	1.2	1.6	2.0
Level position in cylindrical island model, eV	2.329	2.299	2.238	2.180
Level position in planar layer model, eV	2.349	2.332	2.291	2.247

As already mentioned, in view of the specific features in the CdTe/ZnTe band model, the qualitative conclusions of the effect of small island size on the energy and degree of localization are valid for excitons as well. It should be pointed out that, as the spatial size of the exciton in both lateral and perpendicular direction decreases, its binding energy increases. This should result, first, in an increase of the inhomogeneous linewidth caused by fluctuations in geometric size and, second, in a decrease of the homogeneous linewidth, which is due to interaction with optic phonons at high temperatures. This interaction takes place if E_B exceeds the optic-phonon energy $\hbar\omega_{\mathrm{LO}}$.[15] For planar CdTe layers in ZnTe, E_B can be derived by variational calculations.[16] For CdTe thicknesses $L_z = 1-4$ ML we obtain $13 \leqslant E_B(L_z) \leqslant 23$ meV. In the case of islands, numerical calculations are fairly time consuming, and it will be dealt with in a separate publication. Here we shall use qualitative conclusions that can be drawn from the calculations made[17] for cylindrical GaAs/$Ga_{1-x}Al_xAs$ islands. As far as we know, this is at present the only work where the exciton energy and wave function were calculated for finite electron and hole barriers. Extrapolation of the results obtained in Ref. 17 to the case of CdTe islands in ZnTe suggests that within the interval $1 \leqslant L_z \leqslant 4$ ML the exciton binding energy E_B may exceed E_B in ZnTe by more than a factor three. Because $\hbar\omega_{\mathrm{LO}} = 26$ meV, the inequality $E_B > \hbar\omega_{\mathrm{LO}}$ will hold, and exciton-phonon coupling may weaken.

As for the inhomogeneous linewidth Γ_{inh}, its substantial decrease with a decrease of both the thickness and lateral size of islands allows a qualitative interpretation if one notes the corresponding increase of the exciton to island volume ratio. As a result, fluctuations in island size will result in a smaller difference between exciton energies. The smallest value of Γ_{inh} of 3.1 meV was observed in the W1 structure containing CdTe submonolayers. The results obtained for this structure will be presented below first of all. It was found that on the whole they differ qualitatively from those relating to structures containing CdTe layers with $L_z > 1$ ML.

4. The emission line in W1 is due to excitons localized at islands in two closely lying submonolayers.[2,3] An analysis of its temperature dependence reveals an appreciable variation of the line width Γ and of its shape at high temperatures; indeed, Γ increases by more than a factor of three and approaches a Lorentzian shape while at low temperatures it is closer to a Gaussian. This suggests that the linewidth at low temperatures is determined by inhomogeneous broadening, while at high temperatures it is dominated by the intrinsic exciton-level broadening.[18] The most significant interaction producing exciton energy-level broadening in II-VI semiconductors is the Fröhlich coupling with optic phonons. In this case the $\Gamma(T)$ relation for quantum wells can be written[18]

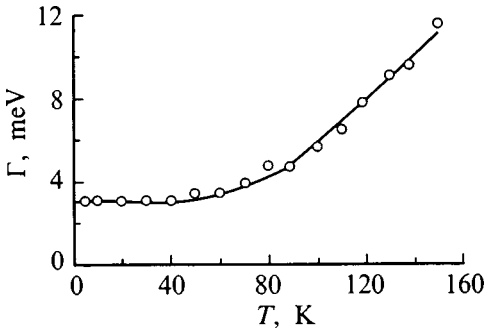

FIG. 2. $\Gamma(T)$ relation for the $W1$ structure: circles—experimental data, solid line—fitting against Eq. (4).

$$\Gamma(T)=\Gamma_{\text{inh}}+\frac{\Gamma_{\text{ph}}}{\exp\left(\frac{\hbar\omega_{LO}}{kT}\right)-1}, \tag{4}$$

where Γ_{ph} is the exciton-phonon coupling constant, $\hbar\omega_{\text{LO}}$ is the optic-phonon energy, and k is the Boltzmann constant. The theoretical relation (4) providing the best fit to experimental data is shown in Fig. 2 by a solid line. The parameters used in the least-squares fitting were Γ_{ph} and $\hbar\omega_{\text{LO}}$, with $\Gamma_{\text{inh}}=\Gamma(5\text{ K})=3.1$ meV (the linewidth remains constant up to 40 K). The constants Γ_{ph} and $\hbar\omega_{\text{LO}}$ obtained in this way are 53 and 26 meV, respectively. The energy of the optic phonon is in a very good agreement with that of the LO phonon in the ZnTe barrier. A similar situation is observed in the case of InAs submonolayers in GaAs.[8] This observation, first, serves as an additional argument for an adequate description of experimental data in our work by Eq. (4). Second, it apparently suggests that because of the very small thickness of CdTe islands (one ML) the largest part of the exciton is localized (in the z direction) in the ZnTe barrier. In this case one may expect that the temperature-induced shift of exciton levels, $\Delta(T)$, should be close to the variation of the gap, $\Delta E_g(T)$, in ZnTe. Indeed, as seen from Fig. 3, the experimental relation $\Delta(T)$ reproduces very well the course of $\Delta E_g(T)$ in the barrier.[19] As for the exciton-phonon coupling constant, its value exceeds by a factor 1.8 that of Γ_{ph} for free excitons in ZnTe, 30 meV.[15] Because the exciton binding energy in this system is close to E_B in ZnTe (13 meV), the increase of Γ_{ph} compared to this quantity for free

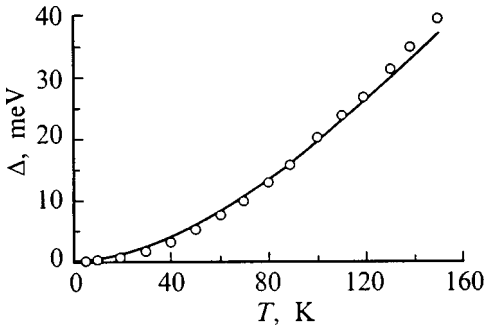

FIG. 3. Shift of the luminescence line maximum with temperature, $\Delta(T)$, in the $W1$ structure: circles—experimental data, solid line—plot of $\Delta E_g(T)$ for ZnTe.

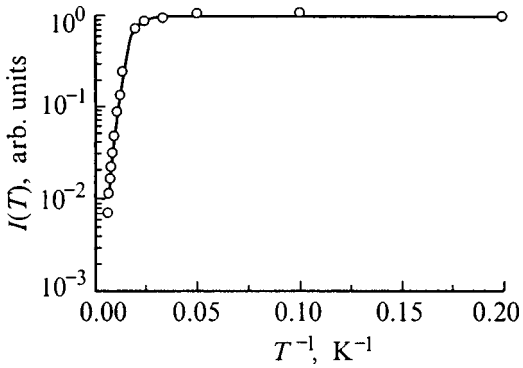

FIG. 4. Temperature dependence of integrated luminescence line intensity for the $W1$ structure [$\log(I(T)/I(5))$ vs $1/T$]: circles—experimental data, solid line—fitting against Eq. (5).

exciton in ZnTe may argue for lateral exciton localization. This is suggested also by the absence of a Stokes shift between the emission and reflectance spectra.[2,3]

Figure 4 plots the temperature dependence of integrated luminescence-line intensity of submonolayers. For $T>40$ K, one observes a noticeable weakening of emission, whose intensity at 150 K is more than two orders of magnitude weaker than that at 5 K. The mechanisms of quenching (weakening) of photoluminescence in quantum wells was studied in a number of works.[20–22] It was shown that in most cases the major mechanism is thermal emission of the carriers localized in quantum wells into the barrier. There is, however, no consensus at present concerning the relation between the so-called activation energy E_a characterizing this emission and the depth of the electron and hole levels, ε_e and ε_h, in a well. In most cases it was found that $E_a\approx\varepsilon_e+\varepsilon_h$.[20] Some authors suggest, however, that $E_a=\min(\varepsilon_e,\varepsilon_h)$,[21] or $E_a=(\varepsilon_e+\varepsilon_h)/2$ (Ref. 22). It appeared of interest to study the mechanisms responsible for the weakening of photoluminescence in systems representing a quantum-dot ensemble and to establish, in particular, which of the above relations between E_a, ε_e, and ε_h is valid. Investigation of the temperature dependences of integrated photoluminescence-line intensities shows quite often that one can separate two portions differing substantially in the luminescence quenching rates at low and high temperatures, which are usually characterized by two different activation energies of nonradiative processes[23–25] with the following relation

$$\frac{I(T)}{I(0)}=\frac{1}{1+A_1\exp\left(-\frac{E_1}{kT}\right)+A_2\exp\left(-\frac{E_2}{kT}\right)}, \tag{5}$$

where E_1 and E_2 are activation energies, and the constants A_1 and A_2 characterize the ratio of nonradiative to radiative recombination rates. As a rule, the larger activation energy E_2 relating to the high-temperature emission-intensity decline can be shown to have a certain physical meaning. It was found that, for our system, E_2 (41 meV) agrees closely with the difference in energies (39 meV) between the free exciton in the barrier and the excitons localized in CdTe submonolayers. Therefore the emission quenching can be

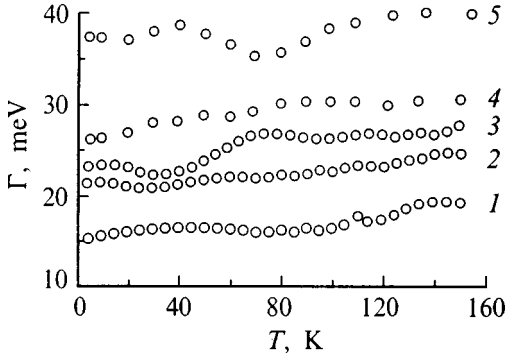

FIG. 5. $\Gamma(T)$ relation for some quantum-island systems: *1*—1.2 ML ($W3$), *2*—1.6 ML ($W3$), *3*—2 ML ($W2$), *4*—3 ML ($W5$), *5*—2 ML ($W5$).

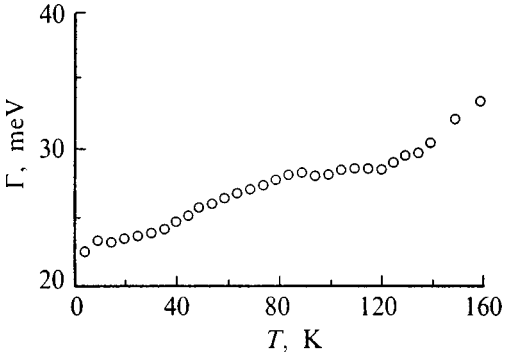

FIG. 6. $\Gamma(T)$ relation for a 4-ML thick CdTe layer ($W4$).

caused by thermal ejection of excitons localized in CdTe islands to free-exciton states in ZnTe. As for E_1 (17 meV), it can be noted that it is close to the exciton binding energy in the given submonolayer structure.

5. Let us turn now to the results obtained for structures with CdTe layer thicknesses above 1 ML. They differ essentially from W1 in that the linewidth here is in most cases (with the exception of $\langle L_z \rangle = 4$ ML) practically temperature independent. Figure 5 illustrates $\Gamma(T)$ measurements made on CdTe layers of differing thicknesses. In contrast to W1, the inhomogeneous contribution to Γ, while remaining mostly practically constant, is dominant at all temperatures. This conclusion was drawn from an analysis of the line shapes made by approximating them with the Voigt profile[26] (a Gaussian folded with a Lorentzian). It was found that the content of the Lorentzian component does not exceed 10% of the total linewidth for all samples and throughout the temperature range covered. Estimates of the exciton-phonon coupling constant show that it does not exceed 20 meV, and that in some cases it may be considerably smaller.

Note that the linewidth in systems with ultrathin InAs layers in GaAs was found in some studies to become narrower with increasing temperature.[27,28] This observation is believed to indicate the onset of lateral migration with increasing temperature, a process by which excitons interacting with phonons transfer from states with a lower localization energy to deeper states. This results in a temperature-induced shift of the radiation maximum, which is sharper compared to the case of the well and barrier materials. We did not observe this phenomenon in our systems. The line shift $\Delta(T)$ was in all cases smaller than $\Delta E_g(T)$ in ZnTe and approached $\Delta E_g(T)$ in CdTe as the exciton level in the well became deeper. These observations, combined with the absence of any temperature dependence of the inhomogeneous width (Figure 5), can be explained by assuming that in structures with thicker CdTe islands, as in submonolayer islands (the W1 structure), excitons are laterally localized and, accordingly, do not migrate. In contrast to W1, however, the size of excitons both in the island plane and in the perpendicular direction is, in accordance with the above, substantially smaller. As already mentioned, this results not only in large inhomogeneous linewidths but also in smaller optic-phonon coupling constants Γ_{ph}, which account for the intrinsic mechanism of broadening at higher temperatures. We note in connection with this that, as shown by an experimental study,[15] in $Zn_{1-x}Cd_xSe/ZnSe$ quantum wells the Γ_{ph} constant becomes smaller for $E_B > \hbar\omega_{\text{LO}}$ than those measured in conventional bulk ZnSe, where $E_B < \hbar\omega_{\text{LO}}$.

$\Gamma(T)$ was observed to increase only for a 4-ML thick CdTe layer (Fig. 6). In contrast to the previous case, this situation is typical and was noted in many systems. It should be pointed out, however, that, unlike the W1 structure, the inhomogeneous contribution is dominant here for all temperatures. An unambiguous analysis of the line profile is difficult to make in this case, however, because a contribution of the oxygen-impurity-bound exciton complexes[29] appears at high temperatures on the long-wavelength side of the line. To understand the nature of the increase of $\Gamma(T)$, measurements of the temperature dependences of emission spectra were carried out under quasi-resonant excitation with a

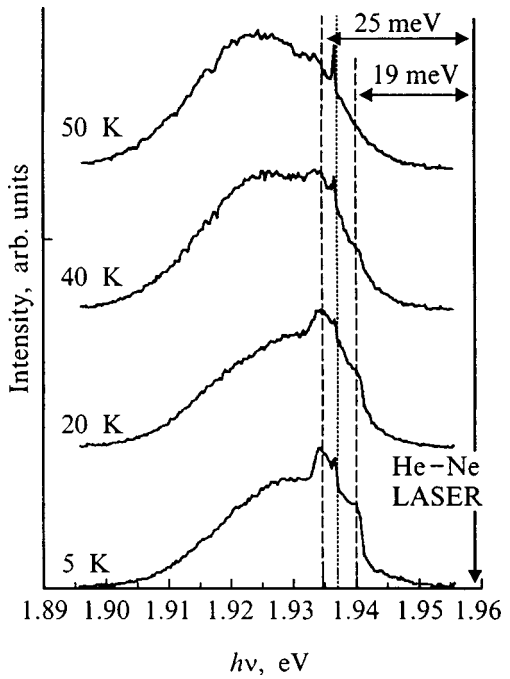

FIG. 7. Photoluminescence spectra for a 4-ML thick quantum well ($W4$) obtained under quasi-resonance excitation by a He-Ne laser at different temperatures. The dashed lines show the features associated with the interface (19 meV) and localized (25 meV) phonons. Shown with dots is the interference laser line.

TABLE III. Activation energies E_1, E_2 and constants A_1 and A_2 characterizing luminescence quenching in CdTe/ZnTe structures.

Structure (Sample)	A_1	E_1, meV	A_2	E_2, meV	A_2/A_1	$\frac{I(5\text{ K})}{I(150\text{ K})}$
0.25 MC (W1)	10	17	2.3×10^3	41	230	145
1.2 MC (W3)	20	10	3.2×10^4	47	1600	1400
1.6 MC (W3)	14	10	1.2×10^4	45	860	420
2 MC (W3)	4	7	3.6×10^3	43	900	140
2 MC (W2)	2	5	3.5×10^3	44	1850	180
3 MC (W4)	11	13	2.2×10^4	58	1950	250
2 MC (W5)	32	24	1.9×10^4	75	600	60
3 MC (W5)	16	25	8×10^4	100	5000	26
4 MC (W4)	7	14	2×10^3	60	280	24

He-Ne laser ($\lambda = 632.8$ nm), whose photon energy is considerably smaller than the band gap in ZnTe and is only 35 meV distant from the maximum of the emission line at $T = 5$ K. The spectra in Fig. 7 suggest several conclusions. First, excitons can be generated fairly efficiently in an ultrathin quantum well by photons having energy in the ZnTe transmission region (the luminescence intensity differs by not more than an order of magnitude from that in the case of barrier excitation). Second, relaxation of the excitons created by a He-Ne laser involves participation of an interface ($\hbar\omega_1 = 19$ meV) and a localized ($\hbar\omega_2 = 25$ meV) phonon, which are due to the presence of a CdTe layer. Note that similar phonons were observed earlier in a study[30] of relaxation kinetics in a 4.3-ML thick CdTe quantum well in ZnTe. The first of the above observations implies the existence of a sufficiently high density of excitonic states which do not contribute to emission at 5 K. Note that this situation is typical of quantum wells with thickness fluctuations. In this case the maximum in the absorption spectrum shifts shortward of the emission maximum.[31] Excitons with higher energies E_{ex} possess a higher mobility in the lateral direction and, hence, are capable of relaxing to states with lower energies by emitting phonons. Excitons generated by a He-Ne laser emit phonons $\hbar\omega_1$ or $\hbar\omega_2$ and, because of this process being fast, cannot emit photons. The subsequent relaxation occurs by a slower process involving emission of acoustic phonons, its probability increasing with temperature. Processes involving absorption of acoustical phonons should be present too, they will increase the population of higher-energy excitonic states, and this is what accounts for the spectral broadening and, accordingly, the increase of $\Gamma(T)$. Finally, the increased probability of the above processes provides explanation for the disappearance from the spectrum with increasing temperature of the features indicated in Fig. 7 by dashed lines. It should be stressed that the population redistribution of excitonic states with different energies is associated with lateral transport.

Table III presents the results illustrating the weakening of integrated photoluminescence intensity, $I(5)/I(150)$, in different structures. These quantities are arranged in the order of decreasing emission photon energy. As the exciton level in the well becomes deeper, the drop in the emission intensity is seen to decrease substantially (by about 60 times). The experimental $I(T)/I(5)$ relations are well fitted in all cases by Eq. (5). In monolayer structures, however, the largest of the activation energies (E_2) does not correlate with the exciton level depth; indeed, E_2 varies from 40 to 100 meV, and ε, from 110 to 460 meV. A similar situation was observed in many quantum-well structures.[28,32,33] The luminescence quenching is usually assigned in these cases to the existence of a nonradiative channel associated with a defect which is located either in the well or near the interface separating the barrier from the well. We have at present no idea of the nature of this defect in our structures.

We note in connection with the data in Table III that the E_1 and E_2 constants and the ratio A_2/A_1 have close values in the $W1$ structure (for all three lines) and in $W2$. This suggests that the nonradiative processes resulting in photoluminescence quenching are similar. A comment concerning the data on the $W5$ structure where the activation energies E_1 and E_2 are maximum appears appropriate here: the emission lines of CdTe layers with an average thickness of 2 and 3 ML lie about 100 meV deeper compared to other CdTe layers with the same $\langle L_z \rangle$. At the same time the inhomogeneous linewidths in this structure are markedly larger. This difference from the other structures is apparently due to the ZnTe surface being misoriented relative to the (001) direction[4] in $W5$. It was pointed out[1] that the fluctuations in geometrical size may be larger in this case. Therefore the anomalous values of the energies E_1 and E_2 in this structure may indicate that the fluctuations in the structure (geometrical and, accordingly, in energy) affect noticeably the temperature dependences.

The authors express gratitude to A. F. Plotnikov for support in this work.

Support of the Russian Fund for Fundamental Research (Grants 96-02-17779 and 97-02-16721), of the Ministry of Science (Project 97-1045), and, partially, of RFRF Grant 96-15-96341 is gratefully acknowledged.

*)E-mail: Zaitsev@sci.lebedev.ru

[1] O. Brandt, L. Tapfer, K. Ploog, R. Bierwolf, M. Hohenstein, F. Philipp, H. Lage, and A. Heberle, Phys. Rev. B **44**, 8043 (1991).
[2] V. S. Bagaev, V. V. Zaĭtsev, V. V. Kalinin, V. D. Kuz'min, S. R. Oktyabr'skiĭ, and A. F. Plotnikov, JETP Lett. **58**, 85 (1993).
[3] V. S. Bagaev, V. V. Zaitsev, V. V. Kalinin, V. D. Kuzmin, S. R. Oktyabrskii, and A. F. Plotnikov, Solid State Commun. **88**, 777 (1993).

[4] V. S. Bagaev, V. V. Zaĭtsev, V. V. Kalinin, V. D. Kuz'min, S. R. Oktyabr'skiĭ, and A. F. Plotnikov, IEE Rev. **58 No. 7**, 97 (1994).
[5] N. Magnea, J. Cryst. Growth **138**, 550 (1994).
[6] U. Neukirch, D. Weckendrup, W. Faschinger, P. Juza, and H. Sitter, J. Cryst. Growth **138**, 849 (1994).
[7] M. Grundmann, J. Christen, N. N. Ledentsov, J. Böhrer, D. Bimberg, S. S. Ruvimov, P. Werner, U. Richter, U. Gösele, J. Heydenreich, V. M. Ustinov, A. Yu. Egorov, A. E. Zhukov, P. S. Kop'ev, and Zh. I. Alferov, Phys. Rev. Lett. **74**, 4043 (1995).
[8] Z. L. Yuan, Z. Y. Xu, B. Z. Zheng, J. Z. Xu, S. S. Li, Weikun Ge, Y. Wang, J. Wang, L. L. Chang, P. D. Wang, C. M. Sotomayor-Torres, and N. N. Ledentsov, Phys. Rev. B **54**, 16919 (1996).
[9] S. Ivanov, A. Toropov, S. Sorokin, T. Shubina, I. Sedova, O. Lyublinskaya, G. Pozina, P. Monemar, and P. Kop'ev, *Abstracts III All-Russian Conf. Physics Semicond.* (Moscow, 1997), p. 345.
[10] V. S. Bagaev, V. V. Zaĭtsev, E. E. Onishchenko, and A. F. Plotmikov, *Abstracts III All-Russian Conf. Physics Semicond.* (Moscow, 1997), p. 155.
[11] H. Mathieu, A. Chatt, J. Allegre, and J. P. Faurie, Phys. Rev. B **41**, 6082 (1990).
[12] Yu. A. Aleshchenko, V. V. Kapaev, Yu. V. Kopaev, and N. N. Mel'nik, Semicond. Sci. Technol. **12**, 1565 (1997).
[13] M. Di Ventra and K. A. Mader, Phys. Rev. B **55**, 13148 (1997).
[14] G. Bastard, *Wave Mechanics Applied to Semiconductor Heterostructures* (Les Éditions de Physique, Les Ulis, 1988).
[15] N. T. Pelekanos, J. Ding, M. Hagerott, A. V. Nurmikko, H. Luo, N. Samarth, and J. K. Furdyna, Phys. Rev. B **45**, 6037 (1992).
[16] Y. X. Liu, Y. Rajakarunanayake, and T. C. McGill, J. Cryst. Growth **117**, 742 (1992).
[17] S. Le Goff and B. Stébé, Phys. Rev. B **47**, 1383 (1993).
[18] J. P. Doran, F. P. Logue, T. Miyajima, R. P. Stanley, J. F. Donegan, and J. Hegarty, Optical Engineering **33**, 3921 (1994).
[19] B. Langen, H. Leiderer, W. Limmer, W. Gebhardt, M. Ruff, and U. Rössler, J. Cryst. Growth **101**, 718 (1990).
[20] S. Weber, W. Limmer, K. Thonke, R. Sauer, K. Panzlaff, G. Bacher, H. P. Meier, and P. Roentgen, Phys. Rev. B **52**, 14739 (1995).
[21] M. Gurioli, J. Martinez-Pastor, M. Colocci, C. Deparis, B. Chastaingt, and J. Massies, Phys. Rev. B **46**, 6922 (1992).
[22] P. Michler, A. Hangleiter, M. Moser, M. Geiger, and F. Scholz, Phys. Rev. B **46**, 7280 (1992).
[23] J. D. Lambkin, L. Considine, S. Walsh, G. M. O'Connor, C. J. McDonagh, and T. J. Glynn, Appl. Phys. Lett. **65**, 73 (1994).
[24] Yi-hong Wu, Kenta Arai, and Takafumi Yao, Phys. Rev. B **53**, 10485 (1996).
[25] E. M. Daly, T. J. Glynn, J. D. Lambkin, L. Considine, and S. Walsh, Phys. Rev. B **52**, 4696 (1995).
[26] G. V. Wertheim, M. A. Butler, K. W. West, and D. N. E. Buchanan, Rev. Sci. Instrum. **45**, 1369 (1974).
[27] Z. Y. Xu, Z. D. Lu, X. P. Yang, Z. L. Yuan, B. Z. Zheng, J. Z. Xu, W. K. Ge, Y. Wang, J. Wang, and L. L. Chang, Phys. Rev. B **54**, 11528 (1996).
[28] D. I. Lubyshev, P. P. González-Borrero, E. Marega, Jr., J. E. Petitprez, N. La Scala, Jr., and P. Basmaji, Appl. Phys. Lett. **68**, 205 (1996).
[29] V. S. Bagaev, V. V. Zaĭtsev, V. V. Kalinin, and E. E. Onishchenko, Fiz. Tverd. Tela (St. Petersburg) **38**, 1728 (1996) [Phys. Solid State **38**, 953 (1996)].
[30] J. H. Collet, H. Kalt, Le Si Dang, J. Cibert, K. Saminadayar, and S. Tatarenko, Phys. Rev. B **43**, 6843 (1991).
[31] U. Jahn, M. Ramsteiner, R. Hey, H. T. Grahn, E. Runge, and R. Zimmerman, Phys. Rev. B **56**, 4387 (1997).
[32] M. Vening, D. J. Dunstan, and K. P. Homewood, Phys. Rev. B **48**, 2412 (1993).
[33] D. R. Storch, R. P. Schneider, Jr., and B. W. Wessels, J. Appl. Phys. **72**, 3041 (1992)

Translated by G. Skrebtsov

Strain-induced photoreflectance spectra in the vicinity of the E_0 transition in GaAs/Si and InP/Si heterostructures

R. V. Kuz'menko, A. V. Ganzha, O. V. Bochurova, and É. P. Domashevskaya

Voronezh State University, 394693 Voronezh, Russia

J. Schreiber and S. Hildebrandt

Fachbereich Physik der Martin-Luther-Universität Halle-Wittenberg, D-06108 Halle/Saale, Deutschland

S. Mo and E. Peiner

Institut für Halbleitertechnik der Technischen Universität Braunschweig, D-38106 Braunschweig, Deutschland

(Submitted September 26, 1998)
Fiz. Tverd. Tela (St. Petersburg) **41**, 725–731 (April 1999)

A study is reported of the structure of photoreflectance (PR) spectra in the vicinity of the E_0 transition from thin ($d=1-5\ \mu$m) n-GaAs and n-InP films ($n=10^{16}-10^{17}\ \mathrm{cm}^{-3}$) grown epitaxially on Si(001) substrates. A quantitative analysis of the spectra involving multicomponent fitting shows that the electronic optical transition from the $\{3/2;\pm 1/2\}$ subband provides a dominant contribution to the intermediate-field electromodulation component in both systems. The splitting observed in the GaAS/Si PR spectra near the main peak are accounted for not by the strain-induced valence-band splitting but rather by a spectral superposition of the intermediate-field component due to the $\{3/2;\pm 1/2\}$ subband with a low-energy excitonic component. The analytically established transition energy $E_0^{3/2;\pm 1/2}$ is used to calculate biaxial strains in epitaxial films. © *1999 American Institute of Physics.*
[S1063-7834(99)03304-3]

Heteroepitaxial growth of III–V semiconductor films on silicon substrates has recently been attracting considerable interest, because it offers a possibility of monolithic integration of optoelectronic elements in Si-based integrated circuits and devices.[1,2] Reducing residual strains in the epilayer to a minimum is a major problem in heteroepitaxial growth technologies.

Strains in GaAs/Si and InP/Si epitaxial layers may arise (a) from a film and substrate lattice mismatch [$a_{\mathrm{Si}}=0.5431$ nm, $a_{\mathrm{GaAs}}=0.5653$ nm, $a_{\mathrm{InP}}=0.5869$ nm (Ref. 3)] and (b) as a result of different thermal expansion coefficients [$\alpha_{\mathrm{Si}}=2.60\times 10^{-6}\ \mathrm{K}^{-1}$, $\alpha_{\mathrm{GaAs}}=5.90\times 10^{-6}\ \mathrm{K}^{-1}$, $\alpha_{\mathrm{InP}}=4.75\times 10^{-6}\ \mathrm{K}^{-1}$ (Ref. 3)]. The stresses in epitaxial layers induced in GaAs/Si and InP/Si systems by lattice mismatch should be compressive. At the growth temperature, however, it can be relieved completely by creating dislocations at the interface.[4,5] When cooling a sample from the growth to room temperature, the difference between the expansion coefficients generates expansion stresses in epitaxial layers.[4] It was reported, however, that the strains determined experimentally at room temperature are substantially smaller than those predicted theoretically.[4,6] It was conjectured[4,6] that tensile strains in films are also relieved above a certain critical temperature T_c through generation of dislocations, and that only at T_c does this process become inoperative.

The problem of high-precision determination of strains in thin epitaxial films within a broad temperature range still cannot be regarded as solved. One of the methods used to study strains in semiconductors, with the highest accuracy a broad temperature range, is optical modulation photoreflectance spectroscopy, based on measuring the strain-induced change in the energy of electronic optical transitions.[7] It offers also such advantages as a high spectral resolution (~ 1 meV) within a broad temperature interval, a possibility of studying thin layers with thicknesses $d\geqslant 100$ nm, a high surface resolution ($\sim 20\times 20\ \mu$m), and a possibility of depth scanning. Despite all these merits, only a few publications report using of PR spectroscopy to determine residual strains in III-V/Si heterostructures.[8–12]

This work reports room-temperature photoreflectance measurements made on InP/Si and GaAs/Si samples with epilayer thicknesses varying from 1 to 5 μm. The experimental spectra are analyzed in terms of a model taking into account the change in the energy of electronic optical transitions from the $\{3/2;\pm 1/2\}$ and $\{3/2;\pm 3/2\}$ valence subbands, as well as the presence of low-energy spectral features.[12] The results obtained show the spectral contribution due to the $\{3/2;\pm 1/2\}$ subband to be dominant, while the weaker $\{3/2;\pm 3/2\}$ component provides only an insignificant contribution to the resultant E_0 PR spectrum. Thus in order to determine residual stresses from measured PR spectra one should use the $E_0-E_0^{3/2;\pm 1/2}$ energy shift relative to the E_0 transition energy in the bulk material. The stresses $\sigma_{\parallel}$ thus obtained are compared with the available data[4,6,9,12,13] on GaAs/Si and InP/Si.

1. EXPERIMENTAL SETUP AND SAMPLES

Measurements of PR spectra were carried out in the 1.35–1.65-eV energy region using a He-Ne laser ($\lambda = 632.8$ nm) in air in an experimental arrangement which is similar in design and principle of operation to the instruments described in the literature.[14] The light-probed area on the sample was varied from $100\times100\,\mu$m to $1000\times1000\,\mu$m. Increasing the spot area did not change the shape of the spectrum, which indicates a high uniformity of the samples. The modulation frequency was varied from 100 to 1000 Hz. The laser excitation density was ~1 W/cm^2, which provided a surface electric-field modulation level $\xi > 0.2$.[15] Additional possibilities for analyzing spectral line shape were provided by a two-channel phase-sensitive amplifier with a preset phase, which permitted one to change both the PR spectral component phase-locked to the reference signal (the so-called fast PR response) and the component shifted by 90° with respect to the reference signal (the so-called slow PR response).[16]

The studies were performed on GaAs/Si and InP/Si samples grown by metalorganic vapor-phase epitaxy.[2,5] The samples consisted of a thick Si(001) substrate, a thin III–V buffer layer (20 nm thick for GaAs and 80 nm for InP), and a thick (1–5 μm), GaAs or InP, main epitaxial layer. The buffer layers were grown for 20 min at a substrate temperature of 400 °C, and the main layers, for 120 min at a substrate temperature of 700 °C for GaAs and 640 °C for InP. The material used to grow the films was nominally undoped, but diffusion of Si atoms from the substrate results in film doping at a level $n = 10^{16}$–10^{17} cm^{-3}.[17]

PR measurements were also carried out on n-GaAs/n^+-GaAs and n-InP/n^+-InP reference homoepitaxial samples with carrier concentrations $n = 10^{16}$–10^{17} cm^{-3}, $n^+ \approx 10^{18}$ cm^{-3}, and epilayer thicknesses $d = 2$–$5\,\mu$m.

2. THEORETICAL BASIS FOR E_0 PR SPECTRUM SIMULATION

The main modulation mechanism responsible for the PR signal is the periodic variation of the surface electric field, which originates from nonequilibrium carriers generated by periodic illumination of the semiconductor surface by laser photons having an energy exceeding the gap width. Electric field modulation produces electromodulation spectral components in the region of direct transitions through the Franz-Keldysh effect. These components can be observed experimentally only in the region of direct electronic optical transitions.

Because the valence band of the GaAs and InP semiconductors is degenerate at the $\Gamma(0,0,0)$ point, their electromodulation spectrum at the E_0 transition is a superposition of two spectral components with identical transition energies

$$\frac{\Delta R}{R} = a_{\{3/2;\pm3/2\}} \times \left(\frac{\Delta R}{R}\right)^{\{3/2;\pm3/2\}}_{E_0^{\{3/2;\pm3/2\}}} + a_{\{3/2;\pm1/2\}} \times \left(\frac{\Delta R}{R}\right)^{\{3/2;\pm1/2\}}_{E_0^{\{3/2;\pm1/2\}}}, \quad (1)$$

where $E_0 = E_0^{\{3/2;\pm3/2\}} = E_0^{\{3/2;\pm1/2\}}$ is the subband transition energy, and the coefficients $a_{\{3/2;\pm3/2\}}$ and $a_{\{3/2;\pm1/2\}}$ are amplitude factors or coefficients of the corresponding components. The amplitude factors depend on the transition matrix element and carrier effective mass in the subbands.[18]

The electromodulation components can have an intermediate- or a low-field line shape. The intermediate-field electromodulation structure near the E_0 transition exhibits a main peak lying in the electronic transition region and high-energy damping Franz-Keldysh oscillations, whose period depends on the surface electric field and is uniquely determined by the electro-optic energy and the level of surface electric field modulation.[19] In the low-field case, the line shape is interpreted as the third derivative of unmodulated reflectance spectrum and represents the so-called resonance structure with two extrema of opposite sign.[20] What spectrum, intermediate or low field, will be observed, is determined by the ratio of electro-optic energy

$$\hbar\Omega = \left(\frac{e^2F^2\hbar^2}{8\mu_\parallel}\right)^{1/3}, \quad (2)$$

where e is the electronic charge, F is the surface electric field, $\hbar$ is the Planck constant, and $\mu_\parallel$ is the reduced effective electron-hole mass along the direction of the electric field, to a phenomenological parameter (or broadening energy) Γ, which is due to the finite carrier lifetime and may also serve as a criterion of structural quality of a sample. From the phenomenological standpoint, for medium doping levels of the n-GaAs and n-InP substrates ($n \approx 10^{16}$ cm^{-3}) the electro-optic energy is, as a rule, larger than the broadening energy, which for such samples is of the order of 5–10 meV, and in these conditions intermediate-field components become observable.[15,19]

The electromodulation intermediate-field component can be considered within a generalized multilayer laminar model[12,21,22] (MLM), which describes the formation of electromodulation signal in terms of the Franz-Keldysh effect with inclusion of electric-field inhomogeneities in the space charge region. The simulation parameters are the electronic optical transition energy E_t, the surface electric field F, the depth of the space charge region d_F, the broadening energy Γ, and the surface electric-field modulation ξ ($0<\xi<1$). When simulating the electromodulation spectrum of a semiconductor in the region of degenerate transitions, each of the spectral components is treated within the MLM model, after which the resultant spectral line shape is constructed in accordance with Eq. (1) with due account of the amplitude factors. In the case of bulk GaAs and InP samples, the amplitude factors for the $\{3/2;\pm3/2\}$ subband exceed the corresponding values for the $\{3/2;\pm1/2\}$ subband (experiment[21,23,24] gives $a_{\{3/2;\pm3/2\}}/a_{\{3/2;\pm1/2\}} \approx 2$ for GaAs and $a_{\{3/2;\pm3/2\}}/a_{\{3/2;\pm1/2\}} \approx 3$ for InP). One should not also over-

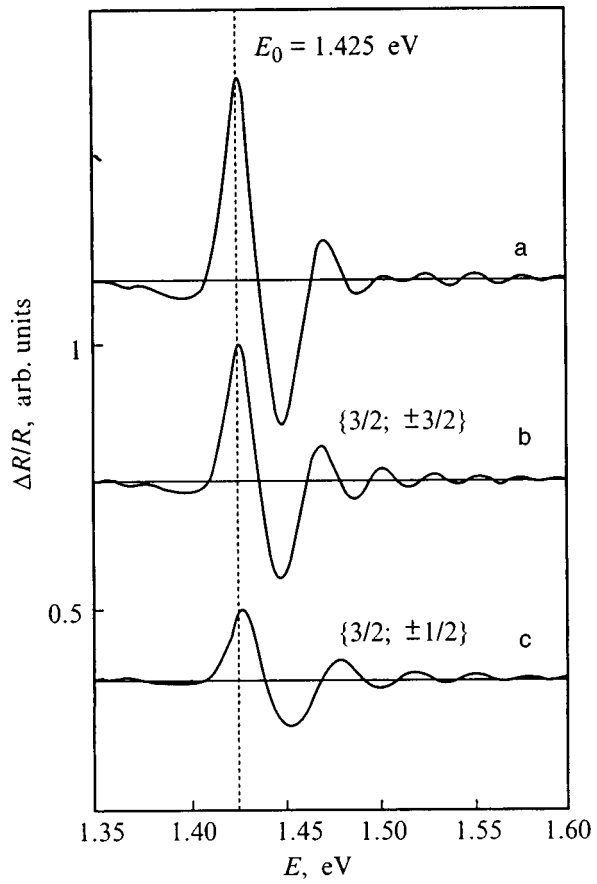

FIG. 1. (a) Model intermediate-field PR spectrum for GaAs and (b,c) subband components. The parameters used in the MLM calculations: $E_0=1.425$ eV, $F=3\times10^6$ V/m, $d_F=300$ nm, $\Gamma=7$ meV, $\xi=1$, $a_{\{3/2;\pm3/2\}}/a_{\{3/2;\pm1/2\}}=2$.

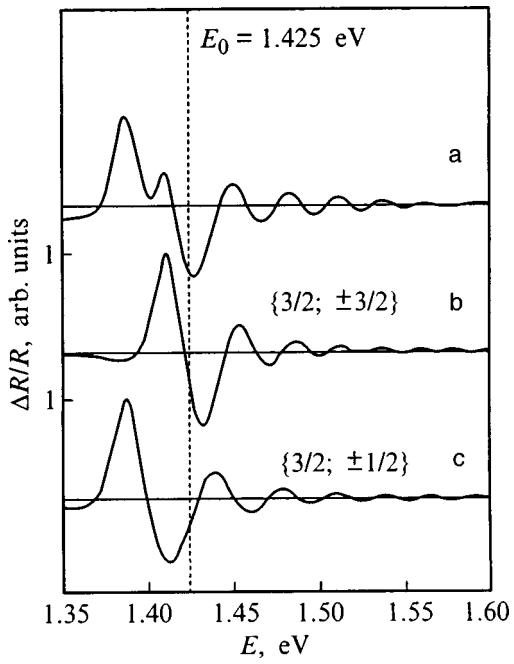

FIG. 2. (a) Model intermediate-field PR spectrum for biaxially stressed GaAs and (b,c) subband components. The parameters used in the calculations: $\sigma_\parallel=3.9\times10^8$ Pa, $E_0^{\{3/2;\pm3/2\}}=1.409$ eV, $E_0^{\{3/2;\pm1/2\}}=1.385$ eV, $F=3\times10^6$ V/m, $d_F=300$ nm, $\Gamma=7$ meV, $\xi=1$, $a_{\{3/2;\pm3/2\}}/a_{\{3/2;\pm1/2\}}=1$. The splitting structure near the main peak indicates valence-band splitting at the Γ point.

look the fact that, because of the difference between the reduced effective hole masses in the subbands, $\mu^{e-h\{3/2;\pm3/2\}}$ and $\mu^{e-h\{3/2;\pm1/2\}}$ and, hence, the electro-optic energies for the subbands differ somewhat, which, in its turn, gives rise to a difference between the Franz-Keldysh oscillation periods for intermediate-field subband components. Figure 1 presents a model spectrum for GaAs calculated using the MLM model.

Biaxial strain in the [100] and [010] directions lowers the zincblende structure symmetry to tetragonal.[25,26] Lattice strain lifts valence-band degeneracy at the $\Gamma(0,0,0)$ point. The energies of the electronic optical transitions can be calculated from the following expressions

$$E_0^{\{3/2;\pm3/2\}}=E_0+\left[\frac{2a}{C_{11}+2C_{12}}-\frac{b}{C_{11}-C_{12}}\right]\sigma_\parallel, \tag{3}$$

$$E_0^{\{3/2;\pm1/2\}}=E_0+\left[\frac{2a}{C_{11}+2C_{12}}+\frac{b}{C_{11}-C_{12}}\right]\sigma_\parallel, \tag{4}$$

where $\sigma_\parallel>0$ for tensile stress and $\sigma_\parallel<0$ for compressive stress, a is the hydrostatic deformation potential, b is the shear deformation potential, and C_{11} and C_{12} are the elastic constants. Tensile stress shifts both transitions toward lower energies with respect to the E_0 transition in unstressed material. The energy shift of the transition from the $\{3/2;\pm1/2\}$ subband is stronger than that from the $\{3/2;\pm3/2\}$ subband. We chose for the calculations the following values of the parameters: $C_{11}=1.18\times10^{11}$ Pa (GaAs), $C_{11}=1.02\times10^{11}$ Pa (InP), $C_{12}=0.54\times10^{11}$ Pa (GaAs), $C_{12}=0.58\times10^{11}$ Pa (InP), $a=-9.8$ eV (GaAs), $a=-8.0$ eV (InP), $b=-2.0$ eV (GaAs), $b=-1.55$ eV (InP), $E_0=1.425$ eV (GaAs), $E_0=1.343$ eV (InP).[3,27]

Strain should also affect the electromodulation spectrum of GaAs and InP in changing the relative magnitude of amplitude factors due to the variation of effective masses in the subbands.[7,25]

The difference between the transition energies $E_0^{\{3/2;\pm3/2\}}$ and $E_0^{\{3/2;\pm1/2\}}$ results in an energy shift of the electromodulation components from the valence subbands with respect to one another. If the amplitude factors of the components are comparable, and the energy splitting is small (~10 meV), one can expect the appearance near the main peak in the electromodulation spectrum of peak structures, or so-called splitting features, which indicate the existence of closely lying electronic transitions (Fig. 2). In these conditions the peak positions can be interpreted, in a first approximation, as energy positions of the corresponding transitions.[8,12]

Although the above model is sufficient for description of electromodulation spectra, experimental E_0 photoreflectance spectra obtained at room temperature on the GaAs and InP semiconductor compounds contain, as a rule, not only the electromodulation E_0 component but also a superimposed low-energy component, which is assigned to excitonic transitions and can be well fitted by the Aspnes relation with the parameter $n=2$.[15,16,19,23] The need of incorporating the low-energy PR components into the model is supported by both the results of our analysis the spectral structures in the case

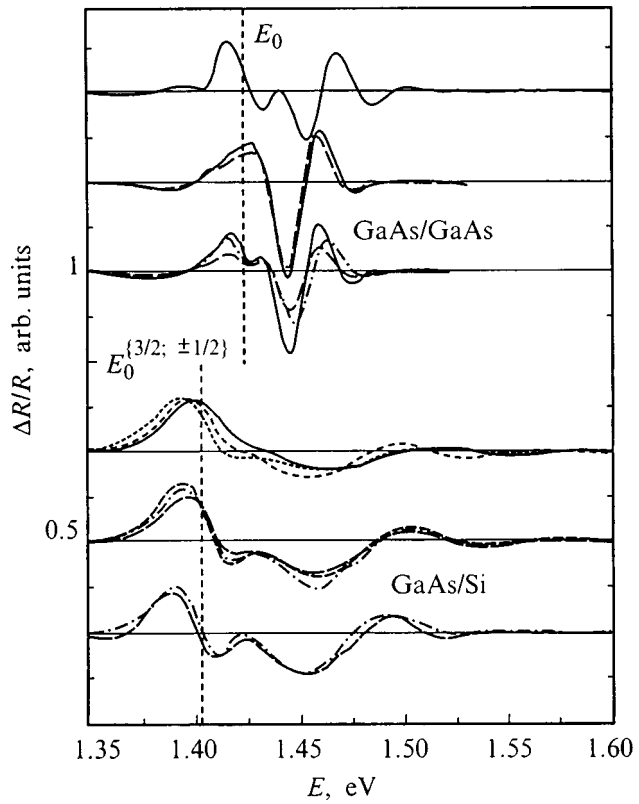

FIG. 3. Comparison of typical experimental E_0 PR spectra obtained from GaAs/GaAs homoepitaxial samples (above) and GaAs/Si heteroepitaxial samples (below). The spectra from the two structures are clearly seen to have common features.

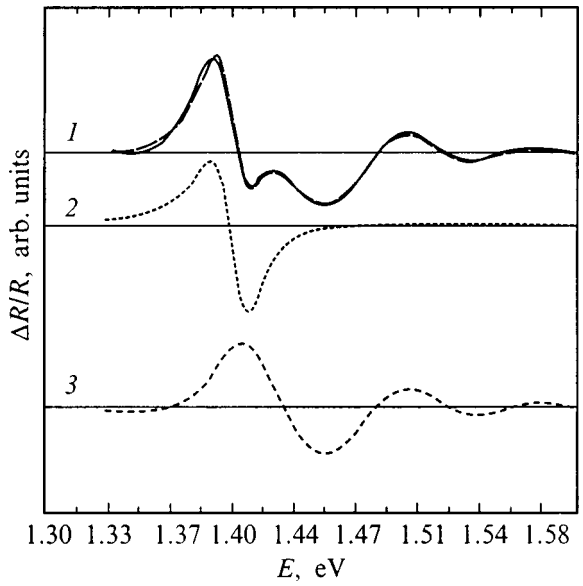

FIG. 4. Fitting of a typical PR spectrum from GaAs/Si. *1*—experimental PR spectrum (solid line) and its fitting (dashed line). *2,3*—spectral components isolated in the analysis. *2*—excitonic component: $E_{\text{exc}}=1.403$ eV, $\Gamma=18$ meV. *3*—intermediate-field component: $E_0^{\{3/2;\pm 1/2\}}=1.406$ eV, $F=9.25\times 10^6$ V/m, $\Gamma=14$ meV.

of GaAs and InP,[15,19] and similar spectral studies by other authors.[14,22–24,28]

Thus a realistic physico-mathematical model applicable to analysis of experimental PR spectra from the GaAs and InP semiconductors should contain a mathematical formalism for simulating the electromodulation and excitonic components.[15,16,23] Simulation of spectra from strained epitaxial GaAs and InP layers should include two electromodulation E_0 components and two excitonic components with different transition energies, $E_0^{\{3/2;\pm 3/2\}}\neq E_0^{\{3/2;\pm 1/2\}}$, $E_{\text{exc}}^{\{3/2;\pm 3/2\}}\neq E_{\text{exc}}^{\{3/2;\pm 1/2\}}$, and different amplitude factors, which correspond to optical transitions from the two subbands.

3. PHOTOREFLECTANCE MEASUREMENTS: RESULTS AND DISCUSSION

Figure 3 displays E_0 PR spectra obtained from GaAs/GaAs homoepitaxial and GaAs/Si heteroepitaxial samples.

PR spectra obtained from homoepitaxial samples in the region of the main peak exhibit different line shapes produced by superposition of a low- and an intermediate-field component. In all spectra, however, the main peak occupies about the same position near the transition energy for bulk unstrained material, $E_0=1.425$ eV (Ref. 3) (see Refs. 15, 16, 23 for a detailed analysis of spectral line shapes in GaAs).

Intermediate-field PR spectra can be measured also on heterostructural samples (see Fig. 3). These spectra are shifted relative to those obtained on homoepitaxial samples toward lower energies, which indicates a decrease in the transition energies for all their spectral components. The low-energy shift of the spectra implies the existence of a residual tensile stress in the films. An estimate of the carrier concentration in the layer based on the Franz-Keldysh oscillation period and made under the assumption that the Fermi level on GaAs surface lies near midgap yields $n\approx 5\times 10^{16}\,\text{cm}^{-3}$. At the high-energy shoulder of the main spectral peak one observes features in the form of peak structures or inflections. Such PR spectra were attributed[8] to a superposition of two intermediate-field components from the $\{3/2;\pm 1/2\}$ and $\{3/2;\pm 3/2\}$ subbands, with the main peak itself assigned to the transition from the $\{3/2;\pm 1/2\}$ subband, and the shoulder peaks, to that from the $\{3/2;\pm 3/2\}$ subband (the so-called splitting structure). We are going to show, however, that this interpretation should be reconsidered, because a purely formal comparison of the spectral structures obtained on homo- and heteroepitaxial samples shows that the ''shoulder'' structures are observed also in PR spectra from homoepitaxial GaAs films (Fig. 3).

To reveal the strain-induced nature of these structures, the experimental PR spectra were treated within the above multicomponent model. The fitting was done with two intermediate-field and two excitonic components with variable transition energies and amplitude factors. The results of the fitting (see Fig. 4 and Table I) show that experimental spectra can be approximated by one excitonic and one intermediate-field component, and that their superposition provides an excellent fit to experimental line shape throughout the spectral region covered. Thus our analysis explains the appearance of a high-energy shoulder or of splitting structures in experimental spectra as due to superposition not of two intermediate-field components as this was assumed in Ref. 8 but rather of one intermediate-field and one excitonic

TABLE I. Parameters of intermediate-field PR spectra and calculated residual stresses.

	Intermediate-field electromodulation component				Excitonic component	
Sample	$E_0^{\text{unstr.}}$ or $E_0^{\{3/2;\pm 1/2\}}$, eV	Broadening energy Γ, meV	Shift $E_0-E_0^{\{3/2;\pm 1/2\}}$, meV	Residual stress $\sigma_\parallel$, 10^8 Pa	Transition energy E_{exc}, eV	Γ, meV
GaAs/GaAs	1.425 ± 0.002	0.1	-	-	1.420 ± 0.002	11.4 ± 1.1
GaAs/Si	1.403 ± 0.003	16.9 ± 7.8	22 ± 2	1.88 ± 0.16	1.400 ± 0.003	17.7 ± 2.5
InP/InP	1.343 ± 0.002	2.5	-	-	-	-
InP/Si	1.335 ± 0.003	8.2 ± 2.3	8 ± 3	0.74 ± 0.27	-	-

component. In accordance with the positions of these spectral components and the results obtained in earlier works,[8,12] they should be assigned to transitions from the $\{3/2;\pm 1/2\}$ subband, although the absence of noticeable spectral contributions of the $\{3/2;\pm 3/2\}$ subband in the spectrum appears somewhat strange, because, while the model predicts a decrease of the amplitude factor for the $\{3/2;\pm 3/2\}$ subband, it should remain comparable in order of magnitude to that for the $\{3/2;\pm 1/2\}$ subband.[7,25]

As already mentioned, our present interpretation of strain-induced PR spectra from the GaAs/Si system is at variance with the assumption[8] that the spectrum is formed by superposition of two intermediate-field electromodulation components. None of our attempts to obtain a good fit using two intermediate-field components has, however, met with success. Moreover, a formal identification of the energy position of the ''shoulder'' peak with the $E_0^{\{3/2;\pm 3/2\}}$ transition energy yields overestimated residual strains, exactly what was obtained in Ref. 8.

Based on the above quantitative analysis of experimental spectra, one can maintain that the residual stresses in epitaxial layers can be derived only from the established change in the E_0 transition energy for the $\{3/2;\pm 1/2\}$ subband, namely, $E_0-E_0^{\{3/2;\pm 1/2\}}$. For the average E_0 transition energy in bulk GaAs we used $E_0=1.425$ eV.[3] As follows from our quantitative analysis of spectra from GaAs/Si heteroepitaxial samples, the values of the E_0 transition energy obtained on the samples studied crowd, irrespective of the GaAs layer thickness, around $E_0^{\{3/2;\pm 1/2\}}=1.403$ eV. Using the difference between the above-mentioned values to calculate the stresses by means of Eq. (4) yields $\sigma_\parallel=(1.88\pm 0.16)\times 10^8$ Pa. This value is in a good agreement with the residual stresses derived[4,6,13] by other means.

PR intermediate-field spectra were also measured on our InP/Si heterostructures. A typical experimental spectrum is presented in Fig. 5. The main spectral peak is seen to lie near 1.335 eV and not to exhibit any features. Because the $E_0+\Delta_0$ transition in InP is close in energy to the E_0 transition, it becomes superposed in the high-energy part of the E_0 spectrum on the $E_0+\Delta_0$ PR spectrum. A comparison of E_0 spectra from InP/Si with PR spectra obtained on homoepitaxial InP/InP samples also shows them to have common features, although the former are shifted to lower energies.

The experimental PR spectra from InP/Si samples were analyzed by the procedure applied to GaAs/Si spectra. Figure 5 illustrates a typical result of such an analysis. We readily see that an E_0 spectrum can be fitted satisfactorily using only one intermediate-field component, which, in accordance with the calculated position of the transition and with our previous results,[12] should be assigned to a transition from the $\{3/2;\pm 1/2\}$ subband. No trace of a low-energy excitonic component was found in the spectrum.

The fit yielded the transition energies $E_0^{\{3/2;\pm 1/2\}}$, which can be used to estimate the residual stresses in InP layers (Table I). A quantitative analysis shows that, similar to the GaAs/Si samples, the $E_0^{\{3/2;\pm 1/2\}}$ transition energies concentrate around the value $E_0^{\{3/2;\pm 1/2\}}=1.335$ eV, irrespective of the thickness of the epitaxial layer. The reference transition energy $E_0=1.343$ eV for an unstrained homoepitaxial InP/InP sample was derived from a quantitative analysis of the spectra and is in agreement with available[24] data.

The residual tensile stress in the layer, $\sigma_\parallel=(0.74\pm 0.27)\times 10^8$ Pa, was extracted from the difference $E_0-E_0^{\{3/2;\pm 1/2\}}$. This value accords with the relatively low residual layer stresses expected[4,12] for InP/Si.

The shift in transition energy $E_0+\Delta_0$ was used also in Ref. 12 to estimate the residual stresses in the InP layer. The values obtained are of the same order of magnitude.

Thus we have studied the structure of strain-induced E_0 PR spectra from the GaAs/Si and InP/Si semiconductor systems. The spectra were analyzed within a theoretico-mathematical model taking into account their multicomponent nature.

While the results of the analysis of the spectral structures observed in the GaAs/Si system support the expected response of the spectrum consisting of its low-energy shift, the interpretation of the splitting structures near the main peak,

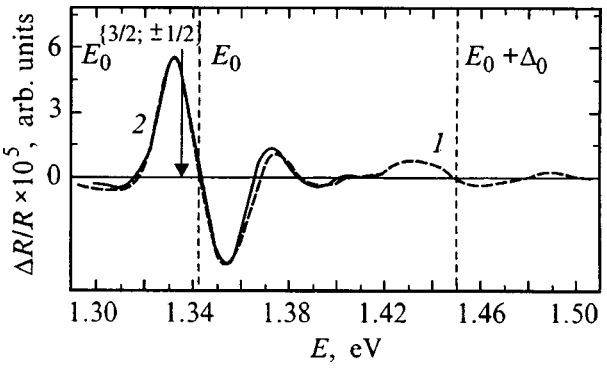

FIG. 5. Fitting of a typical PR spectrum from InP/Si. *1*—experimental PR spectrum, *2*—intermediate-field component isolated in the analysis: $E_0^{\{3/2;\pm 1/2\}}=1.335$ eV, $F=2.9\times 10^6$ V/m, $\Gamma=8$ meV.

which was used in Ref. 8 and was expected from model calculations, as a superposition of two intermediate-field electromodulation components from valence subbands, was not confirmed by our analysis. Despite the relatively large residual strain in the GaAs epitaxial layer and, as a consequence, the substantial splitting at the Γ point, the spectral contribution from the $\{3/2;\pm 3/2\}$ subband was not observed in the spectra because of a strong decrease of the amplitude factor, and the high-energy shoulder peak can be accounted for by superposition of an intermediate-field electromodulation component from the $\{3/2;\pm 1/2\}$ subband on the low-energy excitonic component from the same subband. Thus biaxial tensile stress makes the $\{3/2;\pm 1/2\}$ components dominant in the GaAs E_0 PR spectra, and the stress itself can be derived from the strain-induced shift $E_0-E_0^{\{3/2;\pm 1/2\}}$.

A similar procedure was employed to analyze InP/Si E_0 PR spectra. The electromodulation intermediate-field component from the $\{3/2;\pm 1/2\}$ subband was found to be dominant here too. No noticeable low-energy excitonic component was revealed in the spectra. To derive residual stresses from PR spectra, one should use the strain-induced energy shift of the transition from the $\{3/2;\pm 1/2\}$ subband.

To conclude, the multicomponent theoreticomathematical spectral fitting developed[15,16,19] to study experimental spectral structures has been demonstrated to be a reliable procedure for analysis of spectra not only from unstrained materials but in a more complex case as well, namely, from biaxially strained GaAs and InP epitaxial layers.

[1] D. J. Olego, M. Tamura, Y. Okuno, T. Kawano, and A. Hashimoto, J. Appl. Phys. **71**, 4329 (1992).
[2] A. Lubnow, G.-P. Tang, H.-H. Wehmann, E. Peiner, and A. Schlachetzki, Jpn. J. Appl. Phys., Part 1 **33**, 3628 (1994)
[3] *Numerical Data and Functional Relationships in Science and Technology*, edited by K.-H. Hellwege and O. Madelung (Landolt-Börnstein, Springer, Berlin–Heidelberg, 1984).
[4] M. Sugo, N. Uchida, A. Yamamoto, T. Nishioka, and M. Yamaguchi, J. Appl. Phys. **65**, 591 (1992).
[5] H.-H. Wehmann, G.-P. Tang, and A. Schlachetzki, Solid State Phenom. **32-33**, 445 (1993).
[6] L. Landa, R. Carles, C. Fontaine, E. Bedel, and A. Muñoz-Yagüe, J. Appl. Phys. **66**, 196 (1989).
[7] F. H. Pollak, in *Proc. MRS 1995 Fall Meeting*.
[8] T. Kanata, H. Suzawa, M. Matsunaga, H. Takakura, Y. Hamakawa, H. Kato, and T. Nishino, Phys. Rev. B **41**, 2936 (1990).
[9] N. Bottka, D. K. Gaskill, R. J. M. Griffiths, R. R. Bradley, T. B. Joyce, C. Ito, and D. McIntyre, J. Cryst. Growth **93**, 481 (1988).
[10] A. Dimoulas, P. Tzanetakis, A. Georgakilas, O. J. Glembocki, and A. Christou, J. Appl. Phys. **67**, 4389 (1990).
[11] M. Dutta, H. Shen, S. M. Vernon, and T. M. Dixon, Appl. Phys. Lett. **57**, 1775 (1990).
[12] S. Mo, E. Peiner, A. Bartels, G.-P. Tang, A. Schlachetzki, R. Kusmenko, S. Hildebrandt, and J. Schreiber, Jpn. J. Appl. Phys., Part 1 **35**, 4238 (1996).
[13] Y. Chen, A. Freundlich, H. Kamada, and G. Neu, J. Appl. Phys. **54**, 45 (1983).
[14] N. Bottka, D. K. Gaskill, R. S. Sillmon, R. Henry, and R. Glosser, J. Electron. Mater. **17**, 161 (1988).
[15] R. Kuz'menko, A. Ganzha, J. Schreiber, and S. Hildebrandt, Fiz. Tverd. Tela (St. Petersburg) **39**, 2123 (1997) [Phys. Solid State **39**, 1900 (1997)].
[16] S. Hildebrandt, M. Murtagh, R. Kuzmenko, W. Kircher, and J. Schreiber, Phys. Status Solidi A **152**, 147 (1995).
[17] A. Bartels, E. Peiner, R. Klockenbrink, and A. Schlachetzki, J. Appl. Phys. **78**, 224 (1995).
[18] H. Shen and M. Dutta, J. Appl. Phys. **78**, 2151 (1995).
[19] R. Kusmenko, Thesis (Martin-Luther-Universität, Halle-Wittenberg, Germany, 1993).
[20] D. E. Aspnes, Surf. Sci. **37**, 418 (1973).
[21] R. A. Batchelor, A. C. Brown, and A. Hamnett, Phys. Rev. B **41**, 1401 (1990).
[22] P. L. Jackson and E. G. Seebauer, J. Appl. Phys. **69**, 943 (1991).
[23] J. P. Estrera, W. M. Duncan, and R. Glosser, Phys. Rev. B **49**, 7281 (1994).
[24] R. N. Bhattacharya, H. Shen, P. Parayanthal, F. H. Pollak, T. Coutts, and H. Aharoni, Phys. Rev. B **37**, 4044 (1988).
[25] G. L. Bir and G. E. Pikus, *Symmetry and Strain-Induced Effects in Semiconductors* (Wiley, New York, 1974; Nauka, Moscow, 1972).
[26] C. P. Kuo, S. K. Wong, R. M. Cohen, and G. B. Stringfellow, J. Appl. Phys. **57**, 5428 (1985).
[27] H. Asai and K. Oe, J. Appl. Phys. **54**, 2052 (1983).
[28] H. Shen, F. H. Pollak, and J. M. Woodall, J. Vac. Sci. Technol. B **8**, 413 (1990).

Translated by G. Skrebtsov

Field-emission characteristics of layered systems in high electric fields

T. A. Tumareva

St. Petersburg State Technical University, 195251 St. Petersburg, Russia
(Submitted April 24, 1998)
Fiz. Tverd. Tela (St. Petersburg) **41**, 732–735 (April 1999)

A study has been made of the field-emission characteristics of cerium and BaO films on W within a broad range of field-emission currents and fields. An anomalous broadening of the spectra and a deviation of Fowler-Nordheim characteristics from linearity have been revealed for high (above 10^9 A/m^2) field-emission current densities. The dependence of this anomalous behavior of field-emission characteristics on the work function and topography of the surface has been investigated. Possible reasons for the observed phenomena are discussed.
 [S1063-7834(99)03404-8]

The sharpness, high brightness, and small width of the emitted electron-energy spectra make field-emission cathodes superior to other types of electron sources designed for use in high-resolution electron microprobe analyzers. The spatial resolution of instruments of this type is limited by the minimum size of the visible source, which, in its turn, is determined by the spread in electron velocities. To attain the highest-possible brightness, the field-emission cathode is operated usually at close to limiting current densities j and, accordingly, at high electric fields F. Drawing large cathode currents broadens the field-emission spectra compared to those expected by the Young model.[1] At the same time only a few studies deal with the broadening of the energy spectra of electrons emitted in high electric fields,[2–4] and the observed phenomenon is still awaiting interpretation.

The present work reports a study of field-electron energy spectra and of the Fowler-Nordheim (F–N) characteristics made within a broad range of anode potentials on emitters which are radically different from those investigated earlier. The objects chosen for the study were W–Ce and W–BaO emitting systems. By properly controlling the process of adsorption, one could obtain emitters having different work functions and differing topographies (smooth or made up of three-dimensional adsorbate agglomerates), thus permitting investigation of spectral dynamics for three-dimensional projections and objects with substantially different work functions.

1. EXPERIMENTAL METHOD

The study was performed in a high-vacuum field-emission projector with a high-resolution ($\sim$30 meV) energy analyzer.[5] The temperature of the tip could be varied within a broad range. It could be heated by passing current through the arm to which it was attached, or cooled by introducing liquid nitrogen into the holder on which the cathode assembly was mounted. Thermocouple measurements showed that the tip in this instrument could be cooled down to 120 K. The technique used to obtain BaO coatings of differing structures is described in detail elsewhere.[6] Films of cerium were prepared by depositing it on the tip maintained at temperatures $\geqslant$750 K. These conditions were shown[7] to favor obtaining smooth (uniform in thickness) films. The thickness of a layer was assumed to be proportional to its deposition time. The amount of the adsorbate at which the W–Ce work function was minimum was identified with monolayer coverage. In this work both submonolayer and multilayer films were investigated. The work function φ of the smooth Ce films on W was determined by two methods, namely, from the change in the slope of the F-N characteristic during deposition and by a combined analysis of the slopes of the F-N characteristic and of the low-energy tail in the field-emission electron spectrum, an approach described in detail in Ref. 7. The values of φ and of the field geometry factor β for a submonolayer and a multilayer Ce film on W(111) are listed in Table I. The formation conditions of three-dimensional Ce agglomerates are specified in Ref. 7.

The current density j was derived from the ratio of the current through the probe aperture in the analyzer to the effective area A of the probed surface. The value of A determined from experimental $I-V$ curves and the F-N equation for the corresponding local values of φ and F remained practically constant during adsorption (see Table I).

2. EXPERIMENTAL RESULTS

Figures 1 and 2 display the $I-V$ characteristics and energy spectra of the electrons field emitted from the film system under study. Measurements showed that the $I-V$ curves and the general pattern of the electron spectra (their shape and energy position) are satisfactorily described within a broad range of field-emission currents by Young's equation for metals, by which the energy distribution of field-emitted electrons can be written[1]

$$j_0'(\varepsilon) \propto [1+\exp(\varepsilon/kT)]^{-1} \exp(S_{\mathrm{TED}}\varepsilon), \tag{1}$$

where S_{TED} is the slope of the low-energy tail of the spectrum drawn in the $\ln j_0 vs \varepsilon = E - E_F$ coordinates, E is the total electron energy, E_F is the Fermi energy, and T is the temperature of the emitting surface. For densities $j > 10^9$ A/m^2, however, one observed an anomalous (compared to predictions by Young's theory) broadening of the spectra, which

TABLE I. Probed emitter area A, work function, and field geometric factor β for various emitting systems.

Object of microprobe study	A, Å	φ, eV	$\beta\cdot 10^{-6}$ m^{-1}
(111)W	4400	4.45	0.34
(111)W+Ce, 0.2 ML	4100	3.30	0.34
(111)W+Ce, 6.0 ML	4700	2.6	0.34

involved primarily the steepest high-energy slopes in the spectra. This effect is particularly well seen when comparing the high-energy slopes of curves *3* and *4* to those of curves *1* and *2* (Figs. 2 and 3) obtained at low current densities.

If one presents the experimental results on a semilog scale (Fig. 3), the high-energy portions (curves *3* and *4* in Fig. 4) can be fitted near E_F, in the first approximation, to an exponential, and their slope characterized by a quantity S_T. Applying now Young's relation, one can readily show that the electron gas temperature at the time of emission can be expressed through the slopes of the high-energy (S_T) and low-energy (S_{TED}) portions of the spectra as follows

$$kT(\mathrm{eV})=(|S_T|+S_{\mathrm{TED}})^{-1}.$$

The temperature T can be estimated in this way only provided Young's relation is valid; it was derived, however, under the assumptions which are mathematically justified solely within the temperature interval where the dimensionless form factor $p=kTS_{\mathrm{TED}}\leqslant 0.7$.[8,9]

Attempts at estimating the tip surface temperature from experimental spectra using the above analysis of Young's relation yield effective temperatures T_{eff} which exceed the initial temperature (before the onset of emission) by hundreds of K. For example, for curve *4* in Fig. 1 corresponding to a current density of 6×10^9 A/m^2 one finds $T_{\mathrm{eff}}=900$ K.

Figure 5 presents the values of j and F corresponding to an increase of FWHM, Γ, of the field-electron energy spectrum by about 25% compared to the one expected from Young's model for various values of φ. We readily see that, as the work function decreases, the anomalous broadening of spectra becomes manifest at progressively lower j. The change in spectral shape in high electric fields is accompanied by a deviation of the $I-V$ characteristics from linearity (curves *2–4* in Fig. 1). The onset of a noticeable ($\sim$20%) $I-V$ deviation from linearity also turned out to be dependent on the emitter work function (Fig. 5).

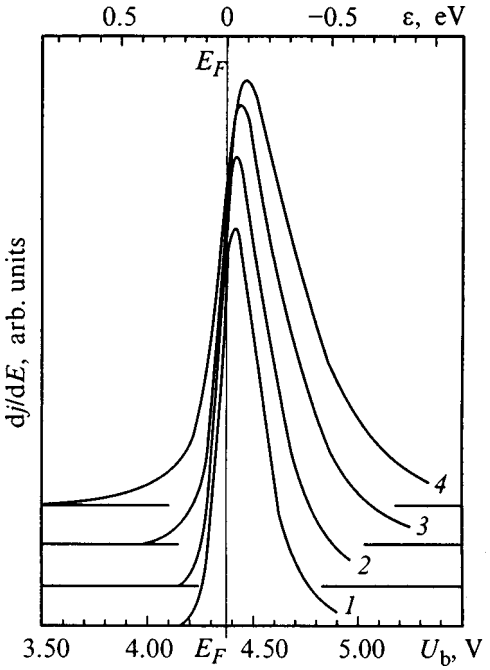

FIG. 2. Energy spectra of field-emitted electrons from a W(111)+Ce (0.2 ML) system. The curves are shifted above each other to make the plots more revealing. The spectra were obtained at $T=300$ K. The position of E_F is identified by a vertical line. The lower scale relates to experimental values of the bias potential U_b at the emitter. The upper scale refers to energies in the solid reckoned from the Fermi level, $F\times 10^{-8}$ (Vm^{-1}): *1*—20.5, *2*—27.4; *3*—31.0; *4*—32.6.

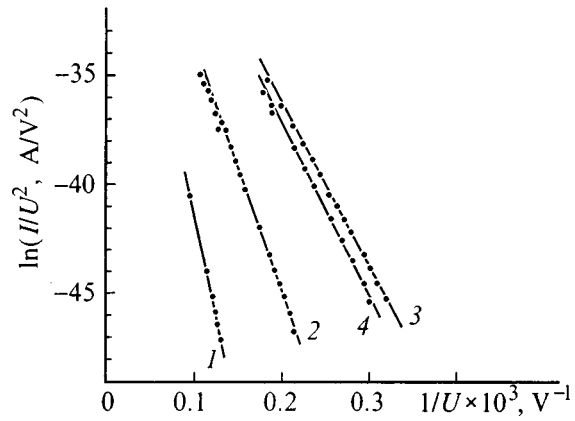

FIG. 1. $I-V$ curves for smooth Ce films on W(111). *1*—clean W(111), $T=300$ K; *2*—W(111)+Ce, 0.2 ML, $T=300$ K; *3*—W(111)+Ce, 6 ML, $T=300$ K; *4*—W(111)+Ce, 6 ML, $T=120$ K.

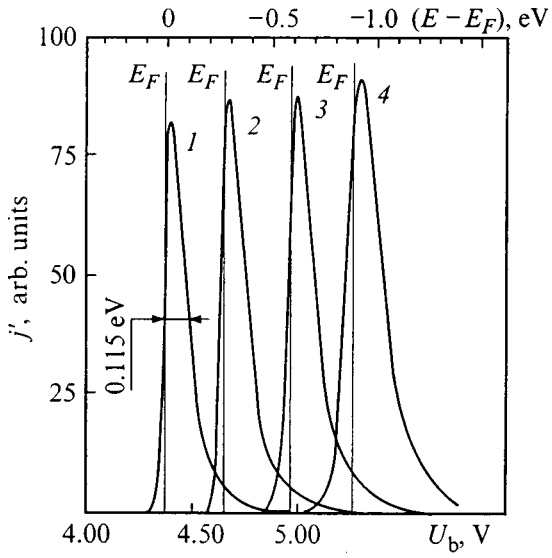

FIG. 3. Energy spectra of field-emitted electrons from a W(111)+Ce (6 ML) system, $T=120$ K. The energy scale directly relates only to curve 1, the other curves are shifted along the energy scale, and each is related to its corresponding Fermi-level position $F\times 10^{-8}$ (Vm^{-1}): *1*—13.5, *2*—15.1; *3*—17.3; *4*—19.1.

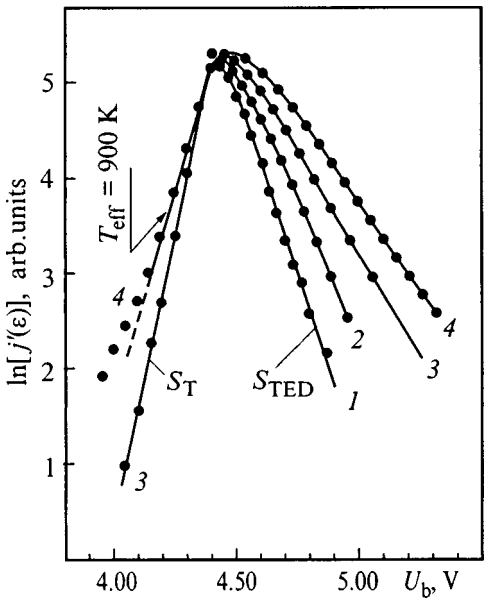

FIG. 4. Energy spectra of field-emitted electrons from a W(111)+Ce (0.2 ML) system drawn on a semilog scale. The spectra are normalized. The curves are numbered in accordance with Fig. 2.

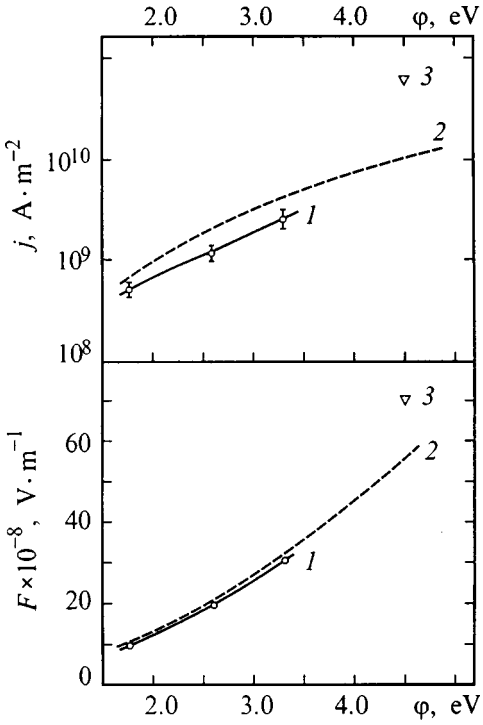

FIG. 5. Current densities j and electric fields F corresponding to the onset of anomalous behavior of the field-emission characteristics plotted vs surface work function. *1*—the data of this work for W–Ce and W–BaO systems ($\varphi = 1.8$ eV) corresponding to the condition $\Delta\Gamma/\Gamma = 25\%$ and $\Delta j/j = 20\%$; *2*—calculation[19] for $\Delta j/j = 50\%$; *3*—experimental estimates[22] for the onset of nonlinearity in the $I-V$ characteristics.

3. DISCUSSION OF EXPERIMENTAL RESULTS

The anomalous broadening of the energy spectra can be caused by thermal effects in the tip associated with high emission currents, or by the space charge of the field-emitted electrons.

Studies[9–15] of the processes involved in the energy release inside the tip suggest that, if the current is uniformly distributed over the surface of the emitter, any substantial heating of the latter is possible only for current densities at the limit of steady-state operation, i.e. $\approx 10^{11}$ A/m^2. It would thus seem that thermal effects should be disregarded in trying to interpret the data obtained. Note, however, that the analysis of thermal processes occurring inside the emitter was carried out under the assumption that the emission is distributed uniformly over the surface. In actual fact, as a result of nonuniformities in the work function and surface microprojections, the field-emission current density can vary considerably over the tip surface, enabling strong overheating of some of its parts. This work permitted discrimination of electron fluxes from various parts of the tip with high spatial resolution (down to 50 Å). While the temperatures of a probed area derived by assuming that the heating is due only to the field-emission current itself may appear too high (hundreds of K), one should not disregard the possibility of temperature variations under emission in high electric fields without performing a special analysis for a nonuniform surface. Besides, when attempting a theoretical evaluation of heat liberation in small objects one should exercise caution in dealing with the basic physical constants characteristic of massive samples.

The influence on emission spectra of the processes occurring in the space charge produced by a high-density field-emitted flux has presently become a subject of a comprehensive analysis.[16–20] Although these studies of the associated phenomena differ somewhat in approach, the prevailing conclusion is that space charge plays a dominant part in field emission in high electric fields. The significance of the effects connected with the electron interaction in the flow between the tip and the first anode is also supported by some of the results in the present investigation on the dependence of spectral broadening on the work function and surface structure. In the case of emitters with a lower work function, the broadening manifests itself at lower values of F (Fig. 5), which can be attributed to the fact that the space charge densities between the tip and the anode needed to initiate the broadening are attained at lower fields. Besides, in the case of three-dimensional cerium projections with the diameters at the base varying typically from 30 to 500 Å,[21] the anomalous broadening of spectra was observed to set in at current densities exceeding by a few times those observed with smooth films with the same work function, which also can be assigned to the effect of space charge on the energy spectrum of field-emitted electrons.

Based on the well-known experimental studies,[22] one would expect strong influence of space-charge effects for j and F larger by far than those at which an anomalous increase of Γ and the deviations of the F–N characteristics from linearity were observed in this work. The disagreement with the results cited in Ref. 22 (Fig. 5) can be associated, however, with different methods used to determine the current density. In Ref. 22, the current densities j were derived by dividing the total current from the tip by the total emitting area, an unjustifiedly straightforward approach. By contrast, in this work one measured directly local values of j, which,

as was found, may exceed considerably the surface-averaged estimates. On the other hand, the values of j and F corresponding to the onset of anomalies in Γ and the F–N characteristics are close to the ones calculated[19] under the assumption of the dominant role of space charge effects.

Summing up, the above does not give grounds for giving preference to either mechanism of anomalous change in field-emission characteristics in high electric fields. The experimental data obtained should prove useful in constructing adequate theoretical models.

The author owes sincere thanks to V. A. Ivanov for assistance in the experiments.

Support of the Russian Fund for Fundamental Research (Grant 97-02-16080) is gratefully acknowledged.

[1] R. D. Young, Phys. Rev. **113**, 110 (1959).
[2] C. Lea and R. Gomer, Phys. Rev. Lett. **25**, 804 (1970).
[3] A. E. Bell and L. W. Swanson, Phys. Rev. B **19**, 3353 (1979).
[4] M. Troyon, J. Microsc. Spectrosc. Electron. **13**, 49 (1988).
[5] V. A. Ivanov, T. S. Kirsanova, and T. A. Tumareva, Fiz. Tverd. Tela (Leningrad) **23**, 664 (1981) [Sov. Phys. Solid State **23**, 377 (1981)].
[6] T. A. Tumareva, V. A. Ivanov, T. S. Kirsanova, and I. V. Vasil'eva, Fiz. Tverd. Tela (Leningrad) **31**, No. 2, 12 (1989) [Sov. Phys. Solid State **31**, 182 (1989)].
[7] V. A. Ivanov, T. S. Kirsanova, and T. A. Tumareva, Fiz. Tverd. Tela (Leningrad) **31**, No. 4, 82 (1989) [Sov. Phys. Solid State **31**, 591 (1989)].
[8] H. Heinrich, M. Essing, and J. Geiger, Appl. Phys. Lett. **12**, 197 (1977).
[9] L. W. Swanson, L. G. Crouser, and F. M. Charbonnier, Phys. Rev. **151**, 327 (1966).
[10] I. L. Sokol'skaya and G. N. Furseĭ, Radiotekh. Elektron. **7**, 1484 (1962).
[11] E. A. Litvinov and A. A. Starobinets, in *Heavy-Current Emission Electronics* [in Russian], edited by G. A. Mesyats (Nauka, Novosibirsk, 1984), p. 41.
[12] M. S. Aksenov, L. M. Baskin, V. M. Zhukov, N. V. Fedorov, and G. N. Furseĭ, Izv. Akad. Nauk SSSR, Ser. Fiz. **43**, 543 (1979).
[13] G. N. Furseĭ, V. M. Zhukov, and L. M. Baskin, in *Heavy-Current Emission Electronics* [in Russian], edited by G. A. Mesyats (Nauka, Novosibirsk, 1984), p. 21.
[14] P. W. Williams and W. T. Williams, J. Phys. D **5**, 280 (1972).
[15] E. E. Martin, J. K. Trolan, and W. P. Dyke, J. Appl. Phys. **31**, 782 (1960).
[16] P. I. Donders and M. I. G. Lee, Phys. Rev. B **35**, 6578 (1987).
[17] M. G. R. Thomson, J. Vac. Sci. Technol. **12**, 3498 (1994).
[18] H. B. Elswijk, T. van Rooy, and C. Schiller, J. Vac. Sci. Technol. **13**, 1037 (1995).
[19] C. B. Wheeler, Proc. IEE **132**, Pt. A, 104 (1985).
[20] W. Knauer, Optik (Stuttgart) **54**, 211 (1979).
[21] A. P. Druchinina, T. S. Kirsanova, I. I. Stolyarov, and T. A. Tumareva, Fiz. Tverd. Tela (Leningrad) **32**, 1653 (1990) [Sov. Phys. Solid State **32**, 964 (1990)].
[22] W. P. Dyke and J. K. Trolan, Phys. Rev. **89**, 799 (1953).

Translated by G. Skrebtsov

Decay kinetics of the delayed annihilation fluorescence of aromatic molecules in Langmuir–Blodgett films

N. Kh. Ibraev*) and V. A. Latonin

Karaganda State University, 470074 Karaganda, Kazakhstan
(Submitted April 23, 1998; resubmitted October 2, 1998)
Fiz. Tverd. Tela (St. Petersburg) **41**, 736–739 (April 1999)

Triplet states of aromatic molecules of the anthracene type in Langmuir–Blodgett films are investigated. It is established that the principal channel for the relaxation of T_1 states is bimolecular triplet-triplet annihilation. The observed nonexponential decay kinetics of delayed annihilation fluorescence is discussed within the formal-kinetic and percolation models.
 [S1063-7834(99)03504-2]

Multimolecular Langmuir–Blodgett (LB) films are an example of artificially organized molecular systems, which are formed by means of the successive transfer of monolayers of organic molecules from a water surface to a solid substrate. One characteristic feature of LB films is their directed molecular orientation and strictly fixed thickness. Owing to their structural features, LB films have several specific properties, which distinguish them from bulk media.[1]

The investigation of the spectral-luminescence properties of LB films of aromatic molecules has been the subject of several papers.[2–7] It was shown that aromatic molecules in both a pure form and in mixtures with molecules of fatty acids form stable monolayers on a water surface and can be transferred intact to a solid substrate. When the concentration of the luminophor in the monolayer was varied, the fluorescence of monomers and excimers was observed.[3,5,7] The spectral-kinetic properties of LB films of anthracene derivatives were studied in Ref. 2, and it was shown that the structure and position of the electronic spectra of LB films are similar to the spectra of anthracene crystals. Nevertheless, the scientific literature on LB films includes virtually no publications devoted to the study of the properties of triplet states, which play a significant role in the conversion of electron excitation energy in molecular systems.

One of the effective channels for the deactivation of triplet states is the bimolecular annihilation of triplet molecules, as a result of which one of the molecules passes into the ground S_0 state, while the other passes into an excited S_1 state. Triplet-triplet annihilation (TTA) is accompanied by delayed fluorescence (DF), whose spectrum coincides with the spectrum of ordinary fluorescence and whose duration is determined by the lifetime of the triplet molecules. Because of the small spatial scale of the exchange interaction underlying TTA, the decay kinetics of annihilation delayed fluorescence depend strongly on the structure of the medium. While the rate of the pair annihilation of triplets in homogeneous liquid solutions and molecular crystals is determined by the diffusion of the reactants and the migration of an exciton,[8,9] the efficiency of TTA in solid-state systems having an irregular structure depends on the nature of the distribution of the molecules and specific details of their interaction.[10]

The present work was devoted to investigate of the properties of the delayed annihilation fluorescence of aromatic molecules in LB films, since it can be expected that new aspects of TTA may become evident in such structures.

1. EXPERIMENTAL METHOD

Zone-purified molecules of anthracene, 1,2-benzanthracene (1,2-BA), pyrene, and 3,4-benzpyrene (3,4-BP) were chosen as objects of investigation. In pure form, the molecules investigated do not form stable monolayers on the water/air interface, since they do not have surface properties. Therefore, mixtures of these molecules with stearic acid were used. The compounds were dissolved separately in chloroform and then mixed in various luminophor:stearic acid mole ratios (1:1, 3:1, and 1:50). A similar method was used in Refs. 6 and 7. Multimolecular layers were obtained on a nonluminescent quartz substrate using an automated Langmuir apparatus. The π-A isotherm (the dependence of the surface pressure on the area per molecule) was recorded for each mixture of a luminophor and stearic acid before the material was deposited on the substrate. The optimum pressure for transferring the monolayer to the substrate was determined from the linear portion of the π-A isotherm, which corresponds to the state of maximum possible packing of the molecules. The time for reaching of this phase state of the monolayer was determined using a Wilhelmy balance. After this the monolayers were successively transferred to a *Z*-type solid substrate.

The π-A isotherms obtained for the mixtures of each luminophor with stearic acid were used to calculate the area per molecule in the solid condensed phase (A_{mol}). The results of the calculations of A_{mol} for the various luminophors are listed in Table I. In all cases the area per molecule approaches the value $A_{\text{mol}}=20.5$ Å^2 for stearic acid as the concentration of stearic acid in the mixed monolayers is increased.

Based on the data obtained it can be presumed that the luminophor molecules are inserted between stearic acid molecules. In such a case a significant increase in the concentra-

TABLE I. Dependence of the area per molecule on the luminophor:stearic acid ratio.

	A_{mol}, Å^2				
Luminophor	1:50	1:1	3:1	5:1	7:1
Anthracene	19.25	16.5	7.5	4	–
1,2-BA	17.6	12.6	7.85	–	–
Pyrene	–	12.4	8.45	5.5	4.3
3,4-BP	–	–	8.60	–	–

tion of luminophor molecules leads to instability of the mixed monolayer. The optimum ratio between the luminophor and stearic acid is 3:1, at which a sufficiently strong monolayer forms. It can be transferred to the substrate, and the solid films obtained exhibit appreciable luminescence.

The spectral-kinetic natures of the samples were measured by an automated system with detection in the photon-counting mode.[11] The samples were placed in a vacuum-pumped optical cryostat for performing experiments over a broad temperature range. Photoexcitation was effected by the output of a nitrogen laser ($\lambda = 337.2$ nm, the energy in a pulse was 3 mJ, and the pulse duration was $\tau = 10$ ns). To eliminate the ordinary fluorescence signal, a mechanical photographic shutter or electronic ''triggering'' by the photomultiplier was employed. The time from the arrival of a laser pulse to the beginning of a measurement was 150 μs in the former case and 10 μs in the latter case. At least 5000 acquisitions were carried out to obtain signals of a satisfactory level. A computer was used to control the apparatus, accumulate the signals, and further process them.

2. EXPERIMENTAL RESULTS AND DISCUSSION

Figure 1 shows the absorption (*1*) and fluorescence (*2*) spectra of 1,2-BA in an LB film. The spectra obtained are red-shifted relative to their spectra in an ethanol solution and more closely approximate the spectra of the crystal. A similar picture was observed for the other luminophors. Pyrene and 3,4-BP molecules exhibited excimer fluorescence along with fluorescence of the monomers. The spectra of the LB films of anthracene are consistent with the data in Ref. 2.

Let us consider the results of measurements of the long-lived luminescence in the example of the LB films of 1,2-BA. When an LB film was excited by the output of a nitrogen laser at $T = 77$ K, delayed fluorescence was observed. Its spectrum coincides with the spectrum of the ordinary fluorescence of the same film. Excimer delayed fluorescence was also observed along with the monomer fluorescence for the pyrene and 3,4-BP films. No appreciable luminescence was detected in the region of the phosphorescence spectra of the luminophors for any of the samples.

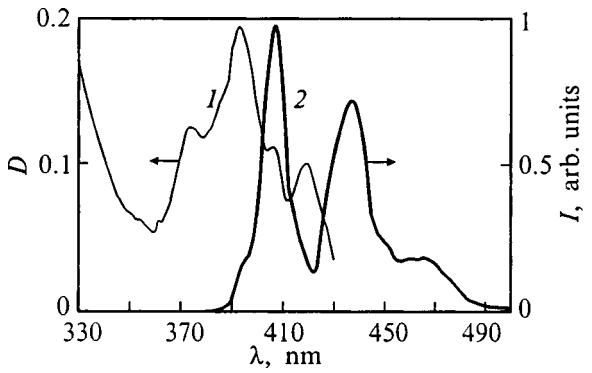

FIG. 1. Absorption (*1*) and florescence (*2*) spectra of LB of 1,2-BA.

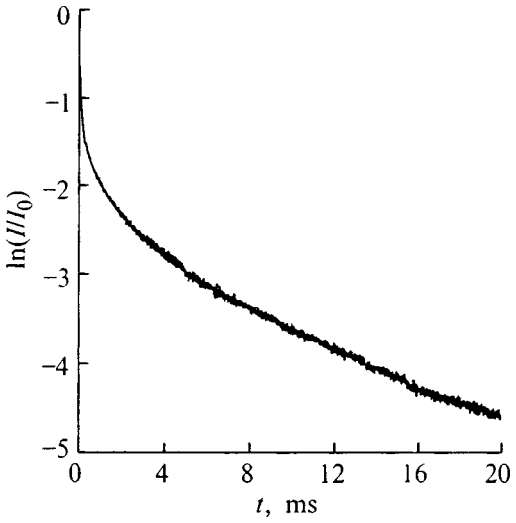

FIG. 2. Decay kinetics of the delayed annihilation fluorescence of an LB film of 1,2-BA.

The form of the kinetic decay curve of the delayed fluorescence of an LB film of 1,2-Ba at $T = 77$ K is shown in Fig. 2. The decay curves for LB films of the other luminophors are not presented here, since similar data were obtained. As can be seen from the figure, nonexponential decay of the delayed fluorescence is observed in the general case. Exponential decay was observed at times $t > 5.0$ ms. The lifetimes of the triplet states (τ_T) and the rate constants of first-order decay (k_1) calculated from the exponential part of the decay curve are presented in Table II.

Along with the formal-kinetic model which describes the laws of the pair annihilation of triplet excitons in molecular crystals,[12] there are static annihilation models for solid isotropic solutions,[13,14] according to which the observed nonexponential DF kinetics are due to the dependence of the rate of TTA on the distance between the reactants. In the case of inhomogeneous media, such as mixed crystals, polymers, porous glasses, etc., percolation theory has proved to be effective for describing the kinetics of annihilation delayed fluorescence.[15,16]

TABLE II. Values of the parameters characterizing the delayed fluorescence of LB films of aromatic molecules.

Luminophor	k_1, s^{-1}	τ_T, ms	n ($I_{DF} \sim t^{-n}$)	$[T_0]\cdot 10^{-14}$, cm^{-3}	k_{ann}, s^{-1}cm^3	h
Anthracene	62.5	16	1.5	3.2	5×10^{-9}	1.01
1,2-BA	55.0	18	1.1	5.2	5×10^{-11}	0.60
Pyrene	22.7	44	1.7	1.0	9×10^{-8}	0.59
3,4-BP	37.0	27	1.3	4.0	1.5×10^{-10}	0.94

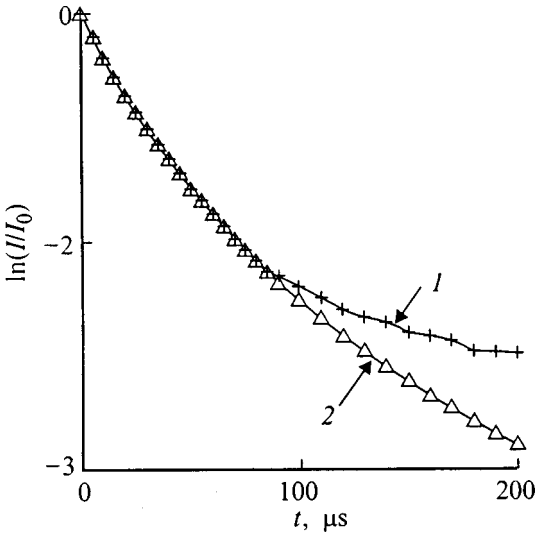

FIG. 3. Comparison of an experimental DF decay curve (*1*) with the theoretical curve (*2*) calculated within the kinetic model.

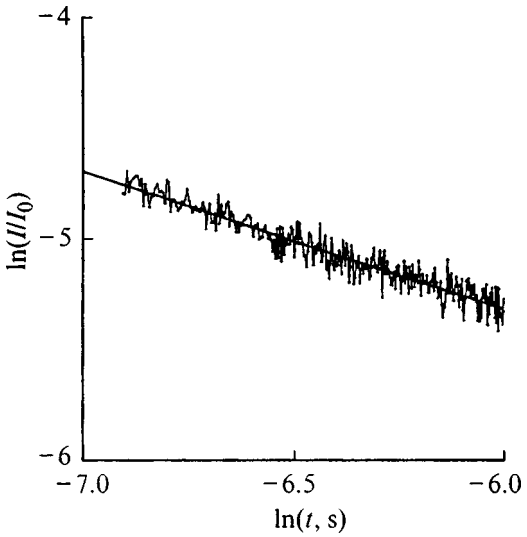

FIG. 4. Description of the kinetics of delayed fluorescence by the percolation model at $t>100\ \mu$s.

The DF decay curves obtained were analyzed according to these models of TTA. The initial portion of the curve ($t<100\ \mu$s) is approximated well by a power function of the form $I_{DF}\sim t^{-n}$. The values of n are listed in Table II. A decrease in the energy of the laser pulse led to transformation of the power law into an exponential dependence. When the energy of the exciting pulse was varied from 3 to 0.12 mJ, the half-life of the luminescence increased from 230 to 405 μs.

The analysis performed on the initial nonexponential portions of the kinetic curves showed that they are described more closely by the formal-kinetic model of TTA in homogeneous systems, according to which the deactivation of triplets is described by the kinetic equation[9]

$$-\frac{d[T]}{dt}=k_1[T]+k_{ann}[T]^2, \tag{1}$$

and the DF intensity is specified by the expression

$$I_{DF}=\left(\frac{k_1^2}{k_{ann}}\right)\left\{\left(1+\frac{k_1}{k_{ann}[T_0]}\right)\exp(k_1t)-1\right\}^{-2}, \tag{2}$$

where k_1 and k_{ann} are the rate constants of monomolecular decay and TTA, respectively, and $[T_0]$ is the initial triplet concentration.

Figure 3 compares the initial portion of the experimental DF decay curve (curve *1*) of a 1,2-BA LB film with the theoretical curve (*2*) calculated from Eq. (2). When the calculated curve was constructed, the approximate value of the initial triplet concentration ($[T_0]$) was estimated with consideration of the energy in the laser pulse, the absorption coefficient of the sample at a wavelength of 337.2 nm, and the quantum efficiency of the luminophor in the triplet state. The values of the pair annihilation rate constant k_{ann} (Table II) of the triplet molecules at which the best agreement between the experimental and calculated curves was observed are qualitatively consistent with the values of the rate constant of the bimolecular annihilation of triplet excitons in molecular crystals.[12]

Thus, the spectral-luminescence data obtained for LB films of the molecules investigated demonstrate their similarity to the analogous characteristics for molecular crystals. The decay kinetics of delayed annihilation fluorescence at the initial decay times are described satisfactorily by the formal-kinetic model of the annihilation of triplet excitons in molecular crystals. At the same time, while the DF kinetic decay curve can be fully described within the excitonic model, in the case of LB films the experimental data agree poorly with the calculated curve (curve *2* in Fig. 3) at $t>100\ \mu$s.

In Refs. 15–17 a percolation model constructed in the fractal approximation was used to account for the laws governing the decay kinetics of long-lived luminescence in inhomogeneous systems. The main difference between the percolation model and the classical formal-kinetic model of annihilation is confined to the time dependence of the annihilation rate constant. According to this model, the equation describing the deactivation of triplets has the form[16]

$$-\frac{d[T]}{dt}=k_1[T]+k_{ann}t^{-h}[T]^2, \tag{3}$$

and the DF intensity is specified by the expression

$$I_{DF}\sim k_{ann}t^{-h}[T]^2. \tag{4}$$

The parameter h characterizes the degree of local inhomogeneity of the medium d_s

$$h=1-d_s/2,\quad 0\leqslant h\leqslant 1. \tag{5}$$

For a strict fractal medium $d_s=1.33$ and $h=0.35$.

The DF kinetic curves were analyzed within the percolation model on the assumption that microscopically inhomogeneous regions can exist in the structure of LB films along with the crystalline regions. Figure 4 shows the result of treating the long-term part of the kinetic curve for 1,2-BA according to the relation (4). It was assumed here that the concentration of triplets varies only slightly during the mea-

surement time. The values of h determined in this way for other luminophors are presented in Table II. The values of h obtained lie in the theoretical limit.

Thus, an analysis of the experimentally obtained decay curves showed that the kinetics of the delayed fluorescence of aromatic molecules in LB films are described satisfactorily by the formal-kinetic model for homogeneous media in the initial period after excitation and are consistent with the percolation model in the later stages of decay ($t>1$ ms).

Generalizing the results obtained, we can conclude that the deactivation of triplet states occurs in Langmuir–Blodgett films of aromatic molecules mainly as a result of biexcitonic annihilation. The kinetics of the initial stage of DF decay probably reflects the existence of crystalline regions having an ordered arrangement of the luminophor molecules, for which the luminescence kinetics are described satisfactorily within the formal-kinetic excitonic model. In addition, the films contain percolation clusters, in which the migration of excitation energy also takes place. The ''fractal'' luminescence, which is clouded by the ''crystalline'' luminescence on the initial portion of the kinetic curve, is displayed more clearly at later decay times.

*)E-mail: nibraev@ism.kargu.krg.kz

[1] L. M. Blinov, Usp. Fiz. Nauk **155**, 442 (1988) [Sov. Phys. Usp. **31**, 623 (1988)].
[2] G. Biesmans, G. Verbeek, B. Verschuere, M. van der Auweraer, and F. C. de Schryver, Thin Solid Films **169**, 127 (1989).
[3] N. Sadovskii, P. Shirov, M. Kuzmin, H. Lemmetyinen, and M. Ikonen, Thin Solid Films **204**, 441 (1991).
[4] T. Yamazaki, N. Tamai, and I. Yamazaki, Chem. Phys. Lett. **124**, 326 (1986).
[5] H. Lemmetyinen, M. Ikonen, and J. Mikkola, Thin Solid Films **204**, 417 (1991).
[6] A. G. Vitukhnovsky, A. G. Sluch, T. G. Warren, and M. C. Petty, Chem. Phys. Lett. **173**, 425 (1990).
[7] A. G. Vitukhnovsky, A. G. Sluch, T. G. Warren, and M. C. Petty, Chem. Phys. Lett. **184**, 235 (1991).
[8] C. A. Parker, *Photoluminescence of Solutions. With Applications to Photochemistry and Analytical Chemistry* (Elsevier, New York, 1968; Mir, Moscow, 1972).
[9] V. L. Ermolaev, E. N. Bodunov, E. B. Sveshnikova, and T. A. Shakhverdov, *Radiationless Transfer of Electron Excitation Energy* [in Russian] (Nauka, Leningrad, 1977).
[10] M. G. Kucherenko, *Kinetics of Nonlinear Photoprocesses in Condensed Molecular Systems* [in Russian] (Izd. Orenburg. Univ., Orenburg, 1997).
[11] N. Kh. Ibraev and V. A. Latonin, Prib. Tekh. Eksp. **5**, 169 (1997).
[12] M. Pope and C. E. Swenberg, *Electronic Processes in Organic Crystals* (Clarendon Press, Oxford; Oxford University Press, New York, 1982; Mir, Moscow, 1985).
[13] N. A. Efremov, S. G. Kulikov, R. I. Personov, and Yu. V. Romanovskiĭ, Fiz. Tverd. Tela (Leningrad) **31**(3), 103 (1989) [Sov. Phys. Solid State **31**, 407 (1989)].
[14] M. G. Kucherenko and M. P. Mel'nik, Zh. Prikl. Spektrosk. **53**, 380 (1990).
[15] E. I. Newhouse and R. Kopelman, Chem. Phys. Lett. **143**, 106 (1988).
[16] L. A. Harmon and R. Kopelman, J. Phys. Chem. **94**, 3454 (1990).
[17] N. A. Borisevich, S. A. Bagnich, and A. V. Dorokhin, Opt. Spektrosk. **69**, 102 (1990) [Opt. Spectrosc. **69**, 62 (1990)].

Translated by P. Shelnitz

FULLERENES AND ATOMIC CLUSTERS

The structure of diamond nanoclusters

A. E. Aleksenskiĭ, M. V. Baĭdakova, A. Ya. Vul', and V. I. Siklitskiĭ

A. F. Ioffe Physicotechnical Institute, Russian Academy of Sciences, 194021 St. Petersburg, Russia
(Submitted September 7, 1998)
Fiz. Tverd. Tela (St. Petersburg) **41**, 740–743 (April 1999)

A model describing the structure of diamond nanoclusters produced by explosive shocks is proposed. The model is based on experimental data obtained from x-ray diffraction and small-angle x-ray scattering. This model considers the diamond nanocluster as a crystalline diamond core coated by a carbon shell having a fractal structure. The shell structure depends both on the cooling kinetics of the detonation products and on the method used to extract from them the diamond fraction. © *1999 American Institute of Physics.*
[S1063-7834(99)03604-7]

The diamond cores in ultradisperse diamond (UDD) clusters obtained by detonation synthesis were found to be 43 Å in size, with a small amount of an amorphous phase with sp^2 and sp^3 hybridized bonds present on their surface.[1] It was shown that UDD clusters are fractal objects, and the variation of the fractal dimension during isothermal anneal was studied in an inert ambient.[2]

This work reports an investigation of the structure of a UDD cluster determined by x-ray diffraction and small-angle x-ray scattering measurements made on UDD samples following consecutive removal of the cluster shell sheets by a high-activity oxidizer.

1. SAMPLES AND EXPERIMENTAL METHOD

The studies were carried out on UDD samples extracted from the carbonaceous residues formed by detonation of explosives containing excess carbon as described in Refs. 3, 4. The UDD samples were obtained by the so-called ''dry'' synthesis,[4] where the detonation products are cooled by a gas; in this case the content of the diamond phase in the detonation-produced carbon does not exceed, as a rule, 35 wt. %.

The diamond phase was extracted by treating the explosion-produced carbon with nitric acid in an autoclave. The amount of the nondiamond phase removed was governed by the temperature of the treatment. After the reaction had come to an end and the material had been taken out of the autoclave, it was washed with distilled water until pH $=7$ was reached. The UDD samples prepared in this way were identical in all parameters, except the amount of the amorphous phase coating the diamond core. The sample with the highest degree of cleaning was obtained by treating the carbon material with ozone. The parameters of the oxidation processes are listed in Table I.

The fractal structure of the nanoclusters was studied in a traditional way[5] by measuring the dependence of the small-angle x-ray scattering intensity I on wave vector q within the interval $0.036<q<0.8\ \text{Å}^{-1}$, which corresponds to scattering angles $0.5<2\Theta_{Br}<10°$. The scattering intensity was measured in Θ, 2Θ geometry on a Dmax-B/RC Rigaku Cor diffractometer in a single-crystal arrangement. Cu radiation ($\lambda = 1.5418$ Å) was used. X-ray diffraction measurements were simultaneous with the small-angle scattering studies on the same samples within a broad range of angles. The data was treated as described in Ref. 2.

2. EXPERIMENTAL RESULTS AND DISCUSSION

The experimental x-ray diffraction and scattering curves are displayed in Figs. 1 and 2. The broad symmetric diffraction maxima observed for all samples at the angles $2\Theta_{Br}=43.9$ and 75.3° correspond to the (111) and (220) reflections from a diamond-type lattice. The halfwidths of the maxima correspond to diffraction from spherical particles having coherent scattering regions about 40 Å in size.

Curve *1* in Fig. 1 (the starting sample of explosion-produced carbon before the oxidizing treatment) also contains a broad diffraction maximum at $2\Theta_{Br}\approx 26°$, which can be assigned to reflection from the (0002) planes of a graphite-type lattice. The halfwidth of the maximum is appropriate for scattering from spherical particles not over 20 Å in size. The integrated-intensity ratio of the diamond, (111), to graphite, (0002), maxima for this sample is $I_D/I_G = 5/8$, which agrees with the expected amount of the diamond fraction of 35%. One can see also narrow maxima corresponding to diffraction from large inclusions of the iron oxide Fe_3O_4 (identified with an asterisk in Fig. 1). At small angles ($2\Theta_{Br}<10°$) a characteristic increase of scattered radiation intensity is observed.

In the first stage of oxidation, iron oxide impurities are removed from the detonation-produced carbon (curve *2* in Fig. 1). A clearly pronounced asymmetry appears in the diffraction maxima at $2\Theta_{Br}\approx 26$ and 75.5°, and the maxima acquire a sawtooth shape typical of diffraction from a two-dimensional grating.[6] The ratio of the integrated intensities

TABLE I. The conditions used for UDD extraction from detonation-produced carbon and scatterer parameters.

Sample No.	Etchant and etch temperature T (°C)	Dimension D and type of fractal	Scatterer size
1		2.51, Surf.	52
2	HNO_3, 50%, 180 °C	2.21, Surf.	$\geqslant 60$
3	HNO_3, 50%, 190 °C	2.93, Surf.	$\geqslant 60$
4	HNO_3, 50% 200 °C	2.85, Surf.	$\geqslant 90$
5	HNO_3, 50% 230 °C	2.34, Surf.	>90
6	HNO_3, 70% 250 °C	2.92, Surf.	45
7	HNO_3, 50% 240–260 °C	2.97, Vol.	52
8	ozone flow	2.93, Vol.	32

Note. The scatterer type, fractal dimension, and size (the first three rows of columns 3 and 4) derived from $I(q)$ relations were obtained by averaging the scattering intensities from graphite nanostructures of different sizes.

of the diamond and graphite maxima changes toward increasing diamond fraction. The ratio $I_D/I_G=3/1$ corresponds approximately to 75 wt. % of the diamond phase in this sample.

The experimental curves obtained on samples subjected to more thorough cleaning exhibit qualitative changes (curves *3* and *4* in Fig. 2), namely, the diffraction maximum corresponding to the graphite phase vanishes, and diffuse scattering (a halo) becomes evident at $2\Theta_{Br}\approx 17°$. The small-angle x-ray scattering pattern also undergoes a qualitative change, so that when plotted on a log-log scale the relations can be well fitted by a power-law function within the $0.2<q<0.8\,\text{Å}^{-1}$ interval (see Fig. 2).

Still deeper cleaning results in a practically complete disappearance of the halo (curve *5*), and a clearly defined maximum appears at small scattering angles (curve *8*).

Our analysis of the diffraction and scattering curves will be based on a model[1,2] in which a UDD cluster consists of a diamond core inside an amorphous carbon shell having a complex structure, and depends on data on the fractal dimension and characteristic size of the scatterer. These parameters determined by the method described in Ref. 2 are presented in Table I.

Obviously enough, the scatterer left after the deepest cleaning stage (ozone treatment) is the diamond core. That the scatterer size is 32 Å, which is less than the typical di-

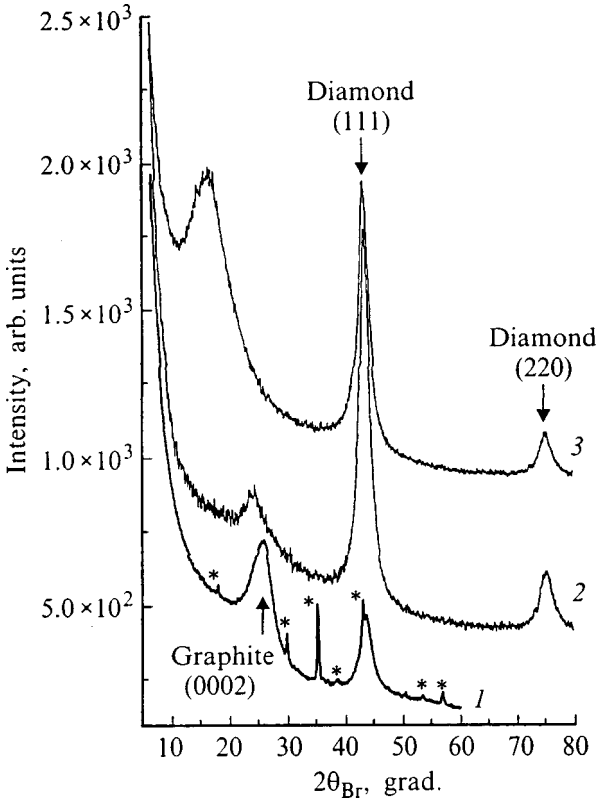

FIG. 1. Diffraction patterns of UDD samples differing in the extent of cleaning. The etching parameters are specified in Table I (the sample numbers coincide with the numbers of the entries). The asterisk identifies the Fe_3O_4 diffraction maxima.

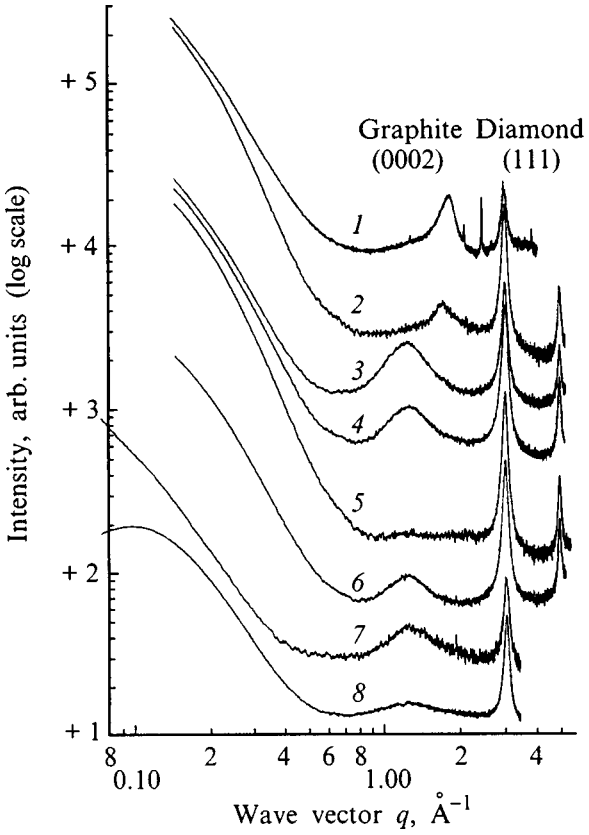

FIG. 2. Small-angle-scattering curves for UDD samples obtained by consecutive oxidation. The oxidation parameters are specified in Table I (the sample numbers coincide with the numbers of the entries).

mension of the coherent-scattering region,[1,7] implies that the diamond core was partially etched off. This conclusion is buttressed also by the broadening of the (111), (220), and (311) diamond reflections. The core fractal dimension is found to be $D=2.93$, which corresponds to a mass (volume) fractal. The weak-intensity halo originates from scattering by an elementary structural block with a characteristic size ~ 2.5 Å. The difference of the fractal dimension from $D=3$ (a smooth ball) indicates a weakly pronounced surface relief. Similar parameters are observed also when oxidizing the amorphous phase in a flow of nitric acid at $T\sim 240-260\,^{\circ}$C (curve *7*). A weak difference is observed only in the size of the scatterer, i.e. the UDD cluster core.

In an earlier stage of cleaning (curve *6*) the scatterer size is $L=45$ Å, which corresponds to the diamond core acting as a coherent scatterer, and the surface exhibits a sharper relief (the halo at 17° is brighter). We associate the observed halo with scattering from the carbon sheets in the onion-like structure. There is more than one argument for this conjecture. First, the halo can be attributed due to scattering from structural elements 2.46 and 2.84 Å in size (which corresponds to the wave vectors $q=1.28$ and $1.11\,\text{Å}^{-1}$, respectively). The break in the small-angle scattering curves at $q\approx 0.55\,\text{Å}^{-1}$ indicates the existence of larger characteristic sizes as well. The ''aromatic'' cluster[8] whose structure is shown in Fig. 3b has such characteristic dimensions. Second, the fractal dimension $D\approx 3$ evidenced by curves *6* and *7* argues for the scatterer being a smooth-surface fractal. Finally, the shell thickness, as shown earlier,[2] does not exceed 5 Å, which corresponds to the observed difference between the scatterer diameters determined for samples *6* and *7*. This size is characteristic of the thickness of the onion-like carbon shell enveloping the core in the initial stages of the diamond-graphite transition during UDD annealing.[9,10] The absence of the halo and of a break in curve *5* for samples studied in earlier stages of cleaning, combined with a substantially sharper relief ($D=2.34$), may be assigned to interference from individual structural elements distributed randomly over the surface of the onion-like UDD-cluster shell.

That the halo and the break in the small-angle scattering curves of samples in earlier stages of cleaning (curves *3* and *4*) are observed at $q\approx 1.2$ and $0.5\,\text{Å}^{-1}$ suggests that the structural element of the scatterer did not change and still remains an aromatic cluster. At the same time the change of the fractal from the mass to surface type with increasing fractal dimension and, simultaneously, increasing scatterer size ($L\geqslant 90$ Å) indicates that the scatterer is a diamond surrounded by an onion-like shell, with sets of equidistant nanosized graphite platelets distributed randomly on its surface. By this model, the decrease of fractal dimension from $D=2.93$ to 2.85, with the etching temperature increasing from 190 to 200 °C, is associated with the formation of channels between these platelet sets (through oxidation of weakly coupled hydrocarbon chains).

The above interpretation of the oxidation process is supported indirectly by the fact that curve *2* obtained at lower oxidation temperatures exhibits diffraction from graphite particles which do not possess three-dimensional symmetry. Such diffraction was observed by us earlier[1] when annealing

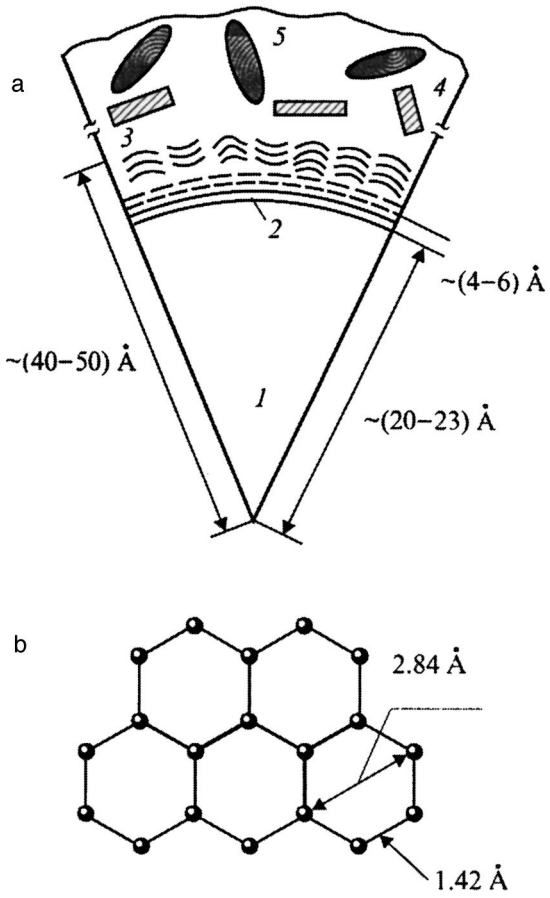

FIG. 3. (a) Model structure of detonation-produced carbon and (b) structure of the aromatic cluster. *1*—diamond core of UDD cluster, *2*—onion-like carbon shell, *3*—nanosized graphite platelets, *4*—graphite particles, *5*—metal-oxide inclusions. The UDD cluster obtained by oxidation of detonation carbon (sample *6*) is made up of a diamond core (*1*) and an onion-like shell.

UDD clusters in an argon ambient at about 1400 K. The structures responsible for such diffraction were described in considerable detail in Ref. 11. They represent a set of equidistant nanosized graphite-like platelets. These graphite-like platelets exhibit structural perfection in two directions in a plane, show only a weak trend to parallel stacking, and, it should be stressed, do not exhibit three-dimensional crystallographic order. Clearly enough, the absence of three-dimensional crystallographic order with, at the same time, a high perfection of the structure as a whole can be achieved in formation of closed and quasiclosed structures. It is these structures that were called the onion-like carbon form.[12]

The change in the shape and the shift of the graphite diffraction maximum in curve 2 compared to the original sample (curve *1*), where the fraction of bulk graphite particles is substantially larger, is thus associated with the change of three-dimensional diffraction from bulk graphite to a two-dimensional one from quasiclosed onion-like structures. Note that the presence in the detonation-produced carbon of graphite particles with a low degree of three-dimensional order along the (001) direction was pointed out in Ref. 9, where it was shown that UDD particles in this carbon are 70–100 Å in size, whereas the graphite-like in-

clusions, are not over 15 Å. These observations are in a good agreement with the size of the scatterers measured by us after the oxidation treatment and, therefore, they were used in drawing the schematic structure of the UDD cluster in Fig. 3.

Thus consecutive removal of UDD sheets permitted us to construct a model of the UDD cluster structure (Fig. 3). It can be maintained that the carbon produced in detonation represents a diamond core coated by an onion-like carbon shell, on which graphite inclusions are distributed. The various impurities and hydrocarbons are located on this shell and are present in the carbon phase. Etching the nondiamond phase away removes consecutively the bulk graphite phase and the impurities; cuts channels dissecting the shell made up of disordered graphite-like quasiclosed sheets, and removes the stacks of the nanosized carbon platelets formed in this way; and, finally, smoothens the surface relief in the last stage by dislodging the onion-like sheets down to the diamond core. Note that depending on the actual extent of cleaning (50 or 70% HNO_3) one can either etch off the nanosized graphite-like platelets from the surface of a closed onion-like shell (sample *7*) or destroy the closed shell altogether (sample *6*).

It becomes clear now that the difference between the UDD obtained in dry and aqueous synthesis[2] consists in different thicknesses of the onion-like shell. Indeed, because the detonation carbon produced in dry synthesis passes the region of kinetic instability of diamond at a lower rate, the thickness of the closed onion-like shell will be larger than that in the process involving water. For equal extents of cleaning used to extract the diamond phase from the detonation carbon the UDD samples produced in the dry and aqueous synthesis will differ naturally only in scatterer size, an observation made by us earlier.[2]

The work was carried out on equipment provided by the St. Petersburg Joint Research Center.

Support of the Russian Fund for Fundamental Research (Grant 96-02-19445) is gratefully acknowledged.

[1] A. E. Aleksenskiĭ, M. V. Baĭdakova, A. Ya. Vul', V. Yu. Davydov, and Yu. A. Pevtsova, Fiz. Tverd. Tela (St. Petersburg) **39**, 1125 (1997) [Phys. Solid State **39**, 1007 (1997)].
[2] M. V. Baĭdakova, A. Ya. Vul', V. I. Siklitskiĭ, and N. N. Faleev, Fiz. Tverd. Tela (St. Petersburg) **40**, 776 (1998) [Phys. Solid State **40**, 715 (1998)].
[3] A. M. Staver, N. V. Gubareva, A. Ya. Lyamkin, and E. A. Petrov, Fiz. Goreniya Vzryva **20**, 100 (1984).
[4] A. Ya. Lyamkin, E. A. Petrov, A. P. Ershov, G. V. Sakovich, A. M. Staver, and V. M. Titov, Dok. Akad. Nauk SSSR **302**, 611 (1988) [Sov. Phys. Dokl. **33**, 705 (1988)].
[5] O. Glatter, J. Appl. Crystallogr. **12**, 166 (1979).
[6] B. E. Warren, Phys. Rev. **59**, 693 (1941).
[7] A. P. Ershov and A. L. Kupershtokh, Fiz. Goreniya Vzryva **27**, 111 (1991).
[8] V. G. Nagornyĭ, D. K. Khakimov, and A. N. Deev, Kristallografiya **20**, 900 (1975) [Sov. Phys. Crystallogr. **20**, 557 (1975)].
[9] V. L. Kuznetsov, M. N. Aleksandrov, I. V. Zagoruiko, A. L. Chuvilin, E. M. Moroz, V. N. Kolomiichuk, V. A. Likholobov, P. M. Brylyakov, and G. V. Sakovitch, Carbon **29**, 665 (1991).
[10] V. L. Kuznetsov, A. L. Chuvilin, Yu. V. Butenko, I. Yu. Malikov, and V. M. Titov, Chem. Phys. Lett. **222**, 343 (1994).
[11] R. Franklin, Acta Crystallogr. **3**, 107 (1950).
[12] H. W. Kroto, J. P. Hare, A. Sarkar, K. Hsu, M. Terrones, and J. R. Abeysinghe, MRS Bull., 51 (November 1994).

Translated by G. Skrebtsov

Influence of crystal dimensions on interatomic distances in dispersed carbon

E. A. Belenkov*) and E. A. Karnaukhov

Chelyabinsk State University, 454136 Chelyabinsk, Russia
(Submitted September 8, 1998)
Fiz. Tverd. Tela (St. Petersburg) **41**, 744–747 (April 1999)

The relationship between the interatomic distances and crystal dimensions in dispersed carbon is studied by x-ray structure analysis and by performing model calculations. It is established that the interatomic distances in dispersed carbon are determined by the dimensions of the crystals along the crystallographic *a* axis (L_a). Small crystal dimensions dictate smaller interatomic distances than in graphite; an increase in the crystal dimensions leads to a corresponding increase in this parameter. The interatomic distances in dispersed carbon depend on the degree in covalency of the bonding, which is a function of L_a. © *1999 American Institute of Physics.* [S1063-7834(99)03704-1]

The conversion of amorphous carbon into graphite during high-temperature treatment has some significant special features. The crystals formed in the amorphous matrix have a turbostratic structure, which differs from the graphite structure.[1,2] The principal parameters of the structure of such crystals are the interlayer distances d_{002} and d_{110} and the dimensions of the coherent scattering regions in the directions of the crystallographic *a* and *c* axes, i.e., L_a and L_c, respectively. For graphite $d_{002}=0.3354$ and $d_{110}=0.1232$ nm, and for the turbostratic structure $d_{002}\in[0.337, 0.360\ \text{nm}]$ and $d_{110}\in[0.1215, 0.1230\ \text{nm}]$. According to Bragg, Lachter, and Aladekomo,[3–5] the differences in the interlayer distances can be attributed to the presence of several metastable phases with structures similar to hexagonal graphite, but with different crystal-lattice parameters. In their opinion, the differences between the interlayer distances in such phases and the values characteristic of graphite are caused by the presence of different types of interlayer carbon atoms.[6] However, it has been shown in several studies that the variation of the interlayer distance d_{002} is governed by the small dimensions of the crystals.[7,8] The correctness of such an approach to the interpretation of the transformation of disordered carbons into graphite is confirmed by the experimentally detected relationship between the interlayer distances and the dimensions of the coherent scattering regions.[9] In the present work an attempt was made to examine the reasons for the deviation of d_{110} from the graphite values on a similar basis. The purpose of the work was to investigate the relationship between the crystal dimensions and the interatomic distances in dispersed carbon.

1. SAMPLES AND INVESTIGATIVE METHODS

Petroleum cokes with various initial concentrations of structural impurities and additions were taken as samples for the investigation (see the caption to Fig. 1). The samples were calcined in an argon atmosphere in the temperature range 1600–2500 °C. The heat treatment was carried out in a Tammann furnace. The heating rate was 300 °C per hour, and the time of isothermal holding at the final temperature was 3 h.

The x-ray structure investigations were performed on a DRON-3 x-ray diffractometer (Cu $K\alpha$ and Co $K\alpha$ radiation). The profiles of the 110 diffraction maxima were recorded on a chart with a rotation rate of the goniometer equal to 1/8 of a degree per minute. The interlayer distances were determined from the center of gravity of the diffraction lines, and the mean dimensions of the coherent scattering regions were determined from the integrated linewidth. Silicon carbide served as a reference.

2. RESULTS OF THE EXPERIMENTAL INVESTIGATIONS

The results of the experimental investigations are presented in Fig. 1. It was found that the interlayer distance d_{110} and, consequently, the interatomic distances ($R_{C-C}=d_{110}/\cos 30°$) in carbonaceous materials depend on the mean dimensions of the coherent scattering regions L_a. Regardless of the content of structural impurities in the samples and the technology used to synthesize them, all the experimental points lie on a single curve (Fig. 1). Small crystal dimensions dictate smaller values of the interlayer separations in comparison to graphite. As L_a increases, the value of d_{110} increases, tending to the value characteristic of graphite.

3. RELATIONSHIP BETWEEN THE DEGREE OF COVALENCY OF THE BONDING AND THE DIMENSIONS OF THE LAYERS

Let us consider the reasons for the difference between the interatomic distances in dispersed carbonaceous materials and the value characteristic of graphite. The literature presents data on the difference between the interatomic distances in various polymorphous modifications of carbon and organic molecules.[10] For example, for diamond $R_{C-C}=0.154$ nm, for graphite $R_{C-C}=0.1422$ nm, and in the benzene and ethylene molecules the interatomic distances are equal to 0.139 and 0.133 nm, respectively. The differences in the interatomic distances are attributed to differences in the

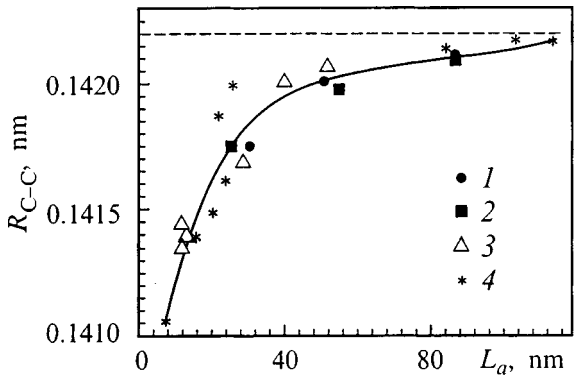

FIG. 1. Variation of the mean interatomic distances R_{C-C} as a function of the mean dimensions of the coherent scattering regions in the direction of the crystallographic *a* axis (L_a) for cokes containing 0.64 wt. % S (*1*), 0.64 wt. % S+0.2 wt. % Fe_2O_3 (*2*), 2.5 wt. % S (*3*), and less than 0.2 wt. % impurities (*4*). The interatomic distance characteristic of graphite (0.1422 nm) is indicated.

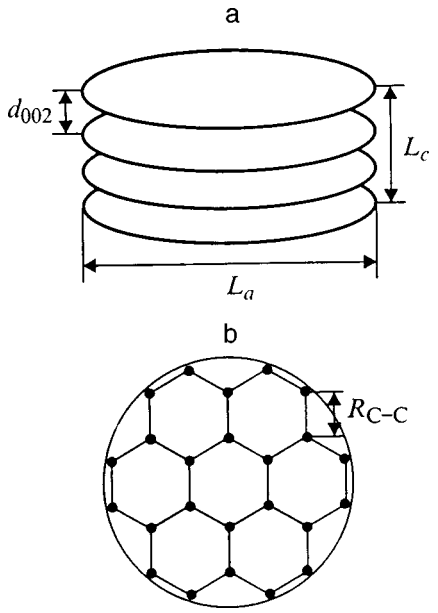

FIG. 2. Diagram of an individual crystal of a carbonaceous material (a) and schematic representation of an individual layer (b).

degree of covalency in the bonding.[10] The degree of covalency is introduced as the parameter χ, which is equal to the ratio of the maximum possible number of covalent bonds formed in the material to the number of bonds actually formed (thus, for diamond $\chi=1$, for graphite $\chi=1.333$, for benzene $\chi=1.5$, and for ethylene $\chi=2$). The interatomic distances for intermediate values of χ can be found using the interpolation polynomial

$$R_{C-C}=A+B\chi+C\chi^2+D\chi^3. \quad (1)$$

In the present work the values of the coefficients *A*, *B*, *C*, and *D* were found from the four pairs of values (R_{C-C}, χ) just presented using the least-squares method.

Let us determine whether the degree of covalency in the bonding depends on the dimensions of the crystals. Let the crystals of the carbonaceous materials be stacks of circular layers, in which the carbon atoms are joined by covalent bonds, and the bonding between the layers is effected by van der Waals interactions (Fig. 2).

Let us find the degree of covalency of the bonding in an individual crystal. We assume that the layers comprising a tiny crystal are equivalent, so that the value of χ for the crystal is identical to the value of χ for an individual layer. The maximum number of bonds in an individual layer equals $4n$ (where n is the number of atoms in the layer). Two bonds actually form for each edge atom (m is the number of edge atoms), and three bonds form for the internal atoms in each layer; therefore,

$$\chi=4n/(3n-m). \quad (2)$$

The ratio between the number of edge atoms and the number of internal atoms depends on the dimensions of the layer L_a. Let us find how χ and, thus, the interatomic distances vary as a function of L_a. This can be done by performing model calculations.

4. MODEL CALCULATION

The model calculations were performed for perfect circular layers, i.e., layers whose edge atoms are joined to the layer by two covalent bonds and which contain no vacancies. Layers in which there were edge atoms joined to the layer by one covalent bond were not considered. Since it was not known *a priori* whether the position of the origin of coordinates relative to the layers influences the results, two cases were studied. In model *1* it was assumed that the center of the layer is located at the midpoint of an interatomic bond (Fig. 3a), and in model *2* it was assumed that it coincides with the center of a hexagon (Fig. 3b). The choice of only

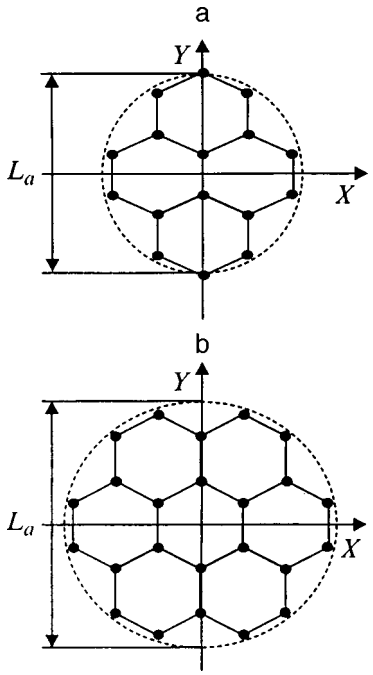

FIG. 3. Diagram of the assignment of graphite-like layers: *a* (model *1*) — for a layer diameter $L_a=0.75$ nm, $n=16$ atoms in a layer, $m=10$ edge atoms; *b* (model *2*) — for a layer diameter $L_a=0.9$ nm, $n=24$ atoms in a layer, and $m=12$ atoms.

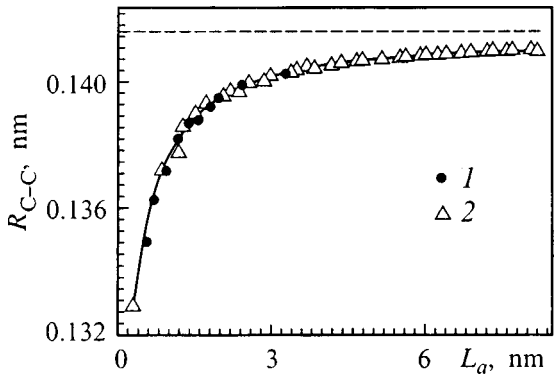

FIG. 4. Model dependence of the interatomic distances R_{C-C} on the crystal dimensions L_a: *1* — model *1*; *2* — model *2*. The interatomic distance characteristic of graphite (0.1422 nm) is indicated.

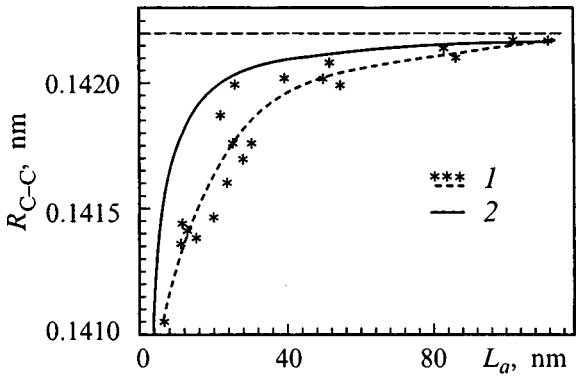

FIG. 5. Dependences of the interatomic distances R_{C-C} on the crystal dimensions L_a: *1* — experimental; *2* — model. The interatomic distance characteristic of graphite (0.1422 nm) is indicated.

perfect layers stipulated discrete variation of the layer dimensions. In model *1* the layers had diameters equal to 0.6, 0.75, 0.95, etc. up to 3.32 nm. In model *2* the dimensions of the layers were 0.3, 0.9, 1.2, etc. up to 8.2 nm. Model *1* has a geometric constraint, i.e., perfect layers with a diameter exceeding 3.32 nm could not be found. Model *2* does not have such a constraint.

The degree of covalency in the bonding [Eq. (2)] was calculated for the layers thus assigned, and then Eq. (1) was used to find the corresponding interatomic distances. The data obtained were used to construct a plot of the dependence of R_{C-C} on the dimensions of the crystal L_a (Fig. 4). The points for models *1* and *2* lie on a single curve, i.e., the result does not depend on the choice of the origin of coordinates relative to the layer. The calculated dependence is accurately interpolated by the equation

$$R_{C-C}=a-1/(bL_a+c), \tag{3}$$

where $a=0.1422$ nm, $b=203.93$ nm^{-2}, and $c=31.44$ nm^{-1} (the coefficients were found by the least-squares method).

The ranges of changes in L_a for calculated and experimental dependences do not coincide (Figs. 1 and 4); therefore, the calculated dependence must be extrapolated in accordance with Eq. (3) to compare them. The course of the dependences is identical, but the experimental points are higher than the calculated ones (Fig. 5). This is probably due to the considerable errors in the experimental determination of the dimensions of the coherent scattering regions and the deviation of the shape of real crystals from cylindrical. The standard x-ray structure methods for determining the dimensions of coherent scattering regions from the shape of the diffraction lines presume constancy of the interplanar distances in all crystals of a material as a starting assumption (only sign-alternating microstrains are allowed).[11] As was shown above, in carbonaceous materials the interplanar distances are a function of the dimensions of the crystals; therefore, the result obtained by conventional methods can be regarded only as a rough first approximation.

5. DISCUSSION

Thus, the experimental data and the results of model calculations show that the small crystal dimensions in the direction of the crystallographic *a* axis specify a value of the interatomic distance that is smaller than in graphite. An increase in dimensions stimulates an increase in the interatomic distances to values characteristic of the graphite structure. The reason for this phenomenon is the variation of the degree of covalency in the bonding in crystals as a function of their size. The results obtained, along with the previously established dependences of d_{002} on L_a (Refs. 7 and 8) allow us to regard the formation of polycrystalline graphite from amorphous and ultradisperse carbonaceous materials as growth of the crystal dimensions, which causes the transformation of the structure of turbostratic carbon into graphite. Such an approach is more correct than treating the formation of graphite as successive phase transitions through a series of metastable states,[3–5] since it enables us to explain the experimentally observed dependences of the interlayer distances in carbonaceous materials on the dimensions of the coherent scattering regions. On the basis of successive phase transitions it is impossible to explain why the formation of graphite is possible in some cokes and anthracites at 1200 $-1700\,^{\circ}$C,[12,13] while graphite does not form in carbon fibers even after thermal treatment at $2500\,^{\circ}$C.[14] The reason is that in some materials there are possibilities for the thermally activated growth of crystals and the removal of structurally incorporated impurities with the resultant formation of graphite in them. In other materials the growth of crystals is impeded, and their structural parameters remain different from those of graphite.

The presence of crystals of different size (and, consequently, with different interatomic distances) in carbonaceous materials causes asymmetry and significant broadening of the x-ray diffraction peaks. The mathematical treatment of such profiles should be reduced to an analysis that yields the size distribution function of the crystals, rather than to a separation into components belonging to different metastable phases.[4] Separation into components is justified only if the size distribution function of the crystals is bimodal, and the ratio between large crystals having a graphite

structure and small crystals with a turbostratic structure must be estimated.[12]

Thus, the results of this study allow us to draw the following conclusions.

1) The interatomic distances in dispersed carbon are proportional to the crystal dimensions along the crystallographic *a* axis. When the dimensions of the crystals are small, the interatomic distances are smaller than in graphite. The growth of crystals leads to an increase in the distances between atoms to the value characteristic of graphite.

2) The value of the interatomic distances in dispersed carbon is determined by the degree of covalency of the bonding. The degree of covalency of the bonding in carbonaceous crystals is a function of their dimensions L_a.

*)E-mail: belenkov@cgu.chel.su

[1] S. V. Shulepov, *Physics of Graphitic Materials* [in Russian] (Metallurgiya, Chelyabinsk, 1990).
[2] D. B. Fishbach, in *Chemistry and Physics of Carbon* (Dekker, New York, 1971), Vol. 7, p. 1.
[3] J. Lachter and R. H. Bragg, Phys. Rev. B **33**, 8903 (1986).
[4] J. B. Aladekomo and R. H. Bragg, Carbon **28**, 897 (1990).
[5] R. H. Bragg and J. B. Aladekomo, J. Appl. Crystallogr. **28**, 14 (1995).
[6] J. Maire and J. Mering, in *Chemistry and Physics of Carbon* (Dekker, New York, 1970), Vol. 6, p. 125.
[7] V. G. Nagornyĭ, in *Carbonaceous Construction Materials* [in Russian] (Metallurgiya, Moscow, 1985), p. 68.
[8] E. A. Belenkov and A. I. Sheĭnkman, Izv. Vyssh. Uchebn. Zaved. Fiz. **10**, 67 (1991).
[9] N. Iwashita and M. Inagaki, Carbon **31**, 1107 (1993).
[10] G. S. Zhdanov, *Crystal Physics* (Oliver and Boyd, Edinburgh, 1965; Moscow State University Press, Moscow, 1961).
[11] Ya. S. Umanskiĭ, Yu. A. Skakov, A. N. Ivanov, and L. N. Rastorguev, *Crystallography, X-Ray Diffraction Analysis, and Electron Microscopy* [in Russian] (Metallurgiya, Moscow, 1982).
[12] E. A. Belenkov, V. A. Tyumentsev, and A. A. Fotiev, Neorg. Mater. **31**, 651 (1995).
[13] V. A. Tyumentsev and E. A. Belenkov *et al.*, Zh. Prikl. Khim. **70**, 21 (1997).
[14] V. A. Tyumentsev, S. A. Podkopaev, E. A. Belenkov, and A. A. Fotiev, Zh. Prikl. Khim. **68**, 1398 (1995).

Translated by P. Shelnitz

Copper-oxygen substructures in carbon allotropes (graphite and fullerites)

V. F. Masterov,* A. V. Prikhod'ko, T. R. Stepanova, A. A. Shaklanov, and O. I. Kon'kov

St. Petersburg State Technical University, 195251 St. Petersburg, Russia
(Submitted July 1, 1998)
Fiz. Tverd. Tela (St. Petersburg) **41**, 748–750 (April 1999)

A comparative study of crystalline graphite and copper-doped fullerite membranes is reported. It is assumed that C_{60} clusters form complexes with oxygen and copper similar to those known to exist in graphite. Above room temperature, these complexes, first, change the symmetry of the fullerite lattice and, second, are responsible for the nonmonotonic temperature dependence of the electrical resistance. © *1999 American Institute of Physics.*
[S1063-7834(99)03804-6]

The experimental observation[1] that oxygen desorption results in an increase in resistance of powder samples of graphite and C_{60} fullerite argues for the electrical activity of the molecular oxygen sorbed on the grain surface, which can affect the electron density at grain boundaries and change the conditions of current percolation through surface barriers.

It was assumed that near room temperature graphite- and fullerite-based powder structures would exhibit percolation conduction over an infinite cluster. As the temperature is increased, the bonds coupling molecular oxygen to the grain boundaries start to break until, at the critical temperature T_c, the endless conducting cluster is destroyed, which results in a growth of resistance and a change in the shape of the I–V characteristics. The close values of the temperature percolation thresholds for both allotropic forms of carbon may be due to close binding energies of oxygen molecules to the graphite and fullerite grain boundaries. In fullerites, oxygen is bound to the hexagons of the C_{60} molecule.[2] At the same time such carbon hexagons are the main building blocks forming the graphite planes. Obviously enough, oxygen molecules penetrate into coarse-grained graphite or loose (weakly pressed) fullerite practically throughout the volume of the sample, so that an increase in temperature brings about only desorption of oxygen. This effect manifests itself in a smooth increase of resistance.

Besides intercalated oxygen, other atoms, for instance, copper can exist on the hexagons.[3] In these conditions, two-dimensional CuO layers form between the graphite layers, and fullerenes transform possibly into CuO-coated hyperclusters.[4] This work reports on a comparative study of the conductivity and structure of crystalline graphite intercalated by copper and oxygen, as well as of polycrystalline copper-containing fullerite samples[5].

1. SAMPLES AND TECHNIQUES

We used as samples copper-intercalated highly-oriented pyrolytic graphite (HOPG),[3] as well as copper-containing polycrystalline fullerite (C_{60}/C_{70}):Cu, prepared by modified sublimation[5] of the pristine fullerite powder in a small thermal chamber. Intercalation of HOPG samples with copper was achieved by keeping them for 20 min in 9.99%-pure molten copper at $T=1473$ K in a vacuum not worse than 10^{-3} Torr. Mass spectrometric analysis of the pristine fullerite powder revealed C_{60} (67%), C_{70} (28%), and $C_{76,78,84}$ (2%) (the powder was prepared and certified within the State Program ''Fullerenes and Atomic Clusters''). Copper was added to the starting powder in the 1:1 ratio. Mass spectrometric measurements yielded about 10^{-3}% for the copper content in the graphite and fullerite samples. The sample resistance R was derived from measurements of nanosecond-range incident (U_i) and reflected (U_r) voltage pulses, where heating of the samples during measurements is insignificant.[6] For sufficiently large sample resistances ($R/\rho \geqslant 10^2$, where ρ is the coaxial-line wave impedance), we limited ourselves to a qualitative estimation of the behavior of R by analyzing ns-range transient processes. It was taken into account that the rise time of the pulse reflected from a sample is equivalent to the time constant.[6]

The sample resistance was calculated from $R=\rho(U_i+U_r)/(U_i-U_r)$, where $U=U_i+U_r$ is the voltage across the sample, and $I=(U_i-U_r)/\rho$.

The change in the pulse leading-edge slope was found from the voltage $U_f \sim 1/R$ at a preset point of the leading edge (0.45 ns). The pulse leading edge was 0.5-ns long. The measurements were carried out in a vacuum of 10^{-3} Torr within the temperature interval of 290–400 K.

X-ray characterization of the samples was performed on a Geigerflec instrument with Cu $K\alpha$ radiation.

2. RESULTS AND DISCUSSION

Figure 1 sums up the results of studying of the effect of intercalated oxygen on the resistance of copper-containing samples of crystalline graphite (Fig. 1a) and of fullerite samples (Fig. 1b). The resistance of the starting HOPG samples increases with temperature above 330 K, and the temperature $T_{c0}=360$ K (curve *1* in Fig. 1a) practically coincides with the temperature at which oxygen desorption from powder graphite is completed.[1] At the same time for (HOPG):Cu samples the value $T_{c1}=306$ K coincides with the position of the desorption peak (305–310 K) characteristic of finely-dispersed dense material. We observed also another feature, the appearance of a second desorption tem-

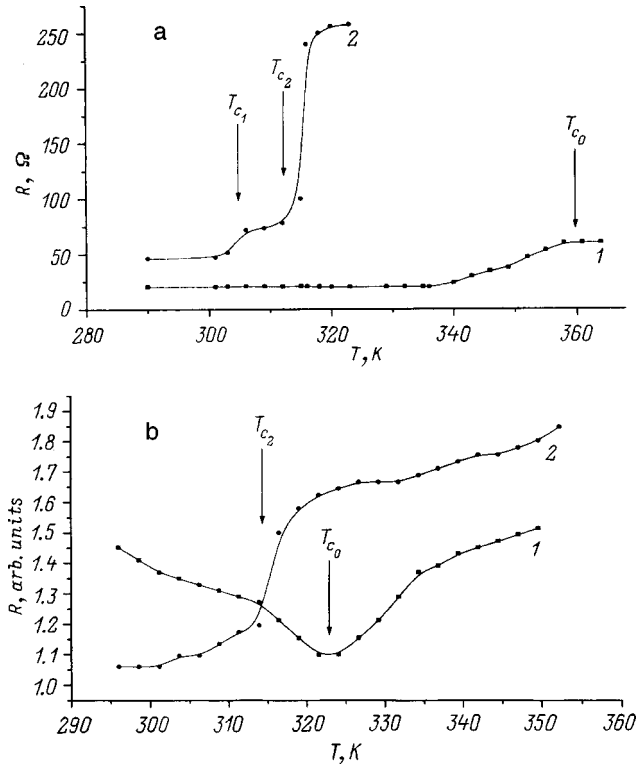

FIG. 1. $R(T)$ dependence for (a) HOPG(Cu) and (b) (C_{60}/C_{70}):Cu samples. Curves *1* relate to the starting samples: (a) HOPG and (b) C_{60}/C_{70}.

perature $T_{c2}=312$ K. Hence desorption proceeds in two stages. The first stage relates to crystalline graphite, and the second, to the copper-containing graphite. Figure 2 shows an $R(U)$ dependence indicating a change in the resistance of HOPG and HOPG(Cu) samples as the critical temperatures T_c are reached. The variation of the I–V curves at T_c is displayed in Fig. 3 in the form of an $I\rho$ vs U plot.

The (C_{60}/C_{70}):Cu samples also exhibit an abrupt change in the slope of the reflected-pulse leading edge (U_f) at about 310 K (curve *2* in Fig. 1b). A comparison of the curves in Fig. 1a and 1b suggests a correlation between the beginning of oxygen desorption in a given sample and that in copper-containing graphite at $T_{c2}=312$ K. In starting samples (C_{60}/C_{70}) one observes an increase in resistance at 320 K,

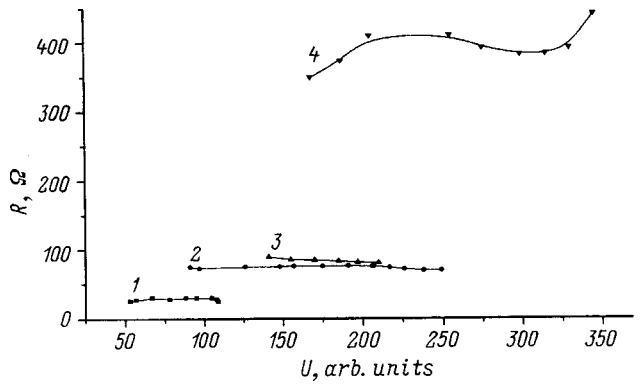

FIG. 2. $R(U)$ dependence for HOPG (*1* — $T_0=297$ K, *2* — $T_{c0}=360$ K) and HOPG(Cu) (*3* — $T_{c1}=306$ K and *4* — $T_{c2}=312$ K).

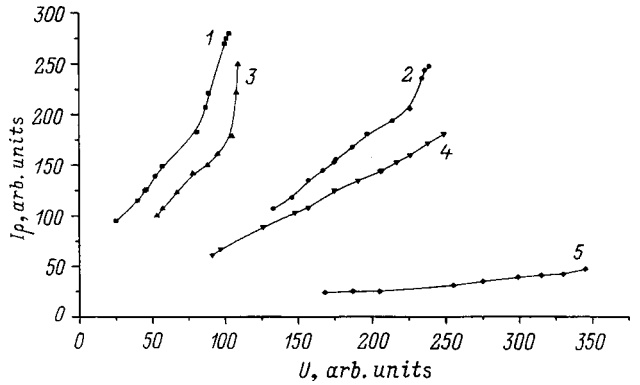

FIG. 3. $I\rho=f(U)$ plot for HOPG (*1* — T_0, *2* — T_c) and HOPG(Cu) (*3* — T_0, *4* — $T_{c1}=306$ K and *5* — $T_{c2}=312$ K).

which we assign to a sharp increase in surface resistance at the frequency of 1 GHz in crystalline graphite.[3]

We carried out a comparative analysis of the x-ray diffraction patterns of the pristine C_{60}/C_{70} and (C_{60}/C_{70}):Cu fullerite samples, as well as of those of HOPG and HOPG(Cu) (Fig. 4). As seen from Fig. 4a, the fullerite samples are polycrystalline without any indication of the presence of an amorphous phase, and the lattice type is in all cases fcc. X-ray diffractograms show the C_{60}/C_{70} lattice to be primarily fcc with $a=14.308$ Å. For (C_{60}/C_{70}):Cu one

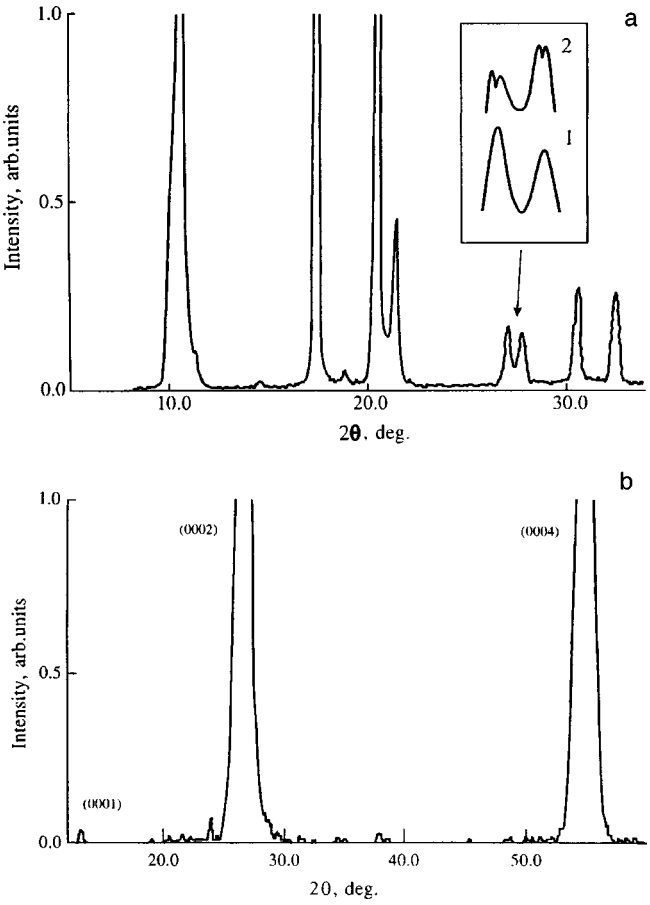

FIG. 4. (a) X-ray diffractogram for C_{60}/C_{70} fullerite samples. The inset shows the change in x-ray reflections at $2\theta=26-29'$ for *1* — C_{60}/C_{70} and *2* — (C_{60}/C_{70}):Cu. (b) X-ray diffractogram for HOPG:Cu samples.

observes a splitting of the x-ray reflections corresponding to a structure with the parameters $a=14.42$ and 14.47 Å (see inset to Fig. 4a). The splitting implies the appearance of tetragonality, i.e. the onset of a transition from fcc to a lower-symmetry structure. The starting HOPG graphite is a $2H$-polytype single crystal with the (0002) and (0004) lines and $d_{0004}=1.681$ Å (the lattice parameter $c=6.725$ Å). The structure of the copper-containing graphite is likewise the $2H$ polytype, but besides the (0002) and (0004) lines one observes also a (0001) line and a narrow reflection at $2\theta=37.5°$ ($d_{1n}=2.371$ Å), which does not belong to any known graphite polytype (Fig. 4b). The lattice parameter of the copper-containing graphite $d_{0004}=1.680$ Å ($c=6.720$ Å). The decrease of the lattice parameter in copper-containing samples is accompanied by a decrease of the coherent-scattering regions in size. This implies strain relaxation in the sample, which is accompanied by diffusion of copper atoms in the crystal. This possibly accounts for the regular pattern of the copper impurity distribution and, accordingly, for the appearance of the (0001) peak. Besides, part of the copper atoms react with oxygen dissolved in graphite to form composite complexes with the graphite lattice atoms. Interaction of these complexes with lattice defects accounts for the substructural reflection with a period of 2.371 Å.

One can thus conjecture that, first, copper and oxygen form composite complexes with the graphite lattice and, second, that C_{60} molecules form complexes with oxygen and copper, which are apparently similar to those existing in graphite. Above room temperature, these complexes change the fullerite lattice symmetry and are also responsible for the desorption features of oxygen trapped in the course of sample preparation. It is known that the carbon hexagonal network may be pictured as an aromatic macromolecule.[7] In this macromolecule, the network edges, or the regions of atomic disorder, form C−OH-type bonds which can attach copper and oxygen atoms. Incorporation of such oxygen complexes into the hexagonal network changes the band structure of the crystal and distorts the electron density on the neighboring carbon atoms, which may account for specific features in the behavior of sample conductivity not only at high but at low temperatures as well.

Support of the ''Fullerenes and Atomic Clusters'' Program (''Gradient'' Project 98063) and of the Russian Fund for Fundamental Research (Grant 96-02-16886a) is gratefully acknowledged.

*Deceased.

[1] V. F. Masterov, A. V. Prikhod'ko, N. I. Nemchuk, A. A. Shaklanov, and O. I. Kon'kov, Fiz. Tverd. Tela (St. Petersburg) **39**, 1703 (1997) [Phys. Solid State **39**, 1522 (1997)].
[2] H. Werner, M. Wohlers, D. Bublak, Th. Belz, W. Bensch, and R. Schlögl, *Electronic Properties of Fullerenes* (Springer Series in Solid-State Sciences, Vol. 117), edited by H. Kuzmany, I. Fink, V. Mehring, and S. Roth (Springer, Berlin, 1993), p. 16.
[3] V. F. Masterov, A. V. Prikhod'ko, O. I. Kon'kov, and A. A. Shaklanov, Fiz. Tverd. Tela (St. Petersburg) **39**, 97 (1997) [Phys. Solid State **39**, 84 (1997)].
[4] M. D. N. Regueiro and M. N. Regueiro, in *Recent Advances in the Chemistry and Physics of Fullerenes and Related Materials*, edited by K. M. Kadish and R. S. Ruoff (Electrochem. Soc., Vol. **92-24**, 1994), p. 647.
[5] V. F. Masterov, A. V. Prikhod'ko, T. R. Stepanova, V. Yu. Davydov, and O. I. Kon'kov, Fiz. Tverd. Tela (St. Petersburg) **40**, 580 (1998) [Phys. Solid State **40**, 535 (1998)].
[6] V. F. Masterov, A. V. Prikhod'ko, O. I. Kon'kov, and E. I. Terukov, Fiz. Tverd. Tela (St. Petersburg) **38**, 1687 (1996) [Phys. Solid State **38**, 931 (1996)].
[7] A. R. Ubbelohde and F. A. Lewis, *Graphite and its Crystal Compounds* (Clarendon Press, Oxford, 1960; Mir, Moscow, 1965, p. 119).

Translated by G. Skrebtsov